Near-infrared imaging spectroscopy and mid-infrared spectroscopy of M 82: revealing the nature of star formation activity in the archetypal starburst galaxy

Dissertation der Fakultät für Physik
der Ludwig-Maximilians-Universität München

vorgelegt von
Natascha M. Schreiber
aus Montréal, Canada

3. November 1998

Gutachter:	Prof. Dr. Reinhard Genzel
	Prof. Dr. Ralf Bender
Tag der mündlichen Prüfung:	14. Mai 1999

Zusammenfassung

Galaxien mit Ausbrüchen verstärkter Sternentstehung im Kernbereich, auch "Starburstgalaxien" genannt, sind eine wichtige Klasse extragalaktischer Objekte. Ein großer Anteil der massereichen Sterne des nahen Universums entsteht in Starburstgalaxien. Starbursts finden sich in einer Vielzahl galaktischer Umgebungen. Untersuchung dieser Galaxien ist wesentlich für das Verstehen sowohl des Sternentstehungsprozesses selbst, als auch der Entwicklung von Galaxien und des intergalaktischen Mediums, und der Geschichte der Sternentstehung im frühen Universum. Es gibt jedoch nur wenig quantitative Informationen über die Eigenschaften der Sternentstehung in einer Starburstumgebung und über die Entwicklung von Starburstaktivität. Genauere Untersuchungen wurden früher durch fehlende räumliche Auflösung und durch Staubextinktion erschwert, die Untersuchungen im optischen und ultravioletten Wellenlängenbereich oft unmöglich macht.

Diese Dissertation stellt die Ergebnisse von Beobachtungen der Starburstgalaxie M 82 im nahen und mittleren Infrarot vor, mit dem Ziel einer detaillerten quantitativen Beschreibung der Starburstaktivität dieses Prototypen der Objektklasse. In diesem Wellenlängenbereich ist Starburstaktivität auffällig und Staubextinktion deutlich weniger störend als im Optischen und Ultravioletten. Die Nähe von M 82 erlaubt Untersuchungen auf räumlichen Skalen die typisch für große Sternentstehungsgebiete und Molekülwolken sind. Die Nahinfrarotbeobachtungen wurden mit dem abbildenden Spektrographen 3D durchgeführt, der gleichzeitig die wesentliche räumliche und spektrale Information gewinnen kann. Die Mittelinfrarotspektroskopie wurde mit dem Short Wavelength Spectrometer (SWS) des Infrared Space Observatory (ISO) gewonnen, das Zugang zum gesamten Spektralbereich $\lambda = 3 - 40$ μm bietet. Zusammen mit der Anwendung von Modellen zur Population- und Entwicklungssynthese dienen diese Daten zur (1) Bestimmung der physikalischen Eigenschaften des interstellaren Mediums innerhalb der Sternentstehungsgebiete, (2) Beschreibung der Populationen heißer, massereicher Sterne und kühler Sterne, (3) Bestimmung der ursprünglichen Massenfunktion (IMF) der Sterne, und (4) Bestimmung von Alters, Dauer und Intensität des Starburst in einzelnen Regionen. Zum Zwecke der Populationssynthese wurde mit

Hilfe von 3D eine Bibliothek von Spektren mittlerer Auflösung von roten Riesen und Überriesen erstellt. Ferner wurden die Entwicklungssynthesemodelle für die Anwendung neuer Untersuchungswerkzeuge aus 3D- und SWS-Beobachtungen optimiert.

Die untersuchten Daten und Modelle zeigen komplexe Starburstaktivität in M 82, die einzelne Sternentstehungsgebiete mit eine Grösse von $\lesssim 25$ pc aufweist. Die typische Dauer einzelner Ausbrüche von einigen Millionen Jahren, und die IMF entsprechen denen von Entstehungsgebieten massereicher Sterne in unserer Galaxie und den Magellanschen Wolken. Insgesamt fand die Starburstaktivität im wesentlichen in zwei aufeinanderfolgenden Episoden statt, die vor 10 und 5 Millionen Jahren abliefen und jeweils einige Millionen Jahre andauerten. Die kurzen Zeitskalen auf allen räumlichen Skalen deuten auf starke negative Rückkoppelung der Starburstaktivität hin. Die erste Sternentstehungsepisode fand in der gesamten Zentralregion von M 82 statt und war in der Umgebung des Kerns der Galaxie besonders stark. Die zweite Episode fand ausserhalb der Kernregion statt, vornehmlich in einem zirkumnuklearen Ring und entlang des stellaren Balkens. Diese Sequenz wird als Ergebnis des Einfalls interstellarer Materie zum Kern interpretiert, ausgelöst zunächst durch gravitative Wechselwirkung zwischen M 82 und dem Nachbarn M 81, und in der Folge durch dynamische Resonanzen und Stoßwellen des interstellaren Mediums aufgrund des durch die Wechselwirkung angeregten stellaren Balkens.

Abstract

Galaxies experiencing vigorous star formation activity in their central regions, or "starburst" galaxies, constitute an important class of extragalactic objects. A substantial fraction of the high-mass star formation in the local Universe takes place in starburst galaxies, and starbursts are found in a wide variety of galactic environments. Studies of these galaxies are crucial for the understanding of the star formation process itself, the evolution of galaxies and of the intergalactic medium, and the star formation history in the early Universe. However, little quantitative information exists on the properties of star formation in starburst environments, and on the evolution of starburst activity. Detailed investigations have been hindered in the past by the lack of spatially resolved data, and by dust obscuration often preventing studies at optical and ultraviolet wavelengths.

This dissertation presents the results of near- and mid-infrared observations of the nearby, archetypal starburst galaxy M 82 aiming at a detailed, quantitative description of its starburst activity. At these wavelengths, starburst activity is conspicuous and dust obscuration is much less important than in the optical and ultraviolet regimes. The proximity of M 82 allows investigations on spatial scales typical of giant star-forming regions and molecular clouds. The near-infrared observations were obtained with the imaging spectrometer 3D, providing simultaneously the essential spatial and spectral information. The mid-infrared observations were obtained with the Short Wavelength Spectrometer (SWS) on board the Infrared Space Observatory, providing access to the complete $\lambda = 3 - 40$ μm spectral region. Together with the application of population and evolutionary synthesis models, the data are used to (1) determine the physical conditions of the interstellar medium within the star-forming regions, (2) characterize the populations of hot massive stars and cool evolved stars, (3) constrain the initial mass function of the stars, and (4) determine the age, timescale and intensity of the starburst in individual regions. For the purpose of population synthesis, a new library of moderate-resolution spectra of red giant and supergiant stars is obtained with 3D. In addition, the evolutionary synthesis models are optimized for applications of new diagnostic tools provided by the 3D and SWS observations.

The data and models reveal complex starburst activity in M 82, with individual starburst sites on scales as small as 25 pc. The typical timescale of a few million years for individual bursts and the initial mass function are similar to those of high-mass star-forming regions in the Milky Way and in the Magellanic Clouds. Globally, starburst activity in M 82 occurred during two successive episodes each lasting a few million years, about 10 and 5 million years ago. The short timescales on all spatial scales indicate strong negative feedback effects of starburst activity. The first starburst episode took place throughout the entire central regions of M 82 and was particularly intense in the nuclear vicinity. The second episode occurred in the extranuclear regions, predominantly in a circumnuclear ring and along a stellar bar. This sequence is interpreted as resulting from the infall of interstellar material towards the nucleus triggered by the gravitational interaction between M 82 and its neighbour M 81, and subsequently from the dynamical resonances and shocks in the interstellar medium due to a stellar bar induced by the interaction.

Contents

List of Tables

List of Figures

Chapter 1

Introduction

1.1 Background

1.1.1 Infrared galaxies

One of the most important discoveries that followed the advent of infrared astronomy in the mid-sixties was that the nuclei of many galaxies are much more luminous in the infrared ($\lambda \approx 1 - 300$ μm) than presumed from observations at other wavelengths (*e.g.* Low & Kleinmann 1968; Kleinmann & Low 1970a,b; Rieke & Low 1972; Rieke & Lebofsky 1978, 1979). The Infrared Astronomical Satellite (*IRAS*), launched in 1983, played a crucial role in this discovery with the detection of tens of thousands of galaxies, the vast majority of which were too faint optically to have been previously catalogued (*e.g.* Sanders & Mirabel 1996). *IRAS* observations led to the identification of the exceptional class of "luminous infrared galaxies", with $L_{8-1000\,\mu\mathrm{m}} > 10^{11}$ $\mathrm{L}_\odot$ (Soifer *et al.* 1987). In these galaxies, the power emitted between $5\,\mu$m and $300\,\mu$m often exceeds that observed in all other spectral ranges combined and represents, in the most extreme cases, almost all the energy radiated. The "ultraluminous galaxies", characterized by $L_{8-1000\,\mu\mathrm{m}} > 10^{12}$ $\mathrm{L}_\odot$, are even more remarkable (Sanders *et al.* 1988). A famous example is the merging system Arp 220, the closest ultraluminous galaxy (76 Mpc), which emits 99% of its $\approx 10^{12}$ $\mathrm{L}_\odot$ luminosity in the infrared (Neugebauer *et al.* 1984; Soifer *et al.* 1984). Although observed in a variety of objects, extreme infrared luminosities seem to be frequently associated with interacting and colliding galaxies. More specifically, the fraction of strongly interacting and merger systems increases from about 10% at $L_{8-1000\,\mu\mathrm{m}} = 10^{10.5} - 10^{11}$ $\mathrm{L}_\odot$, to nearly 100% at $L_{8-1000\,\mu\mathrm{m}} > 10^{12}$ $\mathrm{L}_\odot$ (Sanders & Mirabel 1996, and references therein).

The large infrared luminosity of these galaxies is generally attributed to thermal radiation from dust heated by an energetic source in the nuclear regions. Three hypotheses have been proposed concerning the nature of this source. First, by analogy with star-forming regions and complexes of molecular clouds in our Galaxy, the ultraviolet flux from an exceptionally large population of young, massive stars was very early suspected to heat the interstellar material at the center of infrared galaxies (*e.g.* Harwit & Pacini 1975; Rieke & Lebofsky 1978; Telesco & Harper 1980). This scenario has been widely invoked since and is fully justified in the well-studied examples of M 82 and NGC 253 (*e.g.* Rieke *et al.* 1980, 1993; Engelbracht *et al.* 1998).

Alternatively, active galactic nuclei ("AGN"), where the tremendous energy release likely has a non-stellar origin — presumably from an accretion disk surrounding a black hole — can also provide the energy for the dust heating. In this case, the infrared excess results from the superposition of the thermal spectrum of the dust and the non-thermal spectrum of the AGN itself, in proportions determined by the physical conditions within the host galaxy (*e.g.* Stein & Weedman 1976; Rieke 1978; Carral, Turner & Ho 1990; Condon *et al.* 1991).

Finally, a third energetic process has been proposed that could explain simultaneously the large fraction of interacting and merging systems among luminous infrared galaxies. High velocity shocks between molecular clouds ($v_{\rm shock} \sim 500$ km s^{-1}) in colliding galaxies will produce copious ultraviolet radiation absorbed by the dusty medium and subsequently reemitted at infrared wavelengths (Harwit *et al.* 1987).

The attribution of the infrared luminosity to one or the other mechanism is in many cases controversial. The main difficulty arises from their possible coexistence which, combined with the distance to the object, hampers the determination of their relative spatial distributions and of their respective contributions to the global luminosity. The long-standing debates in the cases of the merging system NGC 6240, of the Seyfert galaxy NGC 1068, or of the ultraluminous infrared galaxies illustrate very well such ambiguities (*e.g.* van der Werf *et al.* 1993; Cameron *et al.* 1993; Sanders *et al.* 1988). Very recently, progress in ground-based instrumentation and observational techniques, as well as the first results emerging from the recent Infrared Space Observatory (*ISO*) mission have raised new hopes for disentangling the energy sources of infrared galaxies. Unprecedented high angular resolution observations (*e.g.* Thatte *et al.* 1997; Smith *et al.* 1998) and the application of new mid-infrared spectroscopic diagnostic tools (*e.g.* Genzel *et al.* 1998) have been particularly useful in determining the main energy mechanisms in infrared luminous galaxies.

1.1.2 The starburst phenomenon

The exceptional amount of energy required for the production of the infrared luminosity observed in the nuclear regions of many galaxies implies high star formation rates. If such rates are maintained, the present gas reservoir in these galaxies will be exhausted in much less than a Hubble time (typically $\sim 10^8$ years; *e.g.* Thronson & Telesco 1986). Consequently, such events must be occurring over relatively short periods of time, and are referred to by the evocative name of "starburst".

Regardless of whether an AGN or radiative shocks coexist with the intense star formation activity, the study of starburst galaxies is of immense interest. A fundamental motivation is the investigation of the star formation process itself which remains, despite extensive studies, not fully understood yet. The wide range of physical conditions and star formation rates in starburst galaxies make them unique laboratories to investigate star formation in a variety of environments. The study of starburst galaxies is also a key element in the understanding of the evolution of galaxies and of the intergalactic medium. Enhanced star formation profoundly affects the dynamics, the contents and the chemical composition of galaxies in two ways: the interstellar gas is consumed and transformed, and young stars and their progeny pump energy back in the interstellar medium (ISM), thereby generating turbulence, more star formation or its inhibition, even expulsion of matter out of the galaxy. Another motivation, which is of cosmological interest, is the important role of nearby starbursts as templates for the characterization of the star formation history and galaxy evolution in the early Universe.

Various causes have been proposed for the origin of starbursts. Interactions and collisions between galaxies favour enhanced star formation activity, as first demonstrated by the models of Larson & Tinsley (1978). In their classical paper, these authors found that the abnormal colours of morphologically peculiar galaxies could be understood as the result of short bursts of star formation induced by galaxy-galaxy interactions. Numerical simulations of galaxy encounters provide support for this interpretation by showing that the interstellar matter, more dissipative than the stellar component, experiences strong large-scale torques and loses its angular momentum rapidly. As a consequence, it falls towards the center of the gravitational potential where it accumulates, eventually resulting in powerful star formation activity (*e.g.* Sundelius *et al.* 1987; Noguchi 1988; Barnes & Hernquist 1996; Mihos & Hernquist 1996). Observations indicate a high incidence of starburst activity among mergers and interacting systems, as well as massive pools of molecular gas providing the fuel for intense star formation events in their central regions (*e.g.* Condon *et al.* 1982; Solomon & Sage 1988; Joseph 1990).

Bars in galactic disks can also trigger starbursts. Both numerical simulations and observations reveal that such non-axisymmetric features induce large-scale flows that drive the gas towards the central regions of the galaxy (*e.g.* Combes & Gérin 1985; Noguchi 1988; Ball 1986; Ondrechen & van der Hulst 1989; Jörsäter & van Moorsel 1995). Various observational studies indicate that barred galaxies are more likely to experience enhanced star formation activity (*e.g.* Hawarden *et al.* 1986; Telesco, Dressel & Wolstencroft 1993; Martinet & Friedli 1997). Telesco & Decher (1988) and Telesco *et al.* (1991) described in more detail how the starbursts in NGC 1068 and M 82 could have resulted from the presence of a bar. Bars may themselves be induced by the proximity of a companion galaxy (*e.g.* Noguchi 1987; Barnes & Hernquist 1991).

Several scenarios relating starbursts to the AGN phenomenon have also been proposed. Amongst others, an AGN could be created from the remnant of a starburst (Weedman 1983). Conversely, star formation could be triggered by the shocks and compression of the interstellar matter induced by the gas flow originating from the active nucleus (Scoville & Norman 1988; Norman & Scoville 1988). Alternatively, co-existing starbursts and AGNs may be indirectly related through a bar responsible for the fueling of both (*e.g.* Telesco & Decher 1988; Heller & Shlosman 1996; Colina *et al.* 1997).

To discriminate between the different possibilities responsible for starburst activity in galaxies, detailed spatial and kinematical studies as well as more elaborated theoretical models are necessary. Although general scenarios may be viable, the diversity of environments in which starbursts occur and the possible relationships between the proposed triggering mechanisms suggest that this triggering depends most probably on the history and physical conditions particular to the host galaxy.

1.2 General properties of starburst galaxies

It is obvious, therefore, that starbursts are found in a variety of objects, including the spectacular infrared-luminous mergers, interacting systems, Seyfert galaxies, barred, spiral and irregular galaxies, and blue compact dwarf galaxies. Enhanced star formation may account for as much as $60\% - 80\%$ of the far-infrared luminosity in the local Universe (Soifer *et al.* 1987). Four starburst galaxies, including M 82 and NGC 253, are responsible for as much as 25% of the high-mass star formation within 10 Mpc of the Milky Way (Heckman 1998). The physical sizes of starburst regions range from $\sim 0.1 - 1$ kpc in nuclear starbursts (as in M 82) or extranuclear starbursts (for example, the giant H II region NGC 604 in M 33), to several kiloparsecs in global bursts that can cover the entire face of a system (as in the colliding pair NGC 4038/4039 or in the Magellanic irregular NGC 4449). Global star formation rates vary from a few $M_\odot\,yr^{-1}$ for the modest starbursts to several thousands of $M_\odot\,yr^{-1}$ for the most powerful ones (*e.g.* Telesco 1988). For comparison, about 3 $M_\odot\,yr^{-1}$ of gas are presently converted into stars throughout the entire Milky Way. The key element which makes even the modest starbursts so outstanding is the much larger star formation rate *per unit volume* compared to more quiescent systems such as our Galaxy.

In addition to a large infrared luminosity, starburst activity exhibits many observational signatures at all wavelengths. Some of the most salient features are:

- strong hydrogen and helium recombination lines from the visible to the millimetric ranges, due to an important population of young massive stars (see the review by Telesco 1988),
- a correlation between the global infrared flux and the radio non-thermal continuum flux, reflecting the coexistence of young stars embedded in dust and supernova remnants where accelerated electrons produce synchrotron radiation (Telesco 1988; Kronberg, Biermann & Schwab 1985; Helou, Soifer & Rowan-Robinson 1985),
- deep absorption bands from the CO molecule longwards of $2.3\,\mu$m due to the presence of an important population of red supergiants, the descendants of young massive OB stars (Walker, Lebofsky & Rieke 1988; Doyon 1991; Goldader *et al.* 1995; Ridgway, Wynn-Williams & Becklin 1994),
- very bright ^{12}CO $J = 1 \rightarrow 0$ emission, implying a massive concentration of molecular gas (Sanders & Mirabel 1985; Young & Scoville 1991).

Starburst activity is particularly conspicuous in the near- and mid-infrared regimes ($\lambda = 1 - 2.5$ μm and $\lambda = 3 - 40$ μm respectively). In addition, starburst regions are very often hidden at short wavelengths by large amounts of dust, but become accessible in the near- and mid-infrared; indeed, obscuration effects by interstellar dust are $\approx 10-100$ times less important at near- and mid-infrared wavelengths than at optical wavelengths. The main characteristics of starburst galaxies in the range $\lambda = 1 - 40\ \mu$m are briefly reviewed in the following subsections.

1.2.1 Near-infrared properties

Much of the knowledge of starburst galaxies in the near-infrared has emerged from spectroscopic studies. The important features are described in the next paragraphs.

- **Atomic hydrogen and helium lines**

Hydrogen recombination lines of the Brackett and Paschen series, in particular Brγ ($n = 7 \rightarrow 4$ at $\lambda = 2.166\ \mu$m), are amongst the strongest emission lines observed in nearby starburst galaxies (Moorwood & Oliva 1988; Ho, Beck & Turner 1990; Kawara, Nishida & Phillips 1989). Helium recombination lines, notably the He I $2^1S - 2^1P$ transition at $\lambda = 2.058\ \mu$m, are also detected in these galaxies (*e.g.* Doyon, Puxley & Joseph 1992; Doherty *et al.* 1995; Vanzi & Rieke 1997). This is not surprising since, in the Milky Way, these lines arise mainly in photoionized regions where intense ultraviolet flux is produced by new-born, hot stars. Their detection in extragalactic objects thus allows the identification of H II regions and the determination of their physical properties such as the mass and luminosity of the ionizing stars, and the interstellar extinction (*e.g.* Lester *et al.* 1990; Satyapal *et al.* 1995; Engelbracht *et al.* 1998).

- **Molecular hydrogen lines**

The discovery of electric quadrupole emission from warm H_2 ($T \sim 1000 - 2000$ K) as a common characteristic of starburst galaxies is one of the key results of near-infrared spectroscopy (*e.g.* Thompson, Lebofsky & Rieke 1978; Fischer *et al.* 1983; Rieke *et al.* 1985; Moorwood & Oliva 1988; Joseph 1989; Kawara, Nishida & Gregory 1987). The strongest line observed is typically the $v = 1-0\,S(1)$ rotational-vibrational transition at $2.122\,\mu$m. In astronomical sources, the H_2 can be excited in two ways: *1)* by absorption of soft ultraviolet photons in the Lyman and Werner electronic bands ($\lambda = 912 - 1108$ Å) followed by fluorescence down to the excited rotational-vibrational levels of the ground electronic state, and subsequent radiative decay, or *2)* by collisional excitation with UV-, X-ray- or shock-heated gas (Shull & Beckwith 1982; Black & van Dishoeck 1987).

In our Galaxy thermal emission from H_2 is observed in various sources including outflows associated with protostars, Herbig-Haro objects, photodissociation regions, planetary nebulae and supernova remnants (*e.g.* Gautier *et al.* 1976; Treffers *et al.* 1976; Elias 1980; Graham, Wright & Longmore 1987; Tanaka *et al.* 1989). Ultraviolet fluorescence, rarer, is also seen in photodissociation regions, and in reflection nebulae (*e.g.* Hayashi *et al.* 1985; Sellgren 1986; Gatley *et al.* 1987; Tanaka *et al.* 1989).

Near-infrared H_2 emission has now been detected in more than 50 extragalactic objects of various types such as interacting and merging systems (*e.g.* Fischer *et al.* 1983; Joseph, Wright & Wade 1984), Seyfert galaxies (*e.g.* Thompson, Lebofsky & Rieke 1978; Kawara, Nishida & Gregory 1987), and bright spiral galaxies (Puxley, Hawarden & Mountain 1988). However, the excitation mechanism remains unclear in most cases. The interpretation of the H_2 emission spectrum is difficult because the line ratios are sensitive to the local physical conditions such as the gas density (Sternberg & Dalgarno 1989) or the shock type and velocity (Hollenbach & McKee 1989). In addition, different sources may excite the H_2, and the emission process (thermal or non-thermal) may not be unique (*e.g.* Doyon, Wright & Joseph 1994; Mouri 1994).

- **[Fe II] lines**

The detection of [Fe II] multiplets in starburst galaxies is another key result of near-infrared spectroscopy (Rieke *et al.* 1980; Joseph *et al.* 1987; Moorwood & Oliva 1988; Kawara, Nishida & Taniguchi 1988). The strongest lines observed correspond to the magnetic dipole transition $a^6D_{9/2} - a^4D_{7/2}$ at $1.257\,\mu$m and the electric quadrupole transition $a^4F_{9/2} - a^4D_{7/2}$ at $1.644\,\mu$m. The [Fe II] lines originate from energy levels excited by the absorption of photons from very hot sources or from interstellar radiative shocks.

The most intense [Fe II] sources in the Milky Way are found in supernova remnants. Supernova shock fronts at $30-60$ km s^{-1} destroy the dust grains, which contain a large fraction of the iron in the ISM, and singly-ionize the liberated iron atoms (Graham, Wright & Longmore 1987; Graham *et al.* 1986; Oliva, Moorwood & Danziger 1989). In photoionization regions such as the Orion nebula, the energetic flux from young, massive stars leads to higher ionization states, thereby inhibiting multiplet [Fe II] emission (*e.g.* Graham, Wright & Longmore 1987). In the Orion nebula, for example, a flux ratio [Fe II]/Brγ of 0.06 is inferred (Lowe, Moorhead & Wehlau 1979) whereas it is as high as 20 to 70 in supernova remnants (*e.g.* Shull & Draine 1987).

In starburst galaxies, where the global [Fe II]/Brγ ratio is close to unity, near-infrared [Fe II] emission is generally attributed to supernova remnants (*e.g.* Moorwood & Oliva 1988; Mouri, Kawara & Taniguchi 1993), for which a high production rate is predicted by theoretical models (*e.g.* Rieke *et al.* 1980), while the hydrogen lines originate in H II regions. Alternatively, [Fe II] emission could originate in large-scale shocks due to a starburst wind, itself generated by high rates of supernova explosions (Kawara, Nishida & Taniguchi 1988; Mouri *et al.* 1990).

• **Stellar absorption features**

The near-infrared continuum spectra of starburst galaxies are generally dominated by photospheric emission from red giants and supergiants, and exhibit a wealth of absorption features produced by various atoms and molecules in the atmospheres of these stars. The strongest features are the first overtone CO bandheads between $2.3\,\mu$m and $2.7\,\mu$m (*e.g.* Walker, Lebofsky & Rieke 1988; Goldader *et al.* 1995; Oliva *et al.* 1995). These bandheads are stronger in cooler and more luminous stars (*e.g.* Kleinmann & Hall 1986). The first overtone CO features in starburst galaxies are often deeper than in elliptical galaxies and bulges of spiral galaxies. This is a natural consequence of the intense star formation activity, since the large number of young, massive stars formed evolve into an important population of red supergiants after $10 - 20$ million years.

1.2.2 Mid-infrared properties

The mid-infrared regime has remained until recently relatively unexplored. Despite important progress in instrumentation development in the past decade, the very low transmission of the Earth's atmosphere over most of the $\lambda = 3 - 40\ \mu$m range as well as the thermal emission from the telescope and instruments still make ground-based observations extremely difficult. Most observations at these wavelengths have been carried out from air-borne and balloon-borne observatories such as the Kuiper Airborne Observatory, or from satellites such as *IRAS*.

The *ISO* satellite, launched in November 1995, has provided a unique access to the infrared regime (Kessler *et al.* 1996). Compared to *IRAS* with its four broad bandpass filters at $12\,\mu$m, $25\,\mu$m, $60\,\mu$m and $100\,\mu$m, the four instruments on board *ISO* have offered a wider wavelength coverage (2.5 times wider), better spatial resolution (down to a few seconds of arc in the mid-infrared, a factor of 60 improvement), greater sensitivity (by a factor of 10 at long wavelengths and 1000 at short wavelengths), more sophisticated instrumentation especially for spectroscopy, and a longer lifetime. *ISO* has contributed significantly to increase the knowledge in many areas of astronomy. Several of the contributions to the knowledge of starburst galaxies are described here.

- **Atomic hydrogen lines**

The brightest hydrogen recombination line from the Brackett series, namely Brα ($n = 5 \rightarrow 4$) at $4.051\,\mu$m, has long been observed in starburst galaxies (*e.g.* Willner *et al.* 1977; Kawara, Nishida & Phillips 1989; Ho, Beck & Turner 1990). Additional lines, including Brβ and several transitions from the Pfund ($n \rightarrow 5$) and Humphreys ($n \rightarrow 6$) series, have now become available through *ISO* observations.

- **Molecular hydrogen lines**

Pure rotational transitions of H_2 in the mid-infrared can be shock- or photo-excited in a similar way as the near-infrared rotational-vibrational lines, but at lower temperatures down to ~ 100 K. These quadrupole emission lines have been previously observed in the Orion Bar and Orion Molecular Cloud (*e.g.* Beck, Lacy & Geballe 1979; Knacke & Young 1980, 1981; Beckwith *et al.* 1983; Brand *et al.* 1988; Parmar, Lacy & Achtermann 1991, 1994). The first detections in various extragalactic sources including starburst galaxies have been obtained with *ISO* (*e.g.* Rigopoulou *et al.* 1996; Moorwood *et al.* 1996; Valentijn *et al.* 1996). The strongest lines are typically the $v = 0 - 0$ $S(5)$, $S(2)$ and $S(1)$ transitions at $6.91\,\mu$m, $12.28\,\mu$m and $17.03\,\mu$m.

- **Fine-structure atomic lines**

Fine-structure emission lines of most abundant atoms (such as Ne, Ar, S and Si) in different low-ionization stages and originating in star-forming regions are commonly observed in starburst galaxies (*e.g.* Gillett *et al.* 1975; Willner *et al.* 1977; Rigopoulou *et al.* 1996; Sturm *et al.* 1996; Kunze *et al.* 1996). The most prominent ones are typically the [Ne II] line at $12.8\,\mu$m, the [S III] line at $33.5\,\mu$m and the [Ar II] line at $6.99\,\mu$m. *ISO* has provided access to numerous additional fine-structure lines, many of which constitute useful diagnostics for electron densities and chemical abundances in H II regions as well as for the temperature of the ionizing stars (*e.g.* Rubin 1985).

• **Dust continuum**

Thermal emission in the mid-infrared from dust grains heated by newly-born stars produces the characteristic featureless continuum steeply rising towards long wavelengths in starburst galaxies. More specifically, very small grains (VSGs) mixed with the photoionized gas are heated by resonantly scattered Lyα photons and, possibly, Lyman continuum photons ($\lambda < 912$ Å) to a few hundred Kelvin and are responsible for the thermal continuum at $\lambda \lesssim 30$ μm. The rising continuum at $\lambda \gtrsim 30$ μm is due to the increasing contribution from cooler, larger dust grains mixed with the neutral gas further away from the heating sources (*e.g.* Telesco 1988 and references therein).

• **Dust emission and absorption features**

Several narrow emission bands are superposed on the thermal continuum of starbursts at 3.3 μm, 6.2 μm, 7.7 μm, 8.6 μm, 11.3 μm and 12.7 μm (the latter discovered with *ISO*). They are generally attributed to polycyclic aromatic hydrocarbon molecules (PAHs) or other carbon-hydrogen rich compounds, transiently heated by the absorption of single ultraviolet photons (*e.g.* Léger & Puget 1984; Allamandola, Tielens & Barker 1985). Alternatively, the carriers of these bands may be closely associated, or identified with, the VSGs (*e.g.* Puget, Léger & Boulanger 1985). Because of their uncertain origin, these features are also referred to as unidentified infrared bands (UIBs).

The PAH features are observed in interstellar Galactic and extragalactic regions exposed to far-ultraviolet radiation such as star-forming complexes, planetary and reflection nebulae, starburst and infrared-luminous galaxies (Cohen *et al.* 1986; Cohen *et al.* 1989; Léger & Puget 1984; Normand *et al.* 1995; Moorwood 1986; Désert & Dennefeld 1988). Despite their stability, PAHs may be destroyed if the ultraviolet radiation field is too strong (*e.g.* Roche & Aitken 1985; Boulanger *et al.* 1988; Helou 1986). Their detection throughout the entire Galactic plane (Giard *et al.* 1989), and in all types of galaxies, including normal ellipticals (Vigroux 1997), has revealed the ubiquity of the interstellar component associated with the PAHs and suggests that, contrary to theoretical predictions, they may also be excited by visible photons alone.

A broad absorption feature centered at 9.7 μm spans the $\lambda = 8 - 14$ μm spectrum of starburst galaxies and other types of extragalactic objects (*e.g.* Gillett *et al.* 1975; Jones & Rodriguez-Espinosa 1984; Rieke & Low 1975b; Frogel, Elias & Phillips 1982; Lebosky & Rieke 1979). This feature is attributed to absorption by cool silicate grains. It has been used, in the early days of infrared astronomy, to support the idea that dust does emit infrared radiation in galaxies (Gillett *et al.* 1975; Rieke & Low 1975a), and to estimate the amount of dust extinction (*e.g.* Gillett *et al.* 1975; Rieke 1974).

1.3 The archetypal starburst galaxy M 82

Despite the fact that starburst galaxies have attracted considerable attention in the past two decades, relatively little *quantitative* information about the processes involved or about the physics of the bursts themselves is available. The main limiting factors have been: *1)* the large amounts of obscuring dust towards the star-forming regions hampering detailed investigations at optical and ultraviolet wavelengths, and *2)* the lack of information on scales small enough to resolve individual star-forming regions and complexes, in particular in the infrared due to instrumental limitations. So far, only nearby or relatively bright objects have been the subject of detailed investigations; for instance, NGC 253 (Engelbracht *et al.* 1998), NGC 6240 (van der Werf *et al.* 1993), NGC 1068 (Blietz *et al.* 1994), NGC 6946 (Engelbracht *et al.* 1996), II Zw 40 (Vanzi *et al.* 1996), and IC 342 (Böker, Förster Schreiber & Genzel 1997). By virtue of its proximity and brightness, the famous galaxy M 82 is one of the best-studied starburst system.

1.3.1 General characteristics of M 82

M 82 (NGC 3034, Arp 337), classified as an irregular galaxy at visible wavelengths, is located 3.3 Mpc away (Freedman & Madore 1988) in the M 81 – M 82 – NGC 3077 group (figure 1.1). It is viewed nearly edge-on, with an inclination angle of about 80°. The global kinematics and mass distribution in M 82 are very peculiar. The rotation curve in the inner 500 pc mimics that for central bulges of spiral galaxies and reveals a comparably high concentration of mass, but declines in the outer parts indicating that extended disk mass is missing (*e.g.* Sofue 1998). Both these characteristics are very different from those of dwarf galaxies with similar total masses (*e.g.* Persic *et al.* 1996). About 30% – 40% of the dynamical mass is contained in molecular gas, a fraction unusually high for normal late-type spiral galaxies and more typical for irregular galaxies (*e.g.* Young & Scoville 1984). These peculiarities together with various other kinematical and morphological properties have been ascribed to tidal disruption or truncation of the disk of M 82 by its massive companion M 81 at a projected distance of 36 kpc (*e.g.* Gottesman & Weliachew 1977; Solinger, Morrison & Markert 1977; Yun, Ho & Lo 1993; Sofue 1998) or, alternatively, to accretion of gas either formerly stripped from M 82 or associated with the M 81 group (*e.g.* O'Connell & Mangano 1978; Young & Scoville 1984).

Because of its disturbed optical morphology as well as its high luminosity at all wavelengths, especially in the infrared with $L_{5-300\,\mu\mathrm{m}} = 3 \times 10^{10}$ L$_\odot$ representing 84%

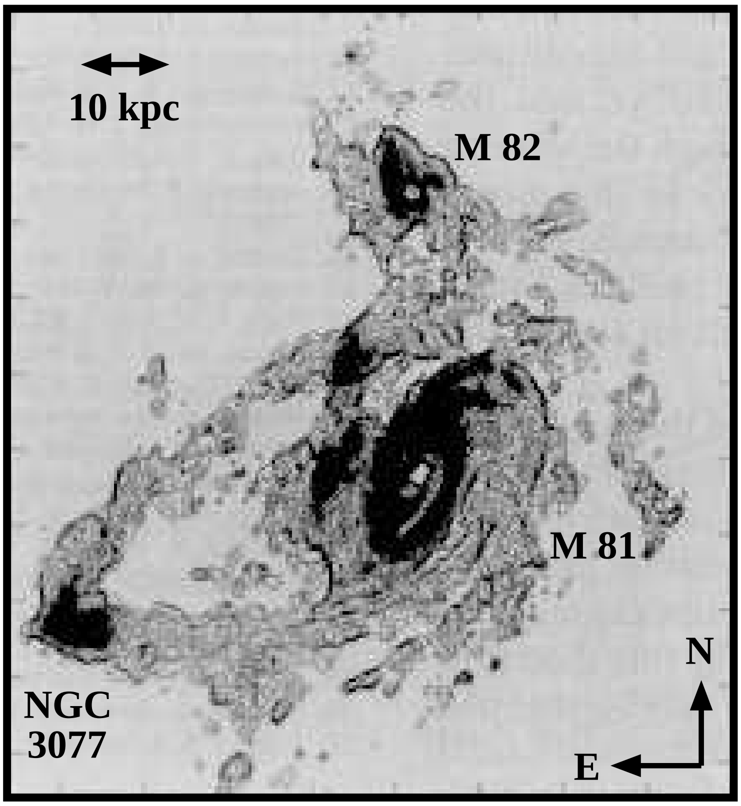

Fig. 1.1.— Integrated H I map of the M 81 – M 82 – NGC 3077 group, obtained by Yun, Ho & Lo (1994). The tidal bridges of material demonstrate the gravitational interaction between the three galaxies.

of its total luminosity (Telesco 1988; see also figure 1.2), M 82 was first suspected to be an exploding galaxy or to host an active nucleus (Lynds & Sandage 1963; Burbidge, Burbidge & Rubin 1964; Schmidt, Angel & Cromwell 1976). Solinger, Morrison & Markert (1977) first proposed the starburst scenario to explain its apparent activity. This hypothesis was supported by the optical spectroscopy of O'Connell & Mangano (1978) and the infrared photometry of Telesco & Harper (1980), and led to the first detailed "starburst models" of Rieke *et al.* (1980). The discovery of a series of time-variable, compact young radio supernova remnants along the galactic plane of M 82 confirmed one of the main predictions of the young starburst theory (Kronberg, Biermann & Schwab 1985; Muxlow *et al.* 1994).

In the past decade, a number of studies have been devoted to M 82 aiming specifically at a better of understanding of its starburst activity (*e.g.* Lester *et al.* 1990; McLeod *et al.* 1993; Rieke *et al.* 1993; Yun, Ho & Lo 1993; Larkin *et al.* 1994; Satyapal *et al.* 1995, 1997). M 82 presents particular advantages that motivated this consider-

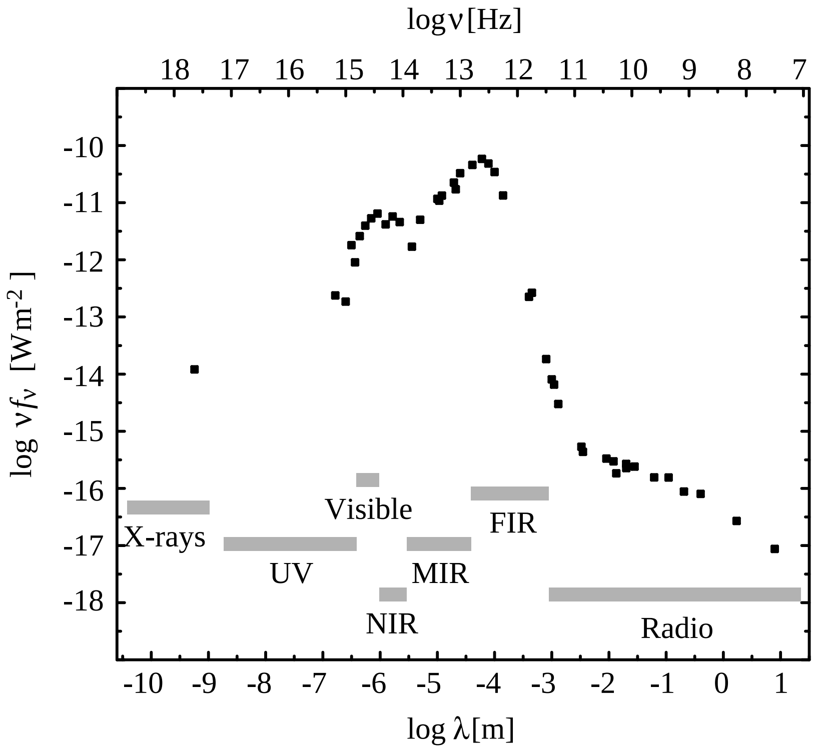

Fig. 1.2.— X-ray to radio continuum energy distribution of M 82. The infrared peak corresponds to dust temperatures of 40 – 50 K. The radio spectrum is dominated by non-thermal synchroton emission from electrons accelerated in supernova remnants. The data are from Fabbiano, Kim & Trinchieri (1992), Rifatto, Longo & Capaccioli (1995), Johnson (1966), Aaronson (1977), Rieke & Low (1972), Dietz *et al.* (1989), *IRAS* Point Source Catalogue, Telesco & Harper (1980), Jaffe, Becklin & Hildebrand (1984), Smith *et al.* (1990), Hughes, Gear & Robson (1990), Elias *et al.* (1978), Thronson *et al.* (1989), Carlstrom & Kronberg (1991), Seaquist, Bell & Bignell (1985) and Klein, Wielebinski & Morsi (1988).

able interest and its promotion as archetype of the class of starburst galaxies. First, its proximity allows detailed studies on scales typical of H II regions, molecular clouds or complexes of such systems; at the distance of M 82, $1'' \approx 15$ pc. In addition, the intense activity it exhibits seems representative of starbursts occurring in other galaxies (Rieke & Lebofsky 1979). Finally, the luminosity associated with the starburst appears to dominate that of the host galaxy (Rieke *et al.* 1980; 1993). The contribution of the host galaxy to the global luminosity can thus be neglected and M 82 can be approached almost as a pure starburst. The qualitative picture of M 82 that has progressively emerged from the wealth of observations is summarized below, and is illustrated in figures 1.3 and 1.4.

1.3.2 The global picture of starburst activity in M 82

Most of the infrared luminosity of M 82 originates from the inner 500 pc and is attributed to thermal radiation of dust heated by an exceptionally large population of massive young stars (see Telesco 1988 and references therein). Near-infrared imaging has shown the evolved stellar population to be distributed in a narrow disk (*e.g.* Rieke *et al.* 1980; Dietz *et al.* 1986; McLeod *et al.* 1993). The peak of the K-band ($2.2\,\mu$m) continuum emission at α_{1950}: $09^{\rm h}51^{\rm m}43\overset{\rm s}{.}53$, δ_{1950}: $+69°55'00\overset{''}{.}7$ (Dietz *et al.* 1986) coincides with the kinematic center (*e.g.* Weliachew, Fomalont & Greisen 1984; Beck *et al.* 1978; Achtermann & Lacy 1995) and is therefore associated with the nucleus of M 82. The $2.2\,\mu$m light distribution provides the strongest evidence for a ~ 1 kpc long stellar bar (Telesco *et al.* 1991; Larkin *et al.* 1994), also hinted at by the morphology and kinematics of the millimetric CO and [Ne II] $12.8\,\mu$m emission (*e.g.* Lo *et al.* 1987; Achtermann & Lacy 1995). Observations of the molecular and neutral gas, including CO, HCN, CS, OH and H I, reveal the existence of a rotating molecular ring or tightly wound spiral arms and of an inner spiral arm at radii of approximately 400 pc and 125 pc respectively (Weliachew, Fomalont & Greisen 1984; Nakai *et al.* 1987; Lo *et al.* 1987; Carlstrom 1988; Loiseau *et al.* 1990; Shen & Lo 1995).

Tracers of H II regions, such as the near-infrared hydrogen recombination lines, the $12.8\,\mu$m [Ne II] line, the mid- and far-infrared continuum emission, and the non-thermal radio emission indicate that the active star formation is taking place in the region enclosed by the molecular ring (Joy, Lester & Harvey 1987; Lester *et al.* 1990; Carlstrom & Kronberg 1991; Telesco *et al.* 1991; Waller, Gurwell & Tamura 1992; Telesco & Gezari 1992; Larkin *et al.* 1994; Satyapal *et al.* 1995; Achtermann & Lacy 1995). The most intense star-forming sites may themselves be concentrated in a smaller rotating ring of diameter ≈ 200 pc and outside this ring, along ridges roughly coinciding with dust accumulations on the leading side of the stellar bar (Telesco *et al.* 1991; Waller, Gurwell & Tamura 1992; Larkin *et al.* 1994; Achtermann & Lacy 1995).

A large-scale bipolar outflow, presumably a superwind resulting from the abnormally high rate of supernova explosions, has been inferred from observations of the diffuse soft X-ray emission (Watson, Stanger & Griffiths 1984; Schaaf *et al.* 1989; Bregman, Schulman & Tomisaka 1995), of the extended radio synchrotron emission (Seaquist & Odegard 1991), and of the emission lines from ionized gas in the ultraviolet and visible (*e.g.* Lynds & Sandage 1963; McCarthy, Heckman & van Breugel 1987; Shopbell & Bland-Hawthorn 1998). Part of the ultraviolet and optical light detected at high latitudes may also be reflection and scattering of radiation escaping along the minor axis of the galaxy (*e.g.* McCarthy, Heckman & van Breugel 1987; Shopbell & Bland-Hawthorn 1998). On smaller scales, the kinematics of the ionized and molecular

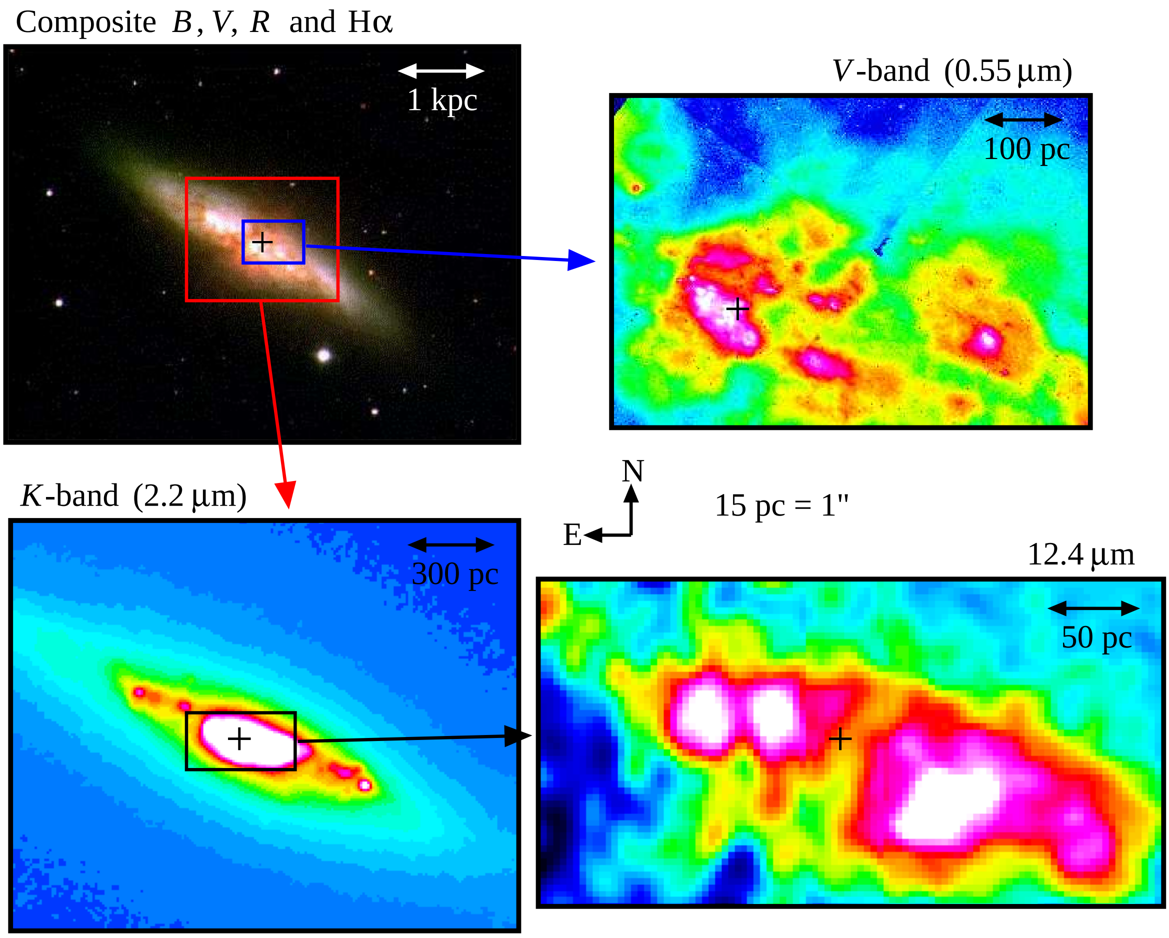

Fig. 1.3.— Optical and infrared images of M 82. The composite image, made up with broad-band B (4400 Å), V (5500 Å), R (7000 Å) and Hα line emission (6563 Å) maps (Kohle & Credner 1995, top left), illustrates the irregular morphology of M 82 at optical wavelengths characterized by prominent knots and complexes superposed on an extended region of more diffuse emission, and strong dust lanes. High spatial resolution imaging in the V-band with the Hubble Space Telescope (O'Connell *et al.* 1995, top right) has resolved the emission knots in over 100 luminous super star clusters typically 3.5 pc in size. The dramatic effects of high and patchy extinction are obvious from the comparison of optical images with the K-band map (Förster 1995, bottom left). The 2.2 μm light distribution, dominated by the cool evolved stars, reveals a conspicuous "inner" disk around the nucleus (marked by a cross in all images), a kiloparsec long bar, several compact clusters along the plane of the galaxy and a smooth envelope at larger radii. The thermal dust emission at 12.4 μm (Telesco & Gezari 1992, bottom right) exhibits the global double-lobe morphology typical of the molecular and ionized gas distributions as well as of the millimetric thermal free-free emission, which breaks up into sub-structures on scales as small as a few tens of parsecs.

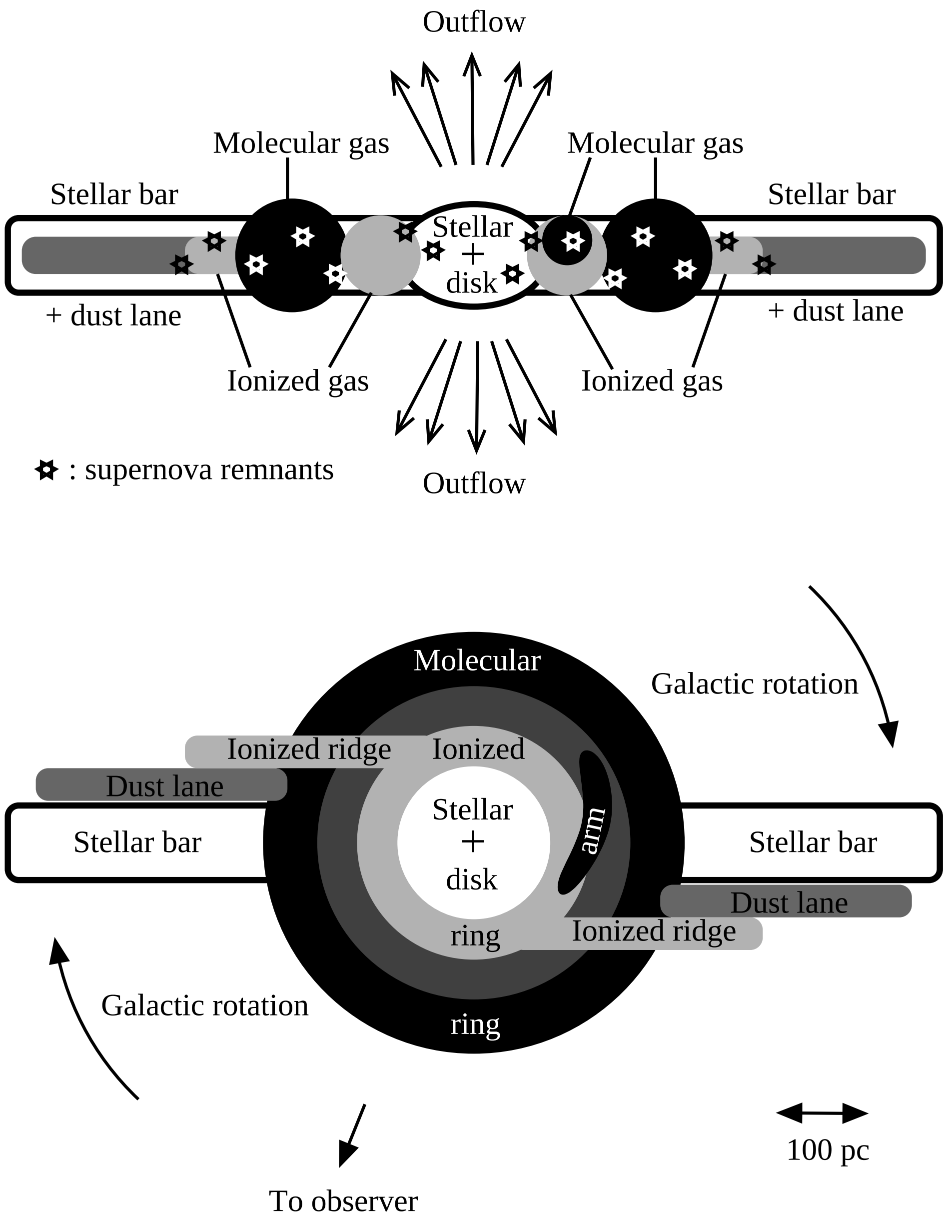

Fig. 1.4.— Edge-on and face-on sketches characterizing the global picture of M 82 (see text for the description).

gas near the center of M 82 show non-circular and possibly out-of-the-plane motions (O'Connell & Mangano 1978; Achtermann & Lacy 1995; Shen & Lo 1995).

The triggering of the burst of star formation in M 82 is generally attributed to tidal interaction with M 81 $\sim 10^8$ years ago or, alternatively, to the stellar bar which may itself have been induced by the interaction (Gottesman & Weliachew 1977; Williams, Caldwell & Schommer 1984; Lo *et al.* 1987; Waller, Gurwell & Tamura 1992; Yun, Ho & Lo 1993, 1994; Telesco *et al.* 1991; Larkin *et al.* 1994; Achtermann & Lacy 1995).

Several authors have applied evolutionary synthesis models to derive the star formation parameters in M 82, such as the age and duration of the starburst, and the initial mass function (IMF) of the stars. These models were optimized to best reproduce the *global* properties of M 82 — including the infrared and radio luminosities, the K-band and ultraviolet fluxes, the dynamical mass, the depth of the near-infrared CO stellar features — with a single burst or two successive burst events (Rieke *et al.* 1980, 1993; Bernlöhr 1992; Doane & Mathews 1993). Although based on different sets of stellar evolutionary tracks and modeling techniques, the best fits from various authors were achieved with similar starburst parameters. The most remarkable outcome from all these models is that an IMF deficient in low-mass stars is required in order to satisfy simultaneously the constraints on the dynamical mass and K-band luminosity. This important conclusion, however, has been recently challenged by Satyapal *et al.* (1997), who also presented the first models for selected, individual regions.

1.3.3 Unsolved issues

A global approach is not sufficient for a detailed investigation of the nature and evolution of starburst activity. Such information is crucial for the understanding of the triggering and propagation mechanisms. The key to further insight resides in a *spatially and spectrally* detailed description providing the location of and the physical conditions within *individual regions* involved in the starburst. Indeed, recent observations of M 82 have revealed small-scale structure ($\lesssim 25$ pc) in the ionized and molecular gas (*e.g.* Larkin *et al.* 1994; Shen & Lo 1995; Achtermann & Lacy 1995). Compact stellar clusters have been observed at optical and near-infrared wavelengths (*e.g.* O'Connell *et al.* 1995; Satyapal *et al.* 1997). These results suggest that the central starburst region is comprised of many smaller individual starburst sites. The two successive starburst events in the models of Rieke *et al.* (1993) and the age dispersion inferred for the young stellar clusters in M 82 (Satyapal *et al.* 1997; O'Connell *et al.* 1995 and references therein) indicate a time sequence in the triggering of the individual bursts.

Despite recent progress revealing more clearly the spatial and chronological evolution of starburst activity in M 82, crucial issues remain pending and are described below.

- **The composition of the evolved stellar population**

This issue has been addressed by many authors in the past because of its direct implication on the age and duration of the starburst but no consensus has been reached yet. From observations within various apertures, several authors infer the presence of an important population of young supergiants (*e.g.* Rieke *et al.* 1980; McLeod *et al.* 1993; Lester *et al.* 1990) whereas others favour an older population of (metal-rich) giants (*e.g.* Gaffney, Lester & Telesco 1993; Lançon, Rocca-Volmerange & Thuan 1996). The stellar population in the central regions of M 82 needs to be further investigated and the possibility of spatial variations has to be considered.

- **The star formation parameters**

The shape and cutoffs of the IMF as well as the starburst age and timescale are essential for the understanding of the starburst phenomenon. However, most of these parameters are still poorly constrained in M 82.

- **The evolution of starburst activity**

The spatial and chronological evolution of starburst activity is still unclear. The scenarios proposed in the past are based on qualitative evidence, on spatially limited information, or on data biased towards a particular stellar population. An "inside-out" propagation of the starburst, from the nucleus towards the outer regions, has been frequently suggested (*e.g.* Rieke *et al.* 1980; McLeod *et al.* 1993; Lançon, Rocca-Volmerange & Thuan 1996). The arguments rely primarily on the spatial distribution of various tracers showing a more centrally concentrated evolved stellar component surrounded by a "ring" of active star-forming sites. Satyapal *et al.* (1997) presented the first quantitative analysis supporting the inside-out scenario from the age of a dozen individual stellar clusters. Other authors have argued in favour of different, even opposite scenarios based on the physical state of the molecular gas and on the spatially extended distribution of the radio supernova remnants (*e.g.* Shen & Lo 1995). The evolution of starburst activity in M 82 needs to be quantitatively constrained from spatially detailed observations tracing *all* of the relevant stellar populations.

1.4 The present work

1.4.1 Motivation

It is obvious from the previous sections that starburst galaxies constitute an important class of extragalactic objects, and that their study has far-reaching consequences for the understanding of star formation, of galaxy evolution at all epochs in the Universe, and of the evolution of the intergalactic medium. However, crucial questions concerning the star formation parameters, and the origin and evolution of starburst activity are still open. Detailed, quantitative investigations have been hindered in the past by dust obscuration often preventing studies at optical and ultraviolet wavelengths, and by the lack of spatially resolved data.

Infrared observations are ideal to study starburst galaxies. Starburst activity is conspicuous in this wavelength regime where, moreover, the effects of dust obscuration are much less important than at optical and ultraviolet wavelengths. Recent progress in infrared instrumentation and the results from the *ISO* mission offer unprecedented opportunities to address the above questions. The recent technique of **integral field spectroscopy** provides **simultaneously spatial and spectral information**. The instruments on board **ISO** provide a **unique access** to the infrared regime, and especially **to the complete mid-infrared spectral region**, difficult to obtain from ground-based telescopes.

This dissertation was therefore motivated by the tremendous potential of such observations for the understanding of the starburst phenomenon. M 82 was chosen as the object of study; its proximity — allowing detailed spatial investigations — and the amount of existing data at all wavelengths — providing important complementary information — make this galaxy an ideal target. Near-infrared imaging spectroscopy from the 3D instrument and mid-infrared spectroscopy from the Short Wavelength Spectrometer on board *ISO* are combined with existing data at other wavelengths, and analyzed with stellar population and evolutionary synthesis models to address the following specific issues:

- the composition and the spatial variations of both the young, massive stellar population and the cool, evolved stellar population,
- the physical conditions of the ISM within the star-forming regions,
- the IMF of the stars associated with the starburst, and
- the age and timescale of starburst activity in individual regions.

This work ultimately aims at a **first, fully quantitative description of starburst activity in M 82** by characterizing:

- the star formation process,
- the detailed spatial and chronological evolution of starburst activity.

The results can then be compared with the properties of star formation in high-mass star-forming regions in the Milky Way and Magellanic Clouds for example. In addition, they provide important constraints on the triggering mechanism of starburst activity in M 82, and on its effects on the environment.

A large part of this thesis work has also been devoted to obtaining a near-infrared library of stellar spectra suitable for population and evolutionary synthesis of stellar populations, and to optimizing an existing evolutionary synthesis code for applications to near- and mid-infrared data. The important lack of near-infrared stellar spectra available at moderate resolution as well as the emergence of new diagnostic tools for the stellar population in both the near- and mid-infrared ranges motivated these complementary projects.

1.4.2 Thesis overview

This thesis is organized as follows. Chapter 2 presents the observations, data reduction and results of the new stellar library, which is then analyzed together with similar existing stellar atlases. Chapter 3 describes the evolutionary synthesis model used, and the improvements and extensions brought to it, for the interpretation of the M 82 data. Chapter 4 presents the observations, data reduction and results for M 82. Chapter 5 describes the nebular analysis to derive the physical conditions of the ISM and the composition of the hot, massive stellar population in M 82. Chapter 6 describes the population synthesis to determine the composition of the evolved stellar population in M 82. Chapter 7 presents the quantitative starburst modeling and discusses the nature and evolution of starburst activity in M 82. Chapter 8 summarizes the main results and conclusions.

Chapter 2

The 3D stellar library

2.1 Introduction

The identification of the spectral types and luminosity classes of stars is important in many branches of astronomy, including stellar evolution, dynamics, and population analysis. In particular, the determination of the stellar contents of clusters and galaxies provides important constraints on the star formation history and parameters. This can be achieved, for instance, by *population synthesis* which consists of isolating, from a complete library of observed or theoretical stellar energy distributions, those constituents that contribute to the energy output of the source of interest. Such stellar libraries are also essential for modeling the integrated properties of evolving stellar populations (see chapter 3).

Extensive stellar libraries now exist in the ultraviolet and optical regimes, and have been applied in numerous studies of Galactic and extragalactic sources (*e.g.* Worthey 1994; Leitherer *et al.* 1996). These are, however, of limited usefulness for obscured systems such as starburst and infrared-luminous galaxies. The near-infrared regime offers an alternative opportunity to probe the stellar populations of regions obscured at shorter wavelengths. In addition, cool ($\sim 3000-6000$ K) stellar populations are best studied at near-infrared wavelengths because their spectral energy distributions peak near $1\,\mu$m. An important application of population synthesis in the near-infrared is to distinguish between populations of red giants and supergiants. Since red supergiants have high-mass progenitors with short main-sequence lifetimes, their presence implies recent ($\sim 10-20$ Myr) star formation. The presence of less massive red giants imply much earlier star formation ($\gtrsim 10^8$ yr). An overview of stellar evolution and a summary of various stellar properties are given in appendix A.

Early near-infrared extragalactic studies mostly consisted of observations with broad-band and narrow-band filters. In particular, two photometric indices have been extensively used to investigate the stellar populations of composite systems: the CO and H_2O photometric indices ($CO_{\rm ph}$ and $H_2O_{\rm ph}$) measuring the depth of the CO absorption bandheads longwards of 2.29 μm, and of the broad H_2O absorption feature centered at 1.9 μm (*e.g.* Frogel *et al.* 1978; Aaronson, Frogel & Persson 1978). However, these indices as well as broad-band photometry have serious drawbacks in the cases of starburst, AGN and infrared-luminous galaxies (*e.g.* Doyon, Joseph & Wright 1994). For instance, they are potentially affected by extinction, by non-stellar continuum emission sources (such as hot dust), by emission lines from ionized and molecular gas (such as H I and He I recombination lines, and H_2 rotational-vibrational lines), and by absorption from the Earth's atmosphere (especially strong and variable in the bandpass used to measure the H_2O absorption near 2 μm). In addition, the filters used cover fixed wavelength ranges, making the colours and photometric indices redshift-dependent.

These problems can be circumvented by turning to spectroscopy and taking advantage of the wealth of absorption features produced by various atoms and molecules in the atmospheres of cool stars. Alternative diagnostics for spectral type and luminosity class can thus be identified, based on more isolated and narrower features, providing redshift- and extinction-independent indicators free from contamination by potential emission lines, and located in spectral regions of optimal atmospheric transmission.

2.1.1 Near-infrared stellar libraries

Early near-infrared spectroscopic studies of stars focussed on cool stars. They were mostly based on low to moderate resolution spectra ($R \equiv \lambda/\Delta\lambda \sim 100 - 3000$), were predominantly qualitative, and were mainly concerned with the identification of the molecular bands and on their approximate temperature and luminosity dependence (*e.g.* Johnson & Méndez 1970; Ridgway 1974; Hyland 1974; Merrill & Stein 1976; Merrill & Ridgway 1979). More quantitative studies have followed (*e.g.* Arnaud, Gilmore & Collier Cameron 1989; Terndrup, Frogel & Whitford 1991). The samples have been extended to hot, luminous stars including OB, luminous blue variable and Wolf-Rayet stars, and to pre-main-sequence stellar objects (Morris *et al.* 1996; Hanson, Conti & Rieke 1996; Meyer 1996; Blum *et al.* 1997). High-resolution spectra were also obtained, aimed at detailed abundance analyses (*e.g.* Hinkle, Lambert & Snell 1976; Lambert & Ries 1981; Ridgway 1984; Lambert *et al.* 1984; Tsuji 1986, 1988, 1991) and improved line identifications (*e.g.* Wallace & Hinkle 1996).

In the past decade, a growing number of efforts have been invested in obtaining atlases of cool stars at moderate resolution for spectral synthesis of stellar clusters and galaxies, especially in the H- and K-band ($\lambda = 1.45 - 1.85$ μm and $\lambda = 1.9 - 2.5$ μm respectively). Kleinmann & Hall (1986, hereafter KH86) assembled a K-band atlas of high signal-to-noise ratio (S/N $\sim 100 - 1000$) spectra at $R \sim 3000$ and analyzed quantitatively the variation with temperature and luminosity of the strongest absorption features. The sample included 26 stars of near-solar metallicity covering spectral types from F8 to M7 and luminosity classes from dwarfs to supergiants. Lançon & Rocca-Volmerange (1992) obtained $1.4 - 2.5$ μm spectra at $R \sim 500$ with S/N $\sim 20 - 300$ of 56 stars of luminosity classes I, III and V between 2000 K and 45000 K. They used their stellar library in evolutionary synthesis models of external galaxies (Lançon, Rocca-Volmerange & Thuan 1996; Lançon & Rocca-Volmerange 1996). The advantage of these data over others is an exceptionally large wavelength coverage and accurate relative flux levels between the H- and K- windows. Origlia, Moorwood & Oliva (1993, hereafter OMO93) studied in detail the variation with stellar parameters of selected features in the H- and K-band by combining spectra at $R \sim 1600$ (H-band) and $R \sim 2500$ (K-band) of 44 G, K and M giants and supergiants with stellar atmosphere models. Their stellar data were applied to extragalactic studies and augmented with observations of template composite stellar populations in subsequent papers (Oliva *et al.* 1995; Origlia *et al.* 1997; Oliva & Origlia 1998). Part of their work was also devoted to establishing a new metallicity scale for populations of red giants and supergiants based on near-infrared indicators.

Additional work include that of Ali *et al.* (1995), who obtained spectra of 33 late-type dwarfs at $R \sim 1380$ in the range $2.15 - 2.35$ μm and studied the temperature dependence of the strongest features in the observed range. Dallier, Boisson & Joly (1996, DBJ96) conducted a similar investigation from their sample of 40 O7 to M3 stars of luminosity classes I, III and V observed at $R \sim 1500$ or $R \sim 2000$ between $1.57\,\mu$m and $1.65\,\mu$m. Ramírez *et al.* (1997) compared their results for 43 K0 to M6 giants observed at $R = 1380$ and $R = 4830$ in the range $2.19 - 2.34$ μm with those from Ali *et al.* (1995) on late-type dwarfs. They also assessed the effects of absorption bands due to the CN molecule on the continuum level at moderate spectral resolution.

Despite these recent efforts, additional near-infrared stellar atlases suitable for population synthesis purposes are needed. A specific problem is the actually quite low number of template spectra with sufficient resolution ($R \gtrsim 1000$) and quality (S/N $\gtrsim 100$) to deblend the numerous closely spaced features in the spectra of cool stars as well as large enough spectral coverage to account for the broad absorption bands that distort the continuum. Another problem resides in the disparity in spectral resolution of the various existing libraries, and in the different definitions of spectroscopic indices used to quantify the strength of the absorption features. Further empirical spectra would also be beneficial to improve the theoretical stellar atmosphere models that still do not satisfactorily reproduce the spectra of the coolest stars (see the discussions in Lançon & Rocca-Volmerange 1992, Oliva & Origlia 1998, and Chiosi, Bertelli & Bressan 1992).

2.1.2 Motivation for the 3D stellar library

In an effort to increase the essential near-infrared stellar database, a new stellar library was assembled, based on observations with the 3D imaging spectrometer. An additional motivation was to provide a reliable database adequate for the investigation of the evolved stellar population in M 82 for the purpose of this thesis work. The 3D atlas focusses on normal red giant and supergiant stars. New K-band spectra at $R \sim 830$ and $R \sim 2000$ with S/N ratios above 100 of 33 late-type giants and supergiants were collected. This sample includes mostly solar-metallicity stars, but also a few with sub-solar abundances, as well as two carbon stars.

The next sections describe the selection of the program stars, the observations and the data reduction procedure. Indices based on equivalent widths (EWs) are defined and applied to measure the depths of the strongest absorption features in the spectra. The results are used to:

- investigate the effects of spectral resolution on the EWs,
- collect data from some of the most relevant existing libraries into a larger database and assess the consistency between the various data sets,
- examine the variation with stellar parameters of the EWs, and
- construct composite indices as indicators of stellar parameters and dilution by featureless continuum sources for applications to extragalactic studies.

2.2 Selection, observations and data reduction of the sample

2.2.1 Selection of program stars

The sample consists of 25 red giants and 6 red supergiants. Except for a few giants with [Fe/H] < -0.3[1], none of the stars are known to have strong abundance anomalies. The sample was selected from the list of optical spectral standards and well-classified stars of Keenan & McNeil (1989). A few additional stars were taken from Cayrel de Strobel *et al.* (1992). The spectral types are given in the revised MK system (Morgan & Keenan 1973) and were cross-checked with Keenan & Yorka (1988), Garrison (1994), Keenan & Pitts (1980) and Morgan & Keenan (1973). In addition, one N-type and one early-R type carbon stars taken from Yamashita (1972, 1975) were observed. Table 2.1 lists the stars with their spectral types, and their metallicities from three literature sources (Taylor 1991; Cayrel de Strobel *et al.* 1992; McWilliam 1990).

2.2.2 Observations

The stars were observed using the Max-Planck-Institut für extraterrestrische Physik near-infrared imaging spectrometer 3D during three observing runs. A first set of spectra was obtained at the 3.5 m telescope in Calar Alto, Spain, on January 12, 18 and 20, 1995. A second set was collected at the 4.2 m William-Herschel-Telescope in La Palma, Canary Islands, on January 2 and 9, 1996. The observations were completed at the 2.2 m ESO telescope in La Silla, Chile, between April 10 and 20, 1996.

3D (Weitzel *et al.* 1996) is an integral field spectrometer that images a square field of view at $0.3'' - 0.5''$/pixel and provides simultaneously the entire H- or K-band spectrum of each spatial pixel at $R \sim 1000$ or $R \sim 2000$. The field of view is sliced in 16 parallel "slits" whose light is dispersed in wavelength by a grism onto a 256×256 HgCdTe NICMOS 3 array. The data are rearranged in a three-dimensional cube during data processing. The intrinsic spectral sampling of 3D is with pixels of size λ/R; Nyquist-sampled spectra are achieved by dithering the sampling by half a pixel on alternate data sets. The Calar Alto and La Palma data were obtained at $R \sim 1000$ in the range $1.9 - 2.4$ μm and the La Silla data, at $R \sim 2000$ in the range $2.18 - 2.45$ μm.

[1] the metallicity is often characterized by the number abundance of Fe relative to H, compared to the solar composition: $[\mathrm{Fe/H}] \equiv \log(\mathrm{n_{Fe}/n_H}) - \log(\mathrm{n_{Fe}/n_H})_\odot$.

Table 2.1: 3D stellar library: program stars

Star	Spectral type	Reference[(a)]	[Fe/H]	Reference[(b)]
HD 44030	K4 II	C92	-0.22; -0.7	T91; C92
HD 78647	K4.5 Ib	KM89	0.23	C92
HD 35601	M1.5 Iab-Ib	KM89	-0.24	C92
HD 36389	M2 Iab-Ib	KM89	0.11	C92
HD 94613	M3+ Ib	KM89		
HD 90382	M3.5 Iab	KM89		
HD 20791	G8.5 III	KM89		
HD 62509	K0 IIIb	KM89	0.01; -0.07; -0.51 to 0.16	T91; Mc90; C92
HD 74442	K0 IIIb	KM89	-0.11; -0.13	T91; Mc90
HD 37160	K0 IIIb Fe-2	KM89	-0.58; -0.63; -0.70 to -0.19	T91; Mc90; C92
HD 49293	K0+ IIIa	KM89	-0.08; -0.12	T91; Mc90
HD 107328	K0.5 IIIb Fe-0.5	KM89	-0.32; -0.48; -0.64 to -0.12	T91; Mc90; C92
HD 89484	K1- IIIb Fe-0.5	KM89	-0.25; -0.49; -0.41 to 0.09	T91; Mc90; C92
HD 85859	K2.5 III	KM89	-0.08; -0.03	T91; Mc90
HD 34334	K2.5 III Fe-1	KM89	-0.26; -0.46; -0.39, -0.25	T91; Mc90; C92
HD 97907	K3 III	C92	-0.09	T91
HD 90432	K4+ III	KM89	-0.24; -0.12	T91; Mc90
HD 133774	K5- III	KM89	-0.41; 0.01	T91; Mc90
HD 82668	K5 III	KM89		
HD 29139	K5+ III	KM89	-0.16; -0.34; -0.33 to 0.00	T91; Mc90; C92
HD 95578	M0 III	KM89		
HD 80874	M0.5 III	KM89		
HD 25025	M0.5 IIIb Ca-1	KM89		
HD 102212	M1 III	KM89	-0.09	C92
HD 119149	M1.5 III	KM89		
HD 120052	M2 III	KM89		
HD 44478	M3 IIIab	KM89	-0.05	C92
HD 80431	M4 III	KM89		
HD 4408	M4 IIIa	KM89		
HD 102620	M4+ III	KM89		
HD 120323	M4.5 III	KM89		
HD 113801	C2,1 (R0)	Y72 (HD)	-0.26	C92
HD 92055	C6,3 (N2)	Y72 (HD)	-0.1	C92

[(a)] C92 : Cayrel de Strobel *et al.* 1992; KM89 : Keenan & McNeil 1989; Y72 : Yamashita 1972; HD : from the *Henry Draper Catalogue*.

[(b)] T91 : average computed by Taylor (1991) from data in the literature; C92 : values collected from the literature by Cayrel de Strobel *et al.* (1992); Mc90 : best fit to high-resolution optical spectra and photometric data using model atmospheres by McWilliam (1990).

Each star was observed in two sequences of several exposures, each sequence taken with spectral sampling shifted by half a pixel with respect to the other. Two similar sequences with an equal number of off-source exposures were obtained to allow proper subtraction of the "background" emission from the sky, the instruments and the observatory. The effects of variable background emission were minimized by taking the off-source positions at most $1'$ away from the stars, and by alternating the on- and off-sequences on timescales of less than 10 minutes. The integration time and number of individual exposures were dictated by the brightness of each star and by the requirement of achieving a S/N $\gtrsim$ 100 per spectral point. B, A, F and early-G type stars were observed each night, before and after the program stars, in order to monitor the atmospheric transmission. Calibration stars close to the program stars in the sky were chosen to optimize the correction for differential airmass and transmission spectrum.

Table 2.2 gives the log of the observations. The K-band magnitudes listed are an inhomogeneous collection of values taken from the literature or computed from V-band magnitudes using the $V - K$ colours given in Koornneef (1983b). They are expected to be only accurate to ~ 0.2 mag and were meant as a guide for calculating integration times. The S/N was evaluated on the relatively clean portion of the spectrum between $2.242\,\mu$m and $2.258\,\mu$m. Since this interval is not completely free of lines (see *e.g.* the KH86 spectra), especially at $R \sim 2000$ and for the carbon stars, this estimate represents a lower limit to the actual S/N. The resolution reported in the table corresponds to the final resolution of the reduced spectra (see section 2.2.3).

2.2.3 Data reduction

The data reduction was carried out using the 3D data analysis package, based on the the GIPSY software package (van der Hulst *et al.* 1992). Because of the different grisms used and of the better tracking from one observing run to the next, the data collected at different telescopes were not reduced in the exact same way. In the following, the reduction of data from different observing runs is described separately.

- **Calar Alto data**

During the Calar Alto run, the lower resolution K-band grism ($R \sim 1000$ in the range $1.90 - 2.40\ \mu$m) was used and the spatial scale was $0.5''$/pixel. The data sets obtained at each wavelength sampling were reduced independently. The non-linear signal response of the detector was first corrected for in all on- and off-source frames. Off-source exposures were averaged and subtracted from the corresponding averaged on-source

Table 2.2: 3D stellar library: log of the observations

Star	K [mag]	$t_{\rm int}$ [a] [s]	S/N [b]	Calibrator	Range [μm]	R [c]	Run [d]
HD 44030	0.00	100	376	PPM 95062 (F8 V)	1.90-2.40	830	CA95
HD 78647	-0.79	10	113	BS 3699 (A8 Ib)	2.18-2.45	2000	LS96
HD 35601	3.37	54	205	PPM 95062 (F8 V)	1.90-2.40	830	CA95
HD 36389	0.07	4.5	213	PPM 95062 (F8 V)	1.90-2.40	830	CA95
HD 94613	2.80	38	99	HD 87504 (B9 III-IV)	2.18-2.45	2000	LS96
HD 90382	2.49	40	85	BS 4037 (B8 IIIe)	2.18-2.45	2000	LS96
HD 20791	3.52	112	251	BS 1153 (B3 V)	1.90-2.40	1000	LP96
HD 62509	-1.21	2.7	218	BS 2890 (A2 V)	1.90-2.40	830	CA95
HD 74442	1.59	14.5	309	BS 3510 (G1 V)	1.90-2.40	830	LP96
HD 37160	1.93	95	343	PPM 95062 (F8 V)	1.90-2.40	830	CA95
HD 49293	2.11	36	277	BS 2779 (F8 V)	1.90-2.40	830	CA95
HD 107328	2.61	40	112	BS 4757 (B9.5 V)	2.18-2.45	2000	LS96
HD 89484	0.13	49	212	BS 4039 (F8 V)	1.90-2.40	830	CA95
HD 85859	2.29	95	108	HD 71459 (B3 V)	2.18-2.45	2000	LS96
HD 34334	1.95	58	349	PPM 95062 (F8 V)	1.90-2.40	830	CA95
HD 97907	0.00	140	418	PPM 158259 (F8 V)	1.90-2.40	830	CA95
HD 90432	0.58	38	155	HD 87504 (B9 III-IV)	2.18-2.45	2000	LS96
HD 133774	1.53	20	107	HD 136664 (B4 V)	2.18-2.45	2000	LS96
HD 82668	-0.54	9.5	83	HD 87504 (B9 III-IV)	2.18-2.45	2000	LS96
HD 29139	-2.81	8.7	323	BS 788 (F9 V)	1.90-2.40	830	CA95
HD 95578	1.00	9	119	HD 87504 (B9 III-IV)	2.18-2.45	2000	LS96
HD 80874	0.98	19	112	HD 71459 (B3 V)	2.18-2.45	2000	LS96
HD 25025	-0.79	14.5	283	BS 788 (F9 V)	1.90-2.40	830	CA95
HD 102212	0.15	49	328	PPM 158259 (F8 V)	1.90-2.40	830	CA95
HD 119149	1.10	40	100	HD 129116 (B3 V)	2.18-2.45	2000	LS96
HD 120052	1.28	19	132	HD 129116 (B3 V)	2.18-2.45	2000	LS96
				BS 4134 (F6 V)			
HD 44478	-1.66	2.7	344	PPM 95062 (F8 V)	1.90-2.40	830	CA95
HD 80431	2.12	100	142	BS 3836 (A5 IV-V)	2.18-2.45	2000	LS96
HD 4408	0.04	22.2	290	HD 4676 (F8 V)	1.90-2.40	830	LP96
HD 102620	-0.23	6	133	BS 4662 (B8 IIIpHgMn)	2.18-2.45	2000	LS96
HD 120323	-1.15	9.5	99	BS 4979 (G3 V)	2.18-2.45	2000	LS96
HD 113801	5.89	600	82	BS 5210 (B5 III)	2.18-2.45	2000	LS96
HD 92055	-0.70	10	25	BS 3836 (A5 IV-V)	2.18-2.45	2000	LS96

[a] Total on-source integration time per spectral point.

[b] S/N evaluated on the final spectra between 2.242 μm and 2.258 μm.

[c] Effective resolution of the reduced spectra.

[d] CA95 : January 1995 run at the 3.5 m telescope at Calar Alto, Spain; LP96 : January 1996 run at the 4.2 m William-Herschel-Telescope on the Canary Islands, Spain; LS96 : April 1996 run at the ESO 2.2 m telescope at La Silla, Chile.

exposures to remove the dark current, the thermal background and the telluric emission lines. Residuals due to spatial and temporal variations in the background emission level were $\lesssim 1\%$. Spatial and spectral flat-fielding, to correct for the differential response of the array pixels, was performed with images of featureless sources, namely the observatory's dome and a glowing Nernst rod. Wavelength calibration was achieved using images of a neon discharge lamp and the data were spectrally redistributed onto a regular grid of spacing $0.002\,\mu$m. The two-dimensional wavelength-calibrated frames were then rearranged in a three-dimensional data cube in which dead and hot pixels were corrected for by interpolation.

The Earth's atmospheric transmission was corrected for with the help of the calibration stars that were reduced in the manner described above. The calibration spectra were first extracted from the reduced data cubes and divided by a black-body curve of the temperature corresponding to that of each reference star. The intrinsic absorption features of the late-F dwarf calibrators are $< 5\%$ of the continuum level at $R \sim 1000$. The spectrum of the A2 V calibrator has a stronger Brγ absorption line at $2.166\,\mu$m but is otherwise featureless. Since the Brγ line lies in a wavelength range where the atmospheric transmission is not very sensitive to the atmospheric conditions, it was removed by simple interpolation in all calibration spectra. The other features in the late-F dwarfs were removed by division with the normalized and Brγ-corrected spectrum of the G3 V star — having similar line strengths — from the KH86 atlas, convolved with a gaussian profile at the resolution of 3D. The resulting spectra include only the variation with wavelength of the telluric and instrumental transmission. The data cubes of the program stars were then ratioed with the calibration spectra. The residuals introduced by inexact cancellation of the intrinsic features of the reference stars are less than 1%.

Since the atmosphere was not monitored simultaneously with the library stars, spatial and temporal variability of the atmospheric transmission led to imperfect cancellation of telluric absorption features. The proximity in time and sky position of the calibration stars kept this effect below 3-4% for $\lambda > 2\ \mu$m. However, at shorter wavelengths, where the atmospheric transmission is poorer and more variable, residuals up to 20% were left in a few spectra. In the case of HD 25025, the spurious features amounted to 12% and 40% longwards and shortwards of $2\,\mu$m respectively. The residuals could be reduced by fine-tuning the airmass assigned to the reference star using synthetic spectra of the atmospheric transmission at various zenithal distances and water vapour column densities generated with the program ATRAN (Lord 1992). An examination of the final spectra reveals that residuals do not persist to more than 1% in most of the band and 5% around $2.0\,\mu$m (except for HD 25025: 10% around $2.0\,\mu$m).

The spectra of the library stars at both wavelength samplings were extracted from the resulting data cubes by summing over the illuminated spatial pixels (with intensity down to 1/10 of the peak). They were normalized in global shape and flux level to one another by polynomial fitting (the differences never exceeded a few percent) and then interleaved, giving the fully sampled, "merged" spectrum. The wavelength calibration and spectral redistribution were performed independently for each wavelength sampling. This procedure caused the final effective resolution to be $R \sim 830$ instead of the expected $R \sim 1000$.

- **La Silla data**

During the La Silla observing run, the higher resolution K-band grism ($R \sim 2000$ in the range $2.18 - 2.45\ \mu$m) was selected and the data were acquired in both $0.5''$/pixel and $0.3''$/pixel scales. The observations were assisted by the tip-tilt adaptive optics system ROGUE II (Thatte *et al.* 1995), with a tracking accuracy better than $0.1''$.

Correction for non-linear detector response, averaging, dark current and background subtraction were performed as described for the Calar Alto data. Due to the accurate tracking, the position of the stars on the array was very stable and each column along the wavelength axis corresponded to the spectrum of the exact same spatial point during one exposure and between successive exposures. Therefore, the background-subtracted object frames at both wavelength samplings could be merged column by column (*i.e.* in wavelength space) before wavelength calibration, following the procedure described for the reduced Calar Alto spectra. Flat fielding, and wavelength calibration and redistribution (onto a grid of spacing $0.0005\,\mu$m) were subsequently performed as for the Calar Alto data but using "merged" flat fields and neon lamp images. The data were then re-arranged in a three-dimensional cube, and bad and hot pixels were corrected for.

Correction for atmospheric transmission was also done similarly as for the Calar Alto data. No intrinsic features were removed for the B- and A-type calibrators since they are not expected to have any between $2.18\,\mu$m and $2.45\,\mu$m. For the F6 and G3 dwarfs, the absorption lines were removed using the G3 V star from KH86, leaving residuals $\leq 1\%$. Differences in airmass between the program and calibration stars introduced features typically $\leq 5\%$ except in the case of HD 94613 (20%). Airmass correction using ATRAN cancelled these features to better than 1%. The final spectra of the library stars were extracted from the resulting data cubes. Since the merging was done before the wavelength calibration, the expected resolution of $R \sim 2000$ was fully achieved.

At the higher spectral resolution, and more importantly for the 0.3″/pixel scale, a complex high-frequency interference pattern appeared in the data, due to multiple reflections at the surface of the detector array. The frequency and position angle of the fringes varied with position on the array and with wavelength sampling, and differed significantly for defocused observations (*e.g.* in the dome images). This pattern multiplicatively modulated the observed counts with a typical peak-to-peak amplitude of 5%-10%. The similar nature of the library and calibration stars as well as the nearly identical technical conditions under which they were observed (telescope pointing close to the zenith, same focus, source positioned at the center of the array) resulted in similar interference patterns in the respective data sets. The division of the library stars by the calibration stars cancelled the fringes to better than 1% except for HD 82668, where they remained at the 3% level at short wavelengths.

- **La Palma data**

During the La Palma run, the lower resolution K-band grism was used ($R \sim 1000$ in the range $1.90 - 2.40$ μm). HD 4408 and HD 74442 were observed without the assistance of ROGUE II. These data were reduced in the same way as the Calar Alto data, with the merging of the wavelength-shifted data sets after data reduction, resulting in $R \sim 830$. HD 20791 was observed with ROGUE II on, enabling successful merging before wavelength calibration, and was reduced as the La Silla data. The spectrum of HD 20791 therefore has a final resolution of $R \sim 1000$. Residuals from intrinsic features of the calibration stars and atmospheric transmission, and from airmass differences are less than a few percents. The noise in the spectra obtained at La Palma is somewhat higher than in the other data sets because of less favourable weather conditions.

2.3 Results

2.3.1 Spectra

The final spectra are displayed in figures 2.1 to 2.3, sorted according to luminosity class and advancing spectral type. They have been normalized to unity in the interval $2.2875 - 2.2910\ \mu$m. They are presented on a linear flux scale and vertically shifted by equal intervals of 0.5 starting at the bottom. The considerable continuum structure is most obvious in the higher resolution spectra. The variation in strength of most features with spectral type and luminosity class is also apparent. The strongest features longwards of $2.15\,\mu$m, identified by comparing their locations with those in KH86, are indicated. Inspection of the high resolution stellar spectra published by Wallace & Hinkle (1996) shows that the absorption features seen at moderate resolution result from the blending of a number of lines from various elements. However, the nomenclature given in KH86 is adopted since it generally corresponds to the species contributing the most to the absorption (see section 2.5.1), and to avoid confusion by respecting the convention established so far. Line identifications in the literature for the complex near-infrared spectra of carbon stars are scarce and uncertain. Therefore, no features are identified for the two carbon star in figure 2.3 except for the ^{12}CO and ^{13}CO bandheads.

To illustrate the quality of the 3D data, several higher-resolution 3D spectra are compared in figure 2.4 with spectra from KH86 convolved at $R \sim 2000$ with a gaussian profile. The KH86 spectra are ratioed with A0 V stars. In order to recover the original energy distributions they were multiplied by a power-law continuum proportional to $\lambda^{-3.94}$ which is the closest representation of an A0 dwarf (Kurucz 1979; as quoted by McGregor 1987). In all cases the 3D and KH86 spectra compare remarkably well.

2.3.2 Equivalent widths of selected absorption features

The strength of the absorption features in the spectra can be quantified by equivalent widths (EWs), defined as:

$$W_\lambda = \int_{\lambda_1}^{\lambda_2} (1 - f_\lambda)\,\mathrm{d}\lambda, \qquad (2.1)$$

where f_λ is the spectrum normalized to a flat continuum slope while λ_1, λ_2 are the integration limits and $\mathrm{d}\lambda$ is expressed in Å. EWs are independent of extinction since the effects of continuous opacity of interstellar dust grains are cancelled by the continuum normalization (dust extinction is described in more detail in chapter 5). The EWs

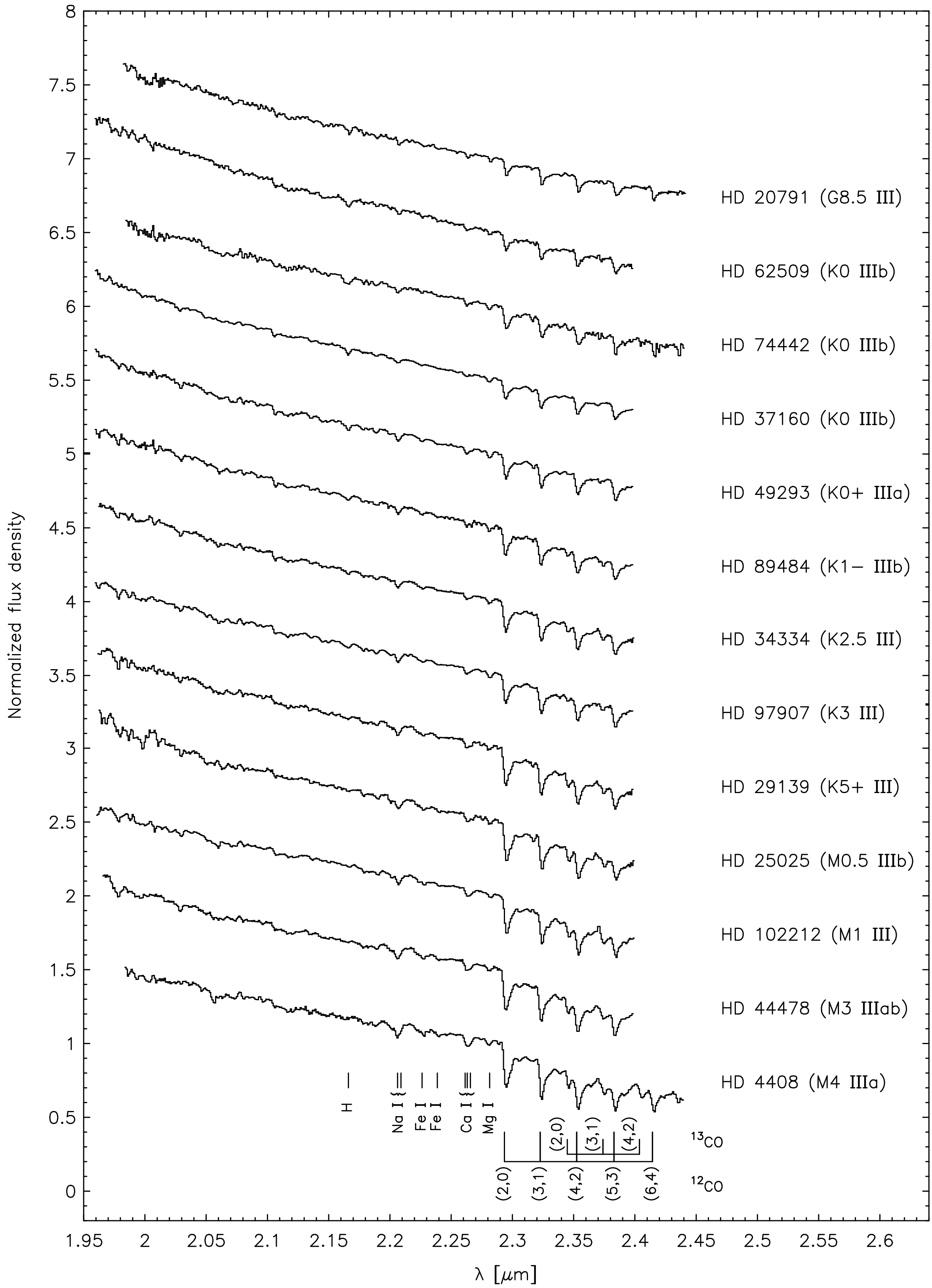

Fig. 2.1.— Spectra of red giants at $R \sim 830$ (the spectrum of HD 20791 has $R \sim 1000$). The spectra are normalized to unity between $2.2875\,\mu$m and $2.2910\,\mu$m. The vertical axis is the appropriate linear flux scale for the bottom spectrum. The other spectra are shifted upwards by intervals of 0.5 relative to one another. The strongest features longwards of $2.15\,\mu$m (marked on the bottom spectrum) were identified from the KH86 atlas.

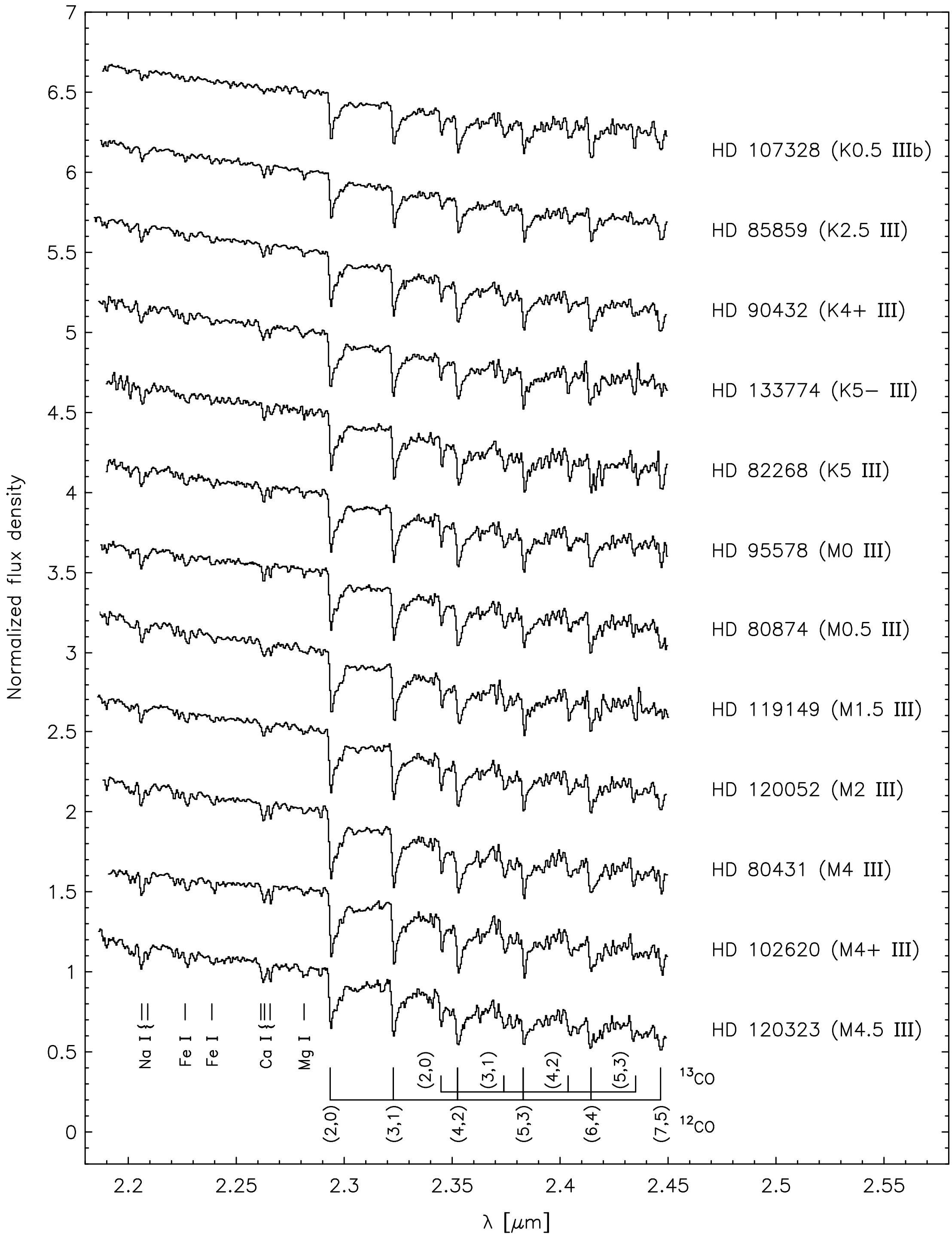

Fig. 2.2.— Same as figure 2.1 for red giants observed at $R \sim 2000$.

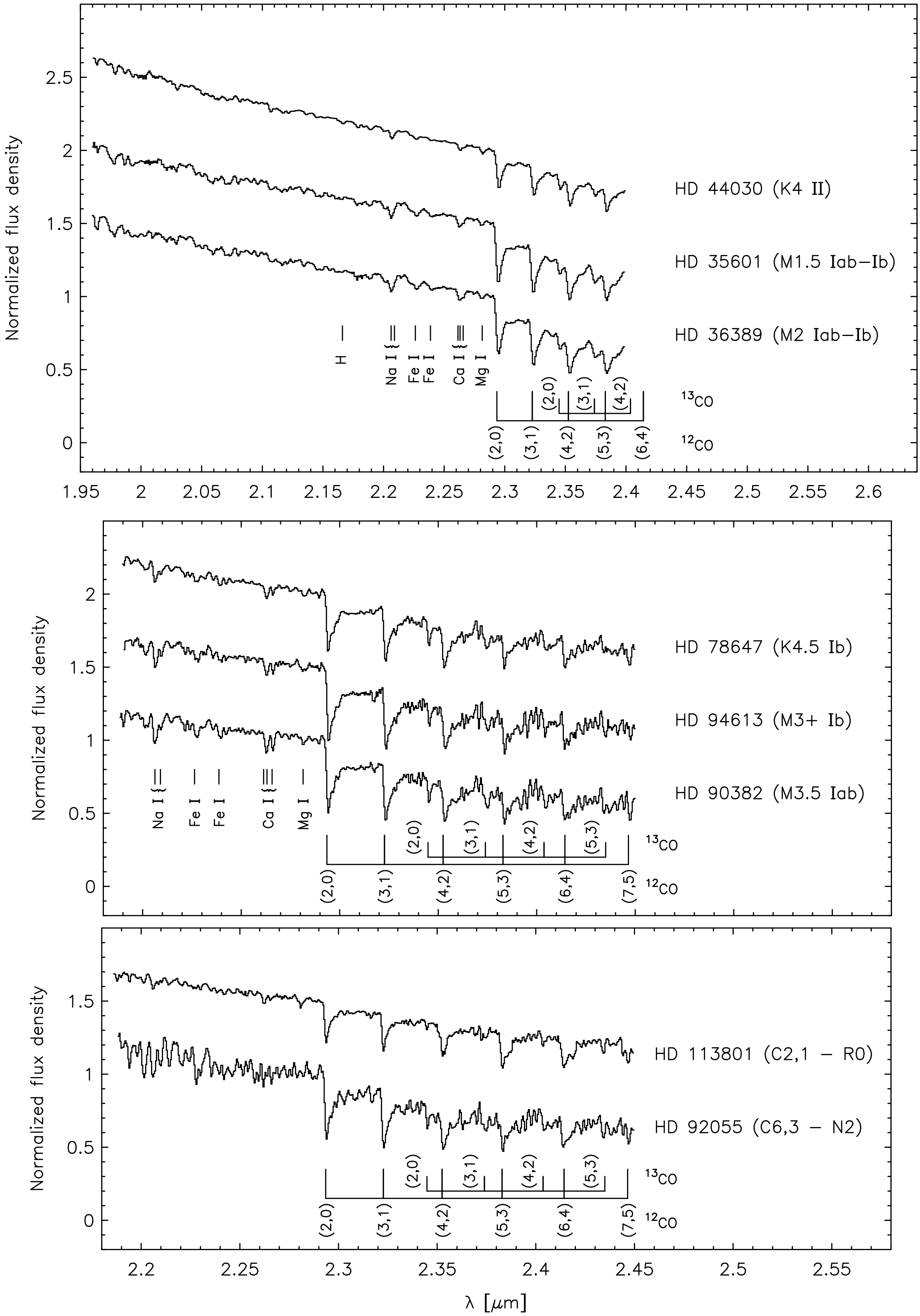

Fig. 2.3.— Same as figure 2.1 for red supergiants observed at $R \sim 830$ (top), and $R \sim 2000$ (middle), and for carbon stars observed at $R \sim 2000$ (bottom).

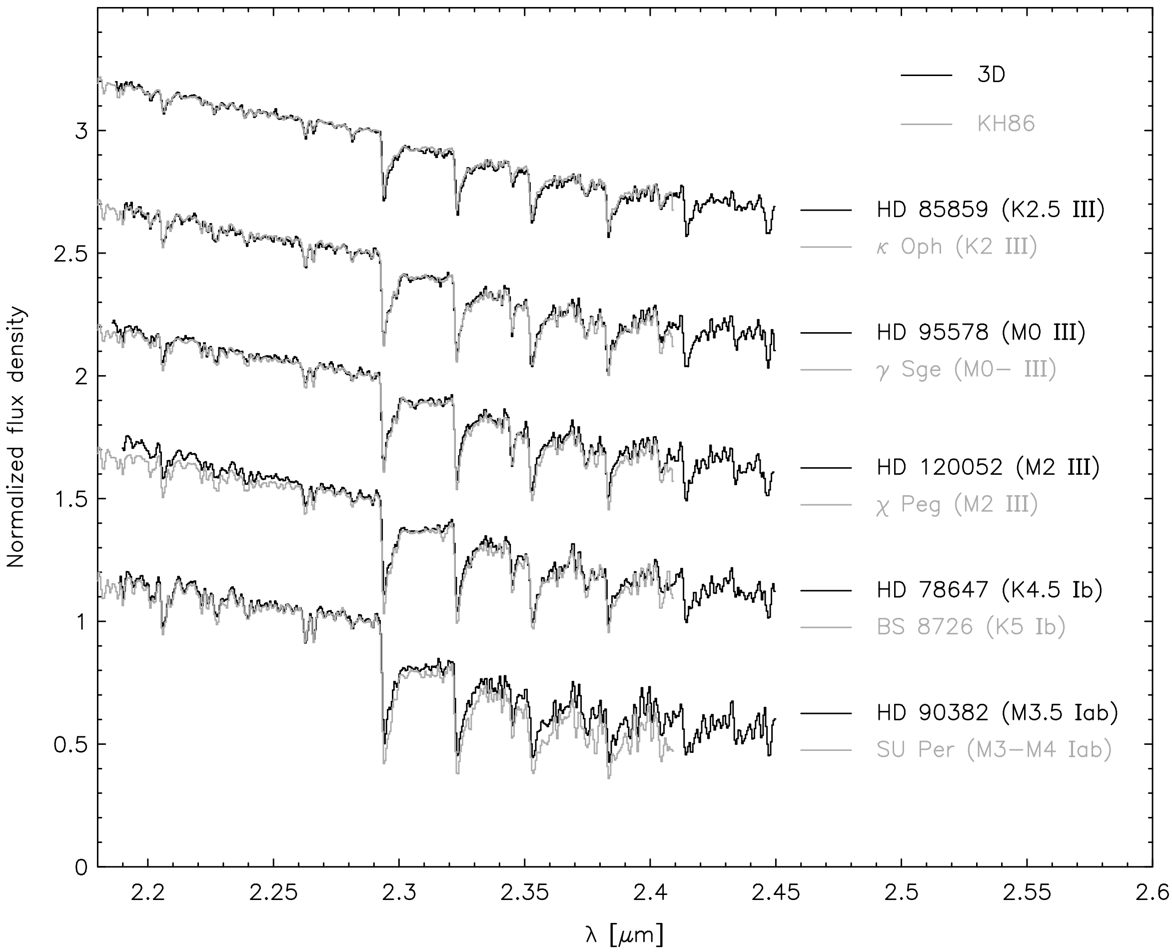

Fig. 2.4.— Comparison of a subset of 3D spectra at $R \sim 2000$ (black lines) with spectra of stars having similar spectral types from the KH86 atlas convolved at the resolution of the 3D data (grey lines). The KH86 spectra have been multiplied by a power law continuum proportional to $\lambda^{-3.94}$ in order to recover the original energy distribution of the stars (see text). All spectra are normalized to unity in the range $2.2875 - 2.2910\ \mu$m. The vertical axis is the appropriate linear flux scale for the bottom pair of spectra, the other pairs being shifted upwards by intervals of 0.5 relative to one another.

were measured for the Na I doublet centered at 2.2076 μm, the Ca I multiplet centered at 2.2636 μm and the ^{12}CO (2,0), ^{12}CO (3,1) and ^{13}CO (2,0) first overtone bandheads at 2.2935 μm, 2.3227 μm and 2.3448 μm respectively (hereafter $W_{\rm Na}$, $W_{\rm Ca}$, $W_{2.29}$, $W_{2.32}$ and $W_{2.34}$). In addition, the EWs for the Fe I lines at 2.2263 μm and 2.2387 μm and of the Mg I line at 2.2814 μm ($W_{\rm Fe1}$, $W_{\rm Fe2}$, $W_{\rm Mg}$) were measured in the higher resolution spectra.

Some authors have defined the normalizing continuum by fitting a straight line to featureless portions of the spectrum over a large wavelength range (*e.g.* KH86; Ali *et al.* 1995). However, this is inappropriate if the continuum shape is distorted by broad features such as the H_2O absorptions around 1.9 μm and 2.7 μm in very cool stars, or affected by extinction and contributions from additional emission sources such as hot dust. The normalizing continuum for each atomic feature of interest here was therefore taken in adjacent regions $0.002 - 0.003$ μm wide on each side of the absorption. Since there is no line-free continuum longwards of the CO bandheads in the 3D spectra, the normalizing continuum was defined at shorter wavelengths only. The continuum for ^{12}CO (2,0) was taken to be the average in the clear band around 2.29 μm. Although the continuum slope is thereby not constrained, the absorption itself is close enough to the continuum interval and narrow enough so that $W_{2.29}$ does not suffer from large uncertainties in the continuum slope. In the case of ^{12}CO (3,1) and ^{13}CO (2,0), for which no close continuum exists, a power-law was fitted to the continuum between 2.21 μm and 2.29 μm to better extrapolate over the bandheads. The continuum-defining intervals were selected in spectral regions free of stellar absorption lines at moderate resolution ($R \sim 1000-2000$), and of potential emission lines from ionized and molecular gas commonly observed in various types of galaxies.

The narrow bands used in the computation of the EWs are reported in table 2.3. The integration limits for the Na I and Ca I features and for the CO bandheads, as well as the continuum definition for ^{12}CO (2,0) are the same as in KH86. In view of the compilation of selected data sets published in the past, the definition of the local continuum and band limits of OMO93 for the strong ^{12}CO (6,3) second overtone bandhead at 1.6187 μm and the Si I feature at 1.5892 μm in the H-band are also listed ($W_{1.62}$ and $W_{1.59}$).

In order to compare the EWs from the 3D spectra taken at different spectral resolution, and ultimately provide a means for comparing observations obtained using different instruments with existing stellar data, the variations of the EWs defined here with instrumental resolution were investigated. This is equivalent to studying the effects of velocity broadening of the absorption features. The Mg I and Fe I lines were excluded from this analysis because their weakness hampers reliable measurements at

Table 2.3: Bandpass edges for the computation of the equivalent widths of the stellar absorption features

Feature	Symbol	Continuum points[a] [μm]	Integration limits [μm]
Si I 1.5892 μm	$W_{1.59}$	1.5850,1.5930	1.5870 – 1.5910
^{12}CO (6,3) 1.6187 μm	$W_{1.62}$	1.6160,1.6270	1.6175 – 1.6220
Na I 2.2076 μm	$W_{\rm Na}$	2.1965,2.2125,2.2175	2.2053 – 2.2101
Fe I 2.2263 μm	$W_{\rm Fe1}$	2.2125,2.2175,2.2323	2.2248 – 2.2293
Fe I 2.2387 μm	$W_{\rm Fe2}$	2.2323,2.2510,2.2580	2.2367 – 2.2402
Ca I 2.2636 μm	$W_{\rm Ca}$	2.2510,2.2580,2.2705,2.2760	2.2611 – 2.2662
Mg I 2.2814 μm	$W_{\rm Mg}$	2.2705,2.2760,2.2900	2.2788 – 2.2840
^{12}CO (2,0) 2.2935 μm	$W_{2.29}$	2.2900	2.2924 – 2.2977
^{12}CO (3,1) 2.3227 μm	$W_{2.32}$	2.2125,2.2175,2.2335,2.2560,2.2705,2.2900	2.3218 – 2.3272
^{13}CO (2,0) 2.3448 μm	$W_{2.34}$	(same as for $W_{2.32}$)	2.3436 – 2.3491

[a] Central wavelength of the $0.002 - 0.003$ μm wide intervals used to fit the normalizing continuum.

$R \lesssim 1000$. The instrumental profiles were assumed to be well approximated by a gaussian function. A grid of stellar spectra convolved with gaussians of velocity dispersion σ ranging from 0 km/s to 400 km/s, in steps of 10 km/s, was first generated using the KH86 spectra for types later than K0. The variations of the EWs with σ did not depend on the chosen templates and were best fitted by second order polynomials. This procedure was repeated with the 3D sample at $R \sim 2000$ and the same results were obtained, within the errors. Velocity dispersions $\sigma < 60$ km/s for the CO bandheads and $\sigma < 20$ km/s for the Na I and Ca I features produced no measurable effect. The dispersion around the fits was less than $\pm 5\%$ for $\sigma \leq 200$ km/s but increased for larger σ, corresponding to $R \lesssim 600$. Since at such low resolving powers, the resolution element λ/R becomes comparable to the integration intervals $\lambda_2 - \lambda_1$, $\sigma \leq 200$ km/s was considered as the range of validity for the empirical corrections.

Oliva *et al.* (1995) used this approach in order to compare the EWs of the ^{12}CO (2,0), ^{12}CO (6,3) and Si I 1.59 μm features in velocity broadened spectra. The correction they found for $W_{2.29}$ (measured as in the present work) using templates at $R \sim 2500$ is given by a linear relationship with σ for $\sigma \geq 60$ km/s. Within the errors, this line is a good approximation to the fit obtained here at $\sigma \leq 200$ km/s. For the sake of consistency with previous work, the relation derived by Oliva *et al.* (1995) for $W_{2.29}$ is adopted. The final empirical relationships are:

$$W_\lambda = W_\lambda(\text{observed})\ [1 + a\,(\sigma - 60)] \qquad 60\ \text{km/s} \le \sigma \le 200\ \text{km/s} \qquad (2.2)$$

for $W_{1.59}$, $W_{1.62}$ and $W_{2.29}$, where $a(1.59) = 8.70 \times 10^{-4}$, $a(1.62) = 7.10 \times 10^{-4}$ and $a(2.29) = 8.75 \times 10^{-4}$,

$$W_\lambda = W_\lambda(\text{observed})\ [1 + a\,(\sigma - 60) + b\,(\sigma - 60)^2] \qquad 60\ \text{km/s} \le \sigma \le 200\ \text{km/s} \quad (2.3)$$

for $W_{2.32}$ and $W_{2.34}$, where $a(2.32) = 4.38 \times 10^{-4}$, $b(2.32) = 3.52 \times 10^{-6}$, $a(2.34) = 1.32 \times 10^{-4}$ and $b(2.34) = 2.61 \times 10^{-6}$,

$$W_\lambda = W_\lambda(\text{observed})\ [1 + a\,(\sigma - 20) + b\,(\sigma - 20)^2] \qquad 20\ \text{km/s} \le \sigma \le 200\ \text{km/s} \quad (2.4)$$

for W_{Na} and W_{Ca}, where $a(\text{Na}) = 1.67 \times 10^{-3}$, $b(\text{Na}) = 4.43 \times 10^{-6}$, $a(\text{Ca}) = 2.33 \times 10^{-4}$ and $b(\text{Ca}) = 6.24 \times 10^{-6}$. The corrections for $R \sim 1000$ amount to $\approx 5\%$ or less except for W_{Ca} (10%) and W_{Na} (22%). At $R \sim 600$, they are $\approx 13\%$ or less, 27% and 48% respectively.

The EWs measured on the 3D spectra, corrected for resolution where appropriate, are listed in tables 2.4 and 2.5. The typical uncertainties are ± 0.5 Å for the atomic features, ± 0.8 Å for $W_{2.29}$, and ± 1.0 Å for $W_{2.32}$ and $W_{2.34}$. The atomic features were not measured for the carbon stars since their spectra are expected to be dominated by numerous absorption bands of carbon compounds such as CN and C_2 (see section 2.5.2). These absorption bands may hide the atomic features and obliterate the continuum, preventing reliable measurements of EWs.

2.3.3 Data from selected stellar atlases in the literature

Three references were chosen to complement the 3D data, because they present data of red giants and supergiants relevant to population synthesis based on near-infrared spectroscopy at moderate resolution. The EWs were measured on the digitally available spectra of DBJ96 and KH86; the EWs given in OMO93 were taken directly because measured according to the definitions adopted here. The variations of the EWs with stellar effective temperature (see section 2.4) are shown in figures 2.5 and 2.6. The EWs for main-sequence stars from KH86 and DBJ96 are included for comparison purposes. **The data obtained from the various references are in excellent agreement.** No systematic deviation of a particular data set is seen, and for the few stars common to two or more samples, the EWs agree within the uncertainties.

Table 2.4: Equivalent widths of the 3D stellar library stars: CO bandheads[(a)]

Star	Type	[Fe/H][(b)]	$W_{2.29}$ [Å]	$W_{2.32}$ [Å]	$W_{2.34}$ [Å]
HD 44030	K4 II	-0.22	12.0	13.0	9.6
HD 78647	K4.5 Ib	0.23	15.3	15.0	9.7
HD 35601	M1.5 Iab-Ib	-0.24	19.7	22.0	14.7
HD 36389	M2 Iab-Ib	0.11	19.2	21.8	15.4
HD 94613	M3+ Ib		20.0	21.8	12.7
HD 90382	M3.5 Iab		19.6	20.9	14.5
HD 20791	G8.5 III		5.1	5.8	1.6
HD 62509	K0 IIIb	0.01	5.5	5.9	1.8
HD 74442	K0 IIIb	-0.11	7.6	8.2	4.4
HD 37160	K0 IIIb Fe-2	-0.58	6.0	6.4	1.8
HD 49293	K0+ IIIa	-0.08	7.8	8.6	3.0
HD 107328	K0.5 IIIb Fe-0.5	-0.32	10.3	10.1	6.5
HD 89484	K1- IIIb Fe-0.5	-0.25	8.5	9.5	5.3
HD 85859	K2.5 III	-0.08	9.7	9.7	5.1
HD 34334	K2.5 III Fe-1	-0.26	9.8	11.0	6.9
HD 97907	K3 III	-0.09	9.1	10.5	5.3
HD 90432	K4+ III	-0.24	11.4	11.3	7.8
HD 133774	K5- III	-0.41	12.8	11.8	7.3
HD 82668	K5 III		11.9	11.5	8.1
HD 29139	K5+ III	-0.16	12.2	11.3	8.0
HD 95578	M0 III		13.6	12.7	8.4
HD 80874	M0.5 III		13.6	13.5	9.9
HD 25025	M0.5 IIIb Ca-1		12.5	12.4	8.5
HD 102212	M1 III	-0.09	12.1	12.6	10.0
HD 119149	M1.5 III		14.2	13.2	9.8
HD 120052	M2 III		13.1	12.5	10.2
HD 44478	M3 IIIab	-0.05	13.5	14.3	11.2
HD 80431	M4 III		16.3	14.7	11.7
HD 4408	M4 IIIa		14.9	16.5	12.2
HD 102620	M4+ III		15.2	14.8	12.3
HD 120323	M4.5 III		13.5	11.6	10.2
HD 113801	C2,1 (R0)	-0.26	9.8	10.1	3.6
HD 92055	C6,3 (N2)	-0.1	17.5	16.8	13.1

[(a)] The typical uncertainties are ±0.8 Å for $W_{2.29}$, and ±1.0 Å for $W_{2.32}$ and $W_{2.34}$.

[(b)] The metallicity from Taylor (1991) has been preferred here when more than one reference was listed in table 2.1.

Table 2.5: Equivalent widths of the 3D stellar library stars: atomic features[a]

Star	Type	[Fe/H][b]	$W_{\rm Na}$ [Å]	$W_{\rm Fe1}$ [Å]	$W_{\rm Fe2}$ [Å]	$W_{\rm Ca}$ [Å]	$W_{\rm Mg}$ [Å]
HD 44030	K4 II	-0.22	2.7			1.7	
HD 78647	K4.5 Ib	0.23	3.1	2.1	1.4	2.5	1.0
HD 35601	M1.5 Iab-Ib	-0.24	4.2			2.9	
HD 36389	M2 Iab-Ib	0.11	4.6			3.1	
HD 94613	M3+ Ib		4.7	2.8	1.5	2.7	1.2
HD 90382	M3.5 Iab		5.0	3.3	2.0	3.7	1.3
HD 20791	G8.5 III		1.4			1.1	
HD 62509	K0 IIIb	0.01	1.3			1.1	
HD 74442	K0 IIIb	-0.11	1.8			1.5	
HD 37160	K0 IIIb Fe-2	-0.58	1.3			0.9	
HD 49293	K0+ IIIa	-0.08	2.3			1.7	
HD 107328	K0.5 IIIb Fe-0.5	-0.32	1.5	0.7	0.5	1.0	0.9
HD 89484	K1- IIIb Fe-0.5	-0.25	2.3			1.3	
HD 85859	K2.5 III	-0.08	2.2	0.9	0.4	1.6	1.0
HD 34334	K2.5 III Fe-1	-0.26	2.0			1.4	
HD 97907	K3 III	-0.09	2.5			1.8	
HD 90432	K4+ III	-0.24	2.6	1.7	1.0	2.1	0.9
HD 133774	K5- III	-0.41	2.9	1.9	1.2	2.8	1.2
HD 82668	K5 III		2.1	1.3	0.8	2.2	0.5
HD 29139	K5+ III	-0.16	2.7			2.2	
HD 95578	M0 III		3.0	1.6	0.9	2.7	1.1
HD 80874	M0.5 III		3.0	1.8	1.1	2.6	1.1
HD 25025	M0.5 IIIb Ca-1		3.1			2.0	
HD 102212	M1 III	-0.09	2.5			2.3	
HD 119149	M1.5 III		3.5	2.3	1.3	2.8	0.7
HD 120052	M2 III		2.3	1.2	0.7	2.6	0.6
HD 44478	M3 IIIab	-0.05	3.5			2.5	
HD 80431	M4 III		3.2	2.4	1.3	3.2	1.1
HD 4408	M4 IIIa		3.3			3.3	
HD 102620	M4+ III		3.5	2.2	1.5	3.4	0.9
HD 120323	M4.5 III		3.7	1.9	1.1	3.9	1.5

[a] The typical uncertainties are ± 0.5 Å.

[b] The metallicity from Taylor (1991) has been preferred here when more than one reference was listed in table 2.1.

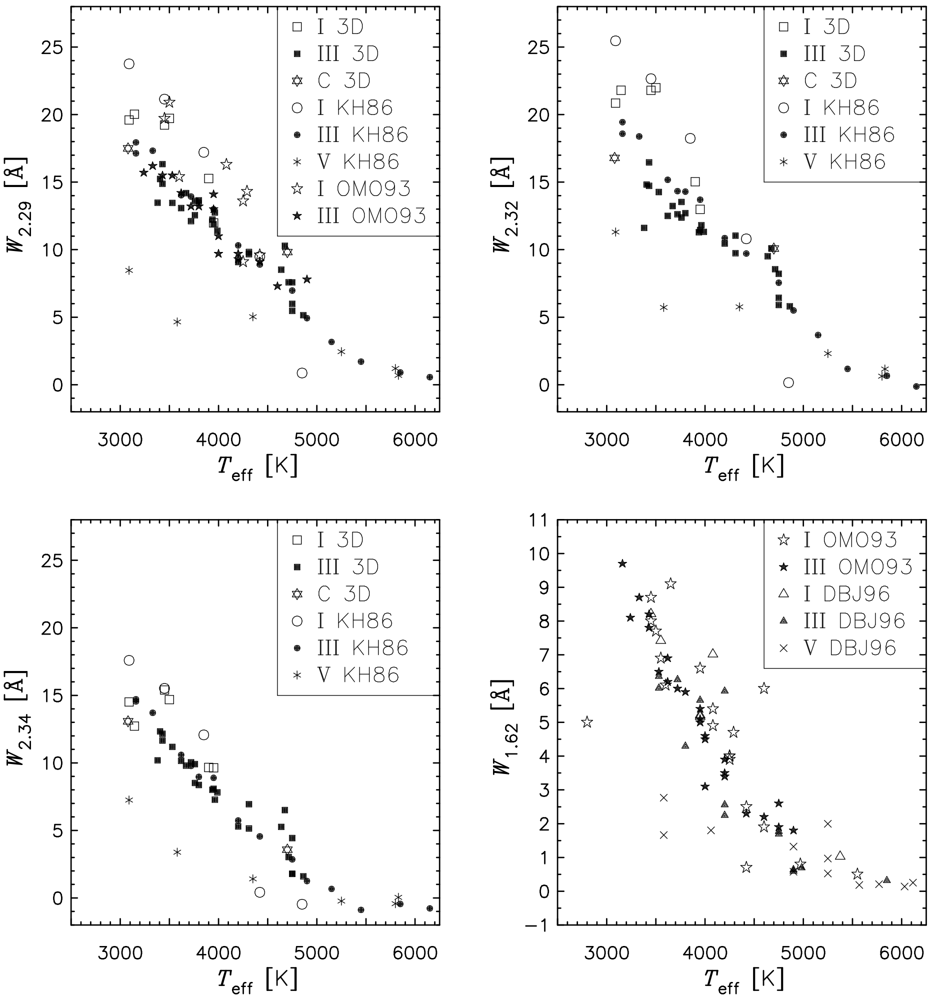

Fig. 2.5.— Variations of the EWs of the molecular absorption features with effective temperature and luminosity class from the 3D sample and from selected existing atlases. *Top left:* ^{12}CO (2,0) bandhead at 2.2935 μm; *top right:* ^{12}CO (3,1) bandhead at 2.3227 μm; *bottom left:* ^{13}CO (2,0) bandhead at 2.3448 μm; *bottom right:* ^{12}CO (6,3) bandhead at 1.6187 μm. Open symbols represent data for supergiants and carbon stars, filled symbols data for giants and crosses, data for dwarfs. Different symbols are also used to distinguish between data from various authors (3D: this work, KH86: Kleinmann & Hall 1986, OMO93: Origlia, Moorwood & Oliva 1993, DBJ96: Dallier, Boisson & Joly 1996). The typical uncertainties are ± 0.8 Å for $W_{2.29}$, ± 1.0 Å for $W_{2.32}$ and $W_{2.34}$, and ± 0.5 Å for $W_{1.62}$.

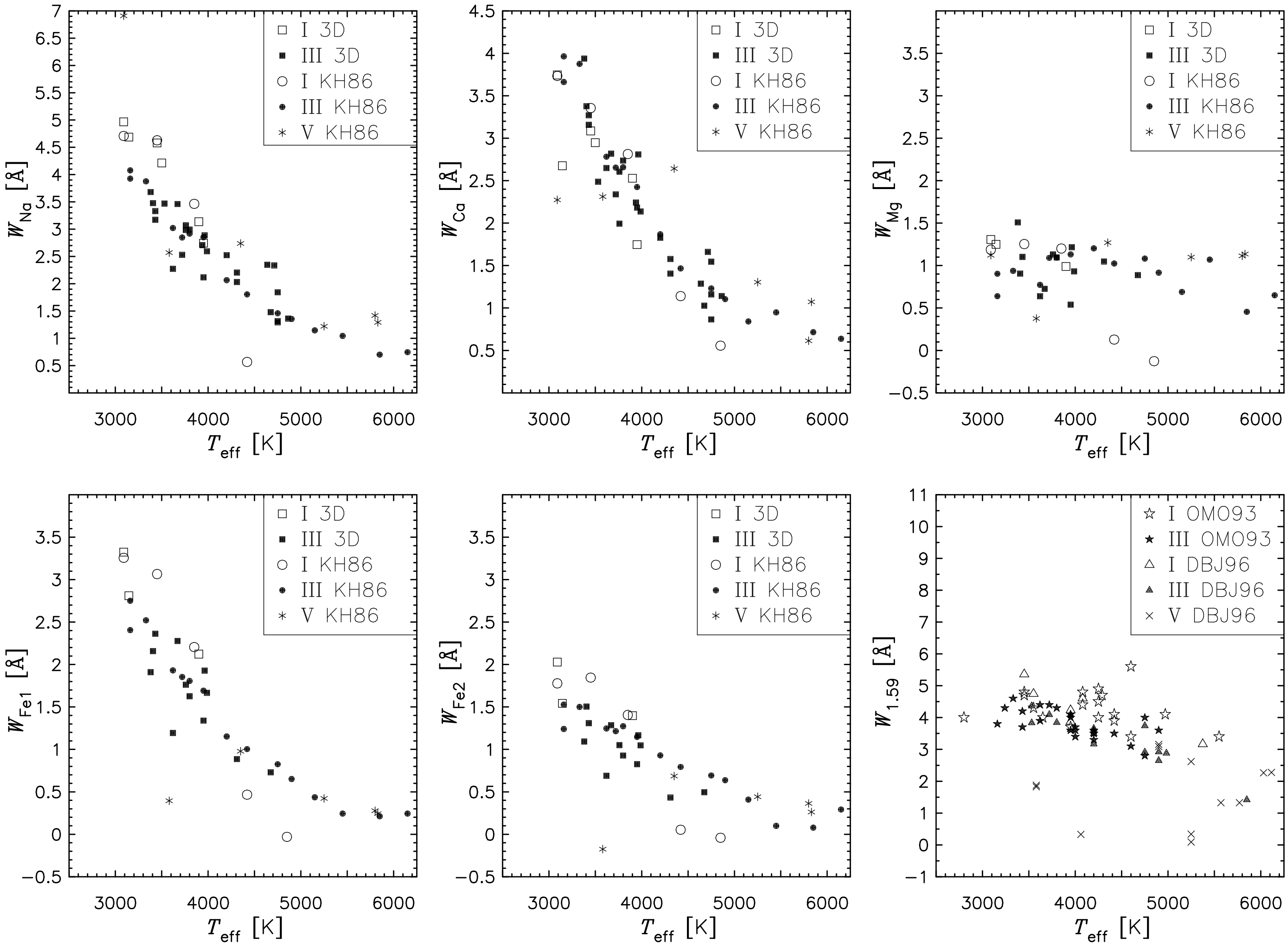

Fig. 2.6.— Variations of the EWs of the atomic absorption features with effective temperature and luminosity class from the 3D sample and from selected existing atlases. *Top left:* Na I feature at 2.2076 μm; *top center:* Ca I feature at 2.2636 μm; *top right:* Mg I feature at 2.2814 μm; *bottom left:* Fe I feature at 2.2263 μm; *bottom center:* Fe I feature at 2.2387 μm; *bottom right:* Si I feature at 1.5892 μm. Open symbols represent data for supergiants, filled symbols data for giants and crosses, data for dwarfs. Different symbols are also used to distinguish between data from various authors (3D: this work, KH86: Kleinmann & Hall 1986, OMO93: Origlia, Moorwood & Oliva 1993, DBJ96: Dallier, Boisson & Joly 1996). The typical uncertainties are ± 0.5 Å.

2.4 The temperature scale

The effective temperature ($T_{\rm eff}$) of stars is generally determined from the observed spectral energy distribution in combination with model atmosphere predictions (*e.g.* Blackwell *et al.* 1990). A more fundamental method based on angular diameters and bolometric fluxes can alternatively be used for nearby stars (*e.g.* Ridgway *et al.* 1980). In both cases, uncertainties arise from the observations, from the assumptions on the structure of the atmosphere and physical conditions (*e.g.* plane-parallel geometry, hydrostatic and local thermodynamic equilibrium) and from the theoretical modeling (*e.g.* limb-darkening corrections, opacities). $T_{\rm eff}$ determinations are particularly difficult for cool stars, notably due to extensive molecular absorptions distorting their spectral energy distributions. Evolved stars (red giants and supergiants, carbon stars) also have complex and expanding atmospheres. In addition, their photometric and spectral properties are often variable, and thermal emission from a surrounding dust shell can contribute to the observed energy distribution.

In order to obtain the most reliable calibrations for supergiants, giants and dwarfs, empirical $T_{\rm eff}$ scales and determinations for G-, K- and M-type stars from various authors were compared (figure 2.7, which also gives the references). The red giants constitute the most complete and consistent sample with respect to $T_{\rm eff}$ determinations, down to spectral type M6. The measurements for supergiants exhibit the largest scatter: $\sigma_{T_{\rm eff,\,I}} \approx 225$ K compared to $\sigma_{T_{\rm eff,\,III,\,V}} \approx 140-170$ K. This reflects the relatively poor knowledge of these objects (less reliable spectral classification, less satisfactory models), due in part to the scarcity of nearby red supergiants for detailed investigations. Fourth-order polynomial fits provide good analytical representations of the empirical data except where there is a break (*e.g.* between K and M giants) and for G-type giants due to ringing effects. The fits for dwarfs and giants are in excellent agreement with those of Ali *et al.* (1995) and Ramírez *et al.* (1997), based on slightly different references. The Schmidt-Kaler (1982) $T_{\rm eff}$ scales follow the analytical fits almost everywhere within the dispersion in the data, and much better reproduce the data in the problematic regions; they are therefore adopted throughout this work.

Several authors have derived temperature scales for carbon stars (*e.g.* Mendoza & Johnson 1965; Bergeat *et al.* 1976; Tsuji 1981a; Ohnaka & Tsuji 1996). However, such calibrations are uncertain, mainly because temperature determinations are still scarce, and the various spectral classification systems proposed in the past have not completely succeeded in providing a consistent temperature sequence. Therefore, it is preferable to use individual determinations. Dominy (1984) derived $T_{\rm eff} = 4700$ K for HD 113801. Given that the MK temperature criteria can be applied to early-R carbon stars, the equivalent oxygen-type for HD 113801 is K1-K2 III (Keenan 1993) and corresponds to

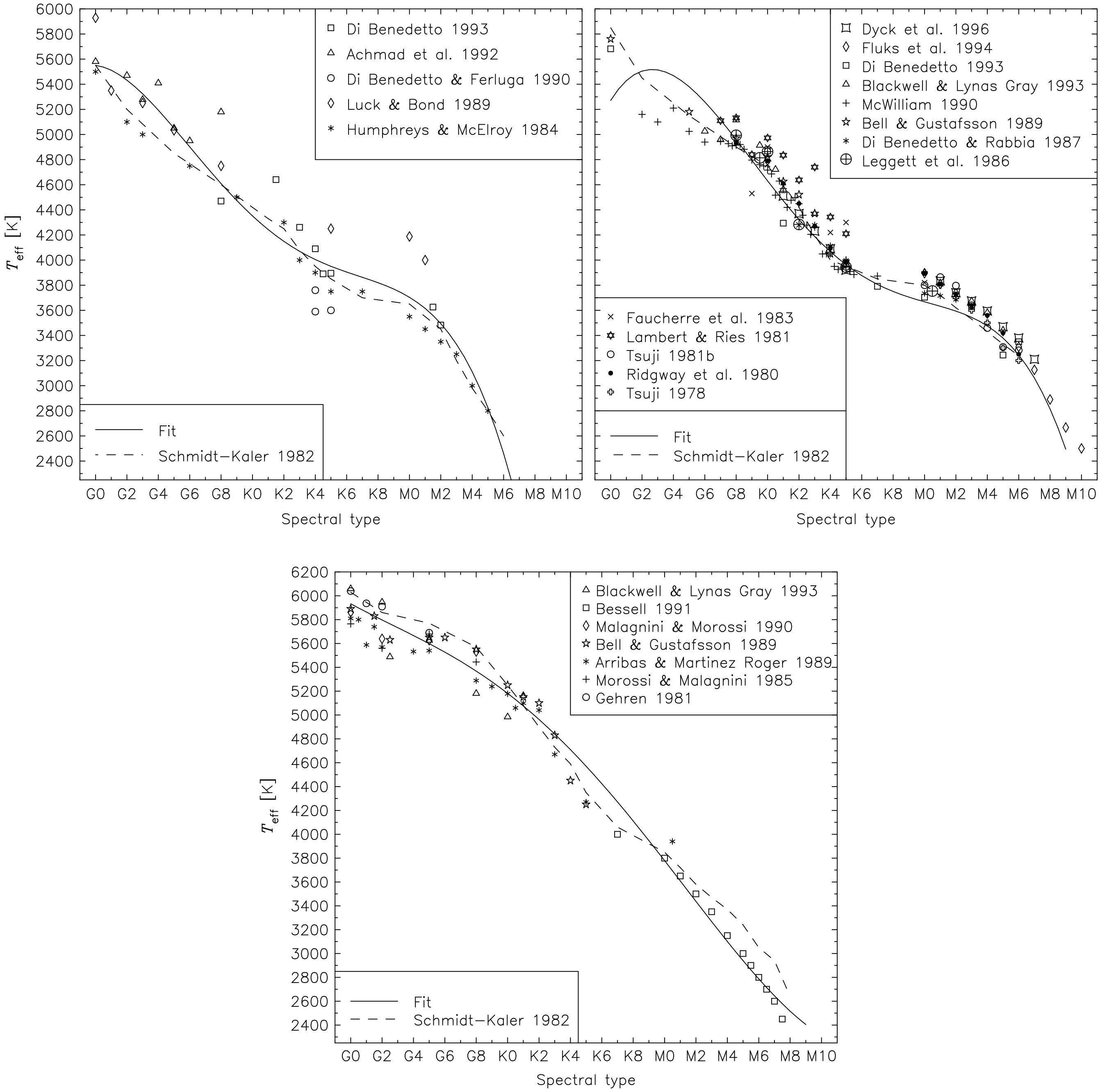

Fig. 2.7.— Empirical effective temperature calibrations and individual determinations for late-type stars: *top left:* supergiants, *top right:* giants, *bottom:* dwarfs. Data from various sources in the literature are represented by different symbols (see insets in each plot). The dashed line in each plot is the Schmidt-Kaler (1982) calibration and the solid line, a fourth-order polynomial fit to the data, excluding Schmidt-Kaler.

$\approx$ 4500 K, close to the result from Dominy. The most reliable $T_{\rm eff}$ determination for the N-type carbon star HD 92055 is from Ohnaka & Tsuji (1996) who accounted for molecular absorptions and extinction, and found $T_{\rm eff} = 3080$ K.

2.5 Discussion

2.5.1 Variations of the equivalent widths with spectral type and luminosity class

As can be seen from figures 2.5 and 2.6, over the range of spectral types considered, the absorption features of interest vary strongly with temperature except for Si I and Mg I. The EWs of the CO bandheads and of the Na I, Ca I and Fe I features in giants and supergiants increase monotonically with decreasing $T_{\rm eff}$ whereas those for Si I and Mg I remain almost constant. The dwarfs are clearly distinguished by lower EWs for $T_{\rm eff} \leq 4000 - 4500$ K, except for Na I and Mg I, even turning over around 4500 K for Ca I and both Fe I. Ali *et al.* (1995) and DBJ96 provide further details on dwarfs. In the rest of this subsection, giants and supergiants are discussed.

In addition to their variation with spectral type, the first overtone CO bandheads longwards of $2.29\,\mu$m also show the long recognized trend with luminosity class for $T_{\rm eff} \leq 4500$ K, supergiants exhibiting deeper absorptions than giants of the same temperature. Below 4000 K, the Na I feature is also stronger in supergiants. A similar but weaker trend is seen for the Fe I lines. The K-band EWs in supergiants seem to decrease more rapidly with increasing $T_{\rm eff}$ above 4500 K than those in giants. However, the range $4500 - 6000$ K at high luminosity is poorly sampled, and this behaviour needs to be confirmed with additional data. The giants generally form a tight distribution in the EWs versus $T_{\rm eff}$ diagrams whereas the supergiants display a larger scatter, especially for the luminosity-sensitive CO bandheads. This can possibly be attributed to the larger uncertainties in the $T_{\rm eff}$ calibration and spectral type assignment as well as the larger range in luminosity within class I (*e.g.* Humphreys & McElroy 1984). The EWs for the first overtone CO bandheads of both carbon stars lie on the loci of giants. However, no conclusion pertaining to these particular types can be reached based on only two measurements.

No metallicity effect is obvious in the data presented here, mainly because of the actually small range in [Fe/H] covered by the samples, with only a few metal-poor and metal-rich stars. From previous empirical and theoretical studies, a variation of the EWs is expected at more extreme metallicities, with an increase from low to high [Fe/H] (*e.g.* Frogel *et al.* 1978; Frogel, Cohen & Persson 1983; Terndrup, Frogel & Whitford 1991; Origlia *et al.* 1997; Oliva & Origlia 1998).

The *observed* variations with spectral type and luminosity class of several of the absorption features considered in this work have been discussed previously by various authors (*e.g.* KH86; Lançon & Rocca-Volmerange 1992; OMO93; Ali *et al.* 1995; DBJ96; Ramírez *et al.* 1997). Efforts have also been made to investigate the dependence of the feature strengths on physical parameters from a *theoretical* point of view using stellar atmosphere models (*e.g.* McWilliam & Lambert 1984; OMO93, Ali *et al.* 1995). However, the complex nature of cool stars has prevented so far a full understanding. In addition, for such purposes, a precise knowledge of the species actually contributing to the observed absorption features is necessary. As emphasized by OMO93, identifications in moderate resolution spectra based on the comparison of line positions may be misleading because different species can produce absorption lines within a given bandpass, and the various line strengths may vary with different stellar parameters.

In this regard, it is instructive to compare the line identifications from Wallace & Hinkle (1996) in their $R \geq 45000$ spectra with the bandpasses used in this work to quantify the strongest features at $R \sim 1000 - 2000$ (figure 2.8). Of all the absorption features discussed here, the Na I, Ca I, Mg I and Fe I features are the most "contaminated", and include contributions from Sc I, Ti I, V I, Si I, S I and HF (1-0) lines. In particular, the variations with temperature and luminosity of the Na I, Ca I and Fe I features seem primarily governed by Sc I, Ti I and V I which may even become the dominant sources of absorption in the coolest giants and supergiants. The identifications adopted by KH86 are actually more appropriate for dwarfs than for giants and supergiants. This is not surprising since these authors identified the features by comparing their spectrum of the K5 V star 61 Cyg A with spectra of sunspots.

It is important to emphasize that the variations of the EWs as discussed here are the *observed variations with spectral type as parametrized by* $T_{\rm eff}$, *and with luminosity class*. These cannot be simply interpreted as direct dependences on stellar $T_{\rm eff}$ and luminosity. Briefly, the contributions from lines of different elements obviously complicate the interpretation of the behaviour of the EWs as a function of the stellar physical parameters. In addition, parameters other than the temperature and luminosity also play an important role in these behaviours, such as the surface gravity, the chemical composition, and the micro-turbulent velocity. A detailed discussion is beyond the scope of this work, but can be found notably in OMO93.

2.5.2 Carbon stars

The spectra of the carbon stars (figure 2.3) are particularly interesting. HD 113801 does not seem to differ from a normal giant, but HD 92055 does. In figure 2.9, the carbon stars are compared to normal giants of similar effective temperature. HD 113801 (C2,1 – R0) is almost identical to its temperature counterpart HD 107328 (K0.5 IIIb). On the

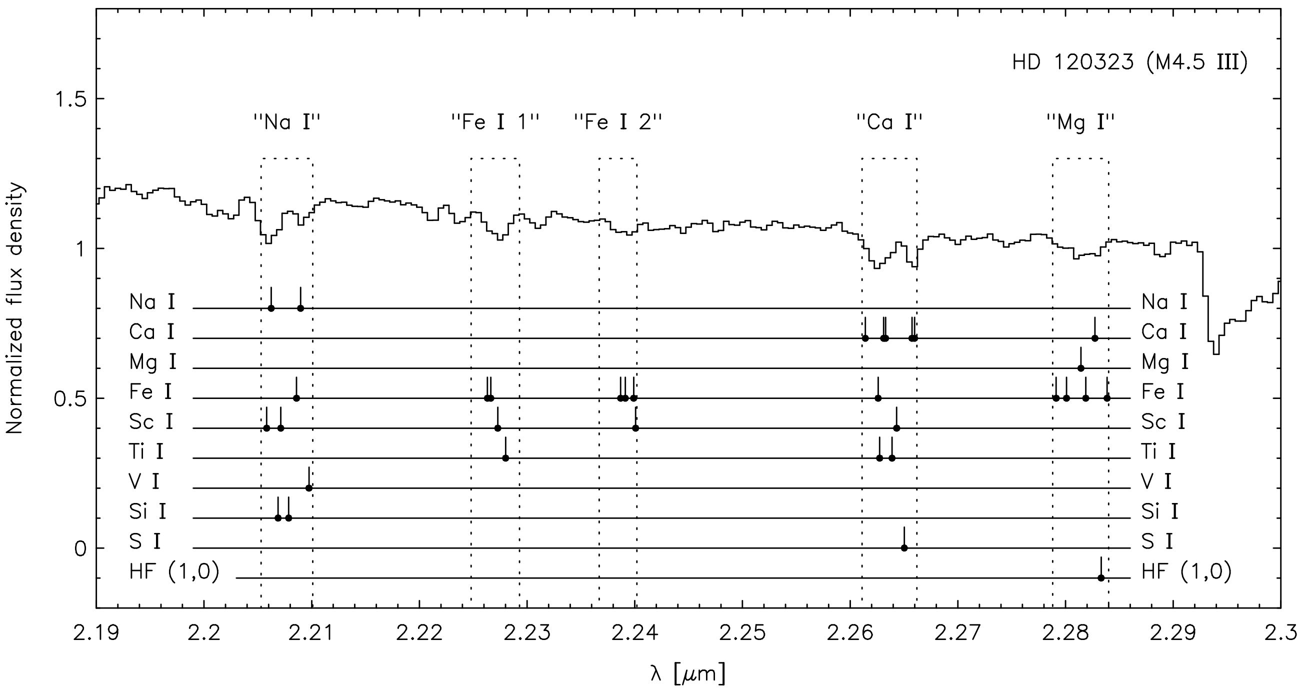

Fig. 2.8.— Positions of the lines of the various elements contributing to the strongest atomic features in medium-resolution spectra of red dwarfs, giants and supergiants as identified by Wallace & Hinkle (1996). The bandpasses used to integrate the depth of the features labeled as "Na I", "Fe I 1", "Fe I 2", "Ca I" and "Mg I" are indicated on the spectrum of HD 120323 by the dashed lines (see table 2.3).

other hand, HD 92055 (C6,3 – N2) shows similar CO bandhead strengths as HD 80431 (M4 III) but a very different continuum riddled with numerous absorption features.

The prominent bands characterizing the optical spectra of carbon stars are mainly due to C_2, CN and CH molecules. Line identifications in the near-infrared are much more uncertain because of the scarcity of empirical spectra and of the lack of laboratory work on some potentially important molecules in the atmosphere of carbon stars. Near-infrared spectra of carbon stars are more complex than those of normal giants and supergiants: the CO lines remain the deepest features but the level of the overall continuum structure is generally elevated and the atomic lines are less prominent (*e.g.* Johnson & Méndez 1970; Wallace & Hinkle 1996). Wallace & Hinkle (1996) identified most of the continuum structure shortwards of 2.29 μm with lines of the CN red system and perhaps some lines of the C_2 Phillips system.

The C_2 and the CN red system bands in the optical are weaker in early-R stars than in N stars — at least in the early-N ones (*e.g.* Yamashita 1972). Assuming C_2 and CN molecules contribute to the near-infrared absorption spectrum of carbon stars, and if the behaviour between early-R and N types of the C_2 and CN features can be

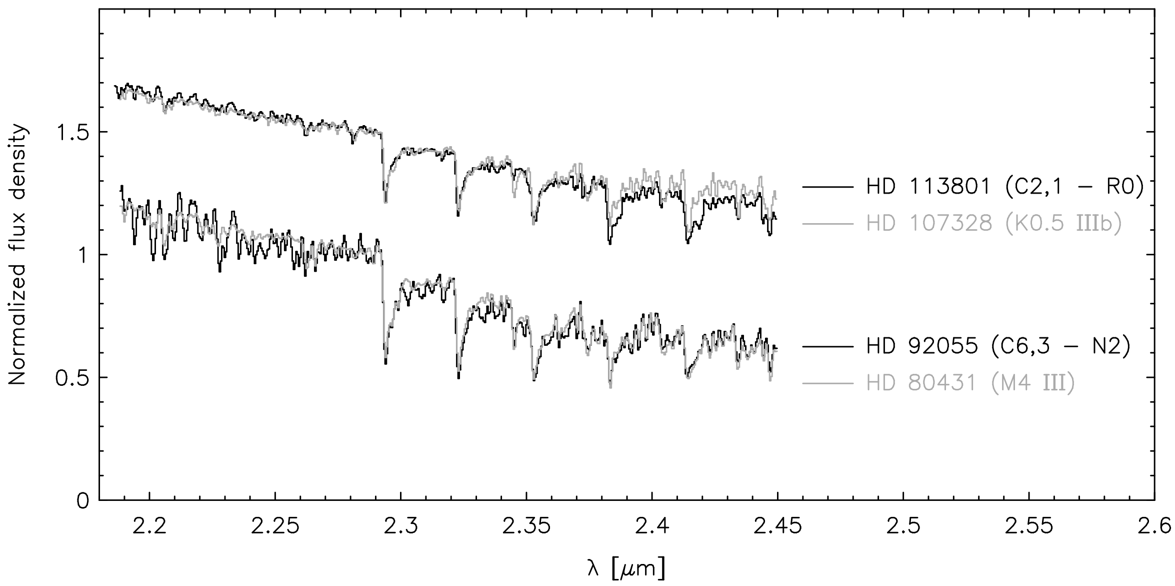

Fig. 2.9.— Comparison of the spectra of the carbon stars HD 113801 and HD 92055 (black lines) with spectra of normal giants of similar effective temperature (grey lines). All spectra have been normalized to unity in the range 2.2875 – 2.2910 μm. The vertical axis is the appropriate linear flux scale for the bottom pair of spectra, the other pair being shifted upwards by an interval of 0.5.

extrapolated at longer wavelengths, the spectra of the two carbon stars presented here could be understood as follows. For both HD 113801 and HD 92055, the first overtone CO bandheads are the most prominent features longwards of 2.29 μm. Shortwards of 2.29 μm, the carbon star features in the early-R type HD 113801 are too weak to be detected at moderate resolution and the striking similarity with early-K giants suggests common sources of opacity for the strongest features. In the N-type star HD 92055, the carbon star features are deep enough to show up clearly and even hide the atomic features.

2.5.3 Stellar temperature and luminosity indicators

In this section, diagnostic tools for population synthesis of composite systems are identified from the EWs discussed above. Empirical relationships constitute useful tools even without the detailed knowledge of the species contributing to the absorptions of interest and their individual dependence on stellar parameters. Because of the restricted range in metallicities of the stellar samples, these tools are reliable only for systems with near-solar abundances.

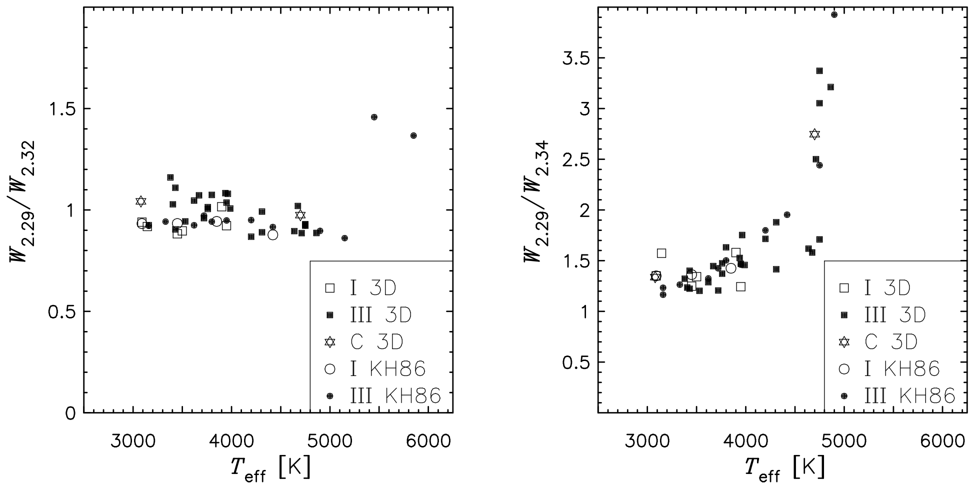

Fig. 2.10.— Variations of the ratios of EWs of the first overtone CO bandheads with effective temperature and luminosity class. *Left:* ^{12}CO (2,0) bandhead at 2.2935μm and ^{12}CO (3,1) bandhead at 2.3227 μm; *right:* ^{12}CO (2,0) bandhead at 2.2935 μm and ^{13}CO (2,0) bandhead at 2.3448 μm. Open symbols represent data for supergiants and carbon stars, and filled symbols data for giants. Different symbols are used to distinguish between data from various authors (3D: this work, KH86: Kleinmann & Hall 1986). The sharp increase of $W_{2.29}/W_{2.34}$ at low temperatures may be an artefact due to the extreme weakness of the ^{13}CO (2,0) bandhead.

$W_{1.62}$ and $W_{\rm Ca}$ constitute pure $T_{\rm eff}$ indicators. All other EWs — except $W_{1.59}$ and $W_{\rm Mg}$ — can also be used to determine the average spectral type but their variation with luminosity class at low temperatures complicates their interpretation. None of the absorption features discussed here varies strictly with luminosity class, so discriminating between giants and supergiants requires prior knowledge of the effective temperature. The most sensitive luminosity indicator is $W_{2.29}$. The ratios $W_{2.29}/W_{2.32}$ and $W_{2.29}/W_{2.34}$ plotted in figure 2.10 show that all three bandheads actually contain the same information about the spectral type and luminosity class for giants and supergiants. The sharp increase of $W_{2.29}/W_{2.34}$ at temperatures above 4500 K likely may be an artefact due to the extreme weakness of the ^{13}CO (2,0) bandhead. For the coolest stars ($T_{\rm eff} \lesssim 4000$ K), $W_{\rm Na}$, $W_{\rm Fe1}$ and $W_{\rm Fe2}$ can in principle also discriminate between luminosity classes if the measurement errors are small enough.

Various combinations of EWs (sums and ratios) were explored as possible temperature and luminosity diagnostic tools. In most cases, the composite indices displayed too large a scatter to provide better indicators than single EWs alone. However, a few proved to be potentially useful and are shown in figure 2.11. As first noted by OMO93, the log ($W_{1.62}/W_{1.59}$) is a very good $T_{\rm eff}$ diagnostic and is not hindered by a luminosity dependence. The log ($W_{1.62}/W_{2.29}$) is also sensitive to temperature and supergiants

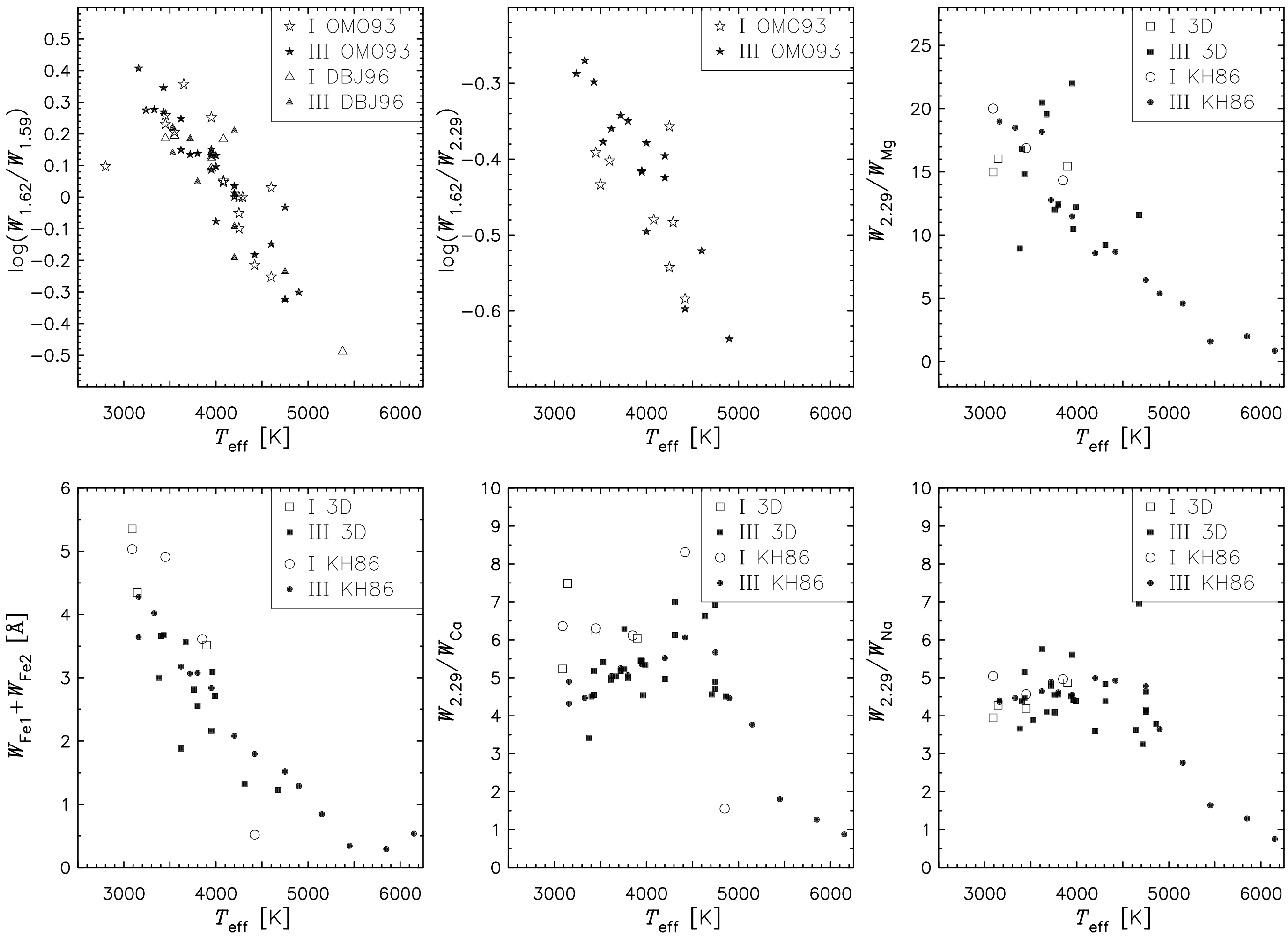

Fig. 2.11.— Variations of composite spectroscopic indices with effective temperature and luminosity class. *Top left:* logarithm of the ratio of EWs of the ^{12}CO (6,3) bandhead at 1.62 μm and of the Si I feature at 1.59 μm; *top center:* logarithm of the ratio of EWs of the ^{12}CO (6,3) and ^{12}CO (2,0) bandheads at 1.62 μm and 2.29 μm respectively; *top right:* ratio of EWs of the ^{12}CO (2,0) bandhead at 2.29 μm and of the Mg I feature at 2.28 μm; *bottom left:* Sum of EWs of the Fe I features at 2.23 μm and 2.24 μm; *bottom center:* ratio of EWs of the ^{12}CO (2,0) bandhead at 2.29 μm and of the Ca I feature at 2.26 μm; *bottom right:* ratio of EWs of the ^{12}CO (2,0) bandhead at 2.29 μm and of the Na I feature at 2.21 μm. Open symbols represent data for supergiants, and filled symbols data for giants. Different symbols are used to distinguish between data from various authors (3D: this work, KH86: Kleinmann & Hall 1986, OMO93: Origlia, Moorwood & Oliva 1993, DBJ96: Dallier, Boisson & Joly 1996).

have a lower ratio than giants. These two indicators have been extensively discussed in OMO93, Oliva *et al.* (1995), Origlia *et al.* (1997) and Oliva & Origlia (1998).

$W_{2.29}/W_{\rm Mg}$ has a pronounced temperature sensitivity, mostly due to $W_{2.29}$, but the number of data points is smaller and the scatter is larger than for $\log(W_{1.62}/W_{1.59})$. The sum of $W_{\rm Fe1}$ and $W_{\rm Fe2}$ provides an additional temperature diagnostic with only marginal luminosity sensitivity, and a higher S/N ratio measurement than the individual Fe I EWs. Combining the sharp increase of $W_{2.29}$ and $W_{\rm Ca}$ with decreasing $T_{\rm eff}$ and the luminosity sensitivity of $W_{2.29}$ at $T_{\rm eff} \lesssim 4500$ K results in a $W_{2.29}/W_{\rm Ca}$ ratio discriminating between giants and supergiants. The $W_{2.29}/W_{\rm Na}$ is also shown in figure 2.11 although since $W_{2.29}$ and $W_{\rm Na}$ exhibit similar behaviours with $T_{\rm eff}$ and luminosity class, their ratio is almost identical in giants and supergiants cooler than 4500 K.

2.5.4 Contamination by featureless continuum sources

The interpretation of the EWs becomes more intricate in objects where featureless continuum sources contribute to the near-infrared emission. For example, thermal emission from hot dust ($T \approx 600 - 1000$ K) or from an important population of young stars, strong free-free emission or non-thermal emission from an AGN can dilute the stellar absorption features. The contribution and spectral shape of these continuum sources are often difficult to constrain. This problem can be circumvented by using dilution-free indicators made up of ratios of EWs of features that are close enough in wavelength to be affected by similar amounts of dilution, so that their ratio is essentially insensitive to dilution.

OMO93 proposed $\log(W_{1.62}/W_{1.59})$ as a dilution-free temperature indicator, and used it in combination with $W_{1.62}$ and $\log(W_{1.62}/W_{2.29})$ to constrain the amount of dilution around $1.6\,\mu$m and $2.3\,\mu$m in various types of galaxies (Oliva *et al.* 1995). In particular, they used spectroscopic equivalents of colour-magnitude plots, namely the $W_{1.62}$ vs $\log(W_{1.62}/W_{1.59})$ and $W_{1.62}$ vs $\log(W_{1.62}/W_{2.29})$ diagrams (figure 2.12). In these plots, undiluted stellar populations of clusters and of elliptical, spiral and even starburst galaxies occupy regions falling on the observed distribution for individual stars (Oliva *et al.* 1995). The amount of dilution near $1.6\,\mu$m is determined from the vertical displacement with respect to the locus of stars in the $W_{1.62}$ vs $\log(W_{1.62}/W_{1.59})$ diagram. Similarly, the amount of dilution around $2.3\,\mu$m is estimated from the horizontal displacement in the $W_{1.62}$ vs $\log(W_{1.62}/W_{2.29})$ diagram once the $W_{1.62}$ has been corrected for dilution. However, because giants and supergiants appear to lie on separate branches in the latter plot, two solutions for the $2.3\,\mu$m dilution are possible unless the luminosity class can be determined independently.

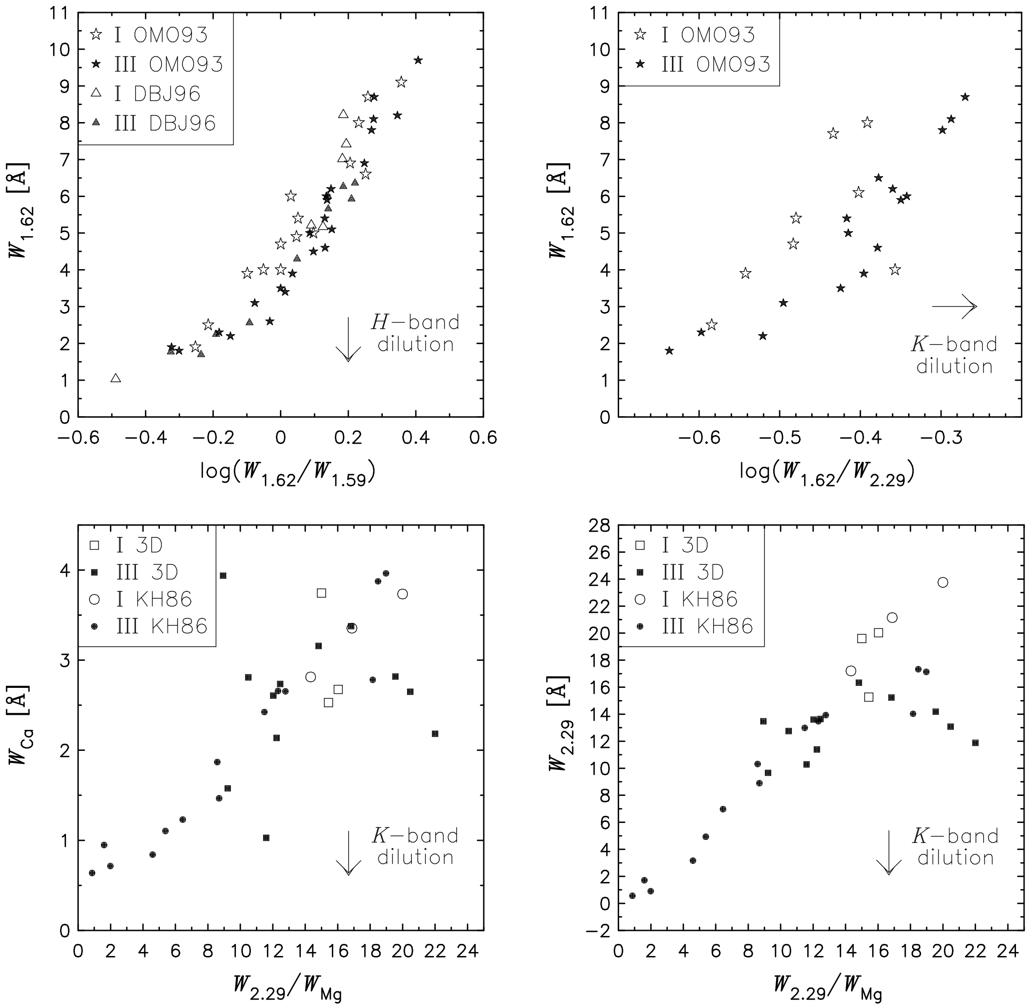

Fig. 2.12.— Variations of the EWs of selected absorption features as functions of temperature-sensitive ratios of EWs, as diagnostics for the amount of dilution by sources of featureless continuum emission. *Top left:* EW of the ^{12}CO (6,3) bandhead at 1.6187 μm versus the logarithm of its ratio with the EW of the Si I feature at 1.5892 μm; *top right:* EW of the ^{12}CO (6,3) bandhead at 1.6187 μm versus the logarithm of its ratio with the EW of the ^{12}CO (2,0) bandhead at 2.2935 μm; *bottom left:* EW of the Ca I feature at 2.2636 μm versus the ratio of the EWs of the ^{12}CO (2,0) bandhead at 2.2935 μm and of the Mg I feature at 2.2814 μm; *bottom right:* EW of the ^{12}CO (2,0) bandhead at 2.2935 μm versus its ratio with the EW of the Mg I feature at 2.2814 μm. Open symbols represent data for supergiants, and filled symbols data for giants. Different symbols also distinguish between data from various authors (3D: this work, KH86: Kleinmann & Hall 1986, OMO93: Origlia, Moorwood & Oliva 1993, DBJ96: Dallier, Boisson & Joly 1996). The arrows indicate the effects of dilution by continuum sources other than late-type stars.

Similar diagrams constructed strictly from the K-band data are less satisfactory mainly because of larger scatter and/or absence of strong enough temperature dependence in ratios of EWs. Furthermore, the variation with luminosity of almost all indices at low temperatures (single and combined EWs) may introduce degeneracy in the determination of the amount of dilution. The best diagrams, in terms of smaller scatter, are $W_{\rm Ca}$ vs $W_{2.29}/W_{\rm Mg}$ and $W_{2.29}$ vs $W_{2.29}/W_{\rm Mg}$, and are shown in figure 2.12. $W_{2.29}/W_{\rm Mg}$ constitutes the dilution-free temperature indicator while $W_{\rm Ca}$ and $W_{2.29}$ also serve as temperature indicators but are potentially affected by dilution, which can then be estimated from the vertical displacement. $W_{\rm Ca}$ vs $W_{2.29}/W_{\rm Mg}$ would in principle be the best K-band tool to constrain the fraction of the continuum around $2.3\,\mu$m not originating from evolved stars because both indices are only sensitive to temperature, yielding unambiguous solutions for the dilution. However, the relatively loose distribution of the data limits the accuracy. The "double-branched distribution" of other similar diagrams in the $T_{\rm eff} \lesssim 4500$ K regime is illustrated in the $W_{2.29}$ vs $W_{2.29}/W_{\rm Mg}$ plot. The difference in dilution inferred assuming a population of supergiants instead of giants can amount to 50% for very cool populations.

By way of conclusion, the ^{12}CO (2,0) and ^{12}CO (6,3) bandheads as well as the Si I feature at 1.59 μm remain at present the most useful and reliable spectroscopic diagnostic tools for studies of stellar populations at moderate spectral resolution in the range $\lambda = 1.5 - 2.5$ μm. Despite some drawbacks, they have the advantage of being amongst the strongest, purest and best-studied features in the near-infrared spectra of red giants and supergiants.

2.5.5 Remaining limitations

The indicators proposed above and partly by the other authors cited in this chapter seem promising at first glance but applications to extragalactic studies have shown some limitations of these tools (see *e.g.* Oliva *et al.* 1995 and chapter 6). Firstly, the frequently limited S/N for extragalactic sources and the dispersion in the stellar data translates in relatively large uncertainties in the derived average spectral type and luminosity class of the evolved population, typical errors on $T_{\rm eff}$ amounting to approximately ± 350 K (see also Ali *et al.* 1995). Secondly, the atomic features in the K-band are intrinsically weak. Thirdly, the amount of dilution can only be determined to within $\approx 10\% - 20\%$ due to the scatter in the template data, and is further complicated by the variations with luminosity class of most indices. In addition, the Si I feature at $1.59\,\mu$m may be contaminated by the hydrogen recombination line Br14 at $1.5881\,\mu$m from H II regions along the line of sight. Although the Br14 line can be removed using the Br13 profile, this increases the uncertainty on $W_{1.59}$ and thus on the useful $\log(W_{1.62}/W_{1.59})$.

The interpretation of the observed EWs (or of the entire spectrum) in terms of a single average spectral type and luminosity class is a simplistic one and may be misleading when distinct evolved populations contribute to the integrated continuum emission, for example young supergiants formed in a recent starburst and older, pre-existing giants. In some cases, the stellar EWs alone are not sufficient to investigate composite systems, and need to be complemented with additional indicators sensitive to the stellar contents and the star formation parameters such as the mass-to-light ratio, and the K-band-, Lyman continuum and bolometric luminosities (see also Oliva *et al.* 1995).

There is still a definite need for additional data covering a wider range of stellar parameters especially in metallicity and at high luminosities, probing more diverse stellar evolutionary stages and including composite systems to *1)* provide a more complete set of empirical templates to which observations of clusters and galaxies can be compared, and *2)* better constrain theoretical models. Indeed, most of the stars for which moderate resolution near-infrared spectroscopy exists have [Fe/H] in the range -0.3 to $+0.1$ and only a few exhibit larger abundance anomalies. In addition, the data for supergiants are still relatively scarce. Consequently, model predictions for high-luminosity stars and stars with more extreme metallicities cannot be thoroughly tested against observations. Moreover, the age-metallicity degeneracy, a well-known problem in stellar population studies from optical and ultraviolet data, has to be clarified in the near-infrared. The work of Origlia, Oliva and coworkers (*e.g.* Origlia *et al.* 1997; Oliva & Origlia 1998) constitutes a valuable effort in this direction. Finally, the lack of spectroscopic observations is most severe for peculiar red giants such as Miras, S stars and N-type carbon stars which are presumably related to the AGB phase. Such stars potentially contribute a non-negligible fraction of the integrated near-infrared output of stellar populations at certain evolutionary phases (*e.g.* Bruzual & Charlot 1993).

2.6 Summary

Moderate resolution K-band spectra of 33 late-type giants and supergiants were obtained with the aim of widening existing near-infrared stellar libraries useful for stellar population synthesis of clusters and galaxies. The EWs of the strongest absorption features were computed: the Na I 2.2076$\,\mu$m and Ca I 2.2636$\,\mu$m features, and the ^{12}CO (2,0), ^{12}CO (3,1) and ^{13}CO (2,0) bandheads. Relationships between these EWs and the spectral resolving power (or, equivalently, the velocity dispersion) were derived, allowing comparison between data sets obtained at different resolution in the range $R \sim 600 - 3000$. In addition, the EWs of the Mg I 2.2814$\,\mu$m feature as well as of the Fe I features at 2.2263$\,\mu$m and 2.2387$\,\mu$m were measured in a subset of the spectra.

The 3D data set was augmented with EWs obtained from other similar stellar libraries, and complemented with EWs of the ^{12}CO (6,3) bandhead and Si I 1.5892$\,\mu$m feature in the H-band. This extended database was used to assess the consistency between the various data sets, and to further investigate spectroscopic diagnostics of spectral type and luminosity class of stars. The main conclusions are:

- The existing data sets compare remarkably well. Compiled together they better constrain the variation of several absorption features with spectral type and luminosity class found by various authors in the past based on smaller samples.
- Several features provide useful tools in stellar population studies of clusters and galaxies. $W_{2.29}$, $W_{1.62}$ and $W_{1.59}$ constitute the best diagnostic tools to constrain the average spectral type and luminosity class of cool evolved stars, and the contribution from featureless continuum sources (young hot stars, non-stellar sources). $W_{\rm Ca}$ and $W_{\rm Mg}$ offer alternatives to $W_{1.62}$ and $W_{1.59}$ in the K-band.
- There is still an important need for data for red supergiants, AGB stars such as Miras and carbon stars, and at both high and low metallicities.

Chapter 3

Evolutionary synthesis models for starburst galaxies

3.1 Introduction

Evolutionary synthesis refers to the modeling of the complete evolutionary path of a stellar system to the presently observed state. Assuming a star formation history, the evolution of the integrated properties and spectrum of an ensemble of stars specified by an initial mass function is followed from the birth of the first stars. Evolutionary synthesis is intrinsically more powerful than the simpler population synthesis in studies of stellar clusters and galaxies, since it allows the investigation of the star formation parameters and history.

The application of evolutionary synthesis to M 82 constitutes a major part of this thesis work (see chapter 7). The modeling of the stellar and nebular properties of individual stellar populations is performed using the stellar evolutionary synthesis code STARS (Kovo, Sternberg & Alexander 1998) and the photoionization code CLOUDY (Ferland 1996). Several improvements were made recently in order to optimize the models for applications to near- and mid-infrared spectroscopic data. Specifically, the set of properties predicted by STARS was augmented with new diagnostic tools available with the 3D imaging spectrometer, namely near-infrared stellar absorption features. In addition, a spectral synthesis routine was developed to generate the detailed integrated spectral energy distribution (SED) used as input to CLOUDY, for comparison with observations of mid-infrared spectra obtained with the Short Wavelength Spectrometer on board *ISO*. In addition, the stellar evolutionary tracks used were extended and new theoretical stellar SEDs were implemented to better account for the evolution and properties of the stellar populations accessible in the range $\lambda = 1 - 40$ μm with 3D and SWS (young, massive stars and cool, evolved stars).

In this chapter, the two main programs STARS and CLOUDY are briefly described, together with the improvements made to STARS and the development of a new program for the purpose of this thesis work:

- the inclusion of the thermally-pulsing asymptotic giant branch phase for intermediate-mass stars,
- the prediction of the near-infrared stellar equivalent widths presented in the previous chapter,
- the prediction of the integrated properties for more realistic starburst populations composed of an ensemble of clusters with a luminosity distribution.

The latter item constitutes an additional step in the modeling of starbursts, performed with the new code CLUSTERS and based on the results obtained with STARS and CLOUDY. Figure 3.1 gives a flow chart providing an overview of the complete modeling procedure, which consists of three steps:

1. the prediction with STARS of the integrated properties of an evolving stellar cluster described by an initial mass function, given a star formation rate;
2. the prediction with CLOUDY of the emission spectrum of a gaseous nebula in response to the impinging SED of the stellar cluster;
3. the modeling with CLUSTERS of the integrated stellar and nebular properties for an *ensemble* of evolving clusters which follow a cluster luminosity function, given a cluster formation rate.

Steps 1 and 2 provide the integrated properties of *single* evolving clusters. Step 3 combines the "cluster evolutionary tracks" generated from steps 1 and 2, weighted according to luminosity and cluster formation rate, to compute the integrated properties of an *ensemble* of evolving clusters.

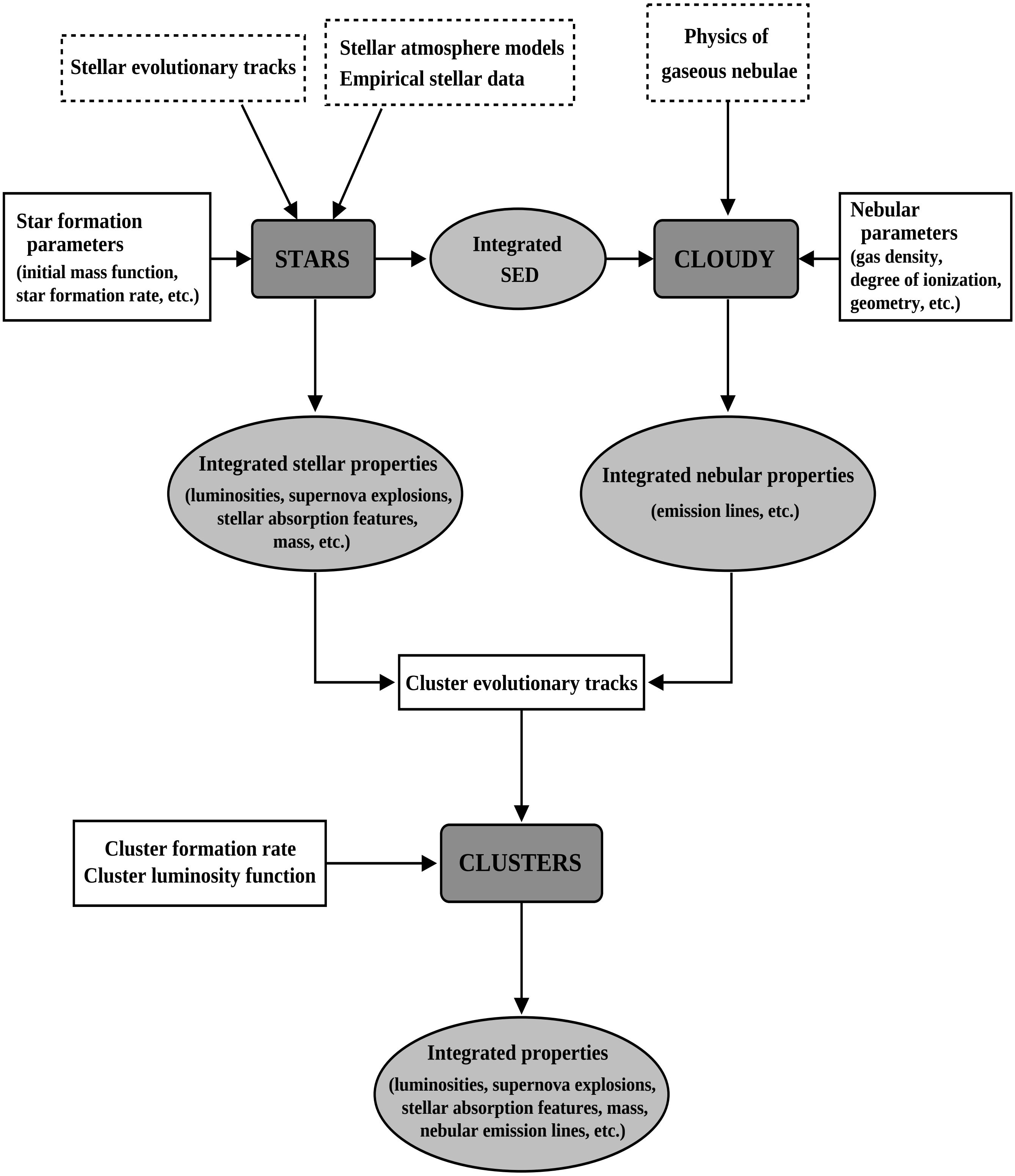

Fig. 3.1.— Flow chart for the evolutionary synthesis models applied in this work, and described in this chapter. The modeling procedure consists of three steps, based on the programs STARS, CLOUDY and CLUSTERS, and represented as dark-shaded boxes (see text). The boxes with dashed borders represent the main "ingredients" used by STARS and CLOUDY. The boxes with solid borders and the light-shaded ovals indicate for each program the direct input and output respectively.

3.2 Modeling of integrated stellar properties

3.2.1 The evolutionary synthesis code STARS

The modeling of integrated properties of evolving stellar populations is based on the evolutionary synthesis code STARS, written by Kovo, Sternberg & Alexander (1998). This code is similar to other models developed by various investigators in the past (*e.g.* Tinsley 1972; Huchra 1977; Bruzual 1983; Guiderdoni & Rocca-Volmerange 1987; Mas-Hesse & Kunth 1991; Doyon, Joseph & Wright 1994; Leitherer & Heckman 1995; Lançon & Rocca-Volmerange 1996). It has been used previously in several studies of starburst systems (*e.g.* Krabbe, Sternberg & Genzel 1994; Genzel *et al.* 1995; Tacconi-Garman, Sternberg & Eckart 1996; Böker, Förster Schreiber & Genzel 1997; Schinnerer *et al.* 1997; Maiolino *et al.* 1998). STARS is briefly described here; appendix B provides a more detailed description of the code, as well as of the theoretical stellar atmosphere models and empirical data used for the energy distributions of individual stars.

STARS is based on the most recent "Geneva" stellar evolutionary tracks, which cover initial stellar masses between 0.8 $M_\odot$ and 120 $M_\odot$ for five metallicities and two assumptions on the mass-loss rates for high-mass stars (Schaller *et al.* 1992; Schaerer *et al.* 1993a, 1993b; Charbonnel *et al.* 1993; Meynet *et al.* 1994). Representative tracks are illustrated in figure A.1 of appendix A, where various stellar evolutionary phases are identified. STARS follows the evolution in the theoretical Hertzsprung-Russell diagram (HRD) of a stellar population whose composition at birth is specified by a power-law initial mass function (IMF)

$$\frac{\mathrm{d}N}{\mathrm{d}m} \propto m^{-\alpha}. \tag{3.1}$$

between a lower and upper mass cutoff, m_{low} and m_{up}. The star formation rate (SFR) is assumed to decline exponentially as

$$R(t_{\mathrm{b}}) = R_0\, e^{-t_{\mathrm{b}}/t_{\mathrm{sc}}}, \tag{3.2}$$

where t_{b} is the time elapsed since the onset of star formation (or "burst age"), t_{sc} is the burst timescale, $R(t_{\mathrm{b}})$ is the SFR at age t_{b}, and R_0 is the initial SFR. The SFR is expressed in $\mathrm{M_\odot\,yr^{-1}}$.

At any given age, the distribution of the stellar population in the HRD is computed and the integrated properties are obtained by summing over those of all the stars present. STARS computes a wide range of stellar properties; the most relevant ones for the purpose of this thesis include the complete spectral energy distribution (SED), the hydrogen ionizing luminosity (or Lyman continuum luminosity $L_{\rm Lyc}$, $\lambda < 912$ Å), the bolometric luminosity ($L_{\rm bol}$), the K-band luminosity (L_K, between $1.9\,\mu$m and $2.5\,\mu$m), the gas mass consumed ($M^\star$) and the rate of supernova explosions ($\nu_{\rm SN}$).

The integrated SED is intended specifically for the computation of the emission spectrum of nebulae photoionized by the stars, such as H II regions (section 3.3). The choice of appropriate SEDs for individual stars is thus crucial, especially for the hot, massive ones. A hybrid grid of stellar SEDs was generated from two libraries of theoretical model atmospheres. The Kurucz (1992) models, which assume local thermodynamical equilibrium (LTE), are used for stars with effective temperatures $T_{\rm eff} \leq 19000$ K. The effects of line blanketing in the rapidly expanding atmospheres of hotter stars are not well represented by LTE models. The new non-LTE stellar atmosphere models for $T_{\rm eff} = 25000 - 65000$ K from Pauldrach *et al.* (1998) are more appropriate and are therefore adopted at $T_{\rm eff} \geq 25000$ K. The SEDs for stars with intermediate temperatures are obtained by interpolating between the Kurucz and the Pauldrach *et al.* models.

Similarly, simple black-body approximations or currently available model atmospheres do not reproduce satisfactorily the energy distributions of cool stars, which are distorted by extensive molecular absorption and potentially contaminated by thermal emission from a circumstellar dust shell. The relevant properties for cool stars (optical and near-infrared luminosities) are therefore derived from the empirical bolometric corrections from Schmidt-Kaler (1982) and the broad-band colours from Koornneef (1983b). The importance of using the more appropriate empirical data is stressed by the fact that red giants and supergiants usually dominate the near-infrared stellar continuum emission from composite systems. The composition of cool, evolved stellar populations provides useful constraints for the star formation history. Therefore, part of the recent improvements made to STARS focussed on cool stars, and are described below.

3.2.2 Extension of the stellar evolutionary tracks: TP-AGB phase

The Geneva tracks follow the evolution of high-mass stars up to the end of the carbon-burning phase, of intermediate-mass stars up to the end of the early asymptotic giant branch (E-AGB), and of low-mass stars up to the He-core flash. Later evolutionary stages for high- and low-mass stars do not have important consequences on the modeling of starburst galaxies. Indeed, the pre-supernova stage for massive stars can be neglected because of its very short duration (a few months to a few years; Woosley & Weaver 1986). For low-mass stars, the post-He-core flash evolution is slower but occurs after a few 10^9 yr or more, so that it is barely relevant in starburst populations, usually much younger. In the cases where an older, pre-existing stellar population has to be accounted for, low-mass stars in post-He-core flash phases (horizontal branch, asymptotic giant branch) will be outshined by other stars in different phases or mass ranges provided the star formation timescale is long enough. In addition, they trace much earlier star formation activity which, in the context of starburst studies, becomes essentially equivalent to that traced by normal red giants.

Intermediate-mass stars, on the other hand, may become important contributors to the integrated properties while undergoing double-shell burning on the thermally-pulsing asymptotic giant branch (TP-AGB), especially at wavelengths between $1\,\mu$m and $5\,\mu$m owing to their large luminosities and low temperatures. Stars with initial masses from 7 $M_\odot$ to 2 $M_\odot$ reach the TP-AGB phase in about 50 Myr to 1 Gyr. Although this evolutionary stage lasts typically no more than about one million years, the combination of large luminosities and IMF-weighting results in measurable effects on various properties predicted from theoretical evolutionary synthesis models (*e.g.* Charlot & Bruzual 1991).

Observationally, TP-AGB stars have been known for a long time to exist in the Magellanic Clouds (Costa & Frogel 1996 and references therein). There is now growing evidence for the presence of important populations of these luminous, intermediate-age stars contributing significantly to the integrated light in the *central regions* or *bulges* of several nearby dwarf elliptical and spiral galaxies, including our own (*e.g.* Blum, Sellgren & DePoy 1996a), M 31 (Rich, Mould & Graham 1993; Rich & Mighell 1995; Davidge *et al.* 1997), M 32 (Freedman 1992; Elston & Silva 1992), M 33 (McLean & Liu 1996) and the M 31 companions (Lee 1996; Lee, Freedman & Madore 1993; Davidge 1994; Martínez-Delgado & Aparicio 1998).

In the past, the TP-AGB phase has been included in evolutionary synthesis modeling optimized for evolved systems such as elliptical galaxies, or for the Magellanic Clouds (*e.g.* Charlot & Bruzual 1991; Bressan, Chiosi & Fagotto 1994; Worthey 1994; Girardi & Bertelli 1998). Lançon & Rocca-Volmerange (1994, 1996) were probably the first to introduce this evolutionary stage in "starburst models", but they barely discuss the implications. The implementation of the TP-AGB phase in STARS, thus, had two motivations. Firstly, it allowed a quantitative investigation of its influence on various cluster properties. Secondly, it seems relevant in studies of the nuclear regions of starburst galaxies — as in this work, and potentially helps to disentangle stars born in earlier bursts or which belong to an underlying population of continuously forming stars, from supergiants associated with recent bursts.

Several uncertainties remain, however, concerning the TP-AGB evolution. The major problem is linked to the "carbon star mystery" (Iben 1981), raised by the observed deficit of high-luminosity carbon stars ($L_{\rm bol} > 10^4$ $L_\odot$) and the excess at lower luminosities in the Large Magellanic Cloud compared to theoretical predictions. The deficit at high luminosities also extends to oxygen-rich AGB stars (Frogel, Mould & Blanco 1990; Reid, Tinney & Mould 1990). Possible theoretical scenarios have been explored to solve this discrepancy but are not completely satisfactory (*e.g.* Iben & Renzini 1983; Groenewegen & de Jong 1993; Boothroyd, Sackmann & Wasserburg 1995). Recent searches for *obscured* luminous AGB stars in the Large Magellanic Cloud remained inconclusive (*e.g.* Reid, Hughes & Glass 1995; Loup *et al.* 1997; van Loon *et al.* 1998). No definitive consensus has been reached yet concerning the details of theoretical modeling and, consequently, on the observational sequence in terms of the stellar types believed to lie on the TP-AGB (*e.g.* Groenewegen & de Jong 1993; Groenewegen, van den Hoeck & de Jong 1995; Wallerstein 1988; Gustafsson 1989; Gautschy & Saio 1996).

Despite the above uncertainties, an estimate of the contribution of TP-AGB stars to integrated properties of evolving stellar populations is possible. Indeed, the morphology and location of the TP-AGB in the HRD does not differ significantly amongst recent models of various authors, and agrees well with the observations for those stars with measured temperatures and luminosities. Both $L_{\rm bol}$ and $T_{\rm eff}$ depend only weakly on the few necessary assumptions made on the input physics (see Charlot & Bruzual 1991). In particular, the average luminosity during the TP-AGB evolution is related to the well-determined core mass in a simple way (Paczyński 1970), and is thus little sensitive to the more uncertain parameters governing mass-loss and photospheric chemical abundances (*e.g.* Groenewegen & de Jong 1993). These have a much larger impact on the duration of the TP-AGB phase and on the line-blanketing throughout the spectrum. Total AGB lifetimes are compared in table 3.1 for models of several authors.

The models of Bedijn (1988) were chosen to extend the Geneva tracks because of their simplicity and because they are representative of other, more complicated models for the parameters of relevance here (age, $T_{\rm eff}$, $L_{\rm bol}$). Another attractive feature of these models is that they reproduce well the statistical properties of local Miras and OH/IR stars, and are closely linked to the most widely accepted evolutionary scenario between different types of TP-AGB stars. Regardless of the details, the assumed scenario is that of an initially unobscured, short-period variable star which becomes progressively cooler, intrinsically more luminous but more obscured due to the building-up of a circumstellar shell resulting from mass-loss, and with a longer variability period. Accordingly, two evolutionary points were added to the Geneva tracks to represent

Table 3.1: Total lifetimes of intermediate-mass stars in the TP-AGB phase[(a)]

M	Lifetimes in 10^5 yr			
[$M_\odot$]	Bedijn	GHJ	V&W	F&C
2.0	13.9	7.5	11.8	—
2.5	13.8	12.1	21.8	—
3.0	13.7	16.2	—	12.2
3.5	—	9.7	4.3	—
4.0	5.5	6.8	—	2.3
5.0	3.2	5.5	2.6	1.3
6.0	4.9	—	—	0.9
7.0	5.2	5.8	—	—

[(a)] The references are Bedijn (1988), Groenewegen, van den Hoek & de Jong (1995; "GHJ"), Vassiliadis & Wood (1993; "V&W") as quoted in Ortiz & Maciel (1996), and Forestini & Charbonnel (1997; "F&C"). The various models compared here are for solar-metallicity stars and, as much as possible, for similar laws and parameters describing mass-loss.

the TP-AGB phase. They correspond to different pulsation modes ("first overtone" and "fundamental" modes) and are associated observationally with short-period optical Mira variables and with long-period OH/IR stars. Bedijn's prescriptions extend smoothly the E-AGB phase from the Geneva tracks (figure 3.2).

Since TP-AGB stars are most conspicuous in the near-infrared, the attribution of the near-infrared photometric properties needs to be considered carefully. Unfortunately, systematic studies of these stars are scarce at near-infrared wavelengths and represent a rather inhomogeneous data set. An alternative approach, similar to that followed by Charlot & Bruzual (1991), was adopted. Given the small dispersion in $T_{\rm eff}$ for stars of various masses on their TP-AGB and since the time spent in the fundamental mode as a long-period OH/IR variable is at most 30% of the total TP-AGB lifetime according to Bedijn's models, the average bolometric correction and broad-band colours of the prototypical Mira variable ω Cet were assigned to all TP-AGB stars. They were derived from the data of Mendoza & Johnson (1965) and Zhou *et al.* (1984), and are given in table 3.2.

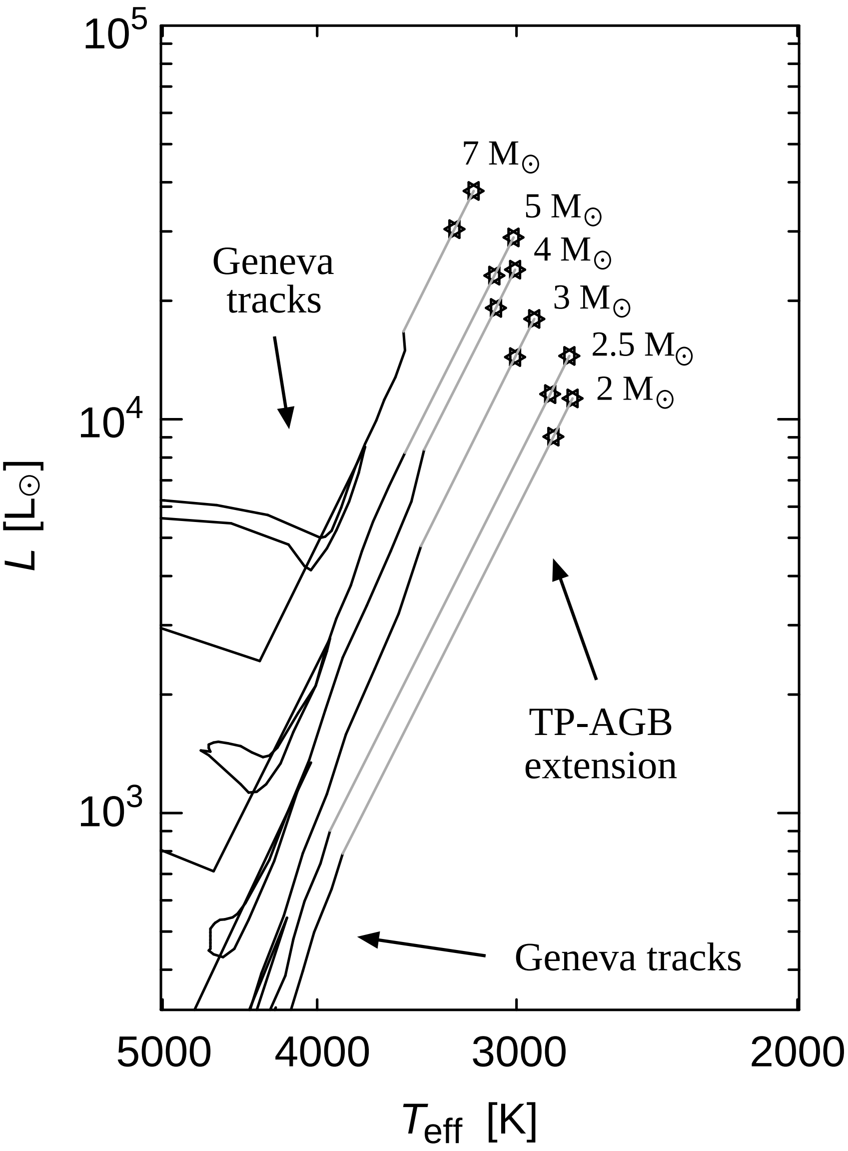

Fig. 3.2.— Evolutionary tracks in the theoretical HRD for the TP-AGB phase of intermediate-mass stars (initial masses between 2 $M_\odot$ and 7 $M_\odot$; grey lines), computed from the models of Bedijn (1988). The two "stars" on each track indicate the evolutionary points corresponding to the two pulsation modes considered (first overtone followed by fundamental mode). The black lines represent the Geneva tracks.

Table 3.2: Adopted photometric properties of TP-AGB stars[a]

Property[b]	Value
BC	-8.0 mag
$V - K$	10.3 mag
$J - K$	1.3 mag
$H - K$	0.3 mag

[a] Characteristic of the prototypical Mira variable ω Cet. The data are from Mendoza & Johnson (1965) and Zhou *et al.* (1984).

[b] The bolometric correction (BC) gives the difference in magnitude between the bolometric and the V-band flux densities. The central wavelengths of the V-, J-, H- and K-band are $0.55\,\mu$m, $1.25\,\mu$m, $1.65\,\mu$m and $2.2\,\mu$m respectively.

3.2.3 Near-infrared stellar absorption features

The set of properties predicted by STARS was augmented with the equivalent widths (EWs) of several near-infrared absorption features observed at moderate spectral resolution in late-type stars discussed in chapter 2: $W_{2.29}$, $W_{1.62}$, $W_{1.59}$, $W_{\rm Na}$ and $W_{\rm Ca}$. First- and second-order polynomial fits were performed to the homogeneized stellar data from figures 2.5 and 2.6. The resulting relationships with $T_{\rm eff}$ for luminosity classes V, III and I below 5700 K were implemented in the code. EWs assigned to hotter stars were identically zero, since the absorption features considered become negligibly small or absent at higher temperatures. The exception is the Si I $1.59\,\mu$m feature, but above ≈ 6000 K, hydrogen is responsible for the absorption feature which then has a different physical meaning. The predicted EWs include the dilution by the featureless free-free and free-bound nebular continuum (see appendix B).

For TP-AGB stars, H- and K-band spectroscopic data at moderate resolution are severely lacking in the literature. From preliminary 3D data which were obtained for a sample of Miras and other TP-AGB stars (S- and N-type stars), the CO bandheads are comparable in strength to those of the latest normal M-type giants. A similar conclusion is reached by inspection of the few spectra published by Johnson & Mendéz (1970) and Wallace & Hinkle (1996), and those obtained by Lançon (private communication). The EWs of normal giants with $T_{\rm eff} = 3000$ K were therefore assigned to all TP-AGB stars.

3.3 Modeling of nebular emission lines

Photoionized nebulae around young, massive stars (H II regions) are often the most conspicuous gaseous nebulae in starburst galaxies. The various processes which occur in H II regions include (*e.g.* Osterbrock 1989):

- photoionization and recombination,
- collisional excitation and de-excitation,
- free-free, free-bound and bound-free interactions between electrons and ions,
- charge-exchange reactions.

These processes result in line emission from the various elements, and continuum emission. When present, dust also contributes to the nebular emission spectrum with thermal continuum and possibly narrow bands such as the PAH features in the mid-infrared. Absorption of photons by gas and dust, and subsequent re-emission modify the stellar radiation field within the nebula.

Nebular recombination and fine-structure lines are particularly important in starburst studies. They allow the determination of the physical conditions of the ionized nebulae. In addition, they probe the shape and intensity of the $\gtrsim 10$ eV ultraviolet radiation field which is usually dominated by the photospheric emission from hot, massive stars. Such information provides important constraints on the properties of the youngest stellar populations such as the luminosity-averaged effective temperature, the global luminosity and the number population. Three mid-infrared emission line ratios, accessible with *ISO* observations, constitute particularly useful temperature indicators: [Ne III] 15.6 μm/[Ne II] 12.8 μm, [Ar III] 8.99 μm/[Ar II] 6.99 μm, and [S IV] 10.5 μm/[S III] 18.7 μm. Because the species involved have very different ionization potentials, they are very sensitive to the SED of the ionizing stars, which is harder for higher stellar temperatures (see appendix B). Furthermore, these line ratios are essentially independent of the chemical abundances of the gas.

For the purpose of this thesis, the modeling of line emission from nebulae photoionized by evolving stellar populations was performed with the photoionization code CLOUDY. A complete description of CLOUDY is given in Ferland (1996). Briefly, CLOUDY predicts the emission spectrum from gaseous nebulae which are heated and ionized by the radiation field of a central object. This is done by simultaneously solving the equations of photoionization equilibrium, of statistical and thermal equilibrium, and of heating-cooling processes under the conditions specified by a set of input parameters. The input parameters provide the physical conditions within the nebula (*e.g.* gas and dust composition, hydrogen gas density $n_{\rm H}$, ionization parameter[1] U), the geometry of the nebula (*e.g.* spherical or plane-parallel geometry, distance R between the source and the illuminated surface of the nebula), and the energy distribution of the impinging radiation field.

Model predictions for the three mid-infrared line ratios of interest here were obtained using the SEDs generated by STARS. The individual line fluxes for a burst timescale of $t_{\rm sc} = 1$ Myr were computed with CLOUDY; they were then convolved by the SFR for longer burst timescales. The ionized nebulae were represented as shells surrounding a central, point-like source (the stellar population), with uniform gas density and nearly plane-parallel geometries. For such nebulae,

$$U \equiv \frac{Q}{4\pi R^2 n_{\rm H} c} \tag{3.3}$$

where Q is the hydrogen ionization rate of the source and c is the speed of light. The gas and dust composition, $n_{\rm H}$ and R were assumed to be time-independent. For the $t_{\rm sc} = 1$ Myr models, U was allowed to vary with burst age proportionally to Q for consistency, and the $U_{\rm max}$ reached at the age for which Q is maximum was specified. This sets the *absolute* flux scale for the SEDs, whose *shape* and *relative* flux scale as the stellar population evolves are determined by STARS. The computations are stopped when $\log U$ becomes smaller than -5.5 dex; at this point, the SFR has dropped by several orders of magnitude compared to the initial SFR and the stellar population is generally expected to have faded away in the galaxy's background population.

The variation of U with Q was not accounted for when convolving for the longer burst timescales. As a consequence, the "generations" of stars with U and Q close to maximum dominate the nebular line emission at each time step, as expected for composite populations with a range of ages. The assumption of constant $n_{\rm H}$ and R and the treatment of U may not be realistic for evolving H II regions. However, for applications to starburst galaxies as in this work, they ensure consistency between the data and the predictions by providing models for which the nebular parameters at any age are close to the observed values.

[1]giving the number of hydrogen ionizing photons impinging at the surface of the nebula per hydrogen atom; see chapter 5

3.4 Model predictions for single evolving clusters

3.4.1 Evolution of the integrated properties

In applications of evolutionary synthesis models, it is generally assumed that the specified IMF applies to the entire stellar population within the observed regions. In other words, the entire population is modelled as if composed of identical clusters with respect to their initial stellar mass distribution, or if it actually consisted of *one, large single cluster*. Such "single cluster" models computed with STARS and CLOUDY as described in the previous sections are here discussed. The evolution with cluster age of the most relevant properties for this work are presented in figures 3.3 to 3.6, including $L_{\rm bol}$, $L_{\rm Lyc}$, L_K, $\nu_{\rm SN}$, $M^{\star}$, EWs of near-infrared stellar absorption features and mid-infrared nebular line ratios. These properties are mostly sensitive to the burst age and timescale, and to the upper mass cutoff of the IMF; the exception is $M^{\star}$ which is actually mainly sensitive to the lower mass cutoff instead of the upper mass cutoff.

Two sets of representative models are shown in the figures to illustrate the general behaviour of the properties with $t_{\rm b}$, $t_{\rm sc}$ and $m_{\rm up}$: *1)* computations for $t_{\rm sc} = 1$ Myr, 5 Myr, 20 Myr and 1 Gyr, with a fixed $m_{\rm up} = 100$ $M_{\odot}$, and *2)* computations for $m_{\rm up} = 25$ $M_{\odot}$, 35 $M_{\odot}$, 50 $M_{\odot}$ and 100 $M_{\odot}$, with a fixed $t_{\rm sc} = 1$ Myr. The range of burst ages covers $10^6 - 10^9$ yr. Time steps equally spaced on a logarithmic scale, with $\Delta \log(t_{\rm b}) = 0.1$ dex, were chosen for a proper sampling of the various evolutionary phases. For all models, the IMF was assumed to have a Salpeter power-law index $\alpha = 2.35$ (Salpeter 1955) and to extend down to $m_{\rm low} = 1$ $M_{\odot}$. The initial SFR was $R_0 = 10$ $M_{\odot}\,{\rm yr}^{-1}$. The stellar tracks for solar metallicity and for the lowest mass-loss rates for massive stars (or "normal" mass-loss rates) were selected. The TP-AGB phase for intermediate-mass stars was accounted for. The nebular parameters for CLOUDY were those appropriate for M 82, as determined in chapter 5: $n_{\rm H} = 300$ cm^{-3}, $\log U_{\rm max} = -2.3$, $R = 10^{19.9}$ cm (25 pc), and solar gas-phase abundances; the effects of interstellar dust mixed with the ionized gas were neglected.

Both $L_{\rm bol}$ and $L_{\rm Lyc}$, which trace the hot young stars, are largest during the early phases of a burst and decrease rapidly as soon as the SFR drops significantly because of the rapid evolution of these stars. For Salpeter-like IMFs, the integrated $L_{\rm Lyc}$ is dominated by the most massive stars while stars in the range $10 - 25$ $M_{\odot}$ contribute to the bulk of $L_{\rm bol}$. Therefore, the $L_{\rm bol}/L_{\rm Lyc}$ ratio is very sensitive to $m_{\rm up}$ in young stellar populations. This ratio also depends on the burst timescale after a few million years because it reflects the relative populations of stars in different mass ranges, which have different main-sequence lifetimes. Similarly, the mid-infrared nebular line ratios vary

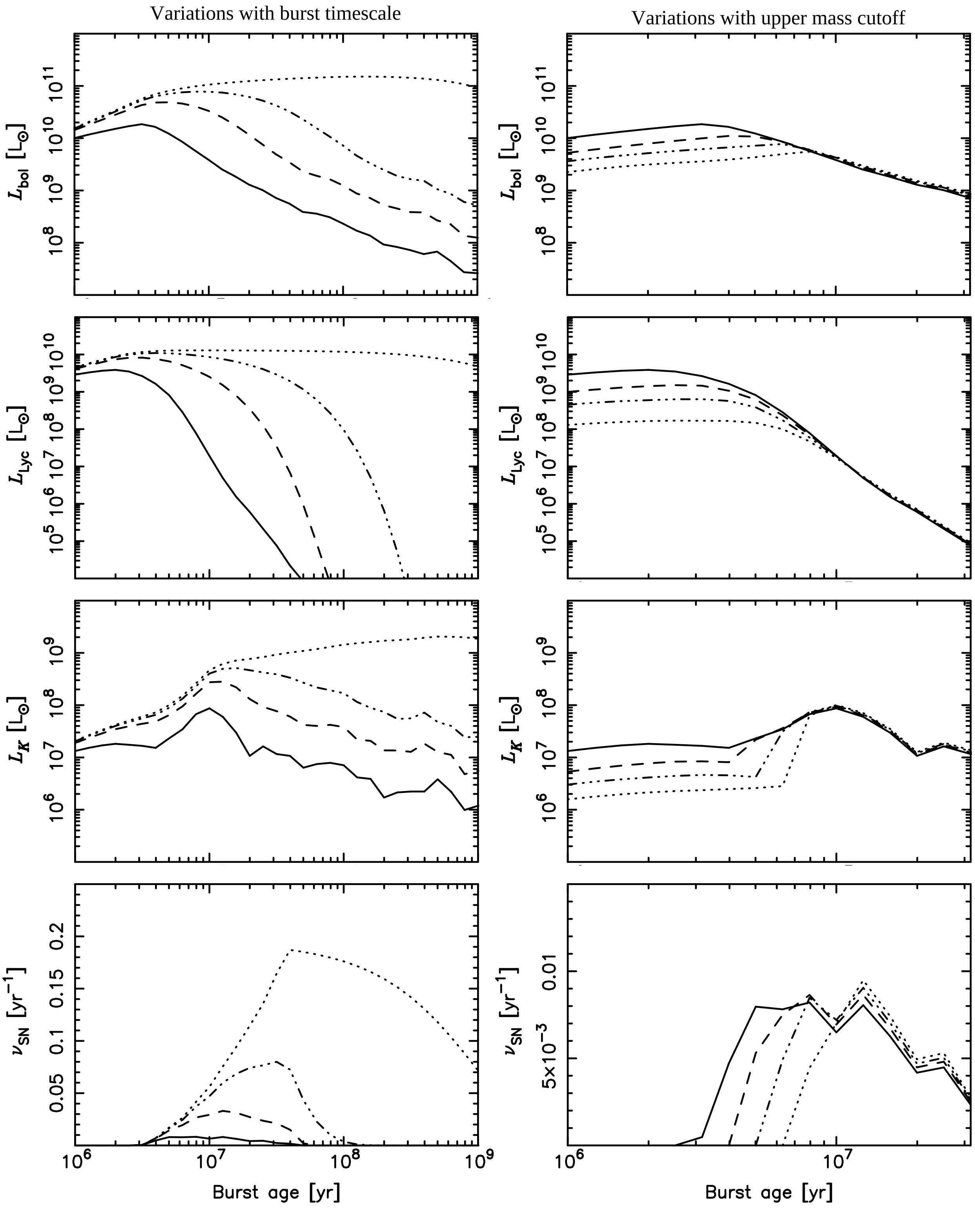

Fig. 3.3.— Variation with burst age and timescale, and with upper mass cutoff of the IMF of $L_{\rm bol}$, $L_{\rm Lyc}$, L_K and $\nu_{\rm SN}$ for a single cluster. *Left panels:* $t_{\rm sc} = 1$ Myr (solid line), 5 Myr (dashed line), 20 Myr (dash-dot-dot-dot line) and 1 Gyr (dotted line); $m_{\rm up} = 100\ {\rm M}_\odot$ for all models. *Right panels:* $m_{\rm up} = 100\ {\rm M}_\odot$ (solid line), 50 $\rm M_\odot$ (dashed line), 35 $\rm M_\odot$ (dash-dot-dot-dot line) and 25 $\rm M_\odot$ (dotted line); $t_{\rm sc} = 1$ Myr for all models. The other model parameters adopted are given in the text. The vertical scales are the same between the left- and right-hand side panels, except for $\nu_{\rm SN}$.

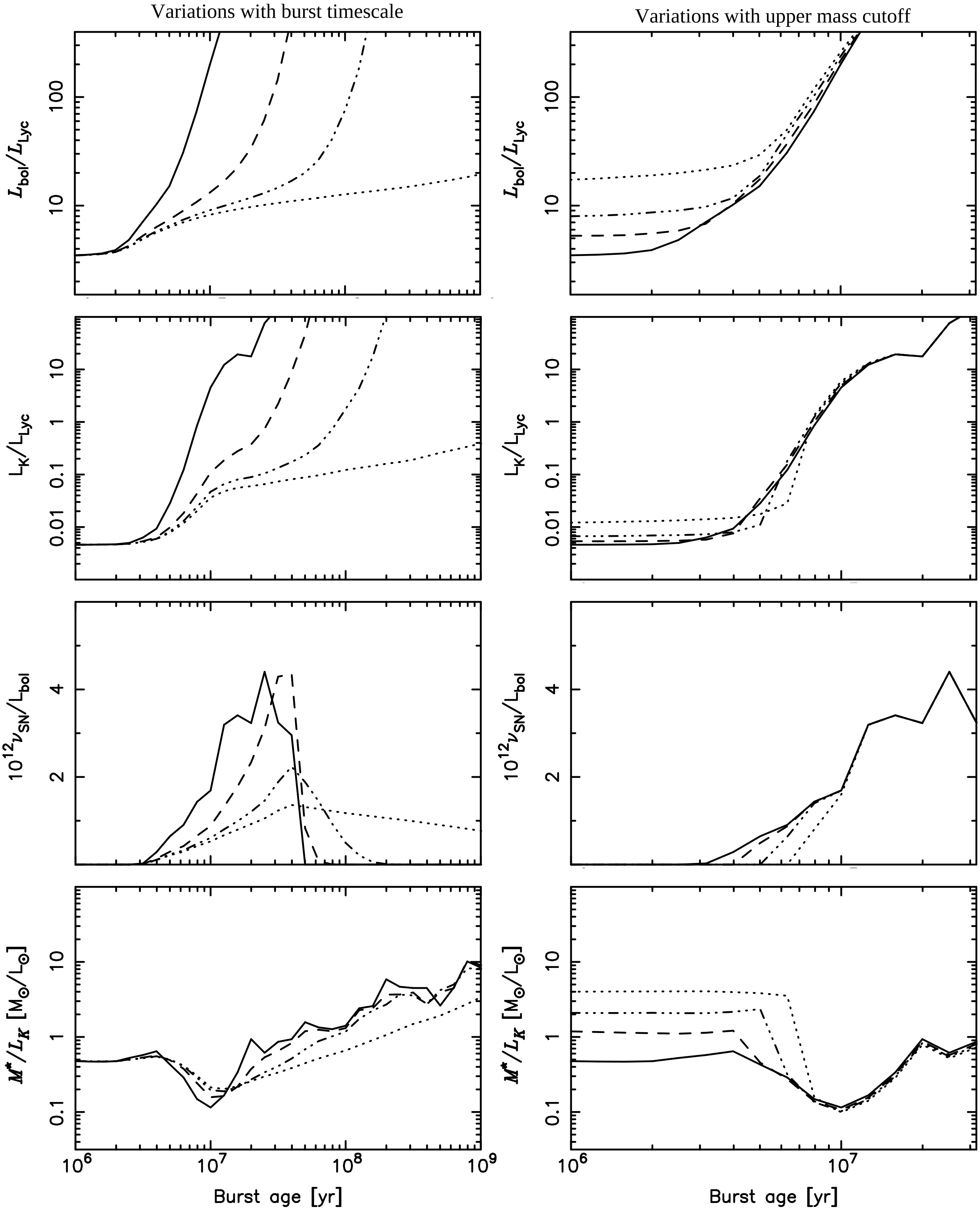

Fig. 3.4.— Variation with burst age and timescale, and upper mass cutoff of the IMF of $L_{\rm bol}/L_{\rm Lyc}$, $L_K/L_{\rm Lyc}$, $\nu_{\rm SN}/L_{\rm bol}$ and $M^\star/L_K$ for a single cluster. *Left panels:* $t_{\rm sc}$ = 1 Myr (solid line), 5 Myr (dashed line), 20 Myr (dash-dot-dot-dot line) and 1 Gyr (dotted line); $m_{\rm up}$ = 100 $M_\odot$ for all models. *Right panels:* $m_{\rm up}$ = 100 $M_\odot$ (solid line), 50 $M_\odot$ (dashed line), 35 $M_\odot$ (dash-dot-dot-dot line) and 25 $M_\odot$ (dotted line); $t_{\rm sc}$ = 1 Myr for all models. The other model parameters adopted are given in the text.

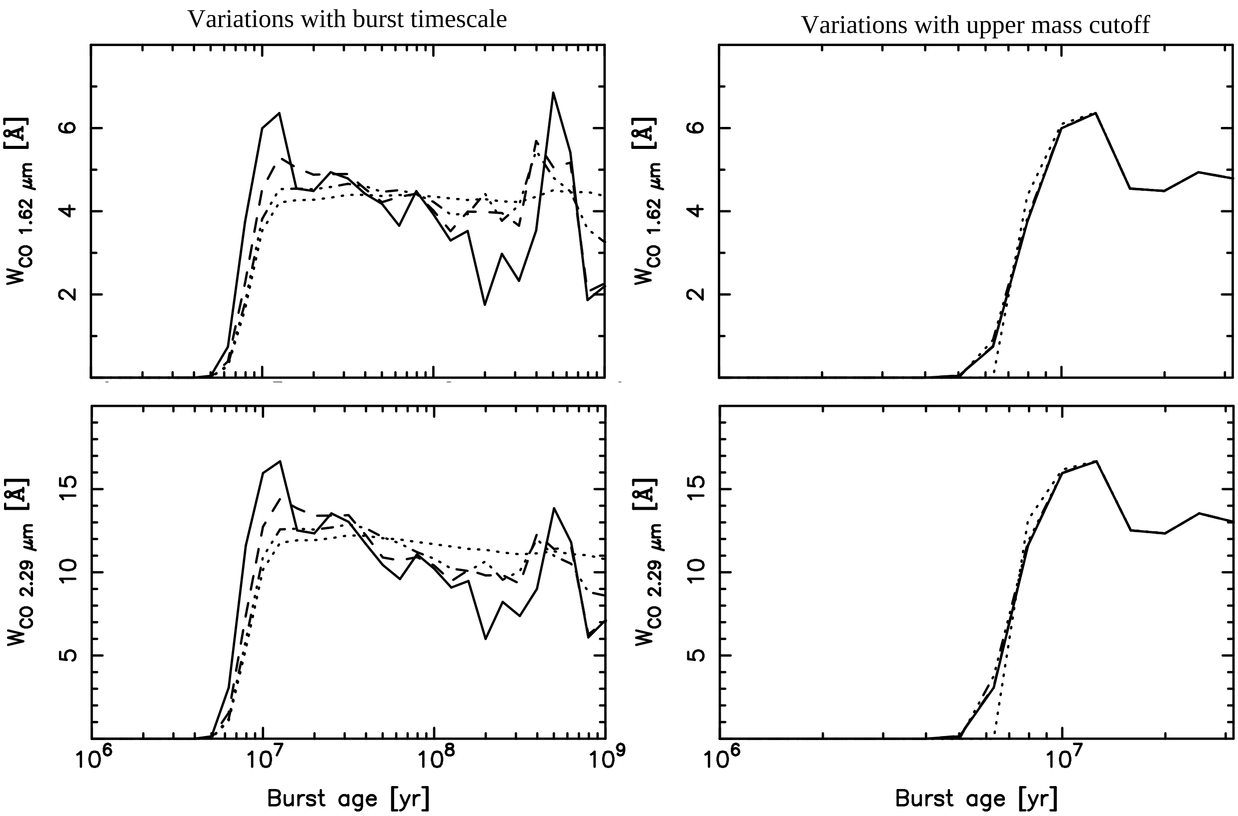

Fig. 3.5.— Variation with burst age and timescale, and upper mass cutoff of the IMF of $W_{1.62}$ and $W_{2.29}$ for a single cluster. *Left panels:* $t_{\rm sc} = 1$ Myr (solid line), 5 Myr (dashed line), 20 Myr (dash-dot-dot-dot line) and 1 Gyr (dotted line); $m_{\rm up} = 100$ M$_\odot$ for all models. *Right panels:* $m_{\rm up} = 100$ M$_\odot$ (solid line), 50 M$_\odot$ (dashed line), 35 M$_\odot$ (dash-dot-dot-dot line) and 25 M$_\odot$ (dotted line); $t_{\rm sc} = 1$ Myr for all models. The other model parameters adopted are given in the text.

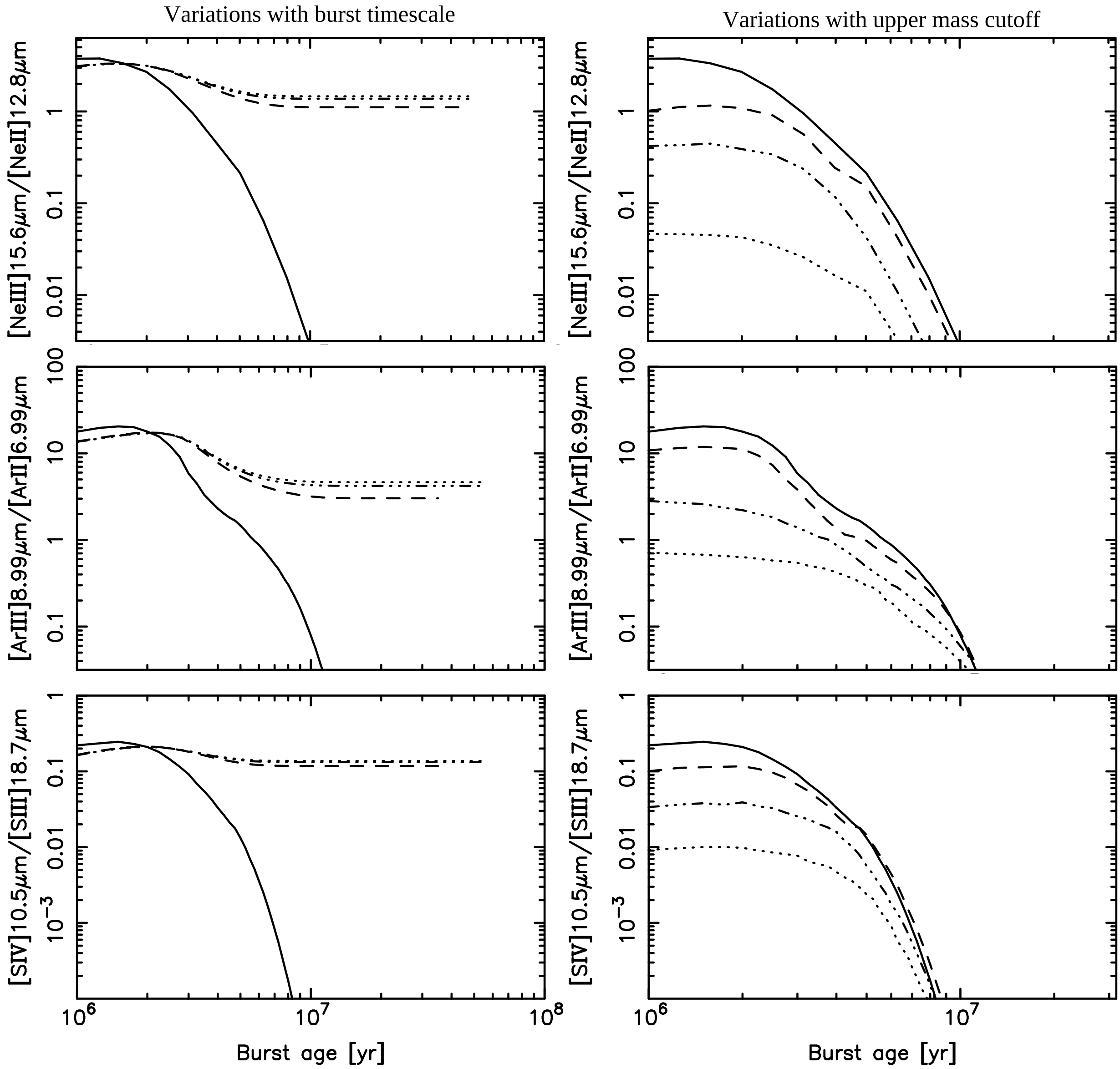

Fig. 3.6.— Variation with burst age and timescale, and upper mass cutoff of the IMF of the [Ne III] 15.6 μm/[Ne II] 12.8 μm, [Ar III] 8.99 μm/[Ar II] 6.99 μm and [S IV] 10.5 μm/[S III] 18.7 μm for a single cluster. *Left panels:* $t_{\rm sc} = 1$ Myr (solid line), 5 Myr (dashed line), 20 Myr (dash-dot-dot-dot line) and 1 Gyr (dotted line); $m_{\rm up} = 100$ M$_\odot$ for all models. *Right panels:* $m_{\rm up} = 100$ M$_\odot$ (solid line), 50 M$_\odot$ (dashed line), 35 M$_\odot$ (dash-dot-dot-dot line) and 25 M$_\odot$ (dotted line); $t_{\rm sc} = 1$ Myr for all models. The other model parameters adopted are given in the text.

strongly with $m_{\rm up}$, $t_{\rm sc}$ and $t_{\rm b}$ since they are very sensitive to the effective temperature, and thus mass, of the ionizing stars.

The evolution of L_K is characterized by a substantial increase marking the appearance of red supergiants at $\approx 10^7$ yr. The subsequent decrease, which occurs at different ages for different burst timescales, corresponds to the less massive and less luminous red giants progressively dominating L_K while the supergiants end their life. Since stars initially more massive than ≈ 25 $M_\odot$ never become red supergiants, L_K is essentially insensitive to $m_{\rm up}$ in the range considered here and for cluster ages above 10 Myr. At younger ages, however, L_K depends on $m_{\rm up}$ due to the contribution of nebular processes (free-free and free-bound interactions), which is large and proportional to $L_{\rm Lyc}$ (see Eq. B.11 in appendix B). For later stages, this contribution becomes negligible owing to the overwhelming near-infrared output from cool, evolved stars. The $L_K/L_{\rm Lyc}$ ratio is strongly dependent on $t_{\rm sc}$ and provides a good measure of the relative populations of massive main-sequence stars and their progeny, cool evolved stars. In addition, it is also sensitive to $m_{\rm up}$ at young ages, for similar reasons as $L_{\rm bol}/L_{\rm Lyc}$.

The rate of supernova explosions is non-negligible for burst ages where stars more massive than 8 $M_\odot$ end their life. Due to the IMF weighting, it is larger when the stars in the lower mass range explode.

According to the convention adopted in STARS, $M^\star$ represents the total mass consumed since the onset of star formation, either locked in stars that are still alive or returned to the ISM via stellar winds and supernova explosions. It therefore increases proportionally to the SFR. Because of the shape of the IMF, it is dominated by the low-mass stars and depends strongly on $m_{\rm low}$. Since L_K is insensitive to contributions from these stars, at least for $t_{\rm b} \lesssim 10^9$ yr, $M^\star/L_K$ is very sensitive to $m_{\rm low}$, as demonstrated in figure 3.7. The dip around 10 Myr is due to the presence of the luminous red supergiants. From models computed with $m_{\rm low} = 1$ $M_\odot$, the correction factor at any age for an IMF extending down to $m_{\rm low}^{\rm true}$ is simply obtained from Eq. B.3 (appendix B):

$$\frac{M^\star(m_{\rm low}^{\rm true})}{M^\star(1\ M_\odot)} = \frac{m_{\rm up}^{-\alpha+2} - (m_{\rm low}^{\rm true})^{-\alpha+2}}{m_{\rm up}^{-\alpha+2} - 1} \qquad \alpha \neq 2, \tag{3.4}$$

$$\frac{M^\star(m_{\rm low}^{\rm true})}{M^\star(1\ M_\odot)} = \frac{\ln m_{\rm up} - \ln m_{\rm low}}{\ln m_{\rm up}} \qquad \alpha = 2, \tag{3.5}$$

The various EWs of the near-infrared stellar absorption features show similar general behaviours mainly governed by variations in the luminosity-averaged effective temperature of cool, evolved stars; only $W_{1.62}$ and $W_{2.29}$ are illustrated in figure 3.5. Before ≈ 10 Myr, the absence of red giants and supergiants, the weakness of the absorption features in cool dwarfs and the large nebular contribution to L_K combine to produce

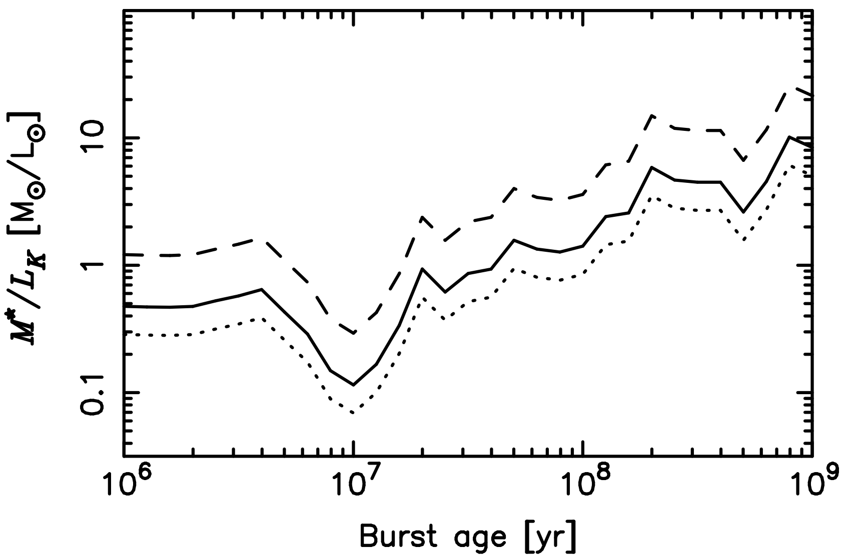

Fig. 3.7.— Variation of the $M^\star/L_K$ ratio with the lower mass cutoff of the IMF for a single cluster: $m_{\rm low}$ = 0.1 M$_\odot$ (dashed line), 1 M$_\odot$ (solid line) and 3 M$_\odot$ (dotted line). $m_{\rm up}$ = 100 M$_\odot$ and $t_{\rm sc}$ = 1 Myr for all curves. The other model parameters are the same as for figures 3.3 to 3.6.

essentially no observable absorption. For later stages, the cool, evolved stars dominate almost completely the near-infrared emission. The first peak near 10 Myr is due to cool, massive supergiants. The subsequent decline results from the longer main-sequence and total lifetimes of stars with progressively lower masses, which have higher temperatures and are characterized by shallower absorption features. The decline is slightly steeper for EWs which are more sensitive to the luminosity class (*e.g.* $W_{2.29}$). The bump around 1 Gyr is produced by intermediate-mass stars when they reach the TP-AGB phase and very low temperatures (the TP-AGB contribution is further discussed below). The TP-AGB feature is more pronounced and comparable in strength to the "supergiant peak" for EWs predominantly sensitive to $T_{\rm eff}$ (*e.g.* $W_{1.62}$). The narrower and more pronounced "supergiant peak" around 10 Myr and "TP-AGB peak" around 1 Gyr for short burst timescales is a natural consequence of the narrower mass range undergoing these phases almost simultaneously. The "dilution" of the absorption features by contributions to the near-infrared light associated with stars in earlier and later evolutionary phases is reduced.

The "oscillations" apparent in the models for some of the properties and especially for short burst timescales (notably for L_K, $M^\star/L_K$ and the stellar EWs) are artefacts inherent to the synthesis method followed in STARS and to the discreteness of the HRD grid where the stars are distributed to compute the integrated properties (see appendix B). The stars are binned in mass, and each mass bin is assigned to one evolutionary track; consequently, stars with a small dispersion in mass associated to a given track may accumulate temporarily in a single, or very few $\log T_{\rm eff} - \log L_{\rm bol}$ bins. For instance, this effect likely exaggerates the peak contribution of TP-AGB stars for the shortest timescales, when stars of similar initial masses reach simultaneously the same low-$T_{\rm eff}$ and high-$L_{\rm bol}$ bin. Such fluctuations are much less important during the supergiant-dominated phase for two reasons: the large spread in $L_{\rm bol}$ in the HRD for the mass range covered by the main-sequence progenitors, and the large spread in $T_{\rm eff}$ for each mass bin due to the extremely rapid post-main-sequence evolution of these stars result in long populated segments along the stellar tracks.

3.4.2 The effects of TP-AGB stars

The contribution to various properties of intermediate-mass stars on the TP-AGB (for ages between 50 Myr and 2 Gyr) can be assessed from figures 3.8 and 3.9. Due to IMF weighting and longer TP-AGB lifetimes, stars in the lower mass range (around 2–3 $M_\odot$) produce the largest effects, at ages $\approx$ 1 Gyr. As expected from the large luminosities and low temperatures of TP-AGB stars, the most important differences occur for $L_{\rm bol}$ and for near-infrared properties. The maximum contribution of TP-AGB stars is about 25% to $L_{\rm bol}$ and 40% to near-infrared luminosities, depending on $t_{\rm sc}$. The models of Charlot & Bruzual (1991) predict smaller contributions which never exceed 10% and 20% respectively. However, given the uncertainties in the assigned properties, and the different evolutionary synthesis method and TP-AGB tracks between this work and Charlot & Bruzual (1991), the agreement is satisfactory. As mentioned in the previous subsection, the contribution of TP-AGB stars is probably artificially enhanced for short burst timescales in the models presented here.

The presence of the cool, luminous TP-AGB stars which have absorption features comparable in strength to those of late-M giants translates into substantial differences in the predicted stellar EWs. Generally, the local maximum in all EWs around 500 Myr is solely attributable to the presence of TP-AGB stars. When the TP-AGB phase is excluded, even the EWs that are only sensitive to the $T_{\rm eff}$ — such as $W_{1.62}$ — exhibit a steeper decline because of the progressively warmer normal giants producing the bulk of the near-infrared light. Figures 3.5 and 3.9 suggest that $W_{2.29}$ together with $W_{1.62}$ can be used to discriminate between populations of young supergiants and older evolved populations with less massive progenitors, namely red giants and TP-AGB stars.

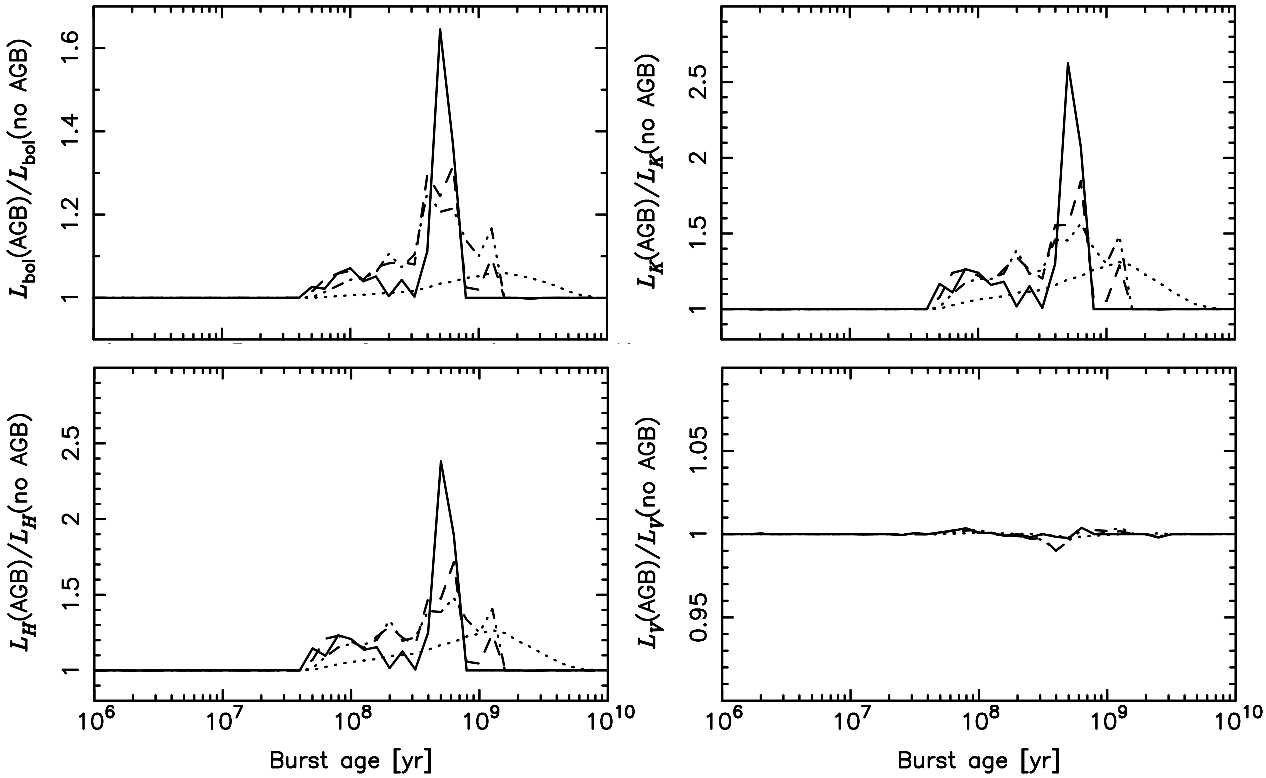

Fig. 3.8.— Effects of intermediate-mass stars on the TP-AGB in the model predictions for the bolometric, K-, H- and V-band luminosities for a single evolving cluster. The curves are the ratios of the luminosities computed including and excluding the TP-AGB phase, for $t_{\rm sc}$ = 1 Myr (solid line), 5 Myr (dashed line), 20 Myr (dash-dot-dot-dot line) and 1 Gyr (dotted line). For all models, $m_{\rm up} = 100$ M$_\odot$, but the results are insensitive to $m_{\rm up}$ since TP-AGB stars have progenitors with masses $\leq 7-8$ M$_\odot$. The other model parameters are the same as for figures 3.3 to 3.6. The contribution of the TP-AGB stars at ≈ 500 Myr is likely exaggerated due to the synthesis technique employed (see text). The horizontal axis extends to 10^{10} yr to show clearly the maximum contribution from the TP-AGB stars.

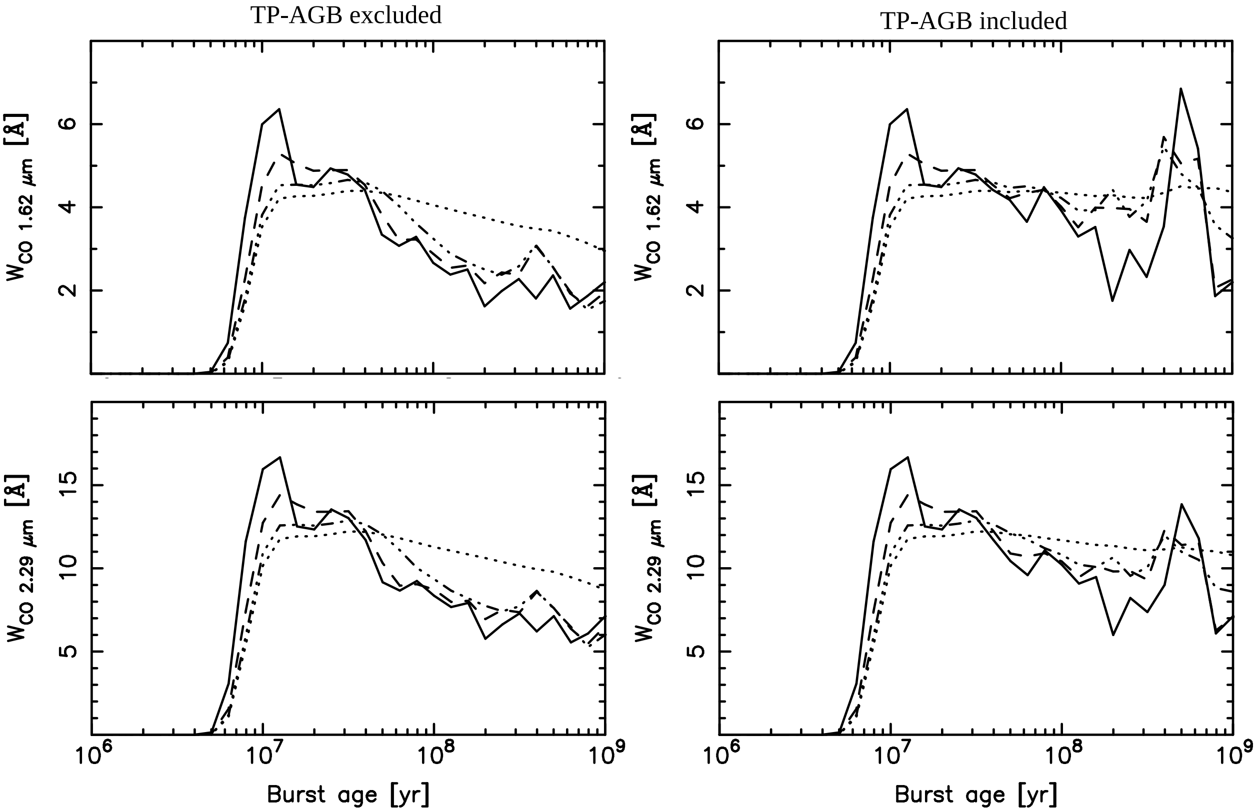

Fig. 3.9.— Effects of intermediate-mass stars on the TP-AGB in the model predictions for $W_{1.62}$ and $W_{2.29}$ for a single evolving cluster. *Left panels:* computations excluding the TP-AGB phase, *right panels:* computations including the TP-AGB phase. The various curves in each plot correspond to $t_{\rm sc} = 1$ Myr (solid line), 5 Myr (dashed line), 20 Myr (dash-dot-dot-dot line) and 1 Gyr (dotted line). For all models, $m_{\rm up} = 100\ {\rm M}_\odot$, but the results are insensitive to $m_{\rm up}$ since TP-AGB stars have progenitors with masses $\leq 7 - 8\ {\rm M}_\odot$. The other model parameters are the same as for figures 3.3 to 3.6. The contribution of the TP-AGB stars at ≈ 500 Myr is likely exaggerated due to the synthesis technique employed (see text).

3.5 Model predictions for ensembles of evolving clusters

Single cluster models as described in the previous section may not be appropriate for entire starburst regions, which potentially include a number of individual clusters. Indeed, compact "super star clusters" with typical sizes ~ 1 pc to ~ 10 pc, in some cases grouped in large associations, have been revealed by observations with the *Hubble Space Telescope* (*HST*) in several nearby starburst galaxies including M 82 (O'Connell *et al.* 1995), NGC 4038/4039 (Whitmore & Schweizer 1995), NGC 1569 and NGC 1705 (O'Connell, Gallagher & Hunter 1994), NGC 1140 (Hunter, O'Connell & Gallagher 1994), and He $2-10$ (Conti & Vacca 1994). Bright compact sources interpreted as young clusters of red supergiants are also seen in high angular resolution near-infrared images of starburst galaxies, notably M 82 (Satyapal *et al.* 1997) and NGC 1808 (Tacconi-Garman, Sternberg & Eckart 1996). Furthermore, important substructure in the ISM on scales $\lesssim 10$ pc is observed or inferred from detailed modeling of starburst regions (*e.g.* Shen & Lo 1995; Achtermann & Lacy 1995; Carral *et al.* 1994).

Most importantly, applications of single cluster models are based on the assumption that the IMF is well populated up to $m_{\rm up}$ in *all* clusters. However, this neglects possible mass constraints: small clusters may not have enough mass available to form the most massive stars for a fixed IMF slope. Therefore, a more realistic assumption is that **ensembles of stellar clusters in starburst regions likely have a distribution of masses**, and that **small clusters may not be able to form very massive stars**.

This hypothesis is supported by observations of OB associations and clusters, and of bright H II regions in the disk of our own Galaxy (*e.g.* McKee & Williams 1997), in nearby spiral and irregular galaxies (*e.g.* Elson & Fall 1985; Kennicutt, Edgar & Hodge 1989; Gonzalez-Delgado *et al.* 1995), as well as in starburst systems like NGC 4038/4039 (Whitmore & Schweizer 1995). These studies show that the number distribution of young clusters and associations in optical light and in ionizing luminosity follows a power-law luminosity function (LF)

$$\Phi(L) \equiv \frac{\mathrm{d}N}{\mathrm{d}(\log L)} \propto L^{-\beta}. \tag{3.6}$$

The LF in the variety of star-forming environments above have remarkably similar indices in the range $\beta = 0.5-1$, down to the faintest luminosities observed. The typical completeness limits correspond to an absolute V-band magnitude of $M_V \approx -10$ mag or to an hydrogen ionizing rate $Q_{\rm Lyc} \sim 10^{50}$ s^{-1}. For comparison, the Orion nebula is powered by OB stars with a total $Q_{\rm Lyc} = 10^{48.85}$ s^{-1} (Kennicutt 1984). In addition, star counts in OB associations and young clusters in the Milky Way and Magellanic Clouds provide no evidence for variations in the shape of the IMF with spatial concentration and richness of the cluster, metallicity, galactocentric distance and morphological type of the host galaxy (*e.g.* Hunter *et al.* 1997; Massey & Hunter 1998; Eisenhauer *et al.* 1998). Therefore, it seems plausible to interpret the observed LF as the result of a cluster mass distribution which determines the mass of the most massive star formed in each cluster (see also Massey & Hunter 1998).

The 3D and *ISO* observations of M 82 presented in this thesis do not resolve individual stellar clusters; the *ISO*-SWS beam corresponds to spatial scales at the distance of M 82 from 200 pc $\times$ 300 pc to 300 pc $\times$ 500 pc depending on wavelength, and the angular resolution of the 3D data is $\approx 15 - 20$ pc. In addition, M 82 is oriented nearly edge-on. Therefore, any region considered for starburst modeling very likely includes contributions from a large number of individual parsec-scale clusters (see also chapter 5). For LFs decreasing with increasing luminosity, a softening of the integrated ionizing radiation field is expected due to the contribution from smaller clusters. More realistic models for ensembles of evolving clusters were therefore developed to assess quantitatively the effects of a distribution of cluster masses and luminosities on the integrated properties of starburst regions. These models are described in this section.

3.5.1 Extrapolation of the cluster LF to low luminosities

The distribution of an ensemble of evolving clusters is parametrized in the models by a power-law LF in hydrogen ionizing rate $Q^{\rm cl}$ (the superscript "cl" designates hereafter integrated cluster properties, and the subscript "Lyc" is omitted for clarity). As there are no observational constraints on the shape of the LF for small clusters, the first step in the modeling consisted in extrapolating the observed LF (for $Q^{\rm cl} \gtrsim 10^{50}$ s^{-1}) at low luminosities. An analytical derivation is inadequate for low-mass clusters containing small numbers of ionizing stars because stochastic effects become important, and because of the steep relationship between the ionizing rate and the mass for individual stars (see appendix A). For example, the formation of a 20 M$_\odot$ star instead of a 15 M$_\odot$ one in a small cluster can change $Q^{\rm cl}$ by close to an order of magnitude.

The derivation of the LF was therefore done using simple Monte Carlo simulations to determine the stellar population of clusters of different masses (see also Thornley *et al.* 1998). The initial cluster IMF was assumed to have a Salpeter slope, and to be filled from the lowest masses upwards (a cluster lower mass cutoff of 0.1 M$_\odot$ was assumed, but the choice has little consequences on the derivation of the LF). The cluster upper mass cutoff ($m^{\rm cl}_{\rm up}$) was therefore constrained by the number of stars in the cluster or, equivalently, the cluster mass. The actual stellar mass distribution of the clusters was then obtained using Poisson statistics. The simulations were run for a sample of 2×10^5 clusters, with the number of stars per cluster ranging from 100 to $10^{7.5}$. Simulations were performed for four different values of the most massive star(s) allowed to form in *any* cluster: $m_{\rm up}^{\rm glob} = 25$ M$_\odot$, 35 M$_\odot$, 50 M$_\odot$ and 100 M$_\odot$. It is emphasized that $m_{\rm up}^{\rm cl}$ applies to *individual clusters in the ensemble* and is different from the *intrinsic, global upper mass cutoff* of the IMF $m_{\rm up}^{\rm glob}$.

Cluster properties as a function of $Q^{\rm cl}$, such as the total mass $M^{\rm cl}$ and the upper mass cutoff $m_{\rm up}^{\rm cl}$, were obtained by averaging over the properties of all clusters in logarithmic bins of width $\Delta\log(Q^{\rm cl}) = 0.1$ dex, covering a specified range. Assuming that the physics underlying the LF is a mass function of the parent molecular clouds, and

$$\frac{{\rm d}N}{{\rm d}(\log M^{\rm cl})} \propto (M^{\rm cl})^{\gamma}, \tag{3.7}$$

the LF can be written as

$$\Phi(Q^{\rm cl}) \propto (M^{\rm cl})^{\gamma}\,\frac{{\rm d}(\log M^{\rm cl})}{{\rm d}(\log Q^{\rm cl})}. \tag{3.8}$$

The cluster mass function can be reasonably expected to have a constant slope (*e.g.* Scoville & Sanders 1987). The entire LF can then be derived from the relationship between $Q^{\rm cl}$ and $M^{\rm cl}$, and by adjusting γ so that the resulting LF at high luminosities matches the observations.

For the models presented here, the mass function was chosen to reproduce the LF for Galactic OB associations determined by McKee & Williams (1997), which has $\beta = 1$ in the observed range of $Q^{\rm cl} \sim 10^{50} - 10^{51}$ s^{-1}. The final LF is assumed to cover the range $Q^{\rm cl} = 10^{45} - 10^{53}$ s^{-1}. These limits were chosen to include the smallest associations susceptible of ionizing an H II region (*i.e.* containing only one early-B star), as well as the most luminous super star clusters such as those detected in M 82 and NGC 4038/4039 (O'Connell *et al.* 1995; Whitmore & Schweizer 1995). The $M^{\rm cl}(Q^{\rm cl})$ relationship exhibits a change of slope near $10^{49.5}$ s^{-1} mainly due to stellar properties, which therefore introduces a change of slope in the LF. The resulting LF can be well approximated by a broken power-law:

$$\Phi(Q^{\rm cl}) \propto (Q^{\rm cl})^{-0.17}, \quad 10^{45}\ {\rm s}^{-1} \leq Q^{\rm cl} < 10^{49.5}\ {\rm s}^{-1} \tag{3.9}$$

and

$$\Phi(Q^{\rm cl}) \propto (Q^{\rm cl})^{-1.0}, \quad 10^{49.5}\ {\rm s}^{-1} \leq Q^{\rm cl} \leq 10^{53}\ {\rm s}^{-1}. \tag{3.10}$$

3.5.2 Modeling of an ensemble of evolving clusters

For the purpose of computing the integrated properties of an ensemble of evolving clusters, a library of single cluster models ("cluster evolutionary tracks") for $t_{\rm sc} = 1$ Myr was generated for $m_{\rm up}^{\rm cl}$ between 5 $M_\odot$ and 100 $M_\odot$. The modeling of ensembles of clusters from this library is analogous to the modeling of single clusters; it constitutes an additional step in which clusters are treated as individual units instead of stars. The two successive steps involved are based on equivalent elements, schematically:

<u>**Individual clusters in the ensemble**</u>	<u>**Ensemble of clusters**</u>
• Stellar evolutionary tracks	• Cluster evolutionary tracks
• Stellar IMF	• Cluster LF
• Star formation rate	• Cluster formation rate

The range $Q^{\rm cl} = 10^{45} - 10^{53}$ s^{-1} considered for the ensemble of clusters was divided in logarithmic bins of width $\Delta \log(Q^{\rm cl}) = 0.05$ dex. For a given $m_{\rm up}^{\rm glob}$, the average $m_{\rm up}^{\rm cl}(Q^{\rm cl})$ relationship obtained from the Monte Carlo simulations is used to assign a single cluster model to each $\log(Q^{\rm cl})$ bin. The models for intermediate $m_{\rm up}^{\rm cl}$ were obtained by interpolation of the library models. The clusters are assumed to follow *at birth* the derived LF (Eqs. 3.9 and 3.10). The single cluster model curves for each bin were therefore scaled so that their zero-age ionizing rates matched the $Q^{\rm cl}$ predicted by the LF. For any burst age, the LF was computed by redistributing the clusters according to their initial number and evolved $Q^{\rm cl}$ in the fixed $\log(Q^{\rm cl})$ grid, normalizing to the total initial number of clusters. The integrated luminosities and emission line fluxes, the gas mass consumed and the rate of supernova explosions were computed following the general equation:

$$L(t_{\rm b}) = \frac{\int_{\log Q_{\rm min}(t_{\rm b})}^{\log Q_{\rm max}(t_{\rm b})} L(Q_0, t_{\rm b})\, \Phi(Q_0)\, {\rm d}(\log Q)}{\int_{\log Q_{\rm min}(t_{\rm b})}^{\log Q_{\rm max}(t_{\rm b})} \Phi(Q_0)\, {\rm d}(\log Q)}, \tag{3.11}$$

where the integration was performed numerically over all clusters including those fainter than the initial lower limit of $Q^{\rm cl} = 10^{45}$ s^{-1}. This ensured continuity in the evolution of the integrated properties when a significant number of clusters have evolved to faint luminosities. All quantities in Eq. 3.11 are cluster properties; the superscript "cl" has been omitted for the sake of clarity. $L(Q_0, t_{\rm b})$ is the luminosity at age $t_{\rm b}$ of the clusters with initial ionizing luminosity Q_0, and $\Phi(Q_0)$ is the number of these clusters. The EWs of the near-infrared stellar absorption features were averaged:

$$W_\lambda(t_\mathrm{b}) = \frac{\int_{\log Q_\mathrm{min}(t_\mathrm{b})}^{\log Q_\mathrm{max}(t_\mathrm{b})} W_\lambda(Q_0, t_\mathrm{b})\, L_\lambda(Q_0, t_\mathrm{b})\, \Phi(Q_0)\, \mathrm{d}(\log Q)}{\int_{\log Q_\mathrm{min}(t_\mathrm{b})}^{\log Q_\mathrm{max}(t_\mathrm{b})} L_\lambda(Q_0, t_\mathrm{b})\, \Phi(Q_0)\, \mathrm{d}(\log Q)}, \tag{3.12}$$

where $W_\lambda(Q_0, t_\mathrm{b})$ and $L_\lambda(Q_0, t_\mathrm{b})$ are the EW and the luminosity at the wavelength of the absorption feature at age t_b of the clusters with initial ionizing rate Q_0.

For longer burst timescales, the number of clusters formed in each $\log(Q^\mathrm{cl})$ bin was assumed to decrease according to an exponentially decaying "cluster formation rate" (CFR) as in Eq. 3.2. The LF was obtained by redistributing all clusters formed since $t_\mathrm{b} = 0$ in the $\log(Q^\mathrm{cl})$ grid according to their initial number and evolved Q^cl. The integrated properties were computed by convolution integrals over time t (numerically with $\Delta t = 1$ Myr, and between 0 and t_b), and over $\log(Q^\mathrm{cl})$ using Eqs. 3.11 and 3.12. Longer SFR for individual clusters were not considered, as studies of young clusters and OB associations show that typical burst timescales are ~ 1 Myr (*e.g.* Leitherer 1998a).

3.5.3 Evolution of the integrated properties

The evolution with burst age of the LF and of the "luminosity-weighted LF", $Q^\mathrm{cl} \times \Phi(Q^\mathrm{cl})$, is shown in figures 3.10 and 3.11 respectively for $m_\mathrm{up}^\mathrm{glob} = 100$ $\mathrm{M}_\odot$, and CFRs with $t_\mathrm{sc} = 1$ Myr and 20 Myr. The slope of the LF at high luminosities is essentially independent of the burst age and of the CFR. This results from the fact that the IMF of clusters with $Q^\mathrm{cl} \gtrsim 10^{50}$ s^{-1} is well populated in very high mass stars which have similar main-sequence lifetimes of about $3-4$ Myr. Consequently, the high-luminosity clusters evolve towards lower luminosities at nearly the same "speed". In addition, due to the flattening of the $Q(m)$ relationship at high stellar masses, "dilution effects" from less massive stars are important: for the parameters illustrated, the Q^cl of high-luminosity clusters is dominated by stars near 60 $\mathrm{M}_\odot$. The high-luminosity LF thus reflects more importantly the mass distribution of the clusters than their high-mass stars contents. The constant shape of the high-luminosity LF is consistent with the similarity of the LFs determined observationally in a variety of objects, which likely have a range of ages and different starburst histories. The assumption made for the modeling that the zero-age clusters are distributed according to the observed LF is thus justified. As the most massive stars die after a few million years, the most luminous clusters evolve towards lower Q^cl rapidly and accumulate in $\log(Q^\mathrm{cl})$ bins corresponding to lower $m_\mathrm{up}^\mathrm{cl}$, where smaller clusters have not yet evolved to lower luminosities. The local "bump" in the evolving LF is thus attributable to stellar lifetimes on the main-sequence and is naturally broader for longer bursts.

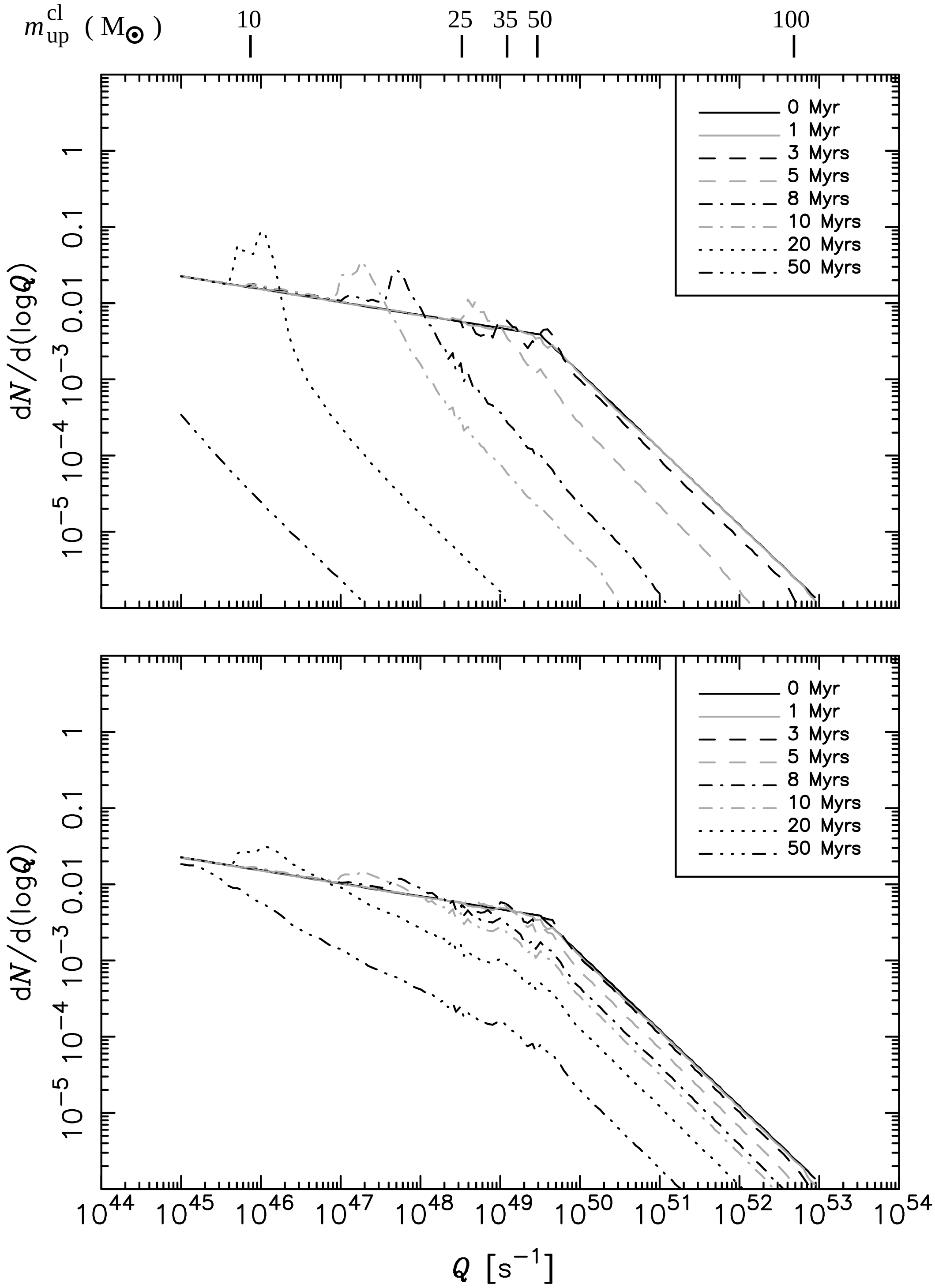

Fig. 3.10.— Evolution of the luminosity function (LF) of an ensemble of clusters. The initial LF is given by Eqs. 3.9 and 3.10. Models are shown for cluster formation rates with timescales of 1 Myr (top panel) and 20 Myr (bottom panel); the global upper mass cutoff for the ensemble of clusters is 100 M$_\odot$. The various lines in each diagram represent the LF for different burst ages as indicated in the insets. The LF is arbitrarily normalized but within each plot, is normalized to the total number of clusters existing at each age. The average cluster upper mass cutoff $m_{\rm up}^{\rm cl}$ obtained from the Monte Carlo simulations is indicated above the top panel for a few $Q^{\rm cl}$.

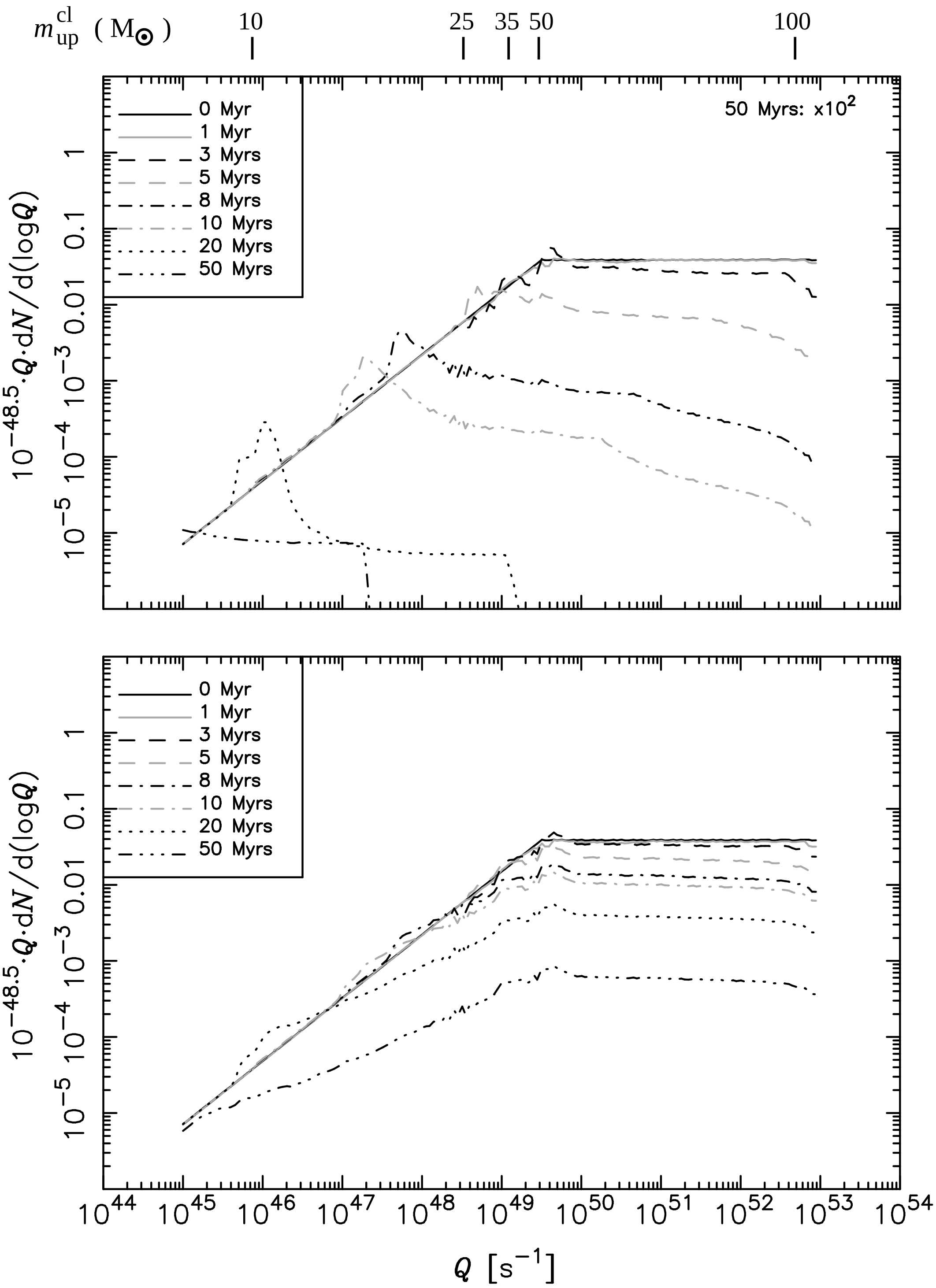

Fig. 3.11.— Evolution of the luminosity-weighted LF of an ensemble of clusters. The curves give simply the number of clusters per luminosity interval from figure 3.10, multiplied by their luminosity. The curve for 50 Myr in the upper panel has been scaled upwards for illustration purposes. The average cluster upper mass cutoff $m_{\rm up}^{\rm cl}$ obtained from the Monte Carlo simulations is indicated above the top panel for a few $Q^{\rm cl}$.

The luminosity-weighted LF gives a more representative measure of the distribution of the ionizing radiation amongst the clusters; figure 3.10 and 3.11 illustrate clearly that despite their much larger numbers, small clusters make only small contributions to the integrated ionizing radiation field as long as the CFR is not negligible.

Model predictions for ensembles of clusters and single clusters with $m_{\rm up} = m_{\rm up}^{\rm glob}$ are compared in figure 3.12. Models are shown for different $m_{\rm up}$ and $t_{\rm sc} = 1$ Myr; the pairs of curves for longer burst timescales exhibit very similar offsets. The introduction of the LF makes the largest differences for the properties which are most sensitive to the massive stars, such as the nebular line ratios, $L_{\rm bol}/L_{\rm Lyc}$ and $10^{12}\,\nu_{\rm SN}/L_{\rm bol}$. The effects on these ratios amount up to about a factor of two; the largest differences are for $m_{\rm up} = 100$ M$_\odot$ and become very small ($10\% - 15\%$) for $m_{\rm up} = 25$ M$_\odot$. This is attributable to the steepening of the relationships between the properties involved (notably $L_{\rm Lyc}$, $L_{\rm bol}$ and the hardness of the ionizing spectrum) and the stellar mass towards lower masses. The properties of individual stars cause the "dilution effects" by less luminous clusters to be more important for higher upper mass cutoffs and younger ages.

The choice of parameters for the LF can affect significantly these results. The most sensitive parameters are the slope of the LF at high luminosities, and the maximum $Q^{\rm cl}$. Shallower slopes as determined for young open clusters in the Large Magellanic Cloud by Elson & Fall (1985), for which $\beta = 0.5$, imply much smaller effects on the integrated properties (at most $\approx 20\%$). On the other hand, a truncation of the LF at $Q^{\rm cl} < 10^{53}$ s^{-1} results in larger effects. However, the LFs in most of the sources studied so far have power-law indices closer to $\beta = 1$, and the super star clusters observed in starburst galaxies, including M 82, support high values for the maximum $Q^{\rm cl}$ in the range $10^{52} - 10^{53}$ s^{-1}. For example, from *HST* photometry, O'Connell *et al.* (1995) measured absolute V-band magnitudes — corrected for extinction — ranging from -9.6 mag to -13.2 mag for the clusters in the most conspicuous emission region at optical wavelengths (region "A"). In addition, the brightest individual cluster in the entire *HST* field of view (known as source "F") has an intrinsic $M_V = -14.5$ mag. For an unevolved stellar population with a Salpeter IMF, these values correspond to $Q = 10^{50.5} - 10^{52.2}$ s^{-1} and $10^{52.7}$ s^{-1} respectively. Accounting for possible evolutionary effects, the observed magnitudes are still consistent with high $Q^{\rm cl}$ up to $\sim 10^{52}$ s^{-1}.

The adopted LF (Eqs. 3.9 and 3.10) therefore seems to be a plausible choice for starburst galaxies in general and for M 82 in particular, and provides a quantitative estimate of the effects of a distribution of cluster masses and luminosities for starburst populations. The models presented in this section demonstrate that these effects are significant, but are not expected to be larger than factors of a few.

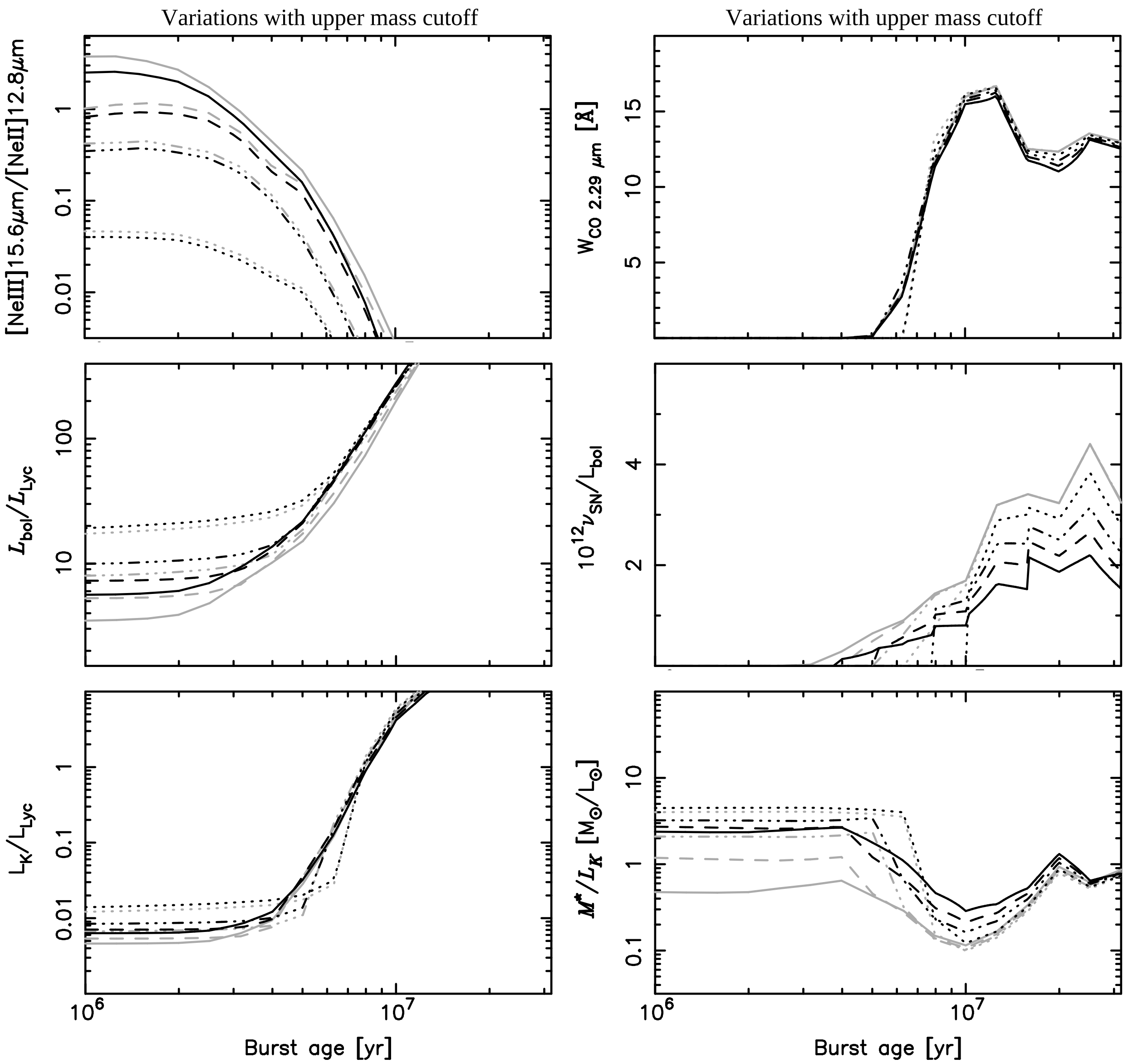

Fig. 3.12.— Comparison between model predictions for single clusters (grey lines; from figures 3.4 to 3.6) and for ensembles of clusters (black lines). The ensembles of clusters are characterized by an initial LF given in Eqs. 3.9 and 3.10. The most massive stars allowed to form in each model pair is the same. The various line types represent $m_{\rm up} = m_{\rm up}^{\rm glob} = 100\ {\rm M}_{\odot}$ (solid lines), 50 $\mathrm{M}_{\odot}$ (dashed lines), 35 $\mathrm{M}_{\odot}$ (dash-dot-dot-dot lines) and 25 $\mathrm{M}_{\odot}$ (dashed lines). The burst timescale is $t_{\rm sc} = 1$ Myr; the offsets between the single cluster and ensemble of clusters models are representative of those for longer timescales.

3.6 Summary

In this chapter, the evolutionary synthesis models applied to M 82 in chapter 7, based on the codes STARS and CLOUDY, have been presented. The improvements and extensions made specifically in the context of this thesis work have been described:

- the extension of the stellar evolutionary tracks for intermediate-mass stars up to the end of the TP-AGB phase,
- the prediction of the EWs of near-infrared stellar absorption features,
- the prediction of the integrated properties for ensembles of clusters with a luminosity distribution.

The main results from this chapter are the following:

- Intermediate-mass stars on the TP-AGB make a non-negligible contribution to the integrated $L_{\rm bol}$ and near-infrared properties of evolving stellar populations at ages between $\approx$ 50 Myr and $\sim$ 1 Gyr. The models presented here predict contributions up to 25% for $L_{\rm bol}$ and 40% at near-infrared wavelengths.
- Various properties which provide useful constraints on the burst age and timescale, and on the cutoffs of the IMF have been discussed from single cluster models. These include notably the [Ne III] 15.6 μm/[Ne II] 12.8 μm nebular line ratio, the EWs of the CO bandheads at 1.62 μm and 2.29 μm, and combinations of $L_{\rm bol}$, $L_{\rm Lyc}$, L_K, $M^\star$ and $\nu_{\rm SN}$.
- Models for ensembles of clusters characterized by a luminosity function have been developed. For the same global $m_{\rm up}$, the effects of a distribution of cluster luminosities on the various integrated properties can amount up to a factor of a few compared to predictions for a single cluster.

Chapter 4

Near- and mid-infrared observations of M 82

The 3D stellar library and the optimization of evolutionary synthesis models presented in the previous chapters were motivated by the new possibilities offered by the recent technique of near-infrared imaging spectroscopy and by the instruments on board the *ISO* satellite. These allow unprecedented detailed studies of starburst galaxies, moreover in wavelength regimes where starburst activity is conspicuous and dust obscuration is much less important than at optical and ultraviolet wavelengths. These new instrumental, empirical and theoretical tools are applied in this work to the nearby galaxy M 82 for a first, fully quantitative investigation of the nature and evolution of its starburst activity. The proximity of M 82 makes it an ideal target for essential spatially detailed studies on scales typical of giant star-forming regions and molecular clouds.

For the purpose of this thesis, observations were obtained with the integral field spectrometer 3D and with the Short Wavelength Spectrometer on board *ISO*. 3D provided **for the first time detailed spectral information over the entire H- and K-band, simultaneously with spatial information on scales of $\approx$ 20 pc** in the central regions of M 82. The *ISO* Short Wavelength Spectrometer provided, also **for the first time, the complete $\lambda = 3 - 40$ μm spectrum** of the starburst core of M 82. This chapter presents:

- the observations and the data reduction,
- the resulting images and spectra.

4.1 Observations and data reduction

4.1.1 Near-infrared observations

M 82 was observed using the Max-Planck-Institut für Extraterrestrische Physik (MPE) 3D instrument (Weitzel *et al.* 1996, described in chapter 2), at the 3.5 m telescope in Calar Alto, Spain, on January 13, 14, 16 and 21, 1995. The observations were completed at the 4.2 m William-Herschel-Telescope in La Palma, Canary Islands, on January 6, 1996.

In order to sample representative starburst regions in M 82, an area approximately 250×150 pc, nearly parallel to the plane of the galaxy, was selected for the observations (see figure 4.1 in section 4.1.3). The entire region mapped includes the nucleus and extends to the west along the major axis up to the inner edge of the molecular ring which surrounds the starburst core. The data were obtained with a spatial scale of $0.5''$/pixel and a spectral resolution of $R \sim 1000$ in both H- and K-band. The 3D field of view being $8'' \times 8''$, four different fields were observed in order to cover the target region, corresponding to $16'' \times 10''$ (at the distance of M 82, $1'' \approx 15$ pc). The center position of each field is given in table 4.1; adjacent fields overlap by approximately $3''$.

Each field was observed in an *object-sky-sky-object* sequence, with the off-source frames taken on blank portions of the sky $2'-4'$ away in the north and south directions. For each field, two data sets were obtained with spectral sampling shifted by half a pixel with respect to each other. The total on-source integration times per field and wavelength channel were 10 minutes for the K-band data, 8 minutes for the Calar Alto H-band data and 15 minutes for the William-Herschel-Telescope H-band data. Typical single-frame exposures were $60 - 100$ s. For atmospheric calibration, B-, late-F or early-G dwarf stars were observed each night, before and/or after M 82. The seeing varied from $1''$ to $1.5''$ during the observations. Table 4.2 gives the log of the observations.

Table 4.1: Center position of the fields observed with 3D on M 82

Field	$\Delta\alpha^{(a)}$	$\Delta\delta^{(a)}$
1	$+2''$	$+1.5''$
2	$+2''$	$-2''$
3	$-3''$	$-1''$
4	$-8''$	$-3''$

$^{(a)}$ Right ascension and declination offsets with respect to the nuclear position defined by the K-band emission peak, at the position α_{1950}: $09^{\mathrm{h}}51^{\mathrm{m}}43\overset{\mathrm{s}}{.}53$, δ_{1950}: $+69°55'00\overset{''}{.}7$ (Dietz *et al.* 1986).

Table 4.2: Log of the 3D observations of M 82

Date	Telescope[a]	Field	Band	t_{int}[b]	Seeing	Atmospheric calibrator
13/01/95	CA	1	K	600 s	$1.5''$	HD 82189 (F5 V)
		2	K	600 s	$1.5''$	HD 82189 (F5 V)
14/01/95	CA	3	K	600 s	$1''$	PPM 17105 (G0 V)
		3	H	480 s	$1''$	HD 87141 (F5 V)
16/01/95	CA	4	K	600 s	$1.3''$	PPM 17105 (G0 V)
21/01/95	CA	1	H	480 s	$1''$	HD 87141 (F5 V)
		4	H	480 s	$1''$	HD 87141 (F5 V)
06/01/96	WHT	2	H	900 s	$1''$	HD 26356 (B5 V)

[a] CA : 3.5 m telescope at Calar Alto, Spain. WHT : 4.2 m William-Herschel-Telescope on the Canary Islands, Spain.

[b] Total on-source integration time per detector pixel.

4.1.2 Near-infrared data reduction

The data reduction was carried out using the 3D data analysis package, based on the GIPSY software package (van der Hulst *et al.* 1992). The procedure was similar to that followed in chapter 2 for the 3D stellar library data obtained at Calar Alto. The data sets for each wavelength sampling were reduced independently as follows.

The non-linear signal response of the detector was first corrected for in all on- and off-source frames. Off-source exposures were averaged and subtracted from the corresponding averaged on-source exposures to remove the dark current, the thermal background and the telluric emission lines. Residuals due to spatial and temporal variations in the sky emission level could not be removed using sky portions of the images because M 82 completely filled all fields, but they were minimized by taking the off-source frames as close as possible in space and time. Spatial and spectral flat-fielding, to correct for the differential response of the array pixels and for the instrumental transmission, was performed with the featureless images of observatory's dome and of a glowing Nernst rod. Wavelength calibration was achieved using images of a neon discharge lamp, and the data were spectrally redistributed onto a regular grid of spacing $0.002\,\mu$m. The two-dimensional wavelength-calibrated frames were then rearranged in a three-dimensional data cube in which dead and hot pixels were corrected for by interpolation.

The atmospheric transmission was corrected for with the help of the calibration stars that were observed immediately before and/or after M 82 and reduced as described above. The procedure followed for the K-band data was quite straightforward and similar to that applied for the stellar library stars in section 2.2.3. The calibration spectra were first extracted from the data cubes and divided by a black-body curve of the appropriate temperature given the spectral type of each reference star. The Brγ absorption line, in a wavelength range where the atmospheric transmission is little sensitive to the atmospheric conditions, was removed by linear interpolation. The other intrinsic features were corrected for by the division with the normalized and Brγ-corrected spectrum of the G3 V star — having similar line strengths as the F5 V and G0 V calibrators — from the Kleinmann & Hall (1986) atlas, convolved at the resolution of the 3D data. The M 82 data cubes were divided by the resulting calibration spectra. The residuals introduced by inexact cancellation of the intrinsic features of the reference stars are less than 1%.

In the H-band, B, late-F and early-G dwarf stars have intrinsic features at $\geq 5\%$ of the continuum level, even at $R \sim 1000$. Since no complete H-band spectra for these types of stars were digitally available, the correction procedure was different than for the K-band data. Composite calibration spectra were constructed as follows. Synthetic spectra were generated between $1.55\,\mu$m and $1.75\,\mu$m, where the atmospheric transmission is most stable, at the proper resolution and sampling as well as zenithal distance using the program ATRAN (Lord 1992). At the edges of the H-band ($\lambda < 1.55\ \mu$m and $\lambda > 1.75\ \mu$m), the transmission is very sensitive to the actual atmospheric conditions and the stars remain the best calibrators for these wavelength ranges. Since they also have no important features bluewards of $1.55\,\mu$m and redwards of $1.75\,\mu$m (within the range observed with 3D), these portions of their spectrum were ratioed with the appropriate blackbody curves and connected to the synthetic spectra. The M 82 data cubes were then divided by the resulting composite calibration spectra.

Since the atmosphere was not monitored simultaneously with M 82, spatial and temporal variability of the atmospheric transmission led to imperfect cancellation of telluric absorption features. The proximity in time and sky position of the calibration stars kept this effect below $3\% - 4\%$ for most of the H- and K-band. Between $1.9\,\mu$m and $2.0\,\mu$m as well as at both edges of the H-band, where the atmospheric transmission is lower and more variable, residuals up to 20% remained. The spurious features were reduced by fine-tuning the airmass assigned to the calibration star with the help of ATRAN. An examination of spectra taken at various positions within the observed regions reveals that residuals do not persist to more than 1% in the K-band and in the middle of the H-band but can amount to 10% at the edges of the H-band.

The resulting data cubes were smoothed with a two-dimensional gaussian to a common spatial resolution of $1.5''$. The small scale structure is thus smeared out in the higher resolution fields, but no important spatial features are lost. This was necessary in order to mosaic properly the various fields of view. The data cubes were flux-calibrated relative to one another by adjusting the mean broad-band flux in the overlapping areas to a common level, and were thereafter combined to produce the final mosaic. Absolute flux calibration was achieved using the broad-band photometric measurements from Rieke *et al.* (1980) in $3.9''$ and $5.8''$ circular apertures centered on the K-band peak. The uncertainties on the absolute fluxes are estimated to be 15% in the H-band and 10% in the K-band. They include possible systematic errors in the relative spatial and spectral flux distribution which may occur in the background subtraction, in the correction for telluric absorption and in the mosaicking (see also section 4.2.2).

4.1.3 Mid-infrared observations and data reduction

Mid-infrared spectroscopy of M 82 was obtained with the Short Wavelength Spectrometer (SWS; de Graauw *et al.* 1996) on board *ISO*[1] (Kessler *et al.* 1996). These observations were carried out as part of the MPE *ISO* Central Program project "Galactic Nuclei" during *ISO* revolution 116 on March 12, 1996. The grating scan mode AOT SWS01 was used to get a full spectrum of the entire SWS range from 2.4 μm to 45 μm. The slowest scan speed was selected to obtain the highest spectral resolution possible in this mode (*i.e.* half of the full SWS resolution). In addition, individual lines were scanned with the grating line profile mode AOT SWS02, to get full SWS resolving power ($R \sim 1000 - 2000$) for the key lines used in the data interpretation.

The SWS rectangular aperture was centered on the western mid-infrared emission peak (actual pointing at α_{1950}: $09^{\rm h}51^{\rm m}42\overset{\rm s}{.}20$, δ_{1950}: $+69°55'00\overset{''}{.}74$). The major axis of the aperture was oriented at a position angle of $64\overset{\circ}{.}5$ so that the SWS field of view was aligned nearly parallel to the galactic plane of M 82. The size of the SWS field of view depends on the "band" in which a line or wavelength range is observed, as reported in table 4.3. The SWS apertures include the regions mapped with 3D, as illustrated in figure 4.1. They extend out to a maximum distance of about 350 pc from the nucleus of M 82 and contain parts of the molecular ring to the west.

The on-source integration time for the individual line observations was of 100 s, with a reset time of 1 s. For the weakest lines, the scans were repeated up to three times to increase the signal-to-noise ratio. The SWS full scan, which covers all bands, took in total $1^{\rm h}50^{\rm m}$.

[1] *ISO* is an ESA project with instruments funded by ESA Member States (especially the PI countries: France, Germany, the Netherlands and the United Kingdom) with the participation of ISAS and NASA. The SWS is a joint project of SRON and MPE.

Table 4.3: *ISO*-SWS aperture size as a function of wavelength

Band	Wavelength range	Aperture size
1	2.38 – 4.05 μm	$14'' \times 20''$
2	4.05 – 12.0 μm	$14'' \times 20''$
3A, 3C, 3D	12.0 – 27.8 μm	$14'' \times 27''$
3E	27.8 – 29.5 μm	$20'' \times 27''$
4	29.5 – 45.2 μm	$20'' \times 33''$

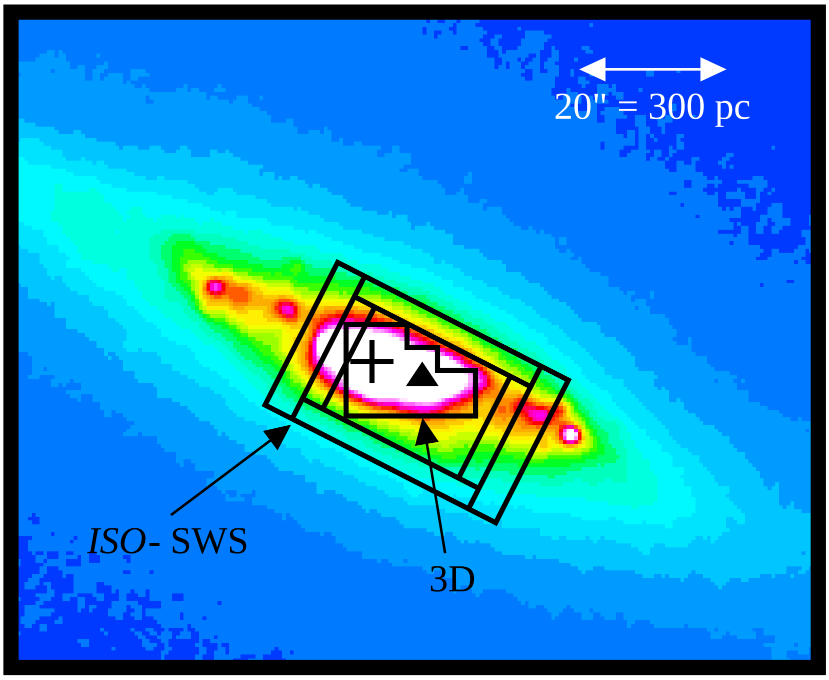

Fig. 4.1.— 3D field of view and *ISO*-SWS apertures shown on a K-band image of M 82 (Förster 1995). The cross and the triangle indicate the positions of the nucleus and of the western mid-infrared peak respectively. The molecular ring, which encloses the starburst core of M 82, is located just outside the bright central concentration in the 2 μm emission.

The *ISO*-SWS data were reduced with the SWS Interactive Analysis package (SIA), using special interactive extensions for glitch tail removal, dark subtraction, up-down correction, flat fielding and defringing. As the combined spectra of the 12 detectors of each SWS band are oversampled, the final data were rebinned to the proper instrumental resolution. The calibration was performed using the SWS calibration tables as of February 15, 1998, equivalent to OLP version 7.0. The overall accuracy of the line and continuum fluxes is estimated to be $\approx 10\% - 20\%$ (Schaeidt *et al.* 1996; Salama *et al.* 1997).

4.2 Results

4.2.1 Near-infrared spectra of selected regions

Three individual regions within the 3D field of view were selected for a particularly detailed analysis in the subsequent chapters: the nucleus, and the Brγ sources located $10''$ west, $5''$ south and $5''$ west, $2''$ south from the nucleus, denoted hereafter "B1" and "B2" (see figure 4.3). B1 is close to the molecular ring, and B2 coincides with the western peak in the mid-infrared continuum emission. All three positions were chosen because they sample representative regions of the starburst core of M 82, with different spectral properties indicative of different stellar populations as described below.

The H- and K-band spectra of the individual regions as well as of the entire 3D field of view were extracted from both 3D data cubes shifted by half a pixel in wavelength space. The were merged in the manner described in section 2.2.3 to obtain full Nyquist sampling, and have a final spectral resolution of $R \sim 1015$ in the H-band and $R \sim 830$ in the K-band. Synthetic apertures of $2.3'' \times 2.3''$ were used for the individual regions, corresponding to 35 pc $\times$ 35 pc. The resulting spectra are shown in figure 4.2. The emission lines were identified from the line positions given in Allen (1976), Morris *et al.* (1996), Black & van Dishoeck (1987), and Nussbaumer & Storey (1988). The absorption features were identified by comparison with the stellar spectra obtained with 3D and from Kleinmann & Hall (1986), Origlia, Moorwood & Oliva (1993) and Lançon & Rocca-Volmerange (1992). All spectra exhibit the typical signatures of starburst activity but the intensity of the emission and absorption features relative to the continuum vary with position. The emission lines become stronger along the radial sequence Nucleus $\rightarrow$ B2 $\rightarrow$ B1. The stellar absorption features show the opposite trend. This reveals important spatial variations on relatively small scales in the stellar populations within the starburst core of M 82, and suggests that the most recent enhanced star formation activity has taken place outside the nucleus, as proposed by several authors (see chapter 1).

The H- and K-band flux densities were computed by averaging over the spectra of each region in the ranges $\lambda = 1.52 - 1.78\ \mu$m and $\lambda = 1.96 - 2.42\ \mu$m respectively, and are reported in table 4.4, together with the area and position of the individual regions. Throughout this work, the photometric system of Wamsteker (1981) is adopted. Its specifications are given in appendix C. The 3D bandpasses do not cover completely those of Wamsteker's system. In addition, the data from Rieke *et al.* (1980) used for the absolute flux calibration of the 3D data cubes are expressed in a slightly different system. However, since the continuum dominates the broad-band emission and is

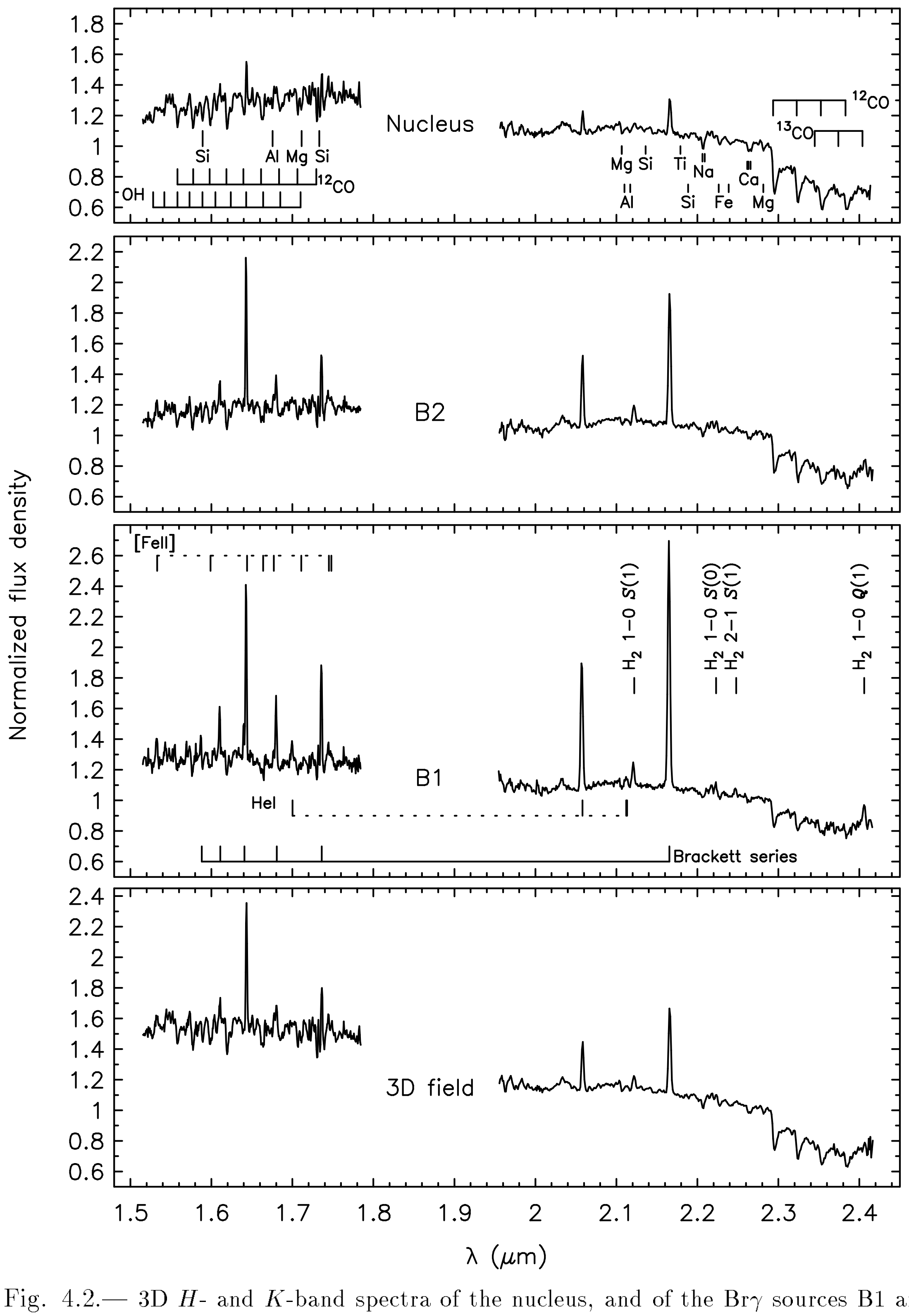

Fig. 4.2.— 3D H- and K-band spectra of the nucleus, and of the Brγ sources B1 and B2 taken in $2.3'' \times 2.3''$ apertures (see table 4.4 and figure 4.3), as well as of the entire 3D field of view. The resolution is $R \sim 1015$ in the H-band and $R \sim 830$ in the K-band. The vertical axis is a linear flux density scale. The spectra are normalized to unity in the interval $2.2875 - 2.2910\ \mu$m. The absolute flux densities in W m$^{-2}\,\mu$m^{-1} can be recovered using the multiplicative factors 6.52×10^{-14} for the nucleus, 2.96×10^{-14} for B2, 1.78×10^{-14} for B1 and 7.24×10^{-13} for the 3D field of view. The positions of various lines are indicated on the spectra of the nucleus (stellar absorptions) and of B1 (emission lines).

Table 4.4: H- and K-band flux densities (f_H and f_K) of selected regions in M 82 (in Jy)[(a)]

Region	Area and location[(b)]	f_H	f_K
Nucleus	$2.3'' \times 2.3''$ at $(0'', 0'')$	0.076	0.104
B1	$2.3'' \times 2.3''$ at $(-10'', -4.25'')$	0.021	0.030
B2	$2.3'' \times 2.3''$ at $(-5.25'', -2'')$	0.032	0.048
3D field	$\approx 16'' \times 10''$ at $\approx (-4'', -1'')$	1.01	1.20

[(a)] The uncertainties on f_H and f_K are estimated to be 15% and 10% respectively.

[(b)] Position relative to the peak of the K-band emission — see table 4.1

relatively flat for the regions observed with 3D, the differences in flux densities measured in these systems are 3% or less. A more detailed discussion is given in appendix C.

The fluxes of various emission lines (H I and He I recombination lines, H_2 rotation-vibration lines and [Fe II] lines) were integrated in the spectra after subtracting the continuum obtained by fitting a straight line to adjacent line-free spectral regions. The continuum-defining intervals were selected by inspection of template spectra of K and M stars from the 3D, Kleinmann & Hall (1986) and Origlia, Moorwood & Oliva (1993) atlases so that the linear interpolation adequately represented the underlying continuum. The validity of this procedure was tested by integrating the line fluxes after subtracting several template spectra of stars within ± 3 spectral classes of the representative type for each region (determined in chapter 6). The average line fluxes are reported in table 4.5, where the uncertainties correspond to one standard deviation of the multiple measurements. At the spectral resolution of 3D, the Br11 and Br12 lines at 1.6807 μm and 1.6407 μm are blended with the [Fe II] lines at 1.6769 μm and 1.6435 μm respectively. In these cases, double gaussian profiles were fitted to the emission features in order to determine the individual line fluxes. The emission lines contribute at most 1.5% to the broad-band flux densities for all four regions.

The equivalent widths (EWs) of several of the most prominent stellar absorption features (CO first and second overtone bandheads at 2.29 μm and 1.62 μm, Si I, Na I and Ca I features at 1.59 μm, 2.21 μm and 2.26 μm) were measured on the spectra according to the definitions and corrections for resolution effects given in chapter 2. The EWs are reported in table 4.6. The Br14 emission line at 1.5881 μm partially fills the Si I feature in all spectra. In order to remove this contamination, the profile of the Br13 line at 1.6109 μm was scaled according to the intrinsic ratio Br14/Br13 = 0.80 assuming case B recombination (Hummer & Storey 1987), and subtracted at the position of Br14. An electron density of $n_e = 300\ \mathrm{cm}^{-3}$ and temperature of $T_e = 5000$ K were adopted, as appropriate for M 82 (see chapter 5). Differential extinction between these lines can be neglected because they are so close in wavelength.

Table 4.5: Near-infrared emission line fluxes of selected regions in M 82 (in 10^{-17} W m^{-2})[a]

Species	Transition[b]	Nucleus	B1	B2	3D field
[Fe II]	$a^4F_{9/2} - a^4D_{5/2}$ (1.5335 μm)	< 0.11	0.75 ± 0.09	0.56 ± 0.04	9.2 ± 2.9
H I	Br13 ($n = 4 - 13$, 1.6109 μm)	0.48 ± 0.30	0.90 ± 0.08	0.71 ± 0.16	13.2 ± 4.5
H I	Br12 ($n = 4 - 12$, 1.6407 μm)	0.33 ± 0.08	0.81 ± 0.19	0.75 ± 0.45	12.9 ± 6.5
[Fe II]	$a^4F_{9/2} - a^4D_{7/2}$ (1.6435 μm)	4.12 ± 0.07	3.53 ± 0.44	4.99 ± 0.44	137 ± 12
[Fe II]	$a^4F_{7/2} - a^4D_{5/2}$ (1.6769 μm)	0.52 ± 0.37	0.22 ± 0.07	0.34 ± 0.13	10.5 ± 3.6
H I	Br11 ($n = 4 - 11$, 1.6807 μm)	0.42 ± 0.25	1.44 ± 0.28	0.90 ± 0.19	14.3 ± 4.1
He I	$3\,^3P - 4\,^3D$ (1.7008 μm)	< 0.16	0.50 ± 0.12	0.38 ± 0.09	6.3 ± 2.8
H I	Br10 ($n = 4 - 10$, 1.7362 μm)	1.22 ± 0.24	2.31 ± 0.18	1.76 ± 0.17	32.2 ± 5.2
He I	$2\,^1S - 2\,^1P$ (2.0581 μm)	2.53 ± 0.28	5.19 ± 0.08	4.34 ± 0.14	74.9 ± 3.3
He I	Blend of $3\,^1P - 4\,^1S$ and $3\,^3P - 4\,^3S$ (2.113 μm)	—	0.48 ± 0.05	—	—
H_2	$1 - 0$ $S(1)$ (2.1213 μm)	1.01 ± 0.21	0.66 ± 0.07	0.98 ± 0.11	21.3 ± 2.4
H I	Brγ ($n = 4 - 7$, 2.1655 μm)	5.25 ± 0.55	10.1 ± 0.2	9.04 ± 0.25	148 ± 6
H_2	$1 - 0$ $S(0)$ (2.2227 μm)	0.67 ± 0.14	0.11 ± 0.03	0.25 ± 0.07	9.8 ± 1.6
H_2	$2 - 1$ $S(1)$ (2.2471 μm)	0.29 ± 0.10	0.28 ± 0.03	0.20 ± 0.06	6.3 ± 1.2
H_2	$1 - 0$ $Q(1)$ (2.4059 μm)	0.92 ± 0.27	1.04 ± 0.22	1.31 ± 0.32	13.2 ± 3.2

[a] The uncertainties represent those of the continuum subtraction (see text). Uncertainties of the absolute flux calibration and systematic errors are estimated to be 15% in the H-band, and 10% in the K-band.

[b] Ionic transitions are given as *lower level - upper level*. H_2 transitions are labeled by the upper and lower vibrational quantum numbers followed by $S(j)$ or $Q(j)$ which refer to transitions for which $j - j'$ equals -2 or 0 respectively, where j and j' are the lower and upper rotational quantum numbers.

Table 4.6: EWs in Å of near-infrared stellar absorption features of selected regions in M 82[a]

Region	$W_{1.59}$[b]	$W_{1.62}$	$W_{2.29}$	$W_{\rm Na}$	$W_{\rm Ca}$	$\log(W_{1.62}/W_{1.59})$	$\log(W_{1.62}/W_{2.29})$
Nucleus	3.6	5.6	15.2	4.1	2.9	0.19 ± 0.05	-0.43 ± 0.03
B1	3.3	3.4	8.4	2.9	1.8	0.01 ± 0.07	-0.39 ± 0.05
B2	3.7	4.6	12.2	3.5	2.1	0.09 ± 0.05	-0.42 ± 0.04
3D field	3.4	4.8	13.0	3.3	2.2	0.15 ± 0.06	-0.43 ± 0.03

[a] Uncertainties are ± 0.4 Å for $W_{1.59}$, ± 0.3 Å for $W_{1.62}$, ± 0.6 Å for $W_{2.29}$ and ± 0.5 Å for $W_{\rm Na}$ and $W_{\rm Ca}$.

[b] Corrected for dilution by the Br14 line at 1.5881 μm as described in the text.

4.2.2 Near-infrared images

Broad-band images and maps of various emission lines and EWs of stellar absorption features were first obtained separately from the wavelength-shifted 3D data cubes by applying to each pixel the procedure described in the previous section for the spectra. The resulting pairs were then averaged together to produce the final images. Selected images and ratio maps are presented in figures 4.3, 4.4 and 4.5, and are briefly discussed below. Three boxes in each image indicate the $2.3'' \times 2.3''$ apertures used to extract the spectra of the individual regions shown in figure 4.2.

The spatial distributions of the H- and K-band emission obtained with 3D agree well with maps in the literature (*e.g.* Dietz *et al.* 1986; Telesco *et al.* 1991; Rieke *et al.* 1980; Larkin *et al.* 1994; Satyapal *et al.* 1995). The emission is generally centrally concentrated about the nucleus, but small-scale structure is apparent, in particular the so-called "secondary peak" $8''$ west from the nucleus. Synthetic circular aperture photometry on the 3D broad-band maps is compared in table 4.7 to selected measurements in the literature. The slight differences between the H- and K-band images are presumably due to spatial variations in the dust obscuration (*e.g.* Telesco *et al.* 1991). The accuracy of the mosaicking can be assessed by comparing the H- and K-band flux densities measured at different positions between the 3D data and the large-scale images at $1''$ resolution from Satyapal *et al.* (1997), which were obtained with a single detector array (table 4.7). The relative flux densities between various regions agree typically to 15% and 10% in the H- and K-band respectively. The differences may be due in part to the different spatial resolution of the data sets.

The Brγ and the He I $2.058\,\mu$m line emission exhibit clumpy morphologies and follow each other very well. The ratio map, however, reveals spatial variations in the He I 2.058/Brγ line ratio. The Brγ image obtained with 3D agrees well with previously published maps (Waller, Gurwell & Tamura 1992; Larkin *et al.* 1994; Satyapal *et al.* 1995). The Brγ line flux was measured in various circular apertures centered on the nucleus and is compared with measurements from the literature in table 4.8. The discrepancies between the various results are very large: up to a factor of 3.5. They are probably attributable to uncertainties in absolute calibration, positioning and continuum subtraction. The spatial distribution of the [Fe II] $1.644\,\mu$m line emission is different, and reveals a prominent arc-like structure nearly centered on the nucleus, on the south side. The contamination of the [Fe II] linemap from the adjacent Br12 emission line due to inaccurate deblending is more important in regions where the Brγ line is stronger, but does not exceed 15%.

Table 4.7: Comparison between H- and K-band photometric measurements from 3D and from the literature

Band	Position[(a)] $(\Delta\alpha, \Delta\delta)$	Aperture diameter [arcsec]	Observed flux[(b)] [Jy]	Literature[(c)] [Jy]
H	(0, 0)	3.9	0.148	0.141 (1)
	(0, 0)	5.8	0.266	0.252 (1)
	(0, 0)	2.0	0.052	0.050 (2)
	(-3.8, -2.6)	2.0	0.022	0.016 (2)
	(-5.0, -0.1)	2.0	0.024	0.017 (2)
	(-7.1, -0.6)	2.0	0.032	0.022 (2)
	(-8.4, -3.9)	2.0	0.015	0.014 (2)
	(-8.9, -1.7)	2.0	0.031	0.027 (2)
	(-10.8, -3.5)	2.0	0.013	0.011 (2)
	(-10.9, -1.8)	2.0	0.018	0.020 (2)
K	(0, 0)	3.9	0.209	0.200 (1)
	(0, 0)	5.8	0.371	0.350 (1)
	(0, 0)	2.0	0.070	0.075 (2)
	(-3.8, -2.6)	2.0	0.031	0.025 (2)
	(-5.0, -0.1)	2.0	0.033	0.025 (2)
	(-7.1, -0.6)	2.0	0.039	0.027 (2)
	(-8.4, -3.9)	2.0	0.022	0.019 (2)
	(-8.9, -1.7)	2.0	0.042	0.036 (2)
	(-10.8, -3.5)	2.0	0.022	0.017 (2)
	(-10.9, -1.8)	2.0	0.027	0.027 (2)

[(a)] Position in arcseconds relative to the peak of the K-band emission — see table 4.1.

[(b)] The uncertainties on the 3D measurements are 15% in the H-band and 10% in the K-band.

[(c)] References: (1) Rieke *et al.* 1980; the uncertainties are $\sim$ 5%. (2) Satyapal *et al.* 1997; the uncertainties are 10%.

The contrast between the distribution of the broad-band emission and of the H I recombination line emission is well delineated by the logarithmic map of the ratio of the K-band to Lyman continuum luminosities, $\log(L_K/L_{\rm Lyc})$. L_K is proportional to the K-band flux density f_K and bandwidth $\Delta\lambda$. $L_{\rm Lyc}$ is computed from the Brγ line flux $F_{\rm Br\gamma}$ assuming case B recombination and using the recombination coefficients from Hummer & Storey (1987). For $\Delta\lambda = 0.6~\mu$m, and for $n_{\rm e} = 300$ cm^{-3} and $T_{\rm e} = 5000$ K,

$$\log\left(\frac{L_K}{L_{\rm Lyc}}\right) = \log\left(3.99 \times 10^{-4}\,\frac{f_K}{F_{\rm Br\gamma}}\right), \tag{4.1}$$

where f_K is expressed in W m$^{-2}\,\mu$m^{-1} and $F_{\rm Br\gamma}$, in W m^{-2}.

Table 4.8: Comparison between Brγ flux measurements from 3D and from the literature

Aperture diameter[(a)] [arcsec]	Observed flux [10^{-17} W m^{-2}]	Source
3.8	11.3 ± 1.8	This work
	20.0 ± 0.4	Lester *et al.* (1990)
	5.7 ± 0.7	Larkin *et al.* (1994)
	17.1 ± 3.4	Satyapal *et al.* (1995)
8	48 ± 8	This work[(b)]
	22 ± 2	Rieke *et al.* (1980)
	26 ± 3	Larkin *et al.* (1994)
	73.6 ± 14.7	Satyapal *et al.* (1995)

[(a)] Aperture centered on the peak of the K-band emission — see table 4.1.

[(b)] An $8''$ aperture slightly exceeds the regions covered by the 3D Brγ map, but the missing flux is estimated to be less than a few percents.

The $W_{2.29}$ and $W_{1.62}$ maps reveal similar spatial variations in the observed EWs, indicating notably very deep absorption features around the nucleus and the "secondary peak", and progressively shallower features at B2 and B1. The ratio of $W_{1.62}$ and $W_{2.29}$ is however not constant throughout the regions observed, as illustrated by the $\log(W_{1.62}/W_{2.29})$ map. In particular, $W_{1.62}$ is enhanced relative to $W_{2.29}$ around B1 and B2. The $W_{2.29}$ image is similar to the CO index map obtained at low spectral resolution by Satyapal *et al.* (1997) within the regions observed with 3D. The $W_{2.29}$ map compares well with the spatial distribution of the K-band emission but even better with the $\log(L_K/L_{\rm Lyc})$ map. The local maximum of $W_{2.29}$ and $W_{1.62}$ around the nucleus does not coincide exactly with the position of the maximum K-band emission but is offset about $1.5''$ west and $0.5''$ south. This corresponds to the maximum of the $\log(L_K/L_{\rm Lyc})$ distribution and to a local minimum in the Brγ, He I 2.058 μm and [Fe II] 1.644 μm emission.

The images demonstrate clearly that the central 35 pc at the nucleus and B1 have the most extreme properties in the entire 3D field of view while B2 has intermediate properties, justifying their choice for a particularly detailed analysis. The maps also support the indication from the spectra in figure 4.2 that the most recent active star formation activity has occurred outside of the central few tens of parsecs.

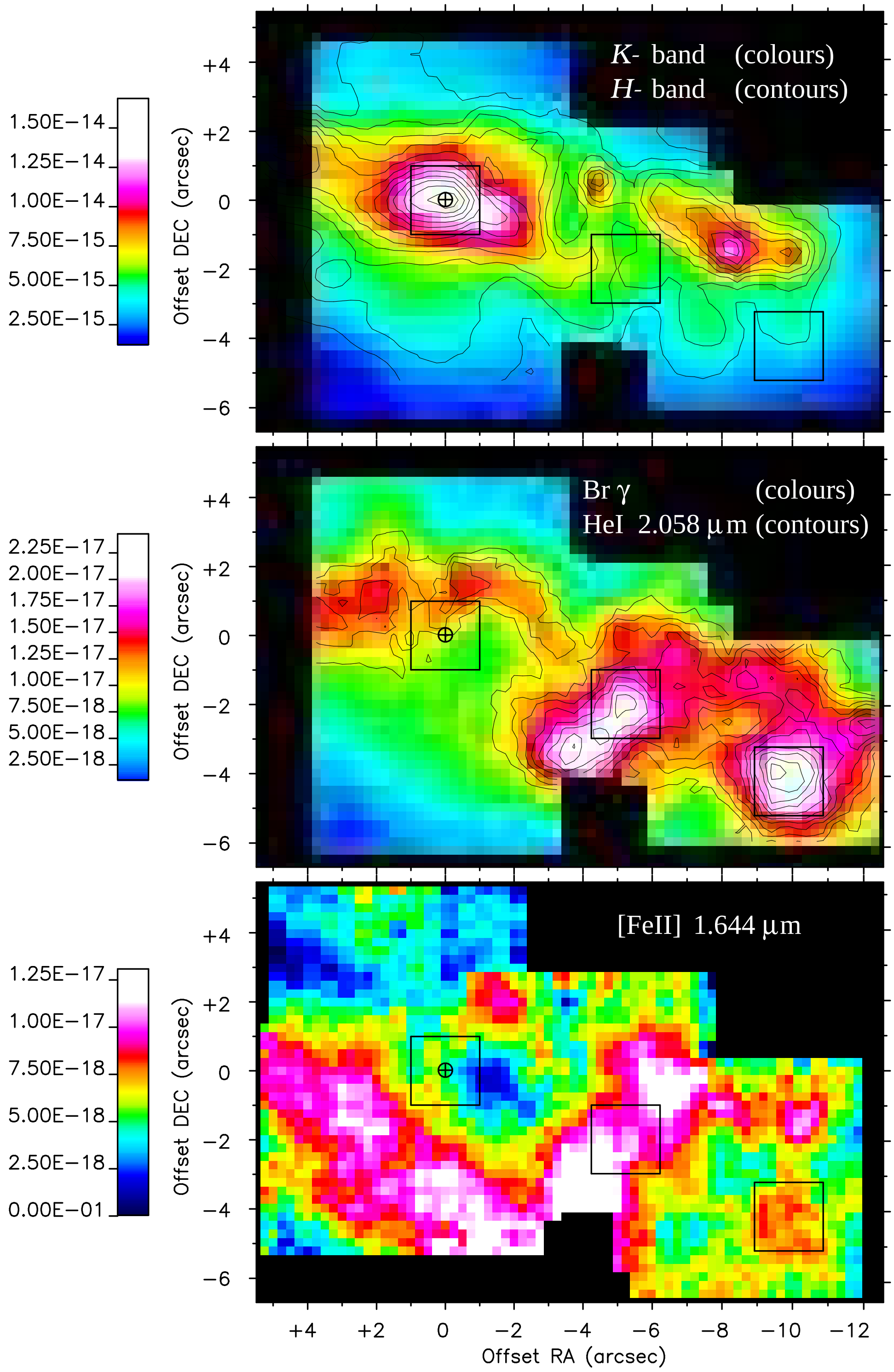

Fig. 4.3.— *Top:* False-colour image of the *K*-band emission in units of $\mathrm{W\,m^{-2}\,\mu m^{-1}\,arcsec^{-2}}$. Contours of the *H*-band emission, from 5.0 to 21.5 in steps of 1.5 and in units of 10^{-15} $\mathrm{W\,m^{-2}\,\mu m^{-1}\,arcsec^{-2}}$. *Middle:* False-colour image of the Brγ line emission in units of $\mathrm{W\,m^{-2}\,arcsec^{-2}}$. Contours of the He I 2.058 μm line emission, from 5.0 to 15.0 in steps of 1.0 in units of 10^{-18} $\mathrm{W\,m^{-2}\,arcsec^{-2}}$. *Bottom:* False-colour image of the [Fe II] 1.644 μm line emission in units of $\mathrm{W\,m^{-2}\,arcsec^{-2}}$. The crossed circle marks the position of the nucleus (table 4.1). The axis coordinates are relative offsets in arcsec from the nucleus. From left to right, the boxes indicate the central 35 pc of M 82, B2 and B1.

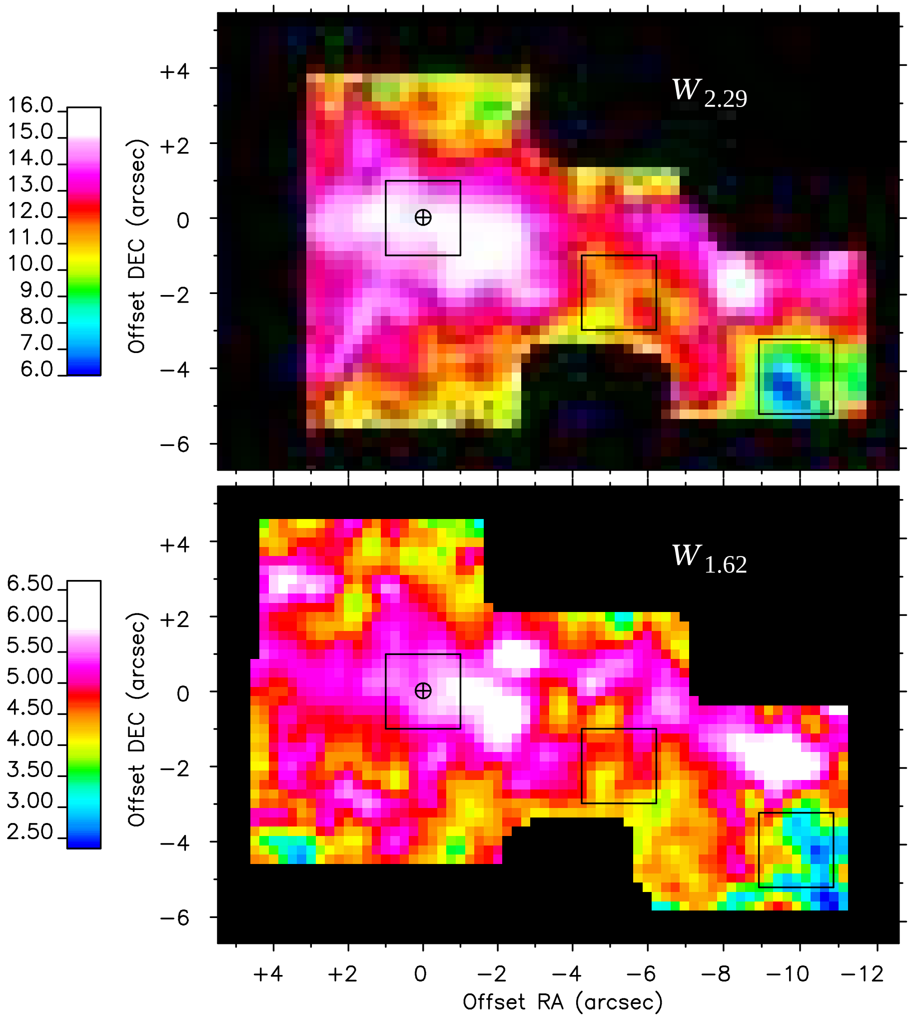

Fig. 4.4.— *Top:* False-colour map of the equivalent width of the ^{12}CO (2,0) bandhead at 2.29 μm, $W_{2.29}$, in units of Å. *Bottom:* False-colour map of the equivalent width of the ^{12}CO (6,3) bandhead at 1.62 μm, $W_{1.62}$, in units of Å. The crossed circle marks the position of the nucleus (table 4.1). The axis coordinates are relative offsets in arcsec from the nucleus. From left to right, the boxes indicate the central 35 pc of M 82, B2 and B1.

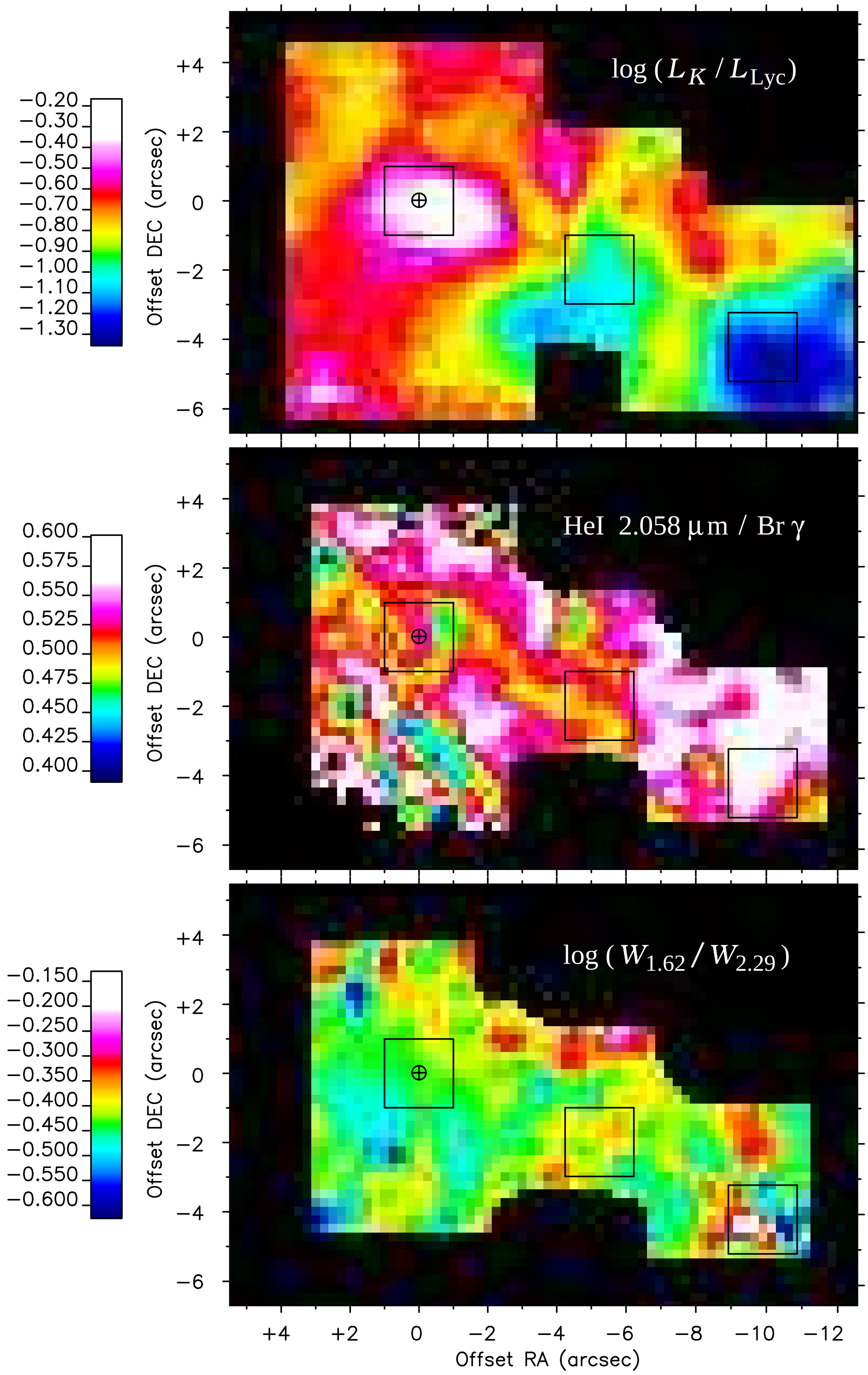

Fig. 4.5.— *Top:* False-colour map of $\log(L_K/L_{\rm Lyc})$ (see text). *Middle:* False-colour map of the He I 2.058/Brγ line ratio. *Bottom:* False-colour map of $\log(W_{1.62}/W_{2.29})$. The crossed circle marks the position of the nucleus (table 4.1). The axis coordinates are relative offsets in arcsec from the nucleus. From left to right, the boxes indicate the central 35 pc of M 82, B2 and B1.

4.2.3 Mid-infrared spectra

The full scan spectrum of M 82 between $2.4\,\mu$m and $45\,\mu$m is shown in figure 4.6. Several hydrogen recombination lines from the Brackett, Pfund and Humphreys series are detected as well as pure rotational lines from H_2 and numerous fine-structure forbidden lines from various atoms mostly in low ionization stages. Broad PAH emission features and absorption features from dust grains are conspicuous. The higher S/N ratio scans obtained for several individual lines are plotted in figure 4.7.

Broad-band flux densities computed from the full scan SWS01 spectrum are reported in table 4.9 and compared to flux densities in large apertures from the literature. The emission line fluxes were measured from both the full scan SWS01 spectrum and the individual line scans SWS02 spectra. A gaussian profile was fitted to the features after subtraction of the continuum baseline obtained by fitting a line to adjacent line-free portions of the spectrum. The line fluxes relevant to this work are given in table 4.10. In order to compare the data obtained with the different SWS apertures, the fluxes are also scaled to the smallest $14'' \times 20''$ aperture. Because most of the line emission arises from the regions within the smallest *ISO*-SWS field of view, the correction has to be smaller than the ratio of aperture areas. The scaling factors were estimated from the [Ne II] $12.8\,\mu$m map of Achtermann & Lacy (1995) and are 0.8 for the $14'' \times 27''$ aperture and 0.7 for the $20'' \times 33''$ one, with 10% uncertainty. The Brα $4.051\,\mu$m, [Ar III] $8.99\,\mu$m and [S IV] $10.51\,\mu$m maps obtained by these authors exhibit morphologies similar to that of the [Ne II] emission, justifying the use of the same scaling factors for all mid-infrared lines. At the resolution of the SWS, the Brβ line ($2.6252\,\mu$m) is blended with the H_2 1-0 $O(2)$ line at $2.626\,\mu$m. However, from the strength of the H_2 1-0 $Q(3)$ at $2.423\,\mu$m (2.65×10^{-16} W m^{-2}) and assuming fluorescent excitation (Black & van Dishoeck 1987), its contribution is estimated to be at most 30% to the Brβ flux. Several line fluxes from *ISO*-SWS are compared with measurements from the literature in table 4.11. Given the morphology of the emission regions (see Achtermann & Lacy 1995), the various results in different apertures are consistent with each other.

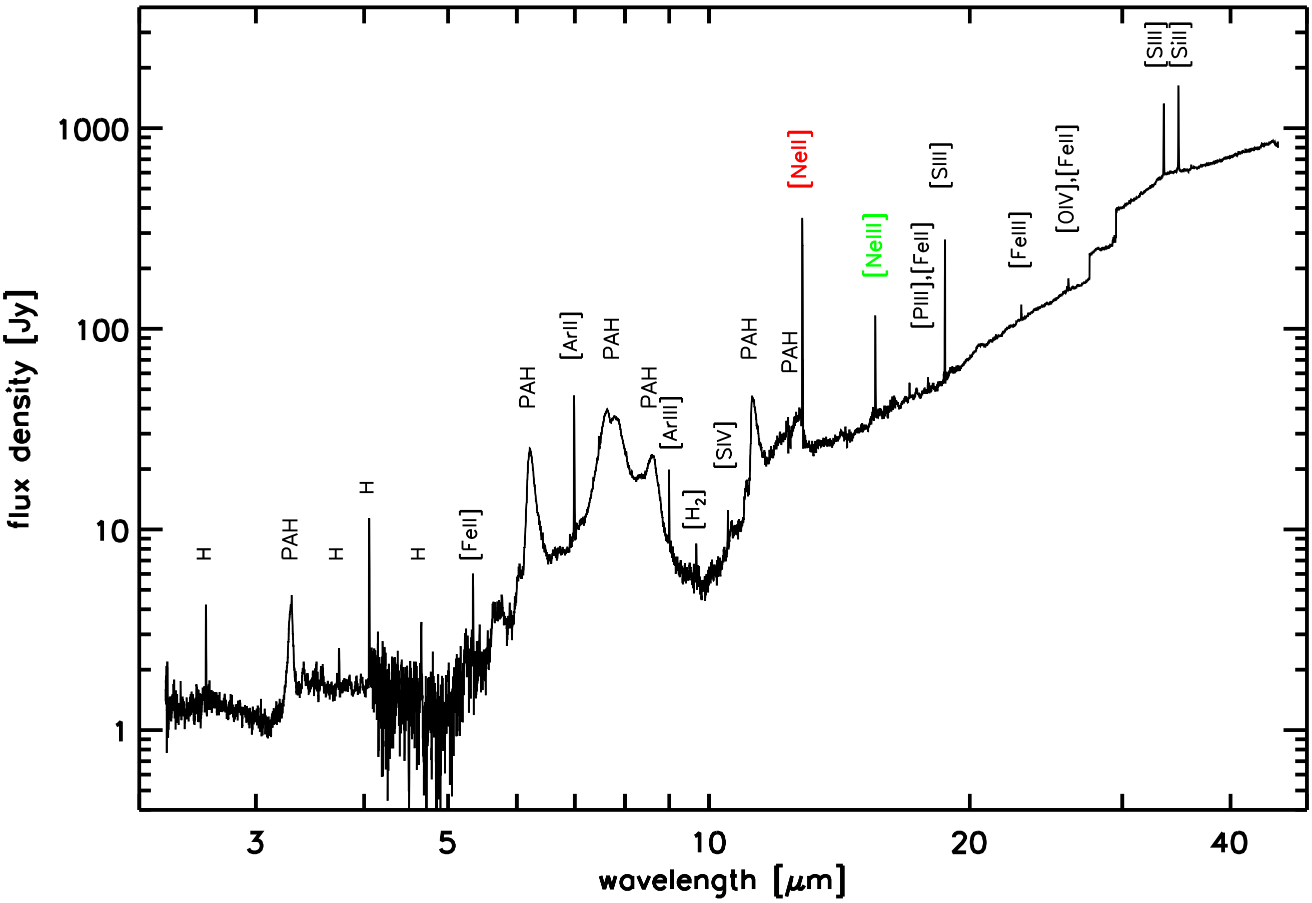

Fig. 4.6.— Mid-infrared spectrum of the central starburst regions of M 82, obtained with the *ISO*-SWS (full scan AOT-SWS01). The spectral resolution varies from ~ 1000 at short wavelengths to ~ 500 at long wavelengths. The "jumps" in the continuum level at 27.8 μm and 29.5 μm are due to the increase in aperture size. The jump at 12.0 μm is smaller and not obvious in this plot.

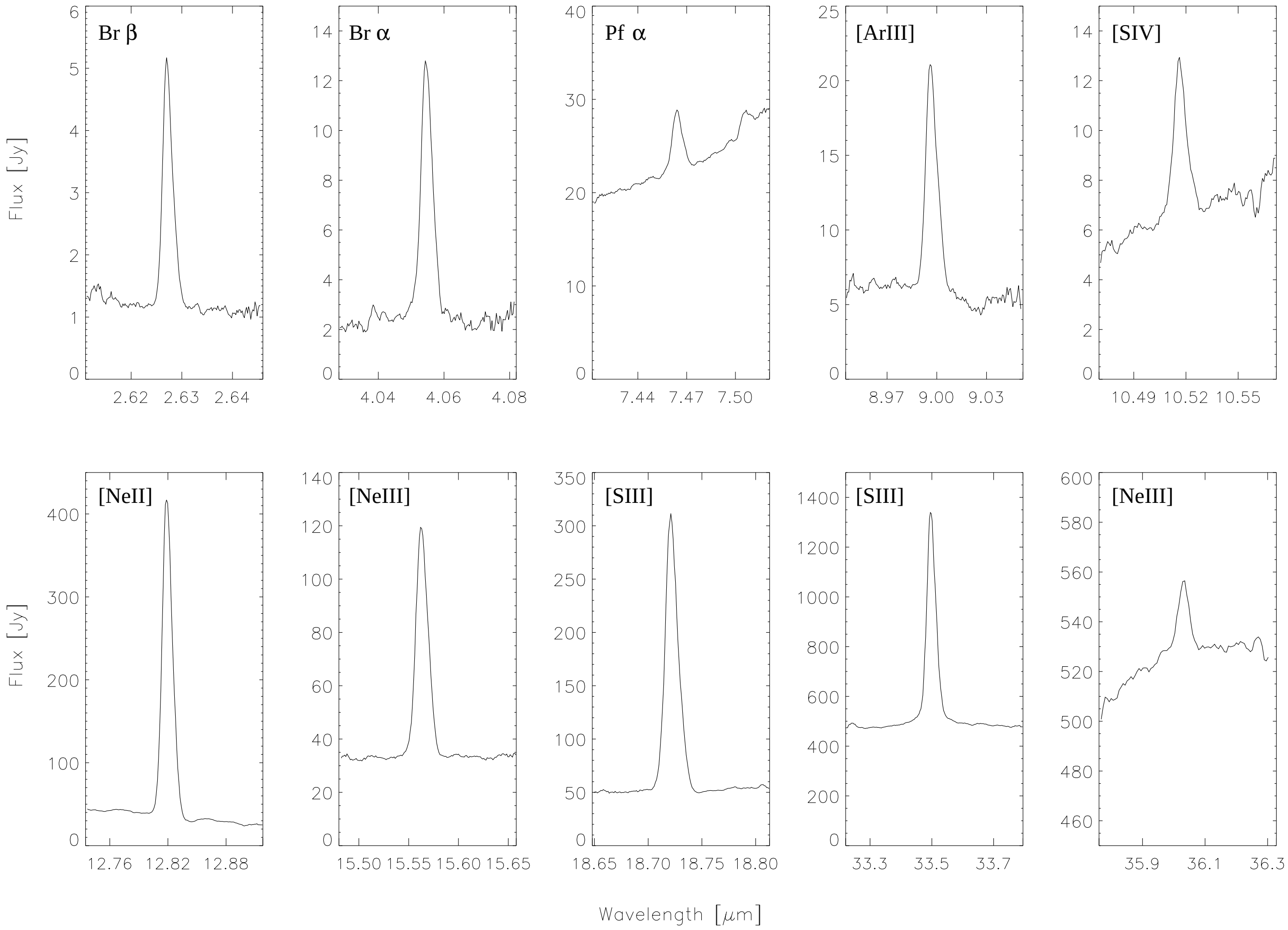

Fig. 4.7.— Higher S/N ratio spectra of individual mid-infrared lines observed in the central starburst regions of M 82 with the *ISO*-SWS (line scans AOT-SWS02). The resolution ranges from ~ 2000 at short wavelengths to ~ 1000 at long wavelengths.

Table 4.9: Comparison between mid-infrared broad-band flux densities from the *ISO*-SWS data[(a)] and from the literature

Band	λ [μm]	Observed flux [Jy]	Aperture[(b)]	Source
L	3.6	1.7 ± 0.3	SWS $14'' \times 20''$	This work
		2.3 ± 0.1	$35''$ diameter	Kleinmann & Low 1970a
M	4.8	1.4 ± 0.3	SWS $14'' \times 20''$	This work
		8.4 ± 1.5	$\approx 30''$ diameter	Rieke & Low 1972
N	10.5	19 ± 4	SWS $14'' \times 20''$	This work
		25 ± 3	$\approx 15'' \times 26''$	Telesco *et al.* 1991[(c)]
		45.4 ± 0.4	$\approx 40'' \times 90''$	Telesco *et al.* 1993
		27 ± 2	$\approx 30''$ diameter	Rieke & Low 1972
$11.8 - 13.0$ μm	12.4	35 ± 7	SWS $14'' \times 27''$	This work
		66 ± 7	$\approx 15'' \times 26''$	Telesco & Gezari 1992
Q	21	79 ± 16	SWS $14'' \times 27''$	This work
		120 ± 8	$\approx 30''$ diameter	Rieke & Low 1972

[(a)] Measured on the *ISO*-SWS01 full scan spectrum.

[(b)] All apertures centered within $8''$ of the nucleus. The rectangular apertures are roughly aligned parallel to the plane of the galaxy.

[(c)] As quoted by Telesco & Gezari (1992).

Table 4.10: Selected mid-infrared line fluxes measured in the central starburst regions of M 82, obtained with *ISO*-SWS

Species	Transition[(a)]	$\lambda_{\mathrm{observed}}$ [μm]	FWHM [μm]	Flux[(b)] [10^{-15} W m^{-2}]	Observation[(c)]	Scaled flux[(d)] [10^{-15} W m^{-2}]
H I	Brβ ($n = 4-6$, 2.6252 μm)	2.62726	0.00295	3.90	01 $14'' \times 20''$	
		2.62720	0.00231	4.10	02 $14'' \times 20''$	
H I	Pfδ ($n = 5-9$, 3.2961 μm)	3.29913	0.00325	0.59	01 $14'' \times 20''$	
H I	Pfγ ($n = 5-8$, 3.7395 μm)	3.74247	0.00501	1.07	01 $14'' \times 20''$	
H I	Hu14 ($n = 6-14$, 4.0198 μm)	4.02301	0.00370	0.13	02 $14'' \times 20''$	
H I	Brα ($n = 4-5$, 4.0512 μm)	4.05437	0.00464	8.75	01 $14'' \times 20''$	
		4.05474	0.00414	8.15	02 $14'' \times 20''$	
H I	Pfβ ($n = 5-7$, 4.6525 μm)	4.65623	0.00447	1.39	01 $14'' \times 20''$	
[Ar II]	$^2P_{3/2} - {}^2P_{1/2}$ (6.9853 μm)	6.98912	0.01083	26.7	01 $14'' \times 20''$	
H I	Pfα ($n = 5-6$, 7.4578 μm)	7.46376	0.00872	2.49	01 $14'' \times 20''$	
		7.46417	0.00727	2.59	02 $14'' \times 20''$	
[Ar III]	$^3P_2 - {}^3P_1$ (8.9914 μm)	8.99664	0.01096	4.89	01 $14'' \times 20''$	
		8.99681	0.00824	4.76	02 $14'' \times 20''$	
[S IV]	$^2P_{1/2} - {}^2P_{3/2}$ (10.5105 μm)	10.51646	0.01468	1.89	01 $14'' \times 20''$	
		10.51639	0.00825	1.49	02 $14'' \times 20''$	
[Ne II]	$^2P_{3/2} - {}^2P_{1/2}$ (12.8136 μm)	12.81923	0.01554	99.1	01 $14'' \times 27''$	79.3
		12.81936	0.01216	89.2	02 $14'' \times 27''$	71.4
[Ne III]	$^3P_2 - {}^3P_1$ (15.5551 μm)	15.56331	0.01685	17.5	01 $14'' \times 27''$	14.0
		15.56337	0.01404	15.7	02 $14'' \times 27''$	12.6
[S III]	$^3P_1 - {}^3P_2$ (18.7130 μm)	18.72210	0.01734	34.7	01 $14'' \times 27''$	27.8
		18.72181	0.01384	31.5	02 $14'' \times 27''$	25.2
[Ar III]	$^3P_1 - {}^3P_0$ (21.8293 μm)	21.84123	0.05191	0.70	02 $14'' \times 27''$	0.6
[S III]	$^3P_0 - {}^3P_1$ (33.4810 μm)	33.49818	0.03873	83.3	01 $20'' \times 33''$	58.3
		33.49816	0.03432	80.3	02 $20'' \times 33''$	56.2
[Ne III]	$^3P_1 - {}^3P_0$ (36.0135 μm)	36.03283	0.04118	2.92	01 $20'' \times 33''$	2.04
		36.03075	0.03535	2.68	02 $20'' \times 33''$	1.88

[(a)] Transitions are given as *lower level - upper level*.

[(b)] The uncertainties on the observed line fluxes are estimated to be 20% for most of the lines, and up to 50% for the faintest lines (including uncertainties of the absolute calibration, continuum subtraction and systematic errors).

[(c)] 01: data from the full scan SWS01 spectrum, 02: data from the individual line scan SWS02 spectra. The SWS02 data are preferred for the analysis because of their higher S/N ratio.

[(d)] Data obtained in the $14'' \times 27''$ and $20'' \times 33''$ apertures are scaled down to the $14'' \times 20''$ aperture using the factors 0.8 and 0.7 respectively (see text). The uncertainties on the scaling factors are estimated to be 10%.

Table 4.11: Comparison between mid-infrared line flux measurements obtained with *ISO*-SWS[a] and from the literature

Line	Position[b] ($\Delta\alpha, \Delta\delta$)	Aperture[b]	Observed flux [10^{-15} W m^{-2}]	Source
Brα 4.05 μm	(-8, -2.5)	$14'' \times 20''$	8.15 ± 1.47	This work
	$\approx(-6, 0)$	$30''$	16	Willner *et al.* 1977
	$\approx(-6, 0)$	$11''$	3.8 ± 0.3	Simon, Simon & Joyce 1979
	—	3 brightest sources	15.8 ± 3.16	Achtermann & Lacy 1995
[Ar II] 6.99 μm	(-8, -2.5)	$14'' \times 20''$	26.7 ± 5.3	This work
	$\approx(-6, 0)$	$28''$	40 ± 10	Willner *et al.* 1977
[Ar III] 8.99 μm	(-8, -2.5)	$14'' \times 20''$	4.76 ± 0.95	This work
	—	3 brightest sources	10.4 ± 2.08	Achtermann & Lacy 1995
[S IV] 10.5 μm	(-8, -2.5)	$14'' \times 20''$	1.49 ± 0.45	This work
	—	3 brightest sources	3.0 ± 0.90	Achtermann & Lacy 1995
[Ne II] 12.8 μm	(-8, -2.5)	$14'' \times 27''$	89.2 ± 17.8	This work
	$\approx(-6, 0)$	$7''$	60	Gillett *et al.* 1975
	$\approx(-6, 0)$	$25'' \times 35''$	300	Gillett *et al.* 1975
	$\approx(-6, 0)$	$30''$	1080 ± 270	Willner *et al.* 1977
	(0, 0)	$30'' \times 20''$	126 ± 38	Beck *et al.* 1978[c]
	—	3 brightest sources	180 ± 27	Achtermann & Lacy 1995
[S III] 18.7 μm	(-8, -2.5)	$14'' \times 27''$	31.5 ± 6.3	This work
	(0, 0)	$25''$	52.1 ± 15.6	Houck *et al.* 1984
[S III] 33.5 μm	(-8, -2.5)	$20'' \times 33''$	80.3 ± 16.1	This work
	(0, 0)	$25''$	116.3 ± 14.0	Houck *et al.* 1984

[a] The measurements from the individual line scan SWS02 data are preferred when available.

[b] Position in arcsecs relative to the peak of the K-band emission — see table 4.1. For circular apertures, the diameter is given. Rectangular apertures are roughly aligned parallel to the plane of the galaxy.

[c] Integrated over the velocity maps as quoted in Lord *et al.* 1996.

Chapter 5

Nebular analysis of the starburst regions in M 82

From the new *ISO*-SWS and 3D data presented in the previous chapter, two main constituents within the central starburst regions of M 82 can be investigated, namely the interstellar medium (ISM) and the stellar population. Various near- and mid-infrared emission lines probe the physical conditions of the ISM and measure the intensity and shape of the ultraviolet radiation field from the hot, young stars. The near-infrared absorption features allow the characterization of the composition of the cool, evolved stellar population.

This chapter presents the nebular analysis of M 82. The physical parameters critical for the interpretation of the nebular line emission are first derived[1], and the composition of the population of OB stars is then investigated. Specifically, the following properties are quantitatively constrained:

- the interstellar extinction towards the H II regions,
- the electron density and temperature within the line-emitting gaseous nebulae,
- the gas-phase chemical abundances for these nebulae,
- the degree of ionization as well as the geometry of the ionized and neutral gas in the H II regions, and
- the average effective temperature and number population of the OB stars.

[1]the derivation of many of the equations used can be found in basic reference work, such as Spitzer (1978) and Osterbrock (1989), and so are not repeated here

5.1 Interstellar extinction

5.1.1 Overview

Interstellar extinction is the obscuration of background light through absorption and scattering by intervening dust grains. The extinction depends on the nature and sizes of the obscuring particles and varies with the wavelength of the incident radiation (*e.g.* Mathis, Rumpl & Nordsieck 1977; Draine & Lee 1984; Emerson 1988; and the review by Mathis 1990). In general, the continuous opacity of interstellar dust grains increases at progressively shorter wavelengths.

The variation of extinction with wavelength ("extinction law") is often expressed in magnitudes and relative to the extinction in the V-band (centered at $\lambda = 0.55$ μm) as A_λ/A_V. The extinction in magnitudes is related to the optical depth τ through

$$A_\lambda = 2.5\,\log(e)\,\tau_\lambda = 1.086\,\tau_\lambda. \tag{5.1}$$

Alternatively, the extinction law can be expressed as the colour excess $E_{\lambda-V}$ relative to E_{B-V} (the B-band is centered at $\lambda = 0.44$ μm). The colour excess between two wavelengths λ_1 and λ_2 is defined as $E_{\lambda_1-\lambda_2} \equiv (m_{\lambda_1} - m_{\lambda_2}) - (m_{\lambda_1} - m_{\lambda_2})_0 = A_{\lambda_1} - A_{\lambda_2}$. The difference in magnitude of the fluxes, $(m_{\lambda_1} - m_{\lambda_2})$ and $(m_{\lambda_1} - m_{\lambda_2})_0$, are the observed and intrinsic colour indices. The absolute amount of extinction at a given wavelength is usually transformed into an equivalent A_V or E_{B-V} by assuming an extinction law.

Observationally, and regardless of the dust properties, the amount of extinction and its wavelength dependence are usually measured by the effects of the obscuring material on the detected light. The differential extinction $A_{\lambda_1} - A_{\lambda_2}$ is determined by comparing the observed fluxes at wavelengths λ_1 and λ_2 from attenuated sources whose intrinsic spectral energy distribution is well-known — such as stars. Similarly, ratios of line fluxes emitted by gaseous nebulae for which the physics are well understood provide solid diagnostics for the extinction, as, for example, the nebular H I recombination lines. Various other methods, including measurements of the dust column density from the strength and profile of dust absorption features (notably the broad feature at 9.7 μm attributed to silicate grains), from the infrared dust continuum emission or from molecular gas emission lines, can alternatively be used (*e.g.* Savage & Mathis 1979; Hildebrand 1983; Roche & Aitken 1985; Makinen *et al.* 1985; Gear 1988).

The relative spatial distribution of the obscuring material and emission sources also affects the extinction. For a uniform, optically thin dust cloud located between the source(s) and the observer (figure 5.1), the intensity of the emergent radiation $I(\lambda)$ is related to that of the incident radiation $I_0(\lambda)$ by

$$I(\lambda) = I_0(\lambda)\, e^{-\tau_\lambda}. \tag{5.2}$$

This particular case is referred to as a *"uniform foreground screen"* model. In astronomical sources, particularly galaxies, the geometry is more complicated. Moreover, any large concentrations of dust present will result in optically thick conditions. Observations at different wavelengths will then probe regions at different *physical* depths since radiation at longer wavelengths can generally penetrate further into dust. As a consequence, for A_λ/A_V decreasing with increasing λ, the equivalent visual extinction will be larger if inferred from diagnostics at longer wavelengths. This behaviour is more pronounced for steeper extinction laws. Radiative transfer calculations for an homogeneous mixture of dust and sources, for clumpy foreground dust or for dust screens interleaved between multiple sources can reproduce the threshold optical depths in complex and optically thick cases (*e.g.* Mathis 1983; Puxley 1991; Witt, Thronson & Capuano 1992; McLeod *et al.* 1993). Two of these cases will be considered in this work, and are illustrated in figure 5.1. For dust and sources uniformly distributed within the same volume, hereafter *"mixed"* model, the attenuation of the radiation is given by

$$I(\lambda) = I_0(\lambda)\, \frac{1 - e^{-\tau_\lambda}}{\tau_\lambda}. \tag{5.3}$$

Here, $I_0(\lambda)$ is the total intrinsic intensity of all the sources, and τ_λ represents the extinction through the region up to the limiting optical depth of the radiation that is measured. For a *"two-screen two-source"* geometry, where the sources are interleaved between two uniform dust screens,

$$I(\lambda) = I_0(\lambda)\, \frac{f + e^{-\tau_\lambda}}{e^{g\tau_\lambda}}. \tag{5.4}$$

The parameters f and g characterize the amount of light and the optical depth of the sources and the screen nearest the observer in terms of the farthest ones. The total source intensity in this case is $(1 + f)\, I_0(\lambda)$.

5.1.2 Previous work on M 82

The large amounts of dust within M 82 make reddening corrections essential for deriving the intrinsic properties of the galaxy even from near- and mid-infrared observations. The amount of extinction measured towards the starburst regions of M 82 has long been a subject of controversy. Measurements have been carried out using a variety of increasingly sophisticated methods, including optical and infrared recombination line studies, near-infrared broad-band photometry, fits to the depth of the 9.7 μm silicate

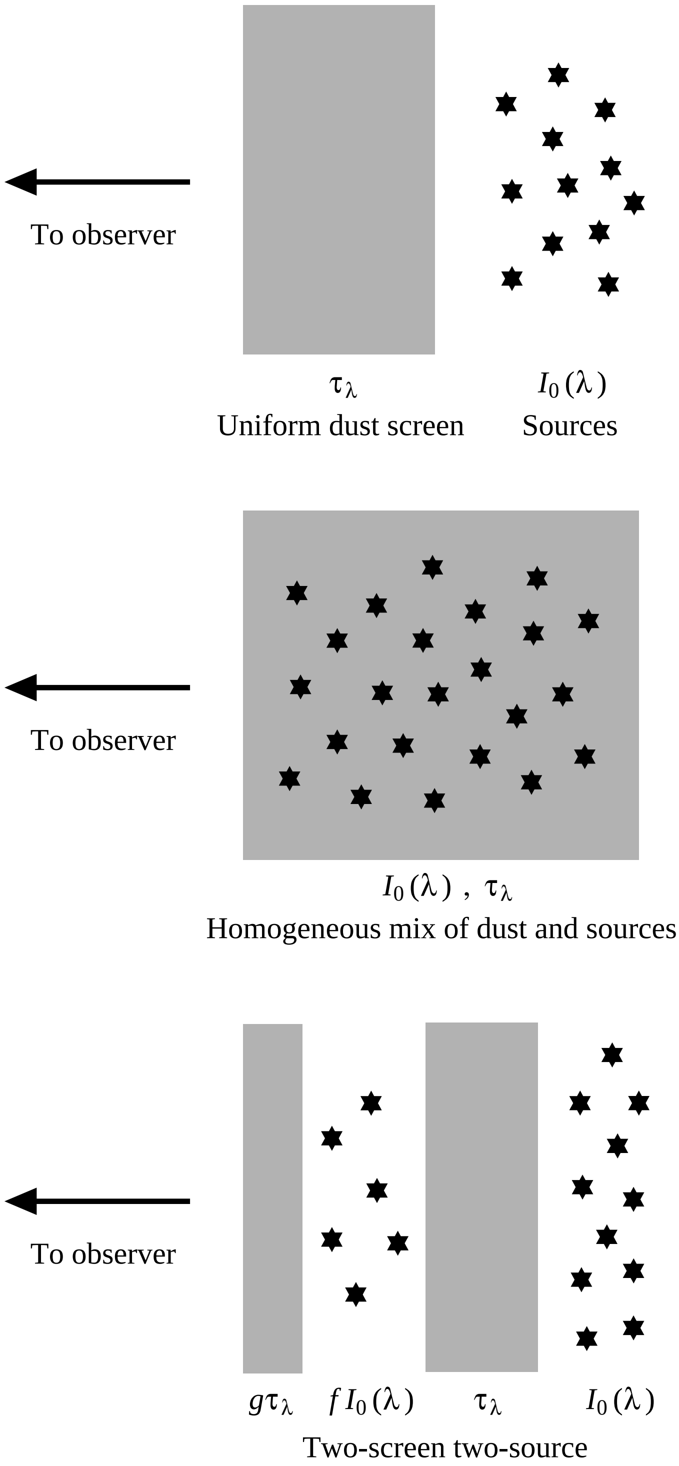

Fig. 5.1.— Three geometries considered in extinction models: a uniform foreground dust screen between the sources — represented as stars — and the observer (top), an homogeneous distribution of dust and sources (middle), and two uniform dust screens separating two emitting regions (bottom).

absorption feature, optical depth measurements from the far-infrared and submillimetric dust continuum emission, and the ratio of the 3.3 mm free-free continuum to Brγ line emission. Various extinction determinations from the literature are summarized in table 5.1.

The results vary considerably depending on the aperture used and position observed, on the method employed to measure the extinction, and on the geometry assumed for the sources and obscuring dust. In particular, determinations made under the assumption of a uniform foreground screen model or based on optical and near-infrared diagnostics yielded A_V from a few to about 15 mag, while $A_V \approx 20 - 60$ mag have been inferred for a mixed model or from diagnostics at longer wavelengths. These important differences can be understood in view of the spatially non-uniform extinction across the disk of M 82, of the large optical depths that prevent the radiation at shorter wavelengths produced in the most obscured regions to escape, and of the large uncertainties in beam-size corrections involved in several studies.

A uniform foreground screen model is probably inappropriate for M 82, as hinted by the systematic increase in derived A_V with increasing wavelength for purely foreground extinction (see table 5.1), and the spatial variations revealed by the existing extinction maps (*e.g.* Telesco *et al.* 1991; McLeod *et al.* 1993; Larkin *et al.* 1994; Satyapal *et al.* 1995). The mixed model and a two screen-two source geometry have been applied to M 82 using data over large wavelength ranges, reproducing satisfactorily the observations (see notably Puxley 1991 and McLeod *et al.* 1993). On the other hand, a few authors have defended *a posteriori* the validity of a simple screen, associated with the molecular ring, based on the correlation of their extinction map with the spatial distribution of the H I optical depth and CO $J = 1 \rightarrow 0$ emission (Telesco *et al.* 1991; Satyapal *et al.* 1995).

One major hindrance in previous studies has been the lack of data in the mid-infrared regime. *ISO*-SWS observations have now filled this gap, with a **consistent set including several H I recombination lines between 3 μm and 10 μm**. In addition, many studies were based on limited data sets not sufficient for probing the most obscured regions and for discriminating between various geometries. In the following, the SWS data are combined with H I recombination line measurements from millimetric to optical wavelengths obtained with 3D and taken from the literature. This extensive collection of data is used to constrain accurately the amount of extinction, and the dust and sources geometry towards the ionized gas in M 82. In addition, the $\lambda = 3 - 10$ μm extinction law is assessed from the SWS lines. Finally, the 3D data are used to constrain the extinction towards individual regions.

Table 5.1: Summary of various extinction determinations towards M 82 from the literature

Work	Diagnostics	Law[(a)]	Model[(b)]	Aperture[(c)]	A_V [(d)] [mag]
Gillett *et al.* 1975	9.7 μm absorption	(1)	—	$7''$	$15 - 60$
Willner *et al.* 1977	Brγ, Brα	vdH#15	UFS	$30''$	≈ 25
Simon *et al.* 1979	Brγ, Brα	vdH#15	UFS	$11''$	14 ± 5
Rieke *et al.* 1980	Brγ, Brα	vdH#12	UFS	$8''$	≈ 26
	JHK colours	vdH#12	MIX	$3.9''$, $5.8''$, $7.8''$	≈ 20
Jaffe *et al.* 1984	400 μm continuum	(2)	—	$42''$	$7.6 - 44$
Pipher *et al.* 1987	$H - K$ colour	L84	UFS	Maps	$6 - 15$
Joy *et al.* 1987	JHK colours	L84	UFS	$6''$	≈ 5
			MIX		≈ 15
	100 μm continuum	(3)	—	Starburst core	$25 - 50$
Young *et al.* 1988	[S III] 9532Å, Hα	W58	UFS	Maps	$\lesssim 8$
Lester *et al.* 1990	Hα, Paβ, Br10, Brδ, Brγ, Brα	L84	UFS	$3.8''$	$5.4 - 15$
	90 GHz continuum, Brγ				5
	[Fe II] 1.257 μm, 1.644 μm				5.7
	JHK colours				$3.7 - 11.1$
Götz *et al.* 1990	Hα, Hβ, Hγ	SM79	UFS	$3'' \times 5''$	$3 - 4.3$
Puxley 1991	Paβ, Br11, Br10, Brδ, Brγ, Brα	L84	UFS	$3.8''$	5.5 ± 2.0
			MIX		24.3 ± 11.4
	JHK colours		UFS		$\gtrsim 5$
			MIX		$\gtrsim 20$
Telesco *et al.* 1991	JHK colours	L84	UFS	Maps	$\lesssim 8$
			MIX		$\lesssim 30$
Waller *et al.* 1992	[S III] 9532Å, Hα	S82	UFS	Maps	$0 - 7$
	$R - I$ colour			Maps	$\lesssim 4$
	Hα, Brγ			Maps	$\lesssim 5$

Table 5.1: — continued

Work	Diagnostics	Law[(a)]	Model[(b)]	Aperture[(c)]	A_V[(d)] [mag]
McLeod *et al.* 1993	Hα, Paδ, Paγ, Paβ, Brγ, Brα	C89/RL85	UFS	$6''$	9
			MIX		55
			2s/2s		20
	Hα, Brα, H53α		UFS	$30''$	9
			MIX		55
			2s/2s		20
	$H-K$ colour	RL85	UFS	Maps	$0-12.5$
Larkin *et al.* 1994	$JHKL'$ colours	RL85	UFS	Maps	$0-11$
	3.3 mm continuum, Brγ	—		$6''$	25
Achtermann & Lacy 1995	Brγ, Brα	D89	UFS	Maps	15 ± 10
Satyapal *et al.* 1995	Paβ, Brγ	L84	UFS	Maps	$2-12$
	JHK colours			Maps	$2-12$
Satyapal *et al.* 1997	JHK colours	L84	UFS	$24''$	7
			MIX		65
			2s/2s		15

[(a)] (1): assuming $A_V/\tau_{9.7\,\mu\mathrm{m}} = 10-40$; (2): using the dust properties from Whitcomb *et al.* (1981) and Hildebrand (1983); (3): assuming $A_V/\tau_{100\,\mu\mathrm{m}} = 500-1000$; vdH#15 and #12: extinction curves # 15 and # 12 from van der Hulst, as quoted in Johnson (1968); L84: Landini *et al.* (1984); W58: Whitford (1958); SM79: Savage & Mathis (1979); S82: Scheffler (1982); C89: Cardelli *et al.* (1989); RL85: Rieke & Lebofsky (1985); D89: Draine (1989).

[(b)] UFS: uniform foreground screen; MIX: homogeneous mixture of dust and sources; 2s/2s: two-screen two-source model, with $f = 0.15$ and $g = 0.1$ for McLeod *et al.* (1993), and $f = 0.3$ and $g = 0.2$ for Satyapal *et al.* (1997).

[(c)] All single-beam apertures are centered on or close to the nucleus, all maps cover most of the central starbursting regions ($\approx 30''$) and include the nucleus.

[(d)] For the cases where the extinction was derived from maps, the A_V was obtained independently for each pixel or resolution element, *i.e.* a non-uniform foreground screen model was assumed. The values reported for A_V correspond to the range found over the mapped regions.

5.1.3 Global extinction towards the H II regions in M 82

H I recombination lines are excellent "standard candles" for extinction determinations because their intrinsic line emissivities ϵ_λ are well determined theoretically. The method employed here to derive the extinction consists of adjusting the extinction parameters for the best fit to

$$\frac{F_\lambda}{F_{\rm ref}} = \left(\frac{\epsilon_\lambda}{\epsilon_{\rm ref}}\right)\left(\frac{X_\lambda}{X_{\rm ref}}\right), \tag{5.5}$$

where $F_\lambda/F_{\rm ref}$ are the observed line fluxes relative to that of a reference line, $\epsilon_\lambda/\epsilon_{\rm ref}$ are the intrinsic ratios of line emissivities, and X_λ and $X_{\rm ref}$ are the attenuation due to extinction at the wavelengths of the lines considered. The goodness-of-fit is measured by the reduced chi-squared, defined as

$$\chi_n^2 \equiv \left(\frac{1}{n-m}\right)\sum_i^n \left[\frac{R_i^{\rm obs} - R_i^{\rm pred}}{\sigma_i}\right]^2, \tag{5.6}$$

where $n-m$ is the number of degrees of freedom, $R_i^{\rm obs}$ and $R_i^{\rm pred}$ are the observed and predicted line ratios, and σ_i are the uncertainties on the measurements. Good fits are characterized by $\chi_n^2 \approx 1$.

The intrinsic line emissivities are taken from Hummer & Storey (1987) assuming case B recombination, *i.e.* that the emitting gas is optically thick in the H I Lyman lines but optically thin in all other lines. An electron density of $n_{\rm e} = 100$ cm^{-3} and temperature of $T_{\rm e} = 5000$ K are adopted, appropriate for M 82 as shown in section 5.2[2]. The extinction laws from Draine (1989) and from Rieke & Lebofsky (1985) are adopted at infrared and optical wavelengths respectively. The extinction is assumed to be zero at millimetric wavelengths.

The three extinction models described in section 5.1.1 are considered, so that the line attenuation X_λ and $X_{\rm ref}$ are given by Eqs. 5.2, 5.3 and 5.4. Deviations from the simple uniform foreground screen model are perceptible only for lines which probe appreciably different optical depths. This is illustrated in figure 5.2, which shows the variation of selected line ratios with A_V for various extinction models. The effects of different geometries in the ranges $\lambda = 1.6 - 2.2$ μm and $\lambda = 2.6 - 7.5$ μm covered by the 3D and the SWS data are essentially indistinguishable, but become significant between optical and mid-infrared wavelengths. The amount of extinction and the dust and sources geometry are closely related. It is thus as important to constrain the geometry as the absolute extinction itself since models which reproduce the observed relative line fluxes over a given wavelength range may result in very different extinction

[2]The electron density is actually in the range $\sim 10 - 500$ cm^{-3}, but the tabulated values for 100 cm^{-3} are used since the line emissivities are little sensitive to $n_{\rm e}$.

corrections, and thus in very different values for the intrinsic properties of interest. Figure 5.2 emphasizes the importance of using data over a wavelength range as large as possible to constrain reliably both A_V and the extinction model in M 82. Moreover, the inclusion of lines which are unobscured is important because even the mid-infrared lines may lead to underestimates of the absolute extinction throughout the galaxy if the sources are severely obscured.

The SWS and 3D data are therefore combined with H I line measurements from the literature, obtained in large apertures (diameter $\gtrsim 20''$), from the optical to the millimetric regime. Since the SWS lines constitute the largest, self-consistent data set available so far, Brα is chosen as the reference line. For an appropriate analysis, the line fluxes outside the mid-infrared regime are scaled to match the SWS $14'' \times 20''$ aperture. Since the most prominent emission regions are included in the SWS field of view (see for example the linemaps from McCarthy, Heckman & van Breugel 1987, Satyapal *et al.* 1995, Achtermann & Lacy 1995 and Seaquist *et al.* 1996), the extinction derived from measurements obtained in the SWS and larger apertures should be representative for the bulk of the ionized gas in M 82. The beam-size correction is applied in two steps: the fluxes are first scaled to a $30''$–diameter aperture centered on the nucleus, and then to the SWS aperture. The latter correction is derived by comparing the various continuum and line flux measurements obtained with the SWS with those reported in the literature (tables 4.9 and 4.11), all of which presumably trace the same sources since they have similar spatial distributions (*e.g.* Telesco *et al.* 1991; Achtermann & Lacy 1995). The scaling factor $30'' \rightarrow$ SWS is 0.5, with 10% uncertainty.

Several hydrogen recombination lines have been observed in M 82 from the submillimetric to the radio regime. However, lines at centimeter wavelengths are potentially affected by stimulated emission and free-free absorption, which introduce considerable complexity in the assessment of the ionizing flux, and thus of the extinction (*e.g.* Seaquist, Bell & Bignell 1985; Seaquist *et al.* 1996). Millimetric and submillimetric lines suffer much less from these effects. The line measurements available in the range $\lambda \sim 1 - 10$ mm include H26α, H27α, H41α (Seaquist *et al.* 1996), H30α (Seaquist, Kerton & Bell 1994), H40α and H53α (Puxley *et al.* 1989). The integrated fluxes for large apertures are consistent with predominantly optically thin, spontaneous emission in local thermodynamical equilibrium (LTE) from H II regions (see references above). The beam size corrections to a $30''$–diameter beam are inferred from the corrections derived by Seaquist, Kerton & Bell (1994) between $19''$, $21''$ and $41''$ apertures and the entire emission region, with an estimated uncertainty of 15%.

At optical wavelengths, the Hα measurement of McCarthy, Heckman & van Breugel (1987) in a $90'' \times 90''$ region is used. An additional estimate is obtained from the Hα

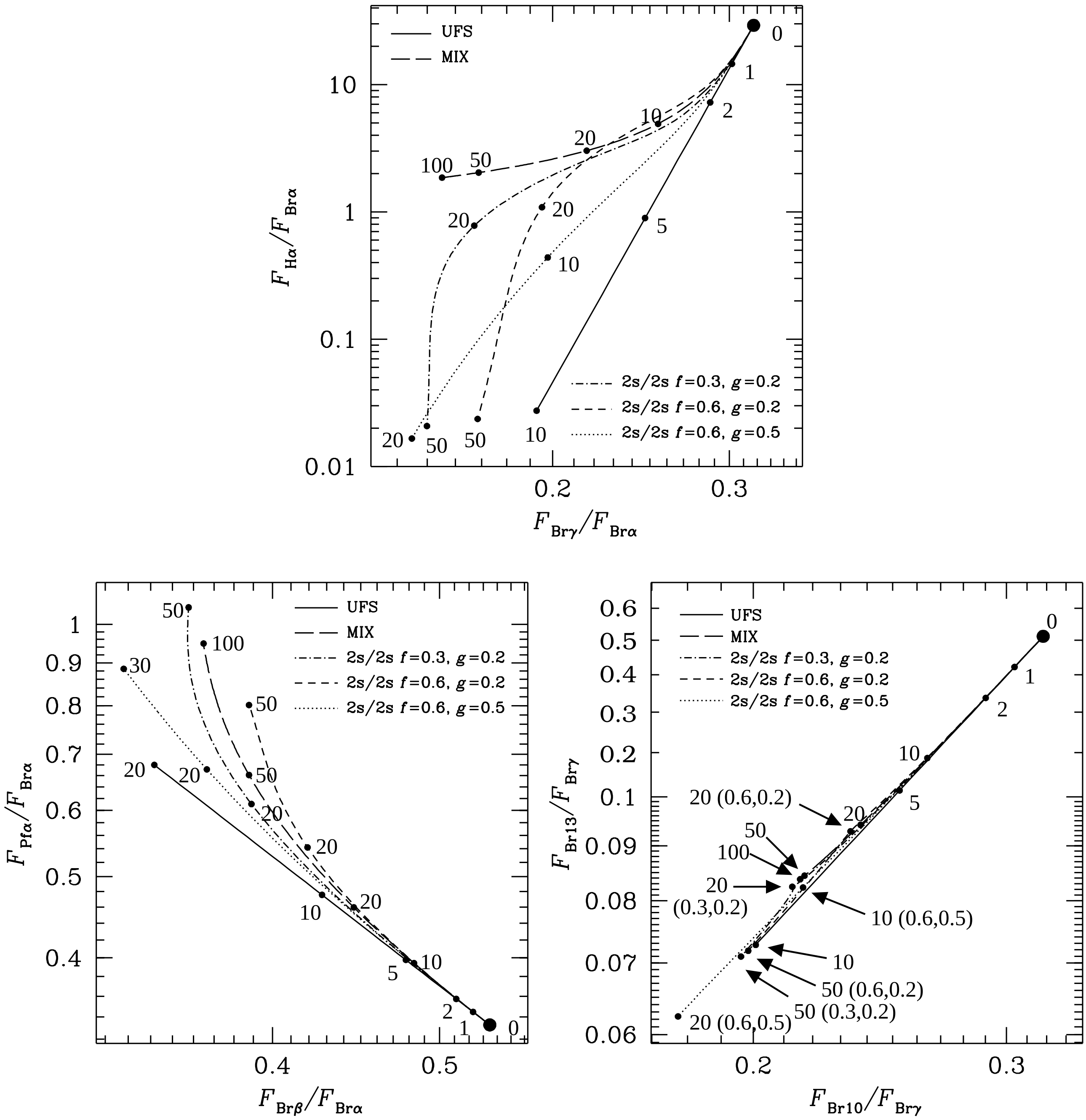

Fig. 5.2.— Variations of selected H I recombination line ratios with A_V for different extinction models (represented by different lines). "UFS", "MIX" and "2s/2s" stand for uniform foreground screen, mixed and two-screen two-source model respectively. The dots on each curve indicate the effects for various A_V as labeled. A_V = 1, 2, and 5 mag refer to the uniform foreground screen model only. A_V = 10, 20, 50 and 100 mag are indicated for the mixed model. In the bottom right plot, the (f, g) pairs for the two-screen two-source models are also indicated for clarity.

+ [N II] $\lambda\lambda 6548, 6584$ Å flux of Young, Kleinmann & Allen (1988) in a $64''$–aperture, assuming a uniform Hα/[N II] ratio of 0.5 (McCarthy, Heckman & van Breugel 1987). Both these apertures contain essentially all of the line emission from M 82 and the beam size correction derived from the millimetric lines is applied. The spatial distribution of the Hα emission exhibits significant differences compared to that of longer wavelength emission lines, probably mostly due to the patchy extinction across the starbursting regions. Scaling factors estimated directly from the Hα maps are, however, consistent with those from the millimetric lines, within $\approx 35\%$.

At near-infrared wavelengths, large discrepancies up to factors of more than three exist between various measurements in the literature. The Brγ and Paβ fluxes obtained by different authors are compared in figure 5.3. Such differences are puzzling. Early measurements from aperture spectroscopy at low resolution are inevitably more uncertain due to the small line-to-continuum ratio at low resolution, and to possible positional errors. However, there is no obvious explanation for recent measurements at higher spectral resolution from well-registered linemaps, as for Larkin *et al.* (1994) and Satyapal *et al.* (1995).

The absolute flux calibration of the 3D data was not performed independently from standard stars at the time of the observations. However, the 3D broad-band photometry (based on multi-aperture measurements from Rieke *et al.* 1980) is in very good agreement with that of Satyapal *et al.* (1997) over the regions mapped with 3D (see table 4.7), confirming the accuracy of the flux calibration of the 3D data cubes. Both the spectral resolution and coverage as well as the quality of the 3D spectra allow a more accurate continuum subtraction than previous studies. In order to derive the flux in a $30''$ aperture, the scaling factor between an $8''$– and $30''$–diameter aperture from the data of Satyapal *et al.* (1995) is applied to the 3D data (with 10% uncertainty). This factor corresponds to a flux proportional to $\theta^{1.5}$, where θ is the aperture diameter. Although the absolute Brγ line fluxes differ importantly between the two data sets, the spatial distribution of the line emission within the regions covered by both agrees very well, giving confidence in the scaling factor employed.

Because of the similar spatial distributions of the Brγ and Paβ line emission (Satyapal *et al.* 1995), the beam-size corrections inferred from Brγ are applied to all near-infrared lines. The 3D Br10, Br11, Br12 and Br13 fluxes in small apertures suffer from relatively large uncertainties due to the weakness of the lines within $\approx 5''$ of the nucleus. The fluxes integrated over the entire 3D map are used instead and multiplied by the ratio of Brγ fluxes in the SWS and 3D fields of view. For Paβ, the fluxes in $3''$– and $6''$–beams from McLeod *et al.* (1993) and Satyapal *et al.* (1995) are scaled according to $\theta^{1.5}$ to a $30''$–beam, then to the SWS aperture, and finally averaged together.

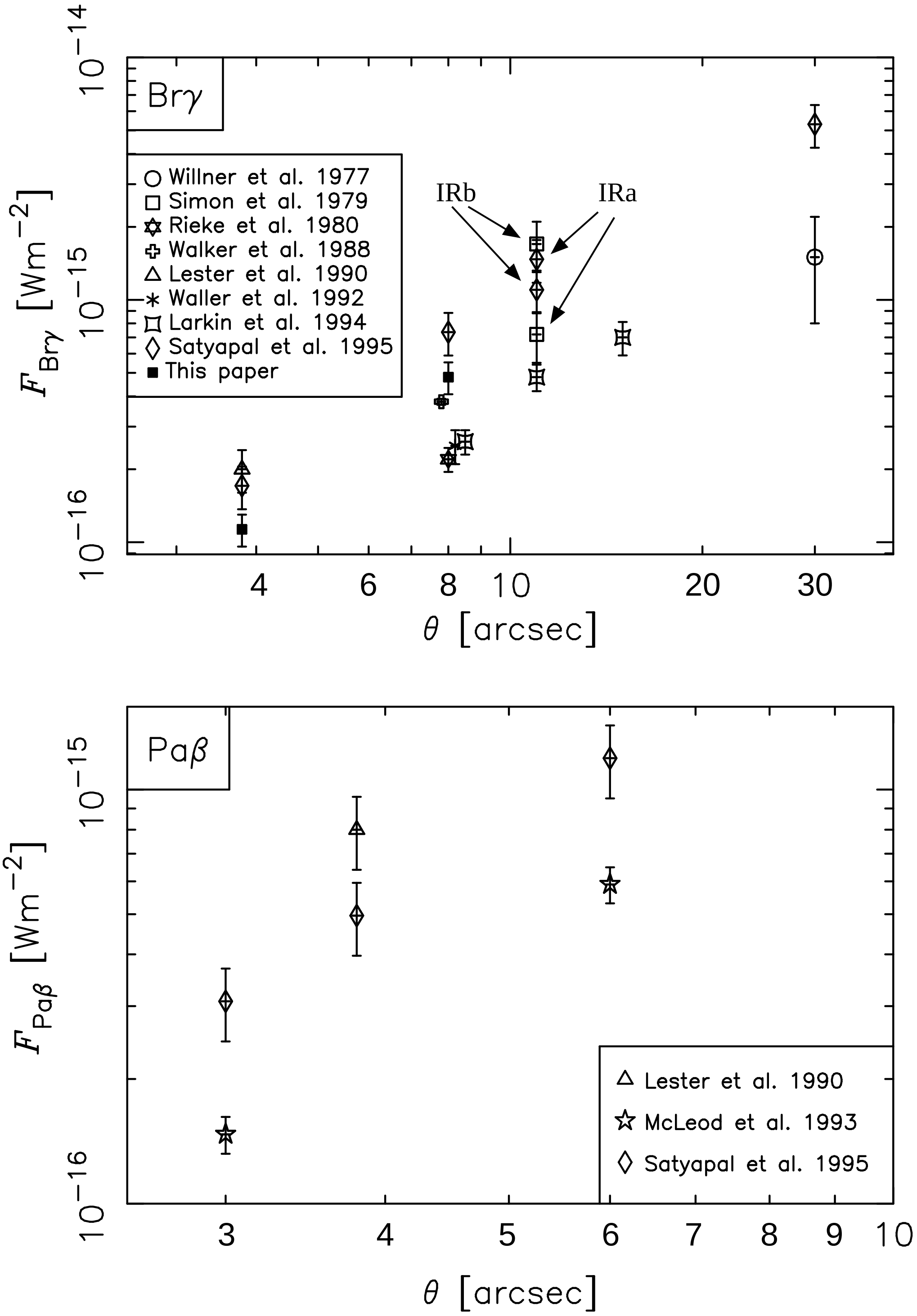

Fig. 5.3.— Comparison of the Brγ and Paβ line fluxes in M 82 from various authors as a function of beam diameter θ. All measurements, obtained either from direct observations through circular apertures or derived from linemaps, correspond to a center position coinciding with the nucleus of the galaxy, except for the Brγ points labeled "IRa" and "IRb" at $11''$ from Simon *et al.* (1979) and Satyapal *et al.* (1995). These were taken at $\Delta\alpha, \Delta\delta = -6'', 0''$ (IRa) and $1'', 4''$ (IRb) relative to the nucleus. For clarity, the measurements for $\theta = 8''$ are shown slightly displaced along the horizontal axis.

Table 5.2 lists the observed line fluxes for the determination of the extinction. Table 5.3 gives the observed fluxes relative to Brα and those for the best-fit extinction parameters for each geometry. The results are also illustrated in figure 5.5, as the intrinsic hydrogen ionization rate Q^0 derived from each of the extinction-corrected line fluxes (figure reported in section 5.1.4; plots labeled "Draine"). The case B recombination coefficients from Hummer & Storey (1987) for $n_e = 100\ \mathrm{cm}^{-3}$ and $T_e = 5000$ K were used to convert the intrinsic line fluxes into ionization rates, assuming an average ionizing photon energy of 15 eV. Assuming that the emission lines originate from the same regions, the predicted Q^0 should be identical for the appropriate A_V and extinction model. The average Q^0 for each geometry is reported in table 5.3. Figure 5.6 shows the reciprocal chi-squared diagrams, $1/\chi^2_n$, as a function of the extinction parameters (section 5.1.4; curves and plots labeled "Draine").

The best fits are achieved with $A_V^{\mathrm{MIX}} = 43 \pm 23$ mag for the mixed model, $A_V^{2\mathrm{s}/2\mathrm{s}} = 73 \pm 35$ mag, $f = 0.6 \pm 0.35$ and $g = 0.05^{+0.01}_{-0.04}$ for the two-screen two-source model, and $A_V^{\mathrm{UFS}} = 4^{+1.5}_{-4}$ mag for the uniform foreground screen model. The latter geometry, however, results in a poor fit to the data, with a minimum $\chi^2_n \approx 8$ compared to $\chi^2_n \approx 1 - 2$ for the mixed and the two-screen two-source models. Figure 5.5 illustrates clearly that purely foreground extinction provides a much less satisfactory fit to the data over the entire wavelength range considered. Rieke *et al.* (1980) first proposed the alternative mixed geometry for M 82 to explain the observed JHK colours, while McLeod *et al.* (1993) first considered the additional two-screen two-source model. The extinction derived for the mixed model is consistent with the results in large apertures obtained by other authors for this geometry (see table 5.1). The parameters for the two-screen two-source model are, on the other hand, different from those obtained by McLeod *et al.* (1993) and Satyapal *et al.* (1997) (see notes to table 5.1).

The data do not allow the discrimination between more or less uniformly mixed dust and sources. However, the mixed and the two-screen two-source models imply comparable extinction corrections at near- and mid-infrared wavelengths (differences of $\approx 20\%$ near $2\,\mu$m and $\approx 30\%$ near $5\,\mu$m), nearly identical Q^0, and consequently, similar values for the intrinsic properties of interest in this work. The true geometry in M 82 is likely a combination of regions with well-mixed ionized nebulae and dust clouds, separated by multiple dust screens. Since the mixed and two-screen two-source models result in similar extinction corrections at the wavelengths of interest, combinations of these models probably would also.

The uncertainties on the extinction parameters are estimated from figure 5.6, with a 1σ error corresponding to a factor of $e^{-1/2}$ from the maximum reciprocal χ^2_n (*i.e.* a gaussian distribution is assumed). The 1σ values for both the mixed and the two-screen two-source models are very large for A_V and f, with the upper bound lying outside

Table 5.2: H I recombination line fluxes used in the derivation of the global extinction towards the ionized gas in M 82

Line	Observed flux[(a)] $[10^{-16}\ \mathrm{W\,m^{-2}}]$	Aperture[(b)]	Scaled flux[(c)] $[10^{-16}\ \mathrm{W\,m^{-2}}]$	Reference[(d)]
Hα 0.6563 μm	450	$90'' \times 90''$	170 ± 68	McCarthy *et al.* 1987
Hα 0.6563 μm	510	$64''$	200 ± 82	Young *et al.* 1988
Paβ 1.2818 μm	86 ± 17	$30''$	43 ± 10	see note (d)
Br13 1.6109 μm	1.32 ± 0.50	3D	1.5 ± 0.6	This work
Br12 1.6407 μm	1.29 ± 0.70	3D	1.5 ± 0.8	This work
Br11 1.6807 μm	1.43 ± 0.50	3D	1.6 ± 0.6	This work
Br10 1.7362 μm	3.22 ± 0.70	3D	3.7 ± 0.9	This work
Brγ 2.1655 μm	4.8 ± 0.8	$8''$	17 ± 4	This work
Brβ 2.6252 μm	41.0 ± 10.5	SWS	41.0 ± 10.5	This work
Pfδ 3.2961 μm	5.9 ± 2.0	SWS	5.9 ± 2.0	This work
Pfγ 3.7395 μm	10.7 ± 3.1	SWS	10.7 ± 3.1	This work
Hu14 4.0198 μm	1.3 ± 0.4	SWS	1.3 ± 0.4	This work
Brα 4.0512 μm	81.5 ± 14.7	SWS	81.5 ± 14.7	This work
Pfβ 4.6525 μm	13.9 ± 4.1	SWS	13.9 ± 4.1	This work
Pfα 7.4578 μm	25.9 ± 4.7	SWS	25.9 ± 4.7	This work
H27α 0.95 mm	$(2.11 \pm 0.43) \times 10^{-2}$	Total	$(8.1 \pm 2.2) \times 10^{-3}$	Seaquist *et al.* 1996
H30α 1.29 mm	$(3.20 \pm 0.38) \times 10^{-3}$	$21''$	$(2.0 \pm 0.4) \times 10^{-3}$	Seaquist *et al.* 1994
H40α 3.03 mm	$(9.22^{+1.38}_{-1.84}) \times 10^{-4}$	$19''$	$(6.2 \pm 1.6) \times 10^{-4}$	Puxley *et al.* 1989
H41α 3.26 mm	$(1.32 \pm 0.22) \times 10^{-3}$	Total	$(5.1 \pm 1.3) \times 10^{-4}$	Seaquist *et al.* 1996
H53α 6.98 mm	$(1.87 \pm 0.28) \times 10^{-4}$	$41''$	$(8.6 \pm 2.0) \times 10^{-5}$	Puxley *et al.* 1989

[(a)] Total uncertainties are given, including those of the absolute flux calibration, continuum subtraction and systematic errors whenever possible. For the Hα measurements, no uncertainties were given in the references, but those of the beam size corrections should dominate for the scaled fluxes.

[(b)] All apertures except the 3D and SWS fields of view are centered approximately on the nucleus of M 82. "Total" refers to measurements integrated over the entire emission regions in M 82.

[(c)] Line fluxes after beam-size correction to match the SWS $14'' \times 20''$ aperture (see text). The uncertainties also account for those of the beam size correction.

[(d)] Reference for the observed line fluxes. The Paβ measurement represents the average of the results derived from measurements in a $3''$– and $6''$–diameter aperture from McLeod *et al.* (1993) and Satyapal *et al.* (1995), as described in the text.

Table 5.3: H I recombination line flux ratios for the best-fit global extinction towards the ionized gas in M 82[(a)]

Ratio	Observed	UFS $A_V = 4$ mag	Mixed $A_V = 43$ mag	2s/2s $A_V = 73$ mag $f = 0.6$, $g = 0.05$
$H\alpha/Br\alpha$	2.1 ± 0.9	1.7	1.7	1.9
$H\alpha/Br\alpha$	2.5 ± 1.1	1.7	1.7	1.9
$Pa\beta/Br\alpha$	$(5.3 \pm 1.5) \times 10^{-1}$	7.6×10^{-1}	3.1×10^{-1}	7.1×10^{-1}
$Br13/Br\alpha$	$(1.8 \pm 0.8) \times 10^{-2}$	2.7×10^{-2}	1.2×10^{-2}	2.4×10^{-2}
$Br12/Br\alpha$	$(1.8 \pm 1.1) \times 10^{-2}$	3.5×10^{-2}	1.6×10^{-2}	3.1×10^{-2}
$Br11/Br\alpha$	$(2.0 \pm 0.8) \times 10^{-2}$	4.7×10^{-2}	2.1×10^{-2}	4.2×10^{-2}
$Br10/Br\alpha$	$(4.5 \pm 1.4) \times 10^{-2}$	6.5×10^{-2}	3.0×10^{-2}	5.8×10^{-2}
$Br\gamma/Br\alpha$	$(2.1 \pm 0.6) \times 10^{-1}$	2.5×10^{-1}	1.4×10^{-1}	2.2×10^{-1}
$Br\beta/Br\alpha$	$(5.0 \pm 1.1) \times 10^{-1}$	4.6×10^{-1}	3.2×10^{-1}	4.1×10^{-1}
$Pf\delta/Br\alpha$	$(7.2 \pm 2.3) \times 10^{-2}$	8.3×10^{-2}	7.0×10^{-2}	7.6×10^{-2}
$Pf\gamma/Br\alpha$	$(1.3 \pm 0.3) \times 10^{-1}$	1.3×10^{-1}	1.2×10^{-1}	1.2×10^{-1}
$Hu14/Br\alpha$	$(1.6 \pm 0.5) \times 10^{-2}$	1.4×10^{-2}	1.4×10^{-2}	1.4×10^{-2}
$Pf\beta/Br\alpha$	$(1.7 \pm 0.5) \times 10^{-1}$	2.1×10^{-1}	2.3×10^{-1}	2.2×10^{-1}
$Pf\alpha/Br\alpha$	$(3.2 \pm 0.5) \times 10^{-1}$	3.6×10^{-1}	4.9×10^{-1}	5.4×10^{-1}
$H27\alpha/Br\alpha$	$(9.9 \pm 3.2) \times 10^{-5}$	2.9×10^{-5}	4.7×10^{-5}	6.6×10^{-5}
$H30\alpha/Br\alpha$	$(2.5 \pm 0.7) \times 10^{-5}$	1.5×10^{-5}	2.5×10^{-5}	3.4×10^{-5}
$H40\alpha/Br\alpha$	$(7.6 \pm 2.3) \times 10^{-6}$	2.8×10^{-6}	4.6×10^{-6}	6.4×10^{-6}
$H41\alpha/Br\alpha$	$(6.3 \pm 1.9) \times 10^{-6}$	2.3×10^{-6}	3.8×10^{-6}	5.3×10^{-6}
$H53\alpha/Br\alpha$	$(1.1 \pm 0.3) \times 10^{-6}$	5.0×10^{-7}	8.1×10^{-7}	1.1×10^{-6}
$\log < Q^0 >$[(b)]	—	$53.49^{+0.21}_{-0.41}$	$53.70^{+0.10}_{-0.14}$	$53.71^{+0.11}_{-0.14}$

[(a)] The results reported for each extinction model are the ratios of the intrinsic line emissivities (from Hummer & Storey 1987) multiplied by the attenuation factors obtained for the best-fit extinction parameters, as in Eq. 5.5. "UFS", "Mixed" and "2s/2s" stand for uniform foreground screen, mixed and two-screen two-source model respectively. The extinction laws from Rieke & Lebofsky (1985) and Draine (1989) were adopted at optical and infrared wavelengths respectively. The extinction was assumed to be zero in the millimetric regime.

[(b)] $< Q^0 >$ is the average hydrogen ionizing rate (in s^{-1}) derived from the extinction-corrected line fluxes, using the recombination coefficients from Hummer & Storey (1987). The uncertainties represent the dispersion of the individual values.

of the range considered for the fits. This reflects the "asymptotic" behaviour of the line ratios for these geometries, characterized by an increasingly slower variation as A_V increases (see figure 5.2). As reasonable uncertainties, the 1σ values defined by the lower bound are adopted for each side of the best-fit A_V and f. For A_V values above the adopted 1σ limit, the optical depth through M 82 at near-infrared wavelengths exceeds 5. Such high obscuration would imply that only a very small fraction of the near-infrared line fluxes from the emitting regions is detected, and originates from the most foreground sources. This would be inconsistent with the similar spatial distributions of the near-infrared line emission and of the millimetric line and free-free continuum emission (*e.g.* Carlstrom & Kronberg 1991; Satyapal *et al.* 1995; Seaquist *et al.* 1996). The best-fit A_V for the two-screen two-source geometry implies very large optical depths at $2\,\mu$m for the screen farthest from the observer, and the very large values of f correspond to most of the emission originating from the nearest, less obscured sources. The resulting uncertainties on the extinction corrections are $\approx 50\%$ near $2\,\mu$m and $\approx 20\%$ near $5\,\mu$m for both the mixed and the two-screen two-source models.

The extinction parameters are fairly insensitive to the choice of electron density and temperature since the relative line emissivities vary slowly with these properties (particularly with $n_{\rm e}$). For example, increasing the density to 10^4 cm^{-3} or the temperature to 10^4 K results in larger A_V's, smaller f and larger extinction corrections, but remain within the 1σ uncertainties for the nominal case with $n_{\rm e} = 100$ cm^{-3} and $T_{\rm e} = 5000$ K. The derived Q^0 values are not very sensitive to $n_{\rm e}$, increasing by $\approx 15\%$ for $n_{\rm e} = 10^4$ cm^{-3}, because the total hydrogen recombination coefficient ($\alpha_{\rm B}$) depends weakly on $n_{\rm e}$; they are more affected by variations of $T_{\rm e}$ (because $\alpha_{\rm B} \propto T_{\rm e}^{-0.81}$; Hummer & Storey 1987), increasing by $\approx 50\%$ for $T_{\rm e} = 10^4$ K.

Part of the Hα emission, particularly from above and below the galactic plane of M 82, may include a component from light escaping along the minor axis scattered by dust grains (*e.g.* O'Connell & Mangano 1978; Notni 1985). This would lead to an overestimate of the observed Hα flux relative to those of lines at longer wavelengths, since the scattering efficiency of interstellar dust grains generally decreases rapidly with increasing λ (*e.g.* Emerson 1988). Fits were thus performed excluding the two Hα measurements. The results for the mixed and two-screen two-source geometries are little affected ($A_V^{\rm MIX} = 44$ mag, and $A_V^{\rm 2s/2s} = 80$ mag, $f = 0.6$, $g = 0.05$ respectively). On the other hand, a substantially larger $A_V^{\rm UFS} = 9$ mag is obtained, as expected since the dust and sources are actually more or less uniformly mixed. The importance of including unobscured lines for determining the extinction towards heavily obscured sources as in M 82 is illustrated by the fact that much smaller A_V for the uniform foreground screen models are derived compared to the other geometries. Fits excluding the millimetric lines result in $A_V^{\rm MIX} = 18$ mag, and $A_V^{\rm 2s/2s} = 7$, $f = 0.15$ and $g = 0.15$.

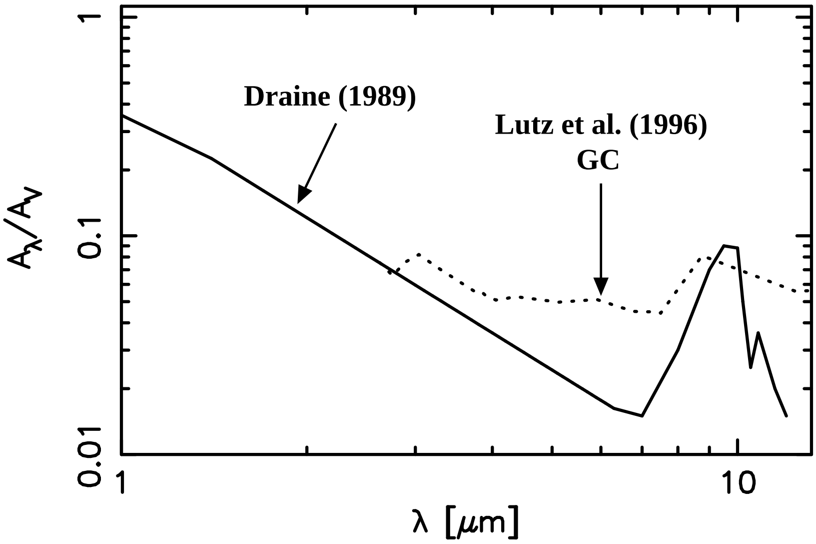

Fig. 5.4.— Comparison of the $3-10$ μm extinction law derived from SWS data towards the Galactic Center (GC) by Lutz *et al.* (1996) with the commonly used law from Draine (1989).

5.1.4 $3-10$ μm extinction law in M 82

Despite the good overall fit for the mixed and two-screen two-source models, figure 5.5 shows that the SWS data are not well reproduced. The extinction law assumed for these wavelengths may not be appropriate however. Indeed, until recently, the extinction law in the $\lambda = 3-10$ μm range was poorly determined because of the difficulties inherent to ground-based observations and because the properties of the template sources accessible so far in this regime were not well-known. The Draine law represents the best fit to various determinations from different authors. *ISO*, and especially the SWS, has now provided observations in various objects of numerous nebular H I recombination lines between $3\,\mu$m and $10\,\mu$m. These lines have been used notably to investigate the extinction law in the direction of the Galactic Center (Lutz *et al.* 1996). Interestingly, the "Galactic Center law" lacks the pronounced minimum in the $4-8$ μm region expected for standard graphite-silicate dust mixtures which are usually assumed (*e.g.* Draine 1989 and references therein), suggesting additional contributors to the extinction. The Galactic Center law from Lutz *et al.* (1996; hereafter simply GC law) is compared with the Draine law in figure 5.4.

The SWS line fluxes in M 82 are much better reproduced if the GC law between $3\,\mu$m and $10\,\mu$m is assumed. The best fits for the different models are $A_V^{\rm MIX} = 52 \pm 17$ mag, $A_V^{\rm 2s/2s} = 32^{+15}_{-10}$ mag with $f = 0.35^{+0.4}_{-0.1}$ and $g = 0.1^{+0.01}_{-0.05}$, and $A_V^{\rm UFS} = 4^{+2}_{-3}$ mag. Table 5.4, and figures 5.5 and 5.6 (plots and curves labeled "GC") show the results for the GC law. The fit for the uniform foreground screen model is still much poorer than

Table 5.4: H I recombination line flux ratios for the best-fit global extinction towards the ionized gas in M 82, using the Galactic Center law[a]

Ratio	Observed	UFS $A_V = 4$ mag	**Mixed**[b] $A_V =$ **52 mag**	2s/2s $A_V = 32$ mag $f = 0.35$, $g = 0.1$
Hα/Brα	2.1 ± 0.9	1.8	2.0	1.9
Hα/Brα	2.5 ± 1.1	1.8	2.0	1.9
Paβ/Brα	$(5.3 \pm 1.5) \times 10^{-1}$	8.1×10^{-1}	3.7×10^{-1}	5.8×10^{-1}
Br13/Brα	$(1.8 \pm 0.8) \times 10^{-2}$	2.8×10^{-2}	1.4×10^{-2}	1.9×10^{-2}
Br12/Brα	$(1.8 \pm 1.1) \times 10^{-2}$	3.7×10^{-2}	1.9×10^{-2}	2.5×10^{-2}
Br11/Brα	$(2.0 \pm 0.8) \times 10^{-2}$	4.9×10^{-2}	2.5×10^{-2}	3.3×10^{-2}
Br10/Brα	$(4.5 \pm 1.4) \times 10^{-2}$	6.9×10^{-2}	3.6×10^{-2}	4.7×10^{-2}
Brγ/Brα	$(2.1 \pm 0.6) \times 10^{-1}$	2.6×10^{-1}	1.7×10^{-1}	1.9×10^{-1}
Brβ/Brα	$(5.0 \pm 1.1) \times 10^{-1}$	4.9×10^{-1}	3.8×10^{-1}	4.0×10^{-1}
Pfδ/Brα	$(7.2 \pm 2.3) \times 10^{-2}$	8.2×10^{-2}	6.7×10^{-2}	6.9×10^{-2}
Pfγ/Brα	$(1.3 \pm 0.3) \times 10^{-1}$	1.3×10^{-1}	1.2×10^{-1}	1.2×10^{-1}
Hu14/Brα	$(1.6 \pm 0.5) \times 10^{-2}$	1.4×10^{-2}	1.4×10^{-2}	1.4×10^{-2}
Pfβ/Brα	$(1.7 \pm 0.5) \times 10^{-1}$	2.0×10^{-1}	2.0×10^{-1}	2.0×10^{-1}
Pfα/Brα	$(3.2 \pm 0.5) \times 10^{-1}$	3.4×10^{-1}	3.7×10^{-1}	3.6×10^{-1}
H27α/Brα	$(9.9 \pm 3.2) \times 10^{-5}$	3.1×10^{-5}	6.8×10^{-5}	7.0×10^{-5}
H30α/Brα	$(2.5 \pm 0.7) \times 10^{-5}$	1.6×10^{-5}	3.5×10^{-5}	3.6×10^{-5}
H40α/Brα	$(7.6 \pm 2.3) \times 10^{-6}$	3.0×10^{-6}	6.6×10^{-6}	6.8×10^{-6}
H41α/Brα	$(6.3 \pm 1.9) \times 10^{-6}$	2.5×10^{-6}	5.4×10^{-6}	5.6×10^{-6}
H53α/Brα	$(1.1 \pm 0.3) \times 10^{-6}$	5.3×10^{-7}	1.2×10^{-6}	1.2×10^{-6}
$\log < Q^0 >$[c]	—	$53.50^{+0.20}_{-0.40}$	$\mathbf{53.79^{+0.08}_{-0.09}}$	$53.76^{+0.08}_{-0.10}$

[a] Same as table 5.3 but the extinction law derived by Lutz *et al.* (1996) towards the Galactic Center from SWS observations was used between $3\,\mu$m and $10\,\mu$m instead of the Draine (1989) law. "UFS", "Mixed" and "2s/2s" stand for uniform foreground screen, mixed and two-screen two-source model respectively.

[b] Adopted result (section 5.1.6).

[c] $< Q^0 >$ is the average hydrogen ionizing rate (in s^{-1}) derived from the extinction-corrected line fluxes. The uncertainties represent the dispersion of the individual values.

for the other geometries. The Q^0 differs by 7% between the mixed and the two-screen two-source models, and the extinction corrections near $2\,\mu$m and $5\,\mu$m differ by 12% and 2% respectively. The uncertainties on these corrections are $\approx 30\%$ (near $2\,\mu$m) and $\approx 25\%$ (near $5\,\mu$m). The $A_V^{\rm MIX}$ is very close to the result from McLeod *et al.* (1993), but both $A_V^{\rm 2s/2s}$ and f are significantly larger than derived by these authors (table 5.1). The data do not allow the accurate determination of the extinction law in M 82, but provide evidence for deviations from the commonly used Draine law similar to those found towards the Galactic Center by Lutz *et al.* (1996).

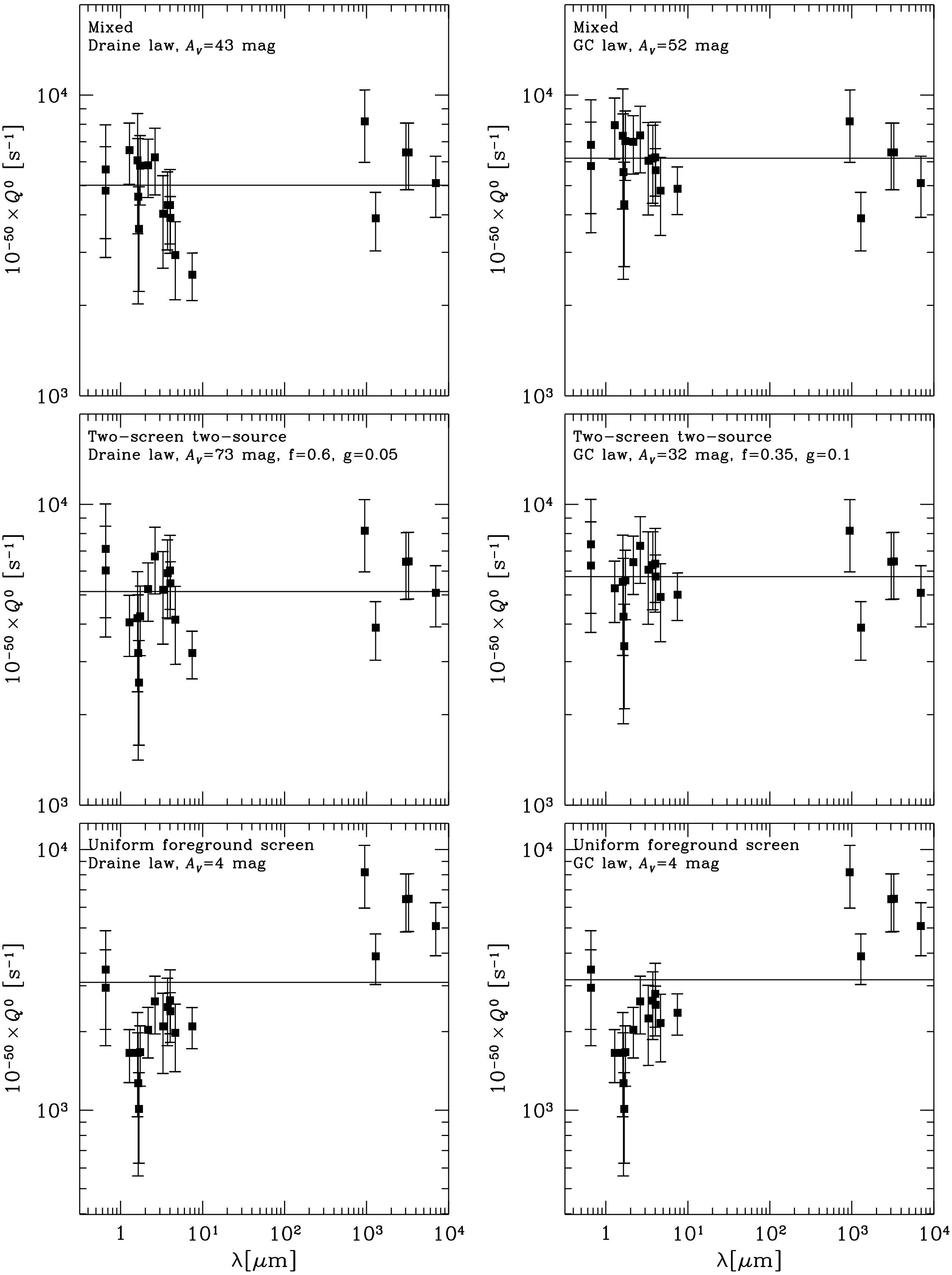

Fig. 5.5.— Intrinsic hydrogen ionization rates Q^0 for the SWS $14'' \times 20''$ aperture, derived from the H I line fluxes corrected for the best-fit extinction parameters for each extinction model and $3-10\ \mu$m law considered. The horizontal lines indicate the average Q^0.

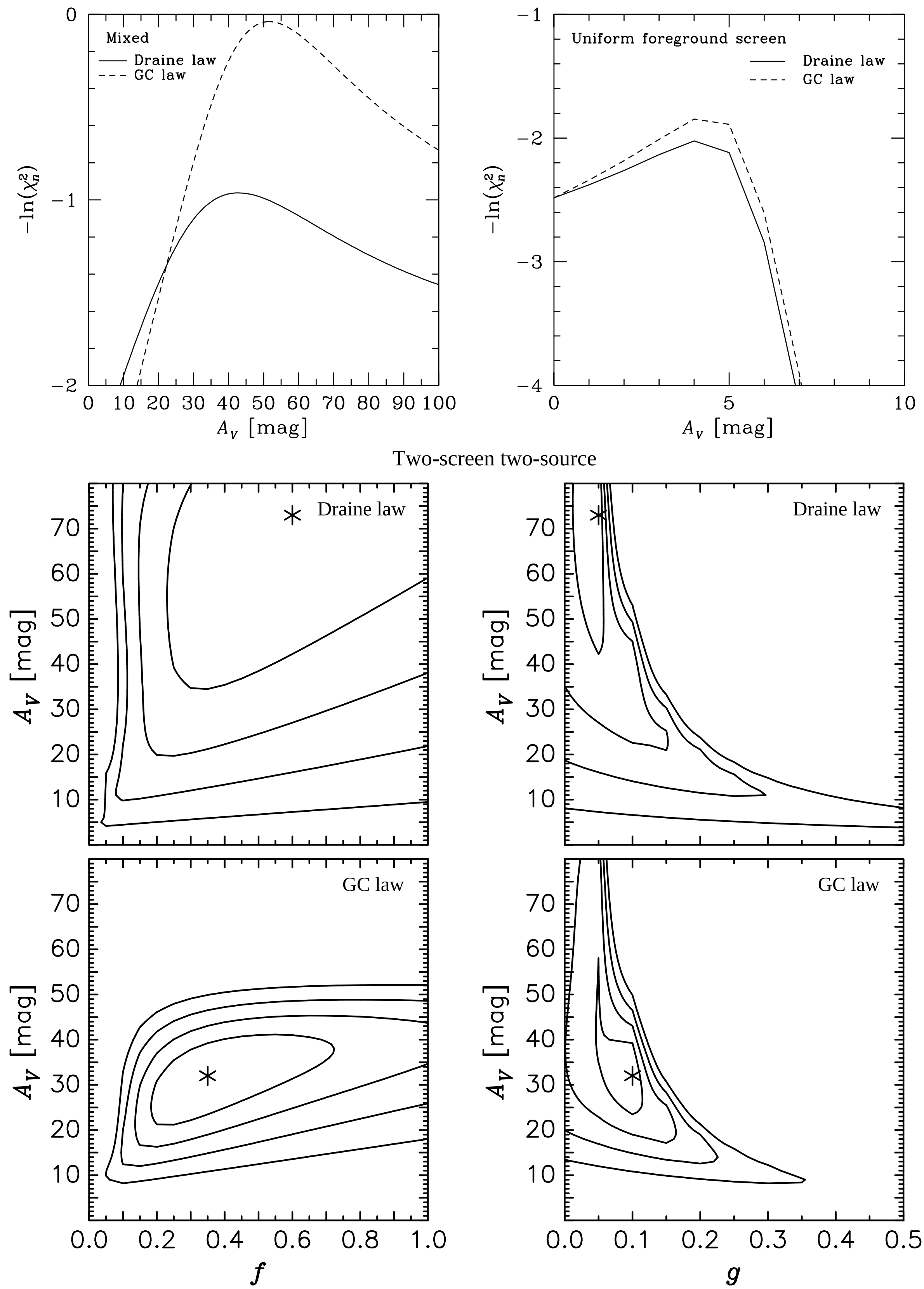

Fig. 5.6.— Variations of $\ln(1/\chi_n^2)$ with extinction parameters for the models and $3-10\ \mu$m laws considered (see text). The contour plots show, for the two-screen two-source model, the projections in the $A_V - f$ and $A_V - g$ planes for the best-fit g and f values respectively. Contours are 1σ, 2σ, 3σ and 4σ from the maximum $\ln(1/\chi_n^2)$ marked with the star symbol (*i.e.* the minimum χ_n^2), where $\sigma \equiv \ln(e^{-1/2})$.

5.1.5 Consistency check from millimeter-wave free-free emission

As a consistency check for the derived extinction, the 3.3 mm (92 GHz) continuum flux density can be used to estimate the intrinsic ionization rate. For spontaneous line emission and optically thin, LTE free-free emission, the recombination line fluxes are directly proportional to the free-free continuum flux density. Because of the minimum in flux density in the spectrum of M 82 around 3.3 mm (see figure 1.2) and since thermal free-free emission has a low spectral index ($S_\nu^{\rm ff} \propto \nu^{-\alpha}$ with $\alpha = 0.1 - 0.2$), this process can only dominate at these wavelengths. Jura, Hobbs & Maran (1978), Seaquist, Bell & Bignell (1985) and Carlstrom & Kronberg (1991) concluded that the continuum emission around 3.3 mm from the starburst core of M 82 is predominantly of thermal free-free origin. Klein, Wielebinski & Morsi (1988) inferred a smaller thermal contribution at 87 GHz of $\approx 25\%$, but point out that this may be an underestimate.

The total continuum measurement obtained at 92 GHz by Carlstrom & Kronberg (1991) of 0.59 ± 0.09 Jy is in very good agreement with those of Seaquist *et al.* (1996) at the same frequency (0.67 ± 0.10 Jy), of Carlstrom & Kronberg (1991) at 91 GHz (0.55 Jy), and of Jura, Hobbs & Maran (1978) and Klein, Wielebinski & Morsi (1988) at 87 GHz (0.54 ± 0.08 Jy and 0.51 ± 0.08 Jy respectively). With the above assumptions on the emission processes,

$$\frac{Q^0}{\rm s^{-1}} = 1.32 \times 10^{53} \left(\frac{D}{\rm Mpc}\right)^2 \left(\frac{\nu}{90\ \rm GHz}\right)^{0.2} \left(\frac{T_{\rm e}}{10^4\ \rm K}\right)^{-0.57} \left(\frac{S_\nu^{\rm ff}}{\rm Jy}\right) \qquad (5.7)$$

where D is the distance to the source, ν is the frequency of the emission observed, and $S_\nu^{\rm ff}$ is the thermal free-free continuum flux density (*e.g.* Spitzer 1978). Adopting the result from Carlstrom & Kronberg (with appropriate beam size correction to match the SWS aperture), $T_{\rm e} = 5000$ K and the distance to M 82 of 3.3 Mpc, Eq. 5.7 yields $\log Q^0 = 53.69^{+0.10}_{-0.12}$. This agrees well with the values in table 5.4 obtained from the intrinsic H I line fluxes assuming the mixed and two-screen two-source models.

5.1.6 Parameters adopted for the global extinction towards the H II regions in M 82

Since the mixed and two-screen two-source models result in similarly good fits, as well as nearly identical Q^0 and extinction corrections at near- and mid-infrared wavelengths, **the mixed model with A_V = 52 mag** will be adopted throughout this thesis as representative of the global extinction towards the bulk of the ionized gas in M 82. The ionizing luminosity for a 30″–diameter aperture is twice that for the SWS field of view, $Q^0 = 1.23 \times 10^{54}$ s^{-1}. The Galactic Center law (Lutz *et al.* 1996) will be adopted between $3\,\mu$m and $10\,\mu$m. For the other wavelength ranges relevant to this work, the extinction law from Rieke & Lebofsky (1985; $\lambda \leq 0.9$ μm) and from Draine (1989; 0.9 μm $< \lambda <$ 3 μm and 10 μm $< \lambda <$ 40 μm) will be used. The validity of the Draine law at near-infrared wavelengths ($A_\lambda \propto \lambda^{-1.75}$), or of similar extinction laws (*e.g.* Landini *et al.* 1984, with $A_\lambda \propto \lambda^{-1.85}$), was confirmed by Satyapal *et al.* (1995).

5.1.7 Local extinction towards the H II regions in M 82

From the spatially resolved Brackett line emission obtained with 3D, the extinction towards individual regions can be derived as described in section 5.1.3 using Brγ as the reference line. As demonstrated in figure 5.2, different geometries result in very similar variations in the Brackett line ratios so that the data do not allow the discrimination between different extinction models; the two-screen two-source model will not be considered here. The $A_V^{\rm UFS}$ and $A_V^{\rm MIX}$ for the central 35 pc of M 82, the Brγ sources B1 and B2, and the 3D field of view are derived from the fluxes listed in table 4.5. The results are reported in table 5.5, together with the Q^0 computed from the Brγ fluxes (the most accurately measured line), corrected for $A_V^{\rm MIX}$. The extinction law from Draine (1989), and the line emissivities and recombination coefficients for $n_e = 100$ cm^{-3} and $T_e = 5000$ K from Hummer & Storey (1987) are adopted. The A_V's are little affected by the choice of $n_{\rm e}$ and $T_{\rm e}$, but the Q^0 values increase by up to 50% for $T_{\rm e} = 10^4$ K.

The lower $A_V^{\rm MIX}$ for the 3D field of view compared to the global extinction derived in the previous subsections is consistent with the fact that the 3D near-infrared lines probe less obscured sources. The resulting extinction correction at 2.2 μm for $A_V^{\rm MIX} = 36$ mag is 3.5 instead of 4.9 for $A_V^{\rm MIX} = 52$ mag. In turn, the larger $A_V^{\rm UFS}$ is consistent with the exclusion of data at optical wavelengths. The differences in A_V between the individual regions are in good agreement with the spatial variations seen in the extinction map

Table 5.5: Extinction towards the ionized gas for selected individual regions in M 82

	Central 35 pc	B1	B2	3D field
$A_V^{\rm UFS}$ [mag]	10 ± 5	8 ± 2	11 ± 2	9 ± 3
$A_V^{\bf MIX}$ [mag]	$\mathbf{23 \pm 10}$	$\mathbf{27 \pm 7}$	$\mathbf{45 \pm 20}$	$\mathbf{36 \pm 16}$
$\log Q^{0\,(\rm a)}$	$\mathbf{52.03^{+0.12}_{-0.17}}$	$\mathbf{52.37^{+0.09}_{-0.11}}$	$\mathbf{52.51^{+0.15}_{-0.23}}$	$\mathbf{53.64^{+0.15}_{-0.23}}$

$^{(a)}$ The mixed model will be adopted. Q^0 (in s^{-1}) derived from the observed Brγ fluxes corrected for $A_V^{\rm MIX}$.

from Satyapal *et al.* (1995) obtained from Brγ and Paβ measurements. For each region, the $A_V^{\rm MIX}$ and $A_V^{\rm UFS}$ imply similar extinction corrections near $2\,\mu$m, to within 35% or less. This is as expected because the lines are so close in wavelength, and therefore probe regions up to similar limiting optical depths. The uncertainties on the extinction corrections are typically $20\% - 40\%$ for both models. As will be discussed in section 5.3, the ionized nebulae are likely mixed with the molecular gas and dust clouds even on scales of a few tens of parsecs. The results for a mixed model in table 5.5 will therefore be adopted for the selected individual regions.

Attempts to generate an extinction map using the 3D Brackett linemaps, rebinned to $1'' \times 1''$ pixels to increase the signal-to-noise ratio, were still hampered by the weakness of the H-band lines over significant areas. In the regions where the signal-to-noise ratio is sufficient, the differences in extinction corrections near $2\,\mu$m between a uniform foreground screen and a mixed model are $\lesssim 20\%$. Furthermore, the corrections implied by the extinction towards the evolved stars derived in chapter 6 are typically within 20% of those inferred here from the extinction towards the ionized gas (for purely foreground obscuration). Therefore, on the smaller spatial scales of individual pixels, the foreground extinction towards the evolved stars provides a satisfactory approximation to the local extinction towards the ionized gas. The extinction from this non-uniform foreground screen model will thus also be applied to the emission line sources when considering the properties of individual pixels throughout this thesis.

5.2 Physical conditions of the ISM

5.2.1 Electron temperature in M 82

The average electron temperature T_e in H II regions can be computed from H I recombination line fluxes combined with thermal free-free continuum flux densities. For optically thin gas in LTE and spontaneous line emission, the line-to-continuum ratio in the millimetric regime is essentially determined only by T_e (*e.g.* Osterbrock 1989 and references below). From the global continuum flux density around 3.3 mm together with various millimetric H I recombination lines, a T_e near 5000 K is inferred for the starburst core of M 82 (Puxley *et al.* 1989; Carlstrom & Kronberg 1991; Seaquist, Kerton & Bell 1994; Seaquist *et al.* 1996). If thermal dust emission or non-thermal synchrotron radiation from supernova remnants contribute to the 3.3 mm continuum, a lower T_e would result from the lower thermal free-free flux density. However, the various authors above have shown that these contributions to the global emission in M 82 are small.

The electron temperature can be estimated on smaller spatial scales from the maps of the H41α line emission (λ = 3.26 mm) and of the underlying continuum emission obtained by Seaquist *et al.* (1996). With the resolution of these data (4.5″), the central 35 pc of M 82, and the Brγ sources B1 and B2 lie in regions of bright continuum emission, for which Seaquist *et al.* (1996) show the line-to-continuum ratio to be consistent with optically thin LTE emission and $T_e = 5000 - 10^4$ K. The H41α map exhibits, however, enhanced emission relative to the continuum at a few locations, indicating LTE temperatures below 2000 K. Seaquist *et al.* (1996) interpret these "cold spots" as due to the presence of dense ($n_e > 10^{4.5}$ cm^{-3}) regions less than 1 pc in size exhibiting primarily stimulated emission, presumably compact H II regions or molecular clouds shock-ionized by the starburst wind. However, the millimetric line ratios for the entire starburst core of M 82 are consistent with spontaneous emission (Seaquist, Kerton & Bell 1994; Seaquist *et al.* 1996). In addition, the central 35 pc of M 82, B1 and B2 do not coincide with the cold spots. Stimulated emission therefore does not affect the determination of T_e in the individual regions considered here.

Electron temperatures in Galactic and extragalactic H II regions fall in the range 5000 − 20000 K, with the lower values corresponding to higher abundances of heavy elements (*e.g.* Smith 1975; Shaver *et al.* 1983). The extensive models of Rubin (1985) show that among the effective temperature of the ionizing stars, the electron density and the metallicity, the latter is the most sensitive factor affecting T_e, mainly because the heavy elements are very efficient coolants. According to these models, electron

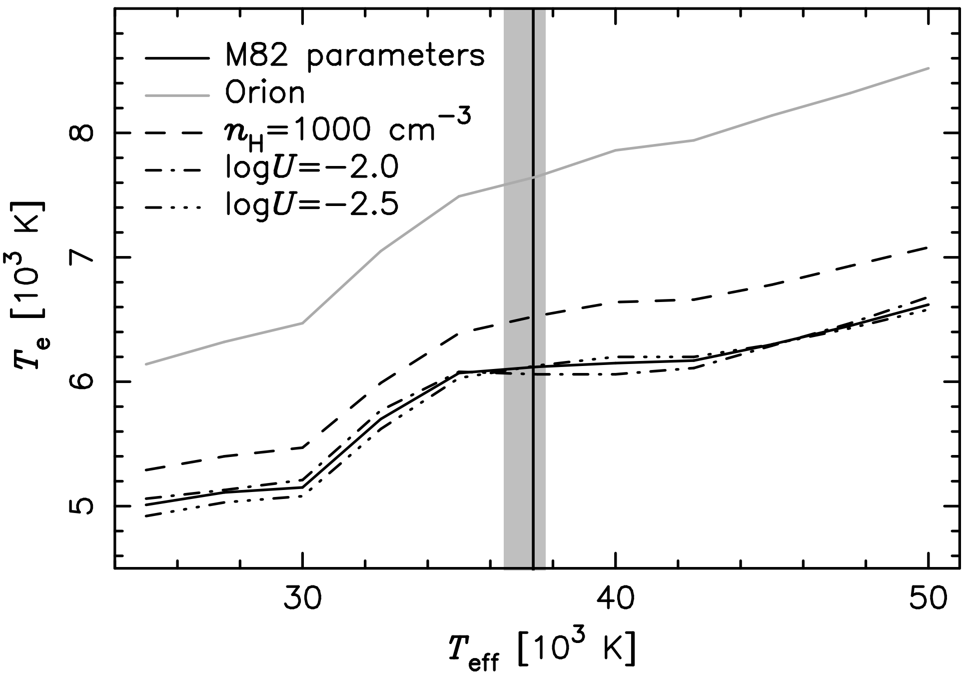

Fig. 5.7.— Variations of T_e with effective temperature of the ionizing stars for various nebular parameters, computed with the photoionization code CLOUDY and the model atmospheres from Pauldrach *et al.* (1998). The solid black curve shows the T_e for the parameters appropriate for M 82 determined in this chapter: $n_e = 300\ \mathrm{cm^{-3}}$, $\log U = -2.3$, $R = 25$ pc, solar gas-phase abundances and no dust grains mixed with the ionized gas. The other curves illustrate the effects of adopting the gas and dust composition typical of the Orion nebula, and of varying n_e ($\approx n_H$) and $\log U$ as indicated in the upper left corner. The vertical line indicates the average temperature for the OB stars which dominate the integrated mid-infrared nebular line emission in the SWS aperture, and the shaded box indicates the dispersion observed across the regions mapped with 3D (section 5.4).

temperatures between $\approx$ 3000 K and 6000 K are predicted for abundances of heavy elements between three times solar and solar respectively, for $n_e = 10^2 - 10^3\ \mathrm{cm^{-3}}$ and a large range in stellar temperatures. The gas-phase abundances determined from various *ISO*-SWS lines in section 5.2.3 below are nearly solar. For the average effective temperature of the OB stars in the SWS and 3D fields of view (section 5.4), photoionization models computed with CLOUDY[3] (assuming $n_e = 300\ \mathrm{cm^{-3}}$, $\log U = -2.3$, $R = 25$ pc, and using the stellar atmosphere models from Pauldrach *et al.* 1998 for solar metallicity main-sequence stars) predict $T_e \approx 6000$ K, in very good agreement with the observations. This is shown in figure 5.7, where the effects of varying the electron density, the ionization parameter or the gas and dust composition are illustrated as well. The density and the ionization parameter have small effects only, while modest gas depletion of heavy elements onto dust grains as in the Orion nebula results in a substantial change in T_e.

[3]described in chapter 3

5.2.2 Electron density in M 82

The electron density n_e in gaseous nebulae can be determined using a variety of techniques, including ratios of collisionally excited lines from species with similar ionization potentials but having different critical densities for collisions with electrons (*e.g.* Osterbrock 1989). The SWS spectrum provides three density-sensitive ratios towards the starburst regions in M 82, namely [S III] 18.7 μm/33.5 μm, [Ne III] 15.6 μm/36.0 μm and [Ar III] 8.99 μm/21.8 μm. All three are fairly insensitive to T_e in the range 5000 − 20000 K. The [S III] ratio is the most reliable one because both lines are amongst the strongest in the SWS spectrum. It is also the most sensitive at low densities because the upper levels of the transitions have the lowest critical densities.

The ratios for the $14'' \times 20''$ SWS aperture corrected for the global extinction of $A_V = 52$ mag (mixed model) are [S III] 18.7 μm/33.5 μm $= 0.71 \pm 0.23$, [Ne III] 15.6 μm/36.0 μm $= 9.0 \pm 4.2$ and [Ar III] 8.99 μm/21.8 μm $= 15.5 \pm 9.3$. The uncertainties include those on the line fluxes, on the scaling factor between the different apertures, and on the extinction. Comparison with the results of computations of collisional excitation in figure 5.8 shows that these ratios lie in the low-density limit, indicating n_e in the range $\sim 10 - 600$ cm^{-3}. This is similar to the average n_e in large apertures obtained previously by various authors using different infrared and radio diagnostics and assuming a single-density model (*e.g.* Houck *et al.* 1984; Duffy *et al.* 1987; Seaquist, Bell & Bignell 1985; Seaquist *et al.* 1996). The [O III] 52 μm/88 μm measured by Duffy *et al.* (1987) in a $48''$–diameter aperture is also shown in figure 5.8. This ratio is more sensitive to n_e at low densities, and indicates $n_e \sim 50 - 500$ cm^{-3}. Such low densities are typical for giant Galactic and extragalactic H II regions, and have been measured in various starburst galaxies as well (*e.g.* Shields 1990; Lutz *et al.* 1996; Rigopoulou *et al.* 1996; Kunze *et al.* 1996). A value of 300 cm^{-3} will be adopted throughout this thesis for the electron density within the H II regions in M 82.

Some studies provide indications of two distinct gas components in M 82: one characterized by a volume filling factor near unity and $n_e \lesssim 100$ cm^{-3}, and the other, by a much smaller volume filling factor ($10^{-4} - 10^{-1}$) and $n_e \gtrsim 10^3$ cm^{-3} (*e.g.* Seaquist, Bell & Bignell 1985; Lugten *et al.* 1986; Seaquist, Kerton & Bell 1994; Seaquist *et al.* 1996). Seaquist, Kerton & Bell (1994) have even proposed a different origin for the millimetric H I lines and the far-infrared forbidden lines such as [O III] 88 μm and [N III] 57 μm, the former being produced in dense, compact star-forming regions and the latter arising in low-density regions. However, the very good spatial correlation between existing near- and mid-infrared H I emission line maps (which are not affected by stimulated emission in high-density gas), the 3.3 mm continuum emission, and the mid-infrared fine-structure line emission — in particular [Ne II] 12.8 μm and [Ar III]

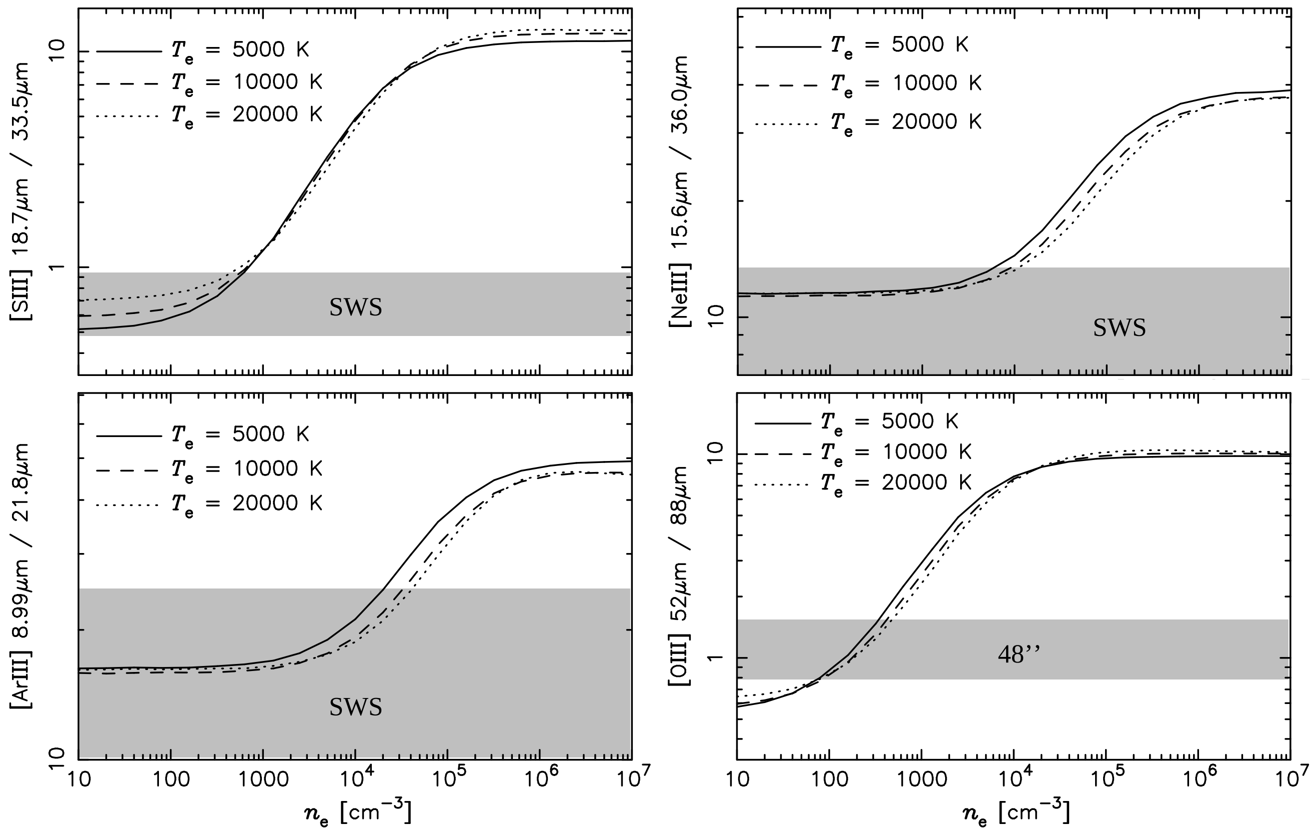

Fig. 5.8.— Determination of the electron density in M 82 from infrared fine-structure line ratios. The various curves are the collisional excitation computations for three electron temperature: 5000 K (solid line), 10^4 K (dashed line) and 2×10^4 K (dotted line). The [S III] 18.7 μm/33.5 μm, [Ne III] 15.6 μm/36.0 μm and [Ar III] 8.99 μm/21.8 μm plots show the measurements obtained with the *ISO*-SWS. The [O III] 52 μm/88 μm ratio from Duffy *et al.* (1987) in a 48″–diameter aperture is shown as well.

8.99 μm — (*e.g.* the 3D Brγ map; Satyapal *et al.* 1995; Seaquist *et al.* 1996; Achtermann & Lacy 1995) suggests that the density derived above from the SWS forbidden lines is representative of n_e in the H II regions observed in the range $\lambda = 1 - 40$ μm.

The spatially resolved 3D data provide the [Fe II] 1.533 μm/1.644 μm line ratio, which is also a good density indicator in the range $n_e = 10^2 - 10^6$ cm^{-3}. The near-infrared [Fe II] line emission, however, does not originate from the star-forming regions but is likely due to collisional excitation by shocks associated with supernova remnants or a starburst wind (e.g. Greenhouse *et al.* 1997). This is obvious from the spatial distribution of the [Fe II] 1.644 μm emission (figure 4.3; see also Greenhouse *et al.* 1997), which is very different from that of the Brγ emission.

The [Fe II] $1.533\,\mu$m/$1.644\,\mu$m ratios measured in individual regions, corrected for the extinction derived in section 5.1.7, can be compared with the theoretical computations by Bautista & Pradhan (1996). The inferred n_e are $2.0^{+1.2}_{-0.7} \times 10^4$ cm^{-3} at B1, $4.0^{+2.3}_{-1.5} \times 10^3$ cm^{-3} at B2, and $2.0^{+1.2}_{-0.7} \times 10^3$ cm^{-3} for the entire 3D field of view. These values are consistent with the densities in Galactic supernova remnants inferred from near-infrared [Fe II] lines by Oliva, Moorwood & Danziger (1989). The non-detection of the [Fe II] $1.599\,\mu$m line in the 3D spectra confirms $n_e < 10^{4.5}$ cm^{-3} (Oliva, Moorwood & Danziger 1989). The upper limit on the [Fe II] $1.533\,\mu$m line flux for the central 35 pc of M 82 implies $n_e \lesssim 500$ cm^{-3}. This is much lower than the estimate of $10^{4.5} - 10^6$ cm^{-3} from McLeod *et al.* (1993) using several lines in the J-band in a $3''$–diameter aperture at the nucleus (central 45 pc), but consistent with the upper limit of $10^{4.5}$ cm^{-3} inferred by Lester *et al.* (1990) from their non-detection of the [Fe II] $1.599\,\mu$m in a $3.8''$–diameter aperture at the nucleus (central 60 pc). It is emphasized that these high densities do not represent those within the ionized nebulae traced by the mid-infrared fine-structure lines considered above and by the H I recombination lines, which are substantially lower.

5.2.3 Gas-phase abundances in M 82

The SWS data allow the determination of the gas-phase abundances of three of the most abundant heavy elements in H II regions, namely Ne, Ar and S, from the fine-structure lines emitted by their ions. The line fluxes for the $14'' \times 20''$ SWS aperture, corrected for extinction, are listed in table 5.6. Detailed models accounting for the ionization structure of the nebulae can be used to derive accurate abundances (*e.g.* Rubin 1985; Shields & Ferland 1994; Simpson *et al.* 1995). However, for the purpose of this work, simpler estimates are sufficient.

In the low-density limit, collisional de-excitation can be neglected. This is the case for the fine-structure lines considered here, which have critical densities for collisions with electrons at $T_e = 5000$ K in the range $\sim 10^4 - 10^6$ cm^{-3}, much larger than the density of $n_e \sim 300$ cm^{-3} determined in the previous section. Assuming a "one-layer" model with uniform density and temperature, the number abundance of a heavy element X in the $i^{\rm th}$ ionization stage relative to H$^+$ can be computed from

$$\frac{F_{\lambda(\mathrm{X}^{+i})}}{F_{\lambda(\mathrm{H}^{+})}} = \frac{n_i n_e \epsilon_{\lambda(\mathrm{X}^{+i})}}{n_{\mathrm{H}^+} n_e \epsilon_{\lambda(\mathrm{H}^{+})}}, \tag{5.8}$$

where $F_{\lambda(\mathrm{X}^{+i})}$ and $F_{\lambda(\mathrm{H}^{+})}$ are the fluxes of the ionic line of interest and of a reference H I recombination line, n_i and n_{H^+} are the densities of ions X$^{+\mathrm{i}}$ and H$^+$, and $\epsilon_{\lambda(\mathrm{X}^{+i})}$ and $\epsilon_{\lambda(\mathrm{H}^{+})}$ are the line emissivities. In H II regions, H is nearly completely ionized so that $n_{\mathrm{H}^+} \approx n_{\mathrm{H}}$. The emissivity of a collisionally excited line (in the low-density limit) is given by

$$\epsilon_{\lambda(\mathrm{X}^{+i})} = \left(\frac{hc}{\lambda}\right) \left(\frac{8.629 \times 10^{-6}}{T_{\mathrm{e}}^{1/2}}\right) \left(\frac{\Upsilon_{12}}{\omega_1}\right) e^{-\chi_{12}/kT_{\mathrm{e}}}\, b, \tag{5.9}$$

where h is Planck's constant, c is the speed of light, k is Boltzmann's constant, T_{e} is the electron temperature, Υ_{12} and χ_{12} are the effective collisional strength and the energy of the transition between levels 2 and 1 giving rise to the line emission, and ω_1 is the statistical weight of the lower energy level 1 (*e.g.* Osterbrock 1989 for Eqs. 5.8 and 5.9). b is the fraction of excitations to level 2 that are followed by emission of a photon in the line of interest; for the cases considered here, $b = 1$.

Taking Brα as reference H I recombination line, its intrinsic line flux is computed from the ionization rate in table 5.4 for $A_V^{\mathrm{MIX}} = 52$ mag, using the total hydrogen recombination coefficient and line emissivities from Hummer & Storey (1987), for the appropriate electron temperature and density for M 82. The effective collisional strengths at $T_{\mathrm{e}} = 5000$ K are taken from Johnson, Kingston & Dufton (1986), Saraph & Tully (1994), Butler & Zeippen (1994), Pelan & Berrington (1995), and Galavís, Mendoza & Zeippen (1995). For ionizing stars with effective temperatures in the range 35000 K – 40000 K, as found for M 82 (section 5.4 below), the Ne, Ar and S are expected to be mostly in the lowest ionization stage observed with SWS, with the Ne^+, Ar^+ and S^{++} zones nearly coinciding with the H^+ zone owing to their comparable ionization potentials in the range 13 eV – 23 eV (see appendix B). Ionization stages higher than those listed in table 5.6 are neglected because the corresponding lines are either very weak or absent in the SWS spectrum. To a good approximation, the elemental abundances correspond therefore to the sum of the ionic abundances determined here. The data and results are given in table 5.6, together with the solar composition for comparison. The uncertainties on the ionic abundances are estimated to be about $\pm 50\%$, and up to a factor of two for those derived from the weakest lines. The relative abundances are nearly solar or slightly above for Ne and Ar, and about one-fourth solar for S. Similar underabundances for S have been found in Galactic H II regions (*e.g.* Simpson *et al.* 1995) and in some extragalactic starburst systems (*e.g.* Genzel *et al.* 1998), and are attributed to depletion of S onto interstellar dust grains.

Most abundance determinations for M 82 in the literature indicate no large depletions or enhancements for most elements compared to the solar neighbourhood composition (*e.g.* Gaffney & Lester 1992; McLeod *et al.* 1993 and references therein; Achtermann & Lacy 1995; Lord *et al.* 1996). The exception is Si, for which Lord *et al.* (1996) found a gas-phase abundance three times larger than in Galactic nebulae, and which they interpret as probably due to partial destruction of silicate grains by fast supernova-driven shocks.

Table 5.6: Gas-phase abundances of Ne, Ar and S within the H II regions of M 82

Transition[(a)]	F_λ^{0}[(b)] [W m^{-2}]	Υ_{12}[(c)] [cm^3 s^{-1} K$^{1/2}$]	ϵ_λ[(d)] [erg cm^3 s^{-1}]	X^{+i}/H[(e)]
Brα (4.05 μm)	2.38×10^{-14}	—	2.29×10^{-26}	—
[Ne II] $^2P_{3/2} - {}^2P_{1/2}$ (12.8 μm)	1.37×10^{-13}	0.277	1.05×10^{-21}	$Ne^+/H = 1.26 \times 10^{-4}$
[Ne III] $^3P_2 - {}^3P_1$ (15.6 μm)	2.17×10^{-14}	0.730	1.89×10^{-21}	$Ne^{++}/H = 1.11 \times 10^{-5}$
[Ne III] $^3P_1 - {}^3P_0$ (36.0 μm)	2.41×10^{-15}	0.227	4.71×10^{-22}	$Ne^{++}/H = 4.92 \times 10^{-6}$
[Ar II] $^2P_{3/2} - {}^2P_{1/2}$ (6.99 μm)	6.51×10^{-14}	2.70	1.55×10^{-20}	$Ar^+/H = 4.03 \times 10^{-6}$
[Ar III] $^3P_2 - {}^3P_1$ (8.99 μm)	1.70×10^{-14}	3.18	1.25×10^{-20}	$Ar^{++}/H = 1.31 \times 10^{-6}$
[Ar III] $^3P_1 - {}^3P_0$ (21.8 μm)	1.09×10^{-15}	1.35	4.39×10^{-21}	$Ar^{++}/H = 2.38 \times 10^{-7}$
[S III] $^3P_1 - {}^3P_2$ (18.7 μm)	5.21×10^{-14}	5.03	1.87×10^{-20}	$S^{++}/H = 2.69 \times 10^{-6}$
[S III] $^3P_0 - {}^3P_1$ (33.5 μm)	7.34×10^{-14}	2.22	1.48×10^{-20}	$S^{++}/H = 4.79 \times 10^{-6}$
[S IV] $^2P_{1/2} - {}^2P_{3/2}$ (10.5 μm)	5.70×10^{-15}	5.85	5.14×10^{-20}	$S^{+++}/H = 1.07 \times 10^{-7}$

X/H[(e)]	Solar composition[(f)]	**M 82**	**([X/H]$_{M82}$)**[(g)]
Ne/H	1.17×10^{-4}	$\approx \mathbf{1.4 \times 10^{-4}}$	**(0.08 dex)**
Ar/H	3.98×10^{-6}	$\approx \mathbf{5 \times 10^{-6}}$	**(0.1 dex)**
S/H	1.62×10^{-5}	$\approx \mathbf{4 \times 10^{-6}}$	**(-0.6 dex)**

[(a)] Ionic transitions are given as *lower level - upper level.*

[(b)] Fluxes for the 14″ × 20″ SWS aperture (table 4.10), corrected for $A_V = 52$ mag (mixed model). The Brα flux is computed from the intrinsic ionization rate (table 5.4) using the recombination coefficient and line emissivities from Hummer & Storey (1987).

[(c)] Effective collisional strengths for $T_e = 5000$ K. [Ne II]: Saraph & Tully (1994); [Ne III]: Butler & Zeippen (1994); [Ar II]: Pelan & Berrington (1995); [Ar III] and [S III]: Galavís, Mendoza & Zeippen (1995); [S IV]: Johnson, Kingston & Dufton (1986).

[(d)] The volume emissivities for the ionic lines are computed from Eq. 5.9 ($b = 1$ for the transitions considered). The volume emissivity for Brα is taken from Hummer & Storey (1987).

[(e)] Ionic or elemental number abundance relative to hydrogen, with estimated uncertainties of approximately ±50%, and up to a factor of two for the ionic abundances derived from the weakest lines.

[(f)] From Grevesse & Anders (1989) and Grevesse & Noels (1993), as given in Ferland (1996).

[(g)] Relative to the solar composition: $[X/H]_{M82} = \log(X/H)_{M82} - \log(X/H)_\odot$.

5.2.4 Dust within the H II regions in M 82

Interstellar dust grains mixed with the ionized gas in H II regions can affect substantially the nebular line emission since dust competes effectively with the gas for absorption of ionizing photons. This can lead to underestimates of the ionizing luminosity of the stars derived from emission line fluxes. In addition, dust will harden the ionizing radiation spectrum within the nebulae since the absorption cross-section of standard interstellar dust grains generally increases at lower ionizing energies (*e.g.* Draine & Lee 1984; Mathis 1990).

In M 82, the presence of dust heated by young, hot stars is supported by the correlation between the spatial distributions of thermal continuum emission and PAH features at infrared wavelengths, and of tracers of ionized gas such as H I recombination lines or the [Ne II] $12.8\,\mu$m line (*e.g.* Telesco & Gezari 1992; Normand *et al.* 1995; Achtermann & Lacy 1995; Satyapal *et al.* 1995). However, spatial variations in the line-to-continuum ratio for the $3.3\,\mu$m PAH feature suggest that the carriers of this emission band are depleted in the central $20''$ of M 82 (Normand *et al.* 1995). Partial destruction of silicate dust grains in the H II regions of M 82 has been proposed by Lord *et al.* (1996) to explain the enhanced Si gas-phase abundance they measured compared to that in Galactic H II regions. Whether — and how much — dust is truly mixed with the ionized gas in M 82, and what are its properties is, however, still very uncertain. Dust grains within H II regions will be ignored in the models applied to M 82 in this work, but their effects will be discussed when appropriate.

5.3 Ionization parameter in M 82

H II regions can be represented as shells surrounding central, point-like stellar clusters. In such models, the nebular conditions are specified by the distance R between the ionizing cluster and the illuminated surface of the gas cloud, the hydrogen number density $n_{\rm H}$ of the gas, and the ionization parameter U defined as

$$U \equiv \frac{\phi}{n_{\rm H}\, c}, \tag{5.10}$$

where ϕ is the stellar Lyman continuum photon flux and c is the speed of light. U thus gives the number of ionizing photons impinging at the surface of the nebula per hydrogen atom. In the simple shell representation,

$$\phi = \frac{Q}{4\pi R^2}, \tag{5.11}$$

where Q is the production rate of ionizing photons from the stars. Since H is the most abundant element in the ISM and is nearly completely ionized in H II regions, and since He (the second most abundant element with typically $n_{\rm He}/n_{\rm H} \approx 0.1$) is not fully ionized in M 82 (section 5.4), $n_{\rm H} \approx n_{\rm e}$ will be hereafter assumed.

U is a particularly critical parameter in photoionization modeling because it affects importantly the ionization structure of the nebula and, in turn, the relative line intensities (*e.g.* Davidson & Netzer 1979; Shields 1993; Shields & Ferland 1994). More specifically, as U decreases, the ionization fronts for the various species become less sharply defined. Consequently, for a given element, a larger fraction of the nebula is in an intermediate ionization state, resulting in a decrease of the ratios of high to low ionization lines, such as [Ne III] 15.6 μm/[Ne II] 12.8 μm. In such complex and distant systems as starburst galaxies, a large number of H II regions may coexist in a relatively small volume and may not be individually resolved by the observations. In this case, the shell geometry is not directly applicable. The spatial distribution of the gas relative to the ionizing sources is crucial in determining ϕ, and in deriving the *effective* U and R to model appropriately the ionized nebulae using the idealized shell geometry.

U is generally poorly determined in starburst galaxies because of the lack of detailed information on small enough spatial scales. M 82 is one exception: owing to its proximity, various observations of the molecular, neutral atomic and ionized gas in the starburst regions of M 82 reveal important structure on scales at least as small as $\approx 20 - 30$ pc (*e.g.* the 3D linemaps in figure 4.3; Shen & Lo 1995; Larkin *et al.* 1994; Achtermann & Lacy 1995; Satyapal *et al.* 1995). Models of the ISM suggest even more extreme properties, with the molecular and the neutral atomic gas confined in very small and dense clouds by a strong but diffuse ultraviolet radiation field (*e.g.* Olofsson

& Rydbeck 1984; Telesco 1988; Wolfire, Tielens & Hollenbach 1990; Lord *et al.* 1996; Stutzki *et al.* 1997). The equilibrium between the strong radiation pressure and thermal gas pressure confines the warm clouds in a small volume and prevents their thermal expansion.

In this section, the 3D and SWS data together with existing data from the literature are used to constrain the degree of ionization of the nebulae within the starburst regions of M 82. Three representative regions are selected for this purpose: a $30''$–diameter aperture centered on the nucleus (hereafter "starburst core"), and the two brightest Brγ sources B1 and B2. For clarity, most numerical results in the following sections are not mentioned in the text but reported directly in tables 5.7 and 5.8 at the end of this section. The 3D and SWS data are complemented with the results from the detailed modeling of photodissociation regions (PDR) by Lord *et al.* (1996). These provide particularly relevant constraints on the properties of the gas and on the radiation field for the present purposes, and are first summarized below.

5.3.1 Properties of the neutral and molecular gas

Lord *et al.* (1996) modeled the global [O I] $63\,\mu$m and [Si II] $35\,\mu$m line emission together with additional data on the molecular gas and far-infrared emission from the literature. These authors considered different spatial distributions for the far-infrared emission, and favoured the case where it arises mainly from two regions about 125 pc in diameter, roughly coinciding with molecular gas concentrations on each side of the nucleus. This is consistent with the general morphology of the infrared continuum emission as well as of the tracers of H II regions. Their models suggest that these lobes contain together $\sim 3 \times 10^5$ clouds with typical masses $M_{\rm cl} \sim 600$ $M_\odot$ and radii $r_{\rm cl} = 0.4 - 1$ pc. These clouds possess thin neutral gas surfaces with temperature ~ 230 K and density $\sim 10^4$ cm^{-3}, and are illuminated by far-ultraviolet fluxes $\sim 10^3$ times the average interstellar value for the Milky Way (see also Duffy *et al.* 1987 and Lugten *et al.* 1986). The inferred cloud core densities are $n_{\rm H_2} \sim 10^4 - 10^5$ cm^{-3}, consistent with the large mass fraction of dense gas inferred from observations of the HCN molecule emission (*e.g.* Shen & Lo 1995; Brouillet & Schilke 1993; Güsten *et al.* 1993). The volume filling factor of the clouds is $\sim 0.01 - 0.1$, and their mean separation is $d_{\rm cl-cl} = 1.5 - 3.8$ pc. The average incident flux on the clouds in each lobe inferred from the PDR modeling is about the same as the beam-averaged radiation field seen in the far-infrared emission, suggesting that the stars, or stellar clusters, are randomly distributed in the starburst core of M 82. The southwestern lobe, which encompasses the regions B1 and B2, has the smallest clouds with $r_{\rm cl} = 0.4$ pc and $M_{\rm cl} = 220$ $M_\odot$.

5.3.2 Geometrical volumes

The geometrical volume V of the regions of interest is critical for several of the properties derived below. For the starburst core, the ionized and molecular gas are assumed to fill an edge-on disk of radius and thickness of 200 pc, consistent with the observations (*e.g.* Satyapal *et al.* 1995; Achtermann & Lacy 1995; Shen & Lo 1995). The $2.3'' \times 2.3''$ square apertures used to extract the spectra at B1 and B2 from the 3D data cubes cover an equivalent circular area of radius 19.5 pc. This is comparable to the full width at half maximum of the emission sources as determined from the Brγ line map. The kinematics of the Brγ, [Ne II] 12.8 μm and millimetric CO emission suggest that the ionized and molecular gas are distributed along a rotating ring or spiral arms (Larkin *et al.* 1994; Achtermann & Lacy 1995; Shen & Lo 1995). The emission regions at B1 and B2 are assumed to occupy cylindrical volumes with lengths corresponding to the intersection along the line-of-sight of the edge-on starburst disk. B1 and B2 are located $10.9''$ and $5.6''$ away from the nucleus, along the plane of the galaxy. The corresponding lengths are thus 230 pc and 365 pc respectively. In all cases, the integrated ionizing flux observed is assumed to be produced by soures distributed uniformly in the entire volume considered.

5.3.3 Mass and distribution of the ionized gas

Using the intrinsic ionization rates and the electron density and temperature determined in the previous sections, the mass and volume filling factor of the ionized gas in the regions of interest are derived assuming a uniform distribution for the ionized gas and case B recombination (Hummer & Storey 1987). The mass of ionized gas is given by

$$\frac{M_{\mathrm{H}^+}}{\mathrm{M}_\odot} = 3.24 \times 10^{-45} \left[\frac{Q}{\mathrm{s}^{-1}}\right] \left[\frac{n_\mathrm{e}}{\mathrm{cm}^{-3}}\right]^{-1} \left[\frac{T_\mathrm{e}}{10^4\ \mathrm{K}}\right]^{0.81} . \tag{5.12}$$

Combining the mass and density of the ionized gas, the volume filling factor is then

$$\Phi_V^{\mathrm{H}^+} = 1.31 \times 10^{-43} \left[\frac{Q}{\mathrm{s}^{-1}}\right] \left[\frac{n_\mathrm{e}}{\mathrm{cm}^{-3}}\right]^{-2} \left[\frac{T_\mathrm{e}}{10^4\ \mathrm{K}}\right]^{0.81} \cdot \left[\frac{V}{\mathrm{pc}^3}\right]^{-1} , \tag{5.13}$$

where V is the geometrical volume of the region considered (*e.g.* Osterbrock 1989).

5.3.4 Mass and distribution of the molecular gas

The mass of molecular gas (M_{H_2}) at B1 and B2 is estimated from the CO $J = 1 \rightarrow 0$ map of Shen & Lo (1995), which has a spatial resolution comparable to the 3D data

(2.5″). The CO intensities at B1 and B2 are converted into H_2 column densities and molecular masses using $N_{\rm H_2}/I_{\rm CO\,1\to0} = 7 \times 10^{19}$ cm^{-2}/K km s^{-1} derived by Wild *et al.* (1992) for regions including these Brγ sources. For the entire starburst core, these authors estimated $M_{\rm H_2} = 1.8\times10^8$ M$_\odot$, which is the mass adopted by Lord *et al.* (1996) for their PDR modeling. The number $N_{\rm cl}$, space density $n_{\rm cl}$ and mean separation $d_{\rm cl-cl}$ of the molecular clouds are computed assuming an average cloud mass $M_{\rm cl}$ of 220 M$_\odot$ at B1 and B2, and 600 M$_\odot$ for the starburst core.

The spatial distribution of the CO $J = 1 \to 0$ emission differs somewhat on small scales from that of the tracers of ionized gas. However, the tracers of dense gas ($n_{\rm H_2} \gtrsim 10^4$ cm^{-3}), such as HCN emission, correlate better with those of H II regions (*e.g.* Shen & Lo 1995; Golla *et al.* 1996). This is consistent with the picture in which the warm cloud remnants are highly pressurized by the intense UV radiation field produced by the numerous new-born stars in the regions where most of the ionized gas emission is observed. The $N_{\rm H_2}/I_{\rm CO\,1\to0}$ conversion factor was derived by Wild *et al.* (1992) from detailed radiative transfer calculations applied to observations of ^{12}CO (up to $J = 6 \to 5$), ^{13}CO and ^{18}CO lines at various positions along the galactic plane of M 82. It should thus account properly for the molecular gas mass at each location.

5.3.5 Ionizing clusters

Usually, the number density of *individual* OB stars with a representative spectral type inferred from optical and/or infrared nebular line ratios is compared to that of gas clouds. Lord *et al.* (1996) estimated an average separation between OB stars of a few parsecs. They argued that this supports a randomized distribution for the stars, since this distance is comparable to the distance massive, new-born stars would travel from motions of $\gtrsim 3$ km s^{-1} induced by star-star and star-cloud gravitational interactions over their main-sequence lifetimes of a few million years, and is consistent with young clusters rapidly disrupted by the dynamical processes occurring in starburst regions.

However, it is likely that the young, massive OB stars in M 82 are still in clusters. Indeed, high-resolution *HST* imaging of M 82 reveals the presence of over 100 super star clusters with typical sizes of 3.5 pc (O'Connell *et al.* 1995). Similar super star clusters are observed in other starburst galaxies as well (*e.g.* Whitmore & Schweizer 1995; O'Connell, Gallagher & Hunter 1994; Conti & Vacca 1994). Due to the high extinction towards the central regions of M 82, these super star clusters are probably mostly foreground, but some of them may also belong to the central regions if they lie in directions of lower extinction. In particular, the conspicuous associations of super-star clusters in the regions denoted "A" and "C" (following O'Connell & Mangano

1978) coincide with regions of lower extinction just south from the nucleus and from the western mid-infrared emission peak (see extinction maps from Telesco *et al.* 1991; McLeod *et al.* 1993; Larkin *et al.* 1994; Satyapal *et al.* 1995). Furthermore, the spatial distribution of the K-band continuum emission and of the stellar CO bandheads at $2.29\,\mu$m and $1.62\,\mu$m (3D maps in figures 4.3 and 4.4; Satyapal *et al.* 1997) reveal distinct compact sources along the galactic plane within $\approx$ 100 pc of the nucleus. From their surface brightness, their sizes and the depth of the CO bandheads, these are associated with young clusters of supergiants with ages near 10^7 yr. Similar clusters have been observed at near-infrared wavelengths in other starburst galaxies as well (*e.g.* Tacconi-Garman, Sternberg & Eckart 1996). The optical and near-infrared clusters are thought to be very young globular clusters, gravitationally bounded.

Therefore, it is more appropriate to compare the number density of ionizing stellar clusters with that of molecular clouds. A plausible cluster luminosity function (LF) for starburst galaxies in general, and M 82 in particular, was derived in chapter 3: $\Phi(Q^\star) \equiv \mathrm{d}N_\star/\mathrm{d}(\log Q^\star) \propto (Q^\star)^{-\beta}$, with $\beta = 0.17$ in the range $Q^\star = 10^{45} - 10^{49.5}$ s^{-1} and $\beta = 1$ in the range $Q^\star = 10^{49.5} - 10^{53}$ s^{-1}. Using this LF[4], the number of ionizing clusters is derived from

$$N_\star = K \int_{45}^{53} \Phi(Q^\star)\mathrm{d}(\log Q^\star), \tag{5.14}$$

where the normalization constant is obtained from the total intrinsic ionizing rate observed Q^0:

$$Q^0 = K \int_{45}^{53} Q^\star \Phi(Q^\star)\mathrm{d}(\log Q^\star). \tag{5.15}$$

From this, the cluster number density $n_\star$ and mean separation $d_{\star-\star}$ is computed.

5.3.6 The geometry of the ionized gas and stellar clusters

The final consideration in the determination of the effective ionization parameter in M 82 is the true geometry of the ionized nebulae relative to the ionizing clusters. The average properties on small spatial scales are very similar to those for the entire starburst core (table 5.7). The dense, small and warm molecular clouds with their thin neutral atomic gas envelope are bathed in the more tenuous and pervasive ionized medium. The mean separation between clusters and between clouds is comparable, supporting a highly uniform distribution of clusters and clouds. The formalism of Wolfire, Tielens & Hollenbach (1990) is followed to derive the effective U (hereafter U_{eff}) for a random distribution of clusters and clouds by comparison with a reference case where the sources are centrally concentrated (hereafter central cluster, or CC

[4] the star symbol is used here to denote stellar clusters, and the subscript "cl" refers to gas clouds

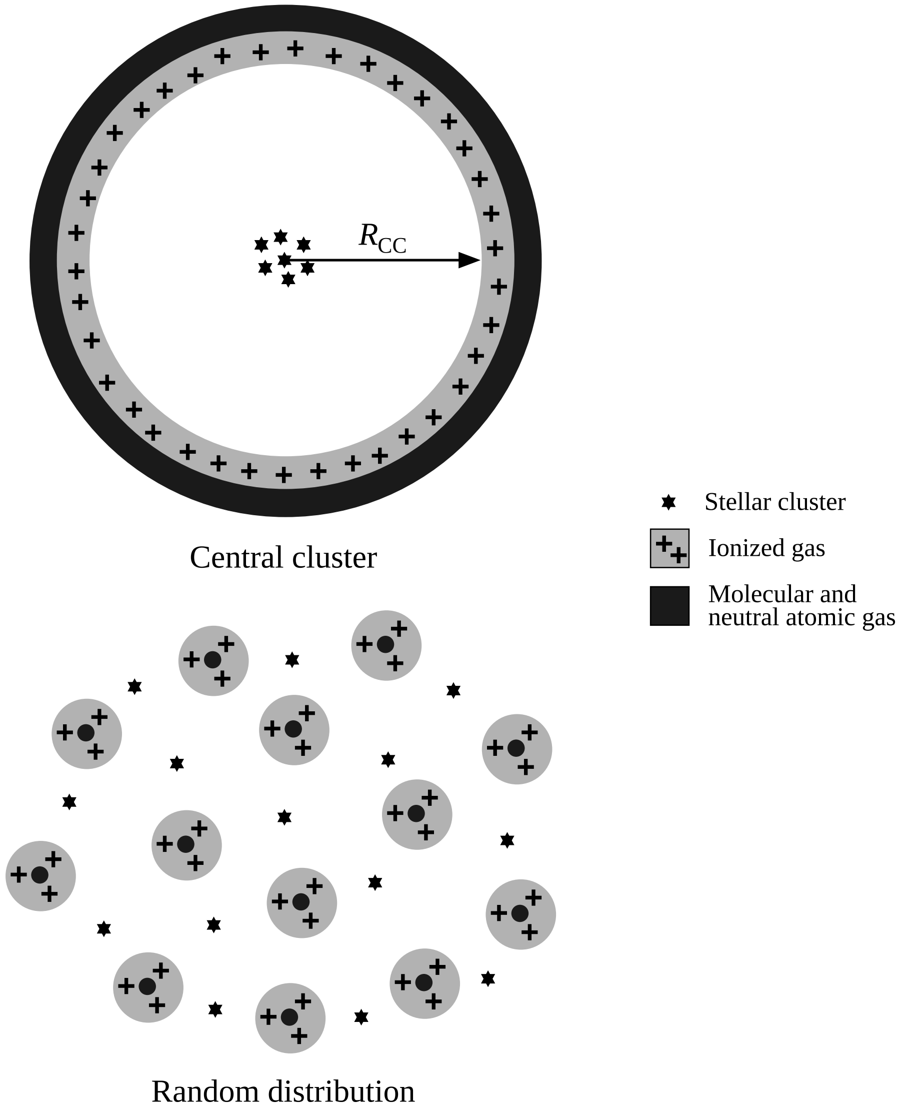

Fig. 5.9.— Two geometries considered in the derivation of $U_{\rm eff}$. *Top:* a central stellar cluster (or association of clusters) illuminates the surrounding gas; *bottom:* a uniform distribution of ionizing clusters and gas clouds.

model) and ionize the clouds located a distance $R_{\rm CC}$ away, with $R_{\rm CC}$ being the radius of the entire region considered. These geometries are illustrated in figure 5.9. In the random distribution model, the volume which is not occupied by the molecular, neutral and ionized gas is assumed to be filled by a hot ($T \sim 10^6$ K), tenuous ($n \sim 1$ cm^{-3}) plasma associated with the interior of evolved supernova remnants, as proposed for NGC 253 by Carral *et al.* (1994).

For convenience, the cylindrical volumes considered for the various regions are divided in spherical sub-units, with appropriate scaling of the luminosity and gas mass. More specifically, for the starburst core, a sphere with radius equal to half of the disk thickness (*i.e.* 100 pc) is treated. For B1 and B2, spheres with radius equal to that of the column cross-section (19.5 pc) are treated. In the CC model, the incident photon flux and corresponding $U_{\rm CC}$ are given by the expressions applicable for the simple shell geometry (Eqs. 5.10 and 5.11), with $R_{\rm CC}$ as the inner radius of the nebula. For a random distribution of stars and clouds within a spherical region of radius $R_{\rm CC}$, the incident radiation field corresponds to the average interstellar radiation field (ISRF) consisting of the contributions from all the clusters reduced by a "shielding factor" ($f_{\rm shield}$): $\phi_{\rm ISRF} = f_{\rm shield}\,\phi_{\rm CC}$. $f_{\rm shield}$ accounts for the interception of part of the radiation along a given light path by intervening clouds. Since the distribution is uniform, this factor is simply

$$f_{\rm shield} = \left(\frac{\lambda}{R_{\rm CC}}\right)\left[1 - e^{-R_{\rm CC}/\lambda}\right], \tag{5.16}$$

where λ is the mean free path of a photon, further discussed below. Consequently, in the logarithmic units used below,

$$\log U_{\rm eff} = \log U_{\rm CC} + \log f_{\rm shield}. \tag{5.17}$$

As long as λ is small compared to the size of the sub-region, the ionizing radiation from adjacent sub-units can be neglected. Otherwise, it is accounted for by adding the $\phi_{\rm ISRF}$ of adjacent sub-units scaled by the ratio $\lambda/R_{\rm CC}$ and assuming 25% of this photon flux is emitted in the direction of the sub-unit considered. The correction factor is denoted $\chi_{\rm adj}$. Two limiting values are given in table 5.8 for $\log U_{\rm eff}$: a lower limit for no contribution from the adjacent sub-units, and an upper limit obtained by (over-) estimating the contribution from the adjacent sub-units as just described.

The shielding factor is crucial for the derivation of $U_{\rm eff}$. Since the ionizing radiation is relevant here, the appropriate radius for the shielding clouds has to account for an ionized layer. Denoting this radius by $r_{\rm shield}$, this means $r_{\rm shield} \geq r_{\rm cl}$ where $r_{\rm cl}$ includes the thin neutral gas surface around the molecular core (see figure 5.10). $r_{\rm shield}$ is set by the requirement that the total volume of ionized gas must equal the fraction of the geometrical volume corresponding to its volume filling factor, *i.e.*

$$\Phi_V^{\rm H^+} V = N_{\rm cl}\frac{4\pi}{3}(r_{\rm shield}^3 - r_{\rm cl}^3). \tag{5.18}$$

Together, $n_{\rm cl}$ and $r_{\rm shield}$ determine the mean free path of ionizing photons:

$$\lambda = \left(n_{\rm cl}\pi r_{\rm shield}^2\right)^{-1}. \tag{5.19}$$

The geometry considered (figure 5.9, bottom) is only valid as long as the ionized thickness

$$l_{\rm H^+} = \frac{\phi_\star}{\alpha_B n_{\rm e}^2} \tag{5.20}$$

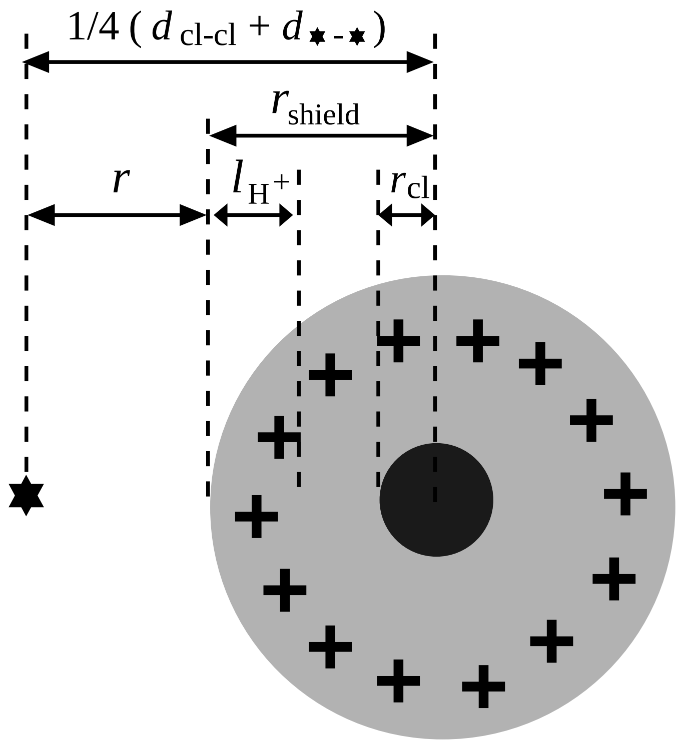

Fig. 5.10.— Local geometry between a cluster and a cloud, indicating the various radii entering in the models.

does not exceed $r_{\rm shield}$ (α_B is the total hydrogen recombination coefficient assuming case B, taken from Hummer & Storey 1987). Otherwise, the clouds become optically thin to ionizing radiation and shield much less efficiently. Note that in Eq. 5.20, the incident photon flux $\phi_\star$ is that produced by a particular cluster on a nearby cloud at a distance $r = 0.25(d_{\star-\star} + d_{\rm cl-cl}) - r_{\rm shield}$.

The atomic and molecular gas has, of course, much larger densities than the surrounding ionized gas itself, so that accurate computation of the ionized thickness should account for a density gradient towards the cloud centers. This also prevents to a large extent the most luminous clusters ($Q^\star \gtrsim 10^{50} - 10^{51}$ s^{-1}) to ionize fully the entire galaxy, in the case where they have blown away most of the dense natal cloud remnants. In addition, the cloud-cloud and cluster-cluster separations, and the distance from clusters to the inner surface of the nebulae derived here are averages for each region. More luminous clusters contain more massive stars whose strong stellar winds will push the surrounding gas left further away than most clusters which are much less luminous. For instance, a cluster with $Q^\star = 10^{52}$ s^{-1} will ionize interstellar gas with $n_{\rm e} = 100$ cm^{-3} located 2 pc away up to a depth of 1.5 kpc, but 60 pc if the distance is increased to 10 pc or if the density is increased to 500 cm^{-3}. For the typical cloud core densities of $n_{H_2} = 10^4 - 10^5$ cm^{-3}, the ionizing radiation would not penetrate further than ≈ 0.1 pc even for a distance of 2 pc, were all the flux to impinge on the cloud core. Again, the small neutral gas clouds present only a small cross-section to the ionizing radiation and most of it impinges on less dense material. To a first approximation, a consistency check for the random distribution model is to compare the average $< l_{H^+} >$ with $r_{\rm shield}$ for an average cluster having $< Q^\star >= Q^0/N_\star$.

5.3.7 The effective ionization parameter

Tables 5.7 and 5.8 summarize the adopted set of parameters, and the derived properties. In all cases, the distance from cluster to center of cloud is taken as half of the average of $d_{\star-\star}$ and $d_{\rm cl-cl}$. The quantity $R_{\rm eff}$ listed in table 5.8 is the effective inner radius that an equivalent shell-like H II region would have for the adopted density, the ionizing rate for a spherical sub-unit, and the derived $U_{\rm eff}$ (through Eqs. 5.10 and 5.11).

The $\log U_{\rm eff}$ for B1, B2 and the entire starburst core for the adopted parameters are between -2.3 dex and -2.5 dex. The average ionized thickness is about 1/4 of the cloud radius including the ionized layer, so that the random distribution model is valid. The ionized gas at B1 and B2 has a volume filling factor $\sim 10^{-1}$, about ten times larger than the molecular and neutral atomic gas. For the entire starburst core, the volume filling factors are more similar, $\sim 10^{-2}$. This is consistent with the fact that B1 and B2 have the brightest Brγ emission, with denser populations of OB star clusters. The mean free path for the ionizing photons is about 20 pc, implying modest shielding for B1 and B2, but substantial shielding for the entire starburst core. The number of luminous clusters ($Q^\star > 10^{50}$ s^{-1}) for the entire starburst core is about 10 times larger than observed with *HST* (O'Connell *et al.* 1995). This is consistent with most of the young clusters being heavily obscured in the central regions of M 82. The $R_{\rm eff}$ are larger than the radius of the spherical sub-units considered in the modeling. This reflects the fact that the shielding afforded by the randomly distributed clouds is effectively equivalent to a larger geometrical dilution by an increase in the size of the region for a shell-like representation. In other words, in terms of effective ionization parameter, a random distribution of clouds and clusters within a region of given radius is equivalent to a central cluster model with a larger radius.

Variations in the input parameters over plausible ranges do not affect substantially the derived $\log U_{\rm eff}$ and $R_{\rm eff}$. These are estimated to be accurate to a few 0.1 dex and to a factor of two respectively. Variations in several parameters have effects which are compensated by opposite, related effects. This is mainly due to the constraint imposed by the volume filling factor of the ionized gas, which ensures some "self-regulation" of $\log U_{\rm eff}$ by adjustments of $r_{\rm shield}$ and r. For instance, increasing $n_{\rm e}$ implies smaller $r_{\rm shield}$ and reduced shielding, but the effect on $\log U_{\rm eff}$ is compensated by the increase of $n_{\rm e}$ itself and of r. For $n_{\rm e} \lesssim 100$ cm^{-3}, $< l_{\rm H^+} > \gtrsim r_{\rm shield}$ but accounting for density gradients would maintain the validity of the random distribution model as discussed in section 5.3.6. Larger, more massive clouds imply larger $r_{\rm shield}$ but thinner ionized layers, and a smaller number of clouds. The mean free path of photons increases, resulting in a more intense radiation field incident on the cloud surfaces, but r increases too and partly compensates for the increase in $\log U_{\rm eff}$ due to the smaller cloud shielding.

The most uncertain parameters are those on the properties of the molecular clouds and on the LF, neither of which can be constrained from the 3D and SWS data. For the LF, substantial differences in the derived $\log U_{\rm eff}$ require either a very flat LF (*e.g.* $\beta < 0.5$ at high luminosities) or a very high lower cutoff (*e.g.* near the inflection point at $Q^\star = 10^{49.5}$ s^{-1}). However, the observed LF in a wide variety of environments — from our own Galaxy to merger systems like NGC 4038/4039 — has a power-law index in the range $\beta = 0.5 - 1.0$ (see chapter 3). In addition, a severe truncation with no clusters below the transition luminosity would imply the unlikely situation that only massive clusters containing at least one O5 star (50 M$_\odot$) can form, excluding the presence of smaller OB associations.

The geometrical volumes are also quite uncertain. Those adopted in table 5.7 for B1 and B2 represent in fact upper limits. Smaller volumes would be more realistic since the ionized ring along which the prominent sources of nebular line emission are distributed has a smaller radius than the entire infrared emitting region (Achtermann & Lacy 1995), and because the ionized gas is clumpy on scales of a few tens of parsecs. The other limiting case corresponds to the situation where the ionizing clusters and gas clouds are confined in spherical volumes, with a radius of 19.5 pc. This results however in a relatively small increase in $\log U_{\rm eff}$ of $0.1 - 0.2$ dex because the increased shielding partly compensates the increased ionizing photon density. Finally, although more realistic, the random distribution is obviously still an ideal description in the sense that the gas clouds are probably distributed in chains or filaments, and the clusters may be grouped in associations. For such geometries, the shielding is reduced — at least locally — but at the same time, the distance between clusters and gas cloud surfaces is larger. Given the high space density for both clouds and clusters, the net effect on $\log U_{\rm eff}$ would probably be small. The limiting case would be the CC geometry, with higher $\log U$ up to ≈ -1.7 (table 5.8).

Table 5.7: Adopted properties of selected regions in M 82 relevant for the determination of the ionization parameter

Property	Units	B1	B2	Starburst core
		Global properties		
Geometry	—	cylindrical	cylindrical	edge-on disk
Radius	pc	19.5	19.5	200
Length	pc	230	365	200
Volume	pc^3	2.7×10^5	4.4×10^5	2.5×10^7
$Q^{(a)}$	s^{-1}	2.34×10^{52}	3.24×10^{52}	1.23×10^{54}
M_{H_2}	$M_\odot$	1.1×10^6	2.3×10^6	1.8×10^8
		Spherical sub-units		
R_{CC}	pc	19.5	19.5	100
V	pc^3	3.1×10^4	3.1×10^4	4.2×10^6
		Cluster luminosity function$^{(b)}$		
$Q^\star_{min}$	s^{-1}	10^{45}	10^{45}	10^{45}
$Q^\star_{max}$	s^{-1}	10^{53}	10^{53}	10^{53}
$Q^\star_{kink}$	s^{-1}	$10^{49.5}$	$10^{49.5}$	$10^{49.5}$
β_1	—	0.17	0.17	0.17
β_2	—	1.0	1.0	1.0
		Neutral cloud properties$^{(c)}$		
r_{cl}	pc	0.4	0.4	0.6
M_{cl}	$M_\odot$	220	220	545
		Ionized gas properties		
n_e	cm^{-3}	300	300	300
T_e	K	5000	5000	5000

$^{(a)}$ Intrinsic hydrogen ionizing rates determined for each region, from tables 5.4 and 5.5 (for the mixed extinction model).

$^{(b)}$ The cluster luminosity function from Eqs. 3.9 and 3.10, described by a broken power-law with index β_1 between the lower cutoff $Q^\star_{min}$ and the inflection point at $Q^\star_{kink}$, and β_2 between $Q^\star_{kink}$ and the upper cutoff $Q^\star_{max}$.

$^{(c)}$ From the PDR modeling of Lord *et al.* (1996).

Table 5.8: Derived properties for selected regions in M 82 relevant for the determination of the ionization parameter[(a)]

Property	Units	B1	B2	Starburst core
		Properties of the ionizing clusters		
$N_\star$	—	2340	3240	1.2×10^5
$N_\star\,(10^{50} - 10^{53})^{(b)}$	—	25	35	1325
$n_\star$	pc^{-3}	8.7×10^{-3}	7.4×10^{-3}	4.8×10^{-3}
$d_{\star-\star}$	pc	6.0	6.4	7.3
$< Q^\star >$	s^{-1}	10^{49}	10^{49}	10^{49}
		Properties of the neutral and molecular gas		
$N_{\rm cl}$	—	4990	10440	3.3×10^5
$n_{\rm cl}$	pc^{-3}	1.9×10^{-2}	2.4×10^{-2}	1.3×10^{-2}
$d_{\rm cl-cl}$	pc	4.7	4.3	5.3
$\Phi_V^{\rm cl}$	—	5.0×10^{-3}	6.4×10^{-3}	1.2×10^{-2}
$n_{\rm H_2}$	cm^{-3}	1.7×10^4	1.7×10^4	1.2×10^4
		Properties of the ionized gas		
$M_{\rm H^+}$	$M_\odot$	1.4×10^5	2.0×10^5	7.6×10^6
$\Phi_V^{\rm H^+}$	—	7.2×10^{-2}	6.1×10^{-2}	4.1×10^{-2}
$r_{\rm shield}$	pc	1.0	0.88	0.98
r	pc	1.7	1.8	2.2
$< l_{\rm H^+} >$	pc	0.23	0.21	0.14
		Geometrical and nebular properties		
λ	pc	17	17	25
$f_{\rm shield}$	—	0.60	0.60	0.24
$\chi_{\rm adj}$	—	1.26	1.29	1.07
$\log U_{\rm CC}$	—	-2.19	-2.25	-1.72
$\log U_{\rm eff}$	—	-2.40 to -2.30	-2.48 to -2.37	-2.30 to -2.32
$R_{\rm eff}$	pc	25.2	25.2	202

[(a)] The number of ionizing clusters and molecular clouds as well as the mass of ionized gas are given for the entire volume of each region.

[(b)] The number of clusters with hydrogen ionization rates in the range $10^{50} - 10^{53}$ s^{-1}.

To summarize, the properties characterizing the spatial distribution of the ionizing clusters and gas clouds, and the degree of ionization of the nebulae are remarkably similar on small scales (B1 and B2) and on large scales (entire starburst core). The average separation between clusters and between molecular clouds are comparable and relatively small: from a few to ≈ 10 pc. This supports the picture of a highly randomized distribution of clusters and clouds, as also concluded by Lord *et al.* (1996) from the simpler consideration of average distance between individual stars. For all plausible sets of parameters, $\log U_{\rm eff}$ is relatively well constrained to values between about -2 and -2.5. For the large $R_{\rm eff}$ inferred, photoionization models are little sensitive to variations of the inner radius. **For all models presented in this work, the nebulae will therefore be described as shells with $\log \mathbf{U_{eff}} = -2.3$ dex and $\mathbf{R_{eff}} = 25$ pc.**

5.3.8 Final remarks

Two final remarks concerning the distribution of clusters and clouds assumed here can be made. Firstly, the large-scale distributions of the molecular and ionized gas in M 82 are not uniform. However, it is emphasized that the aim pursued in this section is to provide an *average picture of the H II regions.* For example, the central 50 pc of M 82 appear depleted in gas and dust, presumably due to the intense nuclear starburst $\sim 10^7$ yr ago and subsequent supernova-driven starburst wind (see chapter 7). The properties in this region are certainly very different from the uniform and closely packed distribution of ionizing clusters and dense, compact clouds assumed above, but this region does not contribute much to the integrated ionized gas emission either.

Secondly, the physics underlying the cluster LF is presumably a mass function for the natal molecular clouds (see chapter 3). The models considered here, in which the clouds all have identical sizes, are not necessarily inconsistent with the existence of a LF. The regions modeled are those in which star formation has already occurred and where the cloud remnants are importantly affected by the intense ultraviolet radiation field, strong stellar winds and supernova explosions. The results of evolutionary synthesis modeling in chapter 7 indicate that starburst activity in M 82 has strong negative feedback effects on the environment, inhibiting further star formation after a few million years only. Star formation activity probably occurs preferentially in regions where the ultraviolet radiation field and the disruptive effects of massive stars are much less important, allowing the molecular gas clouds to follow a more natural mass distribution.

5.4 Young stellar populations in M 82

The average effective temperature of newly-formed OB stars, $T_{\rm eff}^{\rm OB}$, can be determined from the ratios of emission lines from species which have different ionization potentials. Indeed, such line ratios are sensitive to the shape of the ionizing radiation spectrum, which is in turn related to $T_{\rm eff}^{\rm OB}$. The SWS and 3D data provide several diagnostics sensitive to energy differences in the range 13 eV − 41 eV, in particular ratios of atomic fine-structure lines in the mid-infrared, and of He I to H I recombination lines in the near-infrared. The contribution from shock-ionized material to the line emission considered below is not likely to be important in M 82 (McLeod *et al.* 1993; Lutz *et al.* 1998); it will be assumed that the lines originate entirely in gas photoionized by the OB stars. Table B.1 and figure B.2 in appendix B give the ionization potentials of the species involved and illustrate their sensitivity to $T_{\rm eff}^{\rm OB}$.

5.4.1 Mid-infrared fine-structure line ratios

Several diagnostic line ratios are available from the SWS data set for estimating $T_{\rm eff}^{\rm OB}$. In particular, [Ne III] 15.6 μm/[Ne II] 12.8 μm, [Ar III] 8.99 μm/[Ar II] 6.99 μm and [S IV] 10.5 μm/[S III] 18.7 μm have the advantage of being essentially independent of the chemical abundances. The neon ratio is the most reliable one since the lines involved are strong in M 82, the effects of extinction are minimized by their proximity in wavelength, and they were observed through the same aperture.

The line ratios, corrected for extinction and scaled to the same aperture size when appropriate, are reported in table 5.9. The ratios are compared to the predicted variations with $T_{\rm eff}^{\rm OB}$ in figure 5.11. The theoretical predictions were obtained using CLOUDY and the Pauldrach *et al.* (1998) stellar atmosphere models for solar-metallicity main-sequence stars, with the nebular parameters derived for M 82 in the previous sections: $n_{\rm e} = 300$ cm^{-3}, $\log U = -2.3$ dex and $R = 25$ pc. Solar abundances for the gas were assumed, and interstellar dust grains were not accounted for. Details on the treatment of the species involved can be found in Ferland (1996) and Shields & Ferland (1994). The $T_{\rm eff}^{\rm OB}$ derived from each ratio is given in table 5.9.

The effects of varying the gas and dust composition, $n_{\rm e}$ or $\log U$ are also shown in figure 5.11. The most sensitive parameter affecting the line ratios is the ionization parameter. However, varying $\log U$ in the plausible range from −2 dex to −2.5 dex found for M 82 in section 5.3 implies relatively small differences in $T_{\rm eff}^{\rm OB}$: $\leq \pm 1000$ K for the neon and argon ratios, and −2000 K or +4000 K for the sulphur ratio. The $T_{\rm eff}^{\rm OB}$'s inferred from the SWS data are similar to the values in the range 30000 K − 37000 K

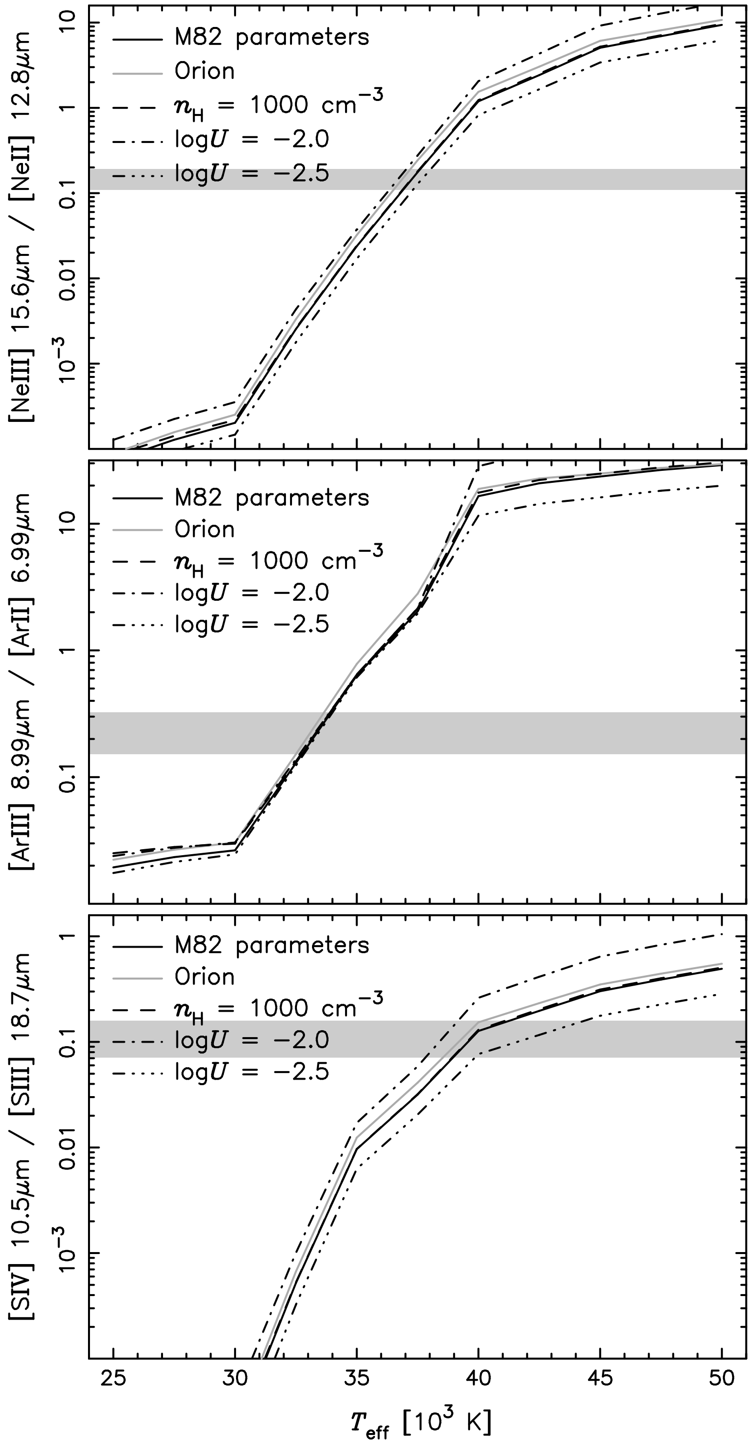

Fig. 5.11.— Mid-infrared fine-structure line ratios in M 82 measured from the SWS spectrum (shaded bars) compared to theoretical predictions of their variation with effective temperature of the ionizing stars. The model predictions were computed using CLOUDY assuming a shell geometry and the nebular parameters derived for M 82: $n_{\rm H} \approx n_{\rm e} = 300\ {\rm cm}^{-3}$, $R = 25$ pc, $\log U = -2.3$ dex, solar composition for the gas and no interstellar dust grains mixed with the ionized gas (solid line). The effects of changing the ISM composition to a gas and dust mixture as in the Orion nebula, the gas density to $n_{\rm H} = 10^3\ {\rm cm}^{-3}$, or $\log U$ between -2 dex and -2.5 dex are illustrated as well (see labels in each plot).

Table 5.9: Mid-infrared $T_{\rm eff}^{\rm OB}$–sensitive fine-structure line ratios in M 82

Diagnostic	Measured ratio[a]	$T_{\rm eff}^{\rm OB}$ [K]
[Ne III] 15.6 μm/[Ne II] 12.8 μm	0.16 ± 0.04	$\mathbf{37400 \pm 400}$[b]
[Ar III] 8.99 μm/[Ar II] 6.99 μm	0.26 ± 0.08	33500 ± 500
[S IV] 10.5 μm/[S III] 18.7 μm	0.11 ± 0.04	39900 ± 1000

[a] Corrected for $A_V = 52$ mag (mixed model). The sulphur lines have been scaled to a common aperture. The uncertainties include those on the line fluxes (continuum subtraction, systematic effects, absolute flux calibration), of the beam size correction (sulphur ratio), and on the extinction.

[b] Adopted result (section 5.4.2).

obtained in the past for the starburst core of M 82 from various infrared and millimetric diagnostic lines (Gillett *et al.* 1975; Willner *et al.* 1977; Puxley *et al.* 1989; McLeod *et al.* 1993; Achtermann & Lacy 1995).

5.4.2 Near-infrared He I to H I recombination line ratios

Three He I emission features are detected in the 3D spectra, namely the $2\,^1S - 2\,^1P$, $3\,^3P - 4\,^3D$ and the blend of $3\,P - 4\,S$ triplet and singlet transition lines at 2.058 μm, 1.701 μm and 2.113 μm respectively. Combined with the nearby Brγ and Br10 lines, they provide sensitive $T_{\rm eff}^{\rm OB}$ diagnostic ratios in the range $\lesssim 55000$ K which are very little affected by extinction. Above this temperature, helium becomes doubly ionized and this complicates the interpretation of the line ratios. However, such hot O stars, corresponding to spectral types earlier than O3, have not been observed in Galactic H II regions (*e.g.* Leitherer 1998a). The low-excitation SWS spectrum and the non-detection of He II lines in the 3D data (for example at 2.189 μm) rule out the presence of important numbers of Wolf-Rayet stars that are hot enough to doubly ionize helium.

Due to sensitivity of the 2.058 μm line to local physical conditions and to degeneracy in $T_{\rm eff}^{\rm OB}$ (through resonance and collisional effects), the traditionally employed He I 2.058/Brγ ratio alone is not sufficient to constrain $T_{\rm eff}^{\rm OB}$ reliably. Similar effects affect the triplet component of the 2.113 μm feature detected at B1. On the other hand, the 1.701 μm line originating from a higher quantum state in the $n\,^3P - n'\,^3D$ series is little sensitive to the effects mentioned above, but the He I 1.701/Br10 saturates above $T_{\rm eff}^{\rm OB} \approx 40000$ K. The combination of the He I 2.058/Brγ, He I 1.701/Br10 and He I 2.113/Brγ ratios allows one to constrain uniquely $T_{\rm eff}^{\rm OB}$. More details on the He I recombination lines and on the model computations obtained using CLOUDY are given in appendix D. A description of the treatment of helium in CLOUDY is given in Ferland (1996) and Shields & Ferland (1994).

Table 5.10: Near-infrared He I to H I recombination line ratios in M 82[(a)]

Region	He I 2.058/Brγ	He I 1.701/Br10	$T_{\rm eff}^{\rm OB}$ (b) [K]
Central 35 pc	0.52 ± 0.08	< 0.13	35700 ± 800
B1	0.55 ± 0.02	0.22 ± 0.06	36000 ± 200
B2	0.52 ± 0.02	0.22 ± 0.06	35600 ± 200
3D field	0.55 ± 0.03	0.20 ± 0.09	36000 ± 300

(a) The ratios are corrected for the (small) extinction effects. The uncertainties on the ratios include those of the continuum subtraction, systematic effects, and extinction correction.

(b) Inferred from the He I 2.058 μm/Brγ ratio.

The He I 2.058/Brγ and He I 1.701/Br10 ratios measured for the central 35 pc of M 82, for the Brγ sources B1 and B2, and for the entire 3D field are reported in table 5.10, and plotted against theoretical predictions in figure 5.12. The He I 2.113 μm blend was detected at B1 only, and the He I 2.113/Brγ ratio is 0.049 ± 0.005. The model predictions were computed for the same nebular parameters as for the mid-infrared line ratios in the previous subsection. The line ratios in table 5.10 are corrected for extinction, but since the lines compared in each case lie so close in wavelength, they are very little affected by dust obscuration (at most 7%).

The He I 2.058/Brγ and He I 1.701/Br10 ratios imply $T_{\rm eff}^{\rm OB}$ near 36000 K for the selected regions considered. The He I 1.701/Br10 ratio clearly rules out the high-$T_{\rm eff}^{\rm OB}$ solutions from the He I 2.058/Brγ ratio. For the temperature range inferred, He I 2.058/Brγ and He I 1.701/Br10 are little affected by variations in $n_{\rm e}$ or $\log U$ within plausible ranges for M 82, or to modest changes in the composition of the ISM (figure 5.12). The He I 2.113/Brγ ratio at B1 is well above the predicted saturation value of ≈ 0.03 from the models in appendix D. This seems to suggest that large optical depths in the $2\,^3S - n\,^3P$ series, not accounted for in the models, affect importantly the triplet component of the 2.113 μm feature.

The He I 2.058/Brγ map obtained with 3D (figure 4.5) supports a general though small increase in $T_{\rm eff}^{\rm OB}$ from the nucleus to larger projected radii along the galactic plane of M 82 to the west. Similar radial variations in $T_{\rm eff}^{\rm OB}$ have been suggested by Satyapal *et al.* (1995), from their ratio map of Brγ to 3.29 μm PAH feature emission. McLeod *et al.* (1993) also suggested such a trend with radial distance from the nucleus on the basis of the lower temperatures derived from mid-infrared line ratios, presumably tracing the innermost stellar population, and the higher temperatures indicated by optical line ratios, tracing foreground, and thus outermost clusters. No clear spatial variations, however, are seen in the relative line fluxes from the Brα, [Ne II] 12.8 μm, [Ar III] 8.99 μm and [S IV] 10.5 μm maps from Achtermann & Lacy (1995). These

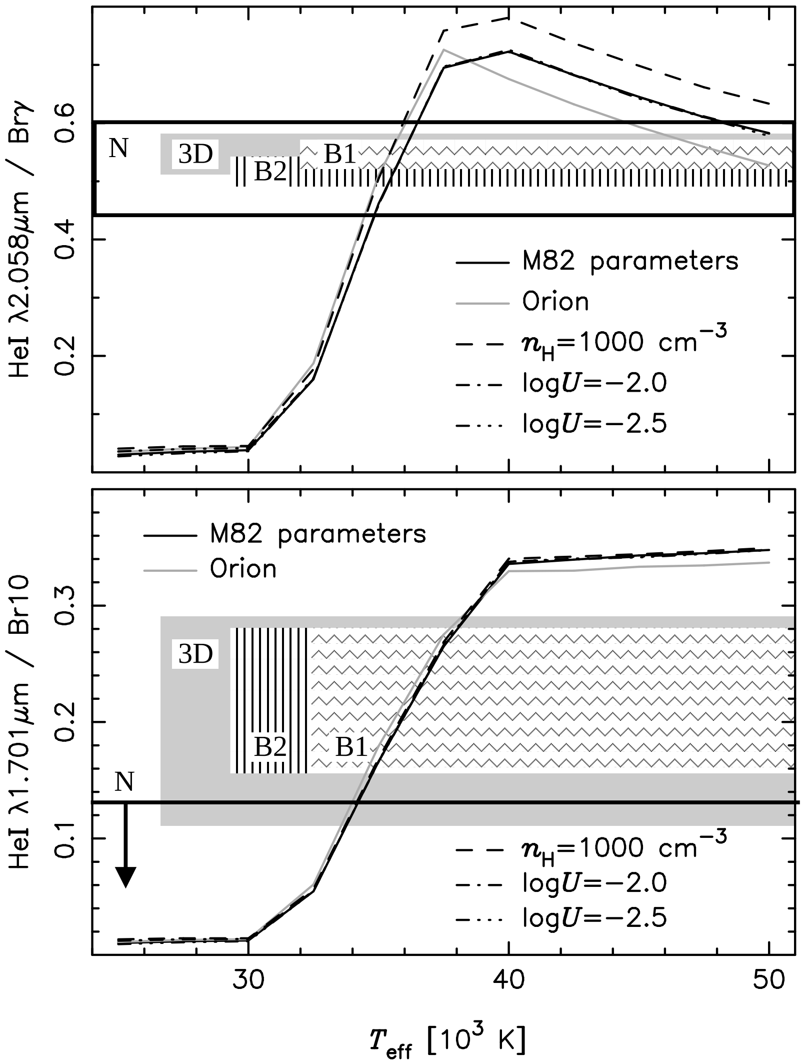

Fig. 5.12.— Near-infrared He I to H I recombination line ratios measured from the 3D spectra for selected individual regions in M 82, compared to theoretical predictions of their variation with effective temperature of the ionizing stars. Different boxes indicate the ratios measured at different locations: central 35 pc at the nucleus (empty box labeled N, and horizontal line marking the upper limit), B1 (broken horizontal lines), B2 (vertical lines) and the entire 3D field of view (shaded box). The various model curves shown are for the same nebular parameters as for figure 5.11.

authors concluded that the excitation, and thus $T_{\rm eff}^{\rm OB}$, is roughly constant across the starburst core of M 82.

To constrain quantitatively the spatial variations in $T_{\rm eff}^{\rm OB}$ across the entire regions mapped with 3D, the He I 2.058 μm and Brγ linemaps were rebinned to $1'' \times 1''$ pixels, in order to increase the signal-to-noise ratio on the line fluxes. The ratios in rebinned pixels are plotted along the model curve for the nebular parameters appropriate for M 82 in figure 5.13 (extinction effects have been neglected, but this introduces errors

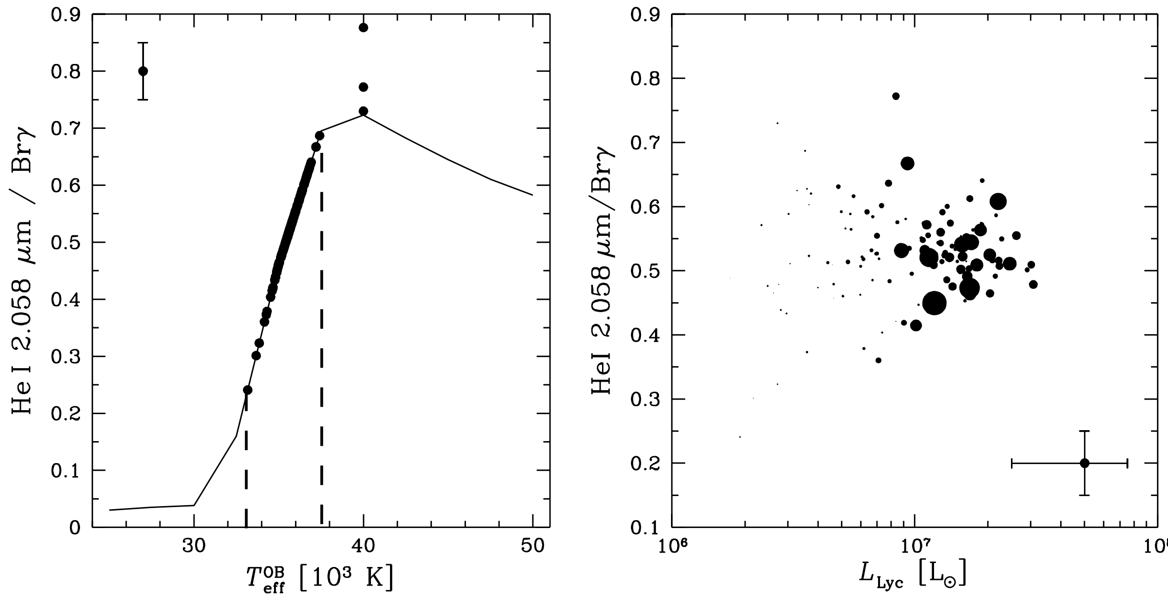

Fig. 5.13.— He I 2.058 μm/Brγ line ratio measured in individual $1'' \times 1''$ pixels across the 3D field of view. The data are compared in the left panel to theoretical predictions from CLOUDY for the nebular parameters appropriate for M 82 ($n_{\rm H} \approx n_{\rm e} = 300~{\rm cm}^{-3}$, $\log U = -2.3$, solar gas abundances and dust grain depletion). The right panel shows the ratio versus the intrinsic Lyman continuum luminosity, given by $L_{\rm Lyc}~[{\rm L}_\odot] = 5.10 \times 10^{23}\,F_{\rm Br\gamma}~[{\rm W\,m^{-2}}]$ for case B recombination, and the $T_{\rm e}$, $n_{\rm e}$ and distance for M 82. The size of the data points is proportional to the intrinsic K-band flux density, given by $L_K[{\rm L}_\odot] = 2.04 \times 10^{20}\,f_K~[{\rm W\,m^{-2}\,\mu m^{-1}}]$ for the distance of M 82 and a K-bandwidth of 0.6 μm. The Brγ flux and K-band flux density are corrected for foreground extinction derived from the $H-K$ colour, as described in chapter 6. The typical uncertainties are shown by the error bars in each plot.

$\lesssim 5\%$ in the ratios). The $T_{\rm eff}^{\rm OB}$ implied by He I 2.058/Brγ varies from 33200 K to 37500 K, excluding the data points which have the largest He I 2.058/Brγ ratios but uncertainties twice as large as the typical uncertainty. There is no apparent correlation with the intrinsic hydrogen ionizing luminosity $L_{\rm Lyc}$ or with the K-band luminosity L_K, as shown in the right-hand panel from figure 5.13. These luminosities are proportional to the Brγ flux and to the K-band flux density respectively (see figure caption); the extinction correction applied for the individual pixels was derived from the observed $H-K$ colour and will be described in chapter 6 (see also section 5.1.7). The average $T_{\rm eff}^{\rm OB}$ is 35700 K with a relatively small dispersion of $1\sigma = 650$ K. The 3D data indicate therefore a **roughly constant $T_{\rm eff}^{\rm OB}$ for the hot massive stars across the regions observed, with only a marginal gradient with projected radius**.

The most reliable diagnostic for the *absolute* $T_{\rm eff}^{\rm OB}$ available from the SWS and 3D data sets is the [Ne III] 15.6 μm/[Ne II] 12.8 μm ratio, because of the quality of the measurement (strong, closely spaced lines observed through the same aperture), and because theoretical modeling of the neon lines does not involve complications as for the He I lines. In addition, the inferred $T_{\rm eff}^{\rm OB}$ is little affected by the uncertainties on the physical conditions within the nebulae. On the other hand, the uncertainties on the He abundance and of the theoretical predictions (optical depth effects for the He I 2.058 μm line, He I 1.701 μm intensity obtained indirectly from optical He I line intensities) make He I 2.058/Brγ and He I 1.701/Br10 less reliable indicators for the absolute $T_{\rm eff}^{\rm OB}$. However, for the typical ratios observed in M 82 and the corresponding $T_{\rm eff}^{\rm OB}$'s, optical depth effects are much less important than at high $T_{\rm eff}^{\rm OB}$ and the He I to H I line ratios are little sensitive to nebular conditions. These ratios constitute reliable diagnostics for the *relative* $T_{\rm eff}^{\rm OB}$ between different regions (assuming negligible variations in He abundance). Since the SWS aperture nearly coincides with the 3D field of view, the nebular line emission in the respective data sets trace the same stellar populations. In the rest of this work, **the absolute $T_{\rm eff}^{\rm OB}$ from He I 2.058/Brγ in individual regions will therefore be increased by 1400 K**, corresponding to the difference between the $T_{\rm eff}^{\rm OB}$ inferred from the SWS [Ne III]/[Ne II] ratio and from the integrated He I 2.058/Brγ ratio in the 3D field of view.

5.4.3 Number of representative OB stars

Adopting the temperature scale from Vacca, Garmany & Shull (1996), the $T_{\rm eff}^{\rm OB}$ inferred from the [Ne III]/[Ne II] ratio corresponds to O8.5 V stars, with masses of $\approx 28\ {\rm M}_\odot$. The small dispersion in $T_{\rm eff}^{\rm OB}$ from the He I 2.058/Brγ ratio implies the same representative type over most of the regions mapped with 3D. Because of the roughly constant excitation in M 82, and since the SWS and 3D fields of view include half of the integrated emission in a 30″–diameter region centered on the nucleus, the above spectral type is probably representative of the OB stars in the entire starburst core of M 82 as well. The number of equivalent O8.5 V stars required to produce the ionizing luminosity in various regions within M 82 are given in table 5.11, assuming $Q_{\rm O8.5\,V} = 10^{48.72}\ {\rm s}^{-1}$ (Vacca, Garmany & Shull 1996).

Table 5.11: Number of equivalent O8.5 V stars in selected regions in M 82[(a)]

	Central 35 pc	B1	B2	3D field	SWS 14″ × 20″	Starburst core
$N_{\rm O8.5\,V}$	2040	4470	6170	8.3×10^4	1.2×10^5	2.4×10^5

[(a)] Using the intrinsic hydrogen ionization rates derived assuming a mixed model for extinction (tables 5.4 and 5.5). The ionization rate for the entire starburst core, enclosed in a 30″–diameter aperture centered on the nucleus, is twice that measured in the SWS 14″ × 20″ aperture (section 5.1.3).

5.5 The nature of the ISM and of the massive star populations in M 82

The results presented in this chapter reveal two important aspects concerning the ISM and the massive stars in M 82. Firstly, the average properties of the H II regions on all spatial scales are remarkably similar. This is reflected most strikingly in the ionization parameter, in the volume filling factor of the ionized gas, and in the nebular line ratios. The properties of the molecular and neutral atomic gas closely associated with the H II regions are also quite uniform throughout M 82. Such uniformity may seem surprising over spatial scales of $\gtrsim 100$ pc, and given the important sub-structure on scales of a few tens of parsecs of the emission regions. The similar properties suggest similar evolutionary states for the ionizing clusters and their surrounding H II regions. This is confirmed by the evolutionary synthesis models presented in chapter 7, which imply very similar ages for the OB star populations across the starburst core of M 82. Kinematics studies provide evidence that the most prominent sources of ionized gas emission are distributed in a ring-like structure and along a stellar bar between radii of 85 pc and 200 pc (*e.g.* Larkin *et al.* 1994; Achtermann & Lacy 1995). Since M 82 is viewed nearly edge-on, the observed properties can be understood as the combination of star formation triggered nearly simultaneously along the "ring" and the bar, and projection effects. Strong stellar winds and supernova explosions from important populations of massive stars in the closely-packed clusters severely disrupt the ISM, consistent with the geometrical parameters inferred for the H II regions, and may thereby contribute to some homogeneization on timescales of a few million years.

Secondly, a large fraction of the integrated ionized gas line emission comes from a diffuse component. For instance, the bright Brγ sources B1 and B2 contribute only $\approx 10\%$ of the total intrinsic emission in the regions observed with 3D and SWS. In turn, these regions include most of the prominent sources but contribute about half of the integrated emission from the entire starburst core. The diffuse component could be attributable to ionizing radiation escaping from the evolved H II regions in the surrounding medium. Alternatively, it could be due to an underlying population of smaller clusters, for which large numbers are predicted from plausible cluster luminosity functions. In this context, Meurer *et al.* (1995) interpreted the large fractional contributions from diffuse emission at ultraviolet wavelengths seen in several nearby starburst galaxies within the framework of a bi-modal scenario for star formation in starbursts: prominent cluster formation, and dominant diffusely distributed star formation.

5.6 Summary

In this chapter, the physical conditions of the photoionized nebulae and the properties of the young stellar populations in M 82 have been determined, and are summarized in the following table.

PROPERTY	RESULTS
Photoionized nebulae	
Extinction	Global $A_V = 52$ mag Mixed model Galactic Center law between $3\,\mu$m and $10\,\mu$m Spatially variable
Electron temperature	$T_e \approx 5000$ K
Electron density	$n_e \approx 300$ cm^{-3}
Gas-phase abundances	Nearly solar
Effective ionization parameter	$\log U_{\rm eff} \approx -2.3$ dex
Equivalent geometry	Shell of radius $R_{\rm eff} = 25$ pc
OB stars	
Effective temperature	$< T_{\rm eff}^{\rm OB} >= 37400$ K Fairly uniform, with only a marginal increase with distance from the nucleus
Equivalent spectral type	O8.5 V, with mass ≈ 28 M$_\odot$

The most important results concern the extinction towards the ionized gas, and the state and spatial distribution of the gas closely associated with the young OB stars:

- Purely foreground extinction towards the ionized gas is definitively ruled out. The new SWS data provide evidence for deviations from the Draine extinction law between $3\,\mu$m and $10\,\mu$m consistent with the extinction law towards the Galactic Center (Lutz *et al.* 1996), indicating more extinction than produced by standard graphite-silicate dust mixtures.
- The photoionized nebulae across the entire starburst regions are characterized by similar values for the ionization parameter and similar excitation, with little spatial variations at a resolution of ≈ 20 pc. This suggests similar evolutionary states for the populations of OB stars, similar distributions of the ionized nebulae relative to the ionizing clusters, and a large degree of uniformity within and between the H II regions complexes throughout the starburst core of M 82.

Chapter 6

Stellar population synthesis for M 82

From the nebular analysis presented in the previous chapter, the properties of the young stellar populations of massive OB stars and of their surrounding H II regions were constrained using the near- and mid-infrared nebular line emission observed with 3D and the *ISO*-SWS. The 3D data allow the investigation of additional constituents of M 82, most importantly the populations of cool, evolved stars.

In general, the near-infrared continuum emission of pure starburst galaxies is composed of

- the integrated light of the evolved stellar population,
- the integrated light of the young stellar population,
- the nebular emission originating around OB stars in the H II regions, and
- the thermal emission from dust heated at $T \sim 600 - 1000$ K by OB stars.

Each of these components can be affected by extinction, which may differ from one source to the other. Red giants and supergiants, when present, usually dominate the near-infrared continuum emission of composite stellar populations because of their temperatures about 3000 K – 5000 K and their large luminosities. Cool main-sequence stars are too faint in comparison to make a significant contribution despite their larger numbers. Populations of supergiants, in turn, outshine the more numerous but less luminous giants. The characterization of the evolved stellar population provides important constraints for the starburst history as, notably, the presence of supergiants implies recent star formation ($10-50$ Myr) whereas populations of giants, much earlier star formation ($\gtrsim 10^8 - 10^9$ yr).

In this chapter, population synthesis is applied to the 3D data of M 82, based on the 3D stellar library and on the diagnostic tools presented in chapter 2. Specifically, the following properties will be constrained:

- the spectral type and luminosity class of the evolved stellar populations,
- the metallicity of the evolved stellar populations,
- the contribution of other sources of near-infrared continuum emission such as hot dust, OB stars and nebular free-free and free-free bound processes, and
- the extinction towards the evolved stellar populations.

In addition, the global properties of the entire starburst core of M 82 (strength of the stellar absorption features, extinction towards the evolved stars) will be derived with the help of existing data in the literature, in view of the evolutionary synthesis modeling in chapter 7. It is not possible to completely quantify independently all the components of the near-infrared continuum emission and this makes such an analysis not straightforward. The following sections illustrate quite well this complex procedure and thus, the difficulty in any attempt to conduct a study of this type, in particular in complex objects such as starburst, AGN, interacting and merging galaxies.

6.1 The composition of the evolved stellar populations in M 82

6.1.1 The giants-supergiants controversy

The nature of the stellar population at the nucleus of M 82 has long been debated. Various diagnostics have been used in the past, including the near-infrared broad-band colours, the $CO_{\rm ph}$ and $H_2O_{\rm ph}$ photometric indices measuring the depth of the CO bandheads longwards of 2.3 μm and of the H_2O absorption feature at 1.9 μm, spectral synthesis in the range 2.18 μm − 2.28 μm and measurements of the $M^{\star}/L_K$ ratio (Walker, Lebofsky & Rieke 1988; Lester *et al.* 1990; Gaffney & Lester 1992; Gaffney, Lester & Telesco 1993; McLeod *et al.* 1993; Lançon, Rocca-Volmerange & Thuan 1996). Application of evolutionary synthesis models has also been used to constrain indirectly the composition of the stellar population in the nuclear vicinity (Rieke *et al.* 1980, 1993; Satyapal *et al.* 1997). However, no consensus has been reached yet. Some of the above studies indicate the presence of young supergiants while others provide evidence for old, metal-rich giants as dominant sources for the near-infrared continuum emission.

Several factors may be responsible for the different conclusions reached by various authors. Firstly, the interpretation of the indicators used so far is complicated by extinction, by emission from hot dust and by the chemical composition of the stars (see the introduction of chapter 2). Secondly, while the observed $CO_{\rm ph}$ in the nuclear regions of M 82 is well-determined, large discrepancies exist between the various measurements of the $H_2O_{\rm ph}$. This has been the main cause for the giants-supergiants controversy. Both indices are sensitive to the temperature *and* to the luminosity of the stars; one index alone is not sufficient to discriminate between giants and supergiants, making $H_2O_{\rm ph}$ critical for interpreting $CO_{\rm ph}$. However, the depth of the H_2O absorption feature is difficult to measure because it lies in a wavelength range where the atmospheric transmission is poor and strongly variable. Thirdly, population synthesis based on spectroscopy in the range 2.18 μm − 2.28 μm at moderate spectral resolution ($R \sim 650$), as applied by Gaffney & Lester (1992) and McLeod *et al.* (1993), suffers from large uncertainties because the stellar absorption features in this range are weak ($\lesssim 5\%$ of the continuum). Finally, the results may be strongly dependent on aperture size if the composition of the stellar population varies spatially.

Another controversy pertains to the contribution of hot dust to the near-infrared continuum emission. Estimates of the amount of hot dust emission in the past were based on the near-infrared broad-band colours and on $CO_{\rm ph}$ (Lester *et al.* 1990; McLeod *et al.* 1993; Larkin *et al.* 1994; Satyapal *et al.* 1997). Some authors have argued against important hot dust contributions in the nuclear vicinity while others have inferred as much as $30\% - 40\%$ contribution. Again, for the indicators employed, the effects of hot dust are intimately related to the composition of the stellar population and to the extinction. In turn, the amount of hot dust emission has important consequences for the characterization of the stellar population and the extinction. The separation between these three components from broad-band colours and photometric indices depends moreover on several assumptions such as the extinction model and the dust temperature, and is not unique.

The spatially resolved 3D data, at a spectral resolution of $R \sim 1000$, allow the application of alternative diagnostic tools from which the crucial issues of the composition of the evolved stellar populations and spatial variations thereof can be reliably constrained.

6.1.2 Analysis of selected stellar absorption features

Spectroscopic indices such as those discussed in chapter 2 constitute powerful diagnostic tools in stellar population studies from moderate-resolution near-infrared spectra. The first overtone ^{12}CO (2,0) bandhead at $2.29\,\mu$m, the second overtone ^{12}CO (6,3) bandhead at $1.62\,\mu$m, and the Si I feature at $1.59\,\mu$m are particularly well suited for applications to obscured starburst galaxies such as M 82. Indeed, they are amongst the strongest absorption features usually observed in such systems and provide sensitive indicators for the effective temperature and luminosity class of evolved stars. Moreover, they lie in spectral ranges of optimal atmospheric transmission. Finally, their equivalent widths ($W_{2.29}$, $W_{1.62}$ and $W_{1.59}$) are independent of extinction and provide a means of constraining the contribution, or "dilution", from sources of featureless continuum emission without requiring any assumptions on their nature and physical properties, which are usually very uncertain.

• Selected individual regions in M 82

The equivalent widths (EWs) of the above features measured for the central 35 pc of M 82, for the Brγ sources B1 and B2, and for the entire 3D field of view (from table 4.6) can be interpreted using the various diagnostic diagrams discussed in chapter 2. The relevant ones are reproduced in figures 6.1 to 6.3, where the measurements for M 82 are compared to stellar data. Figures 6.1 and 6.2 give the effective temperature ($T_{\rm eff}$) and luminosity class implied by the EWs, while figure 6.3 allows the determination of the amount of dilution near $1.6\,\mu$m ($D_{1.6}$) from the vertical displacement relative to the locus of stars in the $W_{1.62}$ versus $\log(W_{1.62}/W_{1.59})$ diagram, and near $2.3\,\mu$m ($D_{2.3}$) from the horizontal displacement in the $W_{1.62}$ versus $\log(W_{1.62}/W_{2.29})$ diagram once $W_{1.62}$ is corrected for dilution. Quantitatively, the fraction of the continuum emission attributable to the dilution sources is evaluated by comparing the observed and intrinsic EWs using

$$\frac{W_\lambda^{\rm obs}}{W_\lambda^{\rm intr}} = 1 - D_\lambda. \qquad (6.1)$$

For composite stellar populations, such an analysis provides the average properties of the stars which contribute the most to the emission that is measured. The integrated EWs are expected to fall on the distributions of stars in the $W_{1.62}$ vs $\log(W_{1.62}/W_{1.59})$ and $W_{1.62}$ vs $\log(W_{1.62}/W_{2.29})$ diagrams, and this is indeed the case for undiluted populations observed by Oliva *et al.* (1995) in Galactic globular clusters and young clusters in the Large Magellanic Cloud, as well as in the central regions of elliptical and spiral galaxies.

For the central 35 pc at the nucleus of M 82, both $W_{1.62}$ and $\log(W_{1.62}/W_{1.59})$ indicate an average effective temperature in the range 3600−4100 K, implying negligible dilution around $1.6\,\mu$m. The $W_{2.29}$ is characteristic of either giants with $T_{\rm eff} = 3200 - 3600$ K or supergiants with $T_{\rm eff} = 3600 - 4200$ K. Therefore, **the strengths of both CO bandheads are only consistent with each other if supergiants dominate the near-infrared continuum emission**, and indicate negligible dilution around $2.3\,\mu$m. If $D_{2.3}$ were not negligible, the intrinsic $W_{2.29}$ would be larger, implying cooler temperatures not consistent with the H-band EWs for any luminosity class. Using the temperature calibration from Schmidt-Kaler (1982), the results correspond to an **average spectral type of K5 I**.

For B1, $T_{\rm eff} = 4000 - 4400$ K and negligible $D_{1.6}$ are inferred from $W_{1.62}$ and $\log(W_{1.62}/W_{1.59})$. The observed $W_{2.29}$ indicates higher temperatures and, therefore, dilution around $2.3\,\mu$m. Due to the degeneracy in luminosity of $W_{2.29}$, it is not possible to discriminate between giants and supergiants. The CO bandheads can be reconciled for K3 III stars and $D_{2.3} \approx 10\%$, or for K2 I stars and $D_{2.3} \approx 10\% - 40\%$. The EWs at B2 and for the entire 3D field of view are very similar. They imply populations of supergiants with average temperatures between 3900 K and 4200 K (*i.e.* K3–K4 I), negligible dilution around $1.6\,\mu$m, and $D_{2.3} \approx 0\% - 20\%$ at B2 and $D_{2.3} \approx 0\% - 15\%$ for the 3D field of view, although undiluted emission from K4 III cannot be completely ruled out. The results for each region are summarized in table 6.1.

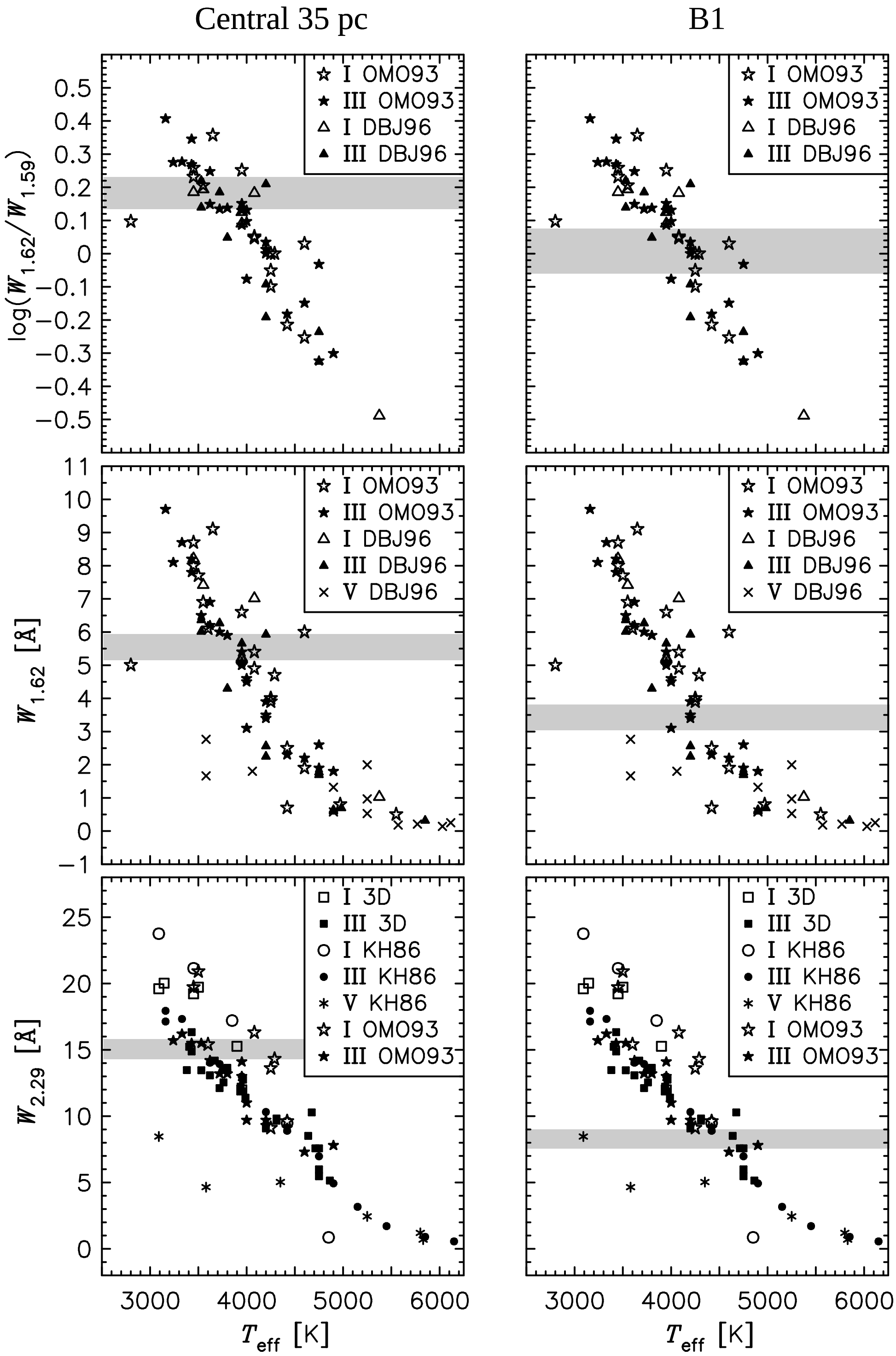

Fig. 6.1.— Determination of the effective temperature and luminosity class of the evolved stellar population for the central 35 pc of M 82 and the Brγ source B1. The shaded bars represent the log $(W_{1.62}/W_{1.59})$, $W_{1.62}$ and $W_{2.29}$ measured for each region. They are compared with the stellar data compiled in chapter 2 from the 3D stellar library (3D), and from the stellar atlases of Kleinmann & Hall 1986 (KH86), Origlia, Moorwood & Oliva 1993 (OMO93), and Dallier, Boisson & Joly 1996 (DBJ96).

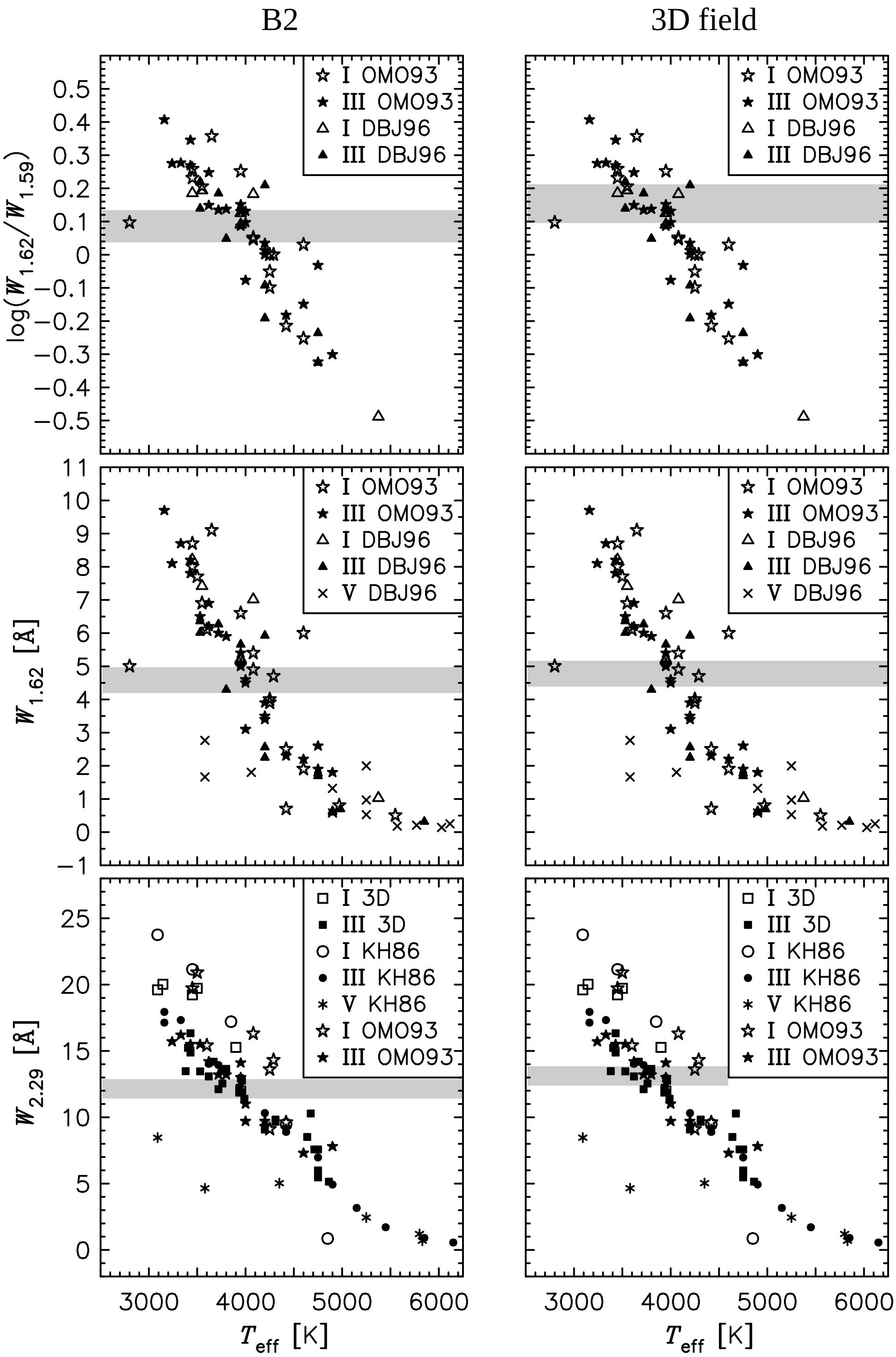

Fig. 6.2.— Same as figure 6.1 for the determination of the effective temperature and luminosity class of the evolved stellar population for the Brγ source B2 and the entire 3D field of view.

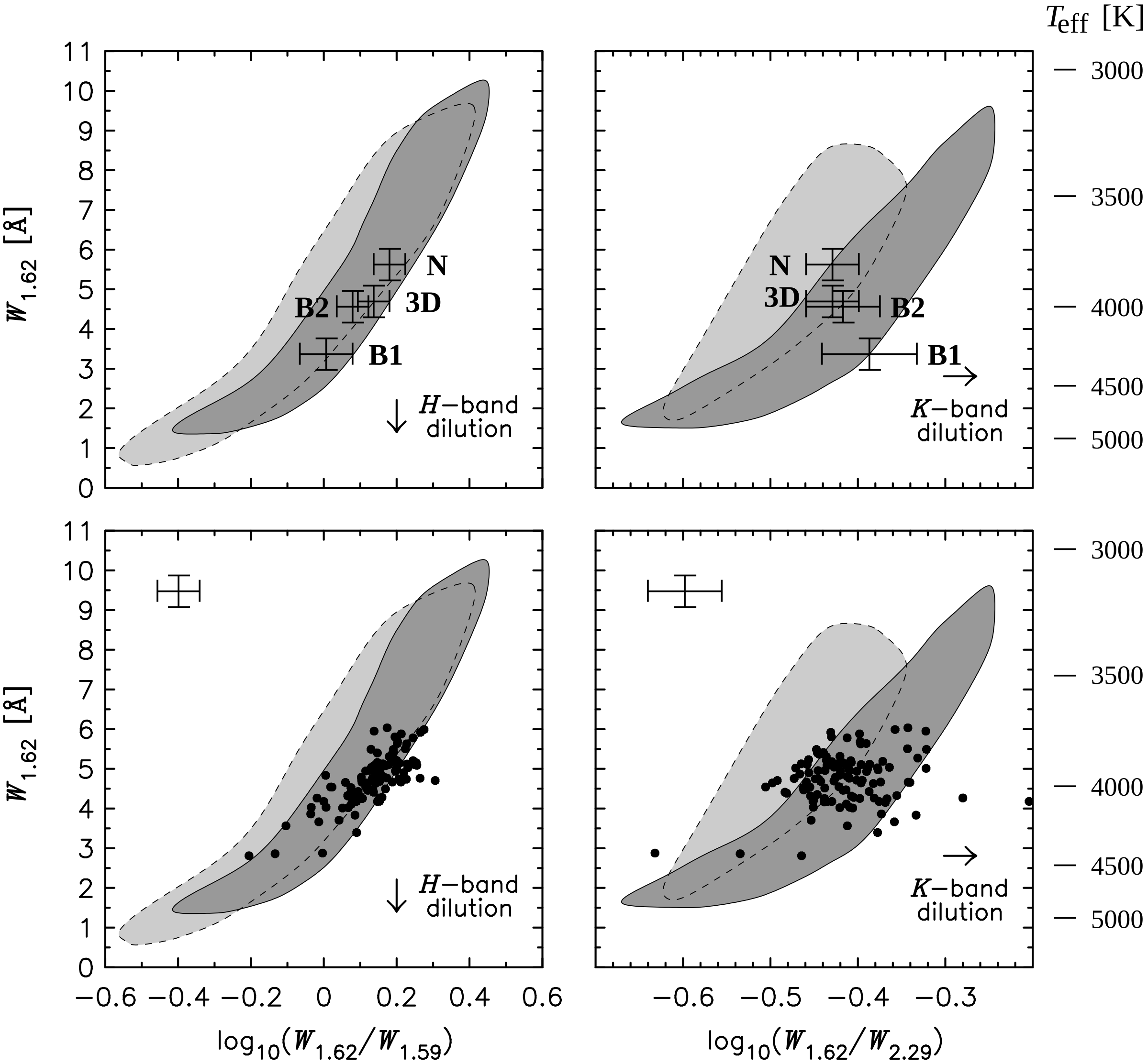

Fig. 6.3.— Estimation of the amount of dilution near 1.6 μm and 2.3 μm in M 82. For clarity, the stellar data are represented by shaded areas corresponding to the loci of giants (dark shade) and supergiants (light shade) from figure 2.12. Undiluted composite populations observed in Galactic globular clusters, Large Magellanic Cloud young clusters, and in the central regions of elliptical galaxies and bulges of spiral galaxies fall on the distributions defined by individual stars (Oliva *et al.* 1995). The arrows indicate the effects of dilution by featureless continuum sources. Stellar effective temperatures corresponding to various $W_{1.62}$ (undiluted) are labeled on the right-hand side diagrams. *Top*: data for the central 35 pc of M 82 (labeled as N), B1, B2 and the entire 3D field of view (labeled as 3D). *Bottom*: data for individual $1'' \times 1''$ pixels from the rebinned 3D maps, with typical uncertainties shown in the upper left corner of the diagrams.

Table 6.1: Results from the analysis of selected stellar absorption features for selected regions in M 82

	Central 35 pc	B1	B2	3D field
Representative type	K5 I	K2 I or K3 III	K4 I	K4 I
$D_{1.6}$[(a)]	0%	0%	0%	0%
$D_{2.3}$[(a)]	0%	25% or 10%	15%	10%

[(a)] Fraction of the continuum emission near 1.6 μm and 2.3 μm contributed by sources of featureless continuum emission. The uncertainties are typically $\pm 10\%$.

- **Spatially detailed analysis**

A similar analysis can be applied for all the regions observed with 3D. Maps of the $W_{1.59}$, $W_{1.62}$ and $W_{2.29}$ were generated from the 3D data cubes rebinned to $1'' \times 1''$ pixels in order to increase the signal-to-noise ratio, especially for $W_{1.59}$. The $W_{1.59}$ map was corrected for contamination by the Br14 emission line ($\lambda = 1.5881$ μm) using a Br13 line map ($\lambda = 1.6109$ μm) obtained from the rebinned H-band data cube, following the procedure described in section 4.2.1. The resulting spectroscopic indices for all pixels are plotted in the $W_{1.62}$ vs $\log(W_{1.62}/W_{1.59})$ and $W_{1.62}$ vs $\log(W_{1.62}/W_{2.29})$ diagrams in the bottom panels of figure 6.3.

Together with the EW maps from figure 4.4, figure 6.3 reveals **spatial variations on scales of a few tens of parsecs in the intrinsic composition of the evolved stellar population**, little dilution around 1.6 μm and variable dilution around 2.3 μm. The ranges of values measured for $W_{1.62}$ and $\log(W_{1.62}/W_{1.59})$ indicate $T_{\rm eff}$'s from 4500 K down to 3600 K, corresponding to spectral types G9 to M0 for supergiants. The average is 4000 K with dispersion of $1\sigma = 200$ K, equivalent to K4 $\pm$ two spectral classes assuming supergiants. Several individual regions exhibit enhanced $W_{2.29}$ relative to $W_{1.62}$, and lie on the locus of supergiants in the $W_{1.62}$ vs $\log(W_{1.62}/W_{2.29})$ diagram. Other regions are characterized by too small $W_{2.29}$ relative to $W_{1.62}$ compared to normal evolved stars, indicating significant dilution up to $\approx 20\%$ assuming an intrinsic population of giants, or $\approx 50\%$ for supergiants. For most individual regions, the $\log(W_{1.62}/W_{2.29})$ does not allow the discrimination between giants and supergiants due to degeneracy in luminosity class and dilution. The analysis of the $M^{\star}/L_K$ ratio provides an additional constraint on the composition of the stellar population which dominates the K-band emission. As will be shown in chapter 7, the very low $M^{\star}/L_K$ ratios measured at all radii in M 82 (from ≈ 10 pc to ≈ 250 pc) compared to those typically found for old populations in elliptical galaxies and bulges of spiral galaxies strongly suggest that the sources of near-infrared continuum emission throughout the entire starburst core of M 82 are young populations of red supergiants.

The above analysis allows the correct interpretation of the $W_{1.62}$ and $W_{2.29}$ maps presented in figure 4.4. Because $W_{1.62}$ is not affected by dilution in M 82, its spatial distribution constitutes essentially a $T_{\rm eff}$ map for the evolved stars. The spatial variations in the $T_{\rm eff}$ of the evolved stellar populations are more complex than simple radial gradients. The coolest populations are found in distinct regions $\lesssim 30$ pc in size around the nucleus and along a ridge extending up to the secondary K-band peak about $8''$ to the west. Just south from this ridge, the $T_{\rm eff}$ increases progressively along the Nucleus $\rightarrow$ B2 $\rightarrow$ B1 sequence. Although affected by dilution, the $W_{2.29}$ map exhibits similar spatial variations, which are mostly attributable to the variations in $T_{\rm eff}$ if supergiants dominate the K-band everywhere. The spatial distributions of $W_{1.62}$ and $W_{2.29}$ follow roughly that of the near-infrared broad-band emission. This is not surprising even if supergiants are the main sources of near-infrared continuum emission, because cooler supergiants are also more luminous.

The correlation between the *intrinsic* stellar L_K, $W_{1.62}$ and $W_{2.29}$ can be assessed from figure 6.4 (left panel). For this purpose, the intrinsic $W_{2.29}$ for each individual pixel was obtained from the stellar data for supergiants, with the $T_{\rm eff}$ inferred from $W_{1.62}$. The amount of dilution at $2.3\,\mu$m was then determined by comparing the observed and predicted $W_{2.29}$ (Eq. 6.1). Finally, from the K-band flux density, corrected for dilution and for the extinction towards the stars derived in section 6.3 below, the intrinsic stellar K-band luminosity was computed. The dispersion in the data is large, but there is a general trend of increasing $W_{2.29}$ (and thus $W_{1.62}$) at larger L_K. The dispersion likely results from a combination of spatial variations in the composition and space density of the stellar clusters, and from projection effects. The centrally concentrated distributions at the nucleus of both EWs and of the continuum emission suggest a large concentration of populations of supergiants within a radius of a few tens of parsecs. Lower surface brightness regions which exhibit very large EWs probably simply trace smaller numbers of clusters containing very cool supergiants.

Figure 6.4 (right panel) also shows the relationship between the amount of dilution and the ratio of stellar K-band to Lyman continuum luminosities ($L_K/L_{\rm Lyc}$), proportional to the ratio of K-band flux density — corrected for dilution — to Brγ flux (see Eq. 4.1). No extinction correction has been applied to the observed fluxes. The extinction towards the evolved stars may differ from that towards the ionized gas, at least for some regions (table 5.5 and 6.3). However, the differences in extinction corrections near $2\,\mu$m found for individual $1'' \times 1''$ pixels are typically $\lesssim 20\%$ (section 5.1.7), so that the observed "undiluted" $L_K/L_{\rm Lyc}$ ratios are close to the intrinsic values. The amount of dilution at $2.3\,\mu$m exhibits a clear anticorrelation with the $L_K/L_{\rm Lyc}$ ratio, confirming that the sources of dilution are closely associated with the OB star clusters.

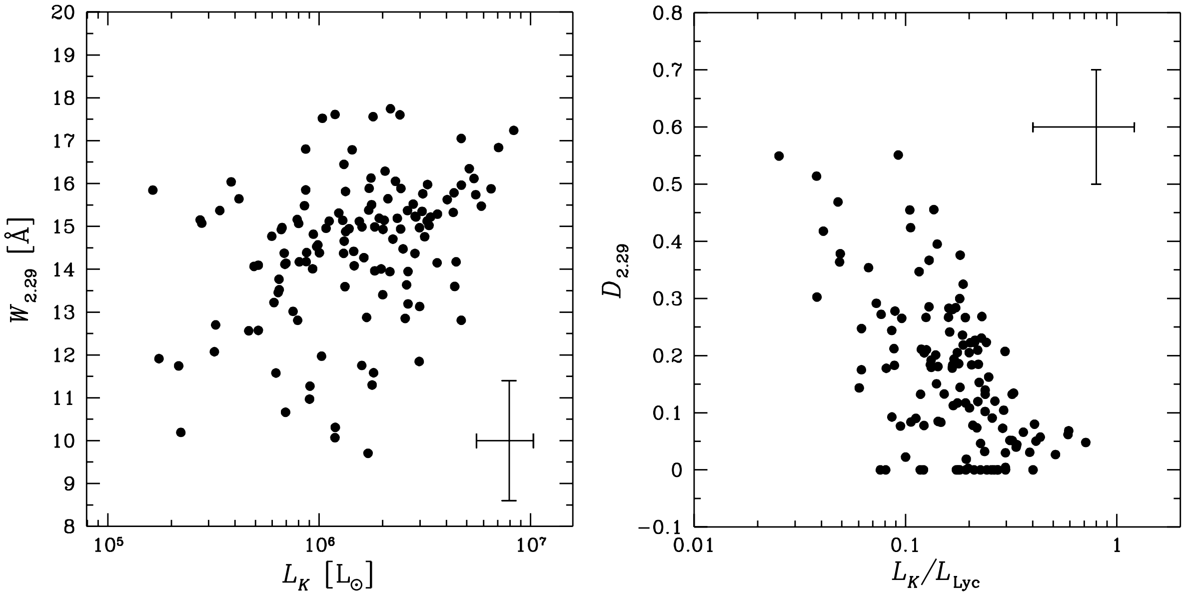

Fig. 6.4.— Relationships between the intrinsic $W_{2.29}$ and L_K, and between the amount of dilution at 2.3 μm and the ratio of K-band to Lyman continuum luminosities for individual $1'' \times 1''$ pixels from the rebinned 3D maps (see text). Typical uncertainties are shown by the error bars.

The important and complex spatial variations in the composition of the evolved stellar population revealed by the 3D data indicate that studies based on data obtained through different apertures or at a few positions only may be misleading. In particular, from a comparison of the $CO_{\rm ph}$ measured at the nucleus and at the secondary peak, Lester *et al.* (1990) and McLeod *et al.* (1993) concluded that there are no gradients in the composition of the stellar population across the starbursting core of M 82. However, the 3D $W_{1.62}$ and $W_{2.29}$ maps clearly show that these regions are "privileged" in the sense that they sample stellar populations with very similar properties. From the comparison of the $H_2O_{\rm ph}$ in different apertures between 3.8″ and 12″, Lançon, Rocca-Volmerange & Thuan (1996) suggested a "radial" picture in which giants dominate the near-infrared continuum in small apertures while supergiants dominate increasingly in larger apertures. The stellar EWs from the 3D data in *both* these apertures are, however, much more consistent with supergiants. The shallower $W_{2.29}$ at increasing radii puts less stringent constraints on the luminosity class, but within 3.8″, it is strong enough to indicate clearly, together with $W_{1.62}$, the presence of supergiants.

The spatial resolution of the 3D images prevents a reliable investigation of the nuclear population on scales smaller than ≈ 20 pc. Gaffney, Lester & Telesco (1993) claimed that an old bulge population dominates the near-infrared continuum emission in the central 15 pc of M 82. Re-examining their arguments, we disagree with this conclusion. Firstly, these authors used an $L_K = 10^8$ $L_\odot$ in their analysis, which is twice as large as the value of 5.6×10^7 L$_\odot$ derived for the central 35 pc in this work (table 6.5 below). Using the K-band flux density of 26 mJy given by Gaffney, Lester & Telesco (1993) themselves, and applying the same extinction correction that they employed (foreground extinction with $\tau_K = 0.8$), $L_K = 7 \times 10^6$ L$_\odot$ is derived, consistent with the 3D measurement. The stellar mass obtained by these authors is 3×10^7 M$_\odot$, which yields $M^\star/L_K = 4.3$ M$_\odot$/L$_\odot$ (instead of 0.3 M$_\odot$/L$_\odot$ with $L_K = 10^8$ L$_\odot$). They argue that the similarity of the $M^\star/L_K$ ratios in M 82 and in the Galactic Center within the same radius of 7.5 pc supports that a nuclear bulge population predating the starburst dominates the near-infrared continuum emission in the nucleus of M 82. The correct ratio of ≈ 4 M$_\odot$/L$_\odot$ is in fact significantly larger than the ratio of 0.5 M$_\odot$/L$_\odot$ they quote for the Galactic Center. Furthermore, the near-infrared light within 7.5 pc of the Galactic Center contains an important contribution from a population of young red supergiants (*e.g.* Haller & Rieke 1989; Blum, Sellgren & DePoy 1996b). The $M^\star/L_K \approx 4$ M$_\odot$/L$_\odot$ is nonetheless significantly lower than the typical ratios of $10 - 30$ M$_\odot$/L$_\odot$ for old populations in the centers of elliptical galaxies and bulges of spiral galaxies, indicating an important contribution to L_K from a young and luminous population of supergiants.

6.1.3 The metallicity of the evolved stellar population

The analysis of the EWs presented above is based on empirical indicators valid for stars with near-solar metallicities. This seems justified for most regions in M 82 since the gas within the H II regions has roughly solar abundances (chapter 5), and the evolved stars presently observed should have formed $\gtrsim 10$ Myr ago from interstellar material with similar or poorer abundances. The recent work by Origlia *et al.* (1997) and Oliva & Origlia (1998) on the effects of metallicity on the indicators used above provides a means of constraining directly the metallicity of the evolved stars in M 82. Their results are here applied *1)* to demonstrate directly that an old *and* metal-rich bulge population is not plausible as dominant near-infrared continuum source in the central 35 pc of M 82, and *2)* to constrain quantitatively the metallicity of the supergiants throughout the regions observed with 3D.

Origlia *et al.* (1997) used theoretical stellar atmosphere models and empirical data of Galactic globular clusters to analyze the dependence of the CO bandheads and Si I feature on metallicity in the range [Fe/H] = +0.4 to −2.2 dex, in K and M giants. They demonstrate that $W_{1.62}$ is significantly affected by metallicity while $W_{2.29}$ varies more importantly with microturbulent velocity (ξ) and $W_{1.59}$ is little affected by changes in these parameters. Qualitatively, if the continuum emission from the central 35 pc of M 82 were dominated by an old, metal-rich population, $W_{1.62}$ would be abnormally large relative to $W_{2.29}$ compared to the EWs for solar-metallicity giants. The opposite behaviour is seen in the data, as expected for supergiants which have larger micro-turbulent velocities than giants. Quantitatively, the diagnostics of micro-turbulent velocity and metallicity proposed by Origlia *et al.* (1997) can be used to derive ξ and [Fe/H] assuming a population of giants. From $W_{1.62}$ and $\log(W_{1.62}/W_{2.29})$, $\xi \approx 3$ km/s. Adopting a solar [C/Fe] = 0.0 dex, $W_{1.62}$ and ξ imply [Fe/H] ≈ -0.5 dex. Assuming a carbon depletion of [C/Fe] $= -0.5$ dex increases the derived [Fe/H] to ≈ -0.2 dex. The 3D data exclude larger carbon depletions; indeed, for [C/Fe] ≤ -0.5 dex, the OH bands at $1.6265\,\mu$m flanking the ^{12}CO (6,3) bandhead become comparably deep or deeper than the CO bandhead (Origlia *et al.* 1997), which is not the case in the 3D spectra. Therefore, **the CO bandheads in the central 35 pc of M 82 are not consistent with an old bulge population of metal-rich giants** dominating the near-infrared light.

In a subsequent paper, Oliva & Origlia (1998) have conducted a similar study for red supergiants. Unfortunately, the metallicity estimates for supergiants depend sensitively on $T_{\rm eff}$, and cannot be very well constrained. Assuming $T_{\rm eff} \approx 3800$ K found in the previous section for the central 35 pc of M 82, the observed $W_{1.62}$ and $W_{2.29}$ imply $\xi \approx 3$ km/s, and [Fe/H] ≈ -0.5 to 0.0 dex is inferred for [C/Fe] = 0.0 to -0.5 dex. Lower temperatures would reduce the inferred metallicity by up to 0.3 dex. Conversely, higher temperatures up to 4300 K would increase the metallicity by up to 0.4 dex. However, the analysis of the EWs in section 6.1.2 leading to a consistent interpretation together with the near-solar abundances of the H II regions support that **the supergiants in the central 35 pc of M 82 have metallicities about solar**, within a factor of ≈ 2.

Similar metallicities are inferred over the entire regions mapped with 3D, assuming supergiants dominate the near-infrared light everywhere and accounting for the variations in $T_{\rm eff}$. The spatial variations in the CO bandheads EWs are not likely due to variations in the metallicity of the stars. Indeed, the observed ranges for $W_{1.62}$ and $W_{2.29}$ would imply variations in the metallicity by factors of at least $4 - 5$. Such large variations on scales of $\sim 10 - 100$ pc are not plausible, particularly for populations of supergiants formed in the past $10 - 50$ Myr, *i.e.* during an interval too short for such substantial chemical enrichment.

6.1.4 Contribution from very cool giant stars

Thermally-pulsing AGB stars such as Mira variables and carbon stars (of type N) exhibit deep absorption features in their near-infrared spectra. Broad H_2O absorption bands centered at 1.9 μm and 2.7 μm severely distort the continuum emission of oxygen-rich AGB stars at both edges of the K-band as well as at the long-wavelength edge of the H-band. A strong Ballik-Ramsey C_2 absorption feature at 1.77 μm and CN absorption bands in the K-band ($\lambda < 2.3\,\mu$m) characterize the near-infrared spectra of carbon-rich AGB stars (*e.g.* Johnson & Mendez 1970; Wallace & Hinkle 1996; see also figures 2.3 and 2.9). None of these extreme features are seen in the 3D spectra. Consequently, these very cool evolved intermediate- and low-mass stars do not contribute importantly to the integrated near-infrared continuum in M 82. Such stars are also very short-lived (appendix A), and the models presented in chapter 3 imply that they contribute $\lesssim 40\%$ to the integrated near-infrared light of stellar clusters of any age. They are therefore not expected to dominate the emission from mixed stellar populations.

6.2 The sources of dilution

The possible sources responsible for the dilution of the stellar absorption features in M 82 include young OB stars, nebular free-free and free-bound processes and hot dust. The broad-band emission from OB stars was estimated using the number of representative O8.5 V stars given in table 5.11 and the photometric properties tabulated by Vacca, Garmany & Shull (1996) and Koornneef (1983b). O8.5 V stars have an absolute V-band magnitude of -4.55 mag, and colours of $V - K = -0.91$ mag and $H - K = -0.05$ mag. The corresponding H- and K-band flux densities at the distance of M 82 are $f_H^{\rm O8.5\,V} = 2.9 \times 10^{-7}$ Jy and $f_K^{\rm O8.5\,V} = 1.7 \times 10^{-7}$ Jy. The H- and K-band flux densities produced by nebular free-free and free-bound processes were computed from the Brγ fluxes corrected for the extinction towards the ionized gas (chapter 5) using the relationships given in Satyapal *et al.* (1995):

$$\frac{f_\lambda^{\rm neb}}{\rm Jy} = C_\lambda \left(\frac{F_{\rm Br\gamma}}{\rm W\,m^{-2}}\right), \tag{6.2}$$

where $C_H = 8.23 \times 10^{12}$, $C_K = 1.02 \times 10^{13}$ for free-free processes, and $C_H = 8.90 \times 10^{12}$, $C_K = 1.11 \times 10^{13}$ for free-bound processes. These coefficients are for case B recombination with $n_{\rm e} = 100$ cm^{-2} and $T_{\rm e} = 10^4$ K. They are little affected by the electron density, but depend more sensitively on the electron temperature. However, for a $T_{\rm e} \approx 5000$ K appropriate for M 82, the nebular flux densities inferred from Brγ would be lower (*e.g.* Joy & Lester 1988). The results are reported in table 6.2.

The contribution from OB stars and nebular emission is thus negligible, leaving hot dust as the most important source of dilution in M 82. Dust at a temperature $T_{\rm HD}$ is usually assumed to emit as a grey body of emissivity λ^{-n} with n in the range $1 - 2$:

$$S_\lambda^{\rm HD} \propto \lambda^{-n}\, B_\lambda(T_{\rm HD}), \tag{6.3}$$

where $B_\lambda(T_{\rm HD})$ is the Planck function (*e.g.* Emerson 1988). Since $D_{1.6}$ is negligible in M 82, even around B1 where $D_{2.3}$ up to $\approx 30\%$ are estimated, the dust temperature cannot exceed ≈ 1000 K.

Table 6.2: Contributions from OB stars and nebular emission in the near-infrared

	Central 35 pc	B1	B2	3D field
$D_H^{\rm OB\,(a)}$	0%	2%	1%	0%
$D_K^{\rm OB\,(a)}$	0%	1%	1%	0%
$D_H^{\rm Neb\,(a)}$	$< 1\%$	$< 8\%$	$< 5\%$	$< 3\%$
$D_K^{\rm Neb\,(a)}$	$< 1\%$	$< 7\%$	$< 4\%$	$< 3\%$

[a] Fraction of the H- and K-band flux densities (corrected for the extinction derived in section 5.1.7 for a mixed model) from OB stars ("OB") and nebular free-free and free-bound processes ("Neb").

6.3 Extinction towards the evolved stars

6.3.1 Selected individual regions

The extinction towards the evolved stars in M 82 can be obtained from the 3D data by two different methods: *1)* from the continuum slope, and *2)* from the observed $H-K$ colour. Both the continuum slope and the $H-K$ colour depend also on the composition of the stellar population and include the contributions from featureless continuum sources. These were constrained in the previous sections from the analysis of the CO bandheads and Si I absorption feature, and estimated from the H I recombination line fluxes. Consequently, the extinction can be determined *independently*.

The amount of extinction was first derived from minimum χ^2-fitting to the 3D spectra in the following way. The K-band spectrum for the average spectral type determined from the selected EWs was combined with a grey-body hot dust emission curve, in the proportions given by the amount of dilution inferred from $\log\left(W_{1.62}/W_{2.29}\right)$. The contributions from OB stars and their associated nebular emission can be neglected. The template stellar spectra were taken from the Kleinmann & Hall (1986) atlas, which provides a larger spectral coverage than the 3D stellar library (chapter 2) for the spectral types of interest, required to better constrain the extinction. The K5 I spectrum was used for all regions except for B1, for which the K0 I and K5 I spectra available were averaged to produce a template K2 I spectrum. The H-band data were excluded from this analysis because of the small wavelength coverage of the Dallier, Boisson & Joly (1996) library. The hot dust was represented by the grey-body emission curve of Eq. 6.3. The temperature and the emissivity index are not well constrained in M 82; $T_{\rm HD} = 800$ K and $n = 1.5$ were adopted, consistent with previous work (*e.g.* Smith *et al.* 1990; Larkin *et al.* 1994). The extinction towards the evolved stars and the hot dust was assumed to be the same. The extinction law from Draine (1989; $A_\lambda \propto \lambda^{-1.75}$) was adopted, and the amount of extinction was varied to achieve the best fit characterized by the minimum χ^2-value. The results from the spectral fits are not significantly affected by the choice of template star within a few spectral classes, by $T_{\rm HD}$ in the range 600 K – 1000 K, by n between 1 and 2, and by the power-law index for the extinction law within 0.1 – 0.2 dex. The assumption that the same extinction applies to the evolved stars and to the hot dust is also of little consequences since the stars dominate strongly the continuum emission.

The A_V derived for two different geometries for the obscuring dust and sources are reported in table 6.3: a uniform foreground screen and a mixed model. As for the determination of the extinction towards the ionized gas from the Brackett lines (chapter

5), the data do not allow the distinction between different geometries for the dust and sources owing to the relatively small wavelength coverage. This would not be possible even including H-band data due to the uncertainties on the hot dust properties, since these become crucial over larger wavelengths intervals. However, the corresponding extinction corrections differ by less than 35% between a uniform foreground screen and a mixed model, except for the central 35 pc ($\approx$ 50%).

To derive the amount of extinction from the $H - K$ colour, only the uniform foreground screen model was considered. The K-band flux densities were first corrected for the hot dust contribution, in order to obtain "undiluted" $H - K$ colours resulting from the stars and from extinction effects only. Intrinsic colours for the $T_{\rm eff}$ inferred from $W_{1.62}$ assuming the stars are supergiants were taken from Koornneef (1983b). The extinction was then determined from the colour excess

$$E_{HK} = (H - K)^{\rm undiluted} - (H - K)^{\rm intrinsic}. \tag{6.4}$$

For the extinction laws from Draine (1989) and Rieke & Lebofsky (1985) at near-infrared and optical wavelengths respectively,

$$E_{HK} = 0.067 A_V. \tag{6.5}$$

The results (table 6.3) are in excellent agreement with those derived from the spectral fits assuming purely foreground obscuration.

The similarity between the correction factors obtained for the two extinction models probably reflects the fact that the emission throughout the H- and K-band probes similar limiting optical depths. Consequently, for the sources which are detected, the choice of the extinction model is not critical. The results for the mixed model will be adopted because such a geometry seems more plausible for populations of clusters of supergiants, which are likely more or less uniformly mixed with interstellar gas and dust clouds, as for the H II regions (chapter 5).

Table 6.3: Determination of the extinction towards the evolved stars for selected regions in M 82[a]

	Central 35 pc	B1	B2	3D field
	From spectral fits to the K-band spectra			
A_V^{UFS} [mag]	10 ± 4	6 ± 3	8 ± 3	6 ± 3
$A_V^{\mathbf{MIX}}$ [mag]	$\mathbf{45 \pm 20}$	$\mathbf{25 \pm 10}$	$\mathbf{28 \pm 10}$	$\mathbf{17 \pm 7}$
	From $H - K$ colour excesses, accounting for the hot dust contribution			
A_V^{UFS} [mag]	10 ± 3	7 ± 2	9 ± 3	6 ± 2
	Equivalent global extinction from the $H - K$ colour excesses, assuming a non-uniform foreground screen model			
$A_{V,\mathrm{eff}}^{\mathrm{UFS}}$ [mag]	—	—	—	8
$A_{V,\mathrm{eff}}^{\mathbf{MIX}}$ [mag]	—	—	—	**18**

[a] The mixed model will be adopted throughout this thesis.

6.3.2 Extinction across the entire 3D field of view

The extinction towards the evolved stars in individual regions across the entire 3D field of view can be determined from the 3D data cubes rebinned to $1'' \times 1''$ pixels. Assuming an intrinsic population of supergiants (section 6.1.2) and purely foreground obscuration along any line of sight, the extinction was derived for each pixel from the $H - K$ colours as described above for the selected regions, after accounting for the hot dust contribution to the K-band emission determined in section 6.1.2. This consists in fact of considering a *non-uniform foreground screen model*. Comparing the flux density integrated over the rebinned, dilution- and extinction-corrected K-band map to the observed integrated flux density, the global correction factor at $2.2\,\mu$m for this model is very close to those obtained from the spectral fits and corresponds to an effective $A_V^{\mathrm{MIX}} = 18$ mag, or $A_V^{\mathrm{UFS}} = 8$ mag.

6.4 Properties of the entire starburst core of M 82

In addition to the regions mapped with 3D and the *ISO*-SWS, the entire starburst core of M 82, enclosed in a 30″–diameter aperture centered on the nucleus, will also be considered for the evolutionary synthesis modeling presented in the next chapter. The various properties considered in this chapter are derived here for the starburst core with the help of existing data in the literature.

Satyapal *et al.* (1997) measured the depth of the CO bandheads longwards of 2.3 μm in a 24″–diameter aperture on the nucleus of M 82. Their spectroscopic index of 0.18 mag (which is independent of extinction) corresponds to $CO_{\rm ph} = 0.20$ mag in the photometric system of Frogel *et al.* (1978). From a calibration between $W_{2.29}$ and $CO_{\rm ph}$ obtained from the 3D and Kleinmann & Hall (1986) atlases, this corresponds to $W_{2.29} = 14.5$ Å, which is essentially the same as the value measured from the spectrum of the entire 3D field of view after correcting for 10% dilution (14.4 Å). Since figure 6.4 shows that the amount of dilution at 2.3 μm decreases with increasing $L_K/L_{\rm Lyc}$ (or, equivalently, with decreasing Brγ equivalent width), and since this ratio is larger for regions outside of the 3D field of view (*e.g.* Satyapal *et al.* 1997), the contribution from featureless near-infrared continuum sources for the entire starburst core is expected to be negligible. Finally, because of the similar intrinsic $W_{2.29}$ for the 3D field of view and the central 30″ of M 82, and because the H- and K-band flux densities for the former constitute a significant fraction ($25\% - 30\%$) of the total emission in the latter, the $W_{1.62}$ measured in the 3D field of view is probably representative for the entire starburst core.

As for the extinction towards the ionized gas, the global extinction towards the evolved stars in M 82 has long been a subject of controversy. While the observed K-band magnitudes measured by various authors agree well with each other, the different extinction values inferred and extinction models assumed have led to very different values for the intrinsic absolute K-band magnitude (M_K), a crucial property in evolutionary synthesis modeling. Various results from the literature are summarized in table 6.4. The global extinction in the central 30″ of M 82 is here re-examined using the results from 3D and *ISO*-SWS. The observed K-band magnitude of 5.43 mag measured by Telesco *et al.* (1991) is adopted.

The morphology of the K-band emission suggests that the sources are mainly concentrated at and around the nucleus, and along the plane of the galaxy, while the tracers of ionized gas suggest a more extended distribution along the line of sight (*e.g.* Telesco *et al.* 1991; Achtermann & Lacy 1995). As argued by Rieke *et al.* (1980), half of the extinction towards the bulk of the ionized gas therefore probably applies to the

Table 6.4: Summary of various determinations of the intrinsic absolute K-band magnitude for the starburst core of M 82 (30″–diameter aperture centered on the nucleus)

Work	Extinction model[a]	Extinction diagnostics	M_K [mag]
Rieke *et al.* 1980	Mixed	H I recombination lines	−23.3
Telesco *et al.* 1991	Non-uniform foreground	$J-H$, $H-K$ colours	−22.6
McLeod *et al.* 1993	Non-uniform foreground	$H-K$ colour	−22.5
Satyapal *et al.* 1997	Non-uniform foreground	H I recombination lines	−22.0
This work	Non-uniform foreground	$H-K$ colour	−23.0
This work	Mixed	Fit to K-band spectrum	−22.9
This work	Mixed	H I recombination lines	−23.2
Adopted			**−23.0**

[a] The extinction determinations assuming a mixed model were derived from integrated fluxes inside an 8″–diameter aperture centered on the nucleus of M 82 for Rieke *et al.* (1980), and the 3D field of view and the SWS aperture (this work). Those based on a non-uniform foreground screen model were derived from maps, assuming a uniform foreground screen model at each pixel.

bulk of the evolved stellar population. The measurement from Telesco *et al.* (1991) is thus corrected for $A_V = 26$ mag, half of the value found in chapter 5 for a mixed extinction model, implying an intrinsic absolute magnitude of $M_K = -23.2$ mag. Similar values are obtained with the extinction for the mixed model derived from the spectral fit to the integrated K-band spectrum of the 3D field of view ($M_K = -22.9$ mag), and with the effective extinction derived from the $H-K$ maps assuming a non-uniform foreground screen model ($M_K = -23.0$ mag).

The intrinsic absolute magnitudes above are consistent with the lower range of values found in the literature. The differences between various determinations correspond to differences of up to a factor of three in the intrinsic L_K, and are mainly attributable to the different assumptions about the geometry of the sources and obscuring dust made by the various authors. It is well established that a simple uniform foreground screen geometry is not appropriate for the global extinction towards the evolved stellar population in M 82 (Rieke *et al.* 1980; Satyapal *et al.* 1997). But again, it is very difficult to distinguish between other geometries because of their similar effects on the relative fluxes at near-infrared wavelengths, where the evolved stars are accessible to observations (*e.g.* Satyapal *et al.* 1997; see also figure 5.2).

Satyapal *et al.* (1997) showed that the integrated near-infrared colours in a $24''$–diameter aperture in M 82 can be reproduced by a mixed and a two-screen two-source model. They claim that their two-screen two-source model (for which $\tau_K = 1.27$, $f = 0.3$ and $g = 0.2$) implies an extinction correction that differs only by a factor of 1.2 from the correction with their uniform foreground screen model (for which $\tau_K = 0.58$). However, the correction for the *total* intensity of the sources for the two-screen two-source model is a factor $(1 + f)$ larger than the factor $[(f + e^{-\tau_K})/e^{g\tau_K}]^{-1}$ they used (see section 5.1.1 and figure 5.1). The correct factor applied to their measurement in a $24''$–diameter aperture would then imply $M_K = -22.4$ mag, in better agreement with the other determinations for a $30''$–diameter aperture.

The intrinsic M_K derived using the extinctions inferred from the 3D near-infrared data corresponds to an intrinsic flux a factor of 1.5 larger than those obtained similarly from near-infrared colour maps (Telesco *et al.* 1991; McLeod *et al.* 1993). This may be partly due to differences in the photometry between the data sets, but also to the fact that the regions mapped with 3D include only sources within at most $\approx 12''$ of the nucleus and along the plane of the galaxy, which likely suffer from more extinction than the average within $30''$. On the other hand, the evolved stellar clusters are probably mixed to some degree with the obscuring material along the line of sight even in $1'' \times 1''$ regions, so that the locally uniform foreground screen may lead to an underestimate of the true extinction. **An average $M_K = -23.0$ mag from our determinations will be adopted, implying an effective global extinction of $A_V^{\rm MIX} = 21$ mag for a mixed model**, or $A_V^{\rm UFS} = 9$ mag for a uniform foreground screen model.

6.5 Number of representative evolved stars

The intrinsic K-band luminosities originating from the cool, evolved stellar populations for the selected individual regions in the 3D field of view were derived by correcting the observed K-band flux densities of table 4.4 for the hot dust contribution and for extinction. Using the K-band luminosity for the appropriate representative spectral type (appendix A), the number of equivalent stars required to produce the intrinsic stellar luminosities were computed. The results, together with those inferred for the entire starburst core in the previous section, are reported in table 6.5.

The results from the population/spectral synthesis are also illustrated in figure 6.5. For B1, the supergiants solution is adopted since, as mentioned in section 6.1.2, supergiants appear to dominate the near-infrared luminosity everywhere across the starburst core of M 82. The template stellar spectra are taken from the atlases of Kleinmann & Hall (1986; KH86) and Dallier, Boisson & Joly (1996; DBJ96), convolved at the resolution of the 3D data. Due to the relatively poor sampling for luminosity class I, the K5 I K-band spectrum from KH86 is used for all regions, except for B1 for which a template K2 I spectrum was obtained by averaging the available K0 I and K5 I spectra. For the H-band, the K4 I spectrum from DBJ96 is used for all regions, including B1 since there are no spectra for earlier K-type supergiants with solar metallicity available from this library.

Table 6.5: Summary of the relevant near-infrared properties of selected regions in M 82

	Central 35 pc	B1	B2	3D field	Starburst core
Representative type	K5 I	K2 I	K4 I	K4 I	K4 I
K-band dilution[(a)]	0%	25%	15%	10%	0%
$A_V^{\rm MIX}$ [mag][(b)]	45 ± 20	25 ± 10	28 ± 10	17 ± 7	21
L_K [10^8 L$_\odot$][(c)]	0.56 ± 0.23	0.074 ± 0.024	0.15 ± 0.05	2.7 ± 0.8	13 ± 4
$N_\star$[(d)]	1.1×10^4	4400	5800	1.0×10^5	5.0×10^5

(a) Contribution to the K-band continuum emission from hot dust, with uncertainties of ±10%. The contributions in the K-band from OB stars and their associated nebular emission, and in the H-band from all these sources, are negligible.

(b) The extinction from the spectral fits to the regions in the 3D field of view, assuming a mixed model, is adopted. For the starburst core, the global effective extinction for a mixed model is adopted (see section 6.4).

(c) Intrinsic K-band luminosity from the evolved stars, obtained from the broad-band flux densities given in table 4.4 corrected for dilution and for extinction.

(d) Number of representative stars producing the intrinsic stellar L_K.

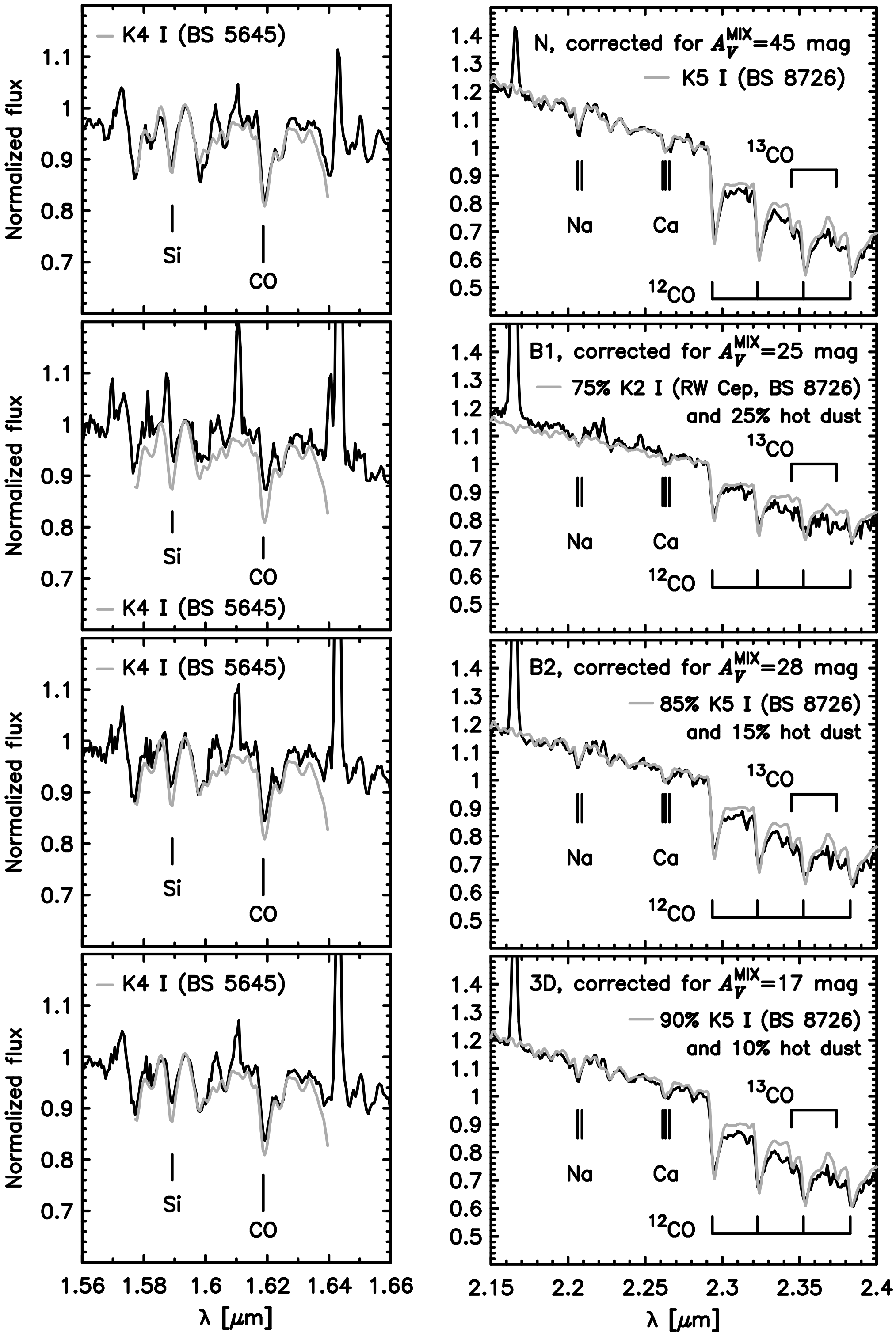

Fig. 6.5.— Spectral synthesis for the central 35 pc of M 82 (top panels, "N"), for the Brγ sources B1 and B2 (middle panels), and for the entire 3D field of view (bottom panels, "3D"). The black lines are the extinction-corrected 3D spectra assuming a mixed model for the extinction. The grey lines are the combination of the template stellar spectra and the hot dust emission ($T_{\rm HD}$ = 800 K and $n = 1.5$) appropriate for each region. The H- and K-band spectra are from Dallier, Boisson & Joly (1996) and Kleinmann & Hall (1986) respectively (see text).

6.6 Summary

In this chapter, the composition of the evolved stellar population, the contribution from near-infrared featureless continuum sources, and the extinction towards the evolved stars have been determined. The main results are summarized in the following table.

PROPERTY	**RESULTS**
Nucleus: central 35 pc	
Evolved stars	Average type K5 I Consistent with solar metallicity
Hot dust emission	Negligible contribution
OB stars and nebular emission	Negligible contribution
Starburst regions within the 3D maps	
Evolved stars	Spatial variations on scales $\lesssim$ 30 pc More complex than a simple radial gradient $< T_{\rm eff} >$ from 3600 K to 4500 K
Hot dust emission	Contribution in the K-band: spatially variable: 0% − 50%, correlated with H II regions Negligible contribution in the H-band
OB stars and nebular emission	Negligible contribution

The most important results concern the composition of the stellar population at the nucleus of M 82 and its spatial variations across the starburst regions:

- The stellar absorption features in the H- and K-band spectrum of the central 35 pc of M 82, particularly the combination of the CO bandheads at 1.62 μm and 2.29 μm, are characteristic of red supergiants with near-solar metallicity. Contributions from old, metal-rich bulge giants or AGB stars (Miras, carbon stars) are small or negligible.

- Important spatial variations are seen in the composition of the stellar populations which dominate the near-infrared emission in M 82, at least within the 3D field of view. In addition to the central 35 pc, several regions along the galactic plane exhibit stellar absorption features with strengths that can unequivocally be attributed to red supergiants. The range of average effective temperatures indicate different evolutionary stages for the evolved stellar populations in different regions within the starburst core of M 82.

Chapter 7

Evolutionary synthesis: starburst modeling of M 82

The nebular analysis and population synthesis presented in chapters 5 and 6 provide information on the present state of the interstellar medium and of the stellar populations. Application of evolutionary synthesis allows the interpretation of the observations in the context of an *evolutionary process*. Most previous studies of starburst galaxies attempted to model the integrated properties of entire starburst regions. The small-scale structure and the important differences in the properties of individual regions in M 82, as revealed by the 3D data and by a number of other recent studies, indicate that such a global modeling is too simplistic.

The 3D and SWS data of M 82, combined with the optimized evolutionary synthesis models presented in chapter 3, provide the best tools available to investigate *quantitatively and consistently* the nature and history of starburst activity in this galaxy. Together with data taken from the literature, they are used to constrain:

- the typical burst timescale on various spatial scales,
- the age dispersion of individual regions,
- the relative intensity of star formation activity between individual regions, and
- the upper and lower mass cutoffs of the initial mass function (IMF).

The **detailed spatial modeling** presented here enables for the first time the **detailed reconstruction of the star formation history in M 82**. This has important consequences for the understanding of starburst activity because it provides constraints on the triggering mechanism and on the effects on the environment of such activity. This chapter ultimately aims at addressing two major, fundamental issues:

- What are the properties of the star formation process in a starburst environment?
- What was the spatial and chronological evolution of starburst activity in M 82?

This chapter is divided as follows. The observational constraints are first summarized in section 7.1 and the modeling procedure is described in section 7.2. Starburst modeling is applied in sections 7.3 and 7.4 to selected, representative regions in order to constrain the general characteristics of starburst activity in M 82. The nature of the sources of low-surface brightness near-infrared continuum emission is investigated in section 7.5. The most useful age indicators identified in section 7.3 are used in section 7.6 for a spatially detailed modeling of the central starburst regions of M 82. Finally, the general picture for starburst activity in M 82 is summarized in section 7.7, and the results, in section 7.8.

7.1 Observational constraints

Table 7.1 summarizes the observational constraints for the modeling of selected regions: the central 35 pc at the nucleus, the H II region complexes B1 and B2, the entire 3D field of view, and the starburst core enclosed in a 30″–diameter region centered on the nucleus. Part of the properties listed were obtained in previous chapters. Additional constraints are derived in this section.

Table 7.1: Observational constraints for selected regions in M 82[(a)]

Property	Units	Central 35 pc	B1	B2	3D field	Starburst core
$L_K{}^{(b)}$	10^8 L$_\odot$	0.56 ± 0.23	0.074 ± 0.024	0.15 ± 0.05	2.7 ± 0.8	13 ± 4
$L_{\rm Lyc}$	10^8 L$_\odot$	0.67 ± 0.25	1.5 ± 0.4	2.0 ± 0.9	27 ± 13	77 ± 23
$L_{\rm bol}$	10^8 L$_\odot$	18 ± 9	8.9 ± 3.1	12 ± 4	220 ± 90	660 ± 120
$M^\star$	10^8 M$_\odot$	$0.79^{+0.22}_{-0.21}$	—	—	—	$6.1^{+2.7}_{-2.5}$
$\nu_{\rm SN}{}^{(c)}$	$10^{-2}\,{\rm yr}^{-1}$	0.25	0.25	0.58	13	6
$W_{1.62}$	Å	5.6 ± 0.3	3.4 ± 0.3	4.6 ± 0.3	4.8 ± 0.3	4.8
$W_{2.29}{}^{(d)}$	Å	15.2 ± 1.2	11.2 ± 1.4	14.4 ± 1.4	14.4 ± 1.4	14.5
$L_K/L_{\rm Lyc}$	—	0.84 ± 0.46	0.049 ± 0.021	0.075 ± 0.041	0.10 ± 0.05	0.17 ± 0.07
$L_{\rm bol}/L_{\rm Lyc}$	—	27 ± 15	5.9 ± 2.5	6.0 ± 2.4	8.1 ± 3.8	8.6 ± 2.3
$M^\star/L_K$	M$_\odot$/L$_\odot$	1.4 ± 0.7	—	—	—	0.47 ± 0.25
$10^{12}\,\nu_{\rm SN}/L_{\rm bol}{}^{(c)}$	${\rm yr}^{-1}$/L$_\odot$	1.4	2.8	4.8	5.9	0.91
[Ne III]/[Ne II][(e)]	—	0.13	0.16	0.12	0.16	0.16 ± 0.04

[(a)] The following properties were obtained in previous chapters: L_K, $W_{1.62}$ and $W_{2.29}$ (chapters 4 and 6); $L_{\rm Lyc}$ (chapter 5); [Ne III]/[Ne II] for the entire starburst core (chapter 5). All luminosities are corrected for extinction.

[(b)] The K-band luminosities are also corrected for the hot dust contribution.

[(c)] The $\nu_{\rm SN}$ and $10^{12}\,\nu_{\rm SN}/L_{\rm bol}$ are uncertain to a factor of two.

[(d)] The $W_{2.29}$ are corrected for hot dust dilution.

[(e)] The [Ne III]/[Ne II] ratio measured in the SWS aperture is assumed to be representative of the ratio for the entire starburst core. The values for the central 35 pc of M 82, B1, B2 and the 3D field of view are the equivalent ratios for the average effective temperature of the ionizing stars inferred from the He I 2.058/Brγ ratios, as described in section 7.1.1. The uncertainties are estimated to be a factor of two.

7.1.1 Equivalent [Ne III]/[Ne II] ratio for individual regions observed with 3D

The nebular line ratios provide a sensitive measure of the average effective temperature of the ionizing stars ($T_{\rm eff}^{\rm OB}$) and constitute, therefore, a crucial constraint for evolutionary synthesis modeling. As discussed in chapter 5 (section 5.4.2), the near-infrared He I to H I recombination line ratios available from the 3D data are likely better indicators of the variations in $T_{\rm eff}^{\rm OB}$ between individual regions than of the absolute $T_{\rm eff}^{\rm OB}$, due to the uncertainties on the He abundance and in theoretical modeling of the He I line emission. In addition, the He I 2.058/Brγ ratio is of limited usefulness in evolutionary synthesis modeling because the degeneracy in $T_{\rm eff}^{\rm OB}$ results in degeneracy in burst age. The [Ne III] 15.6 μm/[Ne II] 12.8 μm constitutes a more reliable diagnostic of absolute $T_{\rm eff}^{\rm OB}$, and varies monotonically with $T_{\rm eff}^{\rm OB}$.

In order to provide the essential constraint on $T_{\rm eff}^{\rm OB}$ for the selected regions in the 3D field of view, an "equivalent" [Ne III]/[Ne II] ratio was obtained in the following way. The $T_{\rm eff}^{\rm OB}$ derived from the He I 2.058/Brγ ratios (table 5.10) were increased by 1400 K from the calibration between the temperatures derived from the SWS [Ne III]/[Ne II] ratio and from the integrated He I 2.058/Brγ ratio measured for the 3D field of view, as described in section 5.4.2. The equivalent [Ne III]/[Ne II] ratios were then inferred from the variations of this ratio with $T_{\rm eff}^{\rm OB}$ plotted in figure 5.11, for the nebular parameters appropriate for M 82. The resulting uncertainties are estimated to be a factor of two.

7.1.2 Bolometric luminosity

In starburst galaxies, two main sources are expected to dominate the bolometric luminosity: the hot, massive stars and the cool, evolved stars. The energy output from young OB stars is partly absorbed by dust and reradiated in the infrared, and partly absorbed by the gas which is thereby ionized. However, for the average O8.5 V spectral type of the stars that dominate the ionizing radiation in M 82, 25% only of the total luminosity is emitted above the Lyman edge (see table A.2 in appendix A). Furthermore, the large extinction derived towards the H II regions implies that most of the recombination line emission is also absorbed by dust. The $L_{\rm bol}$ from hot stars in M 82 is therefore probably well approximated by the infrared luminosity $L_{\rm IR}$ from dust grains, which emit mostly in the range $\lambda = 5 - 300$ μm.

For the entire starburst core, $L_{\rm IR} = 3 \times 10^{10}$ $L_\odot$ (Telesco & Harper 1980). The $L_{\rm IR}$ for the individual regions can be estimated from measurements of the mid-infrared continuum emission such as the N-band ($\lambda = 10.8\ \mu$m, $\Delta\lambda = 5.3\ \mu$m) luminosity. Indeed, observations at mid- and far-infrared wavelengths suggest that the brightest emitting region in M 82 has similar spatial structure at least out to $100\,\mu$m, where the global energy distribution of M 82 peaks (Telesco *et al.* 1991). Consequently, the mid-infrared emission is a good tracer of the infrared luminosity. Telesco, Dressel & Wolstencroft (1993) obtained $L_{\rm IR} = 18\,L_N$ for the entire starburst core of M 82, and found that this relationship also holds for a sample of 11 starburst galaxies, within a factor of two. In order to derive the $L_{\rm IR}$ for the individual regions of interest, the $12.4\,\mu$m map ($\Delta\lambda = 1.2\ \mu$m) from Telesco & Gezari (1992)[1] was actually used, since it has a spatial resolution comparable to that of the 3D data. Comparing the $12.4\,\mu$m measurement with the N-band flux density from Telesco *et al.* (1991) over the starburst core and in a $4'' \times 4''$ region encompassing the western mid-infrared peak yields $f_N = 0.4\,f_{12.4\mu{\rm m}}$ (Telesco & Gezari 1992). The relatively large difference between the flux at $10.8\,\mu$m and $12.4\,\mu$m is mainly due to the larger contribution from the [Ne II] $12.8\,\mu$m line in the $12.4\,\mu$m bandpass and to the stronger depression of the continuum due to the $9.7\,\mu$m silicate absorption feature in the $10.8\,\mu$m bandpass. Combining the above relationships gives

$$\frac{L_{\rm IR}}{{\rm L}_\odot} = 3.25 \times 10^7 \left(\frac{D}{\rm Mpc}\right)^2 \left(\frac{f_{12.4\,\mu{\rm m}}}{\rm Jy}\right). \tag{7.1}$$

Eq. 7.1 includes average extinction effects as well as contributions from PAH emission features, emission lines and the silicate absorption feature in the $10.8\,\mu$m and $12.4\,\mu$m bandpasses for the entire starburst core of M 82. Spatial variations in the extinction and in the emission and absorption features introduce relatively small errors in the application of this relationship to individual regions within M 82, as described below.

The differences in extinction towards the ionized gas obtained in chapter 5 for selected regions within M 82 imply differences of $\approx 20\%$ in the intrinsic $12.4\,\mu$m flux densities. The [Ne II] $12.8\,\mu$m emission line (the strongest in the bandpasses considered) contributes 11% of the $12.4\,\mu$m flux density in the SWS aperture. From the line map of Achtermann & Lacy (1995), similar contributions are estimated for the central 35 pc, B2 and the 3D field of view, and a larger contribution of $\approx 20\%$ is obtained for B1. Spatial variations in the contribution from emission lines are thus estimated to be $\approx 10\%$. The broad PAH emission features at $8.6\,\mu$m, $11.3\,\mu$m and $12.7\,\mu$m contribute in turn about 20% of the N-band and $12.4\,\mu$m bandpasses in the SWS field of view. If the $3.3\,\mu$m PAH emission traces well the other PAH emission features, the line-to-continuum map from Normand *et al.* (1995) implies spatial variations in the PAH contribution. However, because the overall distributions of the [Ne II] line and the $3.3\,\mu$m PAH feature are very similar to that of the mid-infrared continuum

[1] kindly made available in electronic form by the authors

Table 7.2: Estimation of the total bolometric luminosity of selected regions in M 82

Region	$L_{\rm IR}{}^{\rm (a,d)}$ [L$_\odot$]	$L_{\rm bol}^{\rm evolved\ stars(b,d)}$ [L$_\odot$]	$L_{\rm bol}^{\rm tot\,(c,d)}$ [L$_\odot$]
Central 35 pc	$(5.1 \pm 1.8) \times 10^8$	$(1.1 \pm 0.7) \times 10^9$	$(1.8 \pm 0.9) \times 10^9$
B1	$(5.7 \pm 2.0) \times 10^8$	$(1.5 \pm 0.9) \times 10^8$	$(8.9 \pm 3.1) \times 10^8$
B2	$(7.1 \pm 2.5) \times 10^8$	$(2.9 \pm 1.7) \times 10^8$	$(1.2 \pm 0.4) \times 10^9$
3D field	$(1.3 \pm 0.5) \times 10^{10}$	$(5.5 \pm 3.1) \times 10^9$	$(2.2 \pm 0.9) \times 10^{10}$
Starburst core	$(3.0 \pm 0.3) \times 10^{10}$	$(2.7 \pm 0.8) \times 10^{10}$	$(6.6 \pm 1.2) \times 10^{10}$

$^{(a)}$ Infrared luminosity between 5 μm and 300 μm.

$^{(b)}$ Bolometric luminosity from the evolved stellar population.

$^{(c)}$ $L_{\rm bol}^{\rm tot}$ includes $L_{\rm IR}$, $L_{\rm bol}^{\rm evolved\ stars}$ and an additional 30% of $L_{\rm IR}$ ($\pm$10%) to account for light escaping in directions perpendicular to the galactic plane of M 82.

$^{(d)}$ The uncertainties account for those on the absolute calibration of the data used to derive the quantities, on the conversion factors between $f_{12.4\,\mu\rm m}$ and $L_{\rm IR}$, and between L_K and $L_{\rm bol}^{\rm evolved\ stars}$, on the extinction, on the hot dust contribution to L_K, and on the fraction of escaping light.

emission and since their contributions to the bandpasses considered are relatively small, spatial variations should imply only small errors ($\approx$ 10%) in the $L_{\rm IR}$ for individual regions. Variations in the depth of the silicate feature are probably of the same order. Application of Eq. 7.1 to individual regions therefore introduces errors of about 35%.

Part of the stellar light from the inner regions of M 82 likely escapes along the minor axis of the galaxy. This is supported by the pattern of polarization vectors in the ionized filaments above and below the galactic plane of M 82, which indicates that most of the scattered light comes from the central starburst regions (*e.g.* Notni 1985). In addition, the low ratio of [N II] λ6583 Å to Hα emission line in the optical filaments along the minor axis of M 82 suggests that they may be photoionized by light from the central starburst (Shopbell & Bland-Hawthorn 1998). The amount of light that escapes perpendicular to the plane of M 82 is uncertain since it depends on the dust distribution. Following McLeod *et al.* (1993), an additional 30% of the detected $L_{\rm IR}$ is included in $L_{\rm bol}$ to account for escaping light.

The contribution to $L_{\rm bol}$ from the evolved stars cannot be directly measured. Individual giants and supergiants with temperatures between 3500 K and 6000 K have $L_{\rm bol}/L_K \approx 10 - 30$ (see appendix A), similar to the ratio for mixed populations of cool, evolved stars (*e.g.* McLeod *et al.* 1993). The $L_{\rm bol}$ from evolved stars is estimated from the intrinsic L_K using a representative ratio of 20, with 50% uncertainty. The integrated infrared luminosity, the bolometric luminosity from the evolved stellar population and the total bolometric luminosity for each region of interest are reported in table 7.2.

7.1.3 Mass

Götz *et al.* (1990) proposed a mass model for M 82 based on various observations including their own data on the Na D absorption doublet at 5800 Å and Hα absorption line, as well as existing data on the H I 21 cm line (Crutcher *et al.* 1978), the CO $J = 2 \rightarrow 1$ line (Loiseau *et al.* 1990) and the [Ne II] 12.8 μm line (Beck *et al.* 1978). This mass model is compared here with the dynamical mass derived from more recent data obtained at higher spatial and/or velocity resolution. These include observations of the CO $J = 1 \rightarrow 0$ millimetric line at a resolution of 4.1 km s^{-1} and 2.5″ (Shen & Lo 1995), of the [Ne II] 12.8 μm line at 30 km s^{-1} and 2″ (Achtermann & Lacy 1995), of the [S III] λ9069 Å line at 30 km s^{-1} and 2″ (McKeith *et al.* 1993), and of the CO bandhead at 2.3 μm at 15 km s^{-1} in the central 1″ of M 82 (Gaffney, Lester & Telesco 1993).

Assuming a uniform mass distribution and dynamical equilibrium, the dynamical mass enclosed within the projected radius r is given by

$$M_{\rm dyn}(< r) = 3.49 \times 10^3 \left(\frac{r}{\rm arcsec}\right) \left(\frac{v_{\rm rot}}{\rm km\ s^{-1}}\right)^2 , \qquad (7.2)$$

where $v_{\rm rot}$ is the rotational velocity measured at r, estimated from the position-velocity maps presented by the authors above. The data reveal spatially non-uniform gas distributions in the central parts of M 82, with important concentrations at particular radii and relatively little gas elsewhere. These structures are interpreted as rotating rings or spiral arms. $v_{\rm rot}$ was thus properly determined using the maximum, or peak velocity $v_{\rm peak}$ for these concentrations of material, corresponding to their tangent point with the line of sight, corrected for the effects of inclination and resolution (beam and velocity smearing). Various determinations of the inclination angle for the disk of M 82 vary in the range $61° - 82°$ from face-on (*e.g.* Götz *et al.* 1990; Achtermann & Lacy 1995; Telesco *et al.* 1991 and references therein). For such a nearly edge-on orientation, the differences in angle imply differences smaller than 15% in the inclination-corrected $v_{\rm rot}$; an angle of 80° was adopted.

The data above were complemented by the dynamical mass obtained by Gaffney, Lester & Telesco (1993) in the central 1″ of M 82, from stellar velocity dispersion measurements using the CO bandhead at 2.3 μm. The data are reported in table 7.3, and the resulting mass-radius curve is plotted in figure 7.1 along with the mass model proposed by Götz *et al.* (1990). The new data imply larger masses for $r \lesssim 10''$, by up to a factor of ≈ 4 at $r = 0.5''$. Such differences are not surprising since the new data probe much better the central regions of M 82.

The stellar mass, $M^\star$, was obtained by subtracting the gaseous mass from the dynamical mass. The mass of ionized and molecular hydrogen ($M_{\rm H^+}$ and $M_{\rm H_2}$) for the

Table 7.3: Derivation of the enclosed dynamical mass with projected radius for M 82

Source[(a)]	r [arcsec]	$v_{\rm peak}$ [(b)] [$\mathrm{km\,s^{-1}}$]	$v_{\rm rot}$ [(b)] [$\mathrm{km\,s^{-1}}$]	$M_{\rm dyn}$ [$\mathrm{M_\odot}$]
1	0.5	—	—	$(3 \pm 1) \times 10^7$
2	5	—	112 ± 5	$(2.6 \pm 0.2) \times 10^8$
	10	130 ± 20	137 ± 25	$(6.6 \pm 1.7) \times 10^8$
	20	138 ± 20	142 ± 24	$(1.4 \pm 0.3) \times 10^9$
3	7	130 ± 15	147 ± 23	$(5.3 \pm 1.2) \times 10^8$
	15	130 ± 20	140 ± 25	$(1.0 \pm 0.3) \times 10^9$
	23	145 ± 20	149 ± 26	$(1.8 \pm 0.4) \times 10^9$
4	10	110 ± 15	119 ± 20	$(4.9 \pm 1.2) \times 10^8$
	15	98 ± 15	104 ± 19	$(5.7 \pm 1.5) \times 10^8$
	30	88 ± 10	92 ± 14	$(8.9 \pm 1.9) \times 10^8$
	40	93 ± 10	96 ± 14	$(1.3 \pm 0.3) \times 10^9$

[(a)] (1) Gaffney, Lester & Telesco (1993): dynamical mass from the stellar velocity dispersion measured from the CO bandhead at 2.3 μm. (2) Achtermann & Lacy (1995): [Ne II] 12.8 μm line measurements, their model fit for the ionized ring at $r = 5''$ is used directly. (3) Shen & Lo (1995): CO $J = 1 \rightarrow 0$ line measurements. (4) McKeith *et al.* (1993): [S III] λ9069 Å line measurements.

[(b)] The rotational velocity $v_{\rm rot}$ at the projected radius r was computed from the observed tangential velocity $v_{\rm peak}$ corrected for inclination, beam smearing and velocity smearing (see text).

starburst core was estimated in chapter 5. Following the same procedure as described there for B1 and B2, the $M_{\rm H^+}$ for the central 35 pc was computed from the intrinsic $L_{\rm Lyc}$, and the $M_{\rm H_2}$ from the integrated CO $J = 1 \rightarrow 0$ emission map of Shen & Lo (1995) using the conversion factor between the CO intensity and H_2 column density from Wild *et al.* (1992) at the position of the nucleus. The dynamical, gaseous and stellar mass estimates for the central 35 pc and the starburst core of M 82 are given in table 7.4. It is here emphasized that the $M_{\rm H_2}$ adopted for the starburst core, taken from Wild *et al.* (1992), is an upper limit since it was determined in a region larger than 30″ in diameter.

Table 7.4: Dynamical, gaseous and stellar mass estimates for the central 35 pc and the starburst core of M 82

Region	$M_{\rm dyn}$ [$\mathrm{M_\odot}$]	$M_{\rm H_2}$ [$\mathrm{M_\odot}$]	$M_{\rm H^+}$ [(a)] [$\mathrm{M_\odot}$]	$M^\star$ [$\mathrm{M_\odot}$]
Central 35 pc	$(8.0 \pm 2.0) \times 10^7$	$8.2^{+16.4}_{-4.1} \times 10^5$	$6.6^{+25}_{-4.9} \times 10^4$	$7.9^{+2.2}_{-2.1} \times 10^7$
Starburst core	$(8.0 \pm 2.0) \times 10^8$	$(1.8 \pm 0.5) \times 10^8$	$7.6^{+27}_{-5.4} \times 10^6$	$6.1^{+2.7}_{-2.5} \times 10^8$

[(a)] The uncertainties include those on the ionizing luminosity, and on the electron density and temperature.

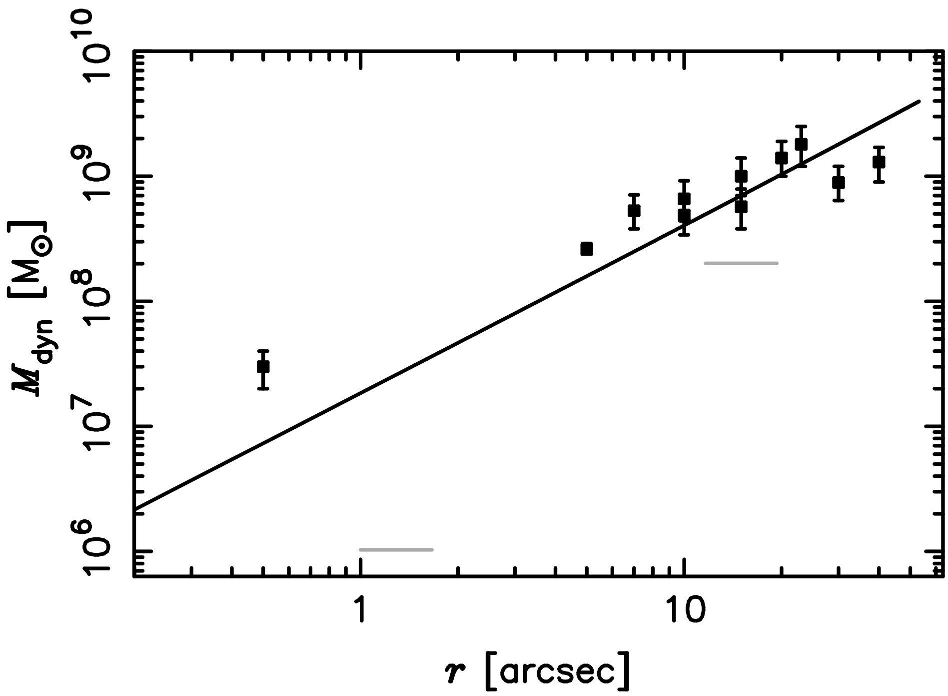

Fig. 7.1.— Enclosed dynamical mass versus projected radius in M 82. The data points are taken from table 7.3. The black line represents the mass model proposed by Götz *et al.* (1990). The grey horizontal line segments at projected radii of 1.3″ and 15″ indicate the contribution from the ionized and molecular hydrogen gas for the central 35 pc and the entire starburst core of M 82.

7.1.4 Rate of supernova explosions

The rate of supernova explosions ($\nu_{\rm SN}$) can be inferred from the radio emission at centimeter wavelengths, which is dominated by non-thermal synchrotron emission from electrons accelerated in supernova remnants (*e.g.* Kronberg, Biermann & Schwab 1985). For the entire starburst core of M 82, estimates vary in the range $0.02 - 0.1$ yr^{-1} (Kronberg, Biermann & Schwab 1985; van Buren & Greenhouse 1994; Huang *et al.* 1994; Muxlow *et al.* 1994; Allen & Kronberg 1998).

Alternatively, $\nu_{\rm SN}$ can be estimated from the [Fe II] 1.644 μm line emission assuming it originates in supernova remnants (SNRs) where the shock fronts sputter the interstellar dust grains and singly-ionize the liberated iron atoms. From the integrated [Fe II] 1.644 μm flux and the total $\nu_{\rm SN}$ from radio observations in M 82, Vanzi & Rieke (1997) have derived the following relationship:

$$\frac{\nu_{\rm SN}}{\rm yr^{-1}} = 1.25 \times 10^{-34} \left(\frac{L_{1.644\,\mu m}}{\rm W}\right), \tag{7.3}$$

assuming a constant [Fe II] $1.644\,\mu$m luminosity over a plausible lifetime of 10^4 yr in the [Fe II] emission phase (Lumsden & Puxley 1995). The average intrinsic line flux of 3×10^{-16} W m^{-2} for four compact sources candidate SNRs observed by Greenhouse *et al.* (1997) implies a calibration which predicts $\nu_{\rm SN}$'s about 50 times smaller.

The uncertainties on these calibrations are actually quite large. The radio and [Fe II] luminosities and lifetimes may be affected by the physical conditions of the interstellar medium (*e.g.* Chevalier 1982; Smith *et al.* 1998). Near-infrared observations may trace a different population of SNRs produced at a different epoch than the radio SNR's, as suggested by Greenhouse *et al.* (1997). The calibration based on the [Fe II] luminosity of individual candidate SNR's therefore likely underestimates $\nu_{\rm SN}$. On the other hand, other mechanisms may also produce [Fe II] emission, in particular collisional excitation by shocks associated with an outflowing starburst wind. The large-scale arc-like structure revealed by the line map from Greenhouse *et al.* (1997) and partly seen in the 3D map (figure 4.3) provides evidence for this hypothesis. This structure together with the more diffuse emission component account for $\approx 90\%$ of the integrated [Fe II] luminosity of M 82. Although the arc-like source may not trace directly the SNR's, it is probably related to $\nu_{\rm SN}$ indirectly since starburst winds presumably result from high rates of supernova explosions in nuclear starbursts (*e.g.* Tomisaka & Ikeuchi 1988; Heckman, Armus & Miley 1990). The calibration from Vanzi & Rieke (1997) based on the integrated [Fe II] luminosity of M 82 may therefore be more appropriate. The $\nu_{\rm SN}$ for the regions within the 3D field of view were estimated using Eq. 7.3 and the [Fe II] $1.644\,\mu$m line fluxes given in table 4.5, corrected for the extinction derived from the Brackett lines in section 5.1.7. The uncertainties are at least a factor of two, since the $\nu_{\rm SN}$ from radio observations is known to a factor of two.

7.2 Evolutionary synthesis modeling procedure for M 82

Evolutionary synthesis modeling is a fairly complex procedure, because of the number of parameters involved and of the complexity of starburst galaxies. Some parameters may be intimately related. Different properties trace different stellar populations which may have formed during distinct starburst events whose combined star formation history may not be well represented by simple monotonic functions. The procedure followed to model M 82 is outlined here.

Regions on scales of ≈ 20 pc to ≈ 450 pc are considered, providing information on the local and global properties of starburst activity in M 82, and on its evolution. The parameters constrained are:

- the upper and lower mass cutoffs of the IMF ($m_{\rm up}$ and $m_{\rm low}$),
- the burst age and timescale ($t_{\rm b}$ and $t_{\rm sc}$), and
- the initial star formation rate (R_0), characterizing the burst strength.

Most of the observational constraints are sensitive to $m_{\rm up}$, $t_{\rm sc}$ and $t_{\rm b}$, which are investigated simultaneously. Since the properties are not sensitive to $m_{\rm low}$ except for the mass, this parameter is constrained independently. R_0 is determined by comparing the predicted L_K and $L_{\rm Lyc}$ to the observed values.

Additional model parameters are kept constant. The IMF is assumed to have a Salpeter power-law index ($\mathrm{d}N/\mathrm{d}m \propto m^{-2.35}$). This choice will be justified in section 7.4. The metallicity of the stars is assumed to be solar (see chapter 6). The mass-loss rate for massive stars is chosen to be "normal" (see appendix B). The nebular parameters for the prediction of the [Ne III]/[Ne II] line ratio are those determined in chapter 5. Table 7.5 summarizes the ranges considered for the parameters to be constrained, and the values adopted for those which are kept constant. The effects of variations in the most critical parameters (such as dust grains mixed with the ionized gas, ionization parameter, shape of the intermediate- and high-mass IMF) will be briefly discussed when appropriate, in order to assess the robustness of the results.

Table 7.5: Summary of model parameters for the evolutionary synthesis of M 82

Parameter	Symbol	Value
	IMF	
Upper mass cutoff	$m_{\rm up}$	25 – 100 $M_\odot$
Lower mass cutoff	$m_{\rm low}$	0.1 – 5 $M_\odot$
Slope	α	2.35 (Salpeter)
	Star formation history	
Burst timescale	$t_{\rm sc}$	1 Myr – 1 Gyr
Burst age	$t_{\rm b}$	1 Myr – 100 Myr
Burst strength[(a)]	R_0	—
	Stellar properties	
Metallicity	—	Solar
Mass-loss rate	—	Normal
	Nebular properties	
Geometry[(b)]	—	Shell
Electron density	$n_{\rm e}$	300 $\rm cm^{-3}$
Ionization parameter[(c)]	$\log U$	−2.3 dex
Inner radius	R	25 pc
Gas-phase abundances	—	Solar
Interstellar dust	—	Neglected

[(a)] Characterized by the initial star formation rate.

[(b)] Geometry assumed for the photoionization modeling. $\log U$ and R are the effective values derived in chapter 5 representing adequately the true nebular conditions in the model geometry.

[(c)] Maximum value of the ionization parameter reached at the burst age for which the Lyman continuum luminosity is maximum (see chapter 3).

The ultimate goal of the modeling of M 82 is to constrain quantitatively the nature and evolution of its starburst activity. This is done by the following steps.

1. The general characteristics of starburst activity in M 82 are first constrained from the properties of selected representative regions; these are the cutoffs of the IMF and the typical burst timescale on various spatial scales (sections 7.3 and 7.4).
2. The contribution to the observed near-infrared properties from a population predating the starburst is constrained across the entire regions mapped with 3D (section 7.5).
3. Having determined the general properties of star formation and identified the most useful age indicators from the first two steps, the modeling is applied to individual regions across the entire 3D field of view to constrain the detailed starburst history and the spatial evolution of starburst activity (section 7.6).

7.3 Modeling of selected regions in M 82

In this section, evolutionary synthesis is applied to the central 35 pc of M 82, the Brγ sources B1 and B2, the entire 3D field of view, and the entire starburst core in order to constrain the upper mass cutoff of the IMF, and the burst age and timescale. The following diagnostic properties are used: [Ne III]/[Ne II], $L_{\rm bol}/L_{\rm Lyc}$, $L_K/L_{\rm Lyc}$, $W_{2.29}$, $W_{1.62}$ and $\nu_{\rm SN}/L_{\rm bol}$. For the typical young ages of starburst regions, none of these properties depends on the lower mass cutoff of the IMF. $m_{\rm low}$ is arbitrarily fixed at 1 $M_\odot$ for the models considered in this section.

The observed quantities from table 7.1 are compared to model predictions for single evolving clusters in figures 7.2 to 7.4. The models in figures 7.2 and 7.3 are computed for $m_{\rm up}$ = 100 $M_\odot$ and burst timescales of 1 Myr, 5 Myr, 20 Myr and 1 Gyr. Of all the properties considered, the [Ne III]/[Ne II] and $L_{\rm bol}/L_{\rm Lyc}$ ratios are the most sensitive to the upper mass cutoff. Models are shown for these two ratios in figure 7.4 for $m_{\rm up}$ = 25 $M_\odot$, 35 $M_\odot$, 50 $M_\odot$ and 100 $M_\odot$, and two burst timescales of 1 Myr and 5 Myr. The formal uncertainties on the measurements are indicated by the width of the horizontal bars in each plot. In addition, uncertainties are associated with the model curves themselves from the assumptions involved. The most important ones will be discussed at the end of this section.

The comparison of the data with the model predictions reveals age differences between the various regions, in particular between the central 35 pc of M 82 (older) and the Brγ sources (younger). The exact ages depend on the upper mass cutoff and on the star formation history, which are constrained first.

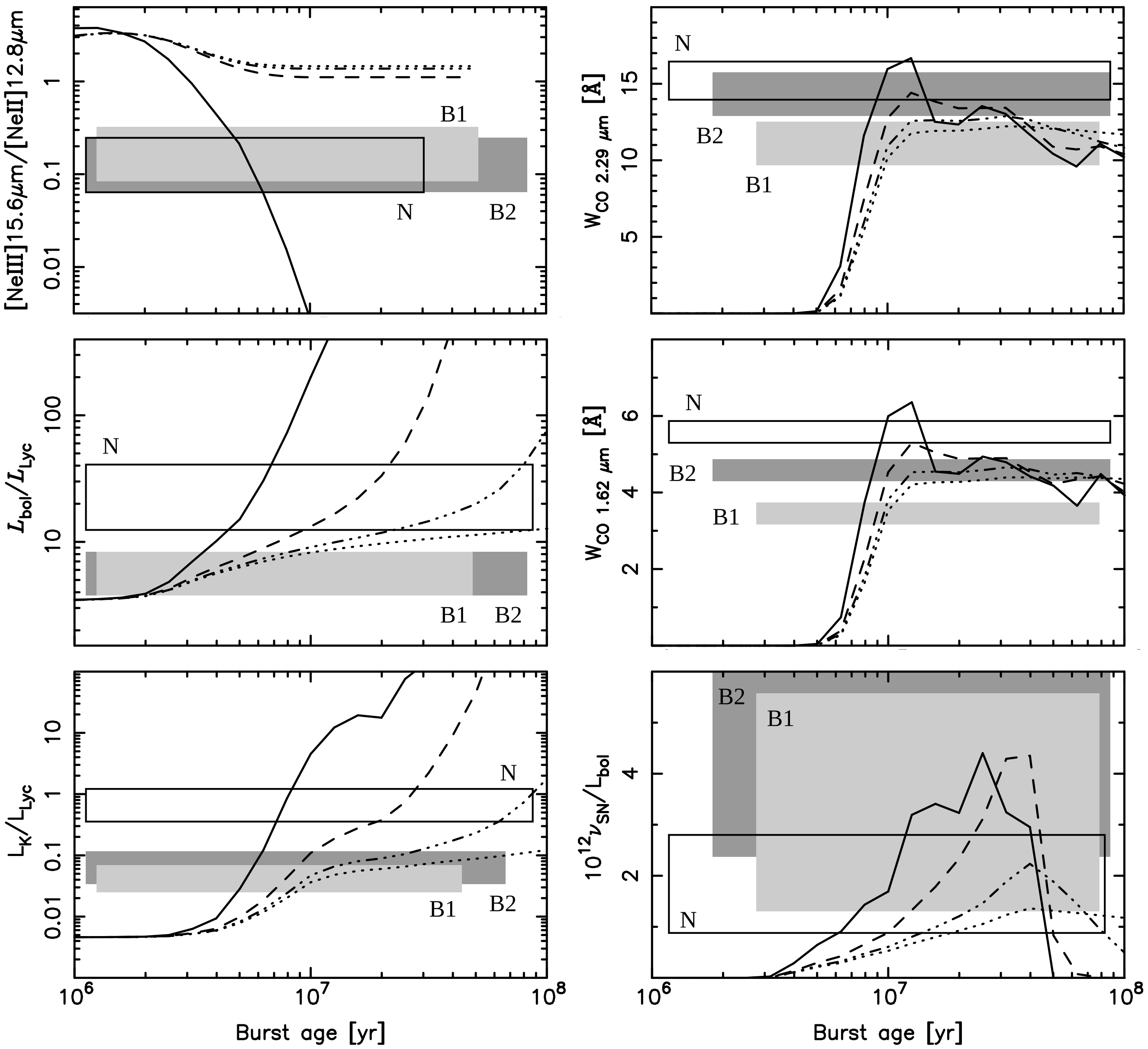

Fig. 7.2.— Comparison of the observed properties of the central 35 pc of M 82, B1 and B2 with model predictions for a single evolving cluster. The curves are computed for $m_{\rm up} = 100\ {\rm M}_\odot$ and four different burst timescales: 1 Myr (solid lines), 5 Myr (dashed lines), 20 Myr (dash-dot-dot-dot lines) and 1 Gyr (dotted lines). The other model parameters are given in the text. The different boxes indicate the measurements for the central 35 pc of M 82 (empty box labeled "N"), B1 (light-shaded box) and B2 (dark-shaded box).

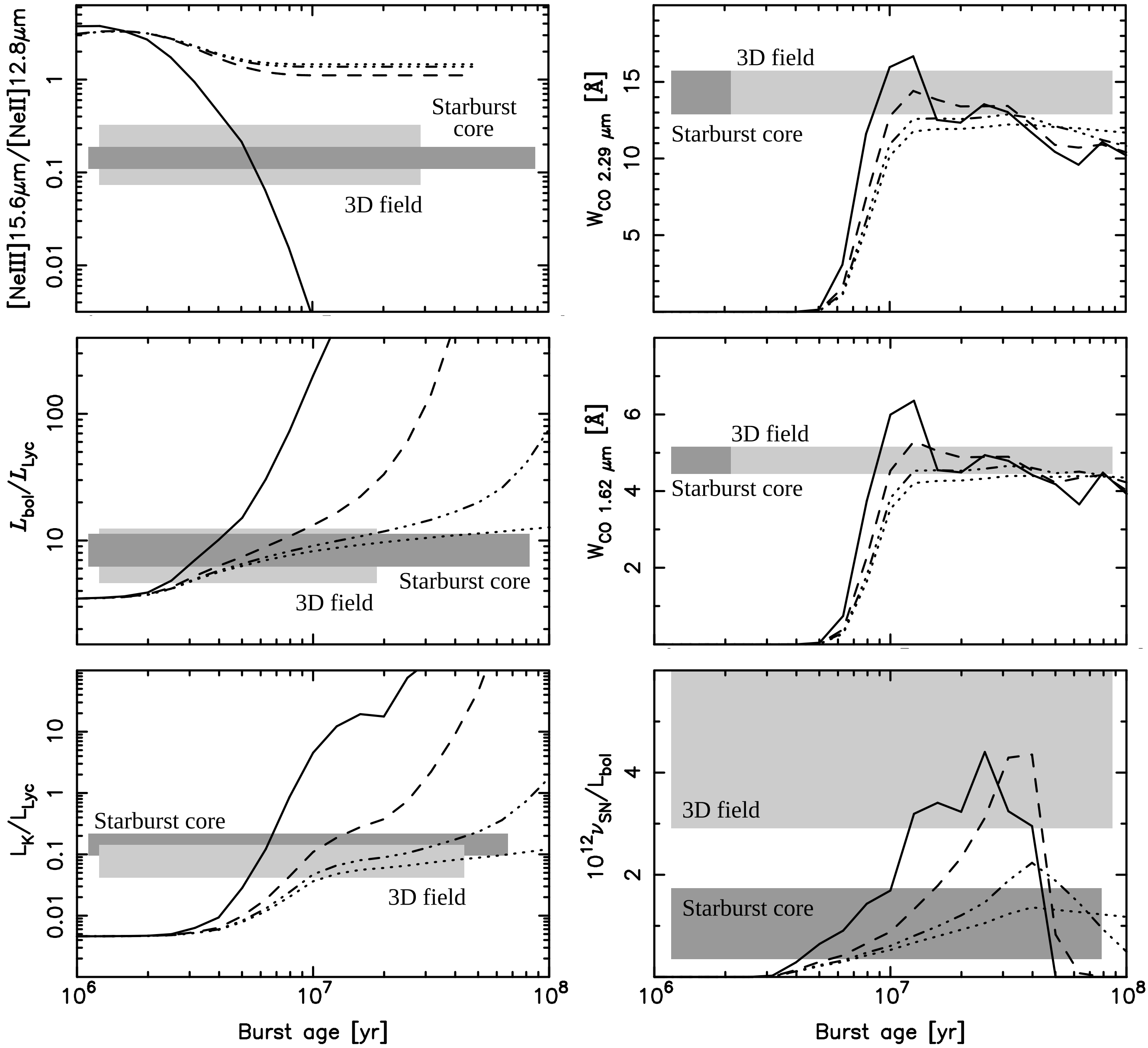

Fig. 7.3.— Comparison of the observed properties of the entire starburst core of M 82 (30″–diameter aperture centered on the nucleus) and for the entire 3D field of view with model predictions for a single evolving cluster. The curves are computed for $m_{\rm up} = 100\ \rm M_\odot$ and four different burst timescales: 1 Myr (solid lines), 5 Myr (dashed lines), 20 Myr (dash-dot-dot-dot lines) and 1 Gyr (dotted lines). The other model parameters are given in the text. The different boxes indicate the measurements for the starburst core of M 82 (dark-shaded box), and the 3D field of view (light-shaded box).

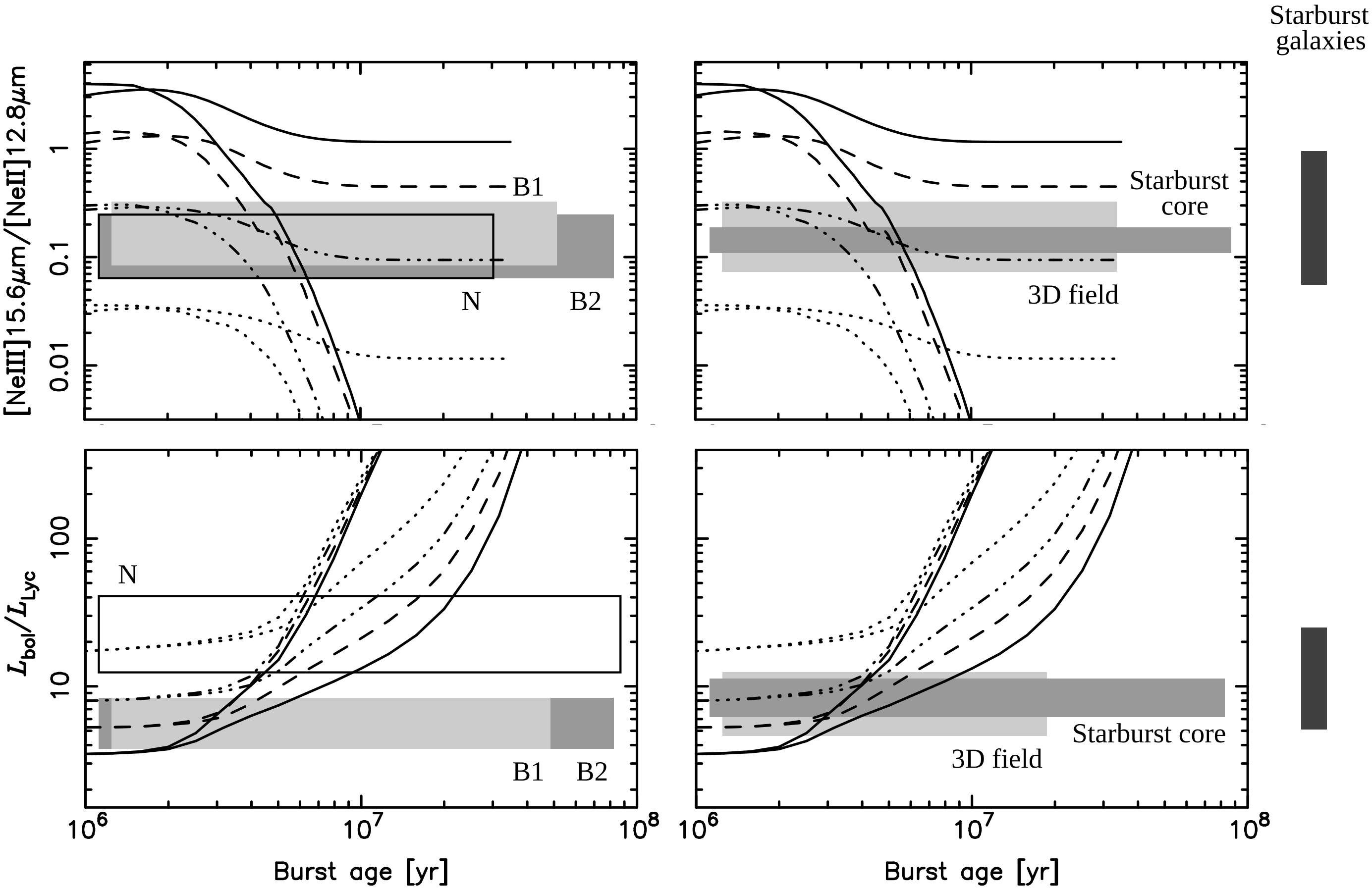

Fig. 7.4.— Comparison of the [Ne III]/[Ne II] and $L_{\rm bol}/L_{\rm Lyc}$ ratios for selected regions in M 82 with model predictions for a single evolving cluster with $m_{\rm up} = 100\ {\rm M}_\odot$ (solid lines), 50 $\rm M_\odot$ (dashed lines), 35 $\rm M_\odot$ (dash-dot-dot-dot lines) and 25 $\rm M_\odot$ (dotted lines). The models are illustrated for burst timescales of 1 Myr (steepest curves) and 5 Myr (flattest curves). The different boxes indicate measurements for different regions as in figures 7.2 (for the left-hand side panels) and 7.3 (for the right-hand side panels). The vertical bars on the right-hand side of the plots indicate the ranges of ratios for a sample of 25 starburst galaxies (with near-solar metallicities) observed with *ISO*-SWS (Thornley *et al.* 1998).

7.3.1 The upper mass cutoff and the burst timescale

The upper mass cutoff of the IMF is best constrained from the properties dominated by the young OB stars shown in figure 7.4. The similar excitation of the ionized gas for the regions considered imply the presence of similar populations of hot massive stars. The differences in $L_{\rm bol}/L_{\rm Lyc}$ between the various regions are mainly due to different contributions from the evolved stars to $L_{\rm bol}$ (table 7.2). These are relatively small for B1, B2 and the 3D field of view, but amount to 40% for the starburst core and 60% for the central 35 pc of M 82. Subtracting these contributions, the $L_{\rm bol}/L_{\rm Lyc}$ characterizing the OB stars (*i.e.* $L_{\rm IR}/L_{\rm Lyc}$) become nearly identical for all regions (in the range $5 - 10$), therefore also indicating similar populations of young stars. These ratios are typical of spectral types O8.5 V or slightly later, consistent with the nebular line ratios (chapter 5).

In general terms, the [Ne III]/[Ne II] ratios indicate relatively low excitation in the $\approx 2 - 4$ Ryd range, while the $L_{\rm IR}/L_{\rm Lyc}$ ratios indicate relatively high excitation at lower energies. From the comparison with the model curves in figure 7.4, two alternative interpretations are possible: *1)* a high upper mass cutoff $\gtrsim 50$ $M_\odot$, a short timescale of at most a few million years, and the softening of the ionizing radiation field attributable to aging of the starburst, *i.e.* very massive stars once formed but are now evolved or dead, or *2)* a lower upper mass cutoff down to ≈ 35 $M_\odot$ with possibly longer timescales, *i.e.* very massive stars never formed. Upper mass cutoffs below 30 $M_\odot$ are definitively ruled out, but the data do not allow us to constrain unequivocally $m_{\rm up}$ and $t_{\rm sc}$ for $m_{\rm up} > 30$ $M_\odot$.

High upper mass cutoffs and short timescales are, however, more plausible given the knowledge on local templates of starburst regions. Indeed, massive stars in the range 50 $M_\odot$ to > 100 $M_\odot$ are directly observed in young clusters and associations of OB stars in the Milky Way and in the Magellanic Clouds, independent of metallicity or other global galactic properties (*e.g.* reviews by Conti 1994, Leitherer 1998a and Massey 1998). Examples are the Galactic star-forming region NGC 3603 (*e.g.* Drissen *et al.* 1995; Eisenhauer *et al.* 1998), several clusters in the Galactic Center (*e.g.* Najarro *et al.* 1994; Krabbe *et al.* 1995; Cotera *et al.* 1996; Figer *et al.* 1998), and the R136 cluster powering the 30 Doradus nebula in the Large Magellanic Cloud (*e.g.* Melnick 1985; Brandl *et al.* 1996; Massey & Hunter 1998). Even the apparent upper mass cutoffs in sparser OB associations have been suggested to result from statistical limitations rather than physical limitations (Massey & Hunter 1998). Young clusters and OB associations in the Local Group of galaxies are thought to be representative of the "starburst units" which compose starburst galaxies although, with a few exceptions such as R136, they are less extreme in their compactness and luminosities than the super star clusters resolved by *HST* in several starburst systems.

Additional support for the formation of very massive stars in M 82 is provided by observations of other large-scale starburst systems. Many emission-line galaxies and giant extragalactic H II regions exhibit emission features characteristic of Wolf-Rayet stars in their integrated spectra, indicative of important populations of stars with initial masses $\gtrsim 30-40$ $M_\odot$ (*e.g.* Conti 1991, 1994; Maeder & Conti 1994). Furthermore, the [Ne III]/[Ne II] and $L_{\rm IR}/L_{\rm Lyc}$ ratios measured in M 82 are within the ranges determined for a sample of 25 dusty, solar-metallicity infrared-luminous starburst galaxies observed with the *ISO*-SWS. These ranges are shown in figure 7.4 and are compatible with $m_{\rm up} = 50-100$ $M_\odot$ or higher, with differences among the sample galaxies attributable to a range in burst ages and timescales (Thornley *et al.* 1998).

Various studies of Galactic and near-extragalactic starburst templates also indicate typical durations for the star-forming events of a few million years or less (see references above). In M 82, evidence for short burst timescales *locally* are the relative spatial distributions and the typical sizes of the line and continuum emission sources. Notably, the morphology of the K-band emission and CO bandhead EWs is very different from that of the ionized gas and thermal dust emission. This implies that star formation activity was not maintained locally at high levels during more than the main-sequence lifetime of the most massive stars which become red supergiants, *i.e.* ≈ 5 Myr. The complexes of ionized and molecular gas are clumpy on scales at least as small as $\approx$ 25 pc (*e.g.* Larkin *et al.* 1994; Achtermann & Lacy 1995; Shen & Lo 1995). The bright, compact K-band sources and the peaks in CO EWs have characteristic sizes of $15-30$ pc and are likely unresolved clusters of red supergiants (figure 4.3 and 4.4; Satyapal *et al.* 1997). Lastly, the super star clusters resolved by *HST* in visible light have typical half-peak intensity sizes of ~ 3.5 pc (O'Connell *et al.* 1995). Massive star formation strongly inhibits further star formation on such physical scales because OB stars inject large amounts of mechanical energy in the ISM. Strong stellar winds and supernova explosions disrupt the surrounding ISM already a few million years after the onset of star formation. The distribution of the ionized and molecular gas in the H II region complexes in M 82 depicted in chapter 5 is consistent with this scenario.

A remarkable result from the modeling is that the integrated [Ne III]/[Ne II] and $L_{\rm bol}/L_{\rm Lyc}$ ratios for the entire 3D field of view and starburst core of M 82 reveal **short burst timescales on large spatial scales** as well. This cannot be due to B1 and B2 dominating the integrated properties, as they contribute together $\approx 10\%$ and $\approx 5\%$ to the total $L_{\rm Lyc}$ and $L_{\rm bol}$ measured in the 3D field of view and central $30''$ of M 82 respectively. This suggests that **not only locally, but also globally, starburst**

activity has strong negative feedback effects inhibiting further star formation. Timescales of a few million years are significantly smaller than the canonical $10^7 - 10^8$ yr commonly assumed for starburst galaxies. This conclusion has important implications for the lifetimes of global starbursts, and dynamical models for the triggering and evolution of starbursts. This will be further discussed in section 7.7.

7.3.2 Successive starburst events

Adopting $m_{\rm up} = 100$ $\rm M_{\odot}$ and $t_{\rm sc} \sim 1$ Myr as justified above, the entire set of properties considered in this section is here examined from figures 7.2 and 7.3. For each region, there is a *systematic increase* from the ages implied by the tracers of hot, young stars ([Ne III]/[Ne II] and $L_{\rm bol}/L_{\rm Lyc}$ ratios) to those implied by the tracers of cool, evolved stars (CO bandheads). The $L_K/L_{\rm Lyc}$ ratios, measuring the relative populations of these stellar components, correspond to intermediate ages. The differences for each region are of a few million years, and are significant compared to the uncertainties in the data and in the models. In particular, single bursts sufficiently evolved for their integrated $W_{2.29}$ and $W_{1.62}$ to match the observed EWs fail to reproduce the observed ionizing luminosities and [Ne III]/[Ne II] ratios by factors of two or more.

This suggests that **the hot, young stars and the cool, evolved stars belong to populations formed in distinct, successive starburst events**. Models consisting of two sequential, short bursts separated in time by more than one timescale can reproduce simultaneously the observed properties much better than single bursts. The "young bursts" account for most of the ionizing radiation while the "old bursts" account for most of the L_K and for the strengths of the CO bandheads. Such two-burst models were first proposed by Rieke *et al.* (1993) for the entire starburst core, for similar reasons. The ages and durations for the two global bursts derived for the 3D field of view and for the starburst core (table 7.7 below) are in good agreement with the models of Rieke *et al.* (1993), despite some differences in the assumed IMF and in the function adopted to represent the star formation rate. These differences have small effects only on the properties relevant for constraining the general characteristics of the star formation history.

The evidence for two successive short bursts on various spatial scales and at different locations in M 82 is another remarkable result. In particular, while multiple events can be reasonably expected for regions extending over $\gtrsim 100$ pc, it seems more surprising for regions on scales of a few tens of parsecs or less. A likely explanation for M 82 is provided again by the morphology of various diagnostic tracers and by the kinematics of the interstellar gas. In particular, the general morphology of the K-band emission is very suggestive of a disk-like distribution for the evolved stars seen nearly edge-on, with a higher concentration towards the nucleus and indications of a stellar bar ~ 1 kpc long (*e.g.* Telesco *et al.* 1991; McLeod *et al.* 1993; Larkin *et al.* 1994). Even the compact sources associated with young clusters of red supergiants are concentrated in the "inner disk" within ≈ 150 pc of the nucleus, and at the edges of the putative stellar bar (*e.g.* Satyapal *et al.* 1997). In addition, the distribution of young radio supernova remnants is quite uniform along the galactic plane and extends over ≈ 600 pc (*e.g.* Kronberg, Biermann & Schwab 1985). In contrast, the spatial distribution and kinematics of the ionized and molecular gas reveal that these components are mainly concentrated in a highly inclined torus or tightly wound spiral arms, at radii between ≈ 80 pc and ≈ 400 pc (*e.g.* Larkin *et al.* 1994; Achtermann & Lacy 1995; Shen & Lo 1995). In particular, in the vicinity of the nucleus, the Brγ emission follows a ridge slightly displaced to the north of the prominent central concentration of K-band emission (figure 4.3), and the corresponding [Ne II] 12.8 μm sources likely lie on the near side of an "ionized ring" (Achtermann & Lacy 1995). This suggests that the young bursts in the central few tens of parsecs are not spatially coincident with the old bursts and, more generally, that the superposition of two starburst populations along various lines of sight results from projection effects.

7.3.3 The burst age and strength

For each region, two successive starburst events thus have to be accounted for. The age for the young and the old bursts are constrained from the indicators tracing exclusively the OB stars ([Ne III]/[Ne II] and $L_{\mathrm{IR}}/L_{\mathrm{Lyc}}$ ratios) and the cool, evolved stars ($W_{2.29}$ and $W_{1.62}$). The initial star formation rates are determined from the observed L_K and L_{Lyc}. For each burst at each region, $m_{\mathrm{up}} = 100$ is assumed and $t_{\mathrm{sc}} = 1$ Myr is chosen to represent the short burst duration.

The ages inferred from both indicators for the young bursts agree marginally, the [Ne III]/[Ne II] ratio implying slightly older ages than the $L_{\mathrm{IR}}/L_{\mathrm{Lyc}}$ ratio[2]. In view of the possible errors on the predicted and equivalent [Ne III]/[Ne II], and on the observed $L_{\mathrm{IR}}/L_{\mathrm{Lyc}}$ ratios, this small discrepancy is however not significant. For instance, the combined uncertainties from the derivation of the equivalent [Ne III]/[Ne II], on the nebular parameters and of the theoretical model atmospheres are estimated to be a factor of $2-3$. L_{IR} could also be underestimated if more than 30% of the light from blue stars escapes in directions perpendicular to the galactic plane of M 82, although it is unlikely that more than half of L_{IR} is missing (for full agreement with the nebular

[2] this discrepancy would not be solved by other choices of m_{up} and t_{sc}

line ratios) in the estimates from mid-infrared flux densities. The small discrepancy is moreover comparable to the burst timescale, and could also be attributed to the fact that an exponentially decaying function may not accurately represent the true star formation rate (see section 7.6). The effects of a distribution of cluster masses and luminosities or of interstellar dust grains, neglected here, would increase the discrepancy as discussed below. The same weight is therefore assigned to both diagnostic ratios in determining the age of the young bursts. If the ages were inferred from [Ne III]/[Ne II] only, larger R_0 would be required to reproduce the observed $L_{\rm Lyc}$ since the predicted $L_{\rm Lyc}$ decreases with age. On the other hand, if $L_{\rm IR}/L_{\rm Lyc}$ only were used, the younger ages would imply lower R_0. Increasing $t_{\rm sc}$ by a few million years would decrease R_0. The uncertainties on the derived R_0 for the young bursts are estimated to be of a factor of a few.

For the old bursts, an accurate age determination is only possible for the central 35 pc of M 82. Indeed, the $W_{2.29}$ and $W_{1.62}$ are very high and the models reproduce such high values only for ages of 8−15 Myr, when massive red supergiants dominate the near-infrared luminosity. The deep CO bandheads further support short burst timescales: for $t_{\rm sc} \geq 5$ Myr, dilution by older populations with shallower bandheads and/or nebular emission associated with main-sequence stars result in predicted integrated EWs lower than observed. Older ages corresponding to those when intermediate-mass stars reach the end of the AGB phase (~ 50 Myr $-$ 1 Gyr) are also ruled out from the $W_{2.29}$, as can be seen from figure 7.5. The age and timescale for the old burst in the central 35 pc of M 82 agree with the average spectral type K5 I found from the population synthesis in chapter 6. Similar conclusions concerning the age of the cool, evolved stellar population were reached by Rieke *et al.* (1980, 1993) for the central 6″ (90 pc) of M 82, and by Satyapal *et al.* (1997) for the central 2″ (30 pc).

For the other selected regions, firm lower limits on the ages for the old bursts can be set, but the EWs alone do not provide strong constraints above these limits. The ranges observed for old ($1 - 10$ Gyr) stellar populations characteristic of the central regions of elliptical galaxies and bulges of spiral galaxies (hereafter "normal populations"; from Oliva *et al.* 1995) are shown in figure 7.5. The EWs at B1 are somewhat lower than for normal populations, and possibly indicate rather an early stage with the first massive stars becoming red supergiants. For B2, the 3D field of view and the entire starburst core, they are slightly higher, and imply possible upper limits on the age of ≈ 50 Myr and on the timescale of ≈ 5 Myr. An additional constraint on the nature of the evolved stellar populations is provided by the $M^{\star}/L_K$ ratio, which will be discussed in section 7.5 below. Briefly, the very low values measured at all radii strongly suggest that luminous red supergiants dominate the near-infrared continuum emission throughout the starburst core of M 82, even in regions of lower surface brightness. Ages $\lesssim 50$ Myr

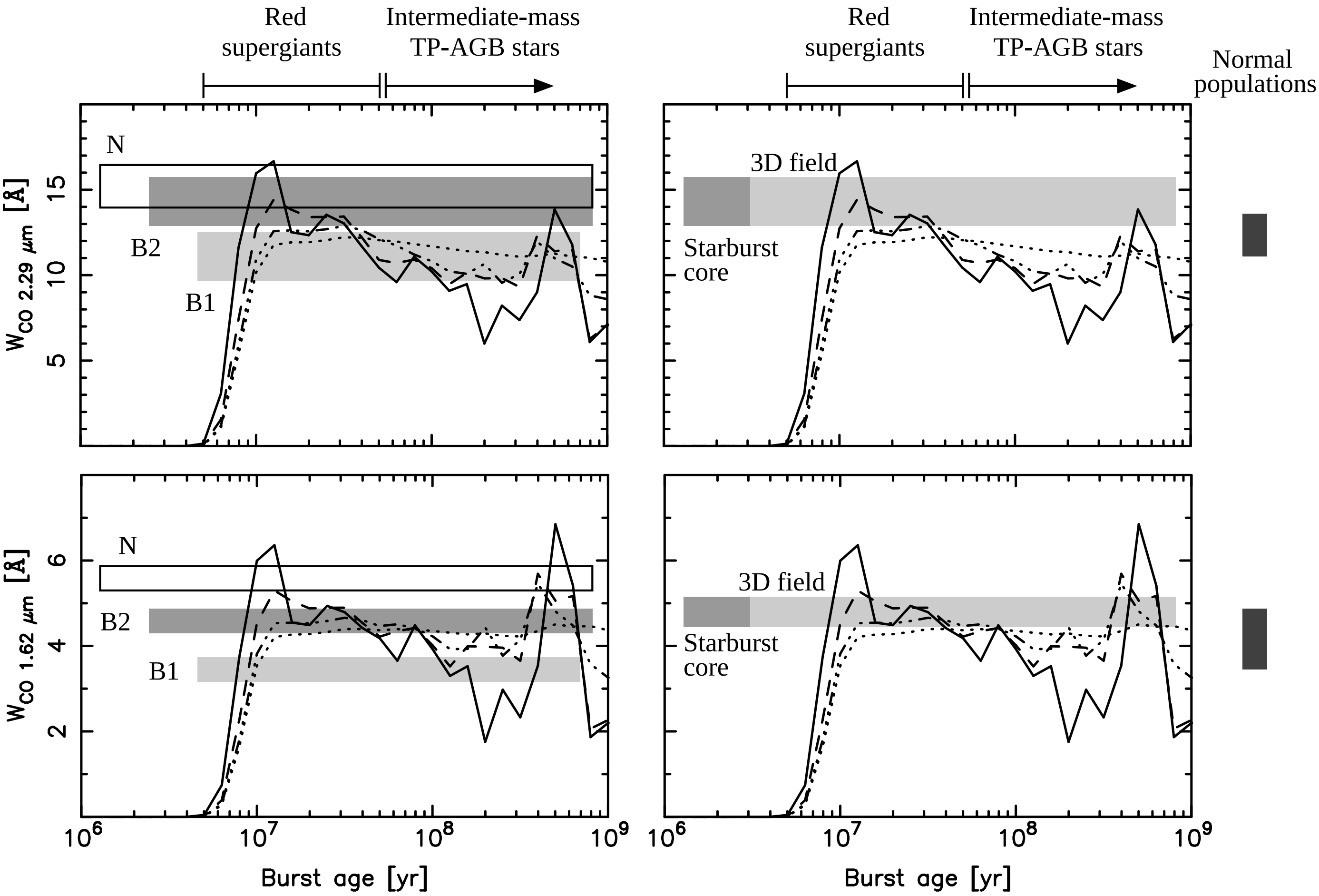

Fig. 7.5.— Comparison of the strength of the CO bandheads measured in selected regions of M 82 with model predictions for single evolving clusters. The model curves are the same as in figures 7.2 and 7.3 ($m_{\rm up} = 100$ M$_\odot$, and $t_{\rm sc} = 1$ Myr, 5 Myr, 20 Myr and 1 Gyr for the solid, dashed, dash-dot-dot-dot and dotted lines respectively). A larger range of burst ages is shown to compare the EWs during the phases when red supergiants dominate the near-infrared continuum emission and when intermediate-mass stars become important contributors, in particular thermally-pulsing AGB (TP-AGB) stars. The vertical bars on the right-hand side of the plots indicate the ranges of EWs observed for normal stellar populations, characteristic of elliptical galaxies and bulges of spiral galaxies (Oliva *et al.* 1995).

are therefore the most plausible; the youngest solutions will be adopted, corresponding to the rising part of the predicted $W_{2.29}$ and $W_{1.62}$. Within the possible ranges in age and timescale, the R_0 for the old bursts would increase for older ages, decrease for timescales longer than 1 Myr, and are uncertain to a factor of a few.

7.3.4 Model results for selected regions in M 82

The two-burst models for the various regions considered in this section are illustrated in figure 7.6 and summarized in tables 7.6 and 7.7. The curves in figure 7.6 are the predictions for the most relevant properties (L_K, $L_{\rm Lyc}$, $L_{\rm bol}$, $W_{2.29}$ and the [Ne III]/[Ne II] ratio) as a function of the time elapsed since the onset of the old burst. The model curves are simply those of figures 7.2 and 7.3 for $m_{\rm up} = 100$ $M_\odot$ and $t_{\rm sc} = 1$ Myr, properly combined for the two bursts, and normalized to the observed values for each property. The models for all regions reproduce the main constraints within a factor of three or better. The predicted masses for the central 35 pc and the starburst core are substantially lower than the observed values. However, the observed stellar masses likely include the contributions from a population predating the starburst (see section 7.4).

For identical IMF parameters and burst timescales, the initial star formation rates R_0 provide a meaningful measure of the relative strengths of the different bursts. The strengths of both successive bursts within each region were comparable — within a factor of two — except for the central 35 pc for which the old burst was about $4-5$ times stronger than the young one. Furthermore, the strengths of the bursts among the small-scale regions were also similar, again with the exception of the old central burst. This contrast is even more striking if the R_0 per unit volume are compared. For B1, B2 and the starburst core, the volumes adopted in the derivation of the effective $\log U$ in chapter 5 are used. For the central 35 pc of M 82, the sources are assumed to occupy a spherical volume of radius 19.5 pc. Although the exact distribution of the sources along the line of sight is relatively uncertain, these crude estimates show the exceptional strength of the old burst in the inner few tens of parsecs of M 82, which was about $1-2$ orders of magnitude more intense than the subsequent young burst, and than both old and young bursts elsewhere. If older ages between 15 Myr and 50 Myr are adopted for B1, B2, the 3D field of view and the starburst core, the old bursts become stronger but the star formation rate densities remain nonetheless factors of several lower than in the central 35 pc of M 82. The R_0 is very sensitive to $m_{\rm low}$ because most of the mass is in low-mass stars. For different $m_{\rm low}$, the correction factor for R_0 is given by Eqs. 3.4 and 3.5 assuming a constant IMF slope over the entire stellar mass range. However, the relevant feature here is the *relative strength* between the various regions, which is independent of $m_{\rm low}$ assuming it is constant throughout M 82.

The models for each region are consistent with the constraints imposed by $\nu_{\rm SN}$ and $10^{12}\,\nu_{\rm SN}/L_{\rm bol}$. A good agreement for the regions included in the 3D field of view is not expected since, as discussed in section 7.1.4, the [Fe II] $1.644\,\mu$m may not be an accurate tracer of the *local* rate of supernova explosions. The ages inferred for the old bursts satisfy the "timing constraint" implied by the extent of the X-ray halo tracing the supernova-driven starburst wind, requiring a minimum age for starburst activity of approximately 10 Myr (Heckman, Armus & Miley 1990; Rieke *et al.* 1993).

7.3.5 Effects of a cluster luminosity distribution

An important consideration concerns the effects of a distribution of cluster masses and luminosities in the interpretation of the observed properties. Model predictions for an *ensemble* of evolving clusters with a luminosity distribution are, in principle, more appropriate for such large-scale regions as the starburst core and 3D field of view, and even for the small-scale regions. Indeed, the ionizing rates measured at B1 and B2 imply at each location the presence of $2000 - 3000$ ionizing clusters, with a few tens of the most luminous and massive ones (see table 5.8). The ionizing rate for the central 35 pc of M 82 is lower, but still implies ≈ 1000 ionizing clusters.

As discussed in chapter 3, plausible luminosity distributions for the young clusters in starburst galaxies can affect the observed properties by factors up to a few. The properties of the entire starburst core, which are also representative of the selected regions considered in this section, are compared in figure 7.7 to model predictions for an ensemble of evolving clusters following the luminosity function derived in chapter 3 (Eqs. 3.9 and 3.10). The global upper mass cutoff is 100 $M_\odot$, and two representative timescales are illustrated: 1 Myr and 5 Myr. Accounting for a distribution of cluster luminosities has small effects only in the interpretation of the data of M 82. These effects tend to reinforce the conclusions of a high upper mass cutoff, and imply similar ages within < 0.5 Myr. Therefore, in the particular case of M 82, modeling based on predictions for single evolving clusters is adequate with regard to the determination of the main star formation parameters.

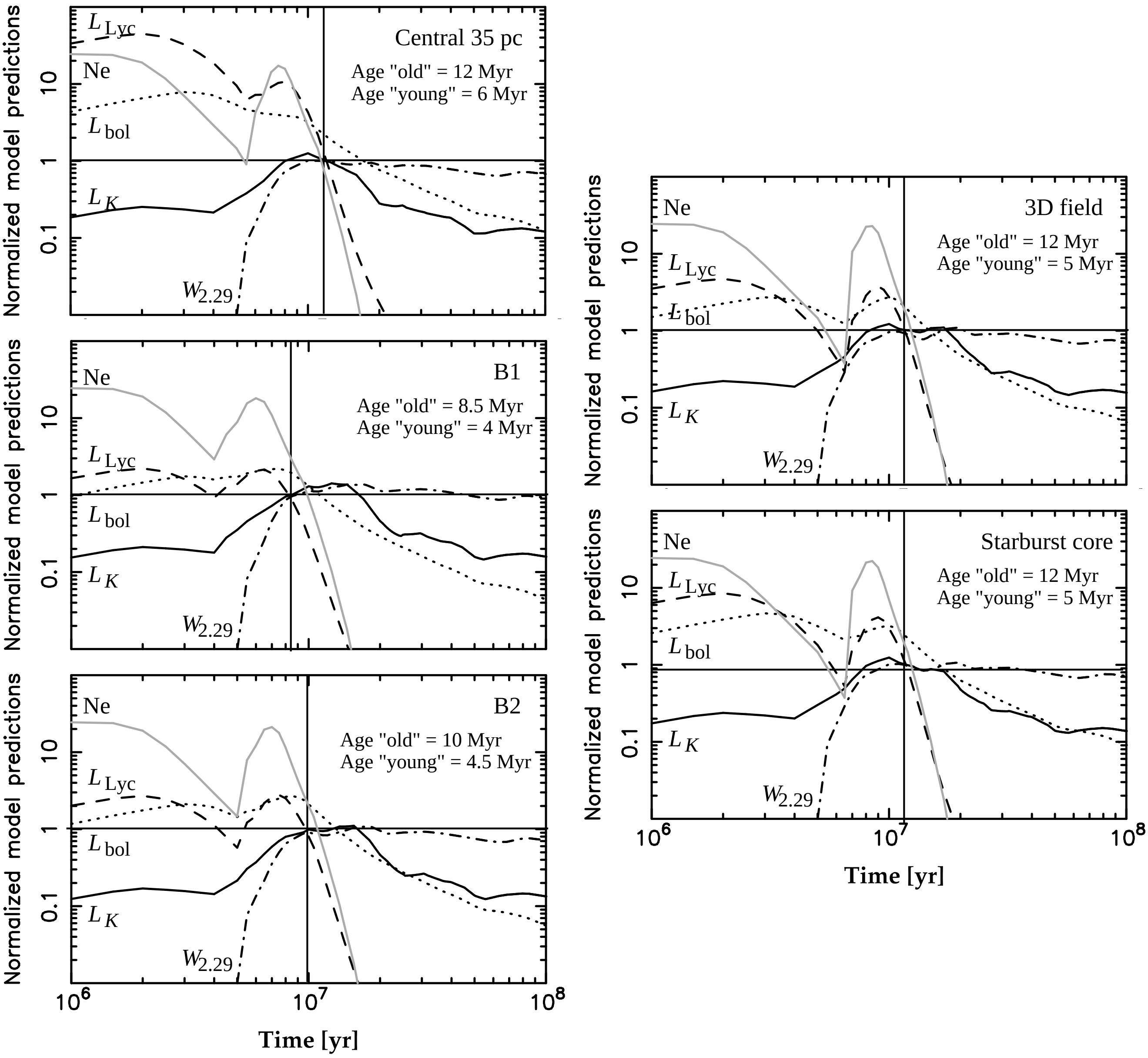

Fig. 7.6.— Starburst models for selected regions in M 82. The various curves (labeled in each plot, with "Ne" denoting the [Ne III]/[Ne II] ratio) represent the evolution of the integrated properties for the two successive short bursts that best reproduce the data. The burst timescale is 1 Myr, and the upper mass cutoff is 100 $M_\odot$. The horizontal axis represents the time elapsed since the onset of the first burst. The ages for the two bursts ("old" and "young") fitted for each region are given in the plots. The onset of the second burst is most apparent in the sudden increase of $L_{\rm Lyc}$ and of the [Ne III]/[Ne II] ratio. The curves are normalized to the observed values. Ideally, they should all meet at unity (horizontal line) at the appropriate age for the old burst (vertical line).

Table 7.6: Starburst models for the central 35 pc of M 82, and the Brγ sources B1 and B2

Central 35 pc

Parameter	Units	Young burst		Old burst	
t_b	Myr	6		12	
R_0	$M_\odot\ yr^{-1}$	1.7		7.8	
$< R_0 >_V$ [(a)]	$M_\odot\ yr^{-1}\ pc^{-3}$	7.6×10^{-5}		3.5×10^{-4}	
Property	**Units**	**Observed**	**Young burst**	**Old burst**	**Total**
L_K	$10^8\ L_\odot$	0.56 ± 0.23	0.054	0.51	0.56
L_{Lyc}	$10^8\ L_\odot$	0.67 ± 0.25	0.61	0.051	0.66
L_{bol}	$10^8\ L_\odot$	18 ± 9	16	21	37
$M^\star$	$10^8\ M_\odot$	$0.79^{+0.22}_{-0.21}$	0.017	0.078	0.095
$W_{1.62}$	Å	5.6 ± 0.3	0.59	6.3	5.7
$W_{2.29}$	Å	15.2 ± 1.2	2.4	16.5	15.2
ν_{SN} [(b)]	$10^{-2}\ yr^{-1}$	0.25	0.13	0.60	0.73
[Ne III]/[Ne II] [(b)]	—	0.13	0.09	0.0004	0.09

B1

Parameter	Units	Young burst		Old burst	
t_b	Myr	4		8.5	
R_0	$M_\odot\ yr^{-1}$	0.8		0.9	
$< R_0 >_V$ [(a)]	$M_\odot\ yr^{-1}\ pc^{-3}$	3.0×10^{-6}		3.3×10^{-6}	
Property	**Units**	**Observed**	**Young burst**	**Old burst**	**Total**
L_K	$10^8\ L_\odot$	0.074 ± 0.024	0.012	0.062	0.074
L_{Lyc}	$10^8\ L_\odot$	1.5 ± 0.4	1.3	0.044	1.3
L_{bol}	$10^8\ L_\odot$	8.9 ± 3.1	12.8	4.4	17.2
$M^\star$	$10^8\ M_\odot$	—	0.008	0.009	0.017
$W_{1.62}$	Å	3.4 ± 0.3	0.0	4.4	3.7
$W_{2.29}$	Å	11.2 ± 1.4	0.0	12.9	10.8
ν_{SN} [(b)]	$10^{-2}\ yr^{-1}$	0.25	0.04	0.07	0.11
[Ne III]/[Ne II] [(b)]	—	0.16	0.47	0.01	0.45

B2

Parameter	Units	Young burst		Old burst	
t_b	Myr	4.5		10	
R_0	$M_\odot\ yr^{-1}$	1.4		1.4	
$< R_0 >_V$ [(a)]	$M_\odot\ yr^{-1}\ pc^{-3}$	3.2×10^{-6}		3.2×10^{-6}	
Property	**Units**	**Observed**	**Young burst**	**Old burst**	**Total**
L_K	$10^8\ L_\odot$	0.15 ± 0.05	0.028	0.12	0.15
L_{Lyc}	$10^8\ L_\odot$	2.0 ± 0.9	1.63	0.027	1.7
L_{bol}	$10^8\ L_\odot$	12 ± 4	20.5	5.4	25.9
$M^\star$	$10^8\ M_\odot$	—	0.014	0.014	0.028
$W_{1.62}$	Å	4.6 ± 0.3	0.02	6.0	4.8
$W_{2.29}$	Å	14.4 ± 1.4	0.08	16.0	13.0
ν_{SN} [(b)]	$10^{-2}\ yr^{-1}$	0.58	0.09	0.09	0.18
[Ne III]/[Ne II] [(b)]	—	0.12	0.32	0.003	0.32

[(a)] Assuming a spherical volume of radius 19.5 pc for the central 35 pc of M 82, and cylindrical volumes with radii of 19.5 pc and lengths of 230 pc and 365 pc for B1 and B2 (as in table 5.7).

[(b)] The constraints on [Ne III]/[Ne II] are uncertain to a factor of two, and on ν_{SN} to a factor of $2-3$.

Table 7.7: Starburst models for the 3D field of view and the starburst core of M 82

3D field of view

Parameter	Units	Young burst		Old burst	
$t_{\rm b}$	Myr	5		12	
R_0	$\rm M_\odot\,yr^{-1}$	26		33	
Property	Units	Observed	Young burst	Old burst	Total
L_K	10^8 $\rm L_\odot$	2.7 ± 0.8	0.59	2.1	2.7
$L_{\rm Lyc}$	10^8 $\rm L_\odot$	27 ± 13	21.1	0.21	21.3
$L_{\rm bol}$	10^8 $\rm L_\odot$	220 ± 90	320	90	410
$M^\star$	10^8 $\rm M_\odot$	—	0.26	0.33	0.59
$W_{1.62}$	Å	4.8 ± 0.3	0.04	6.3	4.8
$W_{2.29}$	Å	14.4 ± 1.4	0.14	16.5	12.9
$\nu_{\rm SN}$ (a)	$10^{-2}\,\rm yr^{-1}$	13	2.0	2.5	4.5
[Ne III]/[Ne II] (a)	—	0.16	0.23	0.0004	0.23

Starburst core (b)

Parameter	Units	Young burst		Old burst	
$t_{\rm b}$	Myr	5		12	
R_0	$\rm M_\odot\,yr^{-1}$	81		170	
$< R_0 >_V$ (b)	$\rm M_\odot\,yr^{-1}\,pc^{-3}$	3.2×10^{-6}		6.8×10^{-6}	
Property	Units	Observed	Young burst	Old burst	Total
L_K	10^8 $\rm L_\odot$	13 ± 4	1.8	11.2	13.0
$L_{\rm Lyc}$	10^8 $\rm L_\odot$	77 ± 23	66.0	1.1	67.1
$L_{\rm bol}$	10^8 $\rm L_\odot$	660 ± 120	990	470	1460
$M^\star$	10^8 $\rm M_\odot$	$6.1^{+2.7}_{-2.5}$	0.8	1.7	2.5
$W_{1.62}$	Å	4.8 ± 0.3	0.04	6.3	5.3
$W_{2.29}$	Å	14.5 ± 1.4	0.14	16.5	14.2
$\nu_{\rm SN}$ (a)	$10^{-2}\,\rm yr^{-1}$	6	6.4	13.3	19.7
[Ne III]/[Ne II]	—	0.16 ± 0.04	0.23	0.0004	0.23

(a) The constraint on [Ne III]/[Ne II] for the 3D field of view is uncertain to a factor of two, and those on $\nu_{\rm SN}$ for both regions, to a factor of $2-3$.

(b) The starburst core corresponds to a $30''$–diameter aperture centered on the nucleus, but the bulk of the sources of emission are assumed to be distributed in an edge-on disk of radius and thickness of 200 pc (as in table 5.7).

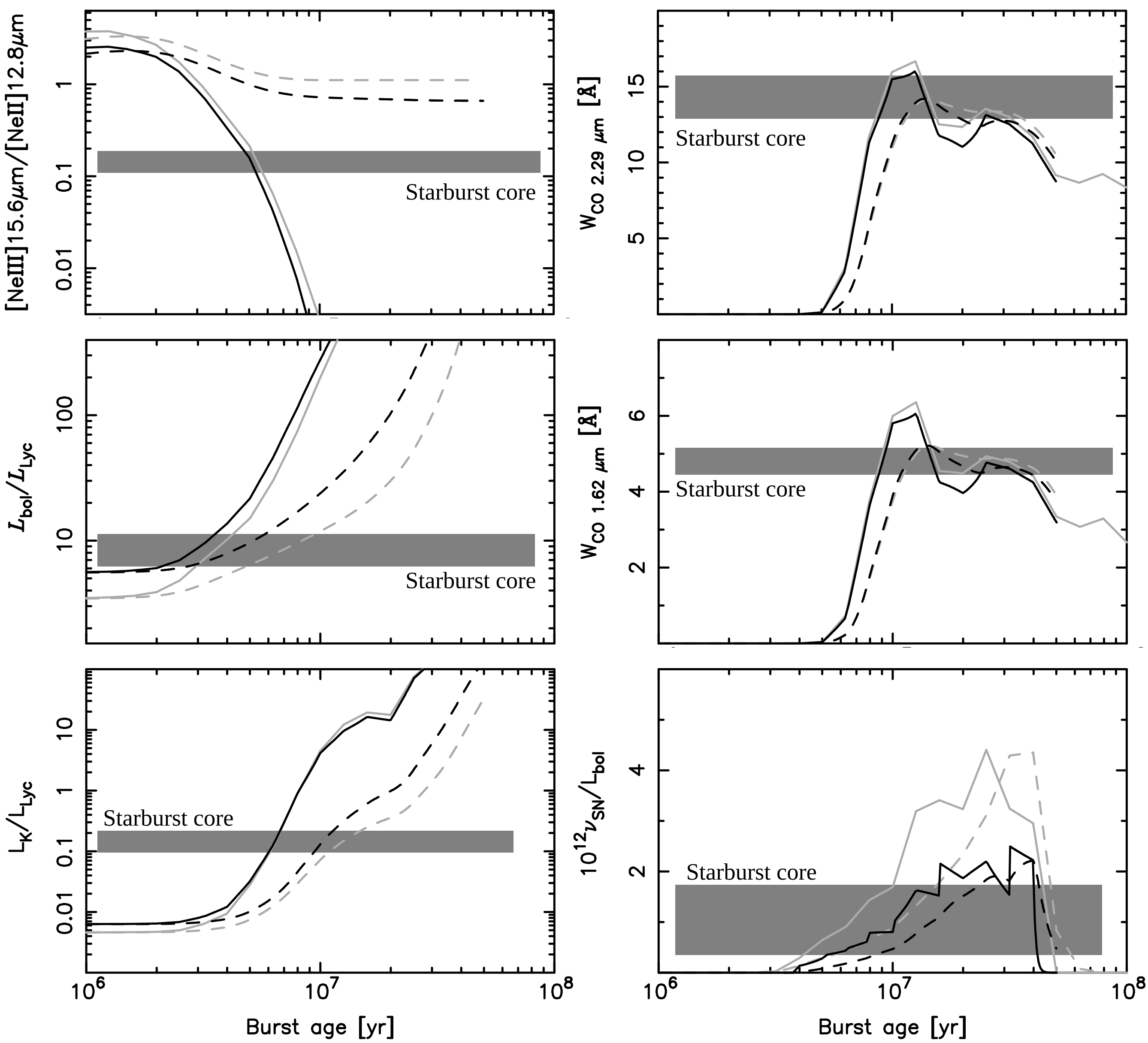

Fig. 7.7.— Effects of a distribution of cluster luminosities in the interpretation of the observed properties for M 82. The data for the entire starburst core, representative of the other selected regions considered in this section, are shown by the horizontal bars. The model curves (black lines) are computed for an ensemble of clusters whose distribution is described by a luminosity function with parameters suitable for starburst galaxies (from Eqs. 3.9 and 3.10 in chapter 3). The global $m_{\rm up}$ for the ensemble of clusters is 100 $M_\odot$. Two representative timescales for the cluster formation rate are illustrated: 1 Myr and 5 Myr (solid and dashed lines respectively). Model predictions for a single cluster are shown for comparison (grey lines), for the same timescales and a cluster $m_{\rm up} = 100\ M_\odot$.

7.3.6 Uncertainties from the model assumptions

The most important uncertainties from the various assumptions made in the modeling presented in this section are discussed here. They do not, however, affect the general characteristics of starburst activity in M 82 derived above (high upper mass cutoff of the IMF, two short successive starburst events, relative strength of the bursts).

- **Effects of nebular parameters**

The most critical nebular parameters for the interpretation of nebular line ratios are the ionization parameter and the assumptions on the ISM composition. For the plausible range of $\log U$ from -2 dex to -2.5 dex derived for M 82 in chapter 5, He I 2.058/Brγ is very little affected and [Ne III]/[Ne II] varies by at most a factor of two relative to the predictions for the adopted $\log U = -2.3$ dex. This is relatively small compared to the variations with the effective temperature of the ionizing stars, and thus to evolutionary effects and to the upper mass cutoff of the IMF. The uncertainties on the ionization parameter do not affect the conclusions concerning $m_{\rm up}$ and $t_{\rm sc}$, and imply uncertainties $\lesssim 0.5$ Myr on the burst ages inferred from the [Ne III]/[Ne II] ratio.

The effects of interstellar dust grains mixed with the ionized gas in the H II regions have been neglected in the models presented here. These effects are potentially important for the nebular line ratios, as discussed in chapter 5, but also for $L_{\rm Lyc}$. Dust competes effectively with gas in absorbing ionizing photons, more importantly at lower ionizing energies since the absorption cross-section for standard interstellar dust grains generally increases at longer wavelengths — in particular between the ionization edges of Ne^0 and Ne^+ (*e.g.* Draine & Lee 1984; Mathis 1990). Accounting for dust grains in the photoionization models would therefore increase the predicted [Ne III]/[Ne II] ratios from the emergent spectrum of the nebulae. Similarly, the He I 2.058/Brγ ratio from which the equivalent [Ne III]/[Ne II] ratio is derived for the regions mapped with 3D would increase. This would be partly compensated by the increased absorption of the resonant He I Lyα photons at 584 Å, reducing the He I 2.058 μm line flux (see appendix D). The ages inferred from the nebular line ratios would thus be slightly larger. The predictions for single star temperatures shown in chapter 5 allow an estimate of the effects of dust: for a dust mixture typical of the Orion nebula and the related depletion of gas-phase heavy elements, the [Ne III]/[Ne II] and He I 2.058/Brγ ratios increase by 30% or less. This implies in turn negligible differences in the burst ages inferred from the nebular line ratios.

Since the $L_{\rm Lyc}$ were inferred from recombination line measurements, they could be significantly underestimated if dust grains were mixed with the ionized gas. Accounting for dust, the ages inferred from $L_{\rm IR}/L_{\rm Lyc}$ would be lower, and would therefore introduce a significant discrepancy with those inferred from [Ne III]/[Ne II]. However, the $L_{\rm IR}/L_{\rm Lyc}$ ratios are already close to the lowest values predicted for the youngest ages and high $m_{\rm up}$, and agree marginally with [Ne III]/[Ne II] for the ages of the young bursts. The effects of dust on the inferred $L_{\rm Lyc}$ are not likely to exceed a factor of two, and are probably smaller.

• Effects of the shape of the IMF

All the properties considered in this section are dominated by high-mass stars (initial masses $\gtrsim 10$ M$_\odot$). The effects of changes in the shape of the high-mass IMF, within the range for OB clusters and associations in the Milky Way and Magellanic Clouds (section 7.4), are small in comparison to evolutionary effects or to the upper mass cutoff. For example, a steeper IMF such as that proposed by Miller & Scalo (1979), which has $\alpha \approx 3.3$ above 10 M$_\odot$ (see section 7.4), implies differences of at most $\approx 50\%$ in the properties used to constrain $m_{\rm up}$, $t_{\rm sc}$ and $t_{\rm b}$ compared to predictions for a Salpeter IMF ($\alpha = 2.35$), with the largest differences for the [Ne III]/[Ne II] and $L_{\rm bol}/L_{\rm Lyc}$ ratios. The conclusions concerning the upper mass cutoff and burst timescale would not change. The burst ages would not be significantly affected (0.5 Myr at most).

• Effects of the shape of the star formation rate

The function chosen to represent the variation of the star formation rate with time affects the shape of the model curves and introduces uncertainties of $1-3$ Myr on the absolute burst ages. The relative ages of the young bursts or of the old bursts between different regions are, however, less affected. For example, using a "half-gaussian" star formation rate ($R(t_{\rm b}) \propto e^{-(t_{\rm b}/t_{\rm sc})^2}$) implies a more rapid variation of the properties with burst age resulting in younger ages by about 1 Myr. The effects of the star formation rate are minimized with burst timescales of ~ 1 Myr since, as they are shorter than, at most comparable to, the main-sequence lifetimes of very massive stars, the variations with age of the integrated properties are largely determined by stellar evolution rather than by the star formation rate. The general conclusions on the star formation parameters and history derived in this section are little affected by the choice of the star formation rate.

7.4 The low-mass end of the starburst IMF in M 82

The low-mass IMF for the starburst populations in M 82 has long been debated. Several authors have argued that it is deficient in stars with initial masses below ≈ 3 $M_\odot$ compared to the solar neighbourhood IMF (Rieke *et al.* 1980, 1993; Bernlöhr 1992; Doane & Mathews 1993). The studies by Rieke and coworkers have been the most influential. In their seminal 1980 paper, they proposed an *IMF truncation at 3.5* $M_\odot$, with no stars produced below this cutoff. In their 1993 paper, they proposed an IMF extending down to 0.1 $M_\odot$ but exhibiting *an important flattening with the inflection point near 3* $M_\odot$, *i.e.* at substantially higher masses than for the solar neighbourhood IMF (see figure 7.9 below). Satyapal *et al.* (1997) have, however, challenged these hypotheses and could model the global K-band luminosity of M 82 with a Salpeter IMF extending down to 0.1 $M_\odot$ without requiring more than $\approx 35\%$ of the dynamical mass involved in the starburst.

The opposite conclusions of Rieke *et al.* 's and Satyapal *et al.* 's can be attributed to the notable differences in the respective data sets and models. The most important ones reside in the intrinsic luminosities (equivalently, the extinction), in the IMF assumed for the entire range of stellar masses formed, and in the star formation history. As recognized by Satyapal *et al.* (1997), their analysis is oversimplified because it assumes a single burst for the entire starburst core of M 82 with the age and timescale not directly constrained from the integrated properties. In this section, the issue of the low-mass IMF in M 82 is therefore re-examined in the light of the new data and models presented in this work. Two regions are considered for this purpose: the central 35 pc and the entire starburst core of M 82.

7.4.1 Re-examination of the low-mass IMF in M 82

Of the various observational constraints available for M 82, the stellar mass is the only one which is sensitive to the low-mass IMF. The first difficulty arises from the possible contribution from a stellar population predating the starburst. The mass involved in the starburst itself ($M^\star_{\rm stb}$) is highly uncertain since it cannot be determined directly. The starburst activity in the nuclear regions of M 82 was presumably triggered by the tidal interaction with its massive companion galaxy M 81. The models of Hernquist (1989) show that such nuclear starbursts have a very short timescale for their development compared to the timescale for the gas settling in the nuclear regions. As argued by McLeod *et al.* (1993), it is therefore unlikely that $M^\star_{\rm stb}$ exceeds half of the dynamical mass in the central regions of M 82. A conservative upper limit for $M^{\star}_{\rm stb}$ of 50% of the total *stellar* mass ($M^{\star}_{\rm tot}$) given in table 7.4 is hereafter adopted.

For convenience, possible modifications to the low-mass IMF can be quantified in terms of the lower mass cutoff $m_{\rm low}$, keeping the IMF slope constant. The $M^{\star}_{\rm stb}$ predicted for the two-burst models derived in the previous section (tables 7.6 and 7.7) for the central 35 pc and central 30″ of M 82 are computed for $m_{\rm low}$ varying in the range $0.1~{\rm M}_{\odot} - 5~{\rm M}_{\odot}$. The IMF is assumed to have a Salpeter power-law index ($\alpha = 2.35$) between $m_{\rm low}$ and 100 $\rm M_{\odot}$. The initial star formation rates R_0 are, as before, adjusted in order to reproduce L_K and $L_{\rm Lyc}$ but essentially scale as the mass following Eqs. 3.4 and 3.5. The results are shown in figure 7.8. The mass constraint is easily met in the central 35 pc of M 82, with $M^{\star}_{\rm stb} < 50\%$ of $M^{\star}_{\rm tot}$ for $m_{\rm low}$ down to 0.1 $\rm M_{\odot}$. The constraint is more stringent for the entire starburst core: $m_{\rm low} \geq 0.7~{\rm M}_{\odot}$ is required for $M^{\star}_{\rm stb}$ not to exceed 50% of $M^{\star}_{\rm tot}$. An IMF which continues to rise as steeply as with a Salpeter-like slope down to an abrupt cutoff is probably not very physical. The above cutoff at 0.7 $\rm M_{\odot}$ is more realistically interpreted as indicative of a flattening of the IMF at low masses. The mass constraint for the entire starburst core of M 82 can be satisfied, for example, with a flat slope ($\alpha = 0$) and the inflection point at 1 $\rm M_{\odot}$, or with an intermediate flattening with $\alpha = 1.35$ and the inflection point at 2.5 $\rm M_{\odot}$.

7.4.2 Factors influencing the low-mass IMF determination

• Observational constraints

As emphasized above, the mass fraction locked in stars formed in the starburst in M 82 is unknown. In particular, a more severe flattening or a turnover of the low-mass IMF cannot be ruled out. Moreover, the gas mass returned to the ISM via stellar winds and supernova explosions, or the mass expelled out of M 82 by the starburst wind are not accounted for. Given that the ages of the bursts are $\lesssim 50$ Myr and that massive stars dominate the mass returned to the ISM but contribute only a small fraction of the total $M^{\star}_{\rm stb}$, neglecting these effects probably does not affect the conclusions.

The intrinsic luminosities, and thus the extinction, are obviously crucial in constraining the low-mass IMF. This has been extensively discussed by McLeod *et al.* (1993), Rieke *et al.* (1993) and Satyapal *et al.* (1997). In that respect, the intrinsic L_K used by Satyapal *et al.* (1997) and the lower limit considered by Rieke *et al.* (1993) are both lower than the value adopted in this work, and allow lower $m_{\rm low}$ for a Salpeter IMF, as shown in figure 7.8 (the mass constraints are similar between all three studies).

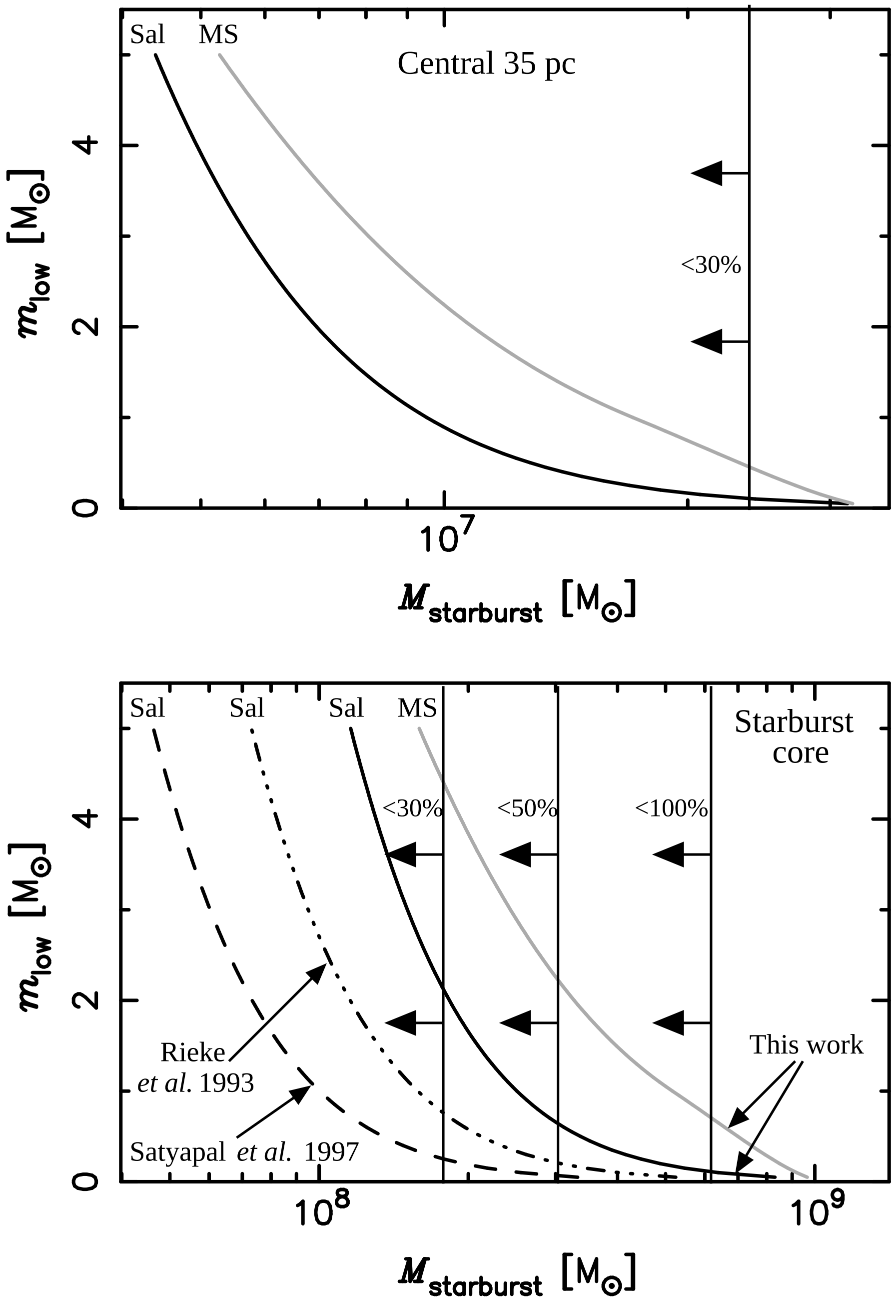

Fig. 7.8.— Mass involved in the starburst for $m_{\rm low}$ in the range 0.1 $M_\odot$ – 5 $M_\odot$, for the central 35 pc and the entire starburst core of M 82. Model predictions are illustrated for a Salpeter IMF (black solid lines labeled "Sal") and for a Miller & Scalo IMF (grey solid lines labeled "MS"). The predictions are computed for the appropriate two-burst models derived in section 7.3, reported in tables 7.6 and 7.7. For the starburst core, additional curves for a Salpeter slope are shown if the intrinsic L_K from Rieke *et al.* (1993) or from Satyapal *et al.* (1997) are used (dash-dot-dot-dot and dashed lines respectively) instead of the estimate based on the extinction derived in chapter 6 from the 3D data. The vertical lines mark various fractions of the *total stellar mass* determined for each region, which are 7.9×10^7 $M_\odot$ and 6.1×10^8 $M_\odot$ for the central 35 pc and the starburst core respectively.

• **The star formation history**

As emphasized by Satyapal *et al.* (1997), the characterization of the low-mass IMF also depends on the star formation history. Longer or older bursts will tend to use up more mass. Moreover, as the luminosities vary rapidly during the first few 10^7 yr, small changes in the ages may result in significant changes in the initial star formation rates, and thus in $M^\star_{\rm stb}$. In this regard, the detailed spatial modeling performed in section 7.6 for the 3D field of view provides an estimate of the possible errors on the predicted $M^\star_{\rm stb}$ from the more simplistic models based on the integrated properties used for figure 7.8. For a Salpeter IMF extending from 1 $M_\odot$ to 100 $M_\odot$, the modeling of the global properties for the 3D field of view in section 7.3 yields $M^\star_{\rm stb} \approx 6 \times 10^7$ $M_\odot$ (table 7.7). This differs by 25% only from $M^\star_{\rm stb} \approx 4.5 \times 10^7$ $M_\odot$ obtained by integrating over the star formation history derived from the modeling of individual pixels (figure 7.15). The $M^\star_{\rm stb}$ inferred from the two-exponential burst models for the central 35 pc and the starburst core of M 82 are therefore probably good approximations even if the variation with time of the star formation rate is not optimized.

• **The shape of the intermediate- and high-mass IMF**

The investigation of the low-mass IMF is intimately related to the slope adopted for the IMF at higher masses. Indeed, steeper IMFs are less efficient at converting the mass into luminosity (*e.g.* L_K, $L_{\rm Lyc}$). In order to reproduce the observed luminosities, which are dominated by stars more massive than $\sim$ 10 $M_\odot$ for the ages of interest here, steeper IMFs imply larger $M^\star_{\rm stb}$. The slope of the high-mass IMF is therefore critical for determining the low-mass IMF. However, the properties considered for the modeling of M 82 in this work are much more sensitive to the upper mass cutoff, and do not allow us to constrain the shape of the high-mass IMF (section 7.3.6).

Figure 7.9 compares "standard" IMFs derived for the solar neighbourhood which are commonly used in studies of starburst galaxies, normalized to unity at 1 $M_\odot$. These include the IMF of Salpeter (1955) adopted in this work, of Miller & Scalo (1979), and of Scalo (1986). The IMF proposed by Rieke *et al.* (1993) for M 82 is illustrated as well. The most remarkable feature of this IMF is the emphasis on the intermediate-mass range ($1 - 10$ $M_\odot$) due to the flattening of the low-mass IMF with the inflection point at 3 $M_\odot$. At high masses, Rieke *et al.* (1993) favoured a steeper slope than Salpeter on the basis of the rate of supernova explosions and the gas-phase oxygen abundances, but recognized the large uncertainties involved. In particular, part of the oxygen may be hidden in the hot gas phase associated with the supernova remnants and the starburst wind, and may be depleted onto interstellar dust grains.

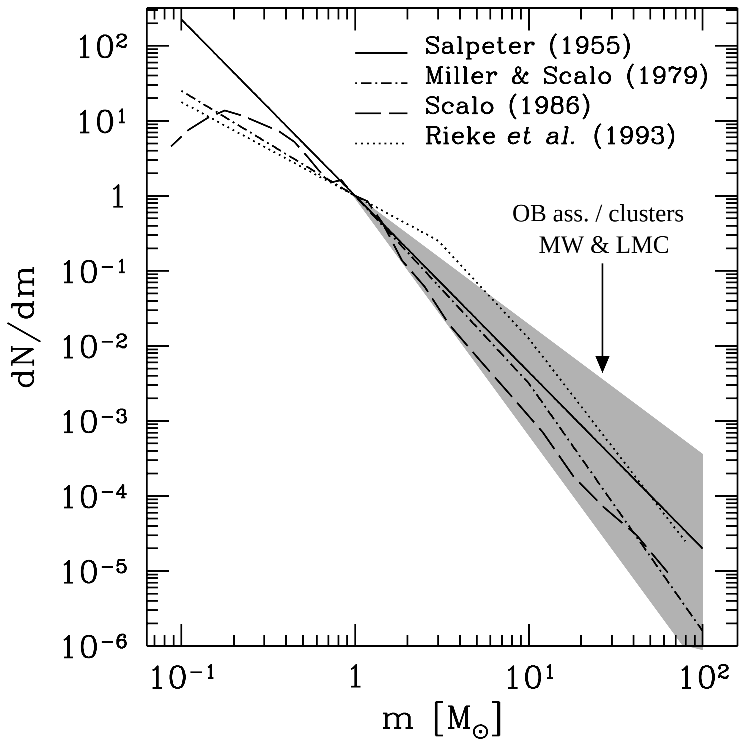

Fig. 7.9.— Comparison of various IMFs, represented by the different lines as labeled in the plot. The IMFs are normalized to unity at 1 $M_\odot$. The shaded region indicates the range of slopes determined in young clusters and OB associations in the Milky Way and in the Large Magellanic Clouds (Hunter *et al.* 1997 and references therein; Brandl *et al.* 1996; Eisenhauer *et al.* 1998; Massey & Hunter 1998; Scalo 1998).

IMF determinations based on star counts now exist for about 50 OB associations and clusters in the Milky Way and in the Magellanic Clouds. The range of slopes found for these local templates of starburst units are also shown in figure 7.9 (*e.g.* Hunter *et al.* 1997 and references therein; Brandl *et al.* 1996; Eisenhauer *et al.* 1998; Massey & Hunter 1998). This range is fairly large, with power-law indices varying by more than 1 dex and encompassing those of the standard IMFs. It may reflect intrinsic variations among clusters and associations, or may be due to differences in the interpretation of the data and observational uncertainties. It is much debated whether these results can be interpreted as evidence for a "universal" IMF for high-mass stars in OB associations and clusters in the Local Group of galaxies. Massey and coworkers (*e.g.* Massey 1998 and references therein) claim that the results support a universal IMF with essentially Salpeter slope. On the other hand, Scalo (1998) concludes that either the uncertainties are so large that the average IMF is poorly constrained, or there are strong indications of IMF variations. One firm conclusion, however, is that the shape of the high-mass IMF in local high-mass star-forming regions does not depend on obvious environmental conditions such as the metallicity, the cluster density and concentration, the galactocentric distance and the galactic morphological type (see references above).

The Salpeter slope was chosen in this work because it appears representative of the range of slopes observed. Variations in the shape of the high-mass IMF imply very small differences in the total mass, but large differences in the conversion of mass into luminosities which can lead to very different inferences on the low-mass IMF. To illustrate these effects, the Miller & Scalo (1979) IMF is considered. For the range $0.1 - 100$ $M_\odot$, the mass fraction locked in stars more massive than 10 $M_\odot$ is small and nearly identical for the Miller & Scalo and the Salpeter IMFs (8% and 12% respectively). The difference is obviously much larger for the mass fraction in stars less massive than 1 $M_\odot$, 44% and 61%. However, since the luminosities, such as L_K, $L_{\rm bol}$ and $L_{\rm Lyc}$, are steeply increasing functions of the stellar mass, the Miller & Scalo IMF predicts substantially less luminosity than the Salpeter one for the same total mass. Normalized to the same luminosities, larger $M^\star_{\rm stb}$ up to a factor of two are predicted for the Miller & Scalo IMF, as shown in figure 7.8. For the central 35 pc of M 82, $m_{\rm low}$ remains essentially unconstrained, but a cutoff near 2 $M_\odot$ for the starburst core is required to satisfy $M^\star_{\rm stb} \leq 50\%$ of $M^\star_{\rm tot}$.

7.4.3 Concluding remarks

As emphasized above, the issue of the low-mass IMF in M 82 is not independent of the assumptions on the slope of the IMF at higher masses. The lack of diagnostic power of the constraints available hamper accurate determinations of the low-mass end of the IMF (truncation, slope), and of its slope above a few $M_\odot$. The strongest constraint on the low-mass IMF is obtained from the properties and modeling of the entire starburst core. For a Salpeter IMF, the data and models presented here provide indications for a truncation near 0.7 $M_\odot$ or, if stars down to 0.1 $M_\odot$ can form in the starburst, for an important flattening with the IMF deficient in low-mass stars compared to most standard IMFs.

The low-mass IMF in local templates of high-mass star-forming regions is still poorly constrained. Even with *HST*, the low-mass stellar contents of OB associations and clusters is difficult to study because of the intrinsic faintness of this sub-population and because of important crowding effects. From high-sensitivity and high angular resolution near-infrared observations of NGC 3603, Eisenhauer *et al.* (1998) found no evidence for a truncation or significant flattening of the IMF down to their observational limit of 1 $M_\odot$. Their IMF is however flatter than Salpeter in the range $1 - 30$ $M_\odot$, with a power-law index $\alpha = 1.73$ defining the lower limit of the range of indices shown in figure 7.9. On the other hand, in a recent investigation based on very deep *HST* images of R136, Sirianni *et al.* (1998; as quoted in Leitherer 1998b) could probe the stellar population down to 0.8 $M_\odot$, and suggest a definite flattening below 3 $M_\odot$ of the IMF, which is close to Salpeter at higher masses. For comparison, the IMF in the solar neighbourhood flattens dramatically below 1 $M_\odot$ and may even turn over near 0.3 $M_\odot$ (*e.g.* Scalo 1986; Rana 1987; Scalo 1998). A bias against the formation of low-mass stars has been suggested for some starburst galaxies other than M 82, (Augarde & Lequeux 1985; Wright *et al.* 1988; Olofsson 1989; Nakagawa *et al.* 1989; Prestwich, Joseph & Wright 1994). Engelbracht *et al.* (1996; 1998) concluded for NGC 6946 and NGC 253 that the particular IMF proposed by Rieke *et al.* (1993) for M 82 was more compatible with the observations than a solar-neighbourhood IMF. To conclude, given the large remaining uncertainties on the low-mass IMF in high-mass star-forming environments but also the possible significant flattening in several of them, the debate whether the starburst IMF in M 82 is "deficient" in low-mass stars may not be relevant anymore.

7.5 The sources of faint K-band emission in M 82

The final consideration before the spatially detailed modeling of M 82 concerns the nature of the evolved stars which dominate the near-infrared emission, especially in regions of lower surface brightness. The strengths of the near-infrared stellar absorption features alone are not sufficient for this purpose. Within the 3D field of view, few regions exhibit CO bandheads which can be unequivocally attributed to red supergiants, and these generally correspond to the brightest K-band emission sources (chapter 6, section 6.1.2). The smoother, low-surface brightness regions have on average $W_{1.62} \approx 4$ Å and $W_{2.29} \approx 11$ Å in the 3D field of view. These EWs do not allow the discrimination between giants and supergiants, as can be assessed from figure 6.3. With a small amount of dilution in the K-band ($\approx 10\% - 15\%$), they are even consistent with those observed for normal evolved populations typical of elliptical galaxies and bulges of spiral galaxies, for which on average $W_{1.62} = 4.4$ Å and $W_{2.29} = 13$ Å (Oliva *et al.* 1995; see figure 7.5).

The $M^{\star}/L_K$ ratios provide useful constraints on the contribution to L_K from a preexisting population. Normal populations have $M^{\star}/L_K$ ratios typically in the range $10 - 30$ $M_{\odot}/L_{\odot}$ (*e.g.* Devereux, Becklin & Scoville 1987; Oliva *et al.* 1995). Assuming the preexisting population in M 82 is characterized by a ratio of 20 $M_{\odot}/L_{\odot}$ and accounts for all the stellar mass, its contribution to the stellar L_K is 7% and 2% in the central 35 pc and the entire starburst core of M 82 respectively. These are upper limits since the starburst population contributes some fraction of the mass as well.

The decrease in $M^{\star}/L_K$ ratio from the central 35 pc to 450 pc ($30''$) suggests an increasing contribution to L_K from the starburst population (see also Gaffney, Lester & Telesco 1993; Lançon, Rocca-Volmerange & Thuan 1996; Satyapal *et al.* 1997). The bright emission region in the inner few tens of parsecs and the compact sources distributed along the galactic plane of M 82 (*e.g.* Pipher *et al.* 1987; Satyapal *et al.* 1997) are not sufficient to maintain or reduce the $M^{\star}/L_K$ ratio with increasing radii. From the 3D data and those of Satyapal *et al.* (1997), these sources contribute only about 70% and 20% of the total intrinsic L_K in the 3D field of view and in the starburst core respectively. This is significantly lower than the minimum $> 90\%$ inferred above. An upper limit for the $M^{\star}/L_K$ ratio of ≈ 0.6 $M_{\odot}/L_{\odot}$ is inferred for the fainter, smoother component assuming it contains all the mass within the central $30''$. This is only marginally larger than the total $M^{\star}/L_K$ ratio for the entire starburst core (0.47 $M_{\odot}/L_{\odot}$), and more than an order of magnitude lower than expected for a preexisting population.

An alternative argument is provided by estimating the fraction of the stellar mass contributed by red giants if they dominate the low surface brightness emission. Typical K-type giants have a mass of ≈ 1 M$_\odot$ and $L_K \sim 10$ L$_\odot$ (table A.3 in appendix A). Such stars would contribute $\sim 15\%$ of the total stellar mass in the starburst core if they were entirely responsible for the $L_K \approx 10^9$ L$_\odot$ inferred for the smoother, fainter emission. This is substantially larger than the typical fractions of $0.2\% - 1\%$ determined empirically for normal populations (*e.g.* Pickles 1985).

Red supergiants, therefore, seem to dominate the near-infrared continuum emission throughout most of the starburst core of M 82. The spatial distributions of the K-band emission and of the CO bandhead EWs can be interpreted as follows. The compact sources distributed along the galactic plane of M 82, interpreted by Satyapal *et al.* (1997) as young clusters of red supergiants on the basis of their sizes and luminosities, likely correspond to clusters with ages for which their integrated L_K is near maximum ($8 - 15$ Myr). This is supported by the general correlation seen in figure 6.4 between the intrinsic CO EWs and L_K, since the maximum $W_{2.29}$ and $W_{1.62}$ occur with maximum L_K. The fairly large dispersion, though, may also indicate that bright sources are partly due to a larger concentration of clusters with a spread in ages. The smoother component likely results from the integrated contribution from numerous, fainter and unresolved clusters of red supergiants which are younger — or older — than the age of maximum L_K. A large space density of ionizing clusters powering the H II region complexes was found in chapter 5 ($\sim 10^{-3} - 10^{-2}$ pc^{-3}, or cluster-to-cluster separations of $5 - 10$ pc). Since the strengths and timescales for the young and old bursts outside the central few tens of parsecs are comparable (section 7.6 below), this implies large densities of clusters of red supergiants as well. Finally, the centrally concentrated morphology of the K-band emission and of the CO bandheads EWs around the nucleus are likely due to age effects as well as to an increasing space density of clusters towards the nucleus.

7.6 The detailed star formation history in M 82

The modeling of selected regions in section 7.3 suggests that two short starburst events took place throughout the central 450 pc of M 82, about 10 Myr and 5 Myr ago. This modeling provided the general characteristics of starburst activity in this galaxy, but only an incomplete picture of its evolution. In particular, a bias towards preferential ages was likely introduced by selecting the small-scale regions as those with brightest continuum or line emission, and with deepest or shallowest CO bandheads. The properties of the large-scale regions are dominated to some extent by the brightest emission sources. To complete the picture, it is therefore important to model *all* individual regions, which have a range in their luminosities and other properties suggesting a range in their evolutionary states and burst strengths. Although along any line of sight the integrated properties will always be dominated by the most luminous populations, a detailed modeling on small spatial scales reduces the bias towards particular ages.

In this section, the 3D data in combination with the 12.4 μm map from Telesco & Gezari (1992) are used to **model individual regions throughout the entire regions observed with 3D**. The results provide for the first time **quantitative constraints on the detailed spatial and chronological evolution of starburst activity in M 82**. Specifically, the following characteristics are determined within the regions mapped with 3D:

- the spatial distribution of burst ages and strengths,
- their variations with projected radius, and
- the integrated star formation history.

These are key elements for the understanding of the local and global processes involved in starburst events, such as the triggering and feedback mechanisms.

7.6.1 Observational constraints

The modeling of selected regions in section 7.3 has enabled the identification of the indicators which are most useful for determining the burst age and strength: the [Ne III]/[Ne II] ratio in combination with the $L_{\rm IR}/L_{\rm Lyc}$ ratio, $W_{2.29}$, L_K and $L_{\rm Lyc}$. The various constraints were derived from the 3D maps, and from the 12.4 μm map from Telesco & Gezari (1992). The latter was smoothed with a synthetic circular gaussian beam to match the spatial resolution of the 3D data. All images were rebinned to $1'' \times 1''$ pixels in order to increase the signal-to-noise ratio.

The K-band map was corrected for the hot dust contribution and for the extinction using the dilution and extinction maps obtained in chapter 6, and the $W_{2.29}$ map was corrected for dilution. The Brγ map was dereddenened assuming that the extinction towards the evolved stars applies to the ionized gas. As discussed in section 5.1.7, the corrections for extinction near 2.2 μm towards the ionized gas and the evolved stars are similar within 20%. The local extinction was assumed to be purely foreground and may underestimate the absolute amount of extinction. However, the spatial variations in the intrinsic properties are relevant for the present purposes, and are much less affected by the extinction model adopted.

The $L_{\rm IR}$ map was computed from the 12.4 μm image using Eq. 7.1. No correction was applied for extinction to the 12.4 μm emission since average extinction effects are included in the $f_{12.4\,\mu\rm m}$ to $L_{\rm IR}$ scaling factor. For the present purposes, the contribution from cool, evolved stars to $L_{\rm bol}$ and the light escaping perpendicular to the galactic plane are neglected, and $L_{\rm bol} = L_{\rm IR}$. The errors introduced by the choice of an inappropriate extinction model for the Brγ emission are potentially more important for $L_{\rm IR}/L_{\rm Lyc}$. However, the very low ratios derived are close to the minimum predicted for young clusters, suggesting that the extinction towards the ionized gas is not importantly underestimated. The final L_K, $L_K/L_{\rm Lyc}$ and $L_{\rm IR}/L_{\rm Lyc}$ maps were then generated. The He I 2.058/Brγ ratio is essentially independent of extinction and was obtained directly from the observed line maps. The "equivalent" [Ne III]/[Ne II] ratio at each pixel was obtained from the He I 2.058/Brγ ratio as described in section 7.1.1.

7.6.2 Modeling of individual pixels

Figure 7.10 compares the data with model curves for a single evolving cluster, as a function of pairs of properties. A Salpeter IMF from 1 $M_\odot$ to 100 $M_\odot$ is assumed, and models for burst timescales of 1 Myr and 5 Myr are illustrated, as justified in the previous sections ($m_{\rm low}$ is irrelevant here). A large fraction of the data points do not fall on the model curves. This is essentially the same behaviour as encountered for the selected regions. More specifically, the [Ne III]/[Ne II] and $L_{\rm IR}/L_{\rm Lyc}$ ratios characterizing the OB stars imply significantly younger ages than those of the evolved stars characterized by $W_{2.29}$. The properties of some of the individual pixels can be reproduced with a single burst if the timescale is increased to 5 Myr. However, these points are mostly those with lower K-band flux densities, while those with higher K-band flux densities have generally deep CO bandheads which can only be reproduced with very short timescales. There is no reason why regions with lower K-band surface brightnesses, also dominated by the light from red supergiants as shown in the previous section, should be preferentially associated with longer burst events. The data points

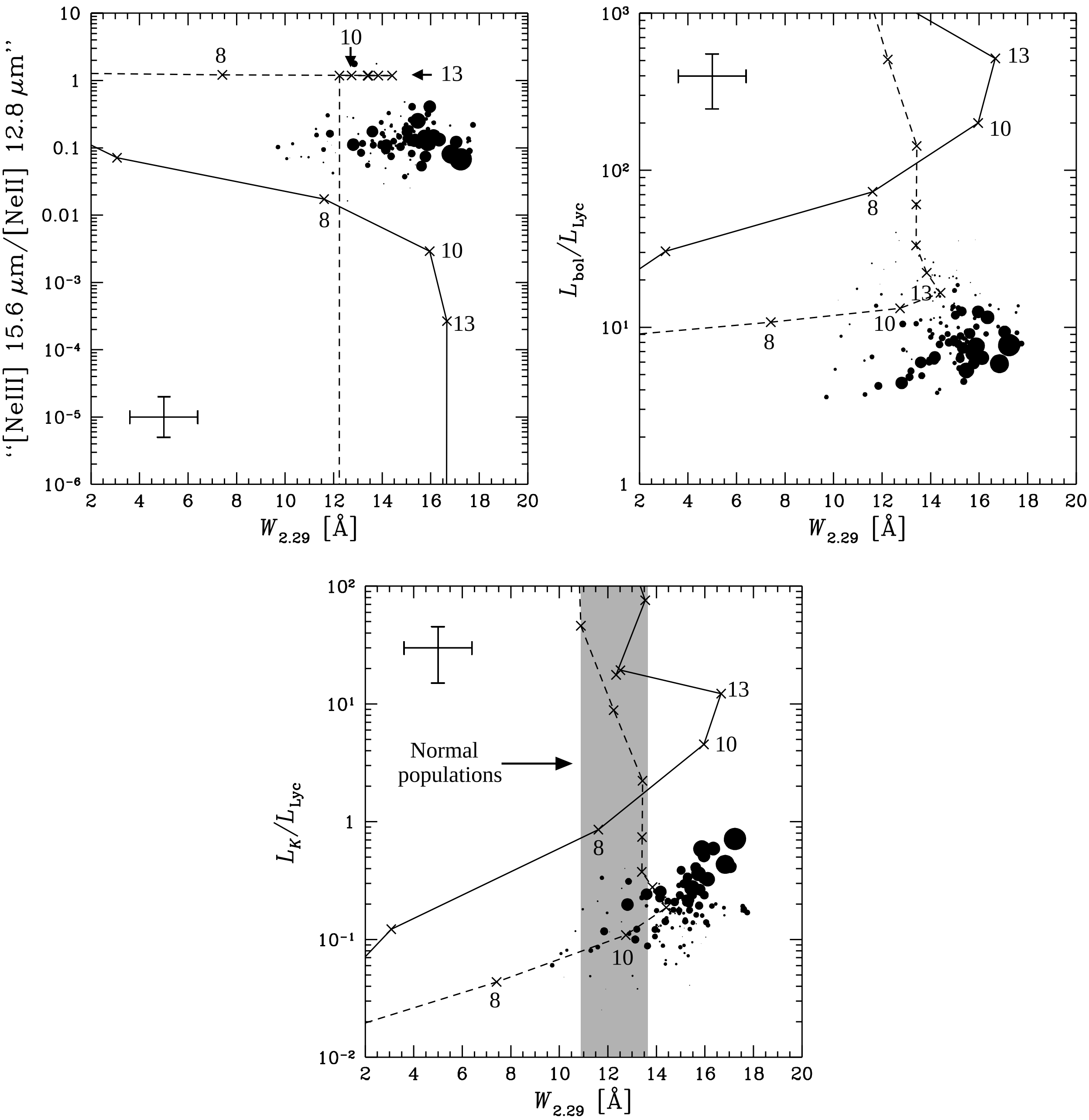

Fig. 7.10.— Comparison of the properties of individual pixels in the 3D field of view with predictions for a single evolving cluster. The model curves are shown for an upper mass cutoff of 100 $M_{\odot}$, and two burst timescales: 1 Myr (solid line) and 5 Myr (dashed line). The crosses on each curve indicate different ages separated in logarithmic intervals of 0.1 dex. A few ages given in Myr are labeled explicitely in each plot. The size of the data points is proportional to the intrinsic stellar K-band luminosity. Typical uncertainties on the data are shown by the error bars in each plot. The shaded area in the bottom panel indicates the range of $W_{2.29}$ measured for "normal" evolved stellar populations characteristic of elliptical galaxies and bulges of spiral galaxies (Oliva *et al.* 1995).

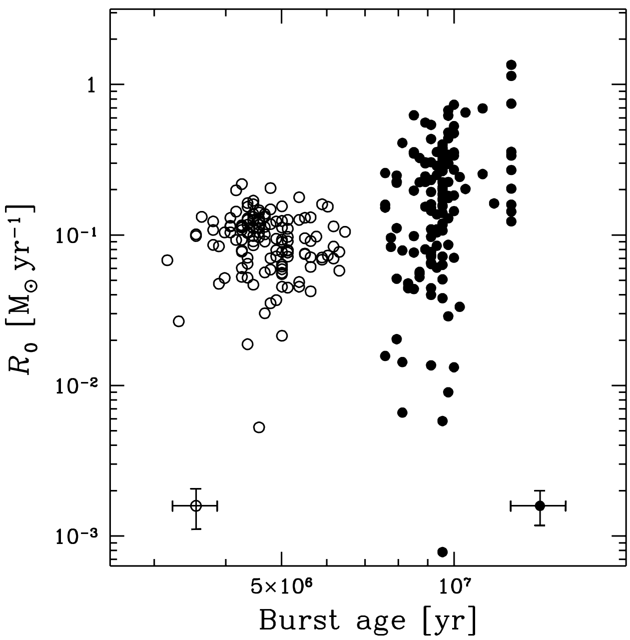

Fig. 7.11.— Model results for individual pixels in the 3D field of view on M 82: initial star formation rate (R_0) versus burst age. Open circles represent the young bursts while filled circles, the old bursts. Typical error bars are indicated at the bottom of the plot, and correspond to 1σ of the results obtained by varying in turn the observational constraints within their typical uncertainties.

in the $L_K/L_{\rm Lyc}$ versus $W_{2.29}$ diagram are distributed along a path which is remarkably parallel to the model curves for $t_{\rm sc} = 1$ Myr, but displaced vertically by about one order of magnitude. The data can be reproduced with **two very short, successive bursts at each location**, with the young bursts producing ≈ 10 times more ionizing luminosity than the older ones responsible for most of the near-infrared luminosity.

For each pixel, a model consisting of two bursts with $t_{\rm sc} = 1$ Myr and a Salpeter IMF between 1 $M_\odot$ and 100 $M_\odot$ was fitted to the constraints. The absolute burst strengths depend on $m_{\rm low}$ or, more generally, on the characteristics of the low-mass IMF. But again, the burst ages and their *relative* strengths are of interest here and are not affected by the low-mass IMF. For each pixel, the age of the young burst was taken as the average of the ages derived from the equivalent [Ne III]/[Ne II] ratio and from the $L_{\rm IR}/L_{\rm Lyc}$ ratio. If the latter was smaller than the minimum $L_{\rm bol}/L_{\rm Lyc}$ in the model predictions, an age of 1 Myr was assigned. The age of the old burst was taken as the youngest solution possible from $W_{2.29}$. Pixels with EWs in excess of the maximum $W_{2.29}$ predicted were assigned the age of maximum $W_{2.29}$. The initial star formation rates (R_0) of the two bursts were determined from L_K and $L_{\rm Lyc}$. The uncertainties on both the burst age and R_0 were estimated by varying in turn the observational constraints by amounts corresponding to the typical uncertainties on the measurements.

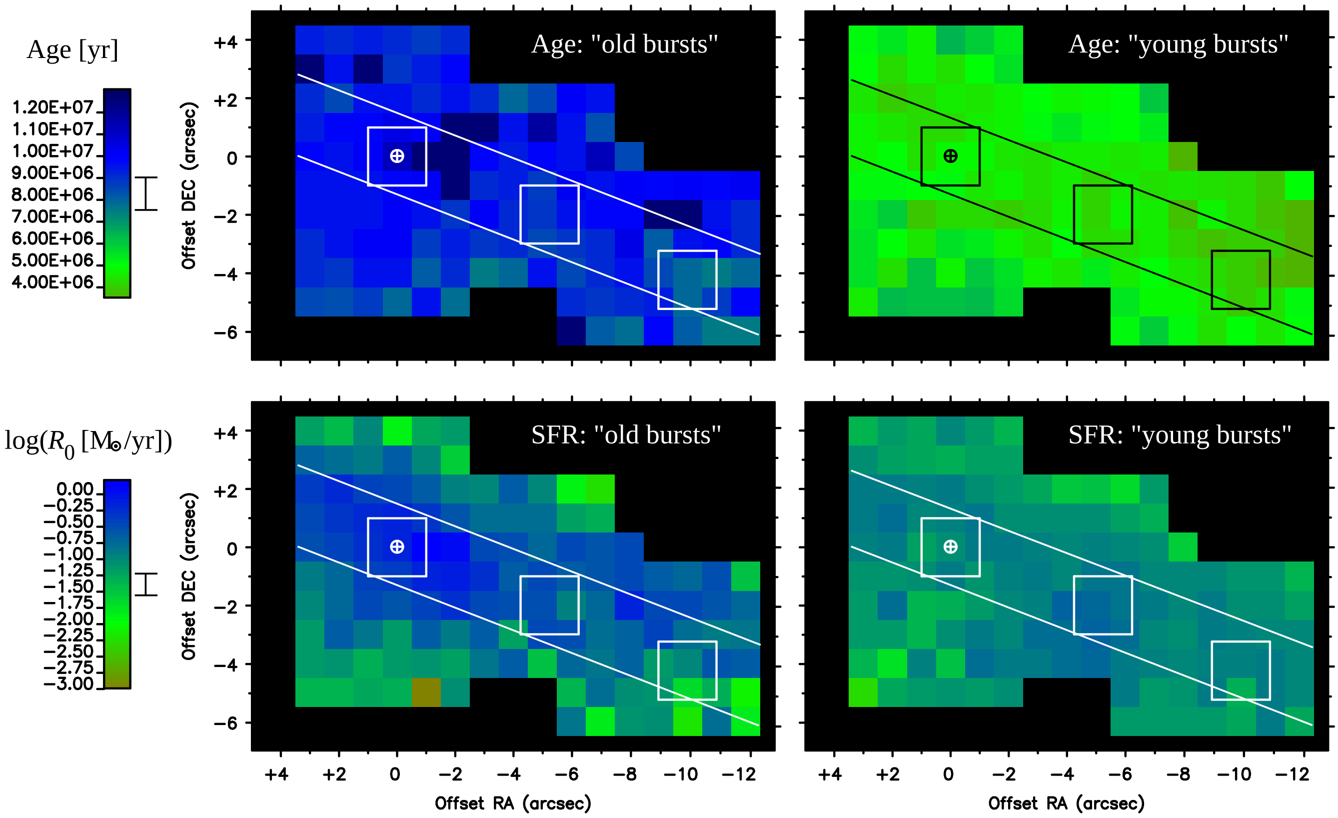

Fig. 7.12.— Model results for individual pixels in the 3D field of view. The top panels show the ages derived for the old and young bursts, and the bottom panels show the initial star formation rates (R_0). Typical uncertainties are shown next to the colour bars. The position of the nucleus is marked by the crossed circle. The square boxes indicate selected regions modelled in section 7.3: the central 35 pc at ($0''$, $0''$), B1 at ($-10''$, $4.25''$), and B2 at ($-5.25''$, $-2''$). The straight lines indicate the $3''$–wide slit along the galactic plane of M 82 used to extract the profiles presented in figure 7.13.

The results of the modeling of individual pixels are shown in figures 7.11 and 7.12. The ages for the young bursts range from 3.2 Myr to 6.5 Myr, with an average of 4.8 Myr and a small dispersion of $1\sigma = 0.6$ Myr. The ages for the old bursts range from 7.6 Myr to 12.6 Myr (the maximum corresponding to maximum $W_{2.29}$), with an average of 9.5 Myr and also a small dispersion of $1\sigma = 1.2$ Myr. The old bursts are oldest near the nucleus and the secondary K-band peak $\approx 8''$ to the west (figure 4.3), and youngest near B1. Large variations are inferred for their strengths, with the most intense star formation having occurred along a ridge roughly parallel to the galactic plane, and peaking around the nucleus. The young bursts are slightly younger near B1. Their strengths are more uniform spatially than for the old bursts, with an average intensity comparable to that for the lower-level old bursts. Not surprisingly, these spatial variations reflect fairly well those of the primary observational diagnostics: He I 2.058/Brγ, and the intrinsic $W_{2.29}$, K-band flux density and Brγ flux.

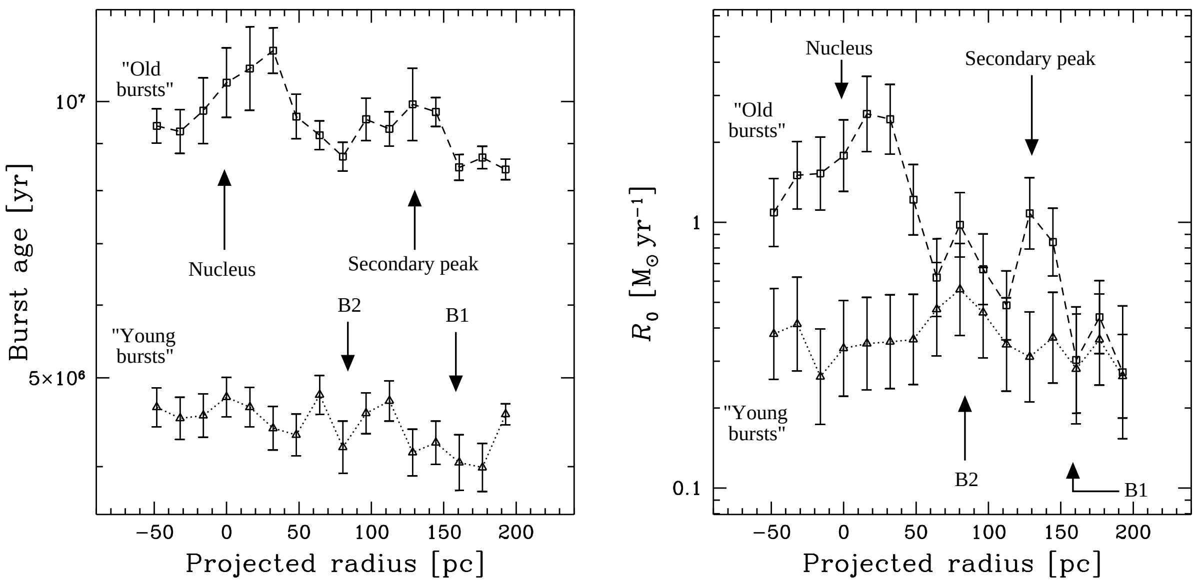

Fig. 7.13.— Variations of the burst age and strength with projected radius from the nucleus of M 82 ($1'' = 15$ pc). The data are taken from the modeling of individual pixels in the 3D field of view, in a slit $3''$–wide along the galactic plane of M 82, as shown in figure 7.12. The results for the young bursts are plotted as dotted lines with triangles, and for the old bursts as dashed lines with squares. The positions of the nucleus, the secondary K-band peak and the Brγ sources B1 and B2 are indicated.

Satyapal *et al.* (1997) investigated the spatial variations in ages for the brightest, compact K-band emission sources in the central 500 pc of M 82, most of which are located within the regions mapped with 3D. Comparing the CO index and the equivalent width of the Brγ emission line (inversely proportional to $L_K/L_{\rm Lyc}$) with the predictions from their own starburst model, they inferred burst ages in the range $4 - 10$ Myr. The agreement between their results on the ages and those presented here is good, given that they modeled the regions as single bursts.

7.6.3 Radial evolution for starburst activity in M 82?

Figure 7.13 shows the average burst age and total burst strength as a function of projected distance from the nucleus in a slit $3''$–wide along the galactic plane of M 82, indicated in figure 7.12. These profiles reveal that **the variations with projected radius of the burst ages and strengths are more complex than for a simple radial picture**. The old bursts are significantly older and stronger near the nucleus, and there is a general decrease in age and strength with increasing projected radius. However, the variations are not monotonic but exhibit an intermediate maximum at a projected radius of $\approx$ 130 pc, near the secondary K-band peak. On the other hand, the younger bursts have comparable ages and strengths at all projected radii, with a marginal trend of decreasing age with increasing projected radius. Local minima in age occur at the locations of the Brγ sources B1 and B2, and the strongest young bursts are found near B2. The models of Satyapal *et al.* (1997) supported a radial picture but were limited to the compact K-band sources, providing less complete information on the spatial evolution of starburst activity.

Starburst activity has thus occurred outside of the central few tens of parsecs of M 82 *prior* to the most recent burst event. This is particularly obvious near the secondary K-band peak, located in projection between the prominent H II region complexes B1 and B2. It is also supported by the analysis of the $M^{\star}/L_K$ ratio in section 7.5, which indicates that red supergiants dominate the near-infrared light out to a projected radius of 225 pc (30″–diameter aperture) and over a large range of surface brightnesses. Additional direct evidence is provided by the spatial distribution of the young radio supernova remnants, which is quite uniform along the galactic plane of M 82 and extends beyond the molecular ring out to projected radii of $\approx$ 300 pc (*e.g.* Kronberg, Biermann & Schwab 1985; Muxlow *et al.* 1994).

7.6.4 The global star formation history

The global star formation history within the 3D field of view can be obtained by integrating the initial star formation rates of all individual pixels. The age bins were chosen arbitrarily to increase logarithmically by 0.05 dex. The resulting global starburst history is shown in figure 7.14. The surface density of star formation rate was also computed by dividing the integrated star formation rate by the total area of the pixels contributing to each age bin. It is illustrated in figure 7.14 as well.

The integrated star formation rate (SFR) exhibits two conspicuous peaks near 5 Myr and 10 Myr, clearly revealing two distinct successive starburst episodes. The increase for the oldest age bin is most likely artificial, and due to the condition that the old bursts for pixels with $W_{2.29}$ in excess of the maximum in the model predictions are assigned the age of maximum $W_{2.29}$. The peaks are remarkably symmetric about the maximum, and very similar in shape. The first starburst episode was globally 3.5 times stronger than the most recent one. The integrated SFR is compared in figure 7.15 with the two exponentially decaying functions representing the SFR of the best model fit to the global properties of the entire 3D field of view in table 7.7. These functions provide reasonable though crude approximations to the detailed SFR.

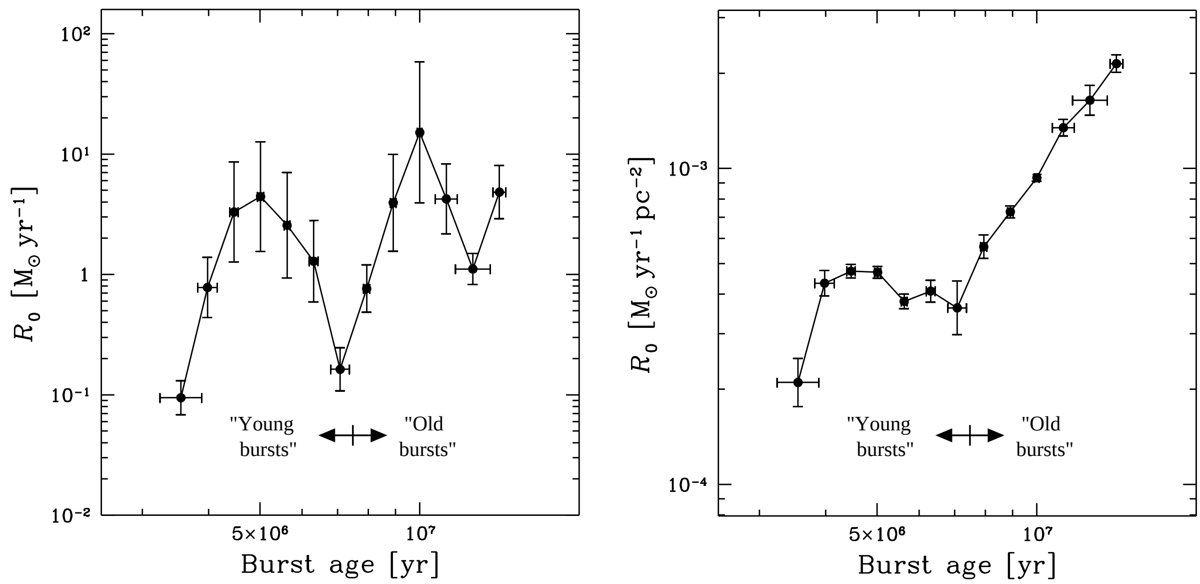

Fig. 7.14.— Global star formation history of M 82 derived from the modeling of individual pixels in the 3D field of view. *Left*: integrated initial SFR per age bin in logarithmic intervals of 0.05 dex. *Right*: initial SFR surface density, obtained by dividing the integrated SFR from the left panel by the total area of the pixels contributing in each age bin. The independent contributions from the "young" and "old" bursts are indicated by the arrows.

In view of the results obtained for the 3D field of view, it is not surprising that Rieke *et al.* (1993) found that a double gaussian profile optimized their model fits for the entire starburst core. The integrated star formation history in the 3D field of view is well reproduced by two semi-logarithmic gaussian profiles centered at 5 Myr and 10 Myr, with amplitudes of $R_0 = 4.4$ $M_\odot\,yr^{-1}$ and 15.1 $M_\odot\,yr^{-1}$, and full-widths at half-maximum of log(age) = 0.13 dex and 0.09 dex (shown in figure 7.15).

The integrated SFR surface density reflects the quite uniform young bursts and the large variations for the old bursts revealed in figure 7.12. The intensities of the old bursts have decreased in time by almost an order of magnitude, down to levels comparable to those of the young bursts. The *present* global SFR per unit area within the 3D field of view is $\approx 3\times10^{-6}$ $M_\odot\,yr^{-1}\,pc^{-2}$. A value of $\approx 7\times10^{-6}$ $M_\odot\,yr^{-1}\,pc^{-2}$ for the entire starburst core (assuming an area corresponding to a 30″–diameter aperture) is implied by the two-burst model fit to the integrated properties (table 7.7); this is likely an overestimate as suggested by the comparison between the two-burst and spatially detailed models for the 3D field of view in figure 7.15. For comparison, an upper limit of a few times 10^{-5} $M_\odot\,yr^{-1}\,pc^{-2}$ has been inferred for various samples of starburst galaxies, assuming a Salpeter IMF between 0.1 $M_\odot$ to 100 $M_\odot$ and a constant SFR during $10^7 - 10^8$ yr (*e.g.* Meurer *et al.* 1995; Lehnert & Heckman 1996; Meurer

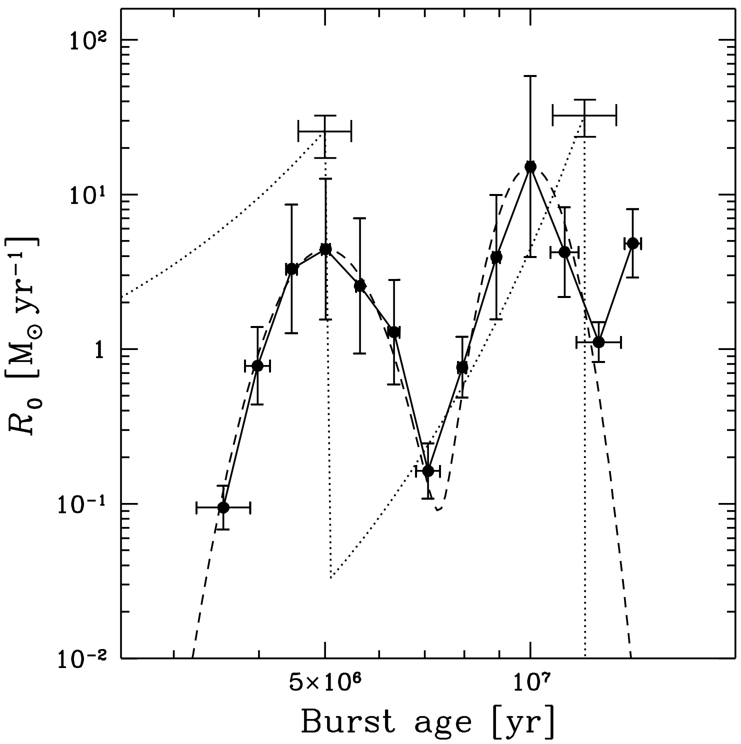

Fig. 7.15.— Integrated SFR (R_0) derived from the modeling of individual pixels in the 3D field of view on M 82 (filled circles and solid line). Two gaussian profiles (linear in R_0 and logarithmic in burst age) provide excellent representations of the integrated SFR (dashed line). The combination of the two exponentially decaying functions corresponding to the best model fit to the global properties of the 3D field of view are illustrated as well (from table 7.7, with uncertainties on the age and R_0 shown by the error bars at the peak SFR).

et al. 1997). This estimate is a factor of 0.4 lower if $m_{\rm low} = 1\ M_\odot$ is adopted instead. It is representative of the present SFRs provided the starburst ages are smaller than the timescales. The present global SFR surface density obtained here for M 82 agrees with the above limit for starburst galaxies, but the model results suggest that the star formation intensity can exceed this upper limit locally and for a short period of time.

7.6.5 Concluding remarks

Admittedly, several additional factors not explicitely accounted for in the formal uncertainties may affect the results, such as uncertainties inherent in the models themselves, and the assumption of identical timescales, identical IMF, and exactly two bursts at each location. For individual pixels, variations in the IMF slope and upper mass cutoff within plausible ranges (range of slopes in local high-mass star-forming regions shown in figure 7.9, $m_{\rm up} > 50$ $M_\odot$ as discussed in section 7.3) imply variations in age $\lesssim 0.5$ Myr and in R_0 of at most a factor of a few. Variations in the low-mass IMF affect R_0 by factors of a few as well. Longer timescales by a few million years result in slightly older ages and lower R_0. The uncertainties on the nebular parameters for the modeling of the [Ne III]/[Ne II] ratio result in similar differences in the derived ages and R_0. Variations in the above parameters would not, however, affect importantly the overall spatial distributions of burst ages and strengths, and the general shape of the radial profiles and integrated star formation history. The data do not allow the distinction between two or more bursts, but the modeling of selected regions in section 7.3 suggests that two bursts are justified and sufficient to fit the properties considered.

Another important consideration is the choice and interpretation of the observational constraints. The effects on the results are discussed here for the integrated star formation rate. If $L_{\rm IR}/L_{\rm Lyc}$ is not used in modeling the young bursts, the equivalent [Ne III]/[Ne II] ratios imply systematically older ages by $\lesssim 0.5$ Myr and slightly higher R_0. Consequently, the integrated peak for the most recent starburst episode ("young peak") shifts slightly to older ages and its amplitude increases by a small factor. On the other hand, if [Ne III]/[Ne II] is not used, the $L_{\rm IR}/L_{\rm Lyc}$ ratios imply systematically younger ages, lower R_0 and a larger age dispersion due to the degeneracy of this ratio below a few million years. As a result, the young peak shifts to younger ages, broadens, and its amplitude decreases. In principle, the $L_{\rm IR}/L_{\rm Lyc}$ ratios alone allow burst timescales longer than 5 Myr. However, such timescales would be inconsistent with the very different spatial distributions of the K-band emission and CO bandhead EWs, and of the ionized gas and thermal dust emission, as discussed in section 7.3. For the old bursts, if older age solutions are adopted for those pixels with EWs for which the model predictions are degenerate, higher R_0 are derived. The "old peak" extends towards older ages, and its amplitude increases. Thus, for a different interpretation of the observational constraints, the integrated star formation history remains qualtitatively the same, with two starburst episodes separated by at least a few million years, of relatively short durations, and with the strength of the most recent episode comparable to or lower than that of the first one.

7.7 The nature of starburst activity in M 82

In this section, the implications on the nature of starburst activity in M 82 of the evolutionary synthesis modeling are discussed. Two aspects are considered: the characteristics of the star formation process itself, and the triggering mechanism and dynamical evolution of starburst activity.

7.7.1 Summary of the model results

The new 3D and *ISO* observations of M 82 together with existing data from the literature are consistent with the formation of very massive stars and the softening of the ionizing radiation field, presently dominated by OB stars with masses near 30 $M_\odot$, attributable to aging of the starburst. The models imply short burst timescales of at most a few million years on all spatial scales. In addition, they strongly suggest that starburst activity has occurred locally and globally during two episodes separated by approximately 5 Myr, with the most recent one taking place about 5 Myr ago. The central few tens of parsecs of M 82 hosted the most intense burst during the first episode. The estimated star formation rate per unit volume for this "nuclear burst" is $1 - 2$ orders of magnitude higher than the average across the galaxy during each episode.

The data do not allow accurate determinations of the general shape of the IMF and its low-mass end. For a Salpeter slope, there are indications of a possible truncation between 0.5 $M_\odot$ and 1 $M_\odot$ or, alternatively, of a significant flattening below one to a few $M_\odot$. The low-mass IMF does not, however, affect the spatial and chronological evolution of starburst activity inferred from the modeling. Within plausible ranges for high-mass star-forming regions, uncertainties in the slope of the IMF above a few $M_\odot$ has no significant effects on the determination of the starburst history either.

7.7.2 Characteristics of the star formation process

The clumpy distribution of the ionized and molecular gas as well as of the infrared-emitting dust on scales at least as small as $\approx$ 15 pc (*e.g.* Telesco & Gezari 1992; Achtermann & Lacy 1995; Shen & Lo 1995), the compact near-infrared continuum sources presumably tracing clusters of red supergiants near their maximum luminosity (*e.g.* Satyapal *et al.* 1997; figures 4.3 and 4.4), and the parsec-scale super star clusters seen at optical wavelengths (O'Connell *et al.* 1995) show that starburst activity in M 82 has occurred in individual burst sites. Their sizes together with the star formation parameters inferred, in particular the short timescales and the high upper mass cutoff of the IMF, make them comparable to Galactic and near-extragalactic massive star-forming regions such as the 30 Doradus nebula and its central cluster R136 in the Large Magellanic Cloud.

This prominent sub-structure probably corresponds to the largest and most luminous burst sites. Smoother and lower surface brightness emission makes indeed a substantial contribution to the integrated properties of M 82. The diffuse ionized gas and thermal dust emission represents roughly 50% of the total emission from the starburst core. The smoother and fainter stellar near-infrared continuum emission contributes at least as large a fraction. These diffuse components correlate roughly with the overall spatial distribution of the brighter and more compact sources. They could be due to the integrated contribution of less massive and less luminous clusters for which large numbers are predicted from plausible cluster luminosity functions, or of clusters with some age spread and thus a range of luminosities, or both. Photons leaking out from the H II regions may be responsible for part of the diffuse ionized gas and thermal dust emission. The state of the interstellar medium (ISM) within the emitting regions described in chapter 5 suggests that the H II region complexes are dynamically evolved and, therefore, may be largely density-bounded with the unabsorbed radiation escaping in the surrounding environment. Large fractional contributions of a diffuse component are also observed at ultraviolet wavelengths in nearby starburst galaxies, with typically 20% of the integrated light coming from bright compact clusters (*e.g.* Meurer *et al.* 1995; Maoz *et al.* 1996). Meurer *et al.* (1995) interpreted these results within the framework of a bi-modal scenario for star formation in starbursts: prominent cluster formation and dominant diffusely distributed star formation.

7.7.3 Triggering and evolution of starburst activity

For a plausible evolutionary scenario of starburst activity in M 82, the model results must be interpreted together with the key morphological features:

- The large-scale tails and bridges of material emanating from M 82 and connecting with its massive neighbour M 81 located about 36 kpc in projection, indicative of a gravitational interaction between the two galaxies (*e.g.* Yun, Ho & Lo 1993).

- The disk-like morphology of the near-infrared continuum emission, peaking at the nucleus and suggesting a $\sim$ 1 kpc–long stellar bar, and the extended distribution of compact non-thermal radio sources along the galactic plane over $\approx$ 600 pc (*e.g.* Telesco *et al.* 1991; Satyapal *et al.* 1997; Kronberg, Biermann & Schwab 1985).

These trace the red supergiants and young supernova remnants (SNRs) formed during the first starburst episode.

- The circumnuclear concentrations of prominent H II regions in a ring of radius ≈ 85 pc and, outside this ring, along ridges presumably on the leading edge of the rotating stellar bar (*e.g.* Larkin *et al.* 1994; Achtermann & Lacy 1995). The "ionized ring" is located just inside of the main concentrations of molecular gas in a toroid or tightly-wound spiral arms as seen in the CO $J = 1 \rightarrow 0$ emission (*e.g.* Shen & Lo 1995). The ionized ring and ridges trace the OB star clusters formed during the second starburst episode. In the 3D images, the Brγ source B2 coincides in projection with the western edge of the ionized ring while B1 is located farther out.

- The bipolar supernova-driven starburst wind along the minor axis of M 82 extending out to about 5 kpc, revealed notably by X-ray and optical observations (*e.g.* McCarthy, Heckman & van Breugel 1987; Tomisaka & Ikeuchi 1988; Bregman, Schulman & Tomisaka 1995; Shopbell & Bland-Hawthorn 1998). The [Fe II] 1.644 μm emission exhibits a prominent arc-like structure on the south side of the galactic plane and centered near the nucleus. This arc may trace shock-ionized gas enriched in iron due to destruction of interstellar grains by the outflowing material (*e.g.* Greenhouse *et al.* 1997; Mouri *et al.* 1990; see also figure 4.3).

- The apparent lack of gas and dust within the central few tens of parsecs of M 82 (*e.g.* Telesco *et al.* 1991; Telesco & Gezari 1992; Larkin *et al.* 1994; Shen & Lo 1995; Normand *et al.* 1995; Achtermann & Lacy 1995; Seaquist *et al.* 1996).

The primary triggering mechanism for starburst activity in M 82 is generally attributed to the M 82 − M 81 tidal interaction $\sim 10^8$ yr ago (*e.g.* Gottesman & Weliachew 1977; O'Connell & Mangano 1978; Lo *et al.* 1987; Yun, Ho & Lo 1993). In this scenario, the ISM in M 82 experienced strong large-scale torques and loss of angular momentum as it was transported towards the dynamical center of the galaxy, in accordance with numerical simulations (*e.g.* Sundelius *et al.* 1987; Noguchi 1987, 1988; Mihos & Hernquist 1996). The increased cloud-cloud collision rate in the disk and the large amounts of material accumulated and compressed in the innermost regions led to the first starburst episode, characterized by very intense star formation activity in the nuclear regions, and lower-level activity elsewhere in the disk. The intense nuclear burst and subsequent high rate of supernova explosions consumed rapidly the gas supply and expelled the remaining gas via the starburst wind, thereby creating the central cavity in the ISM and preventing further star formation. Subsequent evolution of starburst activity in M 82 could be explained by the direct consequences of the presence of the bar, or via "inside-out" propagation, as described below. The global star formation rate derived from the spatially detailed modeling of M 82, characterized by two pronounced peaks, is more consistent with a bar-driven evolution.

• Bar-driven evolution

Numerical simulations show that bars in galactic disks can be induced by galactic interactions and are very effective at driving material towards the central regions of galaxies (*e.g.* Combes & Gérin 1985; Noguchi 1987, 1988; Shlosman *et al.* 1989; Athanassoula 1992). Ring-like or spiral-like dynamical resonances may develop under the action of such non-axisymmetric perturbations. The existence and locations of the resonances depend on the characteristics of the bar (such as the angular velocity) and on the detailed galactic rotation curve, *i.e.* the mass distribution. In the presence of inner Lindblad resonances (ILRs), the radial inflow of material is stopped before it reaches the nucleus of the galaxy and the gas accumulates in a circumnuclear ring. Star formation is triggered by shocks in the ring and along the bar, or its leading dust lanes, and may be particularly enhanced at their intersections.

The second starburst episode in M 82 could thus be explained by the presence of the bar and accompanying ILRs (see also Telesco *et al.* 1991; Lo *et al.* 1987; Achtermann & Lacy 1995). The locations of the gas and dust concentrations are consistent with the two ILRs expected if the bar angular velocity is 50 $\mathrm{km\,s^{-1}\,kpc^{-1}}$, as argued by Telesco *et al.* (1991). An enhancement of star formation activity where the ISM streaming along the bar meets the ionized ring seems supported by the observations of the [Ne II] 12.8 μm emission (Achtermann & Lacy 1995) and by the star formation rate for the young bursts being higher near B2 (figures 7.12 and 7.13). The ionized ridges result from recent star formation due to shocks in the leading dust lanes presumably tracing the inflow (Larkin *et al.* 1994; Achtermann & Lacy 1995). Similar scenarios have been proposed for other starburst galaxies as well as more quiescent spiral galaxies in which circumnuclear rings of enhanced gas density and star formation activity coexist with stellar or gaseous bars (*e.g.* Telesco & Decher 1988; Telesco, Dressel & Wolstencroft 1993; Knapen *et al.* 1995; Böker, Förster Schreiber & Genzel 1997).

The apparent outward progression of starburst activity suggested by the sequence Nuclear supergiants → Ionized ring → Molecular ring may reflect the temporal development of the bar and redistribution of the mass, as suggested by Telesco *et al.* (1991). The bar may have played a role during the first starburst episode by channeling the nuclear inflow before the present dynamical resonances appeared.

The double-peaked shape of the global star formation rate in M 82 can be interpreted as follows: *1)* initial triggering of starburst activity by the M 82 – M 81 interaction and possibly the induced bar, *2)* rapid exhaustion due to severe disruption of the ISM by stellar winds and supernova explosions from massive stars, *3)* subsequent development of dynamical resonances and triggering of starburst activity in a circumnuclear ring and along the bar, and *4)* rapid exhaustion again. The short global burst timescales suggest that the fueling mechanisms providing the gas supply were not sufficient to overcome the strong negative feedback effects of the starburst activity they triggered. Recent numerical simulations of the dynamical evolution of barred galaxies including the effects of star formation show that the intensity of star formation can vary substantially with time, exhibiting a recurrent burst behaviour with typical timescale of ~ 10 Myr which is caused by the ability of massive stars to destroy the flow pattern when a sufficient number of them coexist in a particular place (Heller & Shlosman 1994; Knapen *et al.* 1995).

- **Inside-out propagation**

In this scenario, "self-triggered" star formation activity propagates radially in the disk as a consequence of the powerful nuclear burst and the expanding shock wave generated by the stellar winds and supernova explosions of massive stars. This progression explains naturally the radial sequence of red supergiants, ionized ring and molecular ring. The age difference between the "old burst" in the central 35 pc of M 82 and the "young bursts" along the ionized ring implies a propagation speed of 12 $\mathrm{km\,s^{-1}}$ for a ring radius of 85 pc. If the Brγ source B1 (at a projected radius of 160 pc) is more representative of the present location of the propagating starburst, a speed of 22 $\mathrm{km\,s^{-1}}$ is inferred. Interestingly, these velocities are similar to the normal expansion velocities of H II regions (*e.g.* Yorke 1986; Osterbrock 1989). Also interesting is the fact that the arc-like structure seen in the [Fe II] 1.644 μm 3D map has a projected radius of ≈ 70 pc, close to that of the ionized ring. Satyapal *et al.* (1997) derived significantly larger propagation speeds of $40 - 60$ $\mathrm{km\,s^{-1}}$. However, their estimates were based on the modeling of the compact K-band sources associated to clusters of red supergiants, with a somewhat smaller age difference over a much larger projected distance.

Although inside-out propagation may have contributed to the evolution of starburst activity, the global star formation history determined in this work suggests it is not the dominant factor. Indeed, without dynamical resonances, a smoother, radially decreasing density profile for the ISM is expected. The two pronounced peaks of the integrated star formation rate are difficult to reconcile with an inside-out propagation in such a medium.

7.7.4 The global picture

The scenario proposed for starburst activity in M 82 is sketched in figure 7.16, and illustrated in figure 7.17 with maps of representative tracers of the main phases.

Event	Observational tracer
• Following the gravitational interaction between M 82 and M 81, $\sim 10^8$ yr ago, the ISM in M 82 experienced large-scale torques, loss of angular momentum, and important infall towards the nuclear regions. The stellar bar induced by the interaction possibly played a role in channeling the inflow. In the absence of dynamical resonances, the infalling material can reach the nucleus.	• Bridges and tails of neutral atomic hydrogen are indicative of an interaction between M 82 and its massive neighbour M 81. The distribution of the $2.2\,\mu$m emission provides evidence for the existence of a ~ 1 kpc–long stellar bar.
• The first starburst episode took place $8 - 15$ Myr ago in the central 450 pc of M 82, with short duration. The central few tens of parsecs at the nucleus hosted the most intense star formation activity.	• The CO bandheads, the $2.2\,\mu$m continuum emission and the compact non-thermal radio sources trace the red supergiants and SNRs, the descendants of the massive stars formed during the first starburst episode.
• The second starburst episode was triggered due to bar-induced dynamical resonances. Enhanced star formation has occurred $4 - 6$ Myr ago, predominantly in a circumnuclear ring and along the stellar bar, and has decayed rapidly.	• The Brγ and He I $2.058\,\mu$m line emission trace the H II region complexes powered by the young OB stars formed during the second starburst episode.
• A supernova-driven starburst wind originating in the center of M 82 has broken out of the galactic plane, the dramatic aftermath of the powerful nuclear burst. The outflow component in the disk may have played some role in triggering the second starburst episode.	• The [Fe II] $1.644\,\mu$m emission from shock-excited gas enriched in iron due to dust grain destruction may trace the interaction between the disk ISM and the material entrained by the starburst wind along the minor axis.

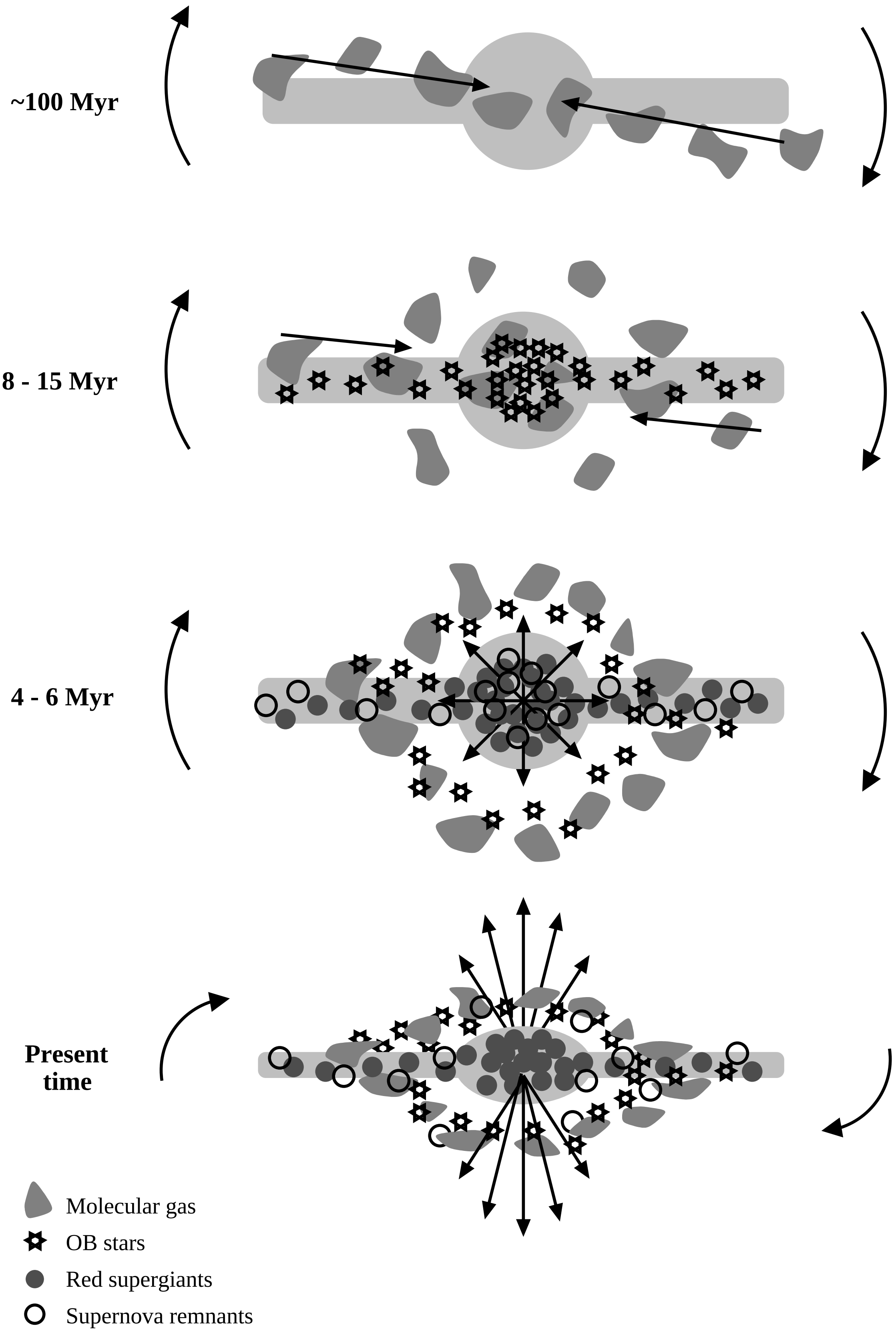

Fig. 7.16.— Sketch of the succession of events related to starburst activity in M 82, as described in the text. The galaxy is illustrated as viewed from above the plane except for the bottom panel, where it is inclined to show the starburst wind.

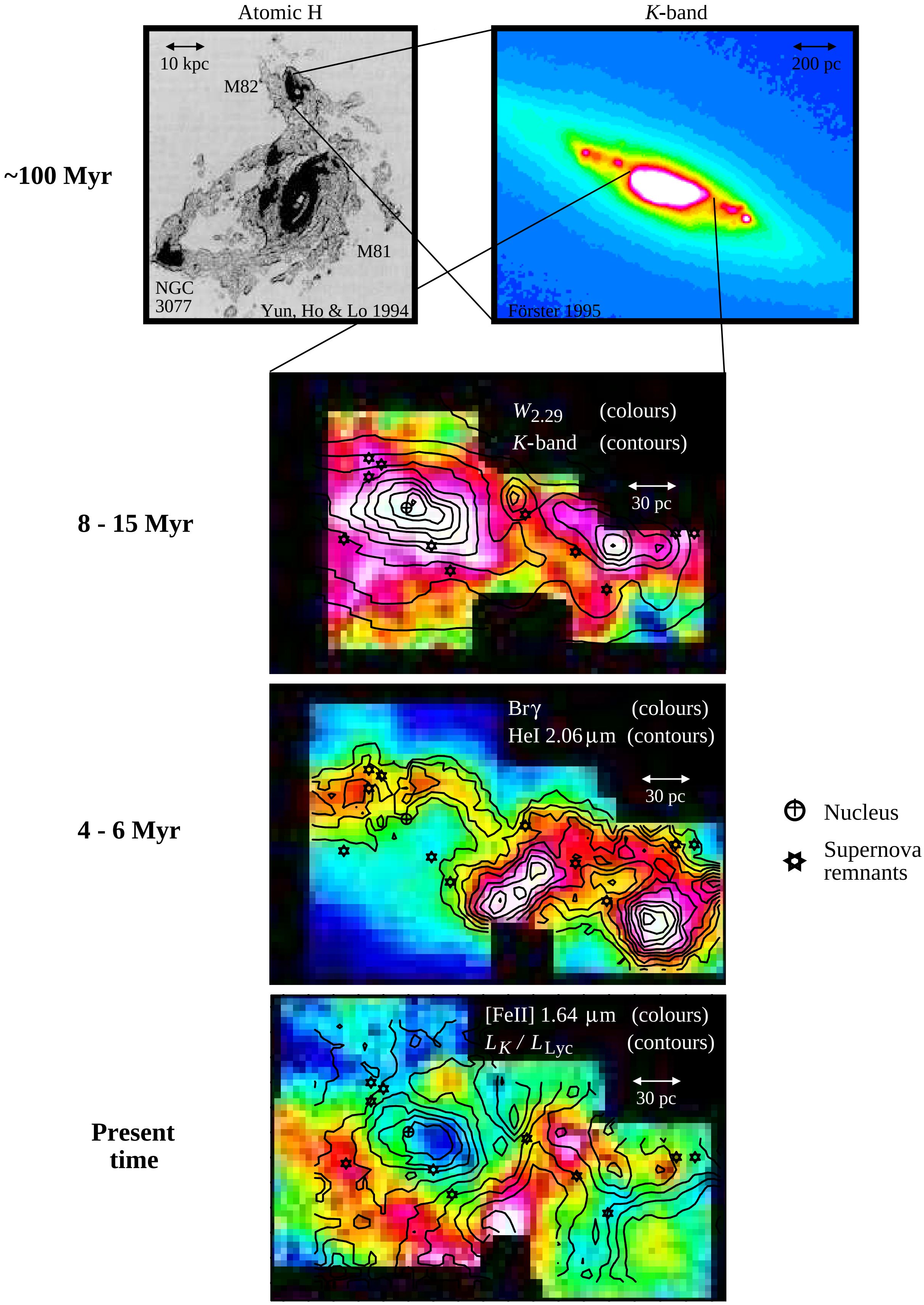

Fig. 7.17.— Representative observational tracers of the succession of events related to starburst activity in M 82, as described in the text. The locations of the supernova remnants are from Kronberg, Biermann & Schwab (1985).

7.8 Summary

In this chapter, the star formation parameters and the spatial and chronological evolution of starburst activity in M 82 have been investigated. The results are summarized in the following table.

STAR FORMATION PROCESS

Initial mass function	Formation of very massive stars in the range 50 $M_\odot$ to > 100 $M_\odot$ Indications of a deficit in low-mass stars
Star formation rate	Burst timescale of a few million years or less on all spatial scales

STARBURST EVOLUTION

Two successive starburst episodes — Bar-driven evolution	
First episode	8 – 15 million years ago Powerful nuclear starburst in the central few tens of parsecs Extended lower level starburst activity throughout the central 450 pc
Second episode	4 – 6 million years ago Starburst activity concentrated in a circumnuclear ring and along the stellar bar Consistent with dynamical resonances associated with the bar

The most important results are:

- Starburst activity in M 82 has occurred in individual burst sites with sizes and star formation properties comparable to those of Galactic and near-extragalactic high-mass star-forming regions.
- The typical burst timescale is very short locally *and* globally, indicating very strong negative feedback effects of starburst activity. Short local timescales reflect the rapid disruption of the surrounding environment by stellar winds and supernova explosions of massive stars. Short global timescales suggest that the important massive star populations formed in the bursts have affected the large-scale dynamical processes fueling starburst activity.
- The global star formation history characterized by two successive episodes is consistent with the first episode triggered by the M 82 – M 81 interaction and possibly by the stellar bar induced, and the second episode due to dynamical resonances and to shocks along the bar.

Chapter 8

Summary and conclusions

The results of this dissertation provide, for the first time, a fully quantitative description of the nature and evolution of starburst activity in M 82. Contrary to most previous studies of starburst galaxies, this work presents a detailed analysis and modeling not only of the global properties of M 82, but also those of *individual* regions on spatial scales typical of giant star-forming regions and molecular clouds. Advantage was taken of the unique opportunities offered by near-infrared imaging spectroscopy with the 3D instrument, and by mid-infrared observations with the Short Wavelength Spectrometer on board the *ISO* satellite. These data provided crucial diagnostics for the physical conditions of the ISM and the composition of the stellar population, several of which were previously inaccessible or very difficult to observe. Together with existing data at other wavelengths and with the application of an evolutionary synthesis model, the 3D and *ISO* data enabled the investigation of crucial star formation parameters, the characterization of the star formation process in a starburst environment, and the determination of the spatial and chronological evolution of starburst activity in M 82. The main results are summarized here.

For the interpretation and modeling of the 3D and *ISO* data, various tools were developed. In chapter 2, a new library of moderate resolution spectra of giants and supergiants obtained with 3D was presented. This new library widens existing near-infrared stellar spectral atlases. The data on several absorption features from these libraries were combined to provide useful diagnostics for the composition of evolved stellar populations and the contributions of featureless sources of continuum emission in studies of composite systems, in particular the CO bandheads at 1.62 μm and 2.29 μm and the Si I feature at 1.59 μm.

In chapter 3, the evolutionary synthesis code STARS was optimized for applications to infrared observations of starburst galaxies. The stellar evolutionary tracks for intermediate-mass stars were extended to the thermally-pulsing asymptotic giant branch phase, during which they make a significant contribution to the integrated bolometric and near-infrared luminosities. The data on near-infrared stellar absorption features from the 3D library and similar atlases were implemented in STARS to augment the number of predicted properties. New models were developed for the evolutionary synthesis of *ensembles* of evolving stellar clusters and of the nebular emission spectrum they excite in surrounding H II regions. These models are based on results from STARS and from the photoionization code CLOUDY. For a given global upper mass cutoff of the IMF, the effects on the integrated properties of a distribution of cluster masses and luminosities can amount up to a factor of a few compared to predictions for a single cluster.

In chapters 5 and 6, nebular analysis and stellar population synthesis were applied to the 3D and *ISO* data of M 82, together with existing data in the literature. The extinction towards the ionized gas and towards the evolved stars was constrained. Extinction models consisting of obscuring dust mixed with the sources are appropriate for the global extinction towards the ionized gas. The *ISO* data suggest possible deviations from the widely used Draine extinction law between $3\,\mu$m and $10\,\mu$m. Extinction laws in this wavelength range were, so far, poorly determined because of the lack of accurate diagnostics. The *ISO* data have now filled this void. The data for M 82 are consistent with the extinction law found from *ISO* observations towards the Galactic Center (Lutz *et al.* 1996), indicating more extinction than predicted for standard graphite-silicate mixtures of interstellar dust. The physical conditions of the ISM within the H II regions of M 82 were determined, including the electron density, the gas-phase abundances and the ionization parameter. The abundances are nearly solar or slightly above for Ne and Ar, and one-fourth solar for S, perhaps due to depletion onto interstellar dust grains. The relative distributions of the ionizing stellar clusters, of the ionized gas, and of the molecular gas were investigated in order to determine the appropriate equivalent geometry and effective ionization parameter for photoionization modeling of M 82. Significant spatial variations in the composition of the stellar population, especially for the evolved stars, are derived on small spatial scales. Red supergiants dominate the near-infrared luminosity over most of the starburst core of M 82, and their metallicity is roughly solar. The contribution to the total near-infrared continuum emission from hot dust also varies spatially and amounts to $30\% - 50\%$ in some regions.

In chapter 7, evolutionary synthesis modeling of M 82 was presented. Application to the global properties as well as to those of *individual* regions on scales as small as a few tens of parsecs led to a detailed quantitative picture of starburst activity in M 82. The data are consistent with the formation of very massive stars, which are now evolved or dead. Starburst activity has occurred in individual burst sites. With typical parsec- or

10-parsec scales, the formation of very massive stars, and short burst timescales of a few million years or less, these burst sites are similar to Galactic and near-extragalactic high-mass star-forming regions. The low-mass IMF is still poorly constrained. The data do not require an abrupt truncation of the IMF at a few solar masses, as often believed. For a Salpeter IMF, stars down to about 0.7 $M_\odot$ can form without exceeding a plausible mass limit for the starburst populations. Alternatively, the IMF can extend down to 0.1 $M_\odot$ provided it flattens sufficiently below 1 $M_\odot$. Finally, if the inflection point is moved to a few solar masses, a less severe flattening is required. This result is difficult to interpret since the low-mass IMF in templates of high-mass star-forming regions in the Milky Way and Magellanic Clouds is also still very uncertain.

The spatial distribution of the burst ages and intensities has made it possible to retrace the detailed spatial and chronological evolution of starburst activity in M 82. The most outstanding result is the episodic nature of the global starbursts, with typical timescale $< 10^7$ yr. This is significantly shorter than the usual assumptions of continuous star formation during $10^7 - 10^8$ yr. While such short burst timescales are expected locally because of the stellar winds and supernova explosions rapidly disrupting the surrounding ISM, this is a surprising result for global star formation activity. This result suggests that intense starburst activity has affected the large-scale dynamical processes which provided the gas supply (for instance bar-driven mechanisms), and therefore also plays a dominant role in its own, global evolution.

This dissertation demonstrates the importance of spatially detailed analyses and modeling for the understanding of the starburst phenomenon. Only with such data can realistic evolutionary scenarios be established and global properties be correctly interpreted. The nature and evolution of starburst activity in M 82 pose important constraints on theoretical modeling of the dynamics of star-forming galaxies. As representative of starburst galaxies as M 82 may be in its global properties, similar studies of other starburst systems in a variety of galactic environments will be crucial to outline the generalities of the starburst phenomenon and identify the characteristics which depend most sensitively on the dynamics and physical conditions of the host system. This is particularly important in order to provide appropriate templates for the investigation of the star formation history and galaxy evolution in the early Universe. A few studies comparable to that presented here have been conducted recently (*e.g.* for NGC 253 and IC 342; Engelbracht *et al.* 1998; Böker *et al.* 1997). With the rapid development of instruments with capabilities similar to or better than 3D and those on board *ISO*, coupled with the new generation of large ground-based telescopes and future satellite missions, such essential detailed studies should be much easier to carry out in the near-future.

Appendix A

Stellar evolution

The present work makes an extensive use of stellar libraries and stellar evolutionary models. This appendix is intended to provide a more general overview of stellar evolution, and to identify the specific stellar populations, and thus evolutionary phases, usually accessible with near- and mid-infrared observations of starburst galaxies.

Stellar evolution theory is amply discussed in a number of astronomy textbooks (*e.g.* Clayton 1983; Kippenhahn & Weigert 1991). Several review articles in the past fifteen years have focused on particular evolutionary phases in light of new observations and improvements in theoretical modeling (*e.g.* Iben & Renzini 1983; Chiosi & Maeder 1986; Chiosi, Bertelli & Bressan 1992; Maeder & Conti 1994). This appendix is based on these references, as well as on various others which provide exhaustive details on theoretical modeling and empirical data related to the evolution of stars, including Maeder & Meynet (1989, 1994), Sweigart, Greggio & Renzini (1990), Boothroyd & Sackmann (1988a,b,c,d), Bedijn (1988), Groenewegen & de Jong (1993), Groenewegen, van den Hoeck & de Jong (1995), Forestini & Charbonnel (1997).

A.1 Basic stellar evolution

Independently of the chemical composition, stars can be classified in three categories according to their initial mass (m_0), evolutionary history and final fate: low-mass stars, intermediate-mass stars and massive stars. Low-mass stars have m_0 between 0.08 $M_\odot$ (the minimum mass for the onset of hydrogen burning at a rapid enough rate to stop the gravitational collapse) and 2 $M_\odot$. Intermediate-mass stars have 2 $M_\odot < m_0 < 8$ $M_\odot$

Table A.1: Typical lifetime of stars in various evolutionary phases (in units of 10^6 years)[(a)]

m_0 [$M_\odot$]	H-burning phase	He-burning phase	TP-AGB phase	C-burning phase
120	2.5614	0.4145	—	0.009498
85	2.8228	0.3923	—	0.006734
60	3.4469	0.4233	—	0.009144
40	4.3032	0.4648	—	0.008947
25	6.4077	0.6297	—	0.009385
20	8.1409	0.7885	—	0.01418
15	11.5842	1.1160	—	0.02793
12	16.0176	1.5689	—	0.04931
9	26.3886	2.6233	—	0.11706
7	43.1880	4.7260	0.52	—
5	94.4591	12.4288	0.32	—
4	164.734	26.1720	0.55	—
3	352.503	86.1926	1.37	—
2.5	584.916	145.365	1.38	—
2	1115.94	240.930	1.39	—
1.7	1827.31	—	—	—
1.5	2694.65	—	—	—
1.25	4912.63	—	—	—
1	9961.73	—	—	—
0.9	15500.30	—	—	—
0.8	25027.88	—	—	—

[(a)] Lifetimes in the H-, He- and C-burning phases are from Schaller *et al.* (1992). Lifetimes in the thermally-pulsing asymptotic giant branch (TP-AGB) phase are from Bedijn (1988).

and massive stars have m_0 above 8 $M_\odot$. The exact limits depend on the chemical composition, and on the details of the modeling.

The physical properties of stars change as they evolve. Their evolution can be partly described in terms of the effective temperature ($T_{\rm eff}$) and bolometric luminosity ($L_{\rm bol}$), and most conveniently by means of the theoretical Hertzsprung-Russell diagram (HRD), illustrated in figure A.1 for representative model stars. Typical lifetimes for various phases are given in table A.1. The initial chemical composition affects somewhat the evolutionary tracks, which also vary between different authors, but the general features remain the same.

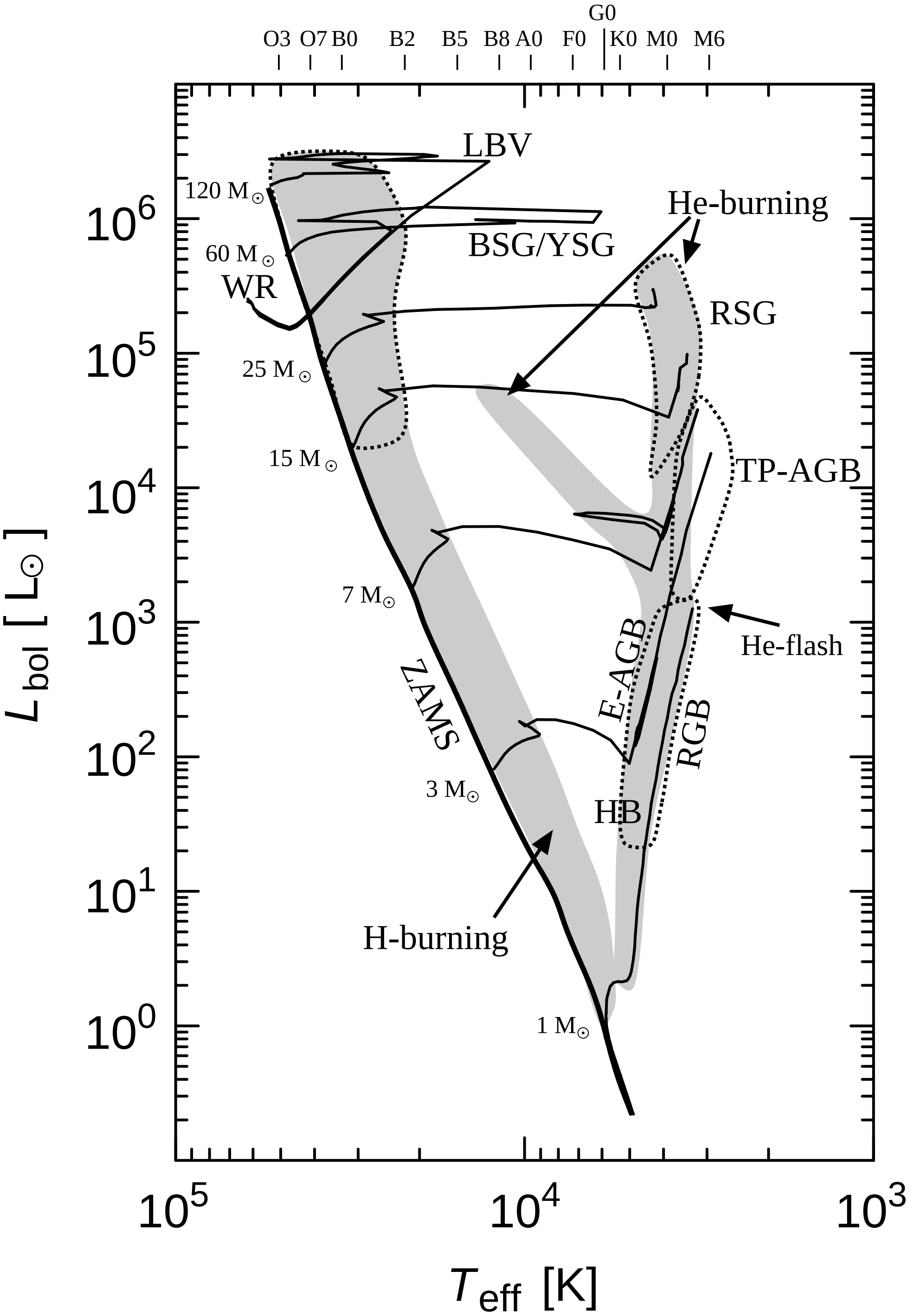

Fig. A.1.— Evolutionary paths in the theoretical HRD of model stars with solar metallicity and different initial masses (Schaller *et al.* 1992: low-mass stars up to the He-flash, intermediate-mass stars up to the end of the E-AGB, high-mass stars up to the end of core-C burning; Bedijn 1988: TP-AGB for intermediate-mass stars). The spectral types for different temperatures are labeled at the top of the diagram. The slow phases of nuclear burning are indicated with grey shade; the particular phases accessible with near- and mid-infrared observations are indicated by the dotted lines. ZAMS stands for zero-age main-sequence; RGB for red giant branch; HB for horizontal branch; E-AGB and TP-AGB for early and thermally-pulsing asymptotic giant branch; BSG, YSG and RSG for blue, yellow and red supergiants; LBV for luminous blue variables; and WR for Wolf-Rayet stars (see text).

A.1.1 Core and shell H-burning, core He-burning

The first — and longest — phase in the life of a star is that of core H-burning, and progressive formation of a He-rich core, on the main sequence (MS). For stars with $m_0 \lesssim 1$ M$_\odot$, this occurs in radiative conditions, whereas in the more massive ones, the nuclear and gravitational energy is transferred by convection. The position on the MS is primarily determined by m_0. Observationally, luminosity class V stars of all temperatures (also called "dwarfs") lie on the MS.

After the MS phase, low-mass stars develop a degenerate helium core and ascend the red giant branch (RGB) until violent core He-burning begins in a thermonuclear runaway (the "He-flash"). The degeneracy is gradually removed and the He-burning proceeds quiescently in a convective core while the star is on the horizontal branch (HB). Meanwhile, hydrogen continues burning in a shell.

Intermediate- and high-mass stars up to about 15 M$_\odot$ evolve rapidly to the red giant/supergiant region, burning hydrogen in a thin shell above a rapidly contracting and heating core, composed essentially of helium. Helium is ignited in non-degenerate conditions when the central temperature and density reach the appropriate threshold values. Convective core He-burning takes place in two regions, first near the Hayashi line[1] at low $T_{\rm eff}$, then in the "blue band" at higher $T_{\rm eff}$ owing to the "blue loops".

The evolution of higher mass stars is more complicated because it is dominated by important mass-loss through stellar winds and by convection. Briefly, the stars become cooler and move redward in the HRD. Stars with m_0 below about 25 M$_\odot$ become red supergiants, those with $m_0 < 20$ M$_\odot$ loop blueward (blue supergiants) and then move back as red supergiants again. Stars with m_0 between about 25 M$_\odot$ and 60 M$_\odot$ first become blue supergiants and then, red supergiants. If mass-loss is important enough, the H-rich envelope is completely lost, the helium core is exposed, the stars move consequently blueward beyond the MS and they become good candidates for Wolf-Rayet stars. The most massive stars, on the other hand, have such strong stellar winds that their outer layers are peeled off rapidly even prior to core He-burning and become Wolf-Rayet stars, after a short time spent as luminous blue variables.

Core He-burning turns helium into carbon, oxygen and traces of heavier elements. After core He-exhaustion, stars are composed of a C-O core, a He-burning shell and, in low- and intermediate-mass stars, an H-rich envelope at the base of which an H-burning shell is active.

[1] defined as the locus of fully convective stars, and representing the borderline between allowed and forbidden regions in the HRD (at lower and higher $T_{\rm eff}$ respectively) for stars in hydrostatic equilibrium and with fully adjusted convection

A.1.2 Later evolutionary phases

Following core He-exhaustion, low- and intermediate-mass stars evolve through the asymptotic giant branch (AGB) phase, itself divided in the early-AGB (or E-AGB) and the thermally-pulsing AGB (or TP-AGB). During the E-AGB, the C-O core becomes degenerate while the H-rich envelope expands, eventually extinguishes, cools, falls back and ultimately reignites. The TP-AGB, or double-shell burning phase, then begins. It is characterized by successive cycles of unstable shell He-burning in a thermonuclear runaway ("He-shell flash"), radial expansion until the He-burning becomes quiescent, followed by shell H-burning once the envelope has fallen back again. H-burning provides most of the luminosity during 90% of the period between two flashes, while He-burning, during only 10%. The TP-AGB phase ends when the H-rich envelope is lost due to stellar winds, leaving a hot, central white dwarf illuminating a planetary nebula. In very low-mass stars ($m_0 \lesssim 1$ M$_\odot$), the ejection of the envelope may be completed even before the TP-AGB phase begins. In principle, stars with $m_0 > 4 - 6$ M$_\odot$ could build up a C-O core reaching the Chandrasekhar limit of 1.4 M$_\odot$, when carbon in the highly degenerate C-O core would ignite in a deflagration; however, this is not confirmed by observations.

Massive stars, on the other hand, develop a non-degenerate C-O core and ignite carbon non-violently. Through a series of nuclear burnings, they proceed either to the construction of an iron core and subsequent photodissociation instability with core collapse and supernova explosion (for $m_0 \gtrsim 12$ M$_\odot$), or following a more complicated scheme, undergo core collapse and supernova explosion (8 M$_\odot$ $< m_0 \lesssim 12$ M$_\odot$). In both cases, the remnant consists of a degenerate neutron star. These stages succeed to one another so rapidly that the details are barely relevant for the understanding of observational HRDs or in the modeling of evolving stellar populations.

A.1.3 Mass-loss and internal mixing

Mass-loss by stellar winds is important during all evolutionary phases in massive stars, and lead to Wolf-Rayet stars for $m_0 \gtrsim 25$ M$_\odot$, as already mentioned above. In lower mass stars, significant mass-loss occurs during the RGB and AGB phases. For instance, OH/IR stars, severely obscured and identified primarily by their 1612 MHz OH maser emission originating in a thick dusty envelope, presumably correspond to a phase of substantial mass-loss on the TP-AGB. Planetary nebulae are thought to be the ejecta resulting from "superwinds" at the end of the AGB evolution.

Mixing between zones of different chemical composition in stellar interiors can occur through a variety of processes such as convection and rotational shears, whose relative importance varies in different types of stars. Various convective instabilities play an important role in the evolution of stars of all masses. In addition, changes in the surface composition of stars are attributed notably to the inward extension of a convective envelope or layer until it reaches processed material which is thereby dredged-up to the surface. This occurs, in low- and intermediate-mass stars, during the RGB phase close to the Hayashi line (first dredge-up), during the E-AGB phase (second dredge-up), and recurrently during the TP-AGB phase (third dredge-up). In particular, in the current picture of TP-AGB evolution, oxygen-rich stars with surface abundance $C/O < 1$ can be transformed into carbon-rich stars with $C/O > 1$ via the third dredge-up. Observationally, these objects are associated notably with oxygen-rich Mira variables and N-type carbon stars respectively. Intermediate stages with C/O of about unity presumably correspond to the MS, S and SC spectral types.

Mass-loss and internal mixing are determinant factors affecting the evolution of stars and the duration of various phases. However, these processes as well as the conditions under which they may occur are still ill-understood, and remain among the major sources of uncertainties in theoretical modeling of stellar evolution and stellar atmospheres (*e.g.* Langer & Maeder 1995; Maeder & Meynet 1996; Gronewegen, van den Hoek & de Jong 1995; van den Hoek & Groenewegen 1997).

A.2 Evolutionary phases accessible with near- and mid-infrared observations of starburst galaxies

Generally speaking, the stars which are *directly* observable at a given wavelength in a composite system are those which, by the combined effects of temperature, luminosity and number, dominate the integrated emission of a stellar population. At near-infrared wavelengths, the coolest stars — late-G, K and M types, with temperatures in the range 2500 K – 5000 K — will dominate the luminosity because their spectral energy distributions peak around $1\,\mu$m. For a normal initial mass function (IMF), red giants are statistically less numerous than red dwarfs because of their shorter lifetimes, but since they are orders of magnitude more luminous, their emission will dominate the near-infrared continuum whenever they are present. Similarly, AGB stars and red supergiants will outshine the more numerous but less luminous red giants. The broad-band colours and the absorption features produced in the atmosphere of cool stars allow the characterization of their average properties, such as temperature, luminosity and chemical composition. In starburst galaxies, red supergiants formed in recent and intense star formation events ($\sim 10 - 50$ Myr ago) often dominate the near-infrared luminosity (*e.g.* Ridgway, Wynn-Williams & Becklin 1994; Goldader *et al.* 1995).

Beyond $3\,\mu$m, stars are usually not directly observable anymore in starburst galaxies, due to their decreasing spectral energy distributions which are by far surpassed by thermal dust emission. However, hot, massive stars become indirectly observable via the emission-line spectra they excite in the surrounding H II regions, in the mid-infrared as well as in the near-infrared (hydrogen and helium recombination lines, fine-structure lines of most abundant atoms). The absolute and relative line intensities depend on the physical conditions and chemical abundances of the nebula, but also on the spectral energy distributions of the ionizing sources. The average temperature and luminosity of the exciting stars can thereby be constrained.

A.3 Stellar properties

Some of the most relevant stellar properties are given in tables A.2, A.3 and A.4 for "normal" main-sequence, giant and supergiant stars. Classes of peculiar stars of interest in this work include variable AGB stars and carbon stars. In contrast to normal stars, no definitive classification in terms of fundamental physical parameters exists for these stars. This is mainly due to the scarcity of systematic and exhaustive studies of these rare stars, and to their complex and variable nature which make temperature and luminosity determinations, for example, very difficult. The main characteristics of AGB and carbon stars are summarized below.

AGB stars can be classified in three categories depending on the nature of their variability: the regular Mira variables, the semi-regular variables of type SRa and SRb, and the irregular variables of type Lb. The periodicity typically ranges from ~ 10 to ~ 2000 days. These classes can be further divided according to surface composition into oxygen-rich (*e.g.* Miras, or very late M-type stars), carbon-rich (*e.g.* N-type carbon stars) and intermediate composition (*e.g.* MS, S and SC stars). All these subtypes are presumably in the TP-AGB phase, except for some oxygen-rich SRb's which are thought to lie on the E-AGB. Additional TP-AGB stars include the OH/IR stars and Infrared Carbon Stars, which generally have very thick oxygen- or carbon-rich dust envelopes and are often completely obscured at optical wavelengths. TP-AGB stars have luminosities of the order of $10^3 - 10^4$ L$_\odot$, temperatures of about $1500 - 3000$ K and mass-loss rates in the range $10^{-8} - 10^{-4}$ M$_\odot$ yr^{-1}. More details can be found notably in Claussen *et al.* (1987), Jura (1988), Jura & Kleinmann (1989, 1992a, 1992b), Jura, Yamamoto & Kleinmann (1993), Epchtein, Le Bertre & Lépine (1990), Lépine, Ortiz & Epchtein (1995), Groenewegen *et al.* (1992), Kerschbaum & Hron (1992), Kerschbaum, Lazaro & Habison (1996).

The term "carbon star" actually designates a heterogeneous group of stars which are related primarily through their spectral properties rather than being associated to a particular evolutionary phase. Carbon stars were originally identified by the effects of deep absorption features from carbon compounds in their optical spectra (*e.g.* Secchi 1868; Cannon & Pickering 1918; Shane 1928; Keenan & Morgan 1941; Yamashita 1972, 1975; Keenan 1993). These stars are usually divided in three subclasses: the N, R and CH types. They correspond to distinct stellar populations differing notably in detailed chemical composition, mean luminosity, temperature range, as well as in space velocity and distribution in our Galaxy (*e.g.* Keenan 1993; Parthasarathy 1991). Their only common property is a photospheric carbon overabundance (C/O > 1). The N stars are concentrated in the Galactic plane, have high luminosities of $10^3 - 10^4$ $L_\odot$, low effective temperatures about 3000 K, enhanced abundances of *s*-process elements such as Ba and Zr, and are often surrounded by circumstellar shells (*e.g.* Wallerstein 1973; Tsuji 1981a, 1981c; Ohnaka & Tsuji 1996). These facts suggest that they lie on the TP-AGB where they undergo double-shell burning and mass-loss.

Early-R and CH stars, on the other hand, have temperatures and luminosities similar to normal field G and K giants. Early-R stars belong to the old disk population, do not exhibit enhancements of *s*-process elements and are ^{13}C-rich. They have presumably not yet experienced double-shell burning and are possibly related to the He-core flash (*e.g.* Dominy 1985; Parthasarathy 1991). The status of late-R stars is still not clear because of the difficulty in distinguishing them from the hottest N stars (Keenan 1993). The CH stars are predominantly population II giants with high *s*-process elements abundances and a high incidence of duplicity, suggesting a connection with barium stars (*e.g.* Dominy 1985; Parthasarathy 1991). Their overabundance of carbon could be due to mass transfer in a binary system (*e.g.* McClure 1989).

Table A.2: Physical parameters of main-sequence stars

Type	$T_{\rm eff}$ [K]	$L_{\rm bol}$ [$L_\odot$]	m [$M_\odot$]	$\log Q_{\rm Lyc}$ [s^{-1}]	L_V [$L_\odot$]	L_K [$L_\odot$]
O3	51230	1.1×10^6	87.6	49.87	2.1×10^3	6.8×10^1
O4	48670	7.6×10^5	68.9	49.70	1.7×10^3	5.5×10^1
O4.5	47400	6.4×10^5	62.3	49.61	1.5×10^3	5.0×10^1
O5	46120	5.3×10^5	56.6	49.53	1.4×10^3	4.5×10^1
O5.5	44840	4.4×10^5	50.4	49.43	1.2×10^3	4.1×10^1
O6	43560	3.7×10^5	45.2	49.34	1.1×10^3	3.7×10^1
O6.5	42280	3.1×10^5	41.0	49.23	1.0×10^3	3.3×10^1
O7	41010	2.5×10^5	37.7	49.12	9.0×10^2	3.0×10^1
O7.5	39730	2.1×10^5	34.1	49.00	8.2×10^2	2.7×10^1
O8	38450	1.7×10^5	30.8	48.87	7.4×10^2	2.4×10^1
O8.5	37170	1.4×10^5	28.0	48.72	6.7×10^2	2.2×10^1
O9	35900	1.2×10^5	25.4	48.56	6.0×10^2	2.0×10^1
O9.5	34620	9.4×10^4	23.3	48.38	5.4×10^2	1.9×10^1
B0	33340	7.6×10^4	21.2	48.16	4.9×10^2	1.7×10^1
B0.5	32060	6.2×10^4	19.3	47.90	4.4×10^2	1.6×10^1
B1	25400	1.6×10^4	13.0	—	1.9×10^2	7.4×10^0
B2	22000	5.7×10^3	9.8	—	4.7×10^1	7.1×10^0
B5	15400	8.3×10^2	5.9	—	2.1×10^1	1.6×10^0
B8	11900	1.8×10^2	3.8	—	1.2×10^1	7.4×10^{-1}
A0	9520	5.4×10^1	2.9	—	5.8×10^0	4.5×10^{-1}
F0	7200	6.5×10^0	1.6	—	8.4×10^{-1}	1.3×10^{-1}
G0	6030	1.5×10^0	1.05	—	1.8×10^{-1}	4.2×10^{-2}
G2	5860	1.1×10^0	1.00	—	1.3×10^{-1}	3.7×10^{-2}
G5	5770	7.9×10^{-1}	0.92	—	9.2×10^{-2}	9.5×10^{-3}
G8	5570	6.6×10^{-1}	0.87	—	6.4×10^{-2}	2.1×10^{-2}
K0	5250	4.2×10^{-1}	0.79	—	4.4×10^{-2}	1.7×10^{-2}
K1	5080	3.7×10^{-1}	0.77	—	3.7×10^{-2}	1.8×10^{-2}
K2	4900	2.9×10^{-1}	0.74	—	2.8×10^{-2}	1.7×10^{-2}
K3	4730	2.6×10^{-1}	0.72	—	2.3×10^{-2}	1.8×10^{-2}
K4	4590	1.9×10^{-1}	0.69	—	1.6×10^{-2}	1.6×10^{-2}
K5	4350	1.5×10^{-1}	0.67	—	1.1×10^{-2}	1.4×10^{-2}
M0	3850	7.7×10^{-2}	0.51	—	3.0×10^{-3}	4.7×10^{-3}
M1	3720	6.1×10^{-2}	0.46	—	1.9×10^{-3}	3.7×10^{-3}
M2	3580	4.5×10^{-2}	0.40	—	1.1×10^{-3}	2.7×10^{-3}
M3	3470	3.6×10^{-2}	0.33	—	7.0×10^{-4}	2.1×10^{-3}
M4	3370	1.9×10^{-2}	0.27	—	3.0×10^{-4}	1.2×10^{-3}
M5	3240	1.1×10^{-2}	0.21	—	1.2×10^{-4}	5.9×10^{-4}
M6	3050	5.3×10^{-3}	0.17	—	4.0×10^{-5}	2.5×10^{-4}

Column 1: spectral type; column 2: effective temperature; column 3: bolometric luminosity; column 4: mass; column 5: logarithm of the production rate of Lyman continuum photons; column 6: V-band luminosity ($\lambda = 5500$ Å, $\Delta\lambda = 890$ Å); column 7: K-band luminosity ($\lambda = 2.2\ \mu$m, $\Delta\lambda = 0.6\ \mu$m). Data are from Vacca, Garmany & Shull (1996) and Schmidt-Kaler (1982). The L_K is computed from the L_V using the broad-band colours from Koornneef (1983b).

Table A.3: Physical parameters of giant stars

Type	$T_{\rm eff}$ [K]	$L_{\rm bol}$ [L$_\odot$]	m [M$_\odot$]	$\log Q_{\rm Lyc}$ [s^{-1}]	L_V [L$_\odot$]	L_K [L$_\odot$]
O3	50960	1.4×10^6	101.4	49.99	2.8×10^3	—
O4	48180	1.1×10^6	82.8	49.86	2.5×10^3	—
O4.5	46800	9.8×10^5	75.8	49.80	2.4×10^3	—
O5	45410	8.6×10^5	68.4	49.73	2.3×10^3	—
O5.5	44020	7.5×10^5	62.0	49.65	2.2×10^3	—
O6	42640	6.6×10^5	56.6	49.58	2.1×10^3	—
O6.5	41250	5.7×10^5	52.0	49.50	2.0×10^3	—
O7	39860	5.0×10^5	47.4	49.41	1.9×10^3	—
O7.5	38480	4.3×10^5	43.0	49.32	1.8×10^3	—
O8	37090	3.7×10^5	39.0	49.22	1.7×10^3	—
O8.5	35700	3.2×10^5	35.6	49.12	1.6×10^3	—
O9	34320	2.7×10^5	32.6	48.97	1.5×10^3	—
O9.5	32930	2.3×10^5	29.9	48.78	1.5×10^3	—
B0	31540	1.9×10^5	27.4	48.55	1.4×10^3	—
B0.5	30160	1.6×10^5	25.1	48.27	1.3×10^3	—
B1	24000	3.9×10^4	17	—	5.8×10^2	—
B2	20300	1.7×10^4	15	—	3.7×10^2	—
B5	15000	1.8×10^3	7	—	7.7×10^1	—
B8	12400	4.6×10^2	5	—	3.0×10^1	—
A0	10100	1.1×10^2	4	—	1.0×10^1	—
F0	7150	2.0×10^1	2.5	—	2.5×10^0	—
G0	5850	3.4×10^1	1.0	—	4.0×10^0	—
G2	5450	4.0×10^1	1.1	—	4.4×10^0	—
G5	5150	4.3×10^1	1.1	—	4.4×10^0	2.4×10^0
G8	4900	5.1×10^1	1.1	—	4.8×10^0	2.7×10^0
K0	4750	6.0×10^1	1.1	—	5.3×10^0	3.6×10^0
K1	4600	6.9×10^1	1.1	—	5.8×10^0	4.4×10^0
K2	4420	7.9×10^1	1.2	—	6.4×10^0	5.3×10^0
K3	4200	1.1×10^2	1.2	—	7.7×10^0	8.7×10^0
K4	4000	1.7×10^2	1.2	—	1.0×10^1	1.5×10^1
K5	3950	2.2×10^2	1.2	—	1.2×10^1	2.8×10^1
M0	3800	3.3×10^2	1.2	—	1.5×10^1	3.5×10^1
M1	3720	4.3×10^2	1.2	—	1.6×10^1	4.5×10^1
M2	3620	5.5×10^2	1.3	—	1.8×10^1	6.3×10^1
M3	3530	7.0×10^2	1.3	—	1.8×10^1	9.6×10^1
M4	3430	8.8×10^2	—	—	1.6×10^1	1.7×10^2
M5	3330	9.3×10^2	—	—	1.3×10^1	3.1×10^2
M6	3240	1.1×10^3	—	—	1.2×10^1	7.1×10^2

Column 1: spectral type; column 2: effective temperature; column 3: bolometric luminosity; column 4: mass; column 5: logarithm of the production rate of Lyman continuum photons; column 6: V-band luminosity ($\lambda = 5500$ Å, $\Delta\lambda = 890$ Å); column 7: K-band luminosity ($\lambda = 2.2\ \mu$m, $\Delta\lambda = 0.6\ \mu$m). Data are from Vacca, Garmany & Shull (1996) and Schmidt-Kaler (1982). The L_K is computed from the L_V using the broad-band colours from Koornneef (1983b).

Table A.4: Physical parameters of supergiant stars

Type	$T_{\rm eff}$ [K]	$L_{\rm bol}$ [L$_\odot$]	m [M$_\odot$]	$\log Q_{\rm Lyc}$ [s^{-1}]	L_V [L$_\odot$]	L_K [L$_\odot$]
O3	50680	1.9×10^6	115.9	50.11	3.7×10^3	—
O4	47690	1.6×10^6	104.7	50.02	3.7×10^3	—
O4.5	46200	1.5×10^6	95.7	49.98	3.7×10^3	—
O5	44700	1.4×10^6	86.5	49.93	3.8×10^3	—
O5.5	43210	1.3×10^6	79.5	49.87	3.8×10^3	—
O6	41710	1.2×10^6	74.7	49.81	3.8×10^3	—
O6.5	40210	1.1×10^6	69.6	49.75	3.8×10^3	—
O7	38720	9.6×10^5	64.3	49.69	3.9×10^3	—
O7.5	37220	8.7×10^5	59.2	49.62	3.9×10^3	—
O8	35730	7.9×10^5	54.8	49.54	3.9×10^3	—
O8.5	34230	7.0×10^5	50.6	49.45	3.9×10^3	—
O9	32740	6.3×10^5	46.7	49.33	4.0×10^3	1.4×10^2
O9.5	31240	5.5×10^5	43.1	49.17	4.0×10^3	1.5×10^2
B0	26000	2.6×10^5	25	—	3.7×10^3	1.5×10^2
B1	20800	1.5×10^5	24	—	3.7×10^3	1.7×10^2
B2	18500	1.1×10^5	23	—	3.7×10^3	2.0×10^2
B5	13600	5.2×10^4	20	—	3.0×10^3	2.1×10^2
B8	11200	4.0×10^4	17	—	3.0×10^3	2.4×10^2
A0	9730	3.5×10^4	16	—	3.3×10^3	3.1×10^2
F0	7700	3.2×10^4	12	—	4.4×10^3	6.1×10^2
G0	5550	3.0×10^4	10	—	3.7×10^3	1.1×10^3
G2	5200	2.9×10^4	11	—	3.3×10^3	1.1×10^3
G5	4850	2.9×10^4	12	—	3.0×10^3	1.2×10^3
G8	4600	2.9×10^4	13	—	2.8×10^3	1.3×10^3
K0	4420	2.9×10^4	13	—	2.5×10^3	1.4×10^3
K1	4330	3.0×10^4	13	—	2.5×10^3	1.6×10^3
K2	4250	2.9×10^4	13	—	2.3×10^3	1.7×10^3
K3	4080	3.3×10^4	13	—	2.3×10^3	2.2×10^3
K4	3950	3.4×10^4	13	—	2.1×10^3	2.6×10^3
K5	3850	3.8×10^4	13	—	2.1×10^3	4.9×10^3
M0	3650	4.1×10^4	13	—	1.8×10^3	4.6×10^3
M1	3550	4.4×10^4	16	—	1.8×10^3	5.3×10^3
M2	3450	5.5×10^4	19	—	1.8×10^3	7.2×10^3
M3	3200	5.6×10^4	21	—	1.8×10^3	1.2×10^4
M4	2980	1.6×10^5	22	—	1.8×10^3	2.2×10^4
M5	2800	3.0×10^5	24	—	1.8×10^3	4.5×10^4
M6	2600	4.5×10^5	25	—	1.8×10^3	—

Column 1: spectral type; column 2: effective temperature; column 3: bolometric luminosity; column 4: mass; column 5: logarithm of the production rate of Lyman continuum photons; column 6: V-band luminosity ($\lambda = 5500$ Å, $\Delta\lambda = 890$ Å); column 7: K-band luminosity ($\lambda = 2.2$ μm, $\Delta\lambda = 0.6$ μm). Data are from Vacca, Garmany & Shull (1996) and Schmidt-Kaler (1982). The L_K is computed from the L_V using the broad-band colours from Koornneef (1983b).

Appendix B

The evolutionary synthesis code STARS

Evolutionary synthesis models presented in this work are based on the code STARS developed by Kovo, Sternberg & Alexander (1998; see also Krabbe, Sternberg & Genzel 1994). STARS was briefly described in chapter 3, along with the details of the improvements made in the context of this thesis. This appendix complements chapter 3 with a more complete description of the basic synthesis algorithm followed in STARS, of the input parameters required, of the properties predicted, and of the theoretical and empirical data used to compute the various output quantities.

B.1 Overview of synthesis techniques

In general, all existing evolutionary synthesis models compute isochrones from available sets of stellar tracks. Various approaches can be followed to obtain the distribution of stars in the theoretical Hertzsprung-Russell diagram (HRD), and these can lead to significant differences in the predicted integrated stellar properties. It is thus important to understand the particularities of different synthesis techniques in order to assess the advantages and limitations of a given technique for applications to a specific study.

STARS is based on the *conventional synthesis* technique, and is similar to other models developed by several investigators in the past (*e.g.* Tinsley 1968, 1972; Huchra 1977; Bruzual 1983; Guiderdoni & Rocca-Volmerange 1987; Doyon, Joseph & Wright 1994; Leitherer & Heckman 1995). In such models, stars are binned in mass and each mass bin is rigidly assigned to a fixed evolutionary track. At a given age, stars in a given mass bin populate a segment on their track whose length is determined by the stars' age dispersion and, in turn, by the star formation timescale. Thus, the HRD of the evolving population at that age is approximated by the collection of the populated segments on the finite number of tracks.

Alternatively, the *fuel consumption theorem* states that the contribution of stars in any post-main-sequence stage to the integrated bolometric luminosity of a burst population is proportional to the amount of nuclear fuel burnt by the stars during that stage (*e.g.* Renzini 1981; Renzini & Buzzoni 1986; Buzzoni 1989). Models based on this theorem usually assume that for an instantaneous burst population, a given isochrone can be approximated beyond the main sequence by the evolutionary track of the current main-sequence turnoff mass, and assign the same initial mass function (IMF) weight to all evolved stars.

Finally, Charlot & Bruzual (1991) introduced the *isochrone synthesis* method in applications to evolutionary synthesis of galaxies. Continuous (in mass) isochrones are computed by interpolating in the HRD between the stellar tracks available for evolutionary stages of equivalent physical significance. The number of stars of a given mass on the isochrone is inferred from the IMF. The resulting isochrones for an evolving, coeval stellar population thus vary smoothly. The integrated properties for a burst population with finite star formation rate (SFR) are then inferred by means of convolution integrals. This approach allows a more accurate determination of the distribution of stars in the HRD compared to conventional models and to those based on the fuel consumption theorem. In addition, it overcomes the fluctuations of conventional synthesis in the limit of short bursts (duration $\ll 1$ Gyr) due to the "discreteness" in mass of the populated segments on the finite number of stellar tracks. It also avoids the uncertainties associated with the assumptions involved in the fuel consumption theorem approach, which may underestimate burst ages.

For applications to young starbursts such as in M 82, where the ages are typically $\lesssim 50$ Myr, conventional synthesis is satisfactory. Indeed, because of the very rapid evolution and large range in bolometric luminosities of massive stars, which dominate the integrated properties at such ages, the spread in the HRD of the stellar distribution is large and fluctuations are small or negligible.

B.2 The evolutionary synthesis code STARS

B.2.1 Basic assumptions

The basic assumptions involved in STARS are the following:

- the stellar population is treated as a closed system,
- the SFR varies smoothly with time, independent of the mass of the stars,
- the IMF is a simple function of stellar mass, independent of age,
- the chemical evolution is not important after the onset of star formation,
- the mass return and mechanical energy deposition in the interstellar medium are neglected, and
- the effects of dust and gas are excluded, except for nebular continuum emission.

These simplifications are introduced for convenience only. In particular, there is no solid justification for the independent treatment of the IMF and of the SFR, neither on theoretical nor on observational grounds. In the case of localized bursts, where the star formation occurs during relatively short periods (of the order of $\sim 1 - 10$ Myr), the assumptions adopted provide a very good description of the starburst event. For longer star formation timescales or for very large systems (such as entire galaxies), these approximations may not be appropriate. However, all arbitrary complex star formation histories can in principle be represented by the convolution of a series of single shorter bursts weighted according to their SFR.

The effects of dust extinction and the emission from gaseous nebulae excited by the stars are taken into account separately. More specifically, correction for dust obscuration and for the contribution from nebular emission lines must be applied to the observed data before comparison with the theoretical predictions from STARS. The emission line spectrum from H II regions excited by the OB stars, for example, can be modeled a posteriori from the integrated spectral energy distribution (SED) of the stars using photoionization models. This is done in this work with the code CLOUDY (Ferland 1996), as described in chapter 3.

B.2.2 Stellar evolutionary tracks

STARS makes use of the most recent stellar evolutionary tracks from the Geneva group (Schaller *et al.* 1992; Schaerer *et al.* 1993a, 1993b; Charbonnel *et al.* 1993; Meynet *et al.* 1994). These sets cover initial masses in the range $m = 0.8 - 120$ $M_\odot$ for five metallicities (mass fraction of heavy elements $Z = 0.001, 0.004, 0.008, 0.020, 0.040$) and two assumptions about the mass-loss rates ("normal" and "high"). The evolution of high-mass stars is followed up to the end of the C-burning phase, that of intermediate-mass stars up to the end of the E-AGB phase, and that of low-mass stars up to the He-flash, *i.e.* to the onset of He-core burning.

The Geneva tracks give various parameters (such as age, stellar mass, effective temperature, and bolometric luminosity) for 21 initial masses and 51 evolutionary stages. The actual set of tracks used by STARS is obtained by linear interpolation in $\log m$ of the more widely spaced Geneva tracks. To ensure physical consistency, the interpolation for a given initial mass m is performed between equivalent evolutionary points identified on the existing tracks for adjacent masses m_i and m_{i+1}, on either side of m. The number of interpolated tracks chosen for this work (641) is quite large, in order to reduce the oscillations inherent to conventional synthesis for short burst timescales.

B.2.3 Basic algorithms

A power-law IMF specifies the number of stars formed per unit mass interval between a lower and an upper mass cutoff $m_{\rm low}$ and $m_{\rm up}$:

$$\frac{\mathrm{d}N}{\mathrm{d}m} \propto m^{-\alpha}. \tag{B.1}$$

An exponentially decaying function describes the SFR:

$$R(t_{\rm b}) = R_0\, e^{-t_{\rm b}/t_{\rm sc}}, \tag{B.2}$$

where $t_{\rm b}$ is the time elapsed after the onset of star formation (or burst age), $t_{\rm sc}$ is the burst timescale, $R(t_{\rm b})$ and R_0 are the SFR at age $t_{\rm b}$ and the initial SFR in $M_\odot\,{\rm yr}^{-1}$. An "instantaneous", or "delta" burst is approximated by $t_{\rm b} \gg t_{\rm sc}$ while a "constant" burst corresponds to the limit $t_{\rm b} \ll t_{\rm sc}$.

The total gas mass converted into stars after a time $t_{\rm b}$ is

$$M^{\star}(t_{\rm b}) = \int_0^{t_{\rm b}} \int_{m_{\rm low}}^{m_{\rm up}} \left(\mathcal{A}\, m^{-\alpha+1}\right) \left(R_0\, e^{-t/t_{\rm sc}}\right)\, \mathrm{d}m\, \mathrm{d}t. \tag{B.3}$$

The factor $\mathcal{A}$ is introduced to ensure that the IMF is always normalized in mass to unity independently of $m_{\rm low}$ and $m_{\rm up}$, so that the amplitude of the SFR is completely determined by the user-specified initial SFR R_0; *i.e.*

$$\mathcal{A} = \frac{1}{\int_{m_{\rm low}}^{m_{\rm up}} m^{-\alpha+1}\,{\rm d}m}. \tag{B.4}$$

The total luminosity (bolometric, in a given waveband or at a given wavelength) produced by the stars alive at age $t_{\rm b}$ can be expressed as

$$L_\lambda(t_{\rm b}) = \mathcal{A}\,R_0 \int_0^{t_{\rm b}} \int_{m_{\rm low}}^{m_{\rm up}} L_\lambda(m, t_{\rm b}-t)\,m^{-\alpha}\,e^{-t/t_{\rm sc}}\,{\rm d}m\,{\rm d}t, \tag{B.5}$$

where $L_\lambda(m, t_{\rm b}-t)$ equals the luminosity of a star of initial mass m and age $t_{\rm b}-t$. Any property φ_λ that is not intrinsically flux-calibrated (for example, the equivalent width of a stellar absorption feature) is accordingly weighted by the luminosity at the corresponding wavelength:

$$\varphi_\lambda(t_{\rm b}) = \frac{\mathcal{A}\,R_0}{L_\lambda(t_{\rm b})} \int_0^{t_{\rm b}} \int_{m_{\rm low}}^{m_{\rm up}} \varphi_\lambda(m, t_{\rm b}-t)\,L_\lambda(m, t_{\rm b}-t)\,m^{-\alpha}\,e^{-t/t_{\rm sc}}\,{\rm d}m\,{\rm d}t. \tag{B.6}$$

Finally, the rate and cumulative number of supernova explosions $\nu_{\rm SN}$ and $N_{\rm SN}$ at time $t_{\rm b}$ are computed assuming all stars with initial masses $m \geq 8\ {\rm M}_\odot$ end their life at age $t_{\rm SN}(m)$ as type II supernovae:

$$\nu_{\rm SN}(t_{\rm b}) = \mathcal{A}\,R_0 \int_{8\,{\rm M}_\odot}^{m_{\rm up}} h(m, t_{\rm b})\,m^{-\alpha}\,e^{-t_{\rm b}/t_{\rm sc}}\,{\rm d}m, \tag{B.7}$$

where $h(m, t_{\rm b}) = 1$ if $t_{\rm b} = t_{\rm SN}(m)$ and is zero otherwise, and

$$N_{\rm SN}(t_{\rm b}) = \mathcal{A}\,R_0 \int_{8\,{\rm M}_\odot}^{m_{\rm up}} \int_0^{t_{\rm b}-t_{\rm SN}(m)} m^{-\alpha}\,e^{-t/t_{\rm sc}}\,{\rm d}t\,{\rm d}m. \tag{B.8}$$

The algorithm implemented in STARS performs the above computations in the following way. The stars are binned in mass so that all stars with initial mass in the interval ${\rm d}m$ centered at m move along the track for mass m. The number of stars formed per unit time and unit mass interval at mass m and time t, $n(m,t)$, is simply proportional to the SFR at time t, with the IMF weight. For a burst age $t_{\rm b}$, these stars will occupy a position along their track in the HRD determined by the $T_{\rm eff}$ and $L_{\rm bol}$ they have at an age of $t_{\rm b}-t$. A length element along the track for mass m at time t is defined as ${\rm d}s = \sqrt{({\rm d}T_{\rm eff})^2 + ({\rm d}L_{\rm bol})^2}$. The population in each segment ${\rm d}s$ for the mass range ${\rm d}m$ during the time ${\rm d}t$ required to evolve a length ${\rm d}s$ is thus:

$$\mathcal{N}(m, T_{\rm eff}, L_{\rm bol}, t_{\rm b})\,{\rm d}s = n(m, t_{\rm b}-t)\,{\rm d}m\,{\rm d}t. \tag{B.9}$$

The total distribution in the HRD of the stellar population at age $t_{\rm b}$ is obtained by considering all the evolutionary points (for star ages smaller than $t_{\rm b}-t$) in each evolutionary track for masses between $m_{\rm low}$ and $m_{\rm up}$. The time integration of the right-hand side of Eq. B.9 can be performed analytically since the exponential SFR considered is an integrable function of time. The HRD is then binned in temperature and luminosity (a 64×16 grid with bins of equal width in $\log T_{\rm eff}$ and $\log L_{\rm bol}$ respectively was used for this work), with properties assigned to each individual cell. The integrated properties are obtained by summing over all bins weighting by the number population.

B.2.4 Predicted properties

STARS computes a wide range of broad-band and spectral properties in addition to the gas mass consumed, and to the rate and cumulative number of supernova explosions (either integrated or in the form of HRDs). The assignment of the stellar properties to each HRD bin are based on theoretical models and relationships or on empirical data.

The hydrogen ionizing luminosity, or Lyman continuum luminosity ($L_{\rm Lyc}$) is obtained using the $L_{\rm Lyc}$ versus $T_{\rm eff}$ relationships for main-sequence stars inferred from the Kurucz (1992) and Pauldrach *et al.* (1998) stellar atmosphere models (section B.3.2). The helium ionizing luminosity ($L_{\rm He\,I}$) and the luminosity in the $6 - 13.6$ eV photodissociation band ($L_{\rm PDR}$) are computed similarly. The number of hydrogen and helium ionizing photons produced per unit time ($Q_{\rm Lyc}$ and $Q_{\rm He\,I}$) is computed from $L_{\rm Lyc}$ and $L_{\rm He\,I}$ assuming mean photon energies of 15 eV and 25 eV respectively. The K-band luminosity (L_K) is derived in the black-body approximation assuming that the K-band extends from $1.9\,\mu$m to $2.5\,\mu$m,

$$L_K^{\rm BB} = \frac{\pi B_\nu(T_{\rm eff}) L_{\rm bol}}{\sigma T_{\rm eff}^4}\,\Delta\nu_K, \qquad \text{(B.10)}$$

where $B_\nu(T_{\rm eff})$ is the Planck function, σ is the Stefan-Boltzmann constant, and $\Delta\nu_K$ is the width in frequency of the K-band. In addition, luminosities and colours in the V-, J-, H- and K-band are computed using empirical stellar data (section B.3.1). The contribution of the nebular continuum emission, including free-free and free-bound processes, is accounted for using

$$L_{\Delta\nu}^{\rm neb} = Q_{\rm Lyc}\,\frac{\gamma_\nu^{\rm neb}}{\alpha_B({\rm H}^0, 10^4~{\rm K})}\,\Delta\nu, \qquad \text{(B.11)}$$

where $\Delta\nu$ is the width in frequency of the band considered, $\gamma_\nu^{\rm neb}$ is the nebular continuum emission coefficient at the central band frequency ν (taken from Ferland 1980) and $\alpha_B({\rm H}^0, 10^4~{\rm K})$ is the case B total recombination coefficient for hydrogen at an electron temperature $T_{\rm e} = 10^4$ K.

The input parameters and the various integrated properties computed by STARS are listed in tables B.2 and B.3 at the end of this appendix.

B.3 Recent improvements to STARS

As part of this thesis work, two additional features were implemented in STARS in order to optimize the code for applications to near-infrared observations of starburst galaxies: the extension of the evolutionary tracks for intermediate-mass stars up to the end of the TP-AGB phase, and the prediction of the equivalent widths (EWs) of near-infrared stellar absorption features. The implementation of these features is described in detail in chapter 3.

In addition, empirical photometric data and a new set of model atmospheres for stars hotter than 25000 K were recently included in STARS to better account for the energy distributions of cool, evolved stars and hot, massive stars. Indeed, for such stars, simple black-body approximations or the plane-parallel, static, LTE (local thermodynamic equilibrium) models of Kurucz (1992), optimized for effective temperatures in the range $5000 - 20000$ K, are inappropriate. The empirical data and new model atmospheres are briefly described in the following.

B.3.1 Empirical photometric stellar properties

For the purpose of computing more accurately the integrated properties of cool stars, particularly at near-infrared wavelengths, the empirical bolometric corrections from Schmidt-Kaler (1982) and the broad-band colours from Koornneef (1983b) were implemented in STARS. The transformation between spectral types and effective temperatures for the HRD is based on the temperature scales from Schmidt-Kaler (1982), discussed in chapter 2. The predicted luminosities, magnitudes and colours are expressed in the photometric system defined in Wamsteker (1981, see appendix C), which is very similar to that adopted by Koornneef (1983a).

Such data are more appropriate since cool stars dominate the integrated near-infrared emission but have energy distributions which are difficult to model accurately. For instance, the treatment of molecular opacities is critical but the lack of laboratory data (notably on H_2O) hampers satisfactory theoretical modeling. Furthermore, the assumptions involved in simple black-body approximations or in the Kurucz models, for example, do not hold for cool evolved stars, which experience mass-loss, have extended and expanding atmospheres and may exhibit variability. The differences implied by inadequate energy distributions are illustrated in figure B.1, where the K-band luminosities computed in the black-body approximation and using the empirical data for a simple burst of timescale 1 Myr are compared.

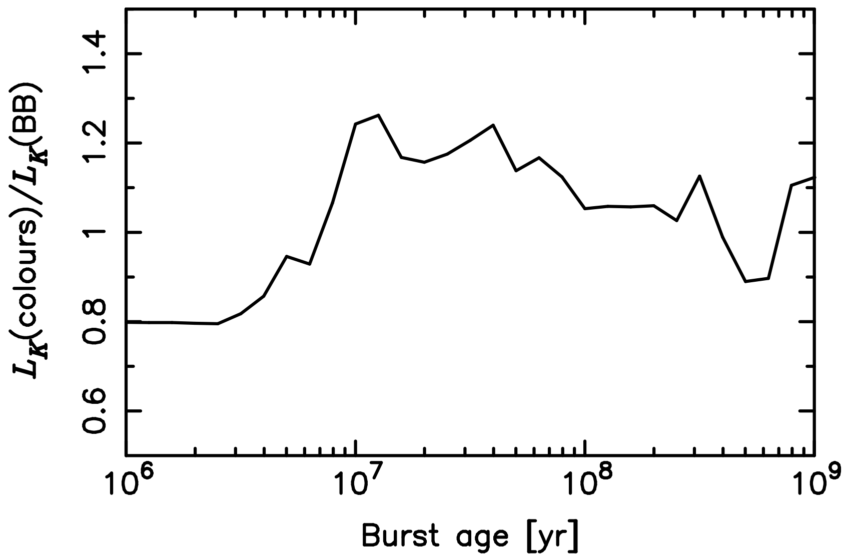

Fig. B.1.— Ratio of the K-band luminosity computed using empirical data for the stellar photometric properties, L_K(colours), to that computed in the black-body approximation, L_K(BB). The predictions are shown for a simple single cluster with a Salpeter IMF ($\alpha = 2.35$) between 1 $M_\odot$ and 100 $M_\odot$, and for a burst with timescale of 1 Myr.

B.3.2 Model atmospheres for hot stars

In the case of hot and massive stars, the most severe deviations to the assumptions involved in the black-body approximation or in the Kurucz models are due to important and rapid mass-loss. Since these stars are the primary energy source in H II regions, and because a key application of the synthetized SEDs generated by STARS is the nebular photoionization modeling to predict the evolution of diagnostic nebular lines in starbursts, the choice of appropriate models is crucial. The recent non-LTE models for stars hotter than 25000 K from Pauldrach *et al.* (1998) were thus implemented. These are more realistic for expanding stellar atmospheres with strong, radiation-driven winds in hot, massive stars.

The main features of the Pauldrach *et al.* atmospheres include accurate atomic data for a very detailed multilevel non-LTE treatment of the metal ions, revised inclusion of extreme ultraviolet and X-ray radiation by shock-heated matter, and, most importantly, the consistent calculation of line blocking and blanketing. This results in generally flatter (*i.e.* harder) SEDs compared to the Kurucz models, as illustrated in figure B.2 for main-sequence stars of various temperatures. These differences have important consequences, notably on line ratios sensitive to the shape of the ionizing spectrum that can be used to infer the star formation parameters in young starbursts.

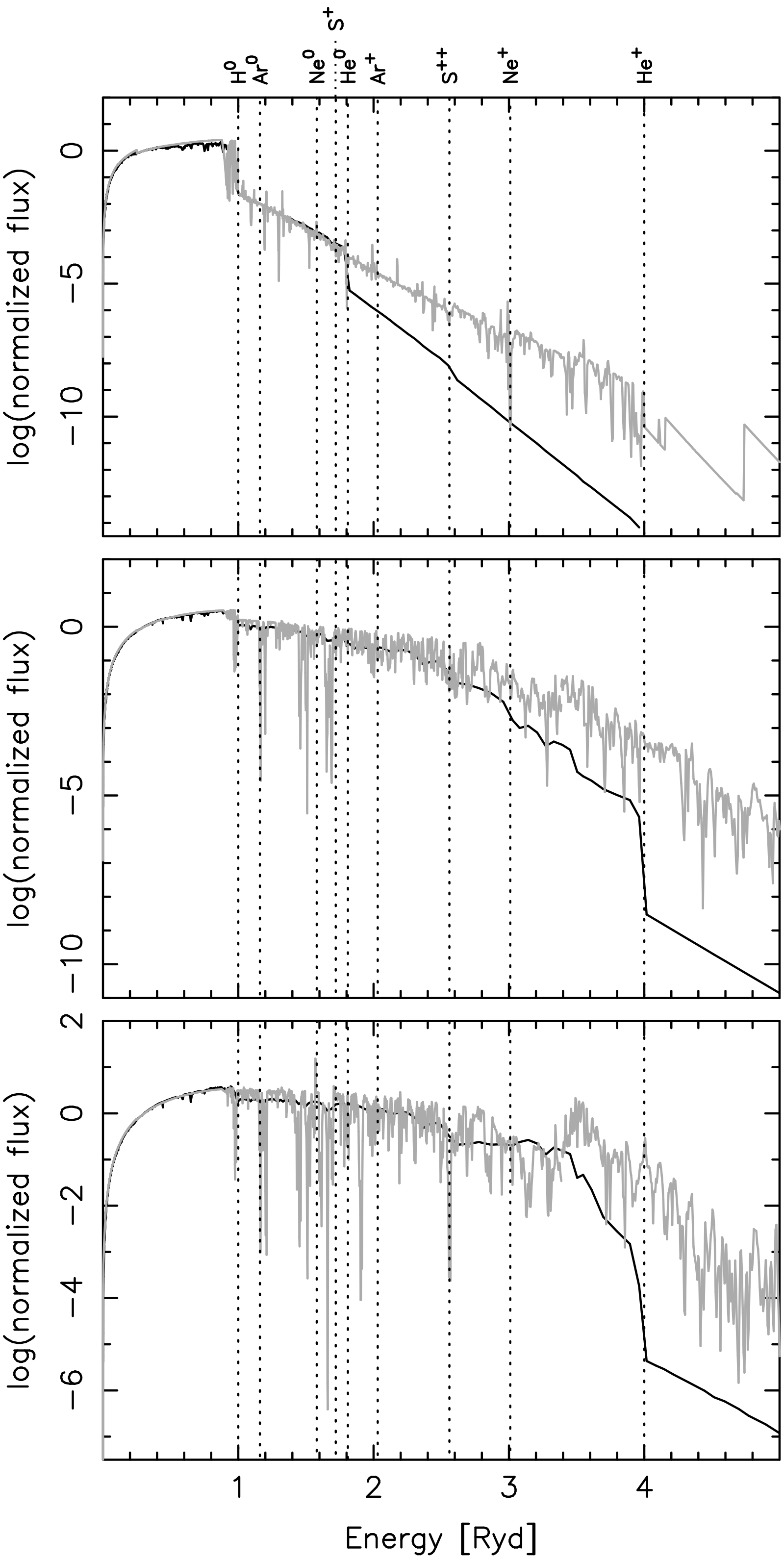

Fig. B.2.— Comparison between the Pauldrach *et al.* (1998) and Kurucz (1992) stellar atmosphere models (grey and black lines respectively) for main-sequence stars of selected effective temperatures. *Top:* SEDs for $T_{\rm eff}$ = 25000 K ($\log g$ = 4.0). *Middle:* SEDs for $T_{\rm eff}$ = 40000 K ($\log g$ = 4.0 for Pauldrach *et al.* and 4.5 for Kurucz). *Bottom:* SEDs for $T_{\rm eff}$ = 50000 K ($\log g$ = 4.0 for Pauldrach *et al.* and 5.0 for Kurucz). The ionization edges for the species of interest in this thesis work are indicated by the vertical lines; the ionization potentials are given in table B.1.

Table B.1: Ionization potentials of selected species (in eV)[(a)]

Z	Element	1st ionization	2nd ionization	3rd ionization
1	H	**13.6**	—	—
2	He	**24.6**	54.4	—
6	C	11.3	24.4	47.9
7	N	14.5	29.6	47.5
8	O	13.6	35.1	54.9
10	Ne	**21.6**	**41.0**	63.5
14	Si	8.2	16.4	33.5
15	P	10.5	19.8	30.2
16	S	10.4	**23.3**	**34.8**
18	Ar	**15.8**	**27.6**	40.7

[(a)] The data are given for species whose emission lines are commonly observed in spectra of H II regions and photodissociation regions around young OB stars. For multi-electron elements, the values listed correspond to the ionization potential to the S term of the resulting ion in its ground configuration. Ionization potentials are bold-faced for the species with emission lines in the range $\lambda = 1 - 40\ \mu$m detected in the 3D and *ISO*-SWS spectra of M 82 that are used in this work to infer the average effective temperature of the ionizing stars (see chapter 5; also figure B.2).

In particular, the [Ne III] 15.6 μm/[Ne II] 12.8 μm ratio — sensitive between 1.6 Ryd and 3 Ryd — increases by factors of up to three for starbursts younger than 5 Myr and a Salpeter IMF extending to 100 $M_\odot$ for computations using the Pauldrach *et al.* atmospheres instead of the Kurucz ones for hot stars.

To ensure an HRD coverage as complete as possible and a smooth transition between the Kurucz and Pauldrach temperature regimes, a hybrid grid in $\log T_{\rm eff} - \log g$ [2] was developed (see also Thornley *et al.* 1998). The Pauldrach models presently available for solar metallicity (consisting of six main-sequence and six supergiant stars from 25000 K to 50000 K; a similar set exists for sub-solar metallicites as well) were interpolated in the range $T_{\rm eff} \geq 25000$ K, and the Kurucz models, in the range $T_{\rm eff} \leq 19000$ K. At the outer boundaries of the range of parameters covered by the existing models, a nearest neighbour approximation was used to extrapolate over the adjacent grid cells. The resulting "Kurucz grid" and "Pauldrach grid" were then interpolated to cover the intermediate temperature range.

[2] g is the stellar surface gravity given by $g = 4\pi G\sigma(m/L_{\rm bol})T^4_{\rm eff}$, where G is the gravitational constant, σ the Stefan-Boltzmann constant and m the stellar initial mass.

Table B.2: Input parameters for STARS

Parameter	Symbol	Values or range available
IMF power-law index	α	—
IMF lower mass cutoff	m_{low}	$0.8 - 120$ $M_{\odot}$
IMF upper mass cutoff	m_{up}	$0.8 - 120$ $M_{\odot}$
Burst age	t_{b}	—
Burst timescale	t_{sc}	—
Initial star formation rate	R_0	—
Stellar tracks metallicity	Z	0.001, 0.004, 0.008, 0.020, 0.040
Mass-loss rate	$\mathrm{d}m/\mathrm{d}t$	"normal", "high"
Two arbitrary wavelengths[a]	λ_X, λ_Y	—
TP-AGB extension	—	(included/excluded)
Stellar atmosphere models	—	Kurucz ($Z = 0.006, 0.020$), Pauldrach ($Z = 0.004, 0.020$), "hybrid"[b]

[a] For the computation of luminosities and colours at arbitrary wavelengths in the black-body approximation.

[b] For spectral synthesis of evolving stellar clusters, three main grids of SEDs are selectable: the Kurucz (1992) model atmospheres for all temperatures, the Pauldrach *et al.* (1998) model atmospheres for $T_{\mathrm{eff}} \geq 25000$ K, and a hybrid grid consisting of the Pauldrach *et al.* models above 25000 K, the Kurucz models below 19000 K and a transition grid obtained by interpolation for intermediate temperatures.

Table B.3: Properties computed by STARS

Quantity	Symbol	Remarks
Number of stars alive	$N^\star$	—
Gas mass converted into stars	$M^\star$	—
Bolometric luminosity	$L_{\rm bol}$	—
Absolute bolometric magnitude	$M_{\rm bol}$	$M_{\rm bol} = -2.5\log(L_{\rm bol}) + 4.75$
Lyman continuum luminosity	$L_{\rm Lyc}$	From model atmospheres[(a)]
Hydrogen ionizing rate	$Q_{\rm Lyc}$	From $L_{\rm Lyc}$[(b)]
He I ionizing luminosity	$L_{\rm He\,I}$	From model atmospheres[(a)]
He I ionizing rate	$Q_{\rm He\,I}$	From $L_{\rm He\,I}$[(b)]
$6 - 13.6$ eV luminosity	$L_{\rm PDR}$	From model atmospheres[(a)]
K-band luminosity	$L_K^{\rm BB}$	Stellar and nebular[(c)]
Rate of supernova explosions	$\nu_{\rm SN}$	Progenitors with $m \geq 8$ M$_\odot$
Cumulative number of supernova explosions	$N_{\rm SN}$	Progenitors with $m \geq 8$ M$_\odot$
Luminosity density at λ_X and λ_Y	F_X, F_Y	Stellar, black-body[(d)]
$X - Y$ colour	$X - Y$	Stellar, black-body[(d)]
V-, J-, H- and K-band luminosities	L_V, L_J, L_H, L_K	Stellar (empirical) and nebular[(e)]
Nebular V-, J-, H- and K-band luminosity densities	$F_V^{\rm neb}$, $F_J^{\rm neb}$, $F_H^{\rm neb}$, $F_K^{\rm neb}$	From Eq. B.11
EWs of near-infrared stellar absorption features	$W_{1.59}$, $W_{1.62}$, $W_{\rm Na}$, $W_{\rm Ca}$, $W_{2.29}$, $W_{2.32}$	Empirical, diluted[(f)]
SED		Stellar, model atmospheres[(g)]

[(a)] The relationships for $L_{\rm Lyc}$, $L_{\rm He\,I}$ and $L_{\rm PDR}$ versus $T_{\rm eff}$ are inferred from the main-sequence model atmospheres of Kurucz (1992) for $T_{\rm eff} < 25000$ K and of Pauldrach *et al.* (1998) for $T_{\rm eff} \geq 25000$ K.

[(b)] Assuming mean hydrogen and helium ionizing photon energies of 15 eV and 25 eV respectively.

[(c)] The stellar contribution is obtained in the black-body approximation from Eq. B.10, and the nebular contribution is computed from Eq. B.11 with the nebular coefficients given in Ferland (1980).

[(d)] Luminosities computed in the black-body approximation (see Eq. B.10); colour computed from $X - Y = -2.5\,[\log(L_X/L_Y) - \log(L_X(T_0)/L_Y(T_0))]$, where $T_0 = 9500$ K is the effective temperature of an A0 V star.

[(e)] The stellar contribution is computed using the bolometric corrections of Schmidt-Kaler (1982) and the broad-band colours tabulated by Koornneef (1983b); the nebular contribution is computed from Eq. B.11.

[(f)] The stellar EWs are computed using the empirical data compiled in chapter 2; dilution by the featureless nebular continuum emission is accounted for.

[(g)] Using the Kurucz (1992) model atmospheres, the Pauldrach *et al.* (1998) model atmospheres, or the hybrid grid (see note (*b*) to table B.2).

Appendix C

Photometric systems

A photometric system is defined by the effective central and cutoff wavelengths of a set of broad-band filters, and by the absolute flux density for a source with zero magnitude in each filter. For spectroscopic data, formulas giving the spectral energy distribution for stars of a specific type with known broad-band magnitude can be used to calibrate the data at each wavelength.

For the 3D data of M 82 presented in this work, no reference star was observed for the purpose of flux calibration. The instrumental transmission profile as a function of wavelength was accounted for by the division with the spectral flat-field. The absolute flux calibration was performed by setting the average flux density in the wavelength ranges observed with 3D equal to the photometric measurements reported in Rieke *et al.* (1980) within identical apertures centered on the nucleus of M 82. The following ranges were covered with 3D for all spatial pixels: H-band: $\lambda = 1.52 - 1.78$ μm, K-band: $\lambda = 1.96 - 2.42$ μm. The filters employed by Rieke *et al.* were centered at 1.6 μm and 2.2 μm with bandwidths of $\Delta\lambda = 0.4$ μm and $\Delta\lambda = 0.5$ μm respectively. Since the continuum emission in M 82 is relatively flat and strongly dominates the broad-band flux densities (the emission lines contribute less than 2% at all positions observed with 3D), the differences in the wavelength ranges between the respective data sets introduce only small errors in the absolute flux calibration of the 3D data. These are estimated to be less than 3% and are thus much smaller than those from other sources of uncertainties, in particular from the mosaicking.

For the data interpretation, the broad-band fluxes are converted into magnitudes and luminosities for the purpose of comparing the results with near-infrared stellar colours and evolutionary synthesis models, and of computing numbers of representative stars. The apparent magnitude m_λ in a bandpass centered at λ is given by

$$m_\lambda = -2.5 \log \left[\frac{f_\lambda}{f_\lambda(0)} \right] \tag{C.1}$$

where f_λ is the observed broad-band flux density and $f_\lambda(0)$ is the flux density of a source with magnitude zero. The luminosity L_λ in the same bandpass can be computed from

$$\frac{L_\lambda}{\mathrm{L}_\odot} = 4\pi \left(\frac{D}{\mathrm{m}} \right)^2 \left(\frac{\Delta\lambda}{\mu\mathrm{m}} \right) \left(\frac{f_\lambda}{\mathrm{W\,m^{-2}}\,\mu\mathrm{m}^{-1}} \right) \left(3.85 \times 10^{26}\ \mathrm{W} \right)^{-1} \tag{C.2}$$

where $\mathrm{L}_\odot = 3.85 \times 10^{26}$ W is the luminosity of the Sun, D is the distance to the object and $\Delta\lambda$ is the bandwidth. The photometric system adopted throughout this thesis is the one described in Wamsteker (1981) and its defining characteristics are given in table C.1. The stellar luminosities and colours used for the data interpretation and implemented in the evolutionary synthesis code STARS are based on the empirical data presented in Koornneef (1983b). These are appropriate for the photometric system described in Koornneef (1983a), which is very close to that of Wamsteker. Again, for the M 82 data, the differences between the ranges covered by the filters in these systems and by 3D introduce errors which are negligible compared to other sources of uncertainties.

Table C.1: Photometric system adopted for optical and near-infrared photometry[(a)]

Band	λ	$\Delta\lambda$	$f_\lambda(0)$	$f_\nu(0)$
	[μm]	[μm]	[$\mathrm{W\,m^{-2}}\,\mu\mathrm{m}^{-1}$]	[Jy]
V	0.55	0.089	3.64×10^{-8}	3670
J	1.25	0.3	3.18×10^{-9}	1650
H	1.65	0.4	1.18×10^{-9}	1070
K	2.20	0.6	4.17×10^{-10}	673

[(a)] From Wamsteker (1981). The table gives the central wavelength, the bandwidth and the flux densities for a source of magnitude zero for the bandpasses relevant to this work (used in the evolutionary synthesis code STARS and for the 3D data).

Appendix D

Near-infrared He I emission

Ratios of emission lines which have different ionization potentials but similar critical densities probe the spectral energy distribution (SED) of the ultraviolet radiation field between the threshold frequencies of the lines considered. Such line ratios therefore give a measure of the luminosity-averaged effective temperature of the ionizing stars, $T_{\rm eff}^{\rm OB}$. Three $T_{\rm eff}^{\rm OB}$ diagnostic ratios available at mid-infrared wavelengths have been discussed in chapter 3, and used in chapter 5 from the *ISO*-SWS data of M 82: [Ne III] 15.6 μm/[Ne II] 12.8 μm, [Ar III] 8.99 μm/[Ar II] 6.99 μm, and [S IV] 10.5 μm/[S III] 18.7 μm. Their variations with $T_{\rm eff}^{\rm OB}$ or their evolution with age for single stellar clusters were modelled directly with the photoionization code CLOUDY (Ferland 1996) using single star SEDs or integrated stellar cluster SEDs (see figures 3.6 and 5.11).

At near-infrared wavelengths, the He I 2.058 μm line has been commonly used in combination with the H I Brγ line at 2.166 μm to estimate $T_{\rm eff}^{\rm OB}$ (*e.g.* Doyon, Puxley & Joseph 1992; Doherty *et al.* 1994, 1995). Precise modeling of this line ratio, as well as of other ratios involving several optical and infrared He I lines is, however, difficult due to complicating radiative transfer effects (*e.g.* Robbins 1968; Clegg 1987; Shields 1993). As a result, these ratios are sensitive to the nebular conditions and to $T_{\rm eff}^{\rm OB}$ in a particular way. Notably, He I 2.058/Brγ does not vary monotonically with $T_{\rm eff}^{\rm OB}$ and needs to be combined with additional ratios, such as He I 1.701/Br10 or He I 2.113/Brγ, to constrain $T_{\rm eff}^{\rm OB}$ uniquely.

This appendix gives a brief overview of the processes affecting the He I recombination line emission (*e.g.* Osterbrock 1989 and references throughout the text below). Predictions for He I 2.058 μm can be obtained directly using CLOUDY, but not for He I 1.701 μm and 2.113 μm. The procedure followed to derive these line fluxes indirectly from predicted optical lines is here described as well.

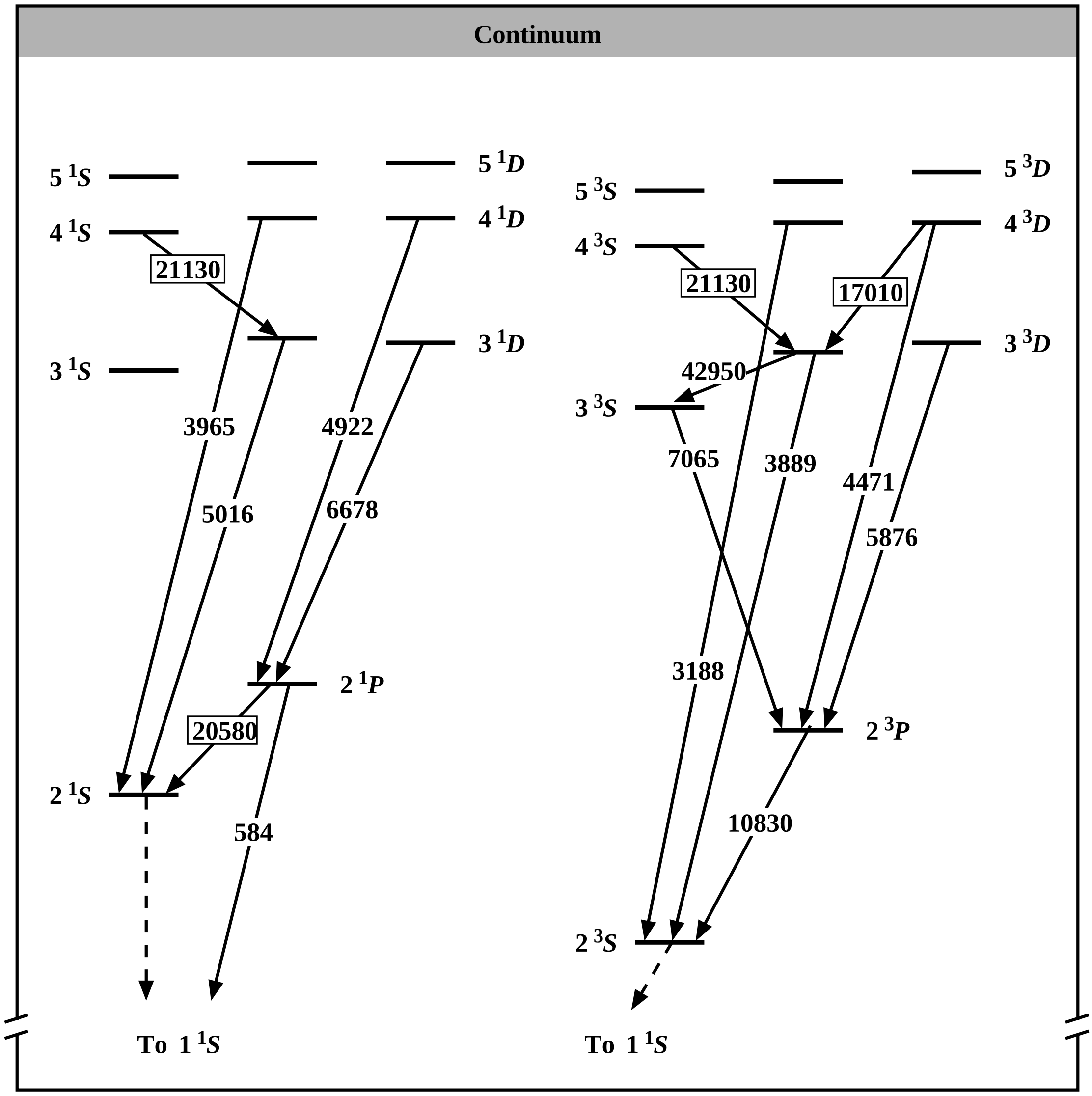

Fig. D.1.— Partial energy-level diagram of He I, showing some of the strongest optical and $\lambda = 1 - 5\ \mu$m lines observed in H II regions as well as the resonant $1\,^1S - 2\,^1P$ line. The wavelengths of the transition lines are given in Å. The near-infrared lines discussed in more detail in the text are indicated with boxes around the respective wavelengths. The $1\,^2S$ level and the terms with $n \geq 6$ or $L \geq 3$ have been omitted for the sake of space and clarity. Transitions are given as *lower level – upper level* in the text.

D.1 Background

Because He I is a two-electron system, it has separate singlet and triplet levels (see figure D.1). All recombinations to singlet levels are followed by radiative cascade leading ultimately to the $1\,^1S$ ground level via the $2\,^1S$ or $2\,^1P$ levels. Atoms in the $2\,^1S$ level quickly decay by two-photon emission to the ground state. Atoms in the $2\,^1P$ level rapidly decay either to the ground state with emission of a resonant He I Lyα photon at 584 Å, or to the $2\,^1S$ level with emission of a $2.058\,\mu$m photon, with relative probability of approximately $1 : 10^{-3}$. Due to the scattering of the 584 Å photons, which constantly re-populates the $2\,^1P$ level, the $2.058\,\mu$m line is amplified by resonance fluorescence. Absorption of 584 Å photons in H ionization, for instance, reduces this effect.

All recaptures to triplets lead ultimately to the highly metastable $2\,^3S$ level through downward radiative cascade. Depopulation of this level occurs *1)* upon absorption of photons in the $2\,^3S - n\,^3P$ series, *2)* by collisional excitation to the $2\,^1S$ or $2\,^1P$ singlets, and *3)* much less importantly, by radiative decay to the $1\,^1S$ level with strongly forbidden emission of 626 Å photons.

The large optical depth in the $2\,^3S - n\,^3P$ series has the following important effects on the line intensities. $1.083\,\mu$m photons emitted in $2\,^3S - 2\,^3P$ transitions are simply scattered, but those resulting from $2\,^3S - n\,^3P$ transitions with $n \geq 3$ may be converted to $n'\,^3S - n\,^3P$ photons with $n' \geq 3,\ n \geq 3$ or to $n'\,^3D - n\,^3P$ with $n' \geq 3,\ n \geq 4$. A simple example is the absorption of a 3889 Å photon, which can lead to the emission of a $3\,^3S - 3\,^3P$ photon at $4.295\,\mu$m, followed by a $2\,^3P - 3\,^3S$ photon at 7065 Å and a $2\,^3S - 2\,^3P$ photon at $1.083\,\mu$m. Thus, the lines in the $2\,^3S - n\,^3P$ series are weakened due to self-absorption whereas those originating from upper levels $n\,^3S$ and $n\,^3D$ are strengthened by resonance fluorescence. Theoretical calculations show, however, that even though the intensity of $2\,^3S - n\,^3P$ and $n'\,^3S - n\,^3P$ lines can vary by large factors, the $n'\,^3D - n\,^3P$ lines are little affected (*e.g.* Robbins 1968).

Collisions between atoms in the $2\,^3S$ level and electrons compete against the effects just described since they involve a spin change, and thus lead to singlets. The probability for collisional excitation to the $2\,^1S$ and $2\,^1P$ levels, which lie at energies above that of $2\,^3S$ comparable to the mean thermal energy of electrons at typical H II region temperatures, is larger than for collisional de-excitation to the ground state. Furthermore, the critical density is only a few 10^3 cm^{-3}. This mode of population of the $2\,^1P$ level contributes in turn to strengthen the $2.058\,\mu$m line. As T_{e} increases, the $2\,^1P$ population becomes more and more enhanced at the expense of the $2\,^1S$ one.

D.2 Predictions for He I to H I line ratios

Theoretical modeling of the He I 2.058/Brγ line ratio by Doyon, Puxley & Joseph (1992), Doherty *et al.* (1994), Shields (1993) and Lançon & Rocca-Volmerange (1994, 1996) all agree on the behaviour at low temperatures. In the absence of dust, the ratio exhibits a steep increase with $T_{\rm eff}^{\rm OB}$ up to about 40000 K (the location and value of the maximum depends somewhat on the model assumptions and on the atomic data used). This primarily reflects the increase of the volume of the He^+ zone within the H^+ zone with stellar temperature or, equivalently, the increase of the number density fraction y^+ of He^+ relative to H^+. At higher temperatures, though, the models of Shields and Lançon & Rocca-Volmerange predict a decrease in the ratio, contrary to those of Doyon, Puxley & Joseph and Doherty *et al.* , which indicate rather that it saturates. As recognized by Doherty *et al.* (1995), the decline is due to the variation with temperature of the ratio y^0 of neutral He to neutral H in the He^+ zone. Indeed, as the radiation becomes harder, y^0 decreases and, consequently, the number of resonant photons at 584 Å is reduced. The He I 2.058/Brγ at high $T_{\rm eff}^{\rm OB}$ is thus very sensitive to the treatment of the He I Lyα opacity, which is one of the major sources of uncertainties in the model predictions (*e.g.* Ferland 1998).

Since He I 2.058/Brγ depends critically on the physical conditions and on $T_{\rm eff}^{\rm OB}$, it is necessary to use additional ratios to constrain $T_{\rm eff}^{\rm OB}$ uniquely. In the $\lambda = 1.5-2.5\ \mu$m range, Vanzi *et al.* (1996) and Doherty *et al.* (1995) have proposed the $3\,^3P - 4^3D$ line at 1.701 μm and the blend of triplet and singlet $3P - 4S$ transition lines at 2.113 μm as useful diagnostics. The 1.701 μm line does not suffer from collisional effects and, because it originates from the $4\,^3D$ level, is also essentially unaffected by self-absorption in the $2\,^3S - n\,^3P$ series. Similarly, the singlet component of the 2.113 μm blend is a "pure" recombination line. However, the triplet component arises from the $4\,^3S$ level and is therefore amplified by resonance fluorescence. It is also potentially affected by variations of the y^0 fraction as the 2.058 μm line, due to the reduction of the number of atoms in the $2\,^3S$ level for absorption of $2\,^3S - n\,^3P$ photons. The intensity of the 2.113 μm blend must therefore be interpreted with caution.

The He I 1.701/Br10 and He I 2.113/Brγ ratios have been used in studies of Galactic H II regions and blue compact dwarf galaxies (Doherty *et al.* 1995; Vanzi *et al.* 1996; Vanzi & Rieke 1997). Unfortunately, the intrinsic weakness of both He I lines make them difficult to detect in strong continuum sources such as infrared-luminous galaxies. They have, therefore, not yet received much attention and no extensive modeling of their intensities with various parameters have been published. From unpublished data by Smits (but details of the theoretical computations can be found in Smits 1991, 1996), Vanzi *et al.* (1996) generated theoretical predictions for $n_e = 100$ cm^{-3} and full ionization (*i.e.* He$^+$ and H$^+$ zones coinciding):

$$\text{He I } 1.701/\text{Br}10 = 3.60\, C_{1.7}(T_e)\, \frac{n_{\text{He}}}{n_{\text{H}}} \tag{D.1}$$

where $C_{1.7}(5000\ \text{K}) = 0.95$, $C_{1.7}(10000\ \text{K}) = 1.00$ and $C_{1.7}(20000\ \text{K}) = 1.05$. Similarly,

$$\text{He I } 2.113/\text{Br}\gamma = 0.40\, C_{2.1}(T_e)\, \frac{n_{\text{He}}}{n_{\text{H}}} \tag{D.2}$$

where $C_{2.1}(5000\ \text{K}) = 0.68$, $C_{2.1}(10000\ \text{K}) = 1.00$ and $C_{2.1}(20000\ \text{K}) = 1.58$. $n_{\text{He}}/n_{\text{H}}$ is the number abundance of He relative to H.

Combining the above equations with model predictions for case B recombination using CLOUDY, the variations of He I 2.058/Brγ, He I 1.701/Br10 and He I 2.113/Brγ with $T_{\text{eff}}^{\text{OB}}$ were derived as follows. Of the lines of interest here, only the He I 2.058 μm line is directly predicted by CLOUDY, which accouns for the collisional and optical depth effects discussed above. The Brγ and Br10 intensities were first computed from the predicted Hβ intensity using the intrinsic emissivities for case B recombination from Hummer & Storey (1987), for the appropriate electron density n_e and temperature T_e. In the photoionization modeling (described in chapter 3), n_e is kept constant but T_e varies for each $T_{\text{eff}}^{\text{OB}}$ (see figure 5.7).

Since triplet transitions originating from high $n\,^3D$ levels are essentially unaffected by collisional effects or scattering from the metastable $2\,^3S$ level, the He I 4471 Å/Br10 ratio was used to derive the He I 1.701/Br10 ratio. The He I 4471 Å line, predicted by CLOUDY, corresponds to the transition $2\,^3P - 4\,^3D$ and thus shares its upper level with the transition producing 1.701 μm photons. The He I 4471 Å/Br10 ratio was scaled by the ratio of the saturation values (reflecting full He I ionization within the H$^+$ zone) for He I 1.701/Br10 from Eq. D.1 and for He I 4471 Å/Br10 as obtained from CLOUDY. The relationship from Smits was interpolated for the appropriate T_e for each $T_{\text{eff}}^{\text{OB}}$. Since collisions are unimportant for both He I lines involved here, especially for the low n_e and T_e ranges of interest in this thesis (chapter 5), Eq. D.1 was also used for n_e up to 10^3 cm^{-3}. A similar procedure was followed for the He I 2.113/Brγ ratio, also using the He I 4471 Å line. However, the triplet component of the 2.113 μm blend does suffer from optical depths effects in the $2\,^3S - n\,^3P$ series and can be enhanced by up to a factor of ≈ 1.6, depending on the physical conditions (Robbins 1968). It is also potentially affected by the decrease in y^0 in the He$^+$ zone as $T_{\text{eff}}^{\text{OB}}$ increases, due to the reduction of the number of atoms in the metastable $2\,^3S$. This effect is not present for the 4471 Å line. Consequently, the predictions for He I 2.113/Brγ derived here are more uncertain. The variations of the three ratios for the nebular parameters appropriate for M 82 are illustrated in figure D.2.

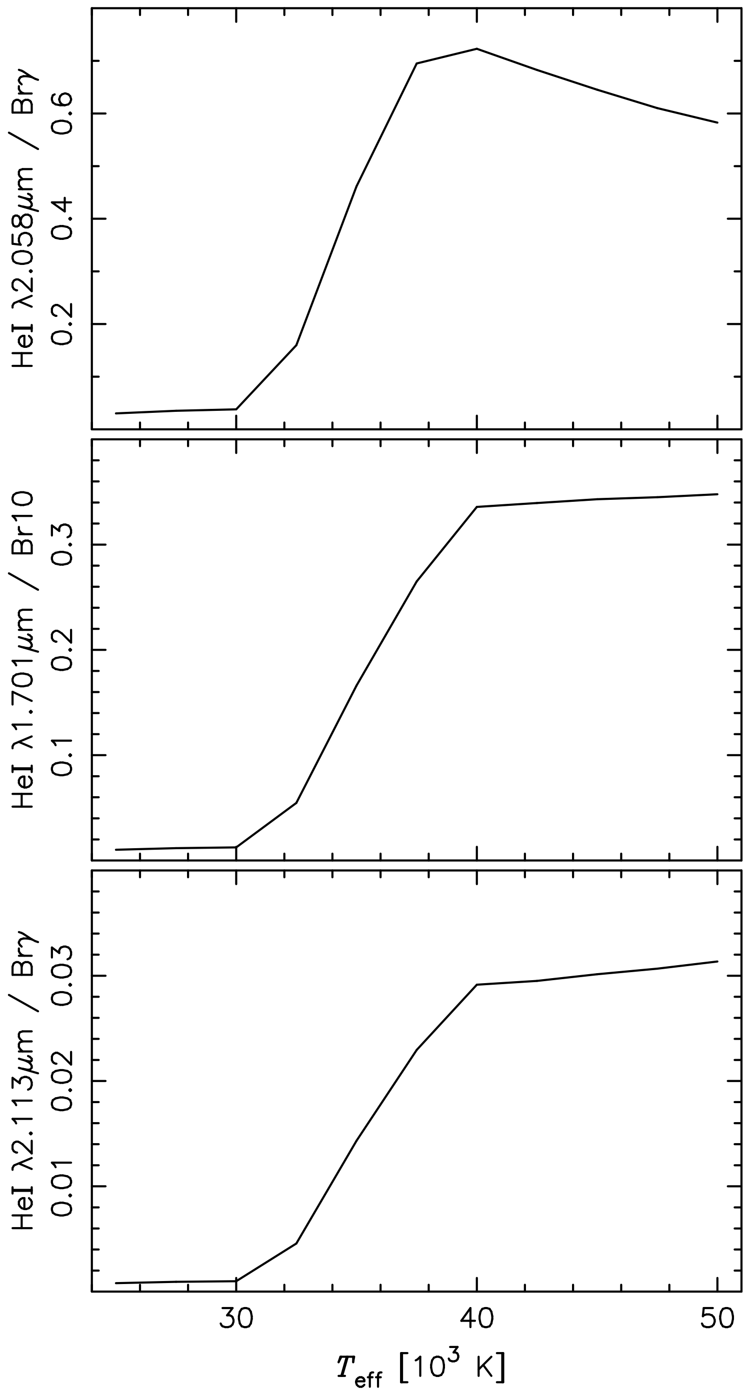

Fig. D.2.— Variations of He I to H I near-infrared recombination line ratios with effective temperature of the ionizing stars. The model predictions were derived by combining photoionization modeling using CLOUDY and theoretical computations from Smits (1991; 1996), as described in the text. The curves are illustrated for the nebular parameters appropriate for M 82 (chapter 5): $n_{\rm H} \approx n_{\rm e} = 300~{\rm cm}^{-3}$, $R = 25$ pc, $\log U = -2.3$ dex, solar gas-phase abundances and no interstellar grains mixed with the ionized gas. Predictions for other nebular parameters are shown in figure 5.12 of chapter 5.

Bibliography

[1] Aaronson, M. 1977, *Ph.D. Thesis*, Harvard University

[2] Aaronson, M., Frogel, J.A. & Persson, S.E. 1978, ApJ, **220**, 442

[3] Achmad, L., Lamers, H.J.G.L.M., Nieuwenhuijzen, H. & Van Genderen, A.M. 1992, A&A, **259**, 600

[4] Achtermann, J.M. & Lacy, J.H. 1995, ApJ, **439**, 163

[5] Ali, B., Carr, J.S., DePoy, D.L., Frogel, J.A. & Sellgren, K. 1995, AJ, **110**, 2415

[6] Allamandola, L.J., Tielens, A.G.G.M. & Barker, J.R. 1985, ApJ, **290**, L25

[7] Allen, C.W. 1976, *Astrophysical quantities* (London: Athlone Press)

[8] Allen, M.L. & Kronberg, P.P. 1998, ApJ, **502**, 218

[9] Arnaud, K.A., Gilmore, G. & Collier Cameron, A. 1989, MNRAS, **237**, 495

[10] Arribas, S. & Martinèz Roger, C. 1989, A&A, **215**, 305

[11] Athanassoula, E. 1992, MNRAS, **259**, 345

[12] Augarde, R. & Lequeux, J. 1985, A&A, **147**, 273

[13] Ball, R. 1986, ApJ, **307**, 453

[14] Barnes, J.E. & Hernquist, L. 1991, ApJ, **370**, L65

[15] Barnes, J.E. & Hernquist, L. 1996, ApJ, **471**, 115

[16] Bautista, M.A. & Pradhan, A.K. 1996, A&AS, **115**, 551

[17] Beck, S.C., Lacy, J.H., Baas, F. & Townes, C.H. 1978, ApJ, **226**, 545

[18] Beck, S.C., Lacy, J.H. & Geballe, T.R. 1979, ApJ, **234**, L213

[19] Beckwith, S., Evans, N.J. II, Gatley, I., Gull, G. & Russell, R.W. 1983, ApJ, **264**, 152

[20] Bedijn, P.J. 1988, A&A, **205**, 105

[21] Bell, R.A. & Gustafsson, B. 1989, MNRAS, **236**, 653

[22] Bergeat, J., Lunel, M., Sibille, F. & Lefevre, J. 1976, A&A, **52**, 263

[23] Bernlöhr, K. 1992, A&A, **263**, 54

[24] Bessell, M.S. 1991, AJ, **101**, 662

[25] Black, J.H. & van Dishoeck, E.F. 1987, ApJ, **322**, 412

[26] Blackwell, D.E. & Lynas-Gray, A.E. 1993, A&A, **282**, 899

[27] Blackwell, D.E., Petford, A.D., Arribas, S., Haddock, D.J. & Selby, M.J. 1990, A&A, **232**, 396

[28] Blietz, M., Cameron, M., Drapatz, S., Genzel, R., Krabbe, A., van der Werf, P., Sternberg, A. & Ward, M. 1994, ApJ, **421**, 92

[29] Blum, R.D., Ramond, T.M., Conti, P.S., Figer, D.F. & Sellgren, K. 1997, AJ, **113**, 1855

[30] Blum, R.D., Sellgren, K. & DePoy, D.L. 1996a, AJ, **112**, 1988

[31] Blum, R.D., Sellgren, K. & DePoy, D.L. 1996b, ApJ, **470**, 864

[32] Böker, T., Förster Schreiber, N.M. & Genzel, R. 1997, AJ, **114**, 1883

[33] Boothroyd, A.I. & Sackmann, I.-J. 1988a, ApJ, **328**, 632

[34] Boothroyd, A.I. & Sackmann, I.-J. 1988b, ApJ, **328**, 641

[35] Boothroyd, A.I. & Sackmann, I.-J. 1988c, ApJ, **328**, 653

[36] Boothroyd, A.I. & Sackmann, I.-J. 1988d, ApJ, **328**, 671

[37] Boothroyd, A.I., Sackmann, I.-J. & Wasserburg, G.J. 1995, ApJ, **422**, L21

[38] Boulanger, F., Beichman, C., Désert, F.X., Helou, G., Pérault, M. & Ryter, C. 1988, ApJ, **332**, 328

[39] Brand, P.W.J.L., Moorhouse, A., Burton, M.G., Geballe, T.R., Bird, M. & Wade, R. 1988, ApJ, **334**, L103

[40] Brandl, B. *et al.* 1996, ApJ, **466**, 254

[41] Bregman, J.N., Schulman, E. & Tomisaka, K. 1995, ApJ, **439**, 155

[42] Bressan, A., Chiosi, C. & Fagotto, F. 1994, ApJS, **94**, 63

[43] Brouillet, N., & Schilke, P. 1993, A&A, **277**, 381

[44] Bruzual A., G. 1983, ApJ, **273**, 105

[45] Bruzual A., G. & Charlot, S. 1993, ApJ, **405**, 538

[46] Burbidge, E.M., Burbidge, G.R. & Rubin, V.C. 1964, ApJ, **140**, 942

[47] Butler, K. & Zeippen, C.J. 1994, A&AS, **108**, 1

[48] Buzzoni, A. 1989, ApJS, **71**, 817

[49] Cameron, M., Storey, J.W.V., Rotaciuc, V., Genzel, R., Verstraete, L., Drapatz, S., Siebenmorgen, R. & Lee, T.J. 1993, ApJ, **419**, 136

[50] Cannon, A.J. & Pickering, E.C. 1918, *Harvard Ann.*, **91**, 10

[51] Cardelli, J.A., Clayton, G.C. & Mathis, J.S. 1989, ApJ, **345**, 245

[52] Carlstrom, J.E. 1988, *Ph.D. Thesis*, University of California, Berkeley

[53] Carlstrom, J.E. & Kronberg, P.P. 1991, ApJ, **366**, 422

[54] Carral, P., Hollenbach. D.J., Lord, S.D., Colgan, S.W.J., Haas, M.R., Rubin, R.H. & Erickson, E.F. 1994, ApJ, **423**, 223

[55] Carral, P., Turner, J.L. & Ho, P.T.P. 1990, ApJ, **362**, 434

[56] Cayrel de Strobel, G., Hauck, B., François, P., Thévenin, F., Friel, E., Mermilliod, M. & Borde, S. 1992, A&AS, **95**, 273

[57] Charbonnel, C., Meynet, G., Maeder, A., Schaller, G. & Schaerer, D. 1993, A&AS, **101**, 415

[58] Charlot, S. & Bruzual A., G. 1991, ApJ, **367**, 126

[59] Chevalier, R.A. 1982, ApJ, **259**, 302

[60] Chiosi, C., Bertelli, G. & Bressan, A. 1992, ARA&A, **30**, 235

[61] Chiosi, C. & Maeder, A. 1986, ARA&A, **24**, 329

[62] Claussen, M.J., Kleinmann, S.G., Joyce, R.R. & Jura M. 1987, ApJS, **65**, 385

[63] Clayton, D.D. 1983, *Principles of Stellar Evolution and Nucleosynthesis*, Second Edition (Chicago: University of Chicago Press)

[64] Clegg, R.E.S. 1987, MNRAS, **229**, 31p

[65] Cohen, L., Allamandola, L.J., Tielens, A.G.G.M., Bregman, J., Simpson, J.P., Witteborn, F.C., Wooden, D. & Rank, D. 1986, ApJ, **302**, 737

[66] Cohen, L., Tielens, A.G.G.M., Bregman, J., Witteborn, F.C., Rank, D.M., Allamandola, L.J., Wooden, D. & Jourdain de Muizon, M. 1989, ApJ, **341**, 246

[67] Colina, L., García Vargas, M.L., Mas-Hesse, J.M., Alberdi, A. & Krabbe, A. 1997, ApJ, **484**, L41

[68] Combes, F. & Gérin, M. 1985, A&A, **150**, 327

[69] Condon, J.J., Condon, M.A., Gisler, G. & Puschell, J.J. 1982, ApJ, **252**, 102

[70] Condon, J.J., Huang, Z.-P., Yin, Q.F. & Thuan, T.X. 1991, ApJ, **378**, 65

[71] Conti, P.S. 1991, ApJ, **377**, 115

[72] Conti, P.S. 1994, Space Science Reviews, **66**, 37

[73] Conti, P.S. & Vacca, W.D. 1994, ApJ, **423**, L97

[74] Costa, E. & Frogel, J.A. 1996, AJ, **112**, 2607

[75] Cotera, A.S., Erickson, E.F., Colgan, S.W.J., Simpson, J.P., Allen, D.A. & Burton, M.G. 1996, ApJ, **461**, 750

[76] Crutcher, R.M., Rogstad, D.H. & Chu, K. 1978, ApJ, **225**, 784

[77] Dallier, R., Boisson, C. & Joly, M. 1996, A&AS, **116**, 239 [DBJ96]

[78] Davidge, T. 1994, in *The Local Group: Comparative and Global Properties*, ESO Conf. and Workshop Proc. vol. 51, eds. A. Layden, R.C. Smith and J. Storm (Garching: ESO), p. 92

[79] Davidge, T.J., Rigaut, F., Doyon, R. & Crampton, D. 1997, AJ, **113**, 2094

[80] Davidson, K. & Netzer, H. 1979, Rev. Mod. Phys., **51**, 715

[81] de Graauw, T. *et al.* 1996, A&A, **315**, L49

[82] Désert, F.X. & Dennefeld, M. 1988, A&A, **206**, 227

[83] Devereux, N.A., Becklin, E.E. & Scoville, N.Z. 1987, ApJ, **312**, 529

[84] Di Benedetto, G.P. 1993, A&A, **270**, 315

[85] Di Benedetto, G.P. & Ferluga, S. 1990, A&A, **236**, 449

[86] Di Benedetto, G.P. & Rabbia, Y. 1987, A&A, **188**, 114

[87] Dietz, R.D., Gehrz, R.D., Jones, T.J., Grasdalen, G.L., Smith, J., Gullixson, C. & Hackwell, J.A. 1989, AJ, **98**, 1260

[88] Dietz, R.D., Smith, J., Hackwell, J.A., Gehrz, R.D. & Grasdalen, G.L. 1986, AJ, **91**, 758

[89] Doane, J.S. & Mathews, W.G. 1993, ApJ, **419**, 573

[90] Doherty, R.M., Puxley, P.J., Doyon, R. & Brand, P.W.J.L. 1994, MNRAS, **266**, 497

[91] Doherty, R.M., Puxley, P.J., Lumsden, S.L. & Doyon, R. 1995, MNRAS, **277**, 577

[92] Dominy, J.F. 1984, ApJS, **55**, 27

[93] Dominy, J.F. 1985, PASP, **97**, 1104

[94] Doyon, R. 1991, *Ph.D. Thesis*, University of London

[95] Doyon, R., Joseph, R.D. & Wright, G.S. 1994, ApJ, **421**, 101

[96] Doyon, R., Puxley, P.J. & Joseph, R.D. 1992, ApJ, **397**, 117

[97] Doyon, R., Wright, G.S. & Joseph, R.D. 1994, ApJ, **421**, 115

[98] Draine, B.T. 1989, in *Proc. of the 22nd ESLAB Symposium on Infrared Spectroscopy in Astronomy*, ed. B.H. Kaldeich (ESA SP-290), p. 93

[99] Draine, B.T. & Lee, H.M. 1984, ApJ, **285**, 89

[100] Drissen, L., Moffat, A.F.J., Walborn, N.R. & Shara, M.M. 1995, AJ, **110**, 2235

[101] Duffy, P.B., Erickson, E.F., Haas, M.R. & Houck, J.R. 1987, ApJ, **315**, 68

[102] Dyck, H.M., Benson, J.A., van Belle, G.T. & Ridgway, S.T. 1996, AJ, **111**, 1705

[103] Eisenhauer, F., Quirrenbach, A., Zinnecker, H. & Genzel, R. 1998, ApJ, **498**, 278

[104] Elias, J.H. 1980, ApJ, **241**, 728

[105] Elias, J.H. *et al.* 1978, ApJ, **220**, 25

[106] Elson, R.A.W. & Fall, S.M. 1985, PASP, **97**, 692

[107] Elston, R. & Silva, D.R. 1992, AJ, **104**, 1360

[108] Emerson, J.P. 1988, in *Formation and Evolution of Low Mass Stars*, eds. A.K. Dupree & M.T.V.T. Lago (Kluwer Academic Publishers), p. 21

[109] Engelbracht, C.W., Rieke, M.J., Rieke, G.H., Kelly, D.M. & Achtermann, J.M. 1998, ApJ, **505**, 639

[110] Engelbracht, C.W., Rieke, M.J., Rieke, G.H. & Latter, W.B. 1996, ApJ, **467**, 227

[111] Epchtein, N., Le Bertre, T. & Lépine, J.R.D. 1990, A&A, **227**, 82

[112] Fabbiano, G., Kim, D.-W. & Trinchieri, G. 1992, ApJS, **80**, 531

[113] Faucherre, M., Bonneau, D., Koechlin, L. & Vakili, F. 1983, A&A, **120**, 263

[114] Ferland, G.J. 1980, PASP, **92**, 596

[115] Ferland, G.J. 1996, *Hazy, a Brief Introduction to Cloudy*, University of Kentucky Department of Physics and Astronomy Internal Report

[116] Ferland, G.J. 1998, private communication

[117] Figer, D.F., Najarro, F., Morris, M., McLean, I.S., Geballe, T.R., Ghez, A.M. & Langer, N. 1998, ApJ, **506**, 384

[118] Fischer, J., Simon, M., Benson, J. & Solomon, P.M. 1983, ApJ, **273**, L27

[119] Fluks, M.A., Plez, B., Thé, P.S., de Winter, D., Westerlund, B.E. & Steenman, H.C. 1994, A&AS, **105**, 311

[120] Förster, N.M. 1995, *M.Sc. Thesis*, Université de Montréal

[121] Forestini, M. & Charbonnel, C. 1997, A&AS, **123**, 241

[122] Freedman, W.L. 1992, AJ, **104**, 1349

[123] Freedman, W.L. & Madore, B.F. 1988, ApJ, **332**, L63

[124] Frogel, J.A., Cohen, J.G. & Persson, S.E. 1983, ApJ, **275**, 773

[125] Frogel, J.F., Elias, J.H. & Phillips, M.M. 1982, ApJ, **260**, 70

[126] Frogel, J.A., Mould, J. & Blanco, V.M. 1990, ApJ, **352**, 96

[127] Frogel, J.A., Persson, S.E., Aaronson, M. & Matthews, K. 1978, ApJ, **220**, 75

[128] Gaffney, N.I. & Lester, D.F. 1992, ApJ, **394**, 139

[129] Gaffney, N.I., Lester, D.F. & Telesco, C.M. 1993, ApJ, **407**, L57

[130] Galavís, M.E., Mendoza, C. & Zeippen, C.J. 1995, A&AS, **111**, 347

[131] Garrison, R.F. 1994, in *The MK Process at 50 Years: a Powerful Tool for Astrophysical Insight*, ASP Conf. Series vol. 60, eds. C.J. Corbally, R.O. Gray and R.F. Garrison (San Francisco: ASP), p. 3

[132] Gatley, I. *et al.* 1987, ApJ, **318**, L73

[133] Gautier, T.N. III, Fink, U., Treffers, R.R. & Larson, H.P. 1976, ApJ, **207**, L129

[134] Gautschy, A. & Saio, H. 1996, ARA&A, **34**, 551

[135] Gear, W.K. 1988, in *Millimeter and Submillimeter Astronomy*, eds. R.D. Wolstencroft and W.B. Burton, (Dordrecht: Kluwer), p. 307

[136] Gehren, T. 1981, A&A, **100**, 97

[137] Genzel, R. *et al.* 1998, ApJ, **498**, 579

[138] Genzel, R., Weitzel, L., Tacconi-Garman, L.E., Blietz, M., Cameron, M., Krabbe, A., Lutz, D. & Sternberg, A. 1995, ApJ, **444**, 129

[139] Giard, M., Pajot, F., Lamarre, J.M., Serra, G. & Caux, E. 1989, A&A, **215**, 92

[140] Gillett, F.C., Kleinmann, D.E., Wright, E.L. & Capps, R.W. 1975, ApJ, **198**, L65

[141] Girardi, L. & Bertelli, G. 1998, MNRAS, **300**, 533

[142] Götz, M., McKeith, C.D., Downes, D. & Greve, A. 1990, A&A, **240**, 52

[143] Goldader, J.D., Joseph, R.D., Doyon, R. & Sanders, D.B. 1995, ApJ, **444**, 97

[144] Golla, G., Allen, M.L. & Kronberg, P.P. 1996, ApJ, **473**, 244

[145] González-Delgado, R.M., Pérez, E., Díaz, A.I., García-Vargas, M.L., Terlevich, E. & Vilchez, J.M. 1995, ApJ, **439**, 604

[146] Gottesman, S.T. & Weliachew, L. 1977, ApJ, **211**, 47

[147] Graham, J.R., Meikle, W.P.S., Allen, D.A., Longmore, A.J. & Williams, P.M. 1986, MNRAS, **218**, 93

[148] Graham, J.R., Wright, G.S. & Longmore, A.J. 1987, ApJ, **313**, 847

[149] Greenhouse, M.A. *et al.* 1997, ApJ, **476**, 105

[150] Grevesse, N. & Anders, E. 1989, in *Cosmic Abundances of Matter*, AIP Conf. Proc. 183, ed. C.J. Waddington (New York: AIP), p. 1

[151] Grevesse, N. & Noels, A. 1993, in *Origin and Evolution of the Elements*, eds. N. Prantzos, E. Vangioni-Flam and M. Casse (Cambridge: Cambridge Univ. Press), p. 15

[152] Groenewegen, M.A.T. & de Jong, T. 1993, A&A, **267**, 410

[153] Groenewegen, M.A.T., de Jong, T., van der Bliek, N.S., Slijkhuis, S. & Willems, F.J. 1992, A&A, **253**, 150

[154] Groenewegen, M.A.T., van den Hoek, L.B. & de Jong, T. 1995, A&A, **293**, 381

[155] Güsten, R., Serabyn, E., Kasemann, C., Schinckel, A., Schneider, G., Schulz, A. & Young, K. 1993, ApJ, **402**, 537

[156] Guiderdoni, B. & Rocca-Volmerange, B. 1987, A&A, **186**, 1

[157] Gustafsson, B. 1989, ARA&A, **27**, 701

[158] Haller, J.W. & Rieke, M.J. 1989, in *The Center of the Galaxy*, IAU Symp. 136, ed. M. Morris (Dordrecht: Kluwer), p. 487

[159] Hanson, M.M., Conti, P.S. & Rieke, M.J. 1996, ApJS, **107**, 281

[160] Harwit, M., Houck, J.R., Soifer, B.T. & Palumbo, G.G.C. 1987, ApJ, **315**, 28

[161] Harwit, M. & Pacini, F. 1975, ApJ, **200**, L127

[162] Hawarden, T.G., Mountain, C.M., Leggett, S.K. & Puxley, P.J. 1986, MNRAS, **221**, 41p

[163] Hayashi, M., Hasegawa, T., Gatley, I., Garden, R. & Kaifu, N. 1985, MNRAS, **215**, 31p

[164] Heckman, T.M. 1998, in *Origins*, ASP Conf. Series vol. 148, eds. C. E. Woodward, J.M. Shull & H.A. Thronson Jr. (San Francisco: ASP), p. 127

[165] Heckman, T.M., Armus, L. & Miley, G.K. 1990, ApJS, **74**, 833

[166] Heller, C.H. & Shlosman, I. 1994, ApJ, **424**, 84

[167] Heller, C.H. & Shlosman, I. 1996, ApJ, **471**, 143

[168] Helou, G. 1986, ApJ, **311**, L33

[169] Helou, G., Soifer, B.T. & Rowan-Robinson, M. 1985, ApJ, **298**, L7

[170] Hernquist, L. 1989, Nature, **340**, 687

[171] Hildebrand, R.H. 1983, QJRAS., **24**, 267

[172] Hinkle, K.H., Lambert, D.L. & Snell, R.L. 1976, ApJ, **210**, 684

[173] Ho, P.T.P., Beck, S.C. & Turner, J.L. 1990, ApJ, **349**, 57

[174] Hollenbach, D. & McKee, C.F. 1989, ApJ, **342**, 306

[175] Houck, J.R., Shure, M.A., Gull, G.E. & Herter, T. 1984, ApJ, **287**, L11

[176] Huang, Z.-P., Thuan, T.X., Chevalier, R.A., Condon, J.J. & Yin, Q.F. 1994, ApJ, **424**, 114

[177] Huchra, J.P. 1977, ApJ, **217**, 928

[178] Hughes, D.H., Gear, W.K. & Robson, E.I. 1990, MNRAS, **244**, 759

[179] Hummer, D.G. & Storey, P.J. 1987, MNRAS, **224**, 801

[180] Humphreys, R.M. & McElroy, D.B. 1984, ApJ, **284**, 565

[181] Hunter, D.A., Light, R.M., Holtzman, J.A., Lynds, R., O'Neil, E.J. Jr. & Grillmair, C.J. 1997, ApJ, **478**, 124

[182] Hunter, D.A., O'Connell, R.W. & Gallagher, J.S. III 1994, AJ, **108**, 84

[183] Hyland, A.R. 1974, Highlights of Astronomy, **3**, 307

[184] Iben, I. Jr. 1981, ApJ, **246**, 278

[185] Iben, I. Jr. & Renzini, A. 1983, ARA&A, **21**, 271

[186] *IRAS Catalogs and Atlases: Point Source Catalog*, 1990 (Washington, DC: US Government Printing Office)

[187] Jaffe, D.T., Becklin, E.E. & Hildebrand, R.H. 1984, ApJ, **285**, L31

[188] Jörsäter, S. & van Moorsel, G.A. 1995, AJ, **110**, 2037

[189] Johnson, C.T., Kingston, A.E. & Dufton, P.L. 1986, MNRAS, **220**, 155

[190] Johnson, H.L. 1966, ApJ, **143**, 187

[191] Johnson, H.L. & Méndez, M.E. 1970, AJ, **75**, 785

[192] Johnson, H.M. 1968, in *Stars and Stellar Systems*, vol. 7, *Nebulae and Interstellar Matter*, eds. B.D. Middlehurst and L.A. Aller (Chicago: Univ. of Chicago Press), p. 199

[193] Jones, B. & Rodriguez-Espinosa, J.M. 1984, ApJ, **285**, 580

[194] Joseph, R.D. 1989, in *Proc. of the 22nd ESLAB Symposium on Infrared Spectroscopy in Astronomy*, ed. B.H. Kaldeich (ESA SP-290), p. 439

[195] Joseph, R.D. 1990, in *Dynamics and Interactions of Galaxies*, ed. R. Wielen (Berlin: Springer), p. 132

[196] Joseph, R.D., Wright, G.S. & Wade, R. 1984, Nature, **311**, 132

[197] Joseph, R.D., Wright, G.S., Wade, R., Graham, J.R., Gatley, I. & Prestwich, A.H. 1987, in *Star Formation in Galaxies*, ed. C.J. Lonsdale (Washington DC: US Government Printing Office), p. 421

[198] Joy, M. & Lester, D.F. 1988, ApJ, **331**, 145

[199] Joy, M., Lester, D.F. & Harvey, P.M. 1987, ApJ, **319**, 314

[200] Jura, M. 1988, ApJS, **66**, 33

[201] Jura, M., Hobbs, R.W. & Maran, S.P. 1978, AJ, **83**, 153

[202] Jura, M. & Kleinmann, S.G. 1989, ApJ, **341**, 359

[203] Jura, M. & Kleinmann, S.G. 1992a, ApJS, **79**, 105

[204] Jura, M. & Kleinmann, S.G. 1992b, ApJS, **83**, 329

[205] Jura, M., Yamamoto, A. & Kleinmann, S.G. 1993, ApJ, **413**, 298

[206] Kawara, K., Nishida, M. & Gregory, B. 1987, ApJ, **321**, L35

[207] Kawara, K., Nishida, M. & Phillips, M.M. 1989, ApJ, **337**, 230

[208] Kawara, K., Nishida, M. & Taniguchi, Y. 1988, ApJ, **328**, L41

[209] Keenan, P.C. 1993, PASP, **105**, 905

[210] Keenan, P.C. & McNeil, R.C. 1989, ApJS, **71**, 245

[211] Keenan, P.C. & Morgan, W.W. 1941, ApJ, **94**, 501

[212] Keenan, P.C. & Pitts, R.E. 1980, ApJS, **42**, 541

[213] Keenan, P.C. & Yorka, S.B. 1988, *Bull. D'Inf. CDS* No. 35, p. 37

[214] Kennicutt, R.C. 1984, ApJ, **287**, 116

[215] Kennicutt, R.C., Edgar, B.K. & Hodge, P.W. 1989, ApJ, **337**, 761

[216] Kennicutt, R.C., Keel, W.C., van der Hulst, J.M., Hummel, E. & Roettiger, K.A. 1987, AJ, **93**, 1011

[217] Kerschbaum, F. & Hron, J. 1992, A&A, **263**, 97

[218] Kessler, M.F. *et al.* 1996, A&A, **315**, L27

[219] Kippenhahn, R. & Weigert, A. 1991, *Stellar Structure and Evolution*, Second Edition (Berlin: Springer)

[220] Klein, U., Wielebinski, R. & Morsi, H.W. 1988, A&A, **190**, 41

[221] Kleinmann, D.E. & Low, F.J. 1970a, ApJ, **159**, L165

[222] Kleinmann, D.E. & Low, F.J. 1970b, ApJ, **161**, L203

[223] Kleinmann, S.G. & Hall, D.N.B. 1986, ApJS, **62**, 501 [KH86]

[224] Knacke, R.F. & Young, E.T. 1980, ApJ, **242**, L183

[225] Knacke, R.F. & Young, E.T. 1981, ApJ, **249**, L65

[226] Knapen, J.H., Beckman, J.E., Heller, C.H., Shlosman, I. & de Jong, R.S. 1995, ApJ, **454**, 623

[227] Koornneef, J. 1983a, A&AS, **51**, 489

[228] Koornneef, J. 1983b, A&A, **128**, 84

[229] Kovo, O., Sternberg, A. & Alexander, T. 1998, in preparation

[230] Krabbe, A., Sternberg, A. & Genzel, R. 1994, ApJ, **425**, 72

[231] Krabbe, A. *et al.* 1995, ApJ, **447**, L95

[232] Kronberg, P.P., Biermann, P. & Schwab, F.R. 1985, ApJ, **291**, 693

[233] Kunze, D. *et al.* 1996, A&A, **315**, L101

[234] Kurucz, R.L. 1979, ApJS, **40**, 1

[235] Kurucz, R.L. 1992, Rev. Mexicana Astron. Astrof., **23**, 181

[236] Lambert, D.L., Brown, J.A., Hinkle, K.H. & Johnson, H.R. 1984, ApJ, **284**, 223

[237] Lambert, D.L. & Ries, L.M. 1981, ApJ, **248**, 228

[238] Lançon, A. & Rocca-Volmerange, B. 1992, A&AS, **96**, 593

[239] Lançon, A. & Rocca-Volmerange, B. 1994, Ap&SS, **217**, 271

[240] Lançon, A. & Rocca-Volmerange, B. 1996, New Astronomy, **1**, 215

[241] Lançon, A., Rocca-Volmerange, B. & Thuan, T.X. 1996, A&AS, **115**, 253

[242] Landini, M., Natta, A., Oliva, E., Salinari, P. & Moorwood, A.F.M. 1984, A&A, **134**, 384

[243] Langer, N. & Maeder, A. 1995, A&A, **295**, 685

[244] Larkin, J.E., Graham, J.R., Matthews, K., Soifer, B.T., Beckwith, S., Herbst, T.M. & Quillen, A.C. 1994, ApJ, **420**, 159

[245] Larson, R.B. & Tinsley, B.M. 1978, ApJ, **219**, 46

[246] Lebofsky, M.J. & Rieke, G.H. 1979, ApJ, **229**, 111

[247] Lee, M.G. 1996, AJ, **112**, 1438

[248] Lee, M.G., Freedman, W.L. & Madore, B.F. 1993, AJ, **106**, 964

[249] Léger, A. & Puget, J.L. 1984, A&A, **137**, L5

[250] Leggett, S.K., Mountain, C.M., Selby, M.J., Blackwell, D.E., Booth, A.J., Haddock, D.J. & Petford, A.D. 1986, A&A, **159**, 217

[251] Lehnert, M.D. & Heckman, T.M. 1996, ApJ, **472**, 546

[252] Leitherer, C. 1998a, in *VIII Canary Islands Winter School of Astrophysics: Stellar Astrophysics for the Local Group*, eds. A. Aparicio, A. Herrero and F. Sánchez (Cambridge: Cambridge Univ. Press)

[253] Leitherer, C. 1998b, preprint (STScI #1254)

[254] Leitherer, C. & Heckman, T.M. 1995, ApJS, **96**, 9

[255] Leitherer, C. *et al.* 1996, PASP, **108**, 996

[256] Lépine, J.R.D., Ortiz, R. & Epchtein, N. 1995, A&A, **299**, 453

[257] Lester, D.F., Carr, J.S., Joy, M. & Gaffney, N. 1990, ApJ, **352**, 544

[258] Lo, K.Y., Cheung, K.W., Masson, C.R., Phillips, T.G., Scott, S.L. & Woody, D.P. 1987, ApJ, **312**, 574

[259] Loiseau, N., Nakai, N., Sofue, Y., Wielebinski, R., Reuter, H.P. & Klein, U. 1990, A&A, **228**, 331

[260] Loiseau, N., Reuter, H.-P., Wielebinski, R. & Klein, U. 1988, A&A, **200**, L1

[261] Lord, S. 1992, Tech. Mem. 103957

[262] Lord, S.D., Hollenbach, D.J., Haas, M.R., Rubin, R.H., Colgan, S.W.J. & Erickson, E.F. 1996, ApJ, **465**, 703

[263] Loup, C., Zijlstra, A.A., Waters, L.B.F.M. & Groenewegen, M.A.T. 1997, A&AS, **125**, 419

[264] Low, F.J. & Kleinmann, D.E. 1968, AJ, **73**, 868

[265] Lowe, R.P., Moorhead, J.M. & Wehlau, W.H. 1979, ApJ, **228**, 191

[266] Luck, R.E. & Bond, H.E. 1989, ApJS, **71**, 559

[267] Lugten, J.B., Watson, D.M., Crawford, M.K. & Genzel, R. 1986, ApJ, **311**, L51

[268] Lumsden, S.L. & Puxley, P.J. 1995, MNRAS, **276**, 723

[269] Lutz, D. *et al.* 1996, A&A, **315**, L269

[270] Lutz, D., Kunze, D., Spoon, H.W.W. & Thornley, M.D. 1998, A&A, **333**, L75

[271] Lynds, C.R. & Sandage, A.R. 1963, ApJ, **137**, 1005

[272] Maeder, A. & Conti, P.S. 1994, ARA&A, **32**, 227

[273] Maeder, A. & Meynet, G. 1989, A&A, **210**, 155

[274] Maeder, A. & Meynet, G. 1994, A&A, **287**, 803

[275] Maeder, A. & Meynet, G. 1996, A&A, **313**, 140

[276] Maiolino, R., Krabbe, A., Thatte, N. & Genzel, R. 1998, ApJ, **493**, 650

[277] Makinen, P., Harvey, P.M., Wilking, B.A. & Evans, N.J. II 1985, ApJ, **299**, 341

[278] Malagnini, M.L. & Morossi, C. 1990, A&AS, **85**, 1015

[279] Maoz, D., Barth, A.J., Sternberg, A., Filippenko, A.V., Ho, L.C., Macchetto, F.D., Rix, H.-W. & Schneider, D.P. 1996, AJ, **111**, 2248

[280] Martinet, L. & Friedli, D. 1997, A&A, **323**, 363

[281] Martínez-Delgado, D. & Aparicio, A. 1998, AJ, **115**, 1462

[282] Mas-Hesse, J.M. & Kunth, D. 1991, A&AS, **88**, 399

[283] Massey, P. 1998, in *The Stellar Initial Mass Function*, ASP Conf. Series vol. 142, eds. G. Gilmore and D. Howell (San Francisco: ASP), p. 17

[284] Massey, P. & Hunter, D.A. 1998, ApJ, **493**, 180

[285] Mathis, J.S. 1983, ApJ, **267**, 119

[286] Mathis, J.S. 1990, ARA&A, **28**, 37

[287] Mathis, J.S., Rumpl, W. & Nordsieck, K.H. 1977, ApJ, **217**, 425

[288] McCarthy, P.J., Heckman, T. & van Breugel, W. 1987, AJ, **92**, 264

[289] McClure, R.D. 1989 in *The Evolution of Peculiar Red Giant Stars*, eds. H.R. Johnson and B. Zuckermann (Cambridge: Cambridge University Press), p. 196

[290] McGregor, P.J. 1987, ApJ, **312**, 195

[291] McKee, C.F. & Williams, J.P. 1997, ApJ, **476**, 144

[292] McKeith, C.D., Castles, J., Greve, A. & Downes, D. 1993, A&A, **272**, 98

[293] McLean, I.S. & Liu, T. 1996, ApJ, **456**, 499

[294] McLeod, K.K., Rieke, G.H., Rieke, M.J. & Kelly, D.M. 1993, ApJ, **412**, 111

[295] McWilliam, A. 1990, ApJS, **74**, 1075

[296] McWilliam, A. & Lambert, D.L. 1984, PASP, **96**, 882

[297] Melnick, J. 1985, A&A, **153**, 235

[298] Mendoza, E.E. V & Johnson, H.L. 1965, ApJ, **141**, 161

[299] Merrill, K.M. & Ridgway, S.T. 1979, ARA&A, **17**, 9

[300] Merrill, K.M. & Stein, W.A. 1976, PASP, **88**, 285

[301] Meurer, G.R., Heckman, T.M., Lehnert, M.D., Leitherer, C. & Lowenthal, J. 1997, AJ, **114**, 54

[302] Meurer, G.R., Heckman, T.M., Leitherer, C., Kinney, A., Robert, C. & Garnett, D.R. 1995, AJ, **110**, 2665

[303] Meyer, M.R. 1996, *Ph.D. Thesis*, University of Massachusetts, Amherst

[304] Meynet, G., Maeder, A., Schaller, G., Schaerer, D. & Charbonnel, C. 1994, A&AS, **103**, 97

[305] Mihos, J.C. & Hernquist, L. 1996, ApJ, **464**, 641

[306] Miller, G.E. & Scalo, J.M. 1979, ApJS, **41**, 513

[307] Moorwood, A.F.M. 1986, A&A, **166**, 4

[308] Moorwood, A.F.M., Lutz, D., Oliva, E., Marconi, A., Netzer, H., Genzel, R., Sturm, E. & de Graauw, T. 1996, A&A, **315**, L109

[309] Moorwood, A.F.M. & Oliva, E. 1988, A&A, **203**, 278

[310] Morgan, W.W. & Keenan, P.C. 1973, ARA&A, **11**, 29

[311] Morossi, C. & Malagnini, M.L. 1985, A&AS, **60**, 365

[312] Morris, P.W., Eenens, P.R.J., Hanson, M.M., Conti, P.S. & Blum, R.D. 1996, ApJ, **470**, 597

[313] Mouri, H. 1994, ApJ, **427**, 777

[314] Mouri, H., Kawara, K. & Taniguchi, Y. 1993, ApJ, **406**, 52

[315] Mouri, H., Nishida, M., Taniguchi, Y. & Kawara, K. 1990, ApJ, **360**, 55

[316] Muxlow, T.W.B., Pedlar, A., Wilkinson, P.N., Axon, D.J., Sanders, E.M. & de Bruyn, A.G. 1994, MNRAS, **266**, 455

[317] Najarro, F., Hillier, D.J., Kudritzki, R.P., Krabbe, A., Lutz, D., Genzel, R., Drapatz, S. & Geballe, T.R. 1994, A&A, **285**, 573

[318] Nakagawa, T., Nagata, T., Geballe, T.R., Okuda, H., Shibai, H. & Matsuhara, H. 1989, ApJ, **340**, 729

[319] Nakai, N., Hayashi, M., Handa, T., Sofue, Y., Hasegawa, T. & Sasaki, M. 1987, PASJ, **39**, 685

[320] Neugebauer, G. *et al.* 1984, ApJ, **278**, L1

[321] Noguchi, M. 1987, MNRAS, **228**, 635

[322] Noguchi, M. 1988, A&A, **203**, 259

[323] Norman, C.A. & Scoville, N.Z. 1988, ApJ, **332**, 124

[324] Normand, P., Rouan, D., Lacombe, F. & Tiphène, D. 1995, A&A, **297**, 311

[325] Notni, P. 1985, Astron. Nach., **306**, 273

[326] Nussbaumer, H. & Storey, P.J. 1988, A&A, **193**, 327

[327] O'Connell, R.W., Gallagher, J.S. III & Hunter, D.A. 1994, ApJ, **433**, 65

[328] O'Connell, R.W., Gallagher, J.S. III, Hunter, D.A. & Colley, W.N. 1995, ApJ, **446**, L1

[329] O'Connell, R.W. & Mangano, J.J. 1978, ApJ, **221**, 62

[330] Ohnaka, K. & Tsuji, T. 1996, A&A, **310**, 933

[331] Oliva, E., Moorwood, A.F.M. & Danziger, I.J. 1989, A&A, **214**, 307

[332] Oliva, E. & Origlia, L. 1998, A&A, **332**, 46

[333] Oliva, E., Origlia, L., Kotilainen, J.K. & Moorwood, A.F.M. 1995, A&A, **301**, 55

[334] Olofsson, K. 1989, A&AS, **80**, 317

[335] Olofsson, H. & Rydbeck, G. 1984, A&A, **136**, 17

[336] Ondrechen, M.P. & van der Hulst, J.M. 1989, ApJ, **342**, 290

[337] Origlia, L., Ferraro, F.R., Fusi Pecci, F. & Oliva, E. 1997, A&A, **321**, 859

[338] Origlia, L., Moorwood, A.F.M. & Oliva, E. 1993, A&A, **280**, 536 [OMO93]

[339] Ortiz, R. & Maciel, W.J. 1996, A&A, **313**, 180

[340] Osterbrock, D.E. 1989, *Astrophysics of Gaseous Nebulae and Active Galactic Nuclei* (Mill Valley, CA: University Science Books)

[341] Paczyński, B. 1970, Acta Astr., **20**, 47

[342] Parmar, P.S., Lacy, J.H. & Achtermann, J.M. 1991, ApJ, **372**, L25

[343] Parmar, P.S., Lacy, J.H. & Achtermann, J.M. 1994, ApJ, **430**, 786

[344] Parthasarathy, M. 1991, A&A, **247**, 429

[345] Pauldrach, A.W.A., Lennon, M., Hoffmann, T.L., Sellmaier, F., Kudritzki, R.-P. & Puls, J. 1998, in *Boulder-Munich Workshop II: Properties of Hot Luminous Stars*, ASP Conf. Series vol. 131, ed. I. Howarth (San Francisco: ASP), p. 258

[346] Pelan, J. & Berrington, K.A. 1995, A&AS, **110**, 209

[347] Persic, M., Salucci, P. & Stel, F. 1996, MNRAS, **281**, 27

[348] Pickles, A.J. 1985, ApJ, **296**, 340

[349] Pipher, J.L., Moneti, A., Forrest, W.J., Woodward, C.E. & Shure, M.A. 1987, in *Infrared Astronomy with Arrays*, eds. C.G. Wynn-Williams and E.E. Becklin (Honolulu: University of Hawaii Press), p. 326

[350] Prestwich, A.H., Joseph, R.D. & Wright, G.S. 1994, ApJ, **422**, 73

[351] Puget, J.L., Léger, A. & Boulanger, F. 1985, A&A, **142**, L19

[352] Puxley, P.J. 1991, MNRAS, **249**, 11p

[353] Puxley, P.J., Brand, P.W.J.L., Moore, T.J.T., Mountain, C.M., Nakai, N. & Yamashita, T. 1989, ApJ, **345**, 163

[354] Puxley, P.J., Hawarden, T.G. & Mountain, C.M. 1988, MNRAS, **234**, 29p

[355] Ramírez, S.V., DePoy, D.L., Frogel, J.A., Sellgren, K. & Blum, R.D. 1997, AJ, **113**, 1411

[356] Rana, N.C. 1987, A&A, **184**, 104

[357] Reid, I.N., Hughes, S.M.G. & Glass, I.S. 1995, MNRAS, **275**, 331

[358] Reid, I.N., Tinney, C. & Mould, J. 1990, ApJ, **348**, 98

[359] Renzini, A. 1981, Ann. Phys. Fr., **6**, 87

[360] Renzini, A. & Buzzoni, A. 1986, in *Spectral Evolution of Galaxies*, eds. C. Chiosi and A. Renzini (Dordrecht: Reidel), p. 195

[361] Rich, R.M. & Mighell, K.J. 1995, ApJ, **439**, 145

[362] Rich, R.M., Mould, J.R. & Graham, J.R. 1993, AJ, **106**, 2253

[363] Ridgway, S.E., Wynn-Williams, C.G. & Becklin, E.E. 1994, ApJ, **428**, 609

[364] Ridgway, S.T. 1974, Highlights of Astronomy, **3**, 327

[365] Ridgway, S.T. 1984, in *Galactic and Extragalactic Infrared Spectroscopy*, eds. M.F. Kessler and J.P. Phillips (Dordrecht: Reidel), p. 309

[366] Ridgway, S.T., Joyce, R.R., White, N.M. & Wing, R.F. 1980, ApJ, **235**, 126

[367] Rieke, G.H. 1974, ApJ, **193**, L81

[368] Rieke, G.H. 1978, ApJ, **226**, 550

[369] Rieke, G.H., Cutri, R.M., Black, J.H., Kailey, W.F., McAlary, C.W., Lebofsky, M.J. & Elston, R. 1985, ApJ, **290**, 116

[370] Rieke, G.H. & Lebofsky, M.J. 1978, ApJ, **220**, L37

[371] Rieke, G.H. & Lebofsky, M.J. 1979, ARA&A, **17**, 477

[372] Rieke, G.H. & Lebofsky, M.J. 1985, ApJ, **288**, 618

[373] Rieke, G.H., Lebofsky, M.J., Thompson, R.I., Low, F.J. & Tokunaga, A.T. 1980, ApJ, **238**, 24

[374] Rieke, G.H., Loken, K., Rieke, M.J. & Tamblyn, P. 1993, ApJ, **412**, 99

[375] Rieke, G.H. & Low, F.J. 1972, ApJ, **176**, L95

[376] Rieke, G.H. & Low, F.J. 1975a, ApJ, **197**, 17

[377] Rieke, G.H. & Low, F.J. 1975b, ApJ, **199**, L13

[378] Rifatto, A., Longo, G. & Capaccioli, M. 1995, A&AS, **114**, 527

[379] Rigopoulou, D. *et al.* 1996, A&A, **315**, L125

[380] Robbins, R.R. 1968, ApJ, **151**, 511

[381] Roche, P.F. & Aitken, D.K. 1985, MNRAS, **215**, 425

[382] Rubin, R.H. 1985, ApJS, **57**, 349

[383] Salama, A. *et al.* 1997, in *First ISO Workshop on Analytical Spectroscopy*, eds. A.M. Heras, K. Leech, N.R. Trams and M. Perry (ESA SP-419), p. 17

[384] Salpeter, E.E. 1955, ApJ, **121**, 161

[385] Sanders, D.B. & Mirabel, I.F. 1985, ApJ, **298**, L31

[386] Sanders, D.B. & Mirabel, I.F. 1996, ARA&A, **34**, 749

[387] Sanders, D.B., Soifer, B.T., Elias, J.H., Madore, B.F., Matthews, K., Neugebauer, G. & Scoville, N.Z. 1988, ApJ, **325**, 74

[388] Saraph, H.E. & Tully, J.A. 1994, A&AS, **107**, 29

[389] Satyapal, S. *et al.* 1995, ApJ, **448**, 611

[390] Satyapal, S., Watson, D.M., Pipher, J.L., Forrest, W.J., Greenhouse, M.A., Smith, H.A., Fisher, J. & Woodward, C.E. 1997, ApJ, **483**, 148

[391] Savage, B.D. & Mathis, J.S. 1979, ARA&A, **17**, 73

[392] Scalo, J.M. 1986, Fund. Cosmic Phys., **11**, 1

[393] Scalo, J.M. 1998, in *The Stellar Initial Mass Function*, ASP Conf. Series vol. 142, eds. G. Gilmore and D. Howell (San Francisco: ASP), p. 201

[394] Schaaf, R., Pietsch, W., Biermann, P.L., Kronberg, P.P. & Schmutzler, T. 1989, ApJ, **336**, 722

[395] Schaeidt, S.G. *et al.* 1996, A&A, **315**, L55

[396] Schaerer, D., Charbonnel, C., Meynet, G., Maeder, A. & Schaller, G. 1993a, A&AS, **102**, 339

[397] Schaerer, D., Meynet, G., Maeder, A. & Schaller, G. 1993b, A&AS, **98**, 523

[398] Schaller, G., Schaerer, D., Meynet, G. & Maeder, A. 1992, A&AS, **96**, 269

[399] Scheffler, H. 1982, in *Astronomy and Astrophysics: LB New Series*, vol. 2c, eds. K. Schaifers and H.H. Voigt (New York: Springer), p. 46

[400] Schinnerer, E., Eckart, A., Quirrenbach, A., Böker, T., Tacconi-Garman, L.E., Krabbe, A. & Sternberg, A. 1997, ApJ, **488**, 174

[401] Schmidt, G.D., Angel, J.R.P. & Cromwell, R.H. 1976, ApJ, **206**, 888

[402] Schmidt-Kaler, T. 1982, in *Astronomy and Astrophysics: LB New Series*, vol. 2b, eds. K. Schaifers and H.H. Voigt (New York: Springer), p. 451

[403] Scoville, N.Z. & Norman, C.A. 1988, ApJ, **332**, 163

[404] Scoville, N.Z. & Sanders, D.B. 1987, in *Interstellar Processes*, eds. D.J. Hollenbach and H.A. Thronson Jr. (Dordrecht: Reidel), p. 21

[405] Seaquist, E.R., Bell, M.B. & Bignell, R.C. 1985, ApJ, **294**, 546

[406] Seaquist, E.R., Carlstrom, J.E., Bryant, P.M. & Bell, M.B. 1996, ApJ, **465**, 691

[407] Seaquist, E.R., Kerton, C.R. & Bell, M.B. 1994, ApJ, **429**, 612

[408] Seaquist, E.R. & Odegard, N. 1991, ApJ, **369**, 320

[409] Secchi, A. 1868, C.R. Acad. Sci. Paris, **67**, 373

[410] Sellgren, K. 1986, ApJ, **305**, 399

[411] Shane, C.D. 1928, Lick Obs. Bull., **13**, 123

[412] Shaver, P.A., McGee, R.X., Newton, L.M., Danks, A.C. & Pottasch, S.R. 1983, MNRAS, **204**, 53

[413] Shen, J. & Lo, K.Y. 1995, ApJ, **445**, L99

[414] Shields, G.A. 1990, ARA&A, **28**, 525

[415] Shields, J.C. 1993, ApJ, **419**, 181

[416] Shields, J.C. & Ferland, G.J. 1994, ApJ, **430**, 236

[417] Shlosman, I., Frank, J. & Begelman, M.C. 1989, Nature, **338**, 45

[418] Shopbell, P.L. & Bland-Hawthorn, J. 1998, ApJ, **493**, 129

[419] Shull, J.M. & Beckwith, S. 1982, ARA&A, **20**, 163

[420] Shull, J.M. & Draine, B.T. 1987, in *Interstellar Processes*, eds. D.J. Hollenbach and H.A. Thronson Jr. (Dordrecht: Reidel), p. 283

[421] Simon, M., Simon, T. & Joyce, R.R. 1979, ApJ, **227**, 64

[422] Simpson, J.P., Colgan, S.W.J., Rubin, R.H., Erickson, E.F. & Haas, M.R. 1995, ApJ, **444**, 721

[423] Sirianni, M., Nota, A., Clampin, M. & Leitherer, C. 1998, in preparation

[424] Smith, H.E. 1975, ApJ, **199**, 591

[425] Smith, H.E., Lonsdale, C.J., Lonsdale, C.J. & Diamond, P.J. 1998, ApJ, **493**, L17

[426] Smith, P.A., Brand, P.W.J.L., Puxley, P.J., Mountain, C.M. & Nakai, N. 1990, MNRAS, **243**, 97

[427] Smits, D.P. 1991, MNRAS, **248**, 193

[428] Smits, D.P. 1996, MNRAS, **278**, 683

[429] Sofue, Y. 1998, PASJ, **50**, 227

[430] Soifer, B.T. *et al.* 1984, ApJ, **283**, L1

[431] Soifer, B.T., Sanders, D.B., Madore, B.F., Neugebauer, G., Danielson, G.E., Elias, J.H., Lonsdale, C.J. & Rice, W.L. 1987, ApJ, **320**, 238

[432] Solinger, A., Morrison, P. & Markert, T. 1977, ApJ, **211**, 707

[433] Solomon, P.M. & Sage, M.J. 1988, ApJ, **334**, 613

[434] Spitzer, L. 1978, *Physical Processes in the Interstellar Medium* (New York: Wiley)

[435] Stein, W.A. & Weedman, D.W. 1976, ApJ, **205**, 44

[436] Sternberg, A. & Dalgarno, A. 1989, ApJ, **338**, 197

[437] Sturm, E. *et al.* 1996, A&A, **315**, L133

[438] Stutzki, J. *et al.* 1997, ApJ, **477**, L33

[439] Sundelius, B., Thomasson, M., Valtonen, M.J. & Byrd, G.G. 1987, A&A, **174**, 67

[440] Sweigart, A.V., Greggio, L. & Renzini, A. 1990, ApJ, **364**, 527

[441] Tacconi-Garman, L.E., Sternberg, A. & Eckart, A. 1996, AJ, **112**, 918

[442] Tanaka, M., Hasegawa, T., Hayashi, S.S., Brand, P.W.J.L. & Gatley, I. 1989, ApJ, **336**, 207

[443] Taylor, B.J. 1991, ApJS, **76**, 715

[444] Telesco, C.M. 1988, ARA&A, **26**, 343

[445] Telesco, C.M., Campins, H., Joy, M., Dietz, K. & Decher, R. 1991, ApJ, **369**, 135

[446] Telesco, C.M. & Decher, R. 1988, ApJ, **334**, 573

[447] Telesco, C.M., Dressel, L.L. & Wolstencroft, R.D. 1993, ApJ, **414**, 120

[448] Telesco, C.M. & Gezari, D.Y. 1992, ApJ, **395**, 461

[449] Telesco, C.M. & Harper, D.A. 1980, ApJ, **235**, 392

[450] Terndrup, D.M., Frogel, J.A., & Whitford, A.E. 1991, ApJ, **378**, 742

[451] Thatte, N., Kroker, H., Weitzel, L., Tacconi-Garman, L.E., Tecza, M., Krabbe, A., & Genzel, R. 1995, Proc. of the SPIE, **2475**, 228

[452] Thatte, N., Quirrenbach, A., Genzel, R., Maiolino, R. & Tecza, M. 1997, ApJ, **490**, 238

[453] Thompson, R.I., Lebofsky, M.J. & Rieke, G.H. 1978, ApJ, **222**, L49

[454] Thornley, M.D. *et al.* 1998, in preparation

[455] Thronson, H.A. Jr. & Telesco, C.M. 1986, ApJ, **311**, 98

[456] Thronson, H.A. Jr., Walker, C.K., Walker, C.E. & Maloney, P. 1989, A&A, **214**, 29

[457] Tinsley, B.M. 1968, ApJ, **151**, 547

[458] Tinsley, B.M. 1972, A&A, **20**, 383

[459] Tomisaka, K. & Ikeuchi, S. 1988, ApJ, **330**, 695

[460] Treffers, R.R., Fink, U., Larson, H.P. & Gautier, T.N. III 1976, ApJ, **209**, 793

[461] Tsuji, T. 1978, A&A, **62**, 29

[462] Tsuji, T. 1981a, JA&A, **2**, 95

[463] Tsuji, T. 1981b, A&A, **99**, 48

[464] Tsuji, T. 1981c, JA&A, **2**, 253

[465] Tsuji, T. 1986, A&A, **156**, 8

[466] Tsuji, T. 1988, A&A, **197**, 185

[467] Tsuji, T. 1991, A&A, **245**, 203

[468] Vacca, W.D., Garmany, C.D. & Shull, J.M. 1996, ApJ, **460**, 914

[469] Valentijn, E.A., van der Werf, P.P., de Graauw, T. & de Jong, T. 1996, A&A, **315**, L145

[470] van Buren, D. & Greenhouse, M.A. 1994, ApJ, **431**, 640

[471] van den Hoek, L.B. & Groenewegen, M.A.T. 1997, A&AS, **123**, 305

[472] van der Hulst, J.M., Terlouw, J.P., Begeman, K., Zwitser, W. & Roelfsema, P.R. 1992, in *Astronomical Data Analysis Software And Systems I*, ASP Conf. Series vol. 25, eds. D.M. Worall, C. Biemesderfer and J. Barnes (San Francisco: ASP), p. 131

[473] van der Werf, P.P., Genzel, R., Krabbe, A., Blietz, M., Lutz, D., Drapatz, S., Ward, M.J. & Forbes, D.A. 1993, ApJ, **405**, 522

[474] van Loon, J.T. *et al.* 1998, A&A, **329**, 169

[475] Vanzi, L. & Rieke, G.H. 1997, ApJ, **479**, 694

[476] Vanzi, L., Rieke, G.H., Martin, C.L. & Shields, J.C. 1996, ApJ, **466**, 150

[477] Vassiliadis, E. & Wood, P.R. 1993, ApJ, **413**, 641

[478] Vigroux, L. 1997, in *Extragalactic Astronomy in the Infrared*, Moriond Astrophysics Meetings Series, eds. G.A. Mamon, T.X. Thuân and J.T.T. Vân (Paris: Editions Frontières), p. 63

[479] Walker, C.E., Lebofsky, M.J. & Rieke, G.H. 1988, ApJ, **325**, 687

[480] Wallace, L. & Hinkle, K. 1996, ApJS, **107**, 312

[481] Waller, W.H., Gurwell, M. & Tamura, M. 1992, AJ, **104**, 63

[482] Wallerstein, G. 1973, ARA&A, **11**, 115

[483] Wallerstein, G. 1988, Science, **240**, 1743

[484] Wamsteker, W. 1981, A&A, **97**, 329

[485] Watson, M.G., Stanger, V. & Griffiths, R.E. 1984, ApJ, **286**, 144

[486] Weedman, D.W. 1983, ApJ, **266**, 479

[487] Weitzel, L., Krabbe, A., Kroker, H., Thatte, N., Tacconi-Garman, L.E., Cameron, M. & Genzel, R. 1996, A&AS, **119**, 531

[488] Weliachew, L., Fomalont, E.B. & Greisen, E.W. 1984, A&A, **137**, 335

[489] Whitcomb, S.E., Gatley, I., Hildebrand, R.H., Keene, J., Sellgren, K. & Werner, M.W. 1981, ApJ, **246**, 416

[490] Whitford, A.E. 1958, AJ, **63**, 201

[491] Whitmore, B.C. & Schweizer, F. 1995, AJ, **109**, 960

[492] Wild, W., Harris, A.I., Eckart, A., Genzel, R., Graf, U.U., Jackson, J.M., Russell, A.P.J. & Stutzki, J. 1992, A&A, **265**, 447

[493] Williams, T.B., Caldwell, N. & Schommer, R.A. 1984, ApJ, **281**, 579

[494] Willner, S.P., Soifer, B.T., Russell, R.W., Joyce, R.R. & Gillett, F.C. 1977, ApJ, **217**, L121

[495] Witt, A.N., Thronson, H.A. Jr. & Capuano J.M. Jr. 1992, ApJ, **393**, 611

[496] Wolfire, M.G., Tielens, A.G.G.M. & Hollenbach, D. 1990, ApJ, **358**, 116

[497] Woosley, S.E. & Weaver, T.A. 1986, ARA&A, **24**, 205

[498] Worthey, G. 1994, ApJS, **95**, 107

[499] Wright, G.S., Joseph, R.D., Robertson, N.A., James, P.A. & Meikle, W.P.S. 1988, MNRAS, **233**, 1

[500] Yamashita, Y. 1972, Ann. Tokyo Astr. Obs., **13**, 169

[501] Yamashita, Y. 1975, Ann. Tokyo Astr. Obs., **15**, 47

[502] Yorke, H.W. 1986, ARA&A, **24**, 49

[503] Young, J.S., Kleinmann, S.G. & Allen, L.E. 1988, ApJ, **334**, L63

[504] Young, J.S. & Scoville, N.Z. 1984, ApJ, **287**, 153

[505] Young, J.S. & Scoville, N.Z. 1991, ARA&A, **29**, 581

[506] Yun, M.S., Ho, P.T.P. & Lo, K.Y. 1993, ApJ, **411**, L17

[507] Yun, M.S., Ho, P.T.P. & Lo, K.Y. 1994, Nature, **372**, 530

[508] Zhou, K., Hao, Y., Chen, P., Zhang, Y. & Gao, M. 1984, Ap&SS, **107**, 373

Acknowledgements

I first wish to thank my advisor Reinhard Genzel for his continuous interest, support and encouragement for this thesis work. I appreciate the freedom he has allowed me to pursue my own scientific interests, and his precious guidance through critical phases. His enthusiasm and the discussions we had have been a source of constant inspiration, and will certainly remain so for my future career. I also wish to thank my co-advisor Linda Tacconi. In addition to her scientific guidance, I am particularly grateful for her presence and for always offering a compassionate ear during the most difficult periods but also every day since my first day at MPE.

I also wish to thank all my colleagues from the 3D and SWS groups at MPE for their scientific, technical and moral support at all times: Lowell Tacconi-Garman, Jack Gallimore, Michele Thornley, Henrik Spoon, Torsten Böker, Niranjan Thatte, Roberto Maiolino, Alfred Krabbe, Dieter Lutz, Dietmar Kunze, Eckart Sturm. I also wish to thank especially Michele and Henrik for their friendship, their cheerful spirits and great teamwork, as well as Linda and Lowell for their availability to help me in many ways, at any time. Special thanks go to Dieter, who considerably improved my german translation of the abstract. Many thanks to the 3D team for help with the observations. My gratitude also goes to Amiel Sternberg, Tino Oliva, Gary Ferland, Bernhard Brandl, Marcia and George Rieke, and Fred Lo for stimulating discussions, for useful and critical comments which helped improve this thesis work, and for communicating some of their research results prior to publication. I am grateful to Amiel Sternberg for modifying part of his evolutionary synthesis code for the purpose of this thesis project. I am also grateful to Charles Telesco and Dan Gezari for providing me with a digital version of their 12.4 μm data on M 82.

Finally, I wish to express my deep gratitude to my closest friends and to my family for always being there no matter how infrequently we saw each other, especially Gerd, Nancy and Manfred, Christine, and Fanny. My family has been the most precious support of all, and I wish to thank them in French. Je tiens à remercier tout particulièrement mon mari Michel, pour son amour et pour avoir partagé les hauts et les bas de ces années. Son soutien et ses encouragements de même que son intérêt pour mon travail ont été des plus précieux à chaque instant. Enfin, je ne saurais exprimer suffisamment ma reconnaisance envers toute ma famille qui m'a encouragée depuis le tout début du long cheminement qui m'a menée au doctorat. Malgré l'océan qui nous sépare, je les sens toujours proches de moi et les en remercie infiniment.

Curriculum vitae

Name:	Natascha M. Schreiber
Date of birth:	8 May 1970
Place of birth:	Montréal, Canada
Civil status:	Married
Nationality:	Canadian-German

Sept. 1976 – June 1982:	Primary school Montréal, Canada
Sept. 1982 – June 1987:	High-school St-Jacques de Montcalm, Canada Diplôme d'Etudes Secondaires granted Sept. 1987
Sept. 1987 – May 1989:	CÉGEP Montréal, Canada Diplôme d'Etudes Collégiales en Sciences granted Nov. 1989
Sept. 1989 – May 1992:	Bachelor of Science in Mathematics-Physics Université de Montréal, Canada B.Sc. bi-disciplinaire Mathématiques-Physique granted June 1992
July 1992 – Nov. 1994:	Master of Science in Physics, specialty Astronomy Thesis: "Etude photométrique et spectroscopique de la galaxie à sursaut de formation d'étoiles M 82 par imagerie infrarouge" Université de Montréal, Canada M.Sc. in Physics granted March 1995
Since Nov. 1994:	Doctorate in Astrophysics Thesis: "Near-infrared imaging spectroscopy and mid-infrared spectroscopy of M 82: revealing the nature of star formation activity in the archetypal starburst galaxy" Ludwig-Maximilians-Universität München and Max-Planck-Institut für Extraterrestrische Physik Garching, Germany